STRUCTURAL AND ELECTRONIC FACTORS THAT INFLUENCE NI VERSUS THIOLATE REDOX FROM SYNTHETIC MODELS OF NISOD

by

RAMSEY ALISON STEINER

(Under the Direction of Todd C. Harrop)

ABSTRACT

Superoxide ($O_2^{\cdot -}$) is a cytotoxic byproduct of aerobic metabolism. As a result, all aerobic organisms possess the metalloenzymes superoxide dismutases (SODs) to catalyze the disproportionation of $O_2^{\cdot -}$ into hydrogen peroxide (H_2O_2) and oxygen (O_2) via alternate oxidation and reduction of their respective metal centers. In 1996, the most recent class of SOD was isolated from *Streptomyces* soil bacteria containing Ni (NiSOD) in an unusual, mixed N/S coordination sphere. The principal question remaining is how this unique coordination sphere promotes both Ni-based redox activity and S-oxidative-stability.

We have successfully developed, synthesized, and characterized Ni complexes with mixed carboxamide/amine and thiolate ligands as low molecular weight synthetic analogues of NiSOD. We designed trimetallic systems to interact via unique inter/intra-molecular H-bonding networks, resulting in properties distinct from their monometallic counterparts. These complexes have shed light onto the role of hydrogen bonding (H-bonding) networks and steric bulk in modulating S-electron density in the frontier molecular orbitals (FMO) and preventing access of

ROS to the Ni/S cluster. We propose that NiSOD employs both steric and electronic protection to avoid thiolate reactivity with ROS.

Reactivity of low molecular weight complexes has also demonstrated reactivity with proton (H^+) or methyl (CH_3^+) donors with NiN_2S_2 complexes containing mixed carboxamide/amine ligands. Our results indicate that S-nucleophilicity of this mixed N-donor set is quite different from the S-nucleophilicity of well-established diamine NiN_2S_2 complexes. We anticipated very little change in donor strength of thioether ligands, as modification of the S-thiolate weakens the σ-donor, but also reduced the Ni(dπ)-S(pπ) repulsive interactions, resulting in little change in bond distance between Ni and S. Coordination of the thioether-containing ligand (N_2S_2-CH_3) to Ni, however, indicated that thioether coordination is not favored and isolation of the Ni-coordinated thiol or thioether is best achieved via modification of a $NiN_{2/3}S_2$ complex. Unlike reported diamine $NiN_{2/3}S_2$ complexes, where monomethylation is favored and dimethylation is unfavored, we observed exclusive dimethylation. Indeed no reaction was observed with stoichiometric H^+/CH_3^+ or at low temperature. The mixed carboxamide/amine N-donor may have unique electronic properties about the Ni center that poise the Cys sulfurs for transient protonation in NiSOD.

INDEX WORDS: Metalloenzyme, superoxide dismutase, nickel, sulfur

STRUCTURAL AND ELECTRONIC FACTORS THAT INFLUENCE NI VERSUS THIOLATE REDOX FROM SYNTHETIC MODELS OF NISOD

by

RAMSEY ALISON STEINER

B.S., Union College, 2012

A Dissertation Submitted to the Graduate Faculty of The University of Georgia in Partial Fulfillment of the Requirements for the Degree

DOCTOR OF PHILOSOPHY

ATHENS, GEORGIA

2018

STRUCTURAL AND ELECTRONIC FACTORS THAT INFLUENCE NI VERSUS THIOLATE REDOX FROM SYNTHETIC MODELS OF NISOD

by

RAMSEY ALISON STEINER

Major Professor:	Todd C. Harrop
Committee:	Michael K. Johnson
	Jeffrey L. Urbauer

Electronic Version Approved:

Suzanne Barbour
Dean of the Graduate School
The University of Georgia
May 2018

ACKNOWLEDGEMENTS

I would like to thank my Ph.D. advisor Dr. Todd Harrop for the opportunity to join his research lab and investing in my scientific and professional development. I am a better scientist, critical thinker, and communicator because of your mentorship. To Dr. Laurie Tyler, thank you for introducing me to bioinorganic chemistry and encouraging me to pursue a graduate degree in chemistry. Thank you to the other members of my advisory committee, Dr. Johnson and Dr. Urbauer, for their thoughtful feedback and support throughout my studies at UGA. Thank you for your letters of recommendation and continued support. Thank you to the Johnson lab for assistance with EPR and CD spectroscopy and the Urbauer lab for NMR assistance. Thank you to Dr. Wei for assistance with X-ray diffraction. Thank you to Dr. Phillips for aid in MS experiments and providing comic relief during data collection. Thank you to Dr. Cui for pairing her NMR expertise with kindness and optimism.

Thank you to current and past members of the Harrop group: Brian Sanders, Melody Rhine Walter, Ellen Broering, and Phan Truong. I am grateful to have been welcomed into the camaraderie, support and laughter of this group. Ellen, thank you for your friendship and constant support throughout the ups and downs of graduate school.

Thank you, Mom, for your encouragement, tough love, and always believing in me. Your determination inspires me. To Dad, thank you for your support and continuous confidence in my abilities. To my siblings, PJ, Margaret and Madeline, thank you for your love and reassurance. To Will, thank you for always being my cheerleader and supporting me. To my running friends, thank you for your love, support and meaningful conversations over many miles in Athens.

TABLE OF CONTENTS

CHAPTER

CHAPTER 1

INTRODUCTION

1.1 Nickel in Biology

The occurrence of nickel (Ni) on Earth is relatively low with average abundances of 75 ppm in the Earth's crust, 8×10^{-3} μM in sea water, 0.04 μM in mammalian blood plasma, and 2 μM in mammalian cells or tissue.[1] In comparison, the abundances of iron (Fe) are 5×10^{4} ppm in the Earth's crust, 1×10^{-3} μM in sea water, 22 μM in blood plasma and 0.001-10 μM in mammalian cells or tissue.[1] While Ni exists in multiple oxidation states in biology (Ni(I), Ni(II), and Ni(III)), redox chemistry during transport is unlikely, as the divalent Ni(II) cation is stable in aqueous media.[1] Ni is considered an essential element for life, but Ni is not required in mammalian physiology.[1] However, Ni is a vital element for prokaryotic microorganisms in the domains of bacteria and archaea.[2] Ni(II) homeostasis must also be tightly regulated because Ni(II) can be toxic.[3] Ni-binding proteins encompass multiple protein classes that include: (i) Transport proteins, which are responsible for recognizing, binding, and transporting Ni(II) into cells, binding and sequestering Ni(II) inside the cell, and inserting Ni(II) into Ni enzymes; (ii) Ni enzymes, with non-redox active and redox-active Ni cofactors (vide infra); and (iii) Ni-dependent regulation proteins, which manage the expression of genes responsible for Ni(II) uptake, sequestration, utilization, efflux and detoxification.[4,5]

1.1.1 Nickel Trafficking

Transport proteins are required for both Ni import into and export out of the cytoplasmic membrane.[5] The primary Ni(II) uptake transport systems are the NikABCDE import pumps and the Ni/Co permeases (NiCoT).[5] In the NikABCDE import system, NikA is a soluble periplasmic binding protein that captures Ni(II) and delivers the metal ion to the membrane components, NikB and NikC, which are channel-forming transmembrane proteins, and then to NikD and NikE, which are cytoplasmic nucleotide binding proteins.[6] NikA plays the crucial role of Ni(II)-receptor for transport into the cell and has a 30 μM binding affinity for $[Ni(EDTA)]^{2-}$ (EDTA = ethylenediaminetetraacetate).[7] X-ray absorption spectroscopy (XAS) studies suggest that NikA binds Ni(II) via six oxygen (O) donors and one methionine (Met) ligand.[8] The secondary transporters of the NiCoT family contain Ni(II)-specific transporters HoxN from *Cupriavidus necator* H16 and NixA of *Helicobacter pylori* with K_M values for Ni(II) ~10-20 nM.[9-15] The NiCoT system likely binds metal ions via the highly conserved His-Xaa_4-Asp-His motif.[11,16,17]

In order to remove superfluous Ni(II) , there are a few Ni(II)-specific efflux transporters (along with several non-specific M(II) efflux mechanisms).[18,19] One example is NreB from *Achromobacter xylosoxidans* 31A, which contains a C-terminus with several His residues and is induced by Ni(II) resulting in reduced Ni(II) accumulation in *E. coli.*[20] Another example of Ni-specific transport is found in the Ni(II)-hyperaccumulating plant, *Thlaspi goesingense*, which stores Ni(II) in leaf vacuoles, utilizing a cation diffusion facilitator TgMTP, which provides resistance to metal-sensitive yeast, allowing Ni(II) to accumulate.[21-23] CznABC found in *H. pylori* and *E.coli* is a Ni(II) export system that pumps Ni(II) across both inner and outer membranes.[18,24] Lastly, RcnA from *E. coli* is also a Ni(II) transmembrane transport protein.[5,25]

Ni(II)-responsive metalloregulators bind Ni(II) ions in order to activate, depress, or repress the transcription of their target genes.[5] Some of these metalloregulators have been

identified as NikR, RcnR, NmtR, KmtR, SrnRQ, and Nur.[5] NikR is a tetrameric protein with two DNA binding sites on opposite sides of the protein. Holo-NikR binds DNA with nM affinity, and binding of this transcriptional regulator results in activation or repression of the Ni(II) uptake *nik*ABCDE genes.[5,26] The four metal-binding sites are all located in the center of the protein, and each site contains two His and one Cys from one subunit and one His from a neighboring subunit to form a square-planar N_3S geometry with a binding affinity of ~10^{-12} M.[27-29] RcnR is a Ni(II)- or Co(II)-responsive regulator that acts as a derepressor (removal of repression) for the efflux transporter RcnA via the *rcn*A gene and Ni(II) binding results in derepression. [5,30] XAS studies indicate that the binding site involves Cys35, His3, His64, the NH_2-terminus, and a sixth His60 ligand for Co(II) and an unresolved sixth ligand for Ni(II).[31] NmtR is a Ni(II)- and Co(II)-responsive transcription factor regulating Ni(II) efflux in *M. tuberculosis*, which requires Ni(II) for urease activity (vide infra).[32,33] NmtR acts as a derepressor for the *nmt*A gene; X-ray absorption spectroscopy (XAS) and site-directed mutagenesis revealed that Ni(II) coordinates in an octahedral geometry with Asp91, His93, His104, His107, His109 and His116.[34] These trafficking proteins play an important role in Ni homeostasis and incorporation of Ni as a cofactor into several Ni-dependent enzymes.

1.1.1 Ni-containing Enzymes

Of the nine known Ni-containing enzymes, five participate in redox reactions or catalyze redox transformations of substrate: nickel superoxide dismutase (NiSOD), carbon monoxide dehydrogenase (CODH), bifunctional acetyl coenzyme A synthase/CODH (ACS/CODH), nickel iron hydrogenase ([NiFe]-H_2ase), and methyl coenzyme M reductase (MCR).[35-41] The remaining four Ni-containing enzymes utilize Ni centers as Lewis acid catalysts and are redox inactive,

namely, urease, glyoxalase I (Glx I), Ni-required acireductone dioxygenase (ARD), and lactate racemase (LarA).[42-47] The activity, structures, and properties of the Ni cofactors in these enzymes are discussed below.

1.1.2 Non-redox active nickel enzymes

The non-redox enzymes urease, Glx I, and ARD utilize Ni(II) as a Lewis acid in catalysis. The function of Ni in LarA is still being explored. Aquated Ni(II) has no biologically relevant redox chemistry, as the Ni(III/II) potential of $[Ni(H_2O)_6]^{2+}$ is > 2 V.[48] Often, electrochemical access to the Ni(III/II) states in biology requires coordination to sulfide, Cys, or other strong-field ligands in order to depress the potential in the biological window (E = –0.18 – 0.91 V vs NHE).[49] Non-redox Ni enzymes are characterized by N- and O-donor active site ligands that often form distorted octahedral coordination geometries that are invariably paramagnetic (S = 1). An exception is LarA (vide infra), which is novel in that the active site Ni is square-planar and contains S-donors, yet is not known to be redox-active, to date (2017).

1.1.2.1 Glyoxalase I (Glx I)

Glx I is an enzyme involved in the detoxification of methylglyoxal, an unwanted byproduct from the reaction between glyceraldehyde-3-phosphate and dyhydroxyacetone phosphate, two intermediates of the glycolysis pathway (Scheme 1.1).[50]

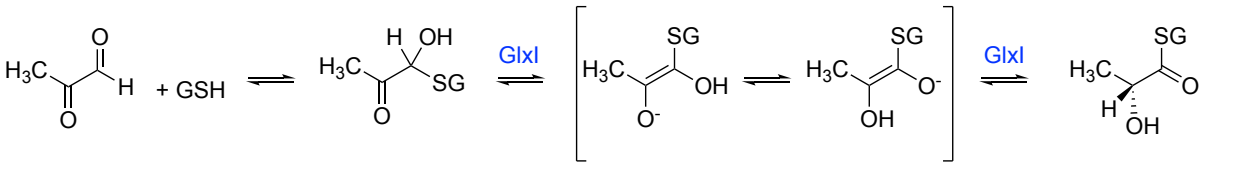

Scheme 1.1. Reaction catalyzed by GlxI, conversion of the hemithioacetal of GSH-bound methylglyoxal to produce S-D-lactoylglutathione

In this detox process, first methylgloxal reacts spontaneously with glutathione (GSH) to form a hemithioacetal.[51] Glx I then converts the hemithioacetal to (S)-D-lactoyl-glutathione through a proposed enediolate intermediate.[51]

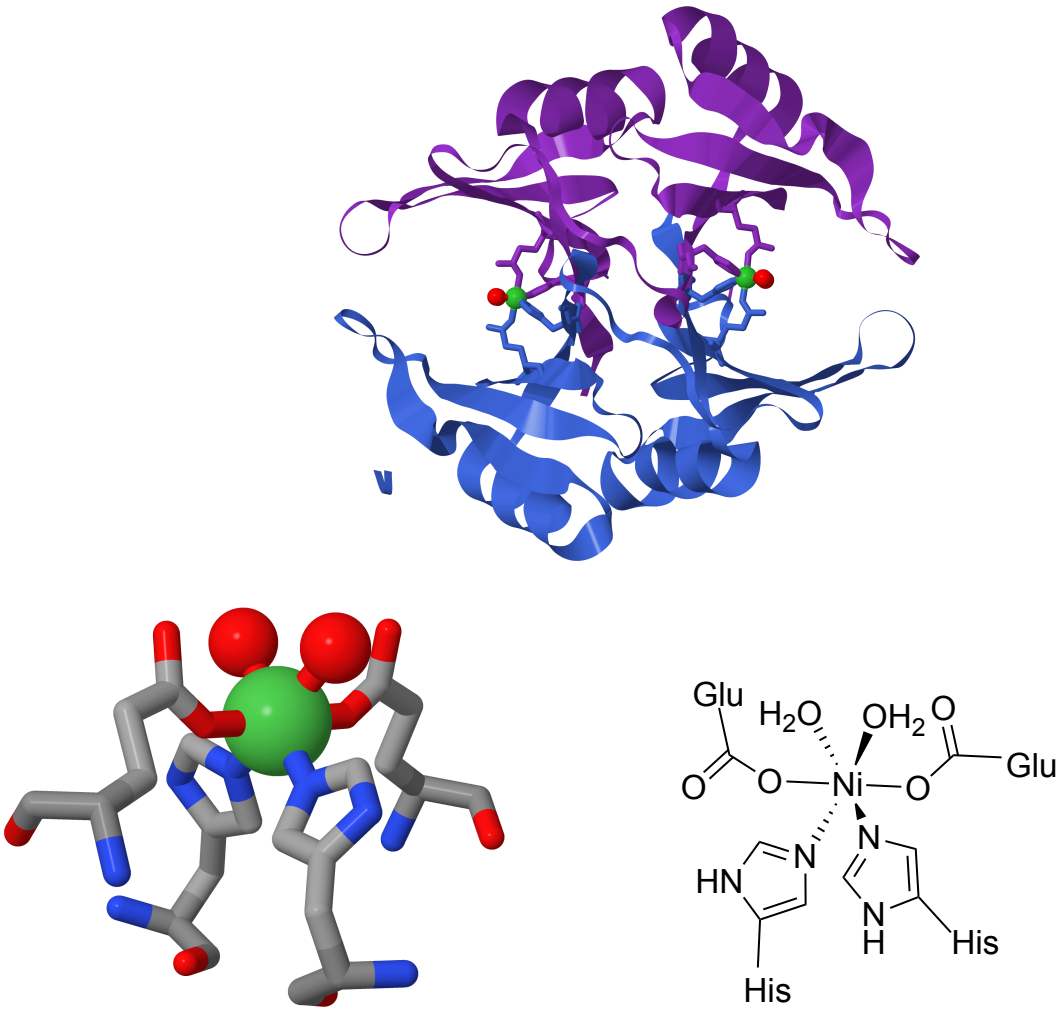

Figure 1.1. X-ray crystal structure of homodimeric Glx I from *M. musculus* (top, 2.5 Å resolution, PDB 1F9Z, Jmol). Ni active site (bottom left). ChemDraw depiction of the Ni active site (bottom right). Ni ions are modeled as green spheres. Ni-bound H_2O is modeled as red spheres.

Finally, glyoxalase II (Glx II) hydrolyses (S)-D-lactoyl-glutathione to lactate and GSH.[51] There are two classes of Glx I; one that is activated by coordination to Zn(II) (Class I) and one that is activated by coordination to Ni(II) (Class II) (Figure 1.1).[52]

In general, most eukaryotic enzymes contain Class I Zn(II)-Glx I, whereas most bacterial enzymes contain Class II Ni(II)-Glx I.[53] Metal preference is not linked to catalytic rates, as the catalytic efficiency (k_{cat}/K_m) is equivalent for both classes (~10^6–10^7 M^{-1} s^{-1}).[54] The Class I Zn(II)-Glx I is a larger protein with ~180 amino acids, as opposed to Class II Ni(II)-Glx I, which contains ~130 amino acids.[52] Both enzymes are homodimers from the βαββββ protein structure superfamily. The Ni(II) form of Glx I is found in *E. coli* and coordinates two cis-His (His5, His75), two monodentate trans-Glu (Glu56, Glu122), and two cis-H_2O ligands to form an octahedral, high-spin Ni(II) active site (Figure 1.1). Both classes are homodimers where two monomeric units coordinate one Glu and one His and bind M(II) at the dimer interface.[55] In *E. coli*, Zn(II) coordination in the Ni(II) active site renders it inactive, and Zn(II) coordinates in a trigonal bipyramidal geometry with loss of one H_2O ligand.[43] There are two proposed mechanisms for Glx I: an inner-sphere and outer-sphere mechanism. In the inner-sphere proposal, the substrate displaces one or both H_2O ligands and Glu when binding to Ni(II), and the displaced Glu abstracts H^+ from the hemithioacetal and subsequently donates H^+ to yield (S)-D-lactoyl-glutathione.[56,57] In the outer-sphere proposal, substrate does not bind to Ni(II), and the bound H_2O ligands act as agents for proton transfer (PT).[57]

1.1.2.2 Acireductone dioxygenase (ARD)

ARD catalyzes the penultimate reaction of the methionine salvage pathway (Scheme

1.2).[58] The ARD found in the bacterium *Klebsiella oxytoca* is unique in that it is the only known ARD that has two different reaction pathways dependent on which metal ion is coordinated (Ni(II) or Fe(II)) and represents the only example of a Ni-containing dioxygenase.[58] The Fe(II) enzyme pathway catalyzes oxidation of 1,2-dihydroxy-3-keto-5-methylthiopentene to formate and 2-keto-4-methylthiobutanoate, which can then be transcarboxaminated to form Met.[51] However, the Ni(II)-containing enzyme catalyzes an off-pathway reaction, and the role of this reaction in bacteria is not clear; this enzyme reacts with 1,2-dihydroxy-3-keto-5-methylthiopentene to form formic acid, carbon monoxide (CO), and 3-methylthiopropionate.[52] One proposal is that CO generation may play a yet undiscovered role as a signaling molecule to regulate the Met salvage pathway.[59] The role of the metal ion in ARD is likely not to activate O_2, but to position the substrate to carry out differing chemistries with O_2.[46] Both the Fe(II)-ARD and Ni(II)-ARD are isolated as almost identical 20.2 kDa proteins belonging to the cupin superfamily, meaning they have a conserved β-barrel fold (Figure 1.2).[58] Both metals coordinate to three His, one monodentate carboxylate ligand from Glu, and two cis-H_2O molecules to form a six coordinate (6C) Ni(II) ion (Figure 1.2).[51] The H_2O molecules are displaced by coordination of the bidentate acireductone substrate.[52] While coordination of Fe(II) is structurally identical to the apo-enzyme, Ni(II) coordination results in small structural changes of the quaternary structure containing a conserved "jelly roll" motif.[51] Indeed, small tertiary structure changes may change the reactivity of these two pathways, as Fe(II)-ARD has an open, solvent exposed active site, and Ni(II)-ARD has a closed site due to a Trp loop.[60] The k_{cat} values of the enzymes in *K. oxytoca* (k_{cat}(Ni(II)-ARD) = 5.0×10^{-2} s^{-1} and k_{cat}(Fe(II)-ARD) = 2.6×10^{-2} s^{-1}) and other kinetic measurements indicate that both acireductone and O_2 need to bind to the active site in order for product release to take place. This activity is likely not a metal-specific reaction mechanism, as

other metal ions such as Mn(II), Co(II), and Mg(II) can bind to the active site and still maintain catalytic activity. [52,58,61] It has been proposed that the two different reactivities of the Fe(II)-ARD and Ni(II)-ARD may be based on either, (i) differing reactivity with H_2O, or (ii) varied electronic structures, where Fe(II) may provide additional stabilization via charge transfer (CT) that is not relevant for a Ni(II) ion, because Fe(II) can donate electrons, but Ni(II) cannot.[52,62-64]

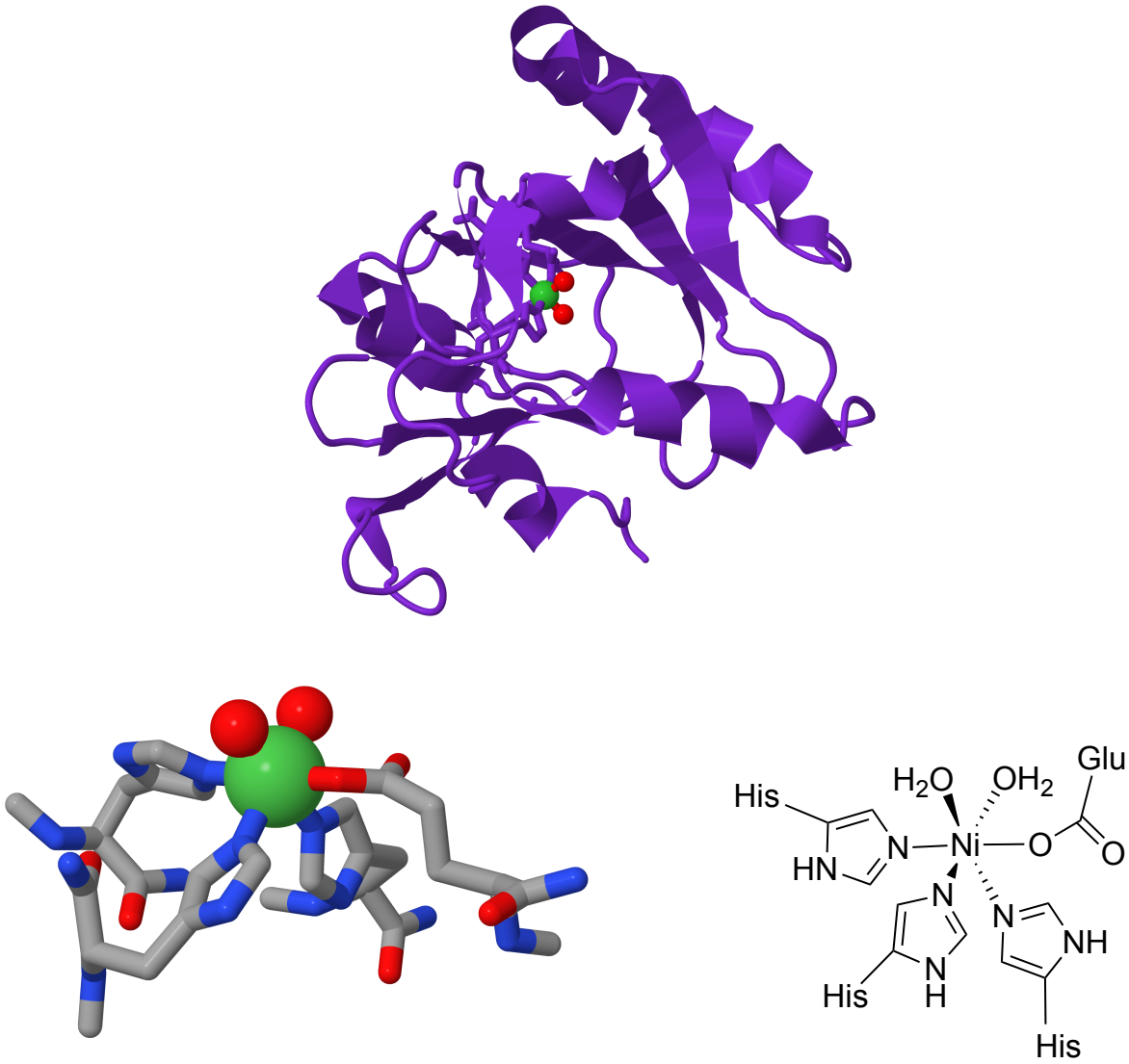

Figure 1.2. X-ray crystal structure of ARD from *K. oxytoca* (top, solution structure, PDB, 1ZRR). Ni active site (bottom left). ChemDraw depiction of the Ni active site (bottom right). Ni

is modeled as green spheres. Ni-bound H_2O molecules are modeled as red spheres.

One proposed mechanism suggests that since neither M(II) is redox-active, O_2 attacks the coordinated acireductone substrate, and the M(II) acts as a Lewis acid by activating acireductone to react with O_2.[51,52,58] One electron radical transfer from bound acireductone would form a transient $O_2^{\bullet-}$, which adds to C–1 to form a C–1 peroxide intermediate.[51,52,58] Ni(II)-ARD and Fe(II)-ARD may form different cyclic peroxide adducts, where the C–1 peroxide would attack C–2 to yield a four-membered cyclic peroxide for Fe(II)-ARD, while the C–1 peroxide would attack C–3 to form a five-membered cyclic peroxide for Ni(II)-ARD.[51,52,58] Metal-based rearrangements would therefore result in different products.[51,52,58]

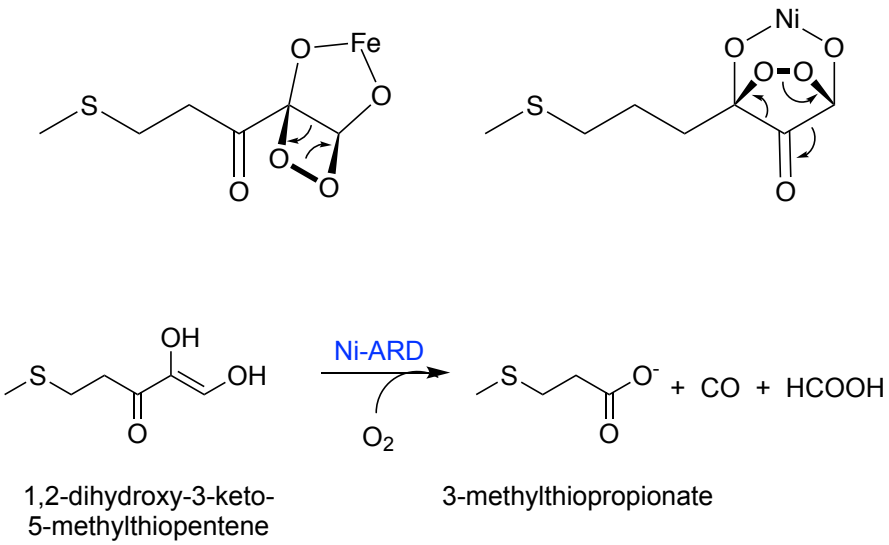

Scheme 1.2. (Top left) Four-membered cyclic peroxide for Fe(II)-ARD. (Top Right) Five-membered cyclic peroxide for Ni(II)-ARD. (Bottom). Reaction catalyzed by Ni(II)- ARD, O_2 insertion resulting in formation CO, formic acid, and 3- methylpropionate.

1.1.2.3 Urease

Urease catalyzes the hydrolysis of urea ($O=C(NH_2)_2$) into ammonia (NH_3) and carbamate ($H_2NCO_2^-$), where $H_2NCO_2^-$ then reacts spontaneously with H_2O to form another molecule of NH_3 and bicarbonate (HCO_3^-) (Scheme 1.3).[51,52]

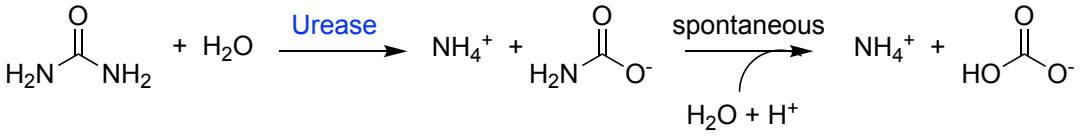

Scheme 1.3. Reaction catalyzed by Ni-urease, the hydrolysis of urea.

Urease proteins have a variety of quaternary structures that can vary from (i) a trimer of trimers $(\alpha\beta\gamma)_3$, where the active site is found in the α subunit, (ii) a trimer of dimers $(\alpha\beta)_3$, (iii) a tetramer of dimers $(\alpha\beta)_4$, where β is a fusion peptide of β and γ, or (iv) a dimer of homotrimers $(\alpha_3)_2$ where α is a fusion peptide of α, β, and γ (Figure 1.3).[52] Despite these variations, the secondary and tertiary structures of urease are conserved: the α subunit contains both a TIM barrel and β-sheet domains, the β subunit is mostly β-sheet domains, and the γ subunit contains both α-helices and β-sheet domains.[52] The active site consists of a bimetallic Ni cluster, where the two Ni(II) ions are bridged by a carbamylated Lys and a OH^-.[42] Each Ni(II) coordinates a terminal H_2O and two His residues, and one Ni(II) (Ni2) coordinates the carboxylate-O of an Asp residue (Figure 1.3).[42]

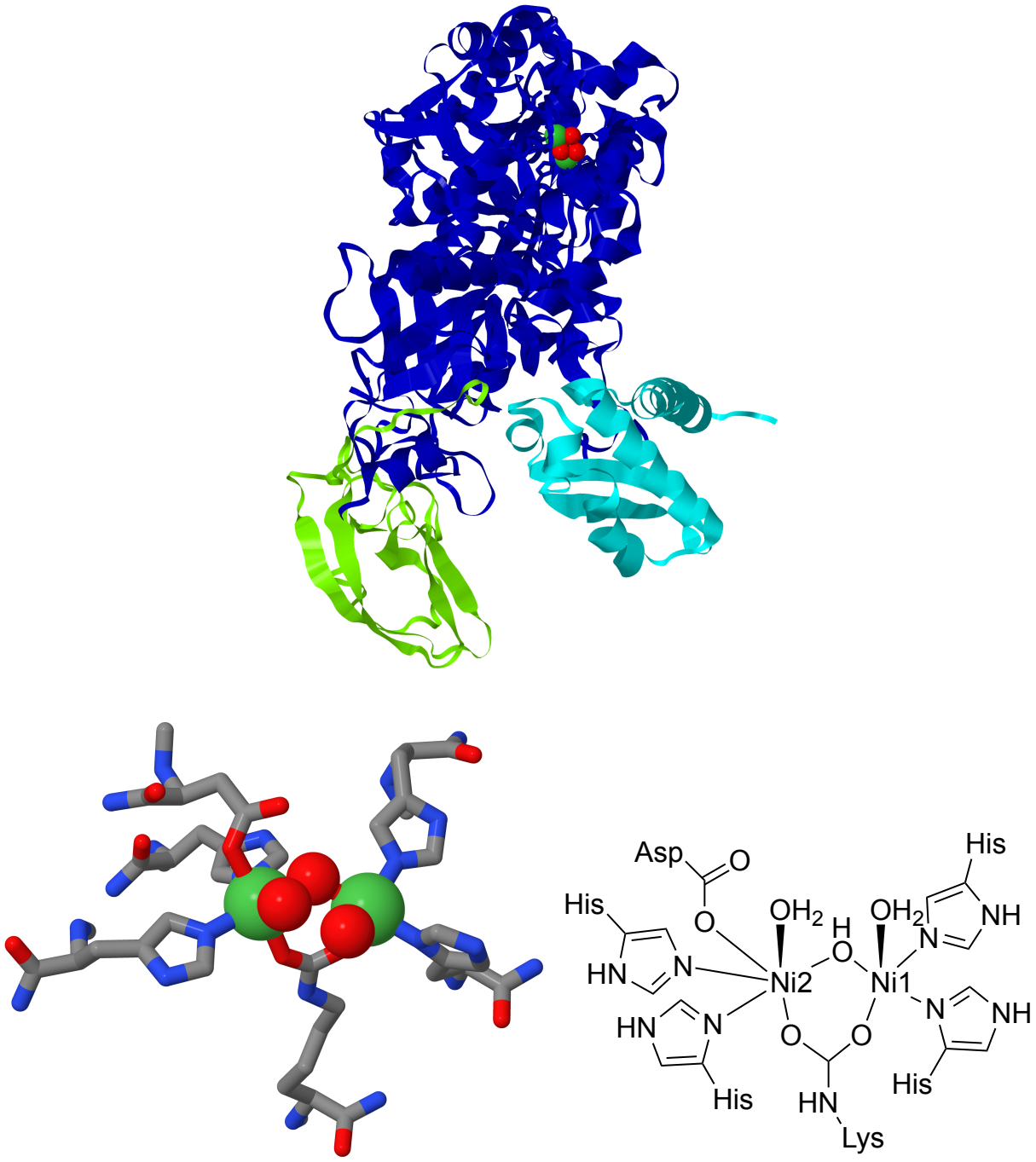

Figure 1.3. X-ray crystal structure of urease (2.2 Å resolution, PDB 1FWJ, Jmol). One monomer of the trimeric *K. aerogenes* urease (top). Dinuclear Ni active site (bottom left). ChemDraw depiction of the Ni active site (bottom right). Ni ions are modeled as green spheres. Ni-bound H_2O molecules are modeled as red spheres.

The k_{cat} and k_{cat}/K_m of urease are strongly dependent on pH.[65] In urease, the bimetallic center acts as a Lewis acid that binds and activates the substrate, while the active site cavity stabilizes the transient tetrahedral intermediate.[51,52] The mechanism begins with replacement of the three H_2O ligands with urea, in which urea initially binds to Ni1 via its carbonyl oxygen and is stabilized with an H-bond involving His222.[52] Closure of the active site channel allows for coordination of the $–NH_2$ group of urea to Ni2.[52] The $–NH_2$ also H-bonds with Ala366, which helps enhance the basicity of the poor Lewis base to facilitate Ni(II) coordination.[52]

The evolutionary choice of Ni(II) in this enzyme is likely due to the binding preferences of Ni for nitrogenous bases.[52] This binding preference has been utilized for protein purification, in which the Hisε tag is used: a string of His residues are added to the N or C terminus of a protein (usually six His residues), which then chelate a Ni(II) ion via metal affinity chromatography. The bidentate coordination of urea to Ni decreases the electron density at the carbonyl carbon and poises it for attack by the bridging OH^-.[52] Attack of the bridging OH^- transforms the sp^2 carbon to a transient sp^3, an intermediate that is stabilized by the active site cavity.[52] This tetrahedral intermediate increases the pK_a of the unbound $–NH_2$ group and decreases the pK_a of the –OH group, facilitating PT via Asp363.[52] His323 stabilizes the positive charge on the $–NH_3^+$ moiety, which promotes breaking of the C–N bond to form $H_2NCO_2^-$ and NH_4. The $H_2NCO_2^-$ intermediate then reacts spontaneously with H_2O and H^+ to yield another equivalent of NH_3 and HCO_3^-.[51,52]

1.1.2.4 Lactate racemase (LarA)

The most recently discovered Ni-dependent enzyme is LarA, which catalyzes the racemization between L- and D-lactic acid, which are vital in the cell wall assembly of many

organisms.[47] The UV-vis spectrum obtained for the holo-protein, yet not observed in the apo-protein, revealed electronic transitions at 375, 440, and 550 nm.[66] LarA contains 16 α-helices and 18 β-strands with a novel fold between two domains (Figure 1.4).[47]

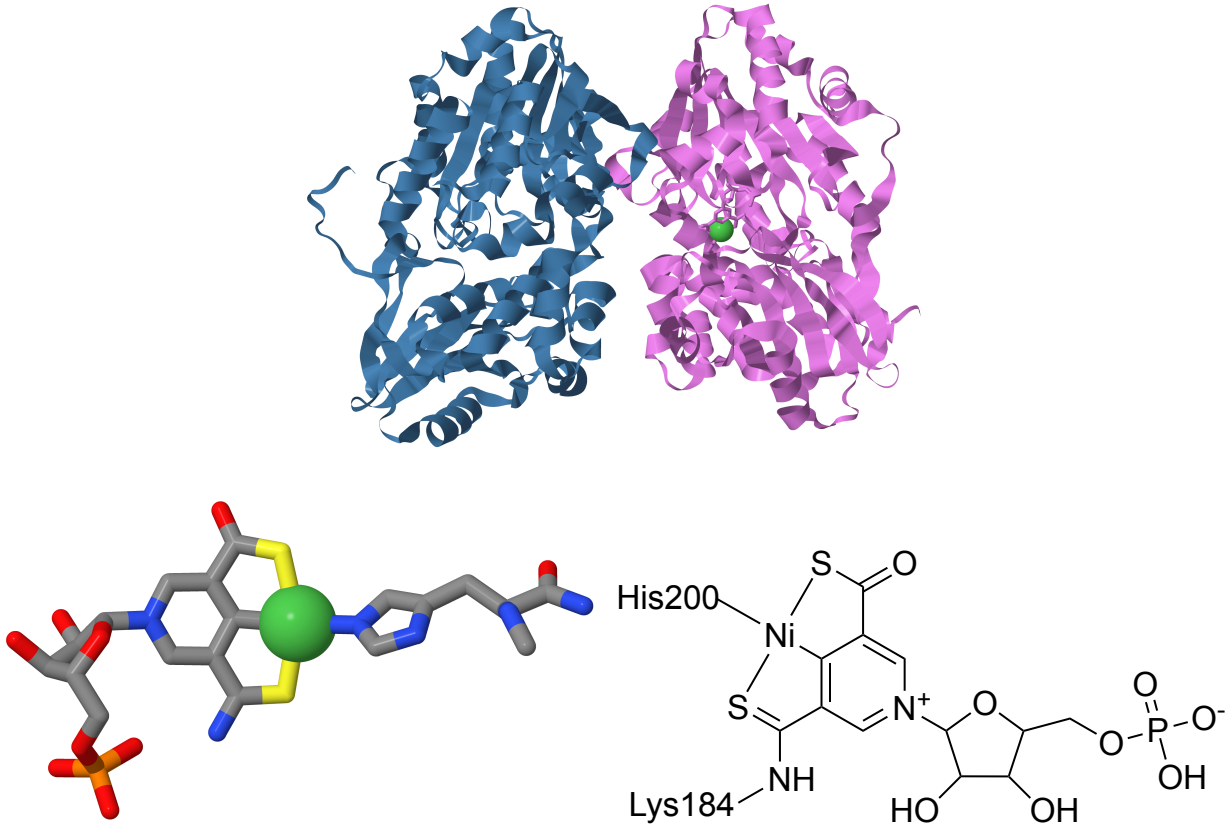

Figure 1.4. X-ray crystal structure of LarA from *L. plantarum* (top, 3.0 Å resolution, PDB 5HUQ, Jmol). Ni active site (bottom left). Ni is modeled as a green sphere. ChemDraw depiction of the Ni active site (bottom right).

Additionally, LC-ESI-MS indicated that the holo-protein contained an additional mass of 451 ± 1 Da (apo-protein was 47,393 Da).[66] It was determined that this mass is due to the vitamin niacin

(nicotinic acid or nicotinamide), which was shown to be essential in maintaining LarA activity. This result suggests that niacin is incorporated into the holo-protein (along with substitution of two deuterium atoms when deuterated niacin was used) and may be a precursor to the Ni-cofactor.[66] X-ray crystallography revealed an active site containing an organometallic Ni(II)-containing prosthetic group, pyridinium-3-thioamide-5-thiocarboxylic acid mononucleotide (a derivative of nicotinic acid mononucleotide) tethered to Lys184 via the C–3 of the pyridinium (Figure 1.4).[66]

The tridentate pincer ligand generates a Ni(II)-SCS complex and contains one Ni–C bond and two Ni–S bonds, where one Ni–S bond arises from thioamide coordination and the second comes from thiocarboxylic acid.[66] Additionally, the Ni(II) binds to His200 to form a square-planar CS_2N coordination-sphere.[66] It is proposed that Ni(II) may play a role in transient hydride (H^-) transfer similar to other metal-free H^- transfer enzymes such as nicotinamide adenine dinucleotide (NAD), although many questions remain about the catalytic mechanism of LarA.[51,66,67] In the structure, sulfate (SO_4^{2-}) binds in the proposed binding site near the Ni-cofactor and is a proposed binding site for lactate.[66] The C–2 of lactate orients itself above the C–4 of the pyridinium ring, which is also near two conserved residues, His108 and His174, which may act as bases for deprotonating/reprotonating an OH^- group of the substrate for racemization.[66] One proposed mechanism involves H^- transfer from lactic acid to the C–4 atom of the Ni(II)-pincer, resulting in transformation of an sp^2 C–Ni bond to an sp^3 C–Ni bond and formation of a reduced, dihydropyridine cofactor (Scheme 1.4).[68]

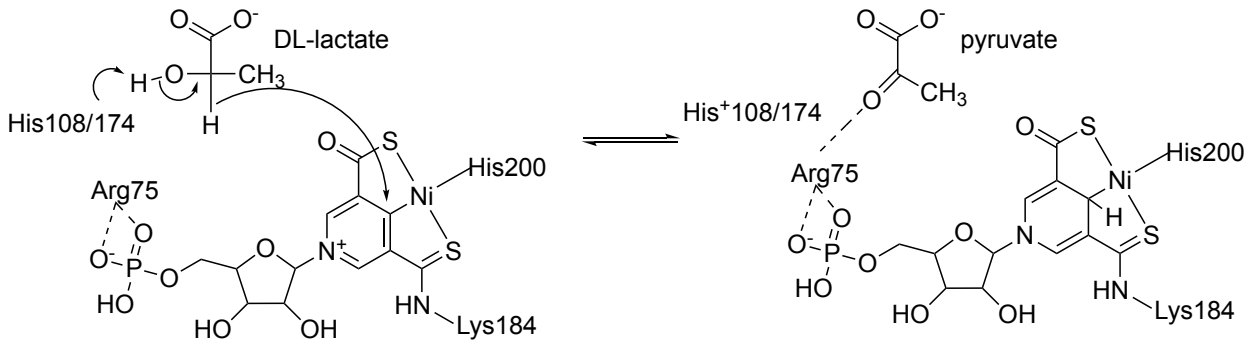

Scheme 1.4. Proposed mechanism for the racemization reaction of lactate by LarA.

At the same time, either His108 or His174 can deprotonate the OH^- group of lactate, to produce a pyruvate substrate intermediate poised for racemization following H^- transfer and reprotonation.[68] Another computationally-based mechanism suggests that racemization occurs through two proton coupled electron transfer (PCET) steps: proton transfer (PT) from lactate to His108 is coupled with electron transfer (ET) from lactate to Ni(III) and vice versa to complete racemization, potentially placing LarA in the redox-active Ni enzyme category.[69]

1.1.3 Redox active nickel enzymes

1.1.3.1 Carbon monoxide dehydrogenase (CODH)

CODH has been isolated in two forms: monofunctional, which catalyzes the reversible transformation of CO and CO_2 at the diffusion controlled rate (2×10^9 M^{-1} s^{-1}), and bifunctional ACS/CODH, where CODH reduces CO_2 to CO and transports CO via a 70 Å gas channel to the ACS active site.[70,71] The monofunctional CODH isolated from the CO-utilizing eubacterium *Carboxydothermus hydrogenoformans* was crystallized in two homodimeric forms, CODH I

(125 kDa, 62.5 kDa subunit) and CODH II (129 kDa, 64.5 kDa subunit), which are both homodimers (CODH II shown in Figure 1.5).[70] It is believed that CODH I generates energy by channeling electrons via ferrodoxins from CO to H_2ase to form H_2, while CODH II assimilates carbon by generating NADPH via reduction of $NADP^+$.[70] CODH is a homodimer with five metal clusters (B, C, D) per monomer (Figure 1.5).[39]

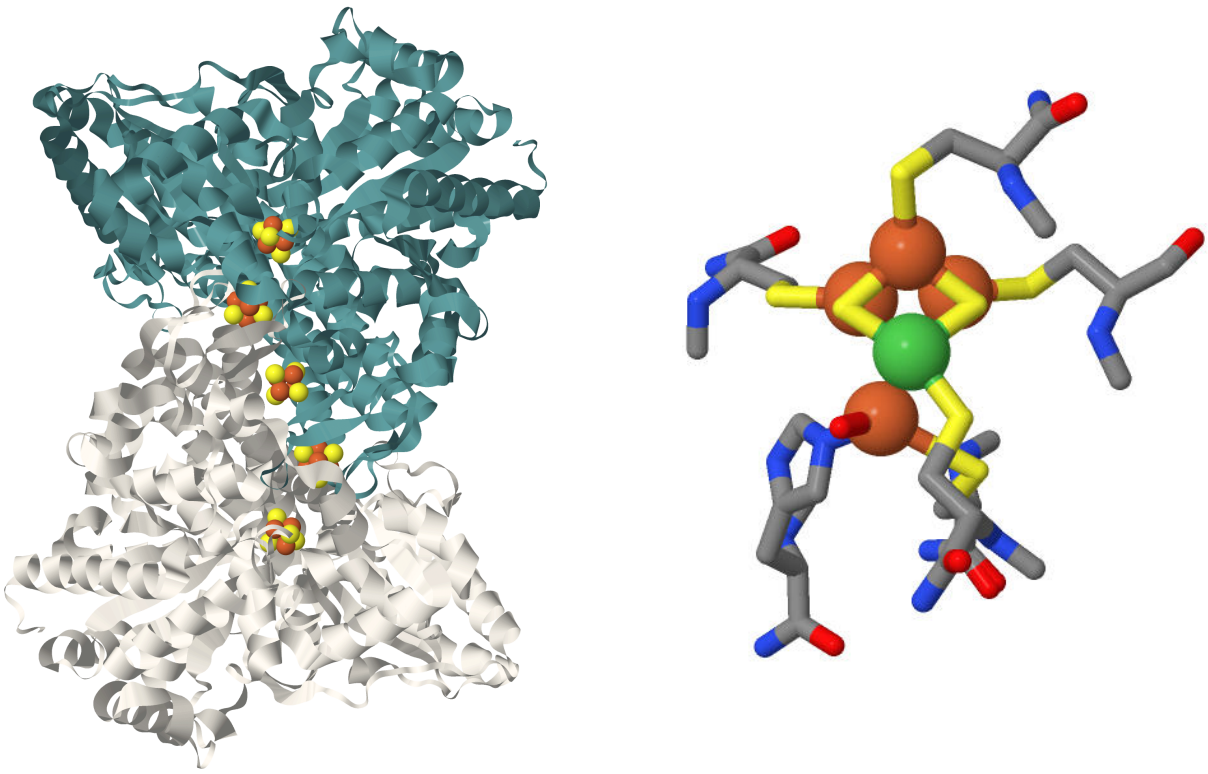

Figure 1.5. X-ray crystal structure of dimeric CODH from *C. hydrogenoformans* (left, 1.5 Å resolution, PDB 3B53, Jmol). Active site (right). Ni is modeled as a green sphere. Iron-sulfur clusters are modeled as orange (Fe) and yellow (S) spheres.

The C-cluster is responsible for the CO ⇄ CO_2 conversion and comprises a [3Fe–4S] cluster that is S-bridged to a cubane-like NiFe cluster, where the Ni is a four coordinate (4C) square-planar sulfide and thiolato species (C_{red1}) (Figure 1.5).[39] There are two channels that have access to the C-cluster: a hydrophobic CO channel and a solvent H_2O channel, both of which allow the two substrates of CODH (CO and H_2O) to access the C-cluster. The B and D clusters contain $[4Fe–4S]^{2+/1+}$ clusters that transfer electrons between the two C-clusters and external redox proteins, and the D-cluster is found at the interface of the two subunits.[72,73] In the proposed mechanism of CODH, CO first binds to Ni(II) axially to form a Ni–CO complex (C_{red1}–CO), while simultaneously, an OH^- bridges the Ni(II) and Fe(II) ions to produce ferrous component II (FCII) (Scheme 1.5).[72,73] The OH^- likely results from reaction with a nearby basic residue, such as Lys562 or His113 near the active site.[72,73] Then, the bridged OH^- attacks the Ni(II)–CO to form a Ni(II)–carboxyl complex (C_{red1}–COOH), which is followed by CO_2 and H^+ release, whereby the cluster is reduced by two electrons (C_{red2}).[72,73] The C-cluster then transfers the two electrons to clusters B and D, which are then transferred to external redox proteins such as ferredoxin to regenerate C_{red1}.[51,71]

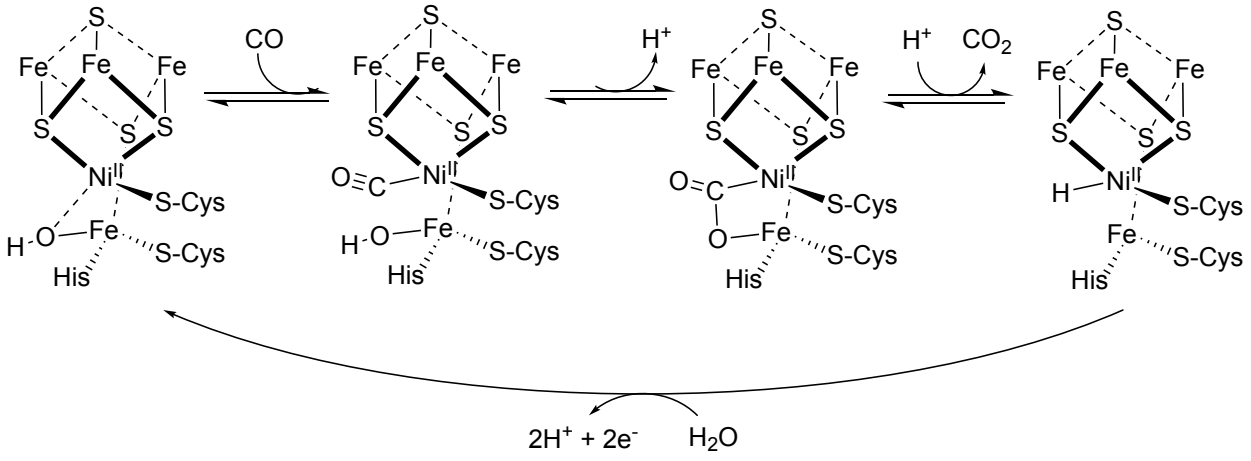

Scheme 1.5. One proposed mechanism of CODH.

1.1.3.2 Bifunctional Acetyl coenzyme A synthase (ACS)/CODH (ACS/CODH)

ACS is a CODH containing enzyme (vide infra); ACS is composed of a CODH dimer (where CO_2 is transformed into CO) and two subunits containing the A cluster (Figure 1.6).

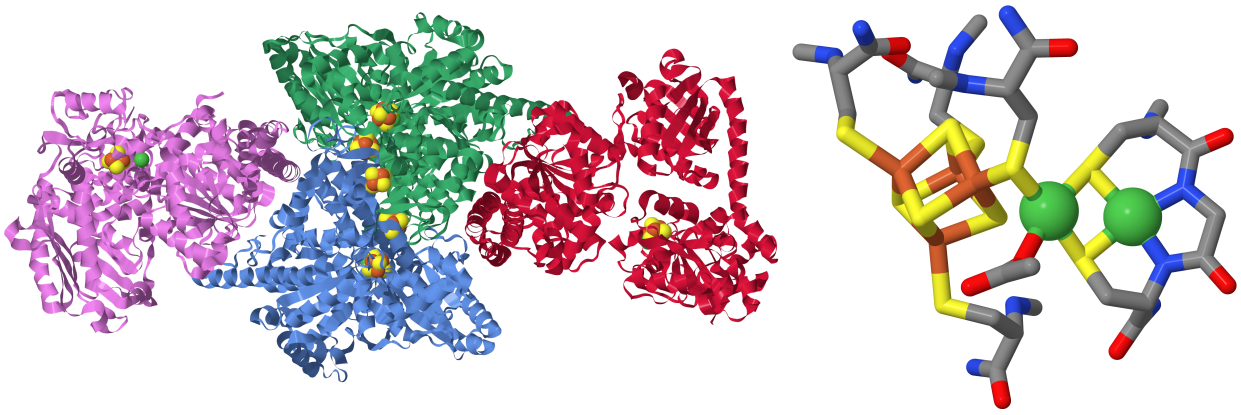

Figure 1.6. X-ray crystal structure of ACS/CODH from *M. thermoacetica* (left, 1.9 Å resolution, PDB 1OAO, Jmol). Active active site (right). The ACS active site is located in the A-cluster represented by purple and red subunits; CODH activity is located in the C-cluster, represented by green and blue subunits. Ni is modeled as green spheres. Iron-sulfur clusters are modeled as orange (Fe) and yellow (S) spheres (right) or rods (left).

For the well-characterized *M. thermoacetica*, the ACS enzyme is quite large at 310 kDa.[74] The A-cluster of ACS reversibly condenses CO with CoA–SH (coenzyme A) and a $–CH_3$ group from a corrinoid/Fe–S protein (CH_3–Co(III)–FeSP) to form acetyl–S–CoA, which is an important enzyme for CO_2 fixation.[38] For ACS/CODH complexes, the k_{obs} of CoA–SH for acetate

degradation in methanogenic *M. thermophila* is 12 s^{-1}, while the k_{obs} for acetate biosynthesis in acetogenic *C. thermoaceticum* is 1.5 s^{-1}.[75] The A-cluster is composed of a diNi cluster bridged by two Cys residues, in which the distal Ni (Ni_d) coordinates two backbone peptido nitrogens and the proximal Ni (Ni_p) coordinates a [4Fe–4S] cluster via a Cys bridge (Figure 1.6).[76]

The Ni_d remains in the Ni(II) oxidation state throughout catalysis, yet the Ni_p is redox active; the Ni_p position is quite promiscuous and can be occupied by Cu(I) or Zn(II), which eliminates activity.[76] In the proposed "paramagnetic" mechanism, CO binds at Ni_p(I) to form the so-called EPR-active NiFeC species, which is likely a $[4Fe–4S]^{2+}$ Ni_p(I) complex (Scheme 1.6).[71]

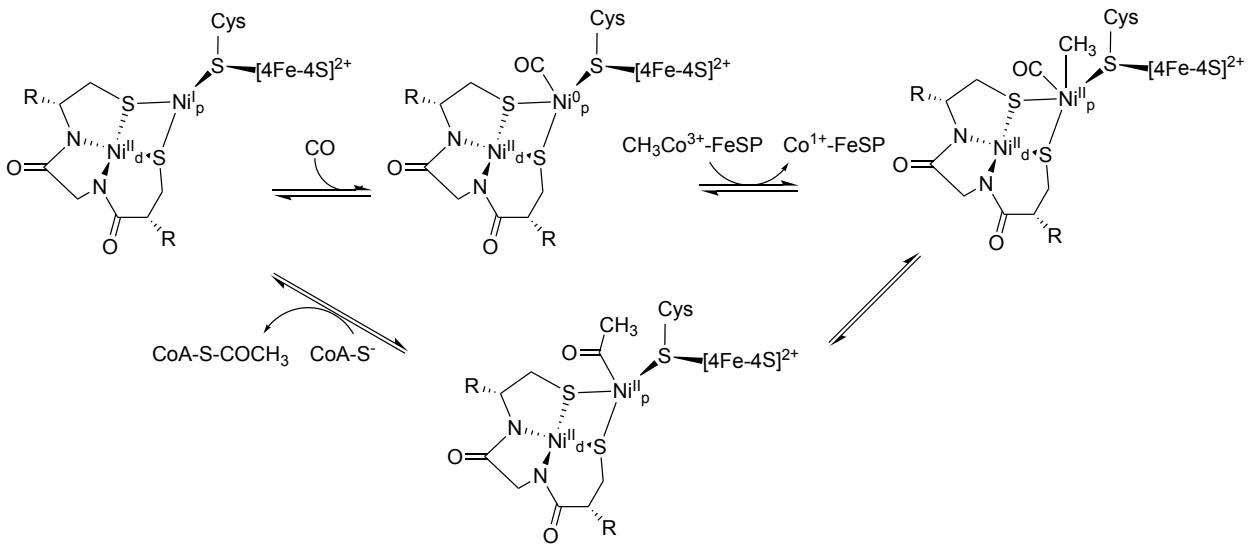

Scheme 1.6. Proposed "paramagnetic" mechanism of ACS.

This reaction is followed by methyl transfer from CH_3–Co(III)–FeSP to Ni_p(I)–CO to result in a transient octahedral Ni_p(III) species, followed by ET to the Fe–S cluster to form a Ni(II)

species.[71] The CO and $–CH_3$ then undergo C–C bond formation to yield an acetyl-Ni species and subsequent acetyl–S–CoA complex following nucleophilic attack by CoA–SH.[71] In the proposed "diamagnetic" mechanism, the $Ni_p(II)$ is pentacoordinate and the oxidation state does not change upon addition of CH_3^+, as two electrons from two nearby Cys donors donate two electrons while forming a disulfide bond coordinated to the Ni(II).[77] The CO then binds in a cis conformation to result in an octahedral Ni(II) geometry, and thereafter the mechanism follows that of the "paramagnetic" mechanism.[77] Questions still remain about the oxidation state of the Fe–S cluster during catalysis in the proposed "diamagnetic" mechanism.[77,78]

1.1.3.3 Nickel iron hydrogenase ([NiFe]-H_2ase)

H_2ase enzymes reversibly catalyze $H_2 \rightleftarrows H^+$ conversion and can be broken into three classes: homodinuclear [FeFe]-H_2ase, heterodinuclear [NiFe]-H_2ase, and mononuclear [Fe]-H_2ase.[79] The mononuclear H_2ase couples H_2 uptake with reduction of the cofactor methylenetetrahydromethanopterin and only contains one Fe atom, while both dinuclear H_2ases ([FeFe]- and [NiFe]-H_2ase) contain Fe/S clusters within their protein scaffolds.[79] [NiFe]-H_2ase is composed of two subunits, one large ~60 kDa subunit is where the NiFe active site is housed, while a smaller subunit (~30 kDa) contains one or more [Fe–S] cluster(s) for ET (Figure 1.7).[73]

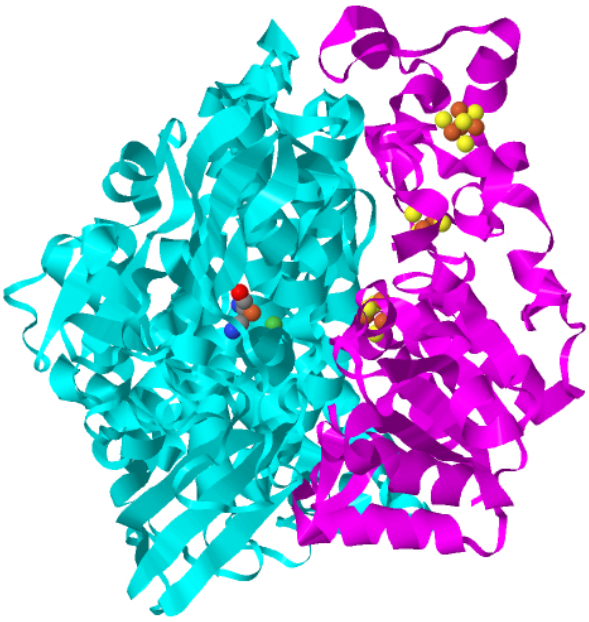

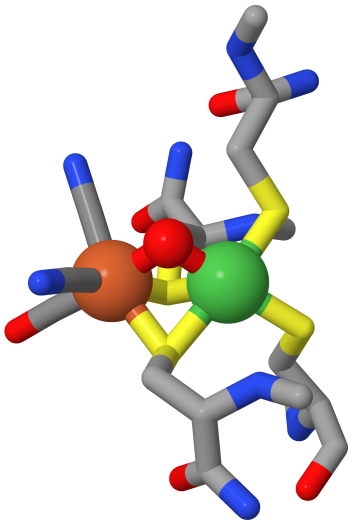

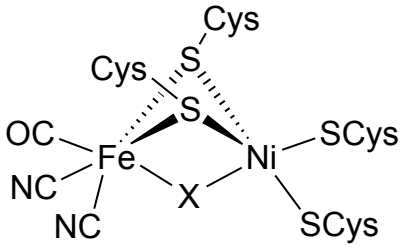

Figure 1.7. X-ray crystal structure of [NiFe]-H_2ase from *D. fructosivorans* (top, 2.1 Å resolution, PDB 1YRQ, Jmol). Ni active site in the OH^--bridged form (bottom left). ChemDraw depiction of the Ni active site (bottom right). Ni is modeled as a green sphere. Iron-sulfur clusters are modeled as orange (Fe) and yellow (S) spheres. The smaller red sphere is a bridging H_2O.

H_2 oxidation is diffusion controlled from [NiFe]-H_2ase (~10^8–10^9 M^{-1} s^{-1}), and the turnover frequency can be as high as 9000 s^{-1}.[80] In the NiFe active site, the Ni and Fe are bridged by two Cys ligands, Ni additionally binds two more Cys residues, and Fe binds two cyanide (CN^-) ligands and one CO ligand (Figure 1.7).[81] The basic catalytic cycle of [NiFe]-H_2ases involves the active site states of Ni–SI_a, Ni–C, and Ni–R (Scheme 1.7). Ni–SI_a is the "resting state" with Ni(II) and Fe(II) oxidation states. Interaction of H_2 with Ni(II) causes polarization of H_2 so that it can be heterolytically split. H^- then bridges between a Ni(II) and Fe(II), and the H^+ is coordinated to one of the terminal Cys ligands of Ni(II), specifically Cys546 from *D. fructosivorans*. Release of the H^+ from Cys546 and an electron from Ni(II) to form Ni(III) yields Ni–C, where the H^-, remains bridged between a Ni(III) and Fe(II). Loss of a H^+ and an electron, both from the bridging H^- returns Ni–SI_a. The H_2 generating pathway proceeds in the opposite direction.[79] The PT ability of the [NiFe]-H_2ase mechanism may prove relevant to Ni superoxide dismutase (NiSOD), as PT via a protonated Cys ligand is a proposal for H_2O_2 generation (vide infra).

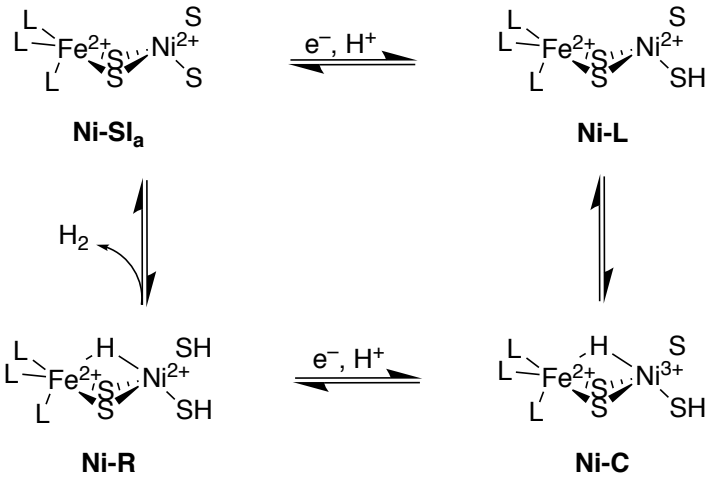

Scheme 1.7. Proposed mechanism of [NiFe]-H_2ase.

There are three main classes of [NiFe]-H_2ase distinguished by their O_2-sensitivity and reaction with O_2: (i) O_2-tolerant, (ii) O_2-resistant, and (iii) O_2-sensitive.[82] O_2-tolerant [NiFe]-H_2ases remain active under aerobic conditions and contain a proximal [4Fe-3S] cluster that contains an unprecedented structure coordinated by six Cys (this is in contrast to the typical proximal [4Fe-4S] cluster coordinated by four Cys).[83,84] The coordination of this unique cluster, in which terminal Cys thiolate ligands outnumber the sulfide ligands, means that the [4Fe-3S] cluster exists in the most oxidized state with three Fe(III) ions and one Fe(II), and it can therefore access three oxidation states at physiological redox potentials.[83] Additionally, O_2-tolerant [NiFe]-H_2ases contain a deprotonated carboxamido-N of the peptide backbone, which coordinates the proximal cluster when oxidized.[84] The proposal is that Glu76 acts as the base to deprotonate the carboxamide-N of Cys20 upon Fe binding and, together with the proximal Fe/S cluster, donates two electrons and one H^+ to reduce O_2 to form H_2O_2 and prevent inactivation of the enzyme.[84,85] In this regard, O_2 acts as a reversible inhibitor to the O_2-tolerant [NiFe]-H_2ases.[86] The current proposal is that the O_2-tolerant enzymes have more positive active site potentials than the O_2-sensitive enzymes due to the proximal cluster which, when oxidized, breaks an Fe–S bond to bind the deprotonated carboxamido-N of Cys20 to reduce O_2 to H_2O with four electrons.[82]

The second class of [NiFe]-H_2ases are O_2-resistant and feature the replacement of a terminal Cys residue on Ni by selenocysteine (Sec) to form a set of [NiFeSe]-H_2ases (Figure 1.8).[51] These enzymes are inactivated under air, but rapidly reactivate when exposed to H_2. SeCys has a lower pK_a, lower bond energies, higher nucleophilicity, and is more polarizable with a larger van der Waals radius than Cys, but less is known about the active site of [NiFeSe]-H_2ases.[79,82,87] The O_2-resistance of these enzymes is due to the Ni–SeCys bond, as the SeCys ligand can be reversibly oxidized to seleninate ($O{=}Se{-}O^-$).[82,87]

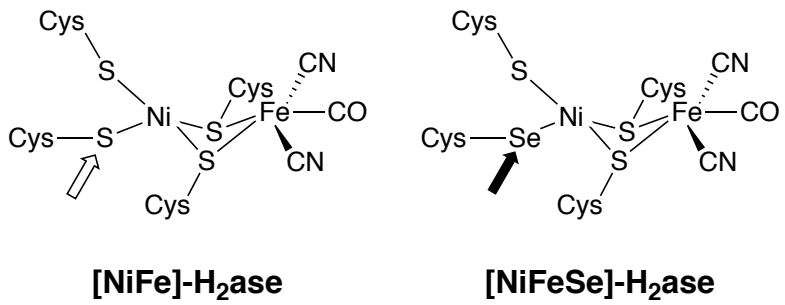

Figure 1.8. Comparison of the active sites the resting states of [NiFe]-H_2ase (left) and [NiFeSe]-H_2ase (right)

The third class of [NiFe]-H_2ases is the O_2-sensitive class that is completely and irreversibly inactivated upon air exposure.[82] These enzymes interact with O_2 by forming reactive oxygen species (ROS), with various deleterious effects to biomolecules, and the inactivated oxidized Ni–A state, which contains a Ni(III) ion, a Ni-Fe bridging OH^- and sulfenate ligands ($Cys–SO^-$).[82,88,89] When the reduced paramagnetic Ni–C state is exposed to O_2, the Ni–B state is formed, which is thought to have a Ni(III) ion and a bridging OH^- ligand and is reactivated under H_2; this reactivation step is designated as the "ready" state.[82,90] Val74Cys (V74C) mutation of *Desulfovibrio fructosovorans* (*Df*) O_2-sensitive [NiFe]-H_2ase results in decreased O_2-sensitivity.[82] In this variant, ~56% of the Ni site occupies a new coordination geometry, denoted Ni′, that resembles the coordination site of NiSOD in that it coordinates two Cys (Cys72 and Cys74), a bridging SH^-, and a main chain peptido-N from Cys75.[82] This strong-field ligand is expected to increase the redox potential of the active site, similar to the Ni(III/II) redox potential observed for NiSOD.[82] This mutation changes the reaction rates of inactivation of the Ni–C state, whereas an initial reaction with O_2 results in O_2 reduction by the H^- to form a transient Ni(III) and peroxide species ($Ni(III)\text{-}OOH^-$).[82] In the WT enzyme, ET from the proximal [4Fe-4S]

cluster is too slow to prevent formation of the inactivated Ni–A state (Ni(III)–OH^- and Cys–SO^-); for the V74C mutant, however, two fast one-electron transfers from the proximal [4Fe-4S] cluster followed by protonation can result in the "ready" Ni–B (Ni(III)–OH^- + H_2O) state.[82] As a result, Fontecilla-Camps and coworkers suggest that metal-peptido bonds (Ni or Fe) partially explain the O_2-tolerance of some classes of [NiFe]-H_2ases and may explain the ROS stability of the active site of NiSOD.[82]

1.1.3.4 Methyl coenzyme M reductase (MCR)

MCR catalyzes the conversion between methyl-coenzyme M (methyl-S-thioethanesulfonate, CH_3–S–CoM) and coenzyme B (*N*-7-mercaptoheptanoylthreonine phosphate, CoB–SH) to methane (CH_4) and the heterodisulfide coenzyme M coenzyme B (CoM–S–S–CoB).[51,91] Methanogenic archaea rely on MCR to produce all biologically-generated CH_4, while other archaea use MCR to oxidize CH_4 anaerobically with sulfate-reducing bacteria.[51,73] The enzyme is isolated as a 300-kDa hexamer in a $(\alpha\beta\gamma)_2$ structure, where the α subunit contains the coenzyme F430, a Ni-tetrapyrrole (Figure 1.9).[41] The Ni(II) state is the inactive form of the enzyme, while the Ni(I) state is catalytically active.[73] The F430 corrinoid contains five double bonds and represents the most reduced corrinoid found in nature to date (2017). In addition to corrinoid ligation, the Ni ion coordinates a Gln in the axial position, while the opposing axial position is available for substrate binding.[41] This enzyme operates at k_{cat} ~100 s^{-1} and has a catalytic efficiency, k_{cat}/K_m(CH_3–S–CoM) = ~1 × 10^5 M^{-1} s^{-1}.[92]

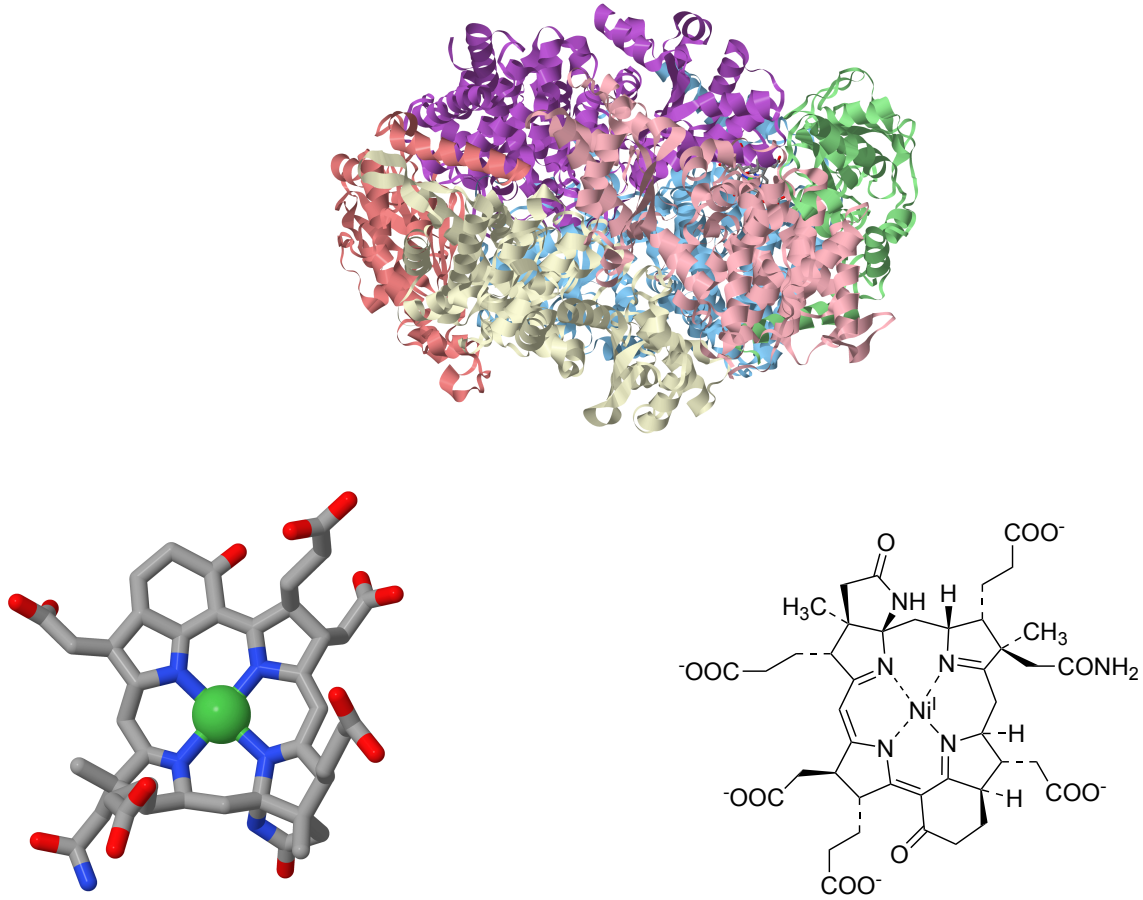

Figure 1.9. X-ray crystal structure of MCR from *M. marburgensis* (top, 1.16 Å resolution, PDB MR1O, Jmol). Ni active site with F430 cofactor (bottom left). ChemDraw depiction of the Ni active site (bottom right).Ni is modeled as a green sphere.

There are two proposed mechanisms for MCR: (i) one that traverses an organometallic CH_3–Ni intermediate and (ii) another that generates a methyl radical ($^{\bullet}CH_3$).[92] The former begins with nucleophilic attack on the CH_3 of CH_3–S–CoM to form a CH_3–Ni(III)–F430 species and CoM–S^- thiolate anion. CoM–S^- is then protonated by CoB–SH (Scheme 1.8).[92]

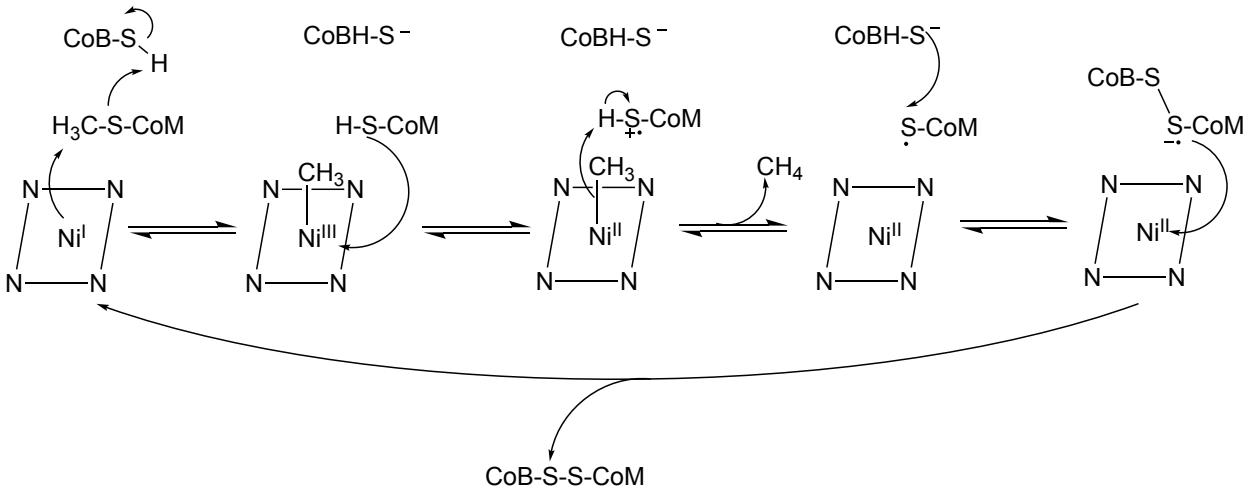

Scheme 1.8. Organometallic intermediate pathway for the production of methane and the disulfide product of CoB-SH and CoM-CH_3 from MCR that traverses an organometallic [Ni-CH_3] intermediate. The 4N square represents the azamacrocycle as depicted in Figure 1.9.

ET from CoM–SH to Ni(III) then yields CH_4 and Ni(II)–F430 and a CoM–S$^{\bullet}$ radical via protonolysis.[92] Linkage between CoM–S$^{\bullet}$ and CoB–S^{-} results in the disulfide radical anion, and subsequent ET from the disulfide radical yields Ni(I)–F430 and disulfide.[92] The second proposed mechanism starts with Ni(I)–F430 inducing catalytic homolytic cleavage of the C–S bond of CH_3–S–CoM to form $^{\bullet}CH_3$ and Ni(II)–S–CoM.[93] The $^{\bullet}CH_3$ then abstracts an H-atom from CoB–SH, forming CH_4 and CoB–S$^{\bullet}$.[93] Combination of CoB–S$^{\bullet}$ an Ni(II)–S–CoM yields the disulfide radical anion and a Ni(II)–F430, which, like the previous mechanism, follows with ET from the disulfide to the Ni to form a Ni(I)–F430 species.[51,93] Researchers have explored how the F430 cofactor stabilizes the Ni(I) state, and it has been proposed that the monoanionic nature of the highly reduced corrinoid promotes both Ni(I) and axial ligand affinity of a thiol.[94] The steric

constraint of the 12- and 13-positions of the corrinoid also prevents ruffling of the macrocycle to force a planar conformation and promotes long Ni–N bonds (calculated 1.99–2.14 Å, as the enzyme has been crystallized in its inactive Ni(II) state).[94] Additionally, it has been proposed that the carbonyl C=O of the 15-*meso*-position also stabilizes the Ni(I) state electronically.[94]

1.1.3.5 *Nickel superoxide dismutase (NiSOD)*

1.1.3.5.1 *Superoxide ($O_2^{\bullet-}$)*

The reduced oxygen molecule superoxide ($O_2^{\bullet-}$) is a cytotoxic byproduct of aerobic metabolism.[95] The damage caused by $O_2^{\bullet-}$ has been implicated in disease states such as diabetes, post-ischemic tissue injury, and neurological disorders such as Parkinson's and Alzheimer's disease.[96-98] Understanding the detoxification of $O_2^{\bullet-}$ as a precursor to $OH^{\bullet}$ and H_2O_2 is vital to understanding one of the many mechanisms biology utilizes to protect against ROS. $O_2^{\bullet-}$ is the conjugate base of hydroperoxy radical (HO_2, pK_a = 4.8) and, as such, $O_2^{\bullet-}$ is the predominant species at physiological pH (pH = 7.4).[99] $O_2^{\bullet-}$ reacts spontaneously to yield H_2O_2 and O_2 via pH and concentration dependent reactions.[100] At pH = pK_a = 4.8, spontaneous disproportionation reaches a maximum rate (k = 9.7 × 10^7 M^{-1} s^{-1}).[100] At pH = 7.4, however, the rate of disproportionation slows to 2 × 10^5 M^{-1} s^{-1}, and $O_2^{\bullet-}$ maintains a half-life of 10 s.[99] Importantly, spontaneous disproportionation is bimolecular, and rates are proportional to $O_2^{\bullet-}$ concentration; under physiological conditions ($[O_2^{\bullet-}] \approx 10^{-6}$-$10^{-9}$ M) and $O_2^{\bullet-}$ can persist for hours.[100] As a result, aerobic organisms have employed SOD to catalyze $O_2^{\bullet-}$ disproportionation at the diffusion controlled limit (10^9 M^{-1} s^{-1}) over a wide pH range (pH = 5-11) with rates dependent only on enzyme concentration.[101-103] There are three classes of SOD: CuZnSOD, Mn or FeSOD, and NiSOD, all of which contain redox-active metal ions that alternately oxidize and reduce $O_2^{\bullet-}$ to

O_2 and H_2O_2, respectively ($E_{1/2}$ ($O_2^{\bullet-}$) = –0.18 V vs NHE).[100,104-107] As a result, SOD can suppress concentrations of $O_2^{\bullet-}$ below 2×10^{-10} M in normal cells and is essential in reducing the lifetime of $O_2^{\bullet-}$ in biology.[100,102,103,108]

1.1.3.5.2 CuZnSOD

Intracellular CuZnSODs are homodimers in almost all eukaryotic organisms; extracellular CuZnSODs are tetrameric and found in both mammals and plants.[100,109-111] Notably, mutations of the human CuZnSOD were associated with the neurodegenerative disease amyotrophic lateral sclerosis (ALS), which is the focus of many CuZnSOD studies.[112] Intracellular CuZnSOD is a 32-kDa homodimeric enzyme where each monomer houses one CuZn active site, and each subunit folds as an eight-stranded Greek-key β-barrel with seven connecting loops. Loop IV contains four Zn-binding amino acids, and loop VII limits access of solvent to the active site.[100] The active site consists of a reduced Cu(I) which coordinates His46, His48, and His120 to form a trigonal-planar geometry, while a nearby Zn(II) coordinates His63, His71, His80, and Asp83 to form a tetrahedral geometry (Figure 1.10).

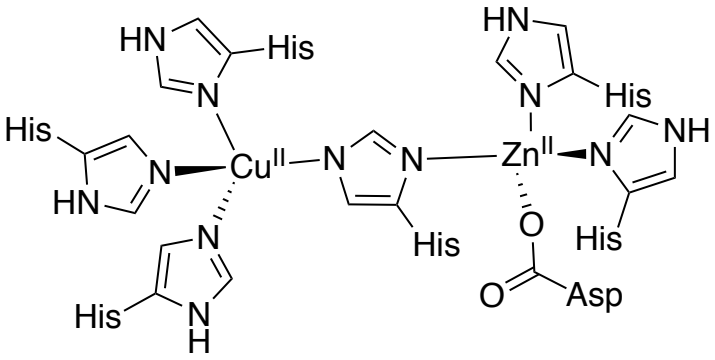

Figure 1.10 Cu/Zn active site in the oxidized Cu(II))state.

Upon oxidation of Cu(I) to Cu(II), the Cu ion coordinates an H_2O molecule and causes His63 to bridge the Cu(II) and Zn(II) ions to result in a distorted square-pyramidal geometry.

$$Cu(II)ZnSOD + O_2^{\bullet-} \rightarrow Cu(I)ZnSOD + O_2 \quad \text{(Eq 1.1)}$$

$$Cu(I)ZnSOD + O_2^{\bullet-} + 2H^+ \rightarrow Cu(II)ZnSOD + H_2O_2 \quad \text{(Eq 1.2)}$$

CuZnSOD catalyzes both half reactions (Eq 1.1-1.2) near the diffusion-controlled rate over a wide pH range of 5.0-9.5.[113] The bridging imidazole provides H^+ for H_2O_2 generation.[100] The role of the positively charged Zn(II) is proposed to help maintain pH independence, as the H_2O_2 producing half reaction is pH dependent in the absence of Zn.[114] Without Zn(II), the bridging imidazole is protonated and dissociates, causing the Cu ion to become fluxional and capable of binding in the Zn(II) site to form a stable, but catalytically inactive, CuCuSOD.[100,114] Electrostatic guidance is also important for CuZnSOD activity, as mutation of Arg143, which is located on the active site lid, results in significant loss of activity. Charge neutralization (Arg143Ile) causes an order of magnitude loss of activity, and charge reversal (Arg143Asp, Arg143Glu) causes an additional order of magnitude loss of activity.[115] CuZnSOD is also inactivated by H_2O_2 likely through peroxidative activity, in which Cu(II)ZnSOD reacts with H_2O_2 to produce $O_2^{\bullet-}$ and Cu(I)ZnSOD reacts with a second equiv of H_2O_2 to yield hydroxyl radical ($OH^{\bullet}$) and OH^-, leading to loss of the Cu ion.[113]

1.1.3.5.3 Mn- or FeSOD

Manganese (Mn), widely found in eukaryotes, and iron (Fe) SOD, found in strict anaerobes and primitive eukaryotes, have similar secondary and tertiary structures and utilize the

same amino acids to coordinate their respective metal ions (Figure 1.11).[100] There are some organisms that exhibit Fe- or Mn-specific activity, while others have Fe or Mn preference, but display some activity with either metal.[100] Other organisms have a gene that typically produces FeSOD, but produces MnSOD in cases of O_2 exposure or Fe deficiency; these cambialistic systems have high SOD activity with either Fe or Mn bound.[116-120] The lack of interchangeability can be explained by redox-tuning of the metal ion by the protein; E^{o}(Fe(III/II)) of $[Fe(H_2O)_6]^{3+/2+}$ is 0.77 V and E^{o}(Mn(III/II) of $[Mn(H_2O)_6]^{3+/2+}$ is 1.5 V vs NHE. Nature requires these potentials of to be depressed by the nearby His and Asp ligands in order to fall within the window of $O_2^{\bullet-}$ disproportionation (E = –0.18 – 0.91 V vs NHE);[49] however, the depression of the E^{o} of Mn(III/II) is greater, suggesting additional depression of E^{o} is carried out by other protein-metal interactions, such as H-bonding to the coordinated H_2O/OH^- ligand to tune the pK_a and E^{o} of the metal ion.[100] Indeed, the E^{o} of Fe is ~0.3 V lower when coordinated to *E. coli* MnSODs and the E^{o} of Mn is ~0.5 V higher when coordinated to *E. coli* FeSOD.[121,122]

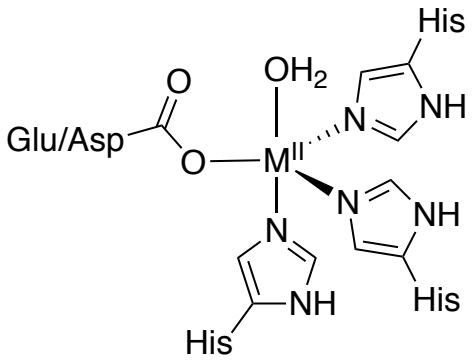

Figure 1.11. Mn-SOD and Fe-SOD active site in the reduced (M(II)) state

1.1.3.5.4 FeSOD

The active site of FeSOD holds the Fe ion in a trigonal bipyramidal geometry, in which the Fe ion is coordinated by His72, His160, and Asp156 as equatorial ligands and His26 and an H_2O/OH^- molecule as axial ligands (Figure 1.11).[100] The varying H_2O/OH^- ligand is in the H_2O form when Fe is in the Fe(II) oxidation state; the ligand is bound as OH^- when Fe is in the Fe(III) oxidation state (Equations 1.3-4).[123] The H_2O/OH^- ligand H-bonds with Asp156 and Gln69 and exhibits a slow H_2O exchange rate, which indicates it is more than a solvent molecule and acts as a ligand.[124-126] The H_2O/OH^- ligand is the beginning of an H-bond network containing His30 and Tyr34 that interconnects the H_2O/OH^- to solvent H_2O molecules and the substrate-binding site. The network also includes Gln69 H-bonded to Asn72 and Trp122, while monomer units are H-bonded together via H-bond pairs His160-Glu159 and His30-Tyr163.[100,125,126] The reaction catalyzed by FeSOD alternates between Fe(III) and Fe(II) oxidation states and also acquires a H^+ in each half reaction via a ping-pong mechanism:

$$O_2^{\bullet-} + H^+ + (HO^-)\text{–Fe(III)SOD} \rightarrow O_2 + (H_2O)\text{-Fe(II)SOD} \qquad \text{(Eq 1.3)}$$

$$O_2^{\bullet-} + H^+ + (H_2O)\text{–Fe(II)SOD} \rightarrow H_2O_2 + (HO^-)\text{-Fe(III)SOD} \qquad \text{(Eq 1.4)}$$

Upon reduction of Fe(III), the OH^- ligand is protonated and can, in turn protonate $O_2^{\bullet-}$. A second protonation step by bulk H_2O results in the formation and release of H_2O_2.[100] The first step of the mechanism of FeSOD involves inner-sphere binding of $O_2^{\bullet-}$ to Fe(III)SOD. This mechanism is supported by small anion coordination to Fe by azide (N_3^-), fluoride (F^-) and OH^-.[104,127,128] Likely, Tyr34 acts as a "gatekeeper Tyr" to exclude larger anions from the active site and promote substrate binding, as the mutant Y34F-Fe(III)SOD has a K_d ($O_2^{\bullet-}$) 3-5 times lower than WT-Fe(III)SOD.[129] $O_2^{\bullet-}$ also coordinates to Fe(III) rather than Fe(II), as Fe(III)SOD has a

binding affinity to F^- that is 20 times higher than Fe(II)SOD.[129] The next step in the disproportionation mechanism involves ET from $O_2^{\bullet-}$ to Fe(III) to yield Fe(II), which occurs very quickly, as no [Fe(III/II)-O_2]$^{-/0}$ adduct has been observed.[130] A H^+ is also taken up from bulk H_2O via the extensive H-bond network around the active site involving Gln69, Tyr34, and His30, where Gln69 donates the H^+ to the OH^- ligand to form an H_2O ligand.[100] Explanations as to why $O_2^{\bullet-}$ does not bind Fe(II)SOD include the trans effect: Asp156 may prevent $O_2^{\bullet-}$ binding in the open coordination site because of the increased strength of the Asp–Fe bond when OH^- becomes H_2O.[100] Also, an HO_2^- ligand would likely cause Fenton chemistry at the active site.[131] NMR evidence of outer-sphere binding indicates that F^- binds to Tyr34 and also perturbs an H-bond between Gln69 and Tyr34.[129,132] In the next step in the FeSOD mechanism, $O_2^{\bullet-}$ is reduced by Fe(II)SOD, and the O_2^{2-} is protonated. It is proposed that the initial protonation arises from the bound H_2O on the proximal O of O_2^{2-} and that the second protonation comes from Tyr34 on the distal O, but the question of protonation site remains under investigation.[100] One argument is that if the distal O of O_2^{2-} were protonated first, it would promote an inner sphere coordination of HO_2^-, which has been shown to be favorable in calculations for MnSOD.[133]

1.1.3.5.5 MnSOD

The active site of MnSOD bears many similarities to that of FeSOD, as the Mn forms a trigonal bipyramidal geometry that coordinates His74, Asp159, and His163 in the equatorial plane and His26 and a bound H_2O/OH^- in the axial positions (Figure 1.11). The MnSOD active site has an H-bond network composed of Gln143, Tyr34, His30 and Tyr166.[100] MnSOD is isolated as both a dimer and a tetramer; dimers are typically found in bacteria and prokaryotes, and tetramers are found in eukaryotes.[100] MnSOD is more mechanistically complex when

compared to the other SODs, as it has different catalytic activities at high and low concentrations of $O_2^{\bullet-}$, a property which has been denoted "gating." At low $O_2^{\bullet-}$ concentrations where [$O_2^{\bullet-}$]:[MnSOD] <5, the redox pathway is similar to that of FeSOD and CuZnSOD.[134-137] At high $O_2^{\bullet-}$ concentration, however, there is an initial fast, first-order, "burst" phase, followed by a slow, zero-order phase (Eq 1.5-6).[134-137]

$$Mn(III)(OH^-) + O_2^{\bullet-} + H^+ \longleftrightarrow Mn(II)(H_2O) + O_2 \qquad \text{(Eq 1.5)}$$

$$Mn(II)(H_2O) + O_2^{\bullet-} + H^+ \longleftrightarrow Mn(III)(OH^-) + H_2O_2 \qquad \text{(Eq 1.6)}$$

One explanation for the differing rates is that reaction of $O_2^{\bullet-}$ with Mn(II) has an alternate pathway, in addition to the mechanism proposed for FeSOD to form O_2 and H_2O_2. In a separate pathway, Mn(II) and $O_2^{\bullet-}$ also form an inhibited or dead-end complex that is possibly a side-on or end-on peroxy ligand.[134-137] In human physiology, high levels of MnSOD are related to tumor suppression, and it has been proposed that in addition to acting as an SOD, MnSOD may also serve a role as a signaling agent.[138-141]

1.1.3.5.6 NiSOD

Nickel superoxide dismutase (NiSOD) is similar to other SODs in that the enzyme disproportionates $O_2^{\bullet-}$ into O_2 and H_2O_2 via one electron oxidation and reduction of its metal center at the diffusion controlled limit (~10^9 M^{-1} s^{-1}).[100,101] This class of SOD is isolated from *Streptomyces* soil bacteria and is found in the genome of cyanobacteria.[142,143] NiSOD is unique in that it contains no sequence homology to other SODs and furthermore contains a unique 80-kDa homohexameric quaternary structure containing one Ni ion per monomeric subunit (Figure

1.12).[35,36] The active site Ni is coordinated to two Cys ligands, which depress the Ni(III/II) redox (286 mV vs NHE) potential, but are unusual ligands for the breakdown of ROS, as they are susceptible to oxidative modification.[35,36] The Ni ion is found in the "Ni-hook" motif that consists of the first nine residues of the N-terminus.[35,36] The enzyme is isolated as a 1:1 mixture of Ni(III) and Ni(II) states, where the Ni(II) ion is in a square-planar geometry, and coordinates to the backbone carboxamide of Cys2, the primary amine from the N-terminus, and two thiolate ligands from Cys2 and Cys6 (Figure 1.12).[35,36]

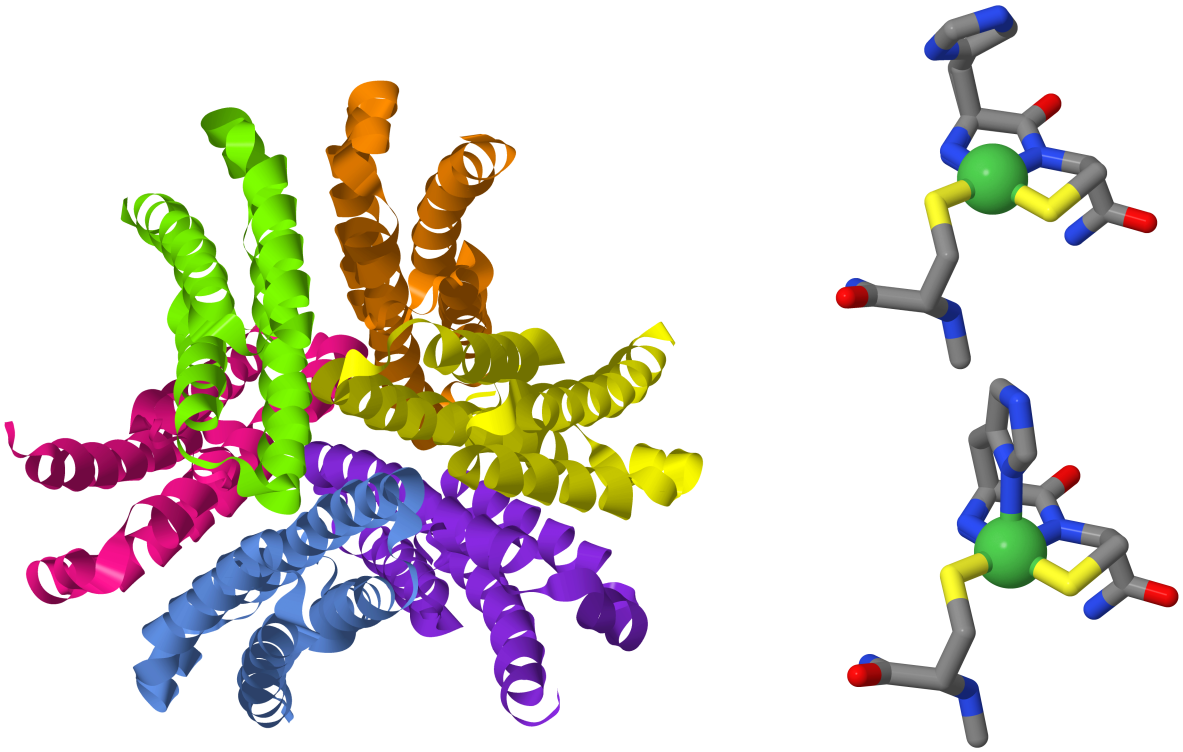

Figure 1.12. X-ray crystal structure of NiSOD from *S. coelicolor* (left, 1.30 Å resolution, PDB 1T6U, Jmol). Ni active site in the Ni(II), His-off coordination (right top) and Ni(III), His-on coordination (right bottom). Ni is modeled as green spheres.

The Ni(III) state additionally binds the Nδ nitrogen of His1 to from a square-pyramidal geometry.[35,36] The Ni(III) ion has a rhombic EPR spectrum with *g*-values = 2.30, 2.24, and 2.01 with a triplet superhyperfine splitting pattern (A_{zz} = 24.9 G) in the g_z component consistent with axial HisN-coordination (Figure 1.13).[35]

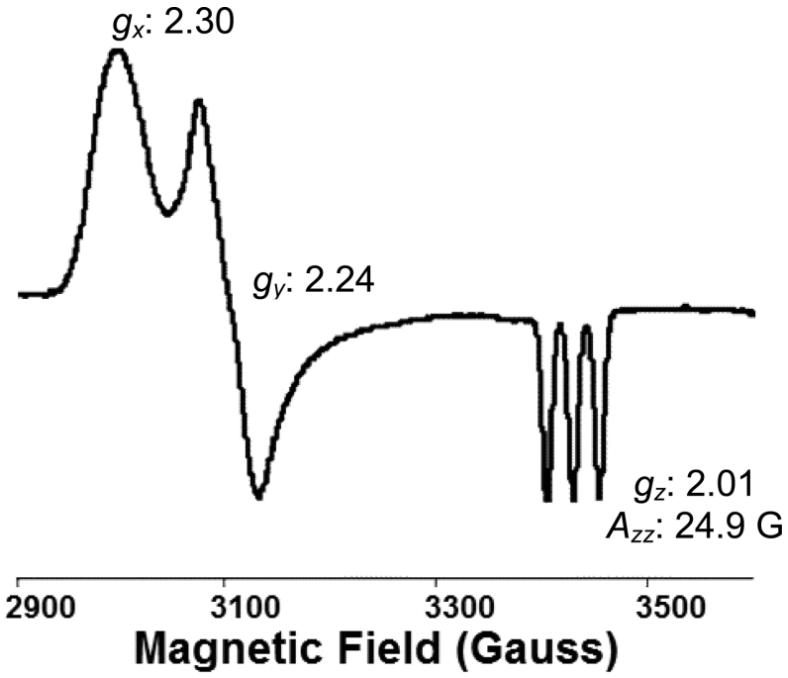

Figure 1.13. EPR spectrum of as-isolated NiSOD in 50 mM HEPES buffer, pH 8.0 (*S. coelicolor*). 55 K, 9.678 GHz, 10 mW, 5 G. Adapted from reference 35.

The UV-vis spectrum of as-isolated NiSOD is dominated by contributions from $NiSOD_{ox}$ (Ni(III) form).[144] To observe the electronic absorbtion of the Ni(II) or $NiSOD_{red}$ form, the enzyme was reduced using dithionite to reveal features at 362 nm (ε: 880 M^{-1} cm^{-1}), 450 nm (ε: 480 M^{-1} cm^{-1}), and 543 nm (ε: 150 M^{-1} cm^{-1}), the latter two or which are characteristic of

Ni(II)N_2S_2 complexes.[144,145] To obtain the $NiSOD_{ox}$ spectrum, the dithionite reduced spectrum was subtracted from the as-isolated spectrum to reveal features at 372 nm (ε: 6800 M^{-1} cm^{-1}) and 502 nm (ε: 1510 M^{-1} cm^{-1}), arising from CT transitions.[144]

From a variety of structural mutations, small molecule complexes, and computational models, it has been determined that the thiolate and imidazole ligands are crucial for depressing the redox potential of Ni to fall within the redox window of disproportionation (E = –0.18 – 0.91 V vs NHE) and to stabilize the low-spin Ni(III) state (vide infra).[49,51] The homohexamer protein orients the Ni ions in an approximately octahedral orientation wherein each Ni ion likely has a balance of His-on and His-off conformations.[146] It has been suggested that this balance of oxidation states is important in maintaining charge neutrality of the hexamer throughout catalysis.[146] Others have proposed that there exists cooperativity between the Ni ions via an intermolecular salt bridge (Asp3-Lys89; Glu49-His53) that connects two trimer subunits to form a dimer of trimers; this bridge may provide a mode of communication between the Ni ions and promote a balance of oxidation states.[146] The role of primary and secondary sphere interactions will be discussed in more detail (vide infra).

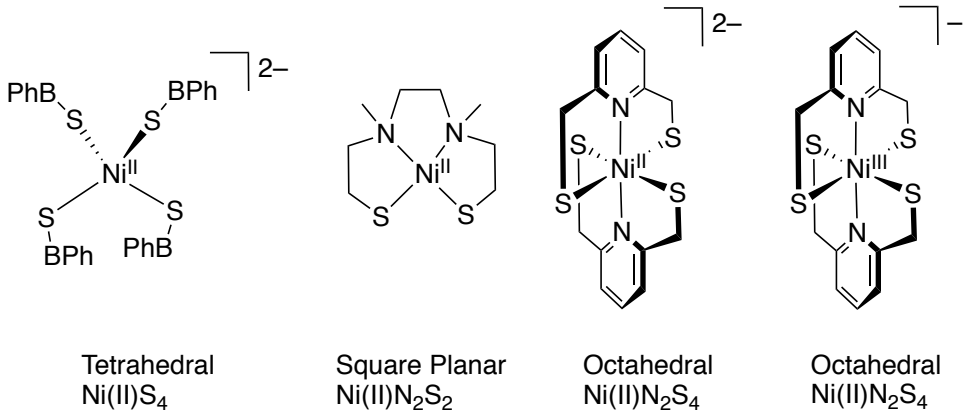

Figure 1.14. Structures of Ni complexes investigated by XAS. BPh = biphenyl.

The Ni-coordinated Cys-thiolates are likely sites of protonation and may serve as the source of H^+ for H_2O_2. XAS analysis by Solomon, Maroney, and coworkers compared the S K-edge spectra of NiSOD to various Ni complexes with different S-ligands (Figure 1.14).[147] The mononuclear Ni(II) complexes have resolved pre-edge features arising from the S(1s) orbital to unoccupied, antibonding Ni/S orbitals and each of the pre-edge features can be assigned to unique Ni–S bonding.[147] The tetrahedral Ni(II)S_4 has a weak pre-edge transition at 2470.5 eV due to weak covalency between the Ni and S orbitals.[147] The octahedral Ni(II)N_2S_4 and square-planar Ni(II)N_2S_2 model complexes exhibited pre-edge transitions at 2470.8 eV with high intensity suggesting a high degree of covalency in the in-plane Ni–S orbitals.[147] The octahedral Ni(III)N_2S_4 complex contains two high-intensity pre-edge transitions at 2469.7 and 2471.0 eV; the first transition is assigned to the additional out-of-plane singly occupied Ni–S orbital (Table 1.1).[147]

Table 1.1 Summary of S K-edge transition energies for various Ni–S bonds

Complex	**Bond**	**Energy (eV)**
Ni(II)S_4, tetrahedral	Ni(II)–S	2470.5
Ni(II)N_2S_4, octahedral	Ni(II)–S	2470.8
Ni(II)N_2S_2, square-planar		
Ni(III)N_2S_4, octahedral	π Ni(III)–S	2469.7
	σ Ni(III)–S	2471.0

These spectroscopic benchmarks are useful in comparing the S K-edge spectrum of NiSOD in its resting state (a mixture of oxidized and reduced Ni centers), which revealed two pre-edge features at 2469.7 and 2470.9 eV, where the former transition can be correlated to a mononuclear Ni(III) feature and the latter transition is likely overlapping mononuclear Ni(II) and Ni(III) features.[147] As the Ni(III) center is photoreduced, the lower energy 2469.7 eV feature disappears, but this photoreduced Ni(II) spectrum is different from the peroxide-reduced Ni(II) spectrum.[147] The peroxide-reduced Ni(II)SOD revealed a broad, structureless S K-edge feature from 2471.8 to 2472.8 eV, which is characteristic of a protonated thiolate.[147] The decreased intensity of the 2470.9 eV feature suggests less Ni/S interaction in the peroxide reduced sample, and the calculated electron donation from protonated Cys ligands to Ni instead predicts a pre-edge feature ~2472.6 eV.[147] One mechanism proposes Ni(III) is initially thiolate-bound, but upon peroxide reduction, Ni(III) is reduced to Ni(II), and a thiolate is protonated via proton coupled electron transfer (PCET).[147] Indeed, Brunold and coworkers have shown via density functional theory (DFT) calculations that Ni–S_{Cys} bonds in NiSOD are derived from covalent σ-bonding and S-protonation eliminates the π-π filled-filled repulsions without disrupting the σ-interactions (Figure 1.15).[144] Cys6 is a likely site of protonation due to the more reactive nature of trans-carboxamide thiolates vs. trans-amine thiolates (vide infra).[148-155] Both the Ni_d of ACS and NiSOD contain square-planar NiN_2S_2 coordination spheres, yet the Ni_d of ACS is redox-inactive, and the Ni ion of NiSOD is capable of catalyzing Ni(III/II) redox cycling. Ni_d of ACS contains bridging Cys ligands, rather than the terminal Cys thiolates found in NiSOD, so perhaps the reduced electron density does not depress the redox potential of Ni_d enough to access the Ni(III) oxidation state. The Ni_d of ACS also contains two peptido N-donors, while NiSOD contains a unique mixed peptido/amine coordination. The two anionic peptide donors in Ni_d contribute

electron density to Ni, but the mixed peptide/amine coordination of NiSOD, in addition to the axial His, may allow stabilization of the Ni(III) state while also preventing S-oxidation (vide infra).[157]

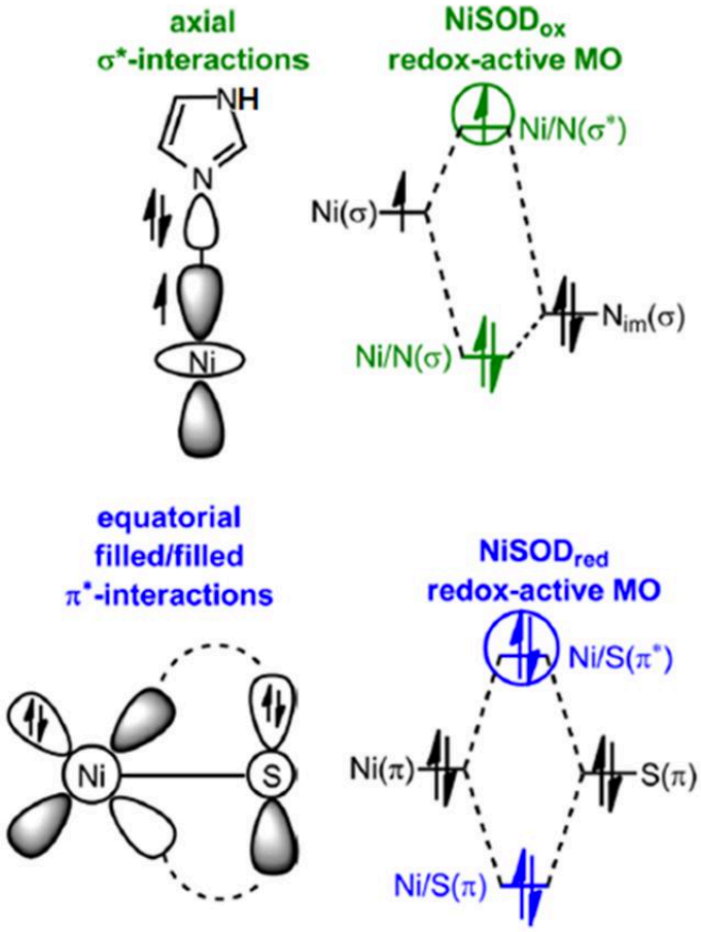

Figure 1.15 Frontier MOs and illustration of the dominant bonding interactions in NiSODox (top) and NiSODred (bottom). This figure was copied with permission from Ref 156.[156]

1.2 NiSOD Structure-Function Studies: Enzyme Mutations

1.2.1 Inner-sphere versus outer-sphere mechanism

The mechanism of NiSOD has yet to be defined, and discussion remains over whether ET occurs by an inner-sphere or outer-sphere mechanism. An outer-sphere mechanism is suggested as a way to protect the Cys residues from S-based modifications by $O_2^{\bullet-}$ and H_2O_2.[36,44] Indeed, the source of H^+ in NiSOD remains a principle question, as NiSOD lacks the bound H_2O ligand of FeSOD and MnSOD that is proposed to tune the redox potential and provide protons in these SODs.[158] Although most biochemical evidence suggests an outer-sphere mechanism, a metallopeptide-based NiSOD model has been isolated with a single Ni-bound cyanide (CN^-) anion. This CN^- coordination serves as limited evidence for small anions binding to the active site.[159]

Disproportionation activity of NiSOD isolated from *Streptomyces seoulensis* was strongly inhibited by excess CN^- (which typically removes Ni) and excess H_2O_2, a byproduct of disproportionation typically decomposed by catalase or a non-specific peroxidase.[101] NiSOD disproportionation is only weakly inhibited by azide (N_3^-), an electronic mimic of $O_2^{\bullet-}$; however, $N_3^-$is 50% larger than $O_2^{\bullet-}$ and is not always an accurate model of $O_2^{\bullet-}$.[100,143,160]

CN^- and N_3^- inhibition of SOD activity were also probed via EPR spectroscopy.[35] The EPR spectrum of oxidized NiSOD (645 μM) treated with 200 mM N_3^- (~300 equiv) reveals a perturbed $g_y = 2.24$ feature, which exhibits shifting and minimal hyperfine splitting.[35] The EPR spectrum of ^{15}N-labeled N_3^- has identical features, which suggest that the hyperfine interactions result from perturbations around the active site, rather than N_3^- binding to the Ni center involving the highest occupied molecular orbital (HOMO) Ni(d_{z2}) orbital.[35] Oxidized NiSOD (683 μM) (spin intensity of 0.72 spins/Ni) treated with 117 mM CN^- (~170 equiv) revealed a complete loss

of the EPR signal.[35] A cocrystal structure (2.05 Å resolution) of NiSOD treated with CN^- showed that Ni had been removed by CN^- chelation resulting in the loss of EPR signal, rather than a transition from EPR-active Ni(III) to an EPR-inactive Ni(II).[35] Taken together, there still remains a lack of structural evidence for small anion binding to Ni.

Ionic strength dependence on catalytic activity is a measure of the electrostatic guidance of charged substrates to the active site of the enzyme, and a strong dependence on ionic strength is often suggestive of an inner-sphere mechanism. For example, CuZnSOD has a positively charged active site and exhibits a decreased k_{cat} with increasing ionic strength.[161] The ionic strength dependence of CuZnSOD is confirmed by site-directed mutagenesis studies that increase positive charge around the active site, which results in faster rates.[162] NiSOD from *S. seoulensis* contains three conserved Lys residues (Lys64, Lys115, Lys27) that form a positive electrostatic potential 10-12 Å away from the Ni ion and may serve as a proposed electrostatic guidance system.[36] NiSOD, however, has very little dependence on ionic strength suggesting that electrostatic guidance of the anionic $O_2^{\bullet-}$ radical is not an important aspect of the catalytic mechanism.[160] Calculations on the electrostatic potential also show that there are no significantly positively charged areas around the active site, which supports the low ionic strength dependence of NiSOD.[36]

The crystal structure of *S. seoulensis* provides additional evidence of an outer-sphere mechanism via structural verification that the active site is blocked by a narrow active site channel, constricted by Pro5 and Tyr9.[36] An outer-sphere mechanism would also allow for added protection of the thiolate ligands from oxidative damage caused by $O_2^{\bullet-}$ and its byproducts, O_2 and H_2O_2. Calculations of the solvent-accessible areas derived from static structures also show

that the four planar ligands of the active site are buried within the globular metalloenzyme structure, which provides little access for the substrate molecule to bind.[36]

1.2.2 Role of primary and secondary sphere residues

The mixed amine/carboxamide coordination in NiSOD represents a unique set of Ni N-donors. In biology, the coordination of a metal ion to a deprotonated peptide nitrogen is rare. and such coordination is only found in three other enzymes: (i) nitrile hydratrases (NHases);[163] (ii) the oxidized P-cluster of nitrogenase;[164] and (iii) the Ni_d site in the A-cluster of ACS.[38,165] The role of peptide coordination in biology has also been explored, and metal-coordinated peptides have the ability to stabilize high oxidation states and have high σ-donor capabilities that can promote lower coordination numbers.[165-168] Peptido nitrogens are also capable of tautomerization to imminolate forms that can modulate the electron density at a metal binding site. Ligation of an N-terminal amine is a unique feature of NiSOD, as there is a paucity of this type of binding motif in nature. It is found in the heme-containing transcription factor, CooA, where an N-terminal nitrogen of proline (Pro) binds in the distal axial position in the Fe(II) state before being displaced by CO binding.[169] An N-terminal amine also coordinates Ni(II) via a CXXCGC motif in HypB, an accessory metallochaperone protein for NiFe-hydrogenase (NiFe-H_2ase).[170] Additionally, albumins contain an amino terminal Cu(II)- and Ni(II)-binding (ATCUN) motif; this binding site is defined by the presence of an NH_2-terminus and has been identified in several albumin species: neuromedins C and K, human sperm protamine P2a, and histatins.[171] A common feature of these proteins is the lability of the metal–N bond arising from the N-terminal amine and its use in transport proteins. NiSOD is unique in that it utilizes both peptide and amine N-donors, combining an anionic deprotonated peptido-N as a strong σ-donor and a neutral N-

terminal amine, which is not labile in this coordination sphere.

Researchers utilize site-directed mutagenesis in structure-function studies to elucidate the role of specific amino acids in an enzyme by assessing how the variant affects function. The role of the primary Cys residues (Cys2 and Cys6) was probed via mutations of Cys to Ser in three different mutants: C2S-NiSOD, C6S-NiSOD, and C2S/C6S-NiSOD (Table 1.2).[44,172] NiSOD's hexameric assembly was preserved in all of the variants with no loss of the six Ni(II) ions; however, the overall stability of the hexameric quaternary structure was lowered.[44] The lowered structure stability was most pronounced when Cys2 was mutated (C2S- and C2S/C6S-NiSOD). Size exclusion chromatography (SEC) revealed C2S-NiSOD as hexameric, trimeric, and tetrameric proteins and C2S/C6S-NiSOD as monomeric, dimeric, trimeric proteins, while C6S-NiSOD is only a hexameric protein, most closely resembling WT-NiSOD.[44] Analogously, by ESI-MS, C6S-NiSOD has a large hexameric envelope most analogous to WT-NiSOD, while C2S- and C2S/C6S-NiSOD have significant envelopes relating to monomer protein.[44] None of these mutants exhibit SOD activity, as k_{cat}/k_M does not change in comparison to spontaneous disproportionation (2×10^5 M^{-1} s^{-1}).[44,173,174] The Ser mutants displayed a different absorption profile from the native enzyme due to the loss of a S-to-Ni(III) CT transition at ~380 nm and the appearance of a new ligand-field transition ~420 nm consistent with a octahedral (S = 1) Ni(II) species.[44] This coordination was confirmed by magnetic circular dichroism (MCD) data that revealed temperature-dependent *C*-term behavior and lack of an EPR signal due to the large zero-field splitting.[172] Additionally, XAS data support that all Ser variants have only N/O-donors including one His ligand.[44] DFT computations reveal that the Ser mutants have frontier MOs that are predominantly Ni(3d) and carboxamide(N/O) antibonding in character.DFT computations further reveal that no orbital contribution arise from the Ser ligands due to the low σ and π-donor

contributions, resulting in a high-spin configuration.[172] Based on a pH-dependent MCD study, in combination with DFT computations, it was proposed that the Ser mutants form a 6C Ni(II) with a weak axial H_2O bond.[172] The Ser mutants are likely in their protonated state, therefore neutral, and can impose a positive charge on the active site, raising the potential of Ni(III/II) to prevent stabilizing a Ni(III) state.[172] Any mutation of either of the Cys2 or Cys6 to Ser prevents coordination of the remaining Cys and results in a paramagnetic Ni(II) state, rather than the planar Ni(II) found in the native enzyme.[44] This change in electronic configuration reveals that the S(σ) and S(π) contributions from both Cys ligands are essential in forming highly-covalent Ni–S bonding interactions in order to lower the Ni(III/II) potential to access the Ni(III) state and fall within the window of $O_2^{\bullet-}$ disproportionation.[44,172] As a result, it has been proposed that coordination to both Cys2 and Cys6 is essential in forming the low-spin Ni(II) configuration and poising the Ni ion for catalysis; furthermore, Cys2 plays an important role in maintaining the overall hexameric structure of the NiSOD enzymes.[44] Cys residues have also been suggested to play a role in PT to and from the active site.[44,175,176]

The role of the backbone carboxamide ligand in NiSOD was explored by Maroney and coworkers via a semisynthetic strategy employing NCL (native chemical ligation) of a pentapeptide (HCDLP) to recombinant *S. coelicolor* NiSOD that lacks the five N-terminal residues and features an N-terminal Cys residue (NΔ5-NiSOD) to produce a variant (H1*-NiSOD), wherein the backbone Cys2 amidate N-donor ligand is altered to a secondary amine.[177] This strategy preserved the backbone N-atom in the protein while altering its chemical properties, including the loss in negative charge of the ligand and the ability to engage in π-bonding.[177] The expected role of the carboxamide ligand is to promote Ni-centered rather than S-centered Ni redox in the Ni(III) electronic structure.[177]

The Ni and S content were determined by ICP-OES and indicted 84% Ni loading into H1*-NiSOD. The protein was analyzed by XAS to reveal a 1s → 4p transition at 8336 eV and no 1s → 3d transition, indicating square-planar Ni coordination. EXAFS analysis specified two N donors (1.98(2) Å) and two S donors (2.14(2) Å). UV-vis spectroscopy is similar to WT-NiSOD, but lacks a ligand-to-metal charge transfer (LMCT) transition (CysS → Ni(III) at 380 nm, consistent with the sample being mostly reduced. These spectroscopic features are similar to the dithionite reduced WT enzyme and other planar nickel complexes and suggest that H1*-NiSOD is structurally very similar to WT-NiSOD and the electronic structure is minimally perturbed by alternation of the carboxamide ligand to a secondary amine.[177]

The EPR spectrum of as-isolated H1*-NiSOD in air revealed a weak, nearly axial signal that accounts for 11% of the nickel in the sample by spin integration (g_x = 2.27, g_y = 2.22, and g_z = 2.02) with hyperfine attributed to the apical His1 imidazole N-donor ligand resolved on g_z, (A_{zz} = 24.2 G). This signal is distinct from rhombic spectrum observed for recombinant WT-NiSOD and semisynthetic WT-NiSOD (g = 2.30, 2.23, and 2.01, A_{zz} = 24.9 G). Thus, the resulting sample contains both Ni(III) and Ni(II) centers, but at a lower Ni(III)/Ni(II) ratio (11%) than the recombinant WT enzyme (50%). The EPR data is consistent with low-spin d^7 Ni with the unpaired electron residing in d_{z2} orbital, similar to WT-NiSOD, but with a more axial signal than rhombic, arising from shift in g_x values from 2.30 to 2.27. The more signal difference is likely due to the change in electronics from the amine-N; the carboxamide N-donor is expected to raise the energy of π-symmetry Ni 3d orbital through a filled π-π interaction that is not present for an amine N-donor, and would perturb the d_{xz} and d_{yz} interactions.[177]

Catalysis was determined by pulse-radiolytically generated $O_2^{\bullet-}$, where the rate constant was measured by monitoring the disappearance of the radical feature at 260 nm. H1*-NiSOD

had a k_{cat} = 5.6 × 10^6 M^{-1} s^{-1} at pH 7.5, which is only 1% of that observed for the recombinant WT NiSOD. The $E_{1/2}$ of H*1-NiSOD was also calculated to be to 0.350 V vs NHE, which is cathodically shifted from WT-NiSOD ($E_{1/2}$ = 0.290 V). TThe higher potential is in-line with the greatly reduced catalytic activity, as it is harder to access Ni(III) and thus inhibits the reduction of $O_2^{\bullet-}$ to H_2O_2. Therefore, the electronic contributions from a mixed carboxamide/amine donor set is essential is achieving full catalytic activity in NiSOD.[177]

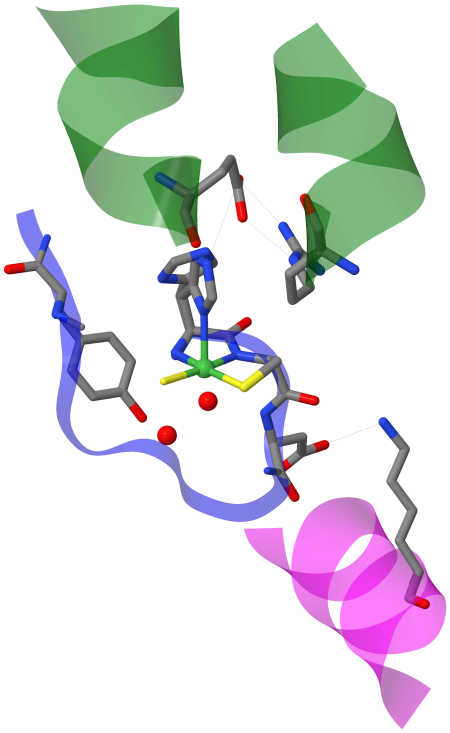

Figure 1.16. X-ray crystal structure of NiSOD where the reduced and oxidized states are superimposed from *S. coelicolor* showing primary and secondary sphere residue interactions (1.30 Å resolution, PDB 1T6U, Jmol). Ni is modeled as a green sphere. H_2O is modeled as red spheres.

Tyr9 has been proposed as a "gatekeeper Tyr" to control anion access to the active site of NiSOD.[146] In the oxidized state of the enzyme, Tyr9 is located opposite the coordinated His1 with a Ni···O distance of 5.47 Å and also participates in H-bonds between two ordered H_2O molecules (Figure 1.16).[35,36] These H_2O molecules have Ni···O distances of 2.57 and 3.15 Å and are H-bonded to Cys6 and Asp3 via peptide-NH protons.[35] There are multiple mechanisms to control anion access to the active sites of SODs such as: (i) size constraint; (ii) electronic steering; and (iii) a "gatekeeper Tyr" and neighboring phenylalanine that is found in Mn- or FeSOD.[161,162,178,179] Maroney and coworkers carried out mutations that perturbed the key conserved Tyr9 (Y9F-NiSOD) residue and Asp3 (D3A-NiSOD) (Table 1.2).[146] These mutants were structurally assessed by EPR and XAS spectroscopies and X-ray diffraction (XRD) and their catalytic activity was assessed.[146]

The Y9F-NiSOD mutant represents the first anion complex of NiSOD that has been structurally characterized, as the structure reveals a Cl^- or Br^- anion close to the Ni ion (Ni···Cl distance 3.5 Å).[146] This suggests a potential anion pocket for the substrate to access Ni with the peptide–N atoms of Asp3, Cys6 and Gly7 are oriented towards the Cl^- or Br^- and are all < 4 Å away.[146] These halide ions are not capable of binding to Ni and therefore provide evidence for a potential outer-sphere mechanism.[146] This mutant has high thermal stability with a scanning melting temperature (T_m) value (86.3 ºC) that compares well to WT enzyme (84.8 ºC).[146] EPR spectroscopy revealed a similar rhombic signal, and integration reveals an approximate 1:1 ratio between Ni(II) and Ni(III), as seen in WT enzyme.[146] Interestingly, XAS characterization of the fully reduced Y9F mutant by sodium dithionite ($Na_2S_2O_4$) reveals two S-donors at very different distances (2.23 and 2.52 Å), contrary to the WT enzyme where both S-donors have similar Ni–S distance (2.16 – 2.19 Å).[146] Loss of the –OH group results in replacement of one of the H-bonded

H_2O with Cl^- or Br^-. This mutation results in loss of the H-bond network near the Ni-hook and therefore perturbs the S-donors, potentially resulting in a mixture of octahedral and square-planar Ni(II).[146] Mutation of the "gatekeeper Tyr" does not perturb the redox potential of the Ni ion (WT-NiSOD $E_{1/2}$(Ni(III/II)) = 286 mV), which is consistent with mutation of Tyr34, the "gatekeeper Tyr" in MnSOD.[146,180] While catalytically active, the Y9F mutant has ~63% of the activity of WT-NiSOD.[146] Surprisingly, at substrate concentrations higher than 5-fold excess, Y9F exhibits saturation kinetics, where the half-life of $O_2^{\bullet-}$ is 41% of the half-life at low substrate concentration.[146] Potentially, the increase in the binding pocket size by elimination of the Tyr–OH group allows other anions to compete with $O_2^{\bullet-}$, but ionic strength measurements utilizing Cl^- and ClO_4^- did not change from WT-NiSOD, suggesting that small anions are not competing with $O_2^{\bullet-}$.[146] It is also proposed that Tyr9 could play a role in preventing H_2O_2 binding and therefore promote product release. This steric blocking would prevent interaction of H_2O_2 with Ni or Cys2/Cys6, and mutation of Y9F may result in saturation behavior due to loss of this function.[146] Alternatively, loss of Tyr may perturb a H^+ donating mechanism to form H_2O_2.[146]

Site-directed mutagenesis of Asp3 to Ala3 provides insight into the intermolecular H-bonds among trimer subunits and Tyr9, as both were perturbed in this variant.[146] Analysis of the D3A-NiSOD mutant reveals that a large amount of monomeric protein was present in the ESI-MS and exhibited a lower T_m (73.9 ºC) compared to WT enzyme (84.8 ºC), indicating weakened interactions between the monomeric subunits.[146] Analogous to the Y9F mutant, EPR analysis showed no change in the electronic structure of the Ni(III) ion, and spin integration revealed a 1:1 ratio between the Ni(III) and Ni(II) states.[146] XAS analysis reveals that the Ni–S distance is 0.03 Å shorter in D3A-NiSOD than in WT-NiSOD, which may be a result of perturbation of the

Ni-hook.[146] Mutation D3A disrupts an intersubunit salt bridge between ion pairs Asp3-Lys89 (H-bond) and Glu4-His53 (H_2O-mediated H-bond) spanning neighboring subunits.[146] This interaction is mirrored to involve 12 ion pairs holding together the dimer of trimers in the hexameric protein (Figure 1.17).[35,36] The absence of the C=O of Asp3 in D3A-NiSOD results in the loss of the H-bond with Lys89 of the opposing trimer.[146] As a consequence, Lys89 and neighboring Glu49 are both shifted ~2.0 Å closer to Ala3, which disrupts the interaction between Glu49 and His53. The loss of this salt bridge likely is responsible for the lack of quaternary stability.[146]

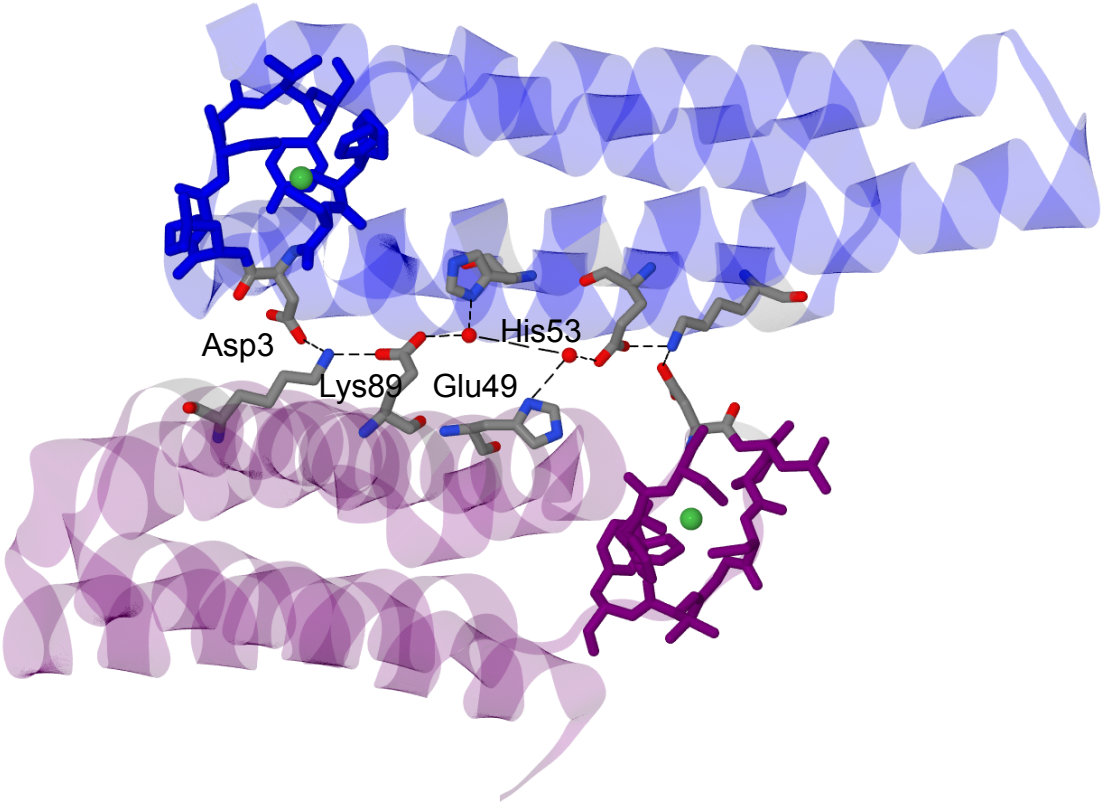

Figure 1.17. Depiction of intersubunit interactions between the dimer of trimers from *S. coelicolor* NiSOD (1.30 Å resolution, PDB 1T6U, Jmol).

This D3A mutation also shifts Tyr9 ~1 Å closer to Ni (WT-NiSOD: Tyr–O–Ni 5.47 Å; D3A-NiSOD Tyr–O–Ni 4.26 Å) resulting in loss of an ordered H_2O in the proposed binding pocket.[146] D3A-NiSOD exhibited sensitivity towards H_2O_2, as SOD catalytic activity was not measureable when incubated with H_2O_2 for 5 min, whereas the activity of WT-NiSOD was unaffected.[146] The ESI-MS was unchanged after incubation with H_2O_2, eliminating the possibility of oxidative damage to the protein; however, EPR spectroscopy revealed a Tyr radical (g = 2.004) representing ~8% of the enzyme, which was confirmed to be Tyr9 by d_4-Tyr.[146] The H_2O_2-activity of D3A-NiSOD supports the possibility that Tyr9 plays an important role in destabilizing the H_2O_2, as the movement of the Tyr9 in the binding pocket may stabilize a Ni–OOH peroxo that is capable of oxidizing Tyr9.[146]

Taken together, these two mutations affect the function of NiSOD and provide evidence of Tyr9 acting as a "gatekeeper Tyr" to control or prevent anion access to the active site.[146] For Y9F, k_{calc} is decreased and exhibits saturation behavior, while D3A loses quaternary stability and forms a Tyr9 radical when incubated with H_2O_2. Indeed, neither D3A or Y9F cause major changes in the overall structure of the enzyme, but they do significantly affect the catalytic activity of these mutants, suggesting important roles in catalysis.[146]

The role of His1 and the H-bond network involving the intersubunit H-bond between His1 and Glu17 and the intrasubunit H-bond between Glu17 and Arg47 was also assessed via site-directed mutagenesis (Figure 1.17).[35,36,181] Interestingly, while His1 is oriented in both a Ni(III)-His_{on} and Ni(II)-His_{off} coordination the Ni, its H-bond with Glu17 is maintained in both oxidation states of the enzyme.[35,36] Maroney and coworkers explored this H-bond network via a family of mutants (H1A, R47A, E17R/R46E, E17A/R47A): H1A-NiSOD eliminates the axial His1 ligand of the Ni ion and the His1-Glu17 H-bond; R47A-NiSOD removes the H-bond

between Glu17 and Arg47; E17R/R47E-NiSOD omits the H-bond between His1 and Glu17 while maintaining an H-bond between Glu17 and Arg47; and E17A/R47A-NiSOD disrupts both the inter- and intramolecular H-bonds (Table 1.2).[181]

The H1A-NiSOD mutant eliminates the axial His ligand, but coordinates in an N_2S_2 ligand environment based on XAS. The H1A mutant exhibits distorted coordination based upon XRD evidence, and it exhibits 4% of the catalytic activity of WT-NiSOD.[181] Additionally, The H1A-NiSOD variant only loaded 0.19 Ni:monomer ratio. SEC reveals a homohexameric protein, suggesting no disruption of the overall structure, and has a melting point (T_m = 77.8 ºC), ~10 ºC lower than WT-NiSOD (88.0 ºC).[181] XAS data for H1A-NiSOD exhibits a Ni 1s→3d transition (8331 eV) and a Ni 1s→4p_z (8336 eV) transition, correlating to a square-planar geometry, with two N and two S scatterers, supporting the expected N_2S_2 environment in this variant.[181] There was no detectable Ni(III) signal in the EPR spectrum, and addition of exogenous imidazole did not yield an EPR-active species.[181] However, an octahedral Ni(II) site with a Ni 1s→3d transition (8331 eV) that lacked the Ni 1s→4p_z (8336 eV) transition was confirmed by XAS.[181] The overall crystal structure of the H1A-NiSOD variant has an unresolved "Ni-hook" motif similar to that of the apo-enzyme.[181] This disorder suggests that the His1···Glu17 H-bond plays an important role in establishing order to Ni-binding and may prevent formation of an octahedral Ni(II) ion by orienting Val8 to impede coordination in the sixth position.[181] The catalytic activity of H1A-NiSOD was not enhanced upon addition of imidazole.[181]

The role of His1 was also explored via DFT computational methods (B3LYP) where the models are composed of Ni coordination to His1, Cys2, and Cys6.[144] The computational models **red** = reduced and **ox-His$_{off}$** have identical ligand contributions, whereas **ox-His$_{off}$** has been oxidized by one electron, but does not contain an axial His1 ligand.[144] This experimental data

from H1A-NiSOD correlate to the **red** and **ox-His$_{off}$** computational models and together reveal that the Ni–NHis1 bond is essential in promoting Ni-centered over S-centered redox reactivity.[144,181] The H-bond network among His1, Glu17, and Arg47 was also explored via computational models of NiSOD$_{ox}$ containing His1, Cys2, and Cys6 and a Ni–NHis1 bond.[144] The models are **ox^1**, with no H-bonding to His1; **ox^2**, containing two H-bonds between His1-Glu17 and Glu17-Arg47; and **ox^3**, composed of an H-bond only between His1-Glu17.[144] These models reveal that H-bonding causes lengthening of the Ni–NHis1$_{imidazole}$ bond from **ox^1** (2.07 Å), where **ox^3** has the largest distance (2.16 Å) and **ox^2** is slightly shortened (2.14 Å), as the H-bond with Arg46 reduces the H-bond accepting ability of Glu17. Based on computations, it has been proposed that this H-bond network may tune the length of the Ni–NδHis1$_{imidazole}$ bond distance by tuning the energy of the Ni 3d$_{z2}$ orbital.[144] The Ni–HisN distance in the crystal structure of NiSOD$_{ox}$ is relatively long (2.3-2.6 Å), which may be explained by the heterogeneity in the crystal structure, due to the presence of both Ni(II) and Ni(III) centers.[35,36]

In the R47A-NiSOD variant, the intramolecular H-bond between Glu17···Arg47 was removed, but the intermolecular H-bond between His1···Glu17 was preserved.[181] This mutant most closely resembles the computational model **ox^3**, which was shown to have a longer Ni–N$_{imidazole}$ bond due to the increased His1···Glu17 interaction.[144] This elongation was confirmed by experiment, where EXAFS analysis revealed that the Ni–N is 2.19(7) Å. For the variants E17R/R47E- and E17A/R47A-NiSOD, the His1···Glu17 is eliminated and resembles the computational model **ox^1**, which predicts a short Ni–N$_{imidazole}$.[144,181] This was confirmed by EXAFS that revealed a Ni–N$_{imidazole}$ bond length of 1.97(5) Å for E17A/R47A-NiSOD and 2.12(3) Å for E17R/R47E.[181] Additionally, these H-bond variants perturb the ratio of Ni(III) and Ni(II), while also decreasing SOD activity.[181] These decreases in Ni(III) content and activity

trend according to the disruption of the H-bond network (R47A < E17R/R47E < E17A/R47A) where the percentage of Ni(III) is ~15, ~8, 0%, respectively, and the order of catalytic activity is reduced by a factor of ~5, ~6, and >10-fold, respectively.[181] This highlights the importance of these H-bonds in accessing and stabilizing a catalytic Ni(III) state.[181] In addition to perturbing the Ni–$N_{imidazole}$ bond and destabilizing the Ni $3d_{z2}$ orbital, the His1···Glu17 interaction also plays an important role in ordering the "Ni-hook" in order to coordinate Ni and prevent axial ligation to form a 6C species.[181]

Table 1.2 Summary of NiSOD mutant properties. Quaternary structure stability was assessed based on [a]size exclusion chromatography (SEC) or [b]ESI-MS.

NiSOD	**Quaternary structure stability:**	**k_{cat} at pH 7.5 ($\times 10^9$ $M^{-1}s^{-1}$)**	**T_m (°C)**	**$E_{1/2}$ (mV vs NHE)**	**Ni(III) EPR integration**
WT	[a]hexamer	0.55	84.8	286	~50%
D3A	[b]hexamer; monomer	0.209	73.9	308(3)	–
R47A	[a]hexamer	0.121	76.4	–	~15%
E17R/R47E	[a]hexamer; trimer	0.095	67.5	–	~8%
E17A/R47A	[a]hexamer; trimer	0.036	68.5	–	silent
Y9F	[b]hexamer	0.371	86.3	297(5)	–

In summary, NiSOD contains a unique set of donor atoms and choice of metal ion to carry out catalysis of ROS. The combination of mixed carboxamide/amine N-donors, two S-thiolates, and axial His are essential for achieving catalytic activity and contributed significantly to the enzyme's spectroscopic properties (UV-vis, EPR). The electronic structure indicates highly covalent Ni/S interactions via strong antibonding Ni(dπ)-S(pπ) interactions in the NiSODred and antibonding Ni-d_{z2}(dσ)-N(pσ) of His in NiSODred. In addition to the primary sphere residues, a number of secondary sphere H-bonding interactions have been identified as essential for maintain catalytic activity and stability of NiSOD and modulating electron density at the active site. The role of these H-bonding interactions and potential protonation or H-bonding to the cysteine thiolates are likely mechanisms for stabilizing S-based molecular orbitals (MOs) and thereby increase Ni-charactere and decrease S-nucleophilicity.

1.3 NiSOD Small Molecule Complexes

1.3.1 Peptide Maquettes and Small Molecule Complexes

The first maquette (metallopeptide) mimic of NiSOD was reported by Shearer and coworkers in 2006 and consisted of the apo-peptide SOD^{M1} representing the first 12 residues from the N-terminus of NiSOD (SOD^{M1} = H_2N–HCDLPCGVYDPA-COOH) (Figure 1.18). Coordination of SOD^{M1} to Ni(II) from $NiCl_2$ under anaerobic conditions was determined to be pH dependent; Ni(II) successfully coordinated to the peptide in a 1:1 ratio to form $NiSOD^{M1}$ (**1**) (0.1 M PBS, pH 7.2), but not when pH ≤ 6, as monitored by UV-vis spectrophotometric titration.

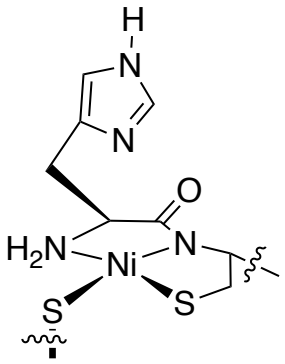

1 and 2

Figure 1.18. Abbreviated structure of Ni(II) coordination to maquettes $NiSOD^{M1}$ (**1**) and $NiSOD^{M2}$ (**2**). Wavy lines indicate continuation of the peptide.

Monomer formation was confirmed by gel permeation chromatography (GPC), and CD spectroscopy revealed a random coil structure in the peptide with some β-turn character. The K_d was calculated to be 1 μM, which was determined spectrophotometrically with Gly as a competitive Ni(II) chelator.[182] ^{1}H NMR indicated that the Ni(II) ion is diamagnetic and no broadening occurs, even when exposed to air, although attempts to oxidize **1** led to degradation. UV-vis spectroscopy reveals absorbances at 337, 458, 552, and 662 nm. Correlating to weak ligand-field transitions and $Ni(3d_{xy})/S(\pi)^* \rightarrow Ni(3d_{x2-y2}/S/N(\sigma))^*$ CT found in $NiSOD_{red}$.[183] Ni K-edge XAS of **1** displays a $1s \rightarrow 4p_z$ transition at 8337.4(2) eV and a $1s \rightarrow 3d$ transition at 8332.9(4) eV, while EXAFS analysis indicated two Ni–N and two Ni–S scatterers at 1.93(2) Å and 2.180(2) Å, respectively, that are consistent with a $Ni(II)N_2S_2$ square-planar complex. Electrochemistry was carried out via protein thin-film voltammetry on a carbon fiber ultramicroelectrode where $E_{1/2}$ Ni(III/II) = 0.710 V vs NHE. SOD disproportionation was measured via the para-nitro blue tetrazolium chloride (NBT)/formazan assay, where NBT reacts

with $O_2^{\bullet-}$ to form formazan (λ_{max} = 580, ε = 35,000 M^{-1} cm^{-1}). Formazan was not produced upon the reaction of **1** with 2800 equiv of $O_2^{\bullet-}$, indicating $O_2^{\bullet-}$ scavenging behavior, although the maquette undergoes degradation after 90 s and the nature of the reaction (Ni-based redox vs ligand modification) is undefined (Table 1.3).

In another peptide maquette, Shearer shortened the peptide fragment to the first seven residues of the Ni-hook, denoted as SOD^{M2} = H_2N–HCDLPCG–COOH (Figure 1.18).[183] The peptide coordinated in a 1:1 Ni-peptide ratio with a K_d for **2** of 5(1) μM, which compared well to **1** (K_d = 1 μM).[183] The UV-vis spectrum of **2** likewise compared well to **1** with λ_{max} = 361 (ε = 656 M^{-1} cm^{-1}), 457 (ε = 345 M^{-1} cm^{-1}), 548 (ε = 130 M^{-1} cm^{-1}), 823 nm (ε = 50 M^{-1} cm^{-1}).[183] Ni K-edge XAS also indicated a Ni(II) square-planar complex with a 1s → 3d transition at 8331.1(1) eV and a 1s → $4p_z$ transition at 3883.3(1) eV. EXAFS analysis indicated two Ni–N scatterers at 1.875(3) Å and two Ni–S scatterers at 2.176(3) Å.[183] Cyclic voltammetry (CV) indicated a quasi-reversible Ni(III/II) redox couple at 0.790 V vs NHE.[183] While no Ni(III) complex was isolated, a putative Ni(III) species was trapped after adding substoichiometric KO_2 to yield an EPR spectrum consistent with a five-coordinate Ni containing an axial N-donor (g_x = 2.32; g_y = 2.26; g_z = 2.02; A_{zz} = 25.2 G), that compares well to $NiSOD_{ox}$ (g_x = 2.30; g_y = 2.24; g_z = 2.01; A_{zz} = 24.9 G).[183] The xanthine/xanthine oxidase assay was carried out, and an IC_{50} value of IC_{50} = 1(1) × 10^{-6} M was reported, which represents the concentration of an SOD active compound required to cause a 50% reduction in the rate of formazan production.[183] Additionally, DFT data on **2** suggest that the axial His remains coordinated during catalysis to avoid reorganization energy, as movement of the His would be unlikely due to the fast (diffusion-controlled) rate of catalysis (Table 1.3).[175,183]

Table 1.3 Summary of selected maquette properties.

Complex	UV-vis λ_{max}, nm (ε, M^{-1} cm^{-1})	Ni–S (Å)	Ni–N (Å)	$E_{1/2}$ (vs NHE)	k_{cat} (M^{-1} s^{-1})
1	485 (355)	2.180(2)	1.93(2)	710 mV	inactive
2	457 (345	2.176(3)	1.875(3)	790 mV	$1(1) \times 10^7$
6	416 (1530)	2.174(3)	1.846(4)	519 mV	inactive
7	459 (427)	2.166(1)	1.898(6)	866 mV	inactive
8	456 (418)	2.168(4)	1.874(8)	680 mV	inactive
9	460 (405)	2.174(2)	1.87(2)	797 mV	$6(2) \times 10^8$
10	464 (410)	2.179(2)	1.89(1)	669 mV	$3(2) \times 10^8$
11	461 (360)	2.182(1)	1.91(1)	481 mV	$6(1) \times 10^6$

A question that remains about the coordination sphere of NiSOD is its unprecedented usage of a deprotonated carboxamide and neutral primary amine as ligands. Researchers have probed the role of the mixed carboxamide/amine coordination by synthesizing and characterizing a series of Ni(II)N_2S_2 complexes containing bis-carboxamide, mixed carboxamide/amine, and bis-amine coordination to elucidate the role of this unique combination of N-ligands in NiSOD. A DFT study (B3LYP TZVPP) compared isostructural Ni(II)N_2S_2 models with variable N-ligands, i.e., dicarboxamide **[Ni(emi)]$^{2-}$] (3)**, emi = *N*,*N*′-ethylenebis-2- mercaptoisobutyramide, a carboxamide/amine **[Ni(BEAAM)]$^-$ (4)**, BEAAM = *N*-{2-[benzyl-(2-mercapto-2-methyl-propyl)-amino]-ethyl}-2-mercapto-2-methyl- propionamide **(4)**, and a diamine **[Ni(bmmp-dmed)] (5)**, bmmp-dmed = *N*,*N*′-bis-2-methyl-mercaptopropyl-*N*,*N*′-dimethylethylenediamine (Figure 1.19).[145,150,152,184,185]

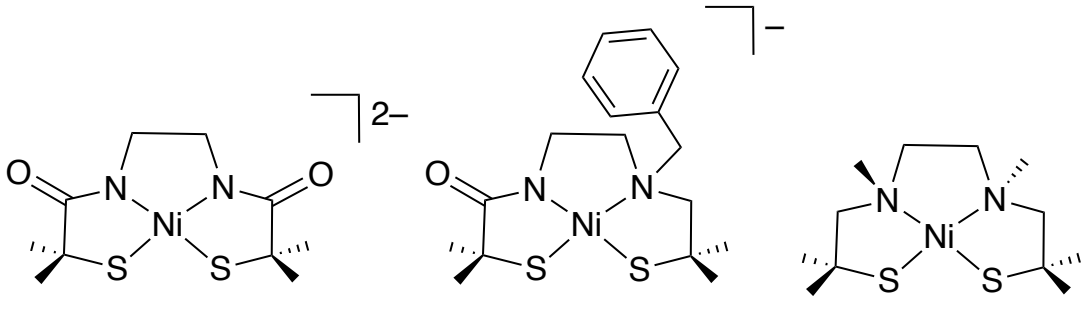

Figure 1.19. Structures of the NiSOD model complexes **3**, **4**, and **5**.

This study revealed that the Ni(π)/S(π)* HOMO increases in energy and in S-character with the increasing number of anionic carboxamide groups: **5** = 74.4% S, **4** = 50.3% S, and **3** = 31.0% S. It was proposed that a biscarboxamide NiN_2S_2 complex would favor Ni-based redox due to the decreased S-character, although the S-donors of a biscarboxamide complex are more prone to S-oxidation. These results are consistent with the increased O_2 reactivity of biscarboxamide vs mixed carboxamide/amine small model complexes.[148,150]

In order to probe the electronic effects of different N-donors, Shearer modified the ligands of **1** by acylating the N-terminus to create a biscarboxamide coordination sphere, **[Ni(SOD^{M1}-Ac)] (6)** (Figure 1.20).[182] Similarly to **1**, **6** coordinated to Ni(II) in a 1:1 ratio at basic pH, where Ni binding was strong at pH 7.5, but no binding occurred below pH 6.2.[182] **6** required a slightly higher pH to coordinate Ni, as **1** (pH 7.2), which is consistent with the requirement to deprotonate two carboxamide-N.[182] **6** exists as a monomer based on ESI-MS and GPC.[182] Ni K-edge XAS confirmed a square-planar NiN_2S_2 species with a weak Ni 1s→3d transition at

8331.9(3) eV and a more intense Ni 1s→4p_z transition at 8339.6(2) eV. EXAFS fitting analysis supports two Ni–N scatterers at 1.846(4) Å and two Ni–S scatterers at 2.174(3) Å.[182] A quasi-reversible Ni(III)/Ni(II) redox couple occurs at 0.519 V vs NHE, a –0.2 V shift from **1** (0.710 V vs NHE). DFT analysis suggests a decrease in Ni/S covalency and lowered S-character in the acylated metallopeptide.[182] The xanthine/xanthine oxidase assay was carried out, which revealed that **6** is less active (IC_{50} = 3(1) × 10^{-5} M) than **1** (IC_{50} = 2(1) × 10^{-7} M) by over two orders of magnitude, providing further evidence that the mixed carboxamide/amine ligation is required for catalysis (Table 1.3).[182]

Modifications of the axial His were carried out on the maquette system **2** by replacing His1 with Ala (H(1)A) or aspartic acid Asp (H(1)D) to form **[Ni(SOD^{M2}H(1)A)] (7)** and **[Ni(SOD^{M2}H(1)D)] (8)**, respectively (Figure 1.20).[183] Both maquettes exhibited similar Ni K_d values to the parent maquette system, **7** (K_d = 6(3) μM) and **8** (K_d = 7(3) μM), suggesting that changing the axial ligand does not change the Ni affinity or binding mode in these maquettes.[183] The UV-vis and CD spectra compared well to **2**, in which the characteristic λ_{max} owing to the Ni($3d_{xy}$)/S(π)* → Ni($3d_{x2-y2}$/S/N(σ))* transition occurs at 459 nm for **7**, 456 nm for **8**, and 457 nm for **2**. XAS/EXAFS analysis also confirmed that both **7** and **8** coordinate as a Ni(II)N_2S_2 square-planar species.[183] CV indicated a quasi-reversible Ni(III/II) couple for **7** at 0.866 V vs NHE, which is a ~ 0.1 V cathodic shift from **2**, while **8** has a quasi-reversible Ni(III/II) couple at 0.680 V vs NHE, which is anodically shifted ~0.1.[183] The mutations also have similar IC_{50} values (IC_{50} **7** = 3(2) × 10^{-5} M; IC_{50} **8** = 5(2) × 10^{-6} M;), although later reports reveal that **7** is catalytically inactive, suggesting the axial His is required for catalysis, as observed in enzyme mutations (vide supra).[183,186]

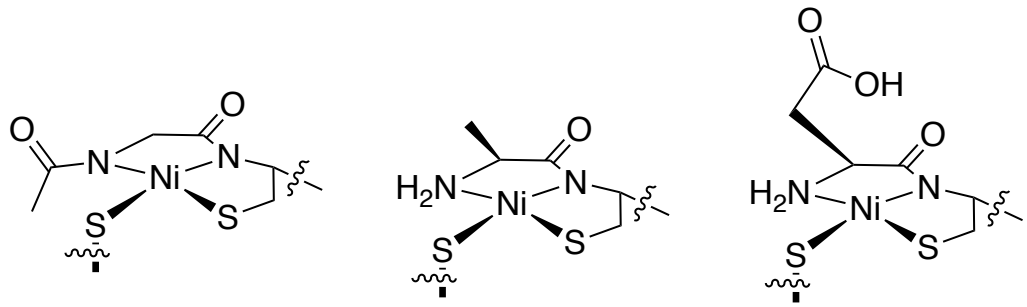

Figure 1.20. Abbreviated structure of Ni(II) coordination to maquettes **6** , **7**, and **8**. Wavy lines indicate continuation of the peptide.

The His1 imidazole was modified by incorporating electron-withdrawing groups to Nε, including tosyl (**[Ni(SOD^{M1}-tos)] (9)**) and 2,4-dinitrophenol (**[Ni(SOD^{M1}-DNP)] (10)** (Figure 1.21). Adding electron-withdrawing groups resulted in a weaker Lewis-basic His with diminished Ni(III)–NHis interactions based on the smaller A_{zz} values (67 and 55 MHz, respectively, compared to 81 MHz for **1**), increased energy in the Ni(III)–S resonance Raman (rR) vibrational modes, and weaker calculated Ni(III)–His force constants ($f_{Ni–His}$ (mdyn Å^{-1}) = 0.22 and < 0.1, respectively, as opposed to 0.52 for **1**.[187] In contrast, a maquette incorporating an electron-donating methyl group (**[Ni(SOD^{M1}H(1)H^{Me})] (11)**) (Figure 1.21), where SOD^{M1}H(1)H^{Me} = H_2N-HMeCDLPCGVYDPA, H^{Me} = Nε-methylhistidine, resulted in a stronger Lewis-basic His with a stronger Ni(III)–His interaction (A_{zz} = 83 MHz; $f_{Ni–His}$ mdyn Å^{-1} = 0.74).[187] Taken together, this data is in-line with the mutations and calculations carried out on His modifications in NiSOD and suggest that His plays an electronic modulating role in order to poise the Ni ion for catalysis, as the length of the Ni–HisN distance in the crystal structure of $NiSOD_{ox}$ is 2.3-2.6 Å.

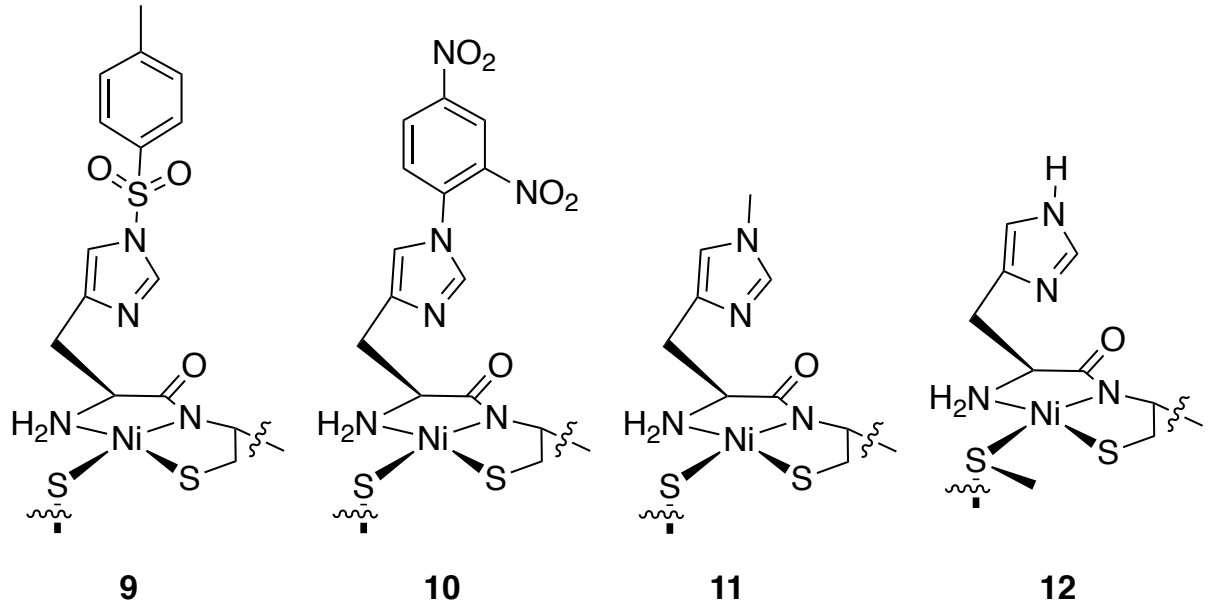

Figure 1.21. Abbreviated structure of Ni(II) coordination to maquettes **9**, **10**, **11**, and **12**. Wavy lines indicate continuation of the peptide.

The mechanism of **11** was investigated in light of the catalytic activity, $k = 6(1) \times 10^6$ M^{-1} s^{-1} at pH 8.0 to probe the role of H^+ donation in the H_2O_2 generating SOD half reaction of NiSOD.[187,188] The reaction carried out in D_2O revealed a solvent kinetic isotope effect (KIE) of 20(4) with a $k_{cat}(D_2O) = 3.1(2) \times 10^5$ M^{-1} s^{-1}, indicating a PCET step.[188] After carrying out experiments to determine the temperature-dependence of k_{cat}, Arrhenius analysis suggests a barrierless reaction with an activation of 0.042(4) cal/mol, which is consistent with a tunneling mechanism.[188] Reactions of **11** with ascorbate (bond dissociation free energy (BDFE) = 73.6 kcal/mol) and TEMPO-H (1-hydroxy-2,2,6,6-tetramethylpiperidine, BDFE = 71.0 kcal/mol), resulted in reduction of Ni(III) to Ni(II), which was reversed with addition of TEMPO$^{\bullet}$ to **11** (Ni(II)) (Scheme 1.9).[188] No reaction occurred with **11** (Ni(III)) and 1,4-dihydroquinone (BDFE = 81.5 kcal/mol) or hydrazine (BDFE = 83.4 kcal/mole), suggesting that there is an H-atom

acceptor site on **11** that has a BDFE = 70-80 kcal/mol (BDFE of cysteine in H_2O = 87 kcal/mol).[188] This site was confirmed via an equilibrium reaction between TEMPO-H and **11** (Ni(III)) with an equilibrium constant K = 26.5(8) at 25.0 ºC and a ΔG = –1.9(7) kcal/mol, translating to a BDFE for the **11** S–H bond = 73(1) kcal/mol.[188] A similar BDFE value was calculated to be ~79 kcal/mol using the $E_{1/2}$ Ni(III/II) (440 mV vs NHE) and pK_a ~ 8.2.[188] These BDFE values are less than the BDFE (O–H) of HO_2^- (81.6 kcal/mol) meaning the reduction of $O_2^{\bullet-}$ through a PCET reaction with **11** is thermodynamically viable.[188] Additionally, S K-edge XAS studies revealed that the absorption spectrum for **11** at pH 9.5 has a pre-edge feature from the S(1s)→Ni(3d)/S(s)* at 2470.4(1) eV and a S(1s)→S(C-Sσ*) transition at 2472.6(1) eV; at pH 7.4 the pre-edge feature disappears and significant broadening occurs for the S(1s)→S(C-Sσ*) transition, suggesting protonation at the one or both of the Cys thiolates.[188] Taken together, this suggests that **11** is catalytically active via a rate-limiting PCET mechanism with a tunneling component, with some evidence that the H-atom comes from a coordinated CysSH moiety.[188] (Table 1.3).[186,188]

Scheme 1.9. Equilibrium reaction between **11** and TEMPO–H.

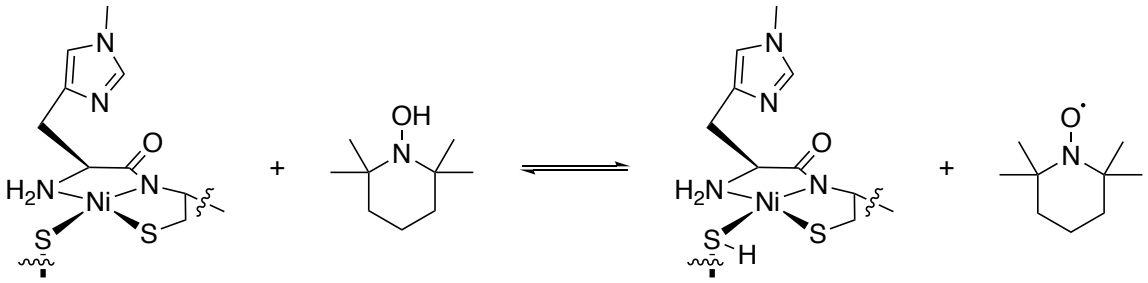

11 **11-H$^+$**

In order to identify the S-thiolate involved in protonation, Shearer and coworkers prepared the S-methylated variant of **1**, namely **[Ni(SOD^{M1}Cys(6)Cys^{Me})] (12)**, where C^{Me} = S-methylcysteine. (Figure 1.21) Cys6 appeared to be the likely site of protonation, as attempts to coordinate Ni(II) to mono-methylated Cys(2)Cys^{Me} or dimethylated Cys(2/6)Cys^{Me} derivatives were unsuccessful.[189] Additionally, computational models indicate that **[Ni(II)(SOD-Cys(6)H$^+$)] (13)** is thermodynamically more stable (ΔG = –4.5 kcal/mol) than **[Ni(II)(SOD-Cys(2)H$^+$)] (14)** (Figure 1.22).[189] Ni K-edge XAS confirmed a square-planar NiN_2S_2 coordination environment for **12** with a small Ni(1s→3d) transition (8331.8(2) eV) and a more intense Ni(1s→4p) transition (8337.7(1) eV) with two Ni–S scatterers (2.19 Å) and two Ni–N scatterers (1.91 Å), but this complex was not redox active from –0.2 to 1.0 V vs NHE.[189] Four computational models were created to probe the electronic effects of thiolate protonation: (i) **[Ni(II)(SOD)]$^-$ (15)**, an approximating model of $NiSOD_{red}$ with Ni(II) coordinated to 2-amino-*N*-(2-mercaptoethyl)-acetamidate; (ii) **[Ni(II)(SOD-Cys(6)Me] (16)**, a methylated variant; (iii) **[Ni(II)(SOD-Cys(6)H$^+$] (13)**, a protonated variant; and (iv) **[Ni(II)(SOD-Cys(6)H$^+$)···H$_2$O] (17)** a protonated variant with an H-bonded H_2O molecule (Figure 1.22).[189] The computational models indicate that S-methylation results in contraction of the Ni–S bond by 0.027 Å, S-protonation resulted in contraction of the Ni–S bond by 0.030 Å, and S-protonation and H-bonding to H_2O resulted in a contraction of the Ni–S bond by 0.045 Å.[189] This contraction is consistent with relief of repulsive filled/filled Ni(3dπ)–S(3pπ) interactions.[189] Molecular orbital analysis indicates that S-methylation and S-protonation yield similar electronic structures with a reduction in S-character and an increase in Ni-character in the LUMO due to reduction in Ni–S covalency upon S-modification.[189] The HOMO for both S-modified models is primarily S/N(π)–Ni(3dπ) antibonding and show a decrease in S-character with S-modification (**15:** 68.5% S; **16:** 57.4% S;

13: 57.1% S; **17:** 59.4% S.[189] The addition of the H-bonding H_2O molecule to the S-protonated model has a similar electronic structure, but with even more S-character in the LUMO due to the increased covalency in the Ni–S bond.[189] The S K-edge XAS spectrum for **12** has a feature corresponding to the thiolate S(1s) transition (2471.8 eV) with 16(4)% S-character and a feature corresponding to the thioether S(1s) transition buried in the edge.[189] The S K-edge XAS spectrum for **1** at pH 9.5 has a similar thiolate S(1s) transition (2472.1 eV) corresponding to 36(6)% S-character; however, at pH 7.4 this peak disappears and the edge broadens.[189] The increased intensity of **1** is due to the two contributing thiolate S, rather than the mixed thiolate/thioether system in **12**.[189] The low pH XAS spectrum of **1** most closely resembles the calculations for **17**, suggesting that protonation and H-bonding to H_2O may be occurring in this system.[189] To explore the role of a protonated cysteine sulfur in NiSOD, small molecule complexes with S-modifications have also been explored.

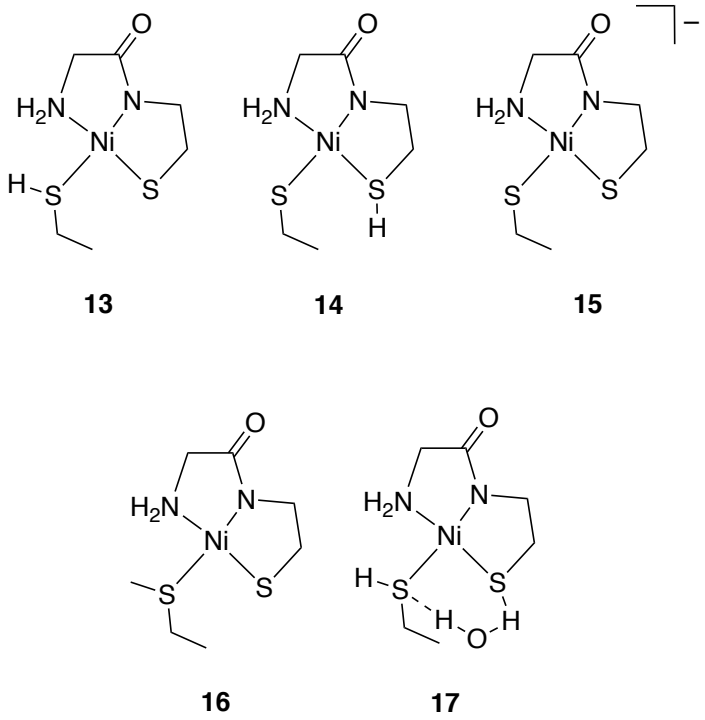

Figure 1.22. Structure of Ni(II) coordination in **13**, **14**, **15**, **16**, and **17**.

1.3.2 Sulfur site modifications in low molecular weight model complexes

Evidence of modification of a Ni-bound thiolate by a H^+ source was first reported in a dimeric, *S*,*S*-bridged complex, **$[Ni(MeN(CH_2CH_2S)_2)]_2$ (18)** (Scheme 1.10).[190] The proposed modification of the terminal thiolate ligand occurred after reaction with one equiv acid ($[H(OEt_2)_2]^+[B[3,5\text{-}(CF_3)_2C_6H_3]_4^-$] or $[H(OEt_2)_2][BAr^F{}_4]$) and exhibited no H/D exchange in the presence of D_2.[190] Titration of **18** with $[H(OEt_2)_2][BAr^F{}_4]$ revealed an isosbestic point at 327 nm, which was reversed upon addition of, diisopropylamine.[190]

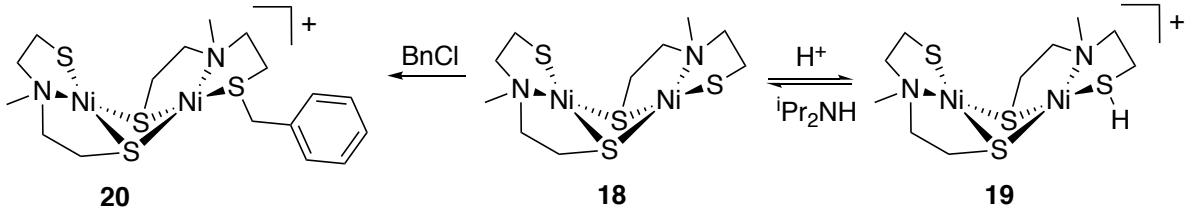

Scheme 1.10. Structures of *S*,*S*-bridged complex **18** and modeled protonation of the terminal thiolate (**19**) and alkylation (**20**).

The S K-edge XAS spectrum showed that protonation to form **19** maintains the dimeric structure with a Ni–N bond at 2.690(3) Å, but the average Ni–S bond is elongated by 0.02 Å and the Ni K-edge shifts from 8339.0(2) to 8339.8(2) eV upon protonation, consistent with a decrease in electron density at the Ni centers.[190] ^{13}C NMR of **19** indicates that protonation has

broken the symmetry of the complex, and ^{2}H NMR (CD_3NO_2) revealed a peak at 1.93 ppm, which is attributed to a protonated thiol.[190] To indicate where the H^+ may add, an analogous alkylation experiment was carried out with one equiv benzyl chloride (BnCl) resulting in monoalkylation of the terminal thiolate to form **20**. XRD revealed Ni–$S_{terminal\text{-}thioether}$ = 2.172 Å, Ni–$S_{terminal\text{-}thiolate}$ = 2.155 Å, indicating a ~0.02 Å lengthening of the Ni–S bond upon methylation.[190] Electrochemistry carried out in CH_2Cl_2 revealed irreversible oxidation features of E_{ox} = +0.390 V vs NHE (**18)**, E_{ox} = 1.2 V vs NHE (**20**), and E_{ox} = 0.960 V vs NHE (**19**), indicating a significant change of redox potential due to S-modification without large changes in structure the dimeric structure or Ni-coordination upon protonation or alkylation.[190]

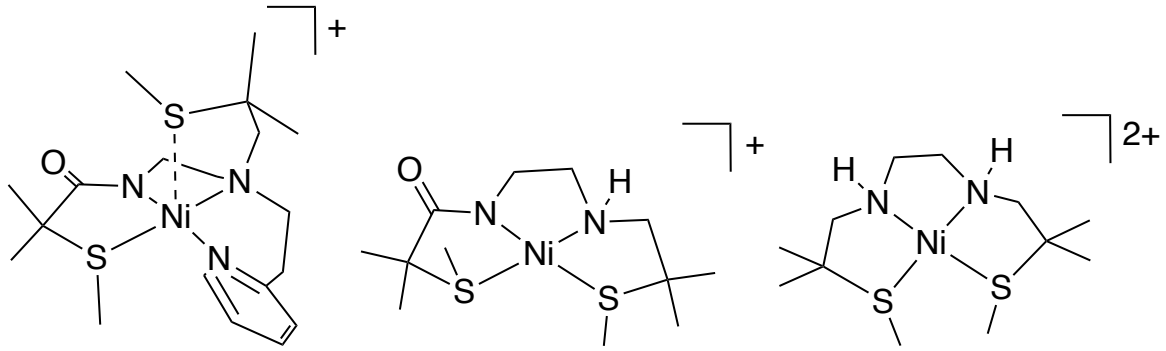

21 **22** **23**

Figure 1.23 Structures of the Ni(II) NiSOD model complexes incorporating thioether ligands **21**, **22**, and **23**.

Masuda and coworkers have synthesized a number of thioether mixed RSR/N-containing ligands, where the thioether methyl is incorporated into the ligand design, rather than

modification via methylating agents as potential NiSOD models (vide infra). Reaction of the deprotonated form of L (L = *N*-(ethylpyridyl)-*N*-(2-mercapto-2-methylpropanoyl)-*N*′-(2-mercapto-2-methylpropyl)-1,2-diaminoethane) with Ni(II) affords the pseudo square-pyramidal ($\tau = 0.06$) complex [Ni(L)] **21** from binding of L through N_3S donors in a planar fashion and a long axial interaction with one of the two thioether-S donors (Ni–S: 2.787(3) Å) (Figure 1.23).[191] This complex has been characterized via XRD to reveal distances for $Ni–N_{carboxamide}$ = 1.870(10) Å, $Ni–N_{amine}$ = 1.969(8) Å, $Ni–N_{pyridine}$ = 1.929(9) Å, $Ni–S_{equatorial}$ = 2.192(4) Å, $Ni–S_{axial}$ = 2.787(3) Å (Table 1.4).[191] The UV-vis spectrum in acetone revealed a λ_{max} absorption band at 472 nm ($\varepsilon = 250\ M^{-1}\ cm^{-1}$), which is consistent with a Ni complex containing mixed N/S donor ligands.[191] A quasi-reversible Ni(III/II) redox wave was observed at 0.99 V vs NHE; bulk oxidation of **21** with cerium ammonium nitrate (CAN) and characterization of the resulting species via EPR revealed a rhombic EPR signal (g = 2.20, 2.13, 2.01), indicating a low-spin Ni(III) ion with asymmetric coordination, but no hyperfine splitting.[191] Complex **21** successfully incorporated two thioether moieties into the ligand synthesis and coordinated to the Ni(II) ion, but the axial position of the thioether ligand and the equatorial position of the pyridine of **21** does not accurately model the active site of NiSOD.[191] This work highlights the utility of the protein scaffold in forming the Ni active site in NiSOD and also the poor donorability of the thioether ligand in coordinating Ni(II).[191]

An asymmetric N_2S_2 ligand with amine, carboxamido, and sterically hindered dithioether ligands was also synthesized by the same group. The Ni complex [Ni(L)] (**22**) (where L = *N*-(2-methylmercapto-2-methylpropanoyl)-*N*′-(2-methylmercapto-2-methylpropyl)-1,2-diaminoethane) was synthesized by coordination to Ni(II) (Figure 1.21).[192] Complex **22** was characterized by XRD to reveal a $Ni–N_{carboxamide}$ = 1.845(3) Å, $Ni–N_{amine}$ = 1.909(2) Å, $Ni–S_{trans-}$

$_{amine}$ = 2.1772(9) Å, and Ni–$S_{trans\text{-}carboxamide}$ = 2.1692(10) Å.[192] The UV-vis spectrum of **22** has a λ_{max} (acetone) = 436 nm (ε = 390 $M^{-1}cm^{-1}$), and CV revealed a reversible Ni(III/II) couple, $E_{1/2}$ at +1.26 vs NHE in acetone.[192] The $E_{1/2}$ value is outside the range of $O_2^{\bullet-}$ disproportionation (E = –0.18 – 0.91 V vs NHE) and is likely due to the overall positive charge of the Ni(II) complex.[49,192] Complex **22** can be oxidized by CAN in MeOH to yield a low-spin Ni(III) EPR signal with a d_{z^2} ground state ($g_\perp$ = 2.22 and $g_\parallel$ = 2.02). In contrast, when **22** is oxidized by KO_2, the Ni(III) d_{z^2} ground state exhibits triplet hyperfine coupling in the $g_\parallel$ component ($g_\perp$ = 2.17 and $g_\parallel$ = 2.05, $|A_\parallel|$ = 1.5 mT). The same hyperfine coupling is seen in the $g_\parallel$ when **22** is oxidized with CAN in the presence of 7.5 equiv imidazole, in addition to triplet hyperfine coupling in the $g_\perp$ ($g_\perp$ = 2.20 $|A_\perp|$ = 1.7 mT; $g_\parallel$ = 2.02, $|A_\parallel|$ = 2.3 mT). In the presence of ^{15}N-labeled imidazole, both $g_\parallel$ and $g_\perp$ changed from triplet hyperfine to doublet hyperfine splitting when oxidized ($g_\perp$ = 2.20 $|A_\perp|$ = 2.5 mT; $g_\parallel$ = 2.02, $|A_\parallel|$ = 3.5 mT).[192] Based on the findings of **21**, in which the thioether ligand became weakly axially coordinated, Masuda proposed that both $O_2^{\bullet-}$ and imidazole are coordinating to **22** upon oxidation. They suggest the amine is coordinated so as to give N-based hyperfine splitting either through (i) the amine after reaction with KO_2 or (ii) coordination of the imidazole. Coordination of the imidazole in **22** reiterates the weak binding nature of the thioether ligand and the importance of secondary sphere interactions in the enzyme.[192] Further investigation of the reactivity of **22** revealed that reaction with $O_2^{\bullet-}$ in DMF results in a $O_2^{\bullet-}$-bound Ni(II) with an EPR spectrum $g_\parallel$ = 2.21, $g_\perp$ = 2.01 and rR spectra $\nu(^{16}O–^{16}O)$ = 1020 cm^{-1} and $\nu(^{18}O\text{-}^{18}O)$ = 986 cm^{-1}. This complex can also be reduced to Ni(II) by superoxide in the presence of 1-methylimidazole and a proton source in DMF. The authors

propose that additional H-bond donors modulate the reactivity of **22** in order to afford a catalytically active complex.

A sterically hindered dithioether diamine complex was synthesized from the ligand, L = *N,N'*-bis(2-methylmercapto-2-methylpropyl)-1,2-diaminoethane (Figure 1.23).[193] The Ni(II) complex (**23**) was characterized by XRD and revealed a square-planar coordination where Ni–N_{avg} = 1.924(3) and Ni–S_{avg} = 2.1981(10), while UV-vis spectroscopy revealed a λ_{max} (MeOH) at 474 nm (ε = 210 M^{-1} cm^{-1}).[193] Electrochemistry reports a quasi-reversible Ni(III/II) couple, $E_{1/2}$ = 1.71 V vs NHE in MeOH.[193] Reaction of **23** with KO_2 in MeOH results in an EPR spectrum suggesting a d_{z^2} ground state with triplet hyperfine splitting in the $g_{\|}$ region ($|A_{\|}|$ = 1.5 mT).[193] The same spectrum is observed after reducing the Ni(II) complex to Ni(I) and exposing it to O_2 in air, which suggests that O_2 oxidizes the Ni(I) species to Ni(III) and that some rearrangement occurs to orient an amine ligand into the axial position.[193] Masuda and coworkers propose that a side-on Ni(III) peroxo could form from reaction of Ni(II) with KO_2 or Ni(III) with O_2, causing structural rearrangement of one of the thioether ligands (Figure 1.24.[193] A rR spectrum was taken of the reaction of Ni(II) with KO_2 at –80 ºC to reveal a ν_{OO} stretching frequency at 923 cm^{-1}, which compares to other ν_{OO} stretches in Ni-dioxygen complexes.[193,194]

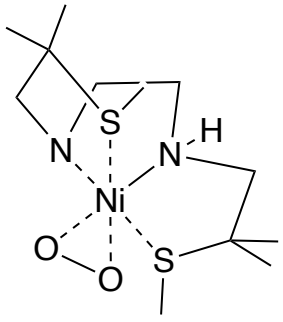

Figure 1.24 Image of proposed $O_2^{\bullet-}$ binding to **23**.

Table 1. 4 Summary of select properties of Complexes **21-23**.

Complex	Bond	Distances (Å)	λ_{max}, nm (ε, M^{-1} cm^{-1})	$E_{1/2}$ (V vs NHE)
21	$Ni–N_{carboxamide}$	1.870(10)	472 (250) (acetone)	0.99
	$Ni–N_{amine}$	1.969(8)		
	$Ni–N_{pyridine}$	1.929(9)		
	$Ni–S_{equatorial}$	2.192(4)		
	$Ni–S_{axial}$	2.787(3)		
22	$Ni–N_{carboxamide}$	1.845(3)	436 (390) (acetone)	1.26
	$Ni–N_{amine}$	1.909(2)		
	$Ni–S_{trans\text{-}amine}$	2.1772(9)		
	$Ni–S_{trans\text{-}carboxamida}$	2.1692(10)		
23	$Ni–N_{avg}$	1.924(3)	474 (210) (MeOH)	1.71
	$Ni–S_{avg}$	2.1981(10)		

Darensbourg and Hegg and coworkers have extensively studied the nucleophilicity of Ni-thiolates in NiN_2S_2 complexes including the complex **$[Ni(ema)]^{2-}$ (24)**, where ema = *N*,*N*′-ethylenebis-2-mercaptoacetamide, with two *cis*-carboxamido donors and two *cis*-dithiolates.[145,148,151] Reaction of **24** with oxygen resulted in **$[Et_4N]_2[Ni(ema)\cdot O_2]$ (25)**, i.e., single S-modification. Reaction of **24** with alkylating agents MeI and $Br(CH_2)_3Br$ has yielded **$[Ni(ema)(Me)_2]$ (26)** and macrocycle **$[Ni(ema)(CH_2)_3]$ (27)**, respectively (Figure 1.25). [145,148,151] Each of these complexes has been characterized by XRD, whereas **24** has $Ni–S_{avg}$ = 2.179 Å and

$Ni–N_{avg}$ = 1.857 Å.[145] Upon sulfinate formation in **25**, the $Ni–S_{sulfinate}$ bond contracts to 2.152(2) Å, while the remaining $Ni–S_{thiolate}$ remains unchanged (2.175(2) Å) (Table 1.5).[145] Additionally, two $\nu_{S=O}$ stretches were observed in the FTIR spectrum: 1150 cm^{-1} (symmetric stretch) and 1020 cm^{-1} (asymmetric stretch).[148] The $Ni–S_{thioether}$ bond distances in **26** are slightly elongated to $Ni–S_{avg}$ = 2.188 Å, while the macrocycle **27** has contracted $Ni–S_{thioether}$ bonds, where $Ni–S_{avg}$ = 2.163 Å, in addition to a restriction of the S–Ni–S angle from 95.4º in **24** to 88.4º in **27**.[148,151]

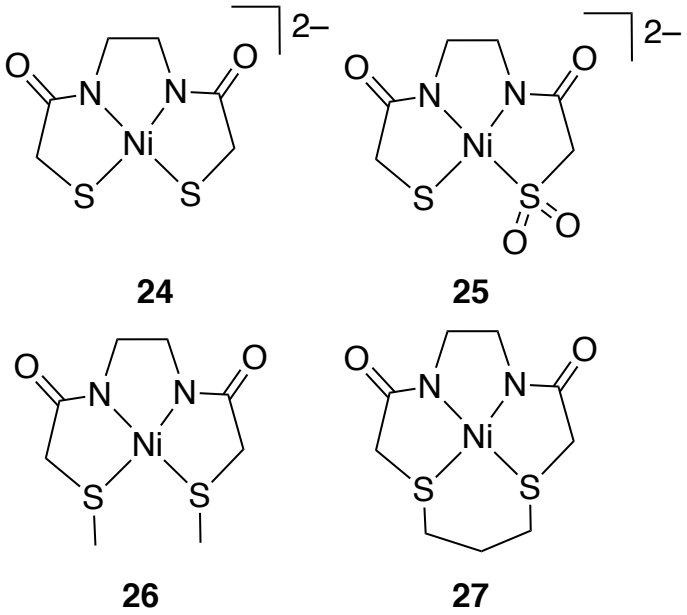

Figure 1.25. Structures of the Ni(II)-N_2S_2 NiSOD model complex **24** and modifications via reaction with O_2, **25**, reaction with MeI, **26**, and reaction with $Br(CH_2)_3Br$, **27**.

S-based modification results in more positive $E_{1/2}$ Ni(III/II) potentials, where the $E_{1/2}$ for **24** = –0.160 V and **25** = –0.114 V vs NHE in DMF.[145,148,151] The neutral alkylated complexes, **26**

and **27** have more positive $E_{1/2}$ Ni(III/II) (0.991 V and 1.05 V vs NHE in DMF, respectively), likely due to S-modification in addition to increased positive charge of the complex.[148,151] Uniquely, **27** has an irreversible Ni(II/I) feature at –1.53 V vs NHE in DMF, which is not seen in the other complexes due to the DMF solvent window.[148,151]

The electronic structures of these complexes were deduced by DFT, where the HOMO of **24** consists of an dπ–pπ asymmetric combination of the S(p_z) orbitals (22% per S) engaging in antibonding overlap with the Ni(d_{xz}) orbital (39%). The HOMO–1 consists of a symmetric contribution of the S(p_z) orbitals (14% per S) with Ni(d_{yz}) (44%) and is nearly degenerate with the HOMO. The LUMO is an antibonding σ-MO between Ni(d_{xy}) (33%), S($p_{x,y}$) (12% per S) and N($p_{x,y}$) (4% per N).[151] DFT shows that for **25**, sulfination breaks the degeneracy of the HOMO and HOMO–1, so that the antibonding orbital has 32% Ni(d_{yz}), 45% $S_{thiolate}$(p_z), 4% $N_{trans\text{-}thiolate}$($p_z$), and 3% $O_{trans\text{-}thiolate}$($p_z$) contributions and the HOMO–1 has 36% Ni(d_{xz}), 20% $N_{trans\text{-}sulfinate}$($p_z$), 13% $O_{trans\text{-}sulfinate}$($p_z$).[151] For the alkylated complexes, **26** and **27**, DFT shows loss of contribution of the S orbital to the frontier molecular orbitals (FMO), where the HOMO consists of the asymmetric combination of N(p_z) orbitals (16-18% per N) and Ni(d_{xz}) (21-22%), while the HOMO–1 consists of N(p_z) (10-15% per N) and Ni(d_{yz}) (19-20%) (Scheme 1.11).[151]

Natural bond order analysis (NBO) and electrostatic potential calculations of **24** show a covalent Ni–S bond (1.95 e^- between Ni and S) and no covalency in the Ni–N bond (1.71 e^- localized on N), indicating a dative bond.[151] Upon oxygenation to form the sulfinate species **25**, the electron density shifts from the thiolate-S to the O lone pairs of the sulfinato, while the electron density of the carboxamido-N is decreased.[151] Sulfination of **24** appears to mimic H-bonding to the modified sulfur and deactivates the remaining thiolate.[151] For the alkylated complexes, NBO analysis reveals that for **26** the Ni–N bonds change from dative to covalent

(1.93 e^- between Ni and N) and the Ni–S bonds switch from covalent to dative (1.72 e^- localized on S). Electrostatic potentials show quenching of the thiolate-S electron density and a formal negative charge on the carboxamide-N.[151] This study of **[Ni(ema)]$^{2-}$** modifications indicate that nucleophilicity of the second thiolate is decreased upon modification of one thiolate, and that nucleophilicity is completely lost once the lone pairs of the thiolate sulfurs are engaged in covalent bond formation.[145,148,151]

Table 1.5 Summary of select properties of Complexes **24-27**.

Complex	Bond	Distances (Å)	$E_{1/2}$ (V vs NHE)	% Composition of HOMO
24	Ni–$S_{avg\ (thiolate)}$	2.179	–0.160	22% per S(p_z)
	Ni–N_{avg}	1.857		39% Ni (d_{xz})
25	Ni–$S_{sulfinate}$	2.152(2)	–0.114	45% S(p_z)
	Ni–$S_{thiolate}$	2.175(2)		32% Ni(d_{yz})
26	Ni–$S_{avg\ (thioether)}$	2.188	0.991	16-18% N(p_z)
				21-22% Ni(d_{xz})
27	Ni–$S_{avg\ (thioether)}$	2.163	1.05	16-18% N(p_z)
				21-22% Ni(d_{xz})

In a related study, DFT has been utilized to study NiN_2S_2 reactivity of diamino **[Ni(bme-dmed)] (28)**, amino-carboxamido **[Ni(mama)]$^-$ (29)**, and dicarboxamido **[Ni(ema)]$^{2-}$ (24)** complexes (Figure 1.26).[145,149,154] Qualitatively, diamino complexes react with O_2 much more

slowly than dicarboxamido complexes, (days vs. minutes).[148-150] This study revealed that, theoretically, a mixed amino/carboxamido donor set would result in less sulfur oxygenation than a dicarboxamido complex.[154] Additionally, S-oxygenation is decreased with H-bonding to one S-thiolate, as it decreases the nucleophilicity of both S-thiolates.[154] Molecular electrostatic potential maps indicate that a single H-bond to an S-thiolate incorporated into the amino-carboxamido **29** complex and dicarboxamido **24** reduces electron density at both S-thiolates and increases the electron density at the Ni center (Figure 1.26).[154]

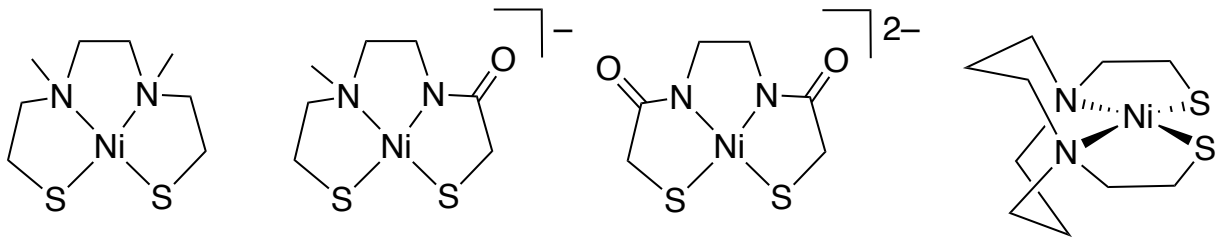

28 **29** **24** **30**

Figure 1.26. Structures of the NiSOD model complexes **28**, **29**, **24**. **30**.

Indeed, S K-edge XAS and DFT calculations on **[Ni(bme-daco)] (30)**, where bme-daco = *N*,*N*′-bis(2-mercaptoethyl)-1,5-diazacyclooctanato, reveal that H-bonding does not affect Ni–S covalency.[195] The S K-edge XAS spectrum of **30** contains a 1s(S) → 3d(Ni) pre-edge transition that correlates to the orbital mixing of the LUMO containing S(3p)- and Ni(3d)- character and gives insight into the Ni–S covalency of the complex.[195] When **30** is a solid, the pre-edge transition occurs at 2470.8 eV and correlates to 46% total 3p S-character.[195] The spectrum is similar when **30** is dissolved in MeCN, while dissolution in H_2O shifts the spectrum ~0.2 eV to

higher energy (2471.0 eV) with no change in intensity.[195] This indicates that the energy shift is due to H-bonding and not solvent coordination to the Ni center.[195] DFT calculations confirm that the 1s(S) orbitals are stabilized by H-bonding with H_2O molecules causing an upshift of the pre-edge transition, but that H-bonding does not change the Ni–S bond length or covalency.[195] This is due to the presence of "passive" H-bonds that interact with the non-bonding thiolate π-orbitals that are perpendicular to the S–Ni–S plane and therefore do not change the Ni–S σ-bond covalency.[195]

Scheme 1.11 Effect of molecular orbitals upon S-modification.

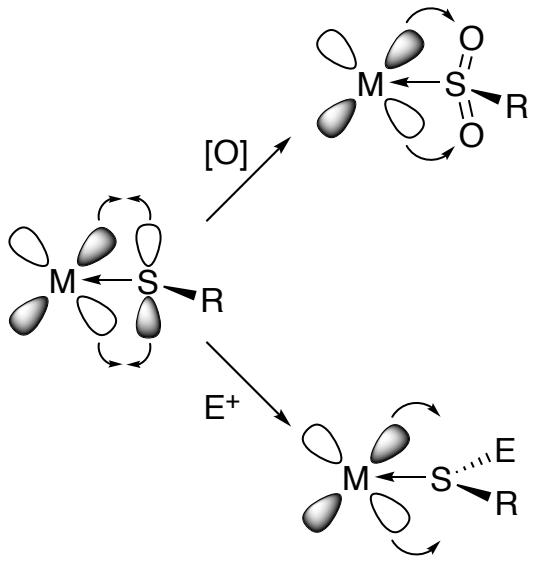

Darensbourg and coworkers have carried out methylation studies on the dithiolate complex **30** to form the thiolate/thioether complex **[Ni(metb-daco)] (31)**, where metb-daco = *N*-(mercaptoethyl)-*N*′-(3-thiabutyl)-1,5-diazacyclooctanato, and the dithioether complex **[Ni(btb-**

daco)] (32), where btb-daco = *N*,*N*′-bis(3-thiabutyl)-1,5-diazacyclooctane (Figure 1.27).[196] The primary structural change upon S-methylation is a subsequent increase in the modified Ni–S bond from 2.159 Å in **30** (S-thiolate) to 2.173 Å in **31** (one S-thioether bond) and 2.204 Å in **32** (two S-thioether bonds). The 0.014-0.045 Å increase in N–S is attributed to the weaker donor strength of thioether-S in comparison to thiolato-S (Table 1.6).

Table 1.6 Select Ni–S bond distances for **30-32**.

Compound	**Bond Type**	**Bond Length (Å)**
30	$Ni–S_{avg\text{-}thiolate}$	2.159(3)
31	$Ni–S_{thiolate}$	2.155(3)
	$Ni–S_{thioether}$	2.173(2)
32	$Ni–S_{thioether}$	2.204(3)
	$Ni–S_{thioether}$	2.211(3)

The methylation also increases $E_{1/2}$ Ni(II/I), where in MeCN the $E_{1/2}$ for Ni(II/I) increases + 0.740 V upon mono-methylation from the dithiolate and + 0.722 V from mono-methylated to dimethylated vs NHE.[196] Carrying out electrochemistry in H_2O reveals that H-bonding to the thiolates increases the Ni(II/I) potentials as the stabilization of **31**, the thiolate/thioether complex, is 0.250 V from MeCN to H_2O, but there is no change for the $E_{1/2}$ value in H_2O from MeCN for **32**, the dithioether.[196] In effect, the S-based modifications either via H-bonds or methylation stabilize the Ni(I) state, but destabilize the Ni(III) state, a trend which is in line with the positive charge and decreased donor ability of the thioether ligand.[196]

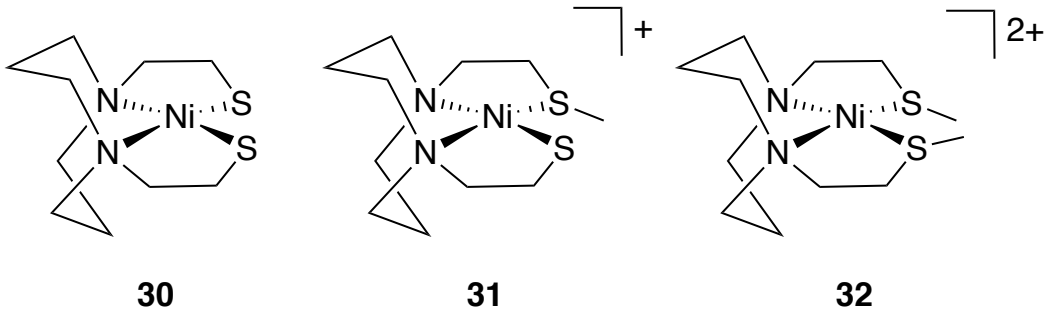

30 **31** **32**

Figure 1.27. Structures of the planar Ni(II)-N_2S_2 NiSOD model complexes **30**, **31**, and **32**.

Single methylation of a thiolate complex with MeI and characterization of the resulting species were carried out by Duboc and coworkers on the Ni(II) diamine dithiolate complex containing the ligand L^{2-} = 2,2′ -(2,2′-bipyridine-6,6′-diyl)bis(1,1-diphenylethanethiolate) **33** (Figure 1.28).[197-199] Methylation was achieved after adding 1.2 equiv of methyl iodide (MeI) in CH_2Cl_2, followed by anion exchange with silver triflate (AgOTf) which yielded the diamine, mixed thiolate/thioether complex, **34** (Figure 1.28).[199] XRD revealed a distorted square-planar geometry with two independent molecules where the $Ni–N_{trans\text{-}thiolate}$ = 1.918(7) and 1.959(8) Å, $N–N_{trans\text{-}thioether}$ = 1.899(8) and 1.914(7) Å, $Ni–S_{thiolate}$ = 2.169(3) and 2.174(3) Å, and $Ni–S_{thioether}$ = 2.172(2) and 2.187(2) Å.[199] These Ni–S distances indicate that methylation has a small effect on the Ni–S bond lengths (0.003 and 0.013 Å lengthening for $Ni–S_{thioether}$ compared to $Ni–S_{thiolate}$, respectively), but methylation has a larger effect on the Ni–N bond lengths (0.019 Å and 0.045 Å contraction for $Ni–N_{trans\text{-}thioether}$ from $Ni–N_{trans\text{-}thiolate}$).[199] The relief of the dπ–pπ antibonding interaction between Ni and S upon methylation counteracts the weak σ-donor character of the thioether ligand, resulting in negligible change in the Ni–S bond distance, as observed in calculations by Brunold (vide supra).[144,199] Complex **34** has a reversible $E_{1/2}$

Ni(III/II) at 1.244 V vs NHE in MeCN and 1.384 V vs NHE in CH_2Cl_2, which is ~ + 0.6 V from the dithiolate system, likely due to the overall positive charge of the thioether complex and reduced donor strength.[199] Bulk electrolysis of **34** indicated that the Ni(III) species was unstable at room temperature. The oxidized state of **34** is proposed to decompose via formation of a thiyl radical followed by disulfide formation, but Ni(III) can be isolated at –30 ºC in either MeCN (UV-vis: λ_{max} = 468, 530 (sh) nm) or CH_2Cl_2 (UV-vis: λ_{max} = 380, 730 (sh) nm) using bulk electrolysis.[199] The EPR spectrum of the Ni(III) complex revealed a rhombic species with g_x = 2.238, g_y = 2.178, g_z = 2.039 and ^{14}N hyperfine lines on the g_z component (A_N = 51 MHz) in CH_3CN (g_x = 2.231, g_y = 2.172, g_z = 2.039 in CH_2Cl_2), consistent with an S = ½ ground state for Ni(III) with the unpaired electron (upe) in the d_{z^2} orbital. The z-axis hyperfine indicates an elongated square-pyramidal geometry with axial coordination by MeCN or triflate/H_2O in the CH_2Cl_2 sample.[199] DFT calculations of the Ni(III) species with no axial ligation revealed that the upe resides in the S(π) MO where the SOMO is composed of 46% S-thiolate and 19% Ni-character, which indicates Ni(II)-thiyl radical-character and contradicts the EPR data.[199] The disconnect between experimental data and theoretical calcuations indicated that a parameter was missting in the calculations; DFT calculations incorporating an axial MeCN ligand ($Ni–N_{MeCN}$ = 2.108 Å) more closely matched the experimental EPR data (calculated: g_x = 2.237, g_y = 2.162, g_z = 2.070, A_N = 44 MHz) in which an upe in the Ni–d_{z^2}-based MO with the SOMO composed of 67% Ni- and 20% S-character suggests that axial N-coordination drastically increases the stability of the Ni(III) complex and reduces the Ni–S covalency in the SOMO.[199] The addition of the thioether results in increased S-character by the unmodified thiolate and decreased Ni-character, as DFT calculations of the analogous dithiolate complex with an axial imidazole indicated the SOMO was composed of 75.9% Ni and 14.3% S.[198,199]

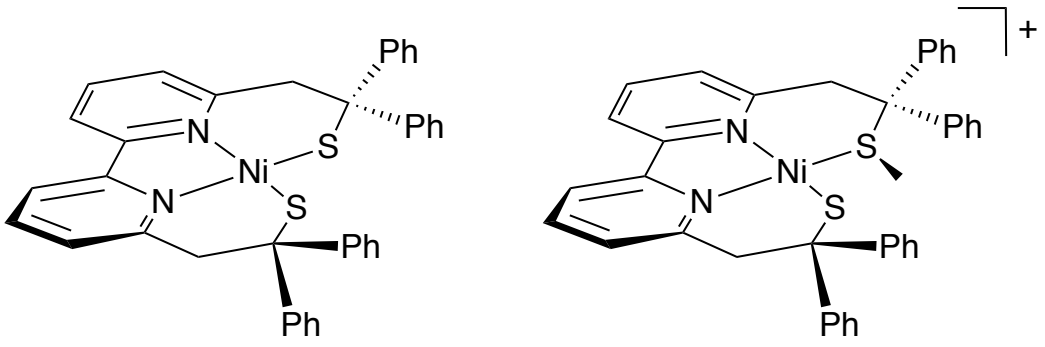

33 **34**

Figure 1.28. Structures of the planar Ni(II)-N_2S_2 NiSOD model complexes **33** and **34**. Ph is phenyl or C_6H_5.

The nucleophilicity of this mono-methylation reaction was explored in more depth, and no dimethylation was observed for the **33** when reacted with MeI, indicating that the nucleophilicity of the thiolate-S is quenched upon methylation of the first sulfur to form **34**.[200] Under pseudo-first-order conditions ($k_{obs} = k_2$[MeI], where MeI >> Ni(II)L), the methylation exhibited second order behavior with $k_2 = 1.25(3) \times 10^{-2}$ M^{-1} s^{-1} at 21 ºC with $\Delta H^{‡} = 47(4)$ kJ/mol and $\Delta S^{‡} = -123(12)$ J/mol·K.[200] These values are consistent with an associative S-alkylation mechanism, where the Ni–S bond remains bound, rather than a dissociative mechanism, where the Ni–S bond would break, followed by addition to the free thiolate. S K-edge XAS data of **33** and **34** and analysis of the pre-edge intensity indicated that the LUMO of **33** had ~22% S-character with ~11% per S-thiolate (pre-edge = 2470.5 eV, 1.16 intensity), while the LUMO of **34** had ~12% S-character for the lone S-thiolate (pre-edge = 2470.2 eV, 0.65 intensity).[200] These orbital compositions indicate that the Ni–$S_{thioether}$ covalency is much weaker than that of the Ni–$S_{thiolate}$ bond, but that methylation does not affect the covalency of the

remaining Ni–$S_{thiolate}$.[200] Additionally, electrostatic potential calculations indicate that the lone pair of the $S_{thiolate}$ of **34** has a charge of –0.052 atomic units (au) on the S-lone pair, while the S-lone pairs of **33** has a charge of –0.069 au. These results are consistent with the negative partial charge of the remaining $S_{thiolate}$ is somewhat quenched upon methylation, reducing its nucleophilicity.[200]

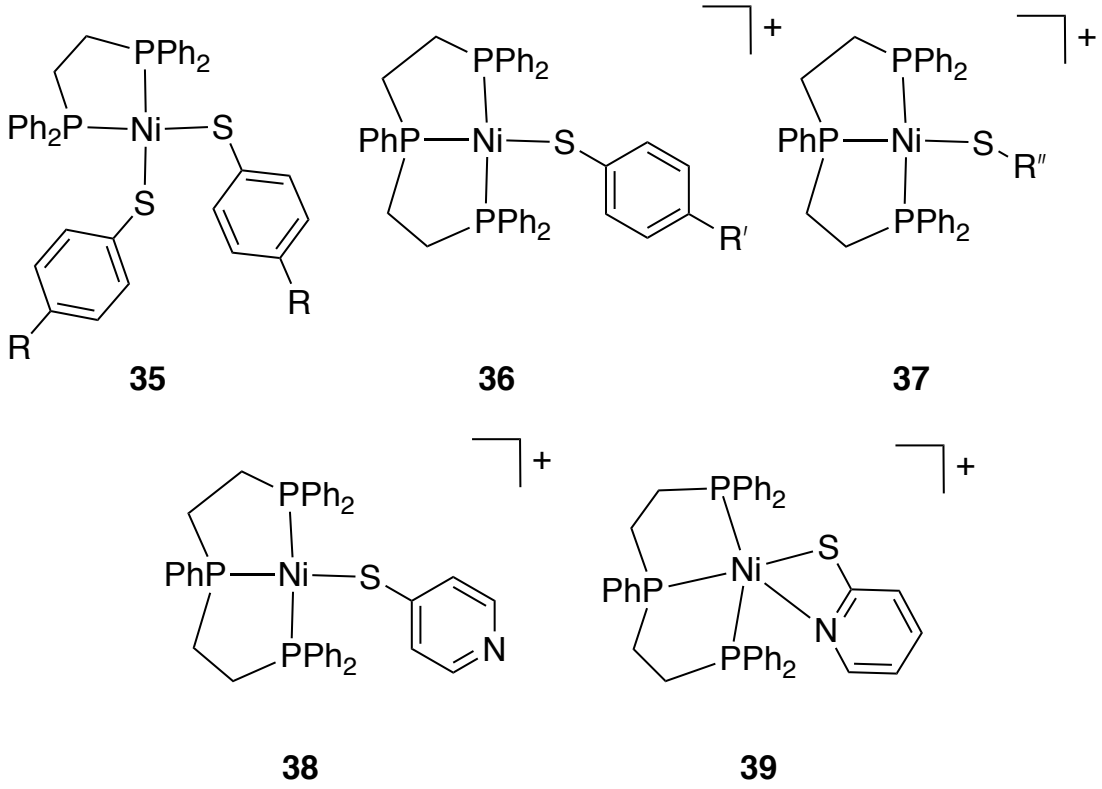

Figure 1.29. Structures of the planar Ni(II)-N_2S_2 complexes used in protonation studies. Complexes **35** where R = MeO, Me, H, Cl, or NO_2 (top left), **36** where R′ = MeO, Me, H, Cl, or NO_2, **37** where R″ = Et, Bu^t, or Cy, **38** and **39**.

To further explore the nucleophilicity of S, Henderson and coworkers have extensively studied the kinetics of equilibrium reactions of Ni-thiolate complexes with the proton donor $[lutH]^+$ where lut = 2,6-dimethylpyridine (pK_a = 6.6). Three families of complexes have been synthesized: (i) the diphosphine dithiolate Ni complexes, $[Ni(SC_6H_4\text{-}R\text{-}4)_2(dppe)]$ **(35)** where R = MeO, Me, H, Cl, or NO_2 and dppe = diphenylphosphinoethane; (ii) triphosphine monothiolate Ni complexes, $[Ni(SC_6H_4R'\text{-}4)(triphos)]^+$ **(36)** where R′ = MeO, Me, H, Cl, or NO_2 and triphos = $PhP\{CH_2CH_2PPh_2\}_2$ and $[Ni(SR'')(triphos)]^+$ **(37)** where R″ = Et, Bu^t, or Cy; and (iii) triphosphine pyridinethiolate Ni complexes, $[Ni(4\text{-}Spy)(triphos)]^+$ **(38)** and $[Ni(2\text{-}Spy)(triphos)]^+$ **(39)** where 4-Spy = 4-pyridinethiolate and 2-Spy = 2-pyridinethiolate (Figure 1.29).

These kinetic studies reveal that protonation of **35**, **36**, and **37** occurs via either a single-step equilibrium reaction or a two-step mechanism where an initial H-bonding step of $[lutH]^+$ occurs before an intramolecular PT. In-line with DFT studies carried out by Brunold, the R substituent has little effect on the pK_a of the coordinated thiolate due to the four electron π-π repulsion between the sulfur lone pairs and the t_{2g}-orbitals of Ni. As the electron density of S increases with electron-donating substituents, the strengthened σ-interaction is countered by the increased π-π repulsion. Furthermore, as the S-density decreases with electron-withdrawing substituents, the weakened σ-interaction between Ni and S would be countered by the decrease in π-π repulsion. For example, the pK_a (MeCN) ranges of the thiolate ligands in **35** (15.1–15.8), **36** (14.3–14.8), and **37** (15.6–16.7) are largely invariable. This is in contrast to analogous 4-substitued phenols (pK_a values in MeCN are unavailable for 4-substituted thiols) that vary from 7-10 pK_a units ($4\text{-}MeC_6H_4OH$ = 10.2, C_6H_4OH = 9.9, $4\text{-}O_2NC_6H_4OH$ = 7.1). This data indicates that the rate and extent of H-bonding to $[lutH]^+$ does not change significantly among the complexes. The extent of PT, however, varies with the basicity of the coordinated thiolate and

the steric hinderance of the bulky phenyl groups of the supporting phosphine ligands. For **35**, only the electron-withdrawing (R = NO_2) substituent revealed a two-step mechanism, whereas the H-bonded intermediate accumulates due to decreased basicity of the coordinated thiol and the decreased steric bulk of the dppe ligand. In the more sterically demanding triphos systems (**36** and **37**), only a two-step mechanism is observed due to the distance PT must travel from [lutH]+ to the buried Ni-thiolate.

The S basicity also has an effect on **36** in which electron-withdrawing substituents have an inverse kinetic isotope effect (KIE), while electron-donating substituents have a primary isotope effect. The S-basicity modulates the position of the proton between the S and the N of lut, where the electron-donating substituents result in an H-bond adduct most closely resembling a coordinated thiol. In contrast, electron-withdrawing substituents yield an H-bond adduct where the proton is more closely associated with the N of lut. In summary, as the S becomes more basic, the KIE becomes larger.

The complexes **38** and **39** shed insight into the preferred protonation site between nitrogen and sulfur ligands in pyridinethiolate complexes. Complex **38** is 4C and square-planar, where the 4-pyridinethiolate coordinates to Ni through the S and not the N. However, complex **39** is 5C and forms a trigonal-bipyramidal geometry with a bidentate coordination of the 2-pyridinethiolate through both S and N.

The reaction kinetics of **38** with $[lutH]^+$ indicates the unbound pyridine-N is protonated and not the coordinated thiolate-S. The reaction kinetics of **39**, in combination with calculations reveal initial protonation occurs at the thiolate-S, followed by dissociation of the pyridine-N, resulting in PT from the coordinated thiol to the uncoordinated pyridine. This result highlights the change in pK_a of pyridine-N and thiolate-S ligands upon metal coordination.

Thermodynamically, pyridine-N is the preferred protonation site compared to free or coordinated thiolate-S, but when pyridine-N is coordinated to a metal, the lone pair is engaged in bonding to the metal, leaving the lone pairs of the thiolate-S available and open for coordination. The reactivity of **39** suggests that protonation of the thiolate-S causes dissociation of the pyridine-N from Ni; the free pyridine-N becomes a more basic protonation site than the coordinate thiol, which causes intramolecular PT from S to N.

In summary, the effect of S-modification of a Ni(II)-N_2S_2 complex does not significantly perturb the bonding distances of S to Ni or Ni coordination geometry. This is due to the simultaneous weakening of the Ni–S σ-bond and reduction of the Ni(dπ)-S(pπ) antibonding repulsion. The coordination of a thioether ligand to Ni, however, does not always result in a planar NiN_2S_2 complex, as seen in **21**. The nucleophilicity of the S-thiolate in NiN_2S_2 complexes containing diamine/dithiolate ligands decreases significantly for the remaining S-thiolate, once mono substitution occurs to form a thioether or sulfinate ligand. Methylation of the S-thiolate resuls in decreases S-contribution to the HOMO. Additionally, the $E_{1/2}$ (Ni(III/II)) is cathodically shifted, making Ni(III) harder to access. We hypothesize transient protonation of the Cys ligands in NiSOD would have less of an effect on the $E_{1/2}$ of NiSOD. Indeed, Lubitz and coworkers have highlighted the potential for H_2ase catalytic activity in a dinuclear [NiFe]-H_2ase model complex that carries out electrocatalytic proton reduction via protonation of the terminal S coordinated to Ni.[201]

1.4 Research objectives and purpose

A principle question about NiSOD that remains is how the enzyme promotes both Ni-based redox activity and S-oxidative-stability. Proposed mechanisms to prevent S-

oxygenation/oxidation chemistry include, (i) hydrogen bonding (H-bonding) networks in the hexameric enzyme and (ii) Ni-coordinated Cys-thiol. We have constructed small molecule mimics of NiSOD to address the impact these mechanisms have on the oxidative-stability of Ni-coordinated thiolates.

To address (i), we synthesized NiSOD analogues that accurately reproduce the reduced state of NiSOD's active site and emulate the multimetallic nature of the enzyme to determine the role of H-bonding networks in the oxidative-stability and catalytic activity of Ni-coordinated thiolates. These complexes are of the general formula $[\{Ni(N_{2/3}S)\}_3(S_3R)]^{3-}$, where S_3R represents a trithiolate ligand tethering three $Ni(N_{2/3}S)$ moieties together via an exogenous S (S_{exo}) and were synthesized by utilizing an established $Ni(N_2S)$ moiety (nmp). Benzene tricarboxamide (BTA) ligands have literature precedent for forming strong, threefold intermolecular H-bonding interactions among the carboxamide functional groups. We have incorporated these unique H-bonding interactions into our multimetallic systems and utilized the BTA moiety as our trimetallic base.[202-207] We can simultaneously influence the type of intermolecular interactions (carboxamide-based H-bonding, π-interactions) and modulate the electronic donating effects of S_3R to determine the role intermolecular interactions and S-electron-donation to the RAMO play in oxidative stability.[208] These trimetallic systems interact via unique inter/intra-molecular H-bonding networks, resulting in properties distinct from their monometallic counterparts. A network of H-bonds sterically protect Ni-S bonds from oxidative modification by impeding access to the Ni ion. Indeed, H-bonding between carboxamides and metal bound thiolates are known to significantly reduce S-nucleophilicity; previously reported $[Ni(nmp)(SR)]^-$ complexes have demonstrated H-bonding to coordinated thiolates stabilizes S-

based MOs relative to Ni(II)-based MOs, allowing for enhanced Ni contribution to the HOMO and protection against S-oxidation.[209-212]

To study (ii), we have synthesized and characterized analogues of NiSOD that model thiol coordination and assessed the mechanistic and electronic implications of Cys-protonation as a protective mechanism against S-oxidation. This approach involves designing $N_{2/3}S_2$-CH_3 ligands to coordinate to Ni, while also modifying $NiN_{2/3}S_2$ complexes via electrophilic addition of H^+ and CH_3^+ to selectively modify the trans-carboxamide thiolate. We expect S-modification decreases S-character in the RAMO to promote N-donor axial binding and favor Ni-based over S-based oxidation. We have modeled S-protonation of the trans-carboxamide-Cys6 of NiSOD by binding H^+ and CH_3^+ to the trans-carboxamide-thiolate of $NiN_{2/3}S_2$ complexes to (a) model a potential H^+ source for H_2O_2 generation, (b) determine the S-nucleophilicity of a mixed carboxamide/amine complex, and (c) probe the role an electron-deficient trans-carboxamide-S plays in promoting Ni-based oxidative chemistry. This synthesis employs different nucleophilicities of the trans-carboxamide vs trans-amine thiolates to selectively bind at the trans-carboxamide-S site via electrophilic addition. We predict selective modification occurs at the trans-carboxamide thiolate based on reactivity studies of diamine and dicarboxamide NiN_2S_2 complexes.[148-153,155,210] Dicarboxamide complexes are more reactive to oxygenation and methylation than their diamine counterparts; for example, dicarboxamide NiN_2S_2 complexes yield S-oxygenated derivatives within minutes, while diamine complexes react on the order of days.[148-153,155,210] Modification of one S also results in inactivation of the remaining S unless conditions are forced.[155] Additionally, modification of the anionic trans-carboxamide-S is not expected to change Ni coordination due to simultaneous relief of the filled-filled dπ-pπ antibonding interaction between the metal and S-orbitals upon protonation or alkylation.[144,213] A

thiol or thioether ligand is expected to decrease the S-character of the RAMO, promoting Ni-based redox activity. N_2S_2-CH_3 monothioether ligands have also been developed for Ni coordination, which offer synthetic control over modification at the trans-carboxamide-S site.

This research aims to probe the role of secondary-sphere interactions in the activity and stability of NiSOD by creating small-molecule analogues of NiSOD. While synthesis and characterization of these complexes provide valuable insight into the physical properties of the active site of NiSOD, ensuring small-molecule catalytic activity remains a challenge. Each aim intends to probe a structure-function aspect in the active site in order to make steps toward an SOD-active model. The goal of this group is to gain insight into the structure-function of redox-active Ni in biology, all of which contain Ni-S bonds. In addition to NiSOD, redox-active Ni can catalyze important transformations for application in alternative energy; NiFe-hydrogenase catalyzes the reversible oxidation of hydrogen and methyl-CoM reductase catalyzes the generation of methane. CO dehydrogenase catalyzes the oxidation of CO to CO_2, an important transformation for environmental remediation. By understanding Ni-based catalytic activity in biology, we can utilize these catalytic transformations for therapeutic, alternative energy, and environmental uses.

1.5 References

(1) Bertini, I.; Gray, H. B.; Stiefel, E. I.; Valentine, J. S., *Biological Inorganic Chemistry*. University Science Books: Sausalito, CA, 2007.

(2) Sawers, R. G., Nickel in Bacteria and Archaea. In *Encyclopedia of Metalloproteins*, Kretsinger, R. H.; Uversky, V. N.; Permyakov, E. A., Eds. Springer New York: New York, NY, 2013; pp 1490-1496.

(3) Kasprzak, K. S.; Sunderman, F. W.; Salnikow, K., Nickel carcinogenesis. *Mutat. Res. Fund. Mol. Mech. Mut* **2003**, *533*, 67-97.

(4) Watt, R. K.; Ludden, P. W., Nickel-binding proteins. *Cell. Mol. Life Sci.* **1999**, *56*, 604-625.

(5) Li, Y. J.; Zamble, D. B., Nickel Homeostasis and Nickel Regulation: An Overview. *Chem. Rev.* **2009**, *109*, 4617-4643.

(6) Navarro, C.; Wu, L. F.; Mandrandberthelot, M. A., The Nik Operon of *Escherichia-Coli* Encodes a Periplasmic Binding-Protein-Dependent Transport-System for Nickel. *Mol. Microbiol.* **1993**, *9*, 1181-1191.

(7) Addy, C.; Ohara, M.; Kawai, F.; Kidera, A.; Ikeguchi, M.; Fuchigami, S.; Osawa, M.; Shimada, I.; Park, S. Y.; Tame, J. R. H.; Heddle, J. G., Nickel binding to NikA: an additional binding site reconciles spectroscopy, calorimetry and crystallography. *Acta. Cryst. D* **2007**, *63*, 221-229.

(8) Allan, C. B.; Wu, L. F.; Gu, Z. J.; Choudhury, S. B.; Al-Mjeni, F.; Sharma, M. L.; Mandrand-Berthelot, M. A.; Maroney, M. J., An X-ray absorption spectroscopic structural investigation of the nickel site in *Escherichia coli* NikA protein. *Inorg. Chem.* **1998**, *37*, 5952-5955.

(9) Eitinger, T.; Suhr, J.; Moore, L.; Smith, J. A. C., Secondary transporters for nickel and cobalt ions: Theme and variations. *Biometals* **2005**, *18*, 399-405.

(10) Eitinger, T.; Friedrich, B., Cloning, Nucleotide-Sequence, and Heterologous Expression of a High-Affinity Nickel Transport Gene from *Alcaligenes-Eutrophus*. *J. Biol. Chem.* **1991**, *266*, 3222-3227.

(11) Fulkerson, J. F.; Garner, R. M.; Mobley, H. L. T., Conserved residues and motifs in the NixA protein of *Helicobacter pylori* are critical for the high affinity transport of nickel ions. *J. Biol. Chem.* **1998**, *273*, 235-241.

(12) Fulkerson, J. F.; Mobley, H. L. T., Membrane topology of the NixA nickel transporter of *Helicobacter pylori*: Two nickel transport-specific motifs within transmembrane helices II and III. *J. Bacteriol.* **2000**, *182*, 1722-1730.

(13) Eberz, G.; Eitinger, T.; Friedrich, B., Genetic-Determinants of a Nickel-Specific Transport-System Are Part of the Plasmid-Encoded Hydrogenase Gene-Cluster in *Alcaligenes-Eutrophus*. *J. Bacteriol.* **1989**, *171*, 1340-1345.

(14) Wolfram, L.; Friedrich, B.; Eitinger, T., The *Alcaligenes-Eutrophus* Protein Hoxn Mediates Nickel Transport in *Escherichia-Coli*. *J. Bacteriol.* **1995**, *177*, 1840-1843.

(15) Hebbeln, P.; Eitinger, T., Heterologous production and characterization of bacterial nickel/cobalt permeases. *FEMS Microbiol. Lett.* **2004**, *230*, 129-135.

(16) Eitinger, T.; Wolfram, L.; Degen, O.; Anthon, C., A Ni^{2+} binding motif is the basis of high affinity transport of the *Alcaligenes eutrophus* nickel permease. *J. Biol. Chem.* **1997**, *272*, 17139-17144.

(17) Degen, O.; Eitinger, T., Substrate specificity of nickel/cobalt permeases: Insights from mutants altered in transmembrane domains I and II. *J. Bacteriol.* **2002**, *184*, 3569-3577.

(18) Nies, D. H., Efflux-mediated heavy metal resistance in prokaryotes. *FEMS Microbiol. Rev.* **2003**, *27*, 313-339.

(19) Grass, G.; Fricke, B.; Nies, D. H., Control of expression of a periplasmic nickel efflux pump by periplasmic nickel concentrations. *Biometals* **2005**, *18*, 437-448.

(20) Grass, G.; Fan, B.; Rosen, B. P.; Lemke, K.; Schlegel, H. G.; Rensing, C., NreB from *Achromobacter xylosoxidans* 31A is a nickel-induced transporter conferring nickel resistance. *J. Bacteriol.* **2001**, *183*, 2803-2807.

(21) Kupper, H.; Lombi, E.; Zhao, F. J.; Wieshammer, G.; McGrath, S. P., Cellular compartmentation of nickel in the hyperaccumulators *Alyssum lesbiacum*, *Alyssum bertolonii* and *Thlaspi goesingense*. *J. Exp. Bot.* **2001**, *52*, 2291-2300.

(22) Kramer, U.; Pickering, I. J.; Prince, R. C.; Raskin, I.; Salt, D. E., Subcellular localization and speciation of nickel in hyperaccumulator and non-accumulator *Thlaspi* species. *Plant Physiol.* **2000**, *122*, 1343-1353.

(23) Persans, M. W.; Nieman, K.; Salt, D. E., Functional activity and role of cation-efflux family members in Ni hyperaccumulation in T*hlaspi goesingense*. *Proc. Natl. Acad. Sci. U.S.A.* **2001**, *98*, 9995-10000.

(24) Stahler, F. N.; Odenbreit, S.; Haas, R.; Wilrich, J.; Van Vliet, A. H. M.; Kusters, J. G.; Kist, M.; Bereswill, S., The novel *Helicobacter pylori* CznABC metal efflux pump is required for cadmium, zinc, and nickel resistance, urease modulation, and gastric colonization. *Infect. Immun.* **2006**, *74*, 3845-3852.

(25) Rodrigue, A.; Effantin, G.; Mandrand-Berthelot, M. A., Identification of rcnA (yohM), a nickel and cobalt resistance gene in *Escherichia coli*. *J. Bacteriol.* **2005**, *187*, 2912-2916.

(26) Schreiter, E. R.; Drennan, C. L., Ribbon-helix-helix transcription factors: variations on a theme. *Nat. Rev. Microbiol.* **2007**, *5*, 710-720.

(27) Chivers, P. T.; Tahirov, T. H., Structure of *Pyrococcus horikoshii* NikR: Nickel sensing and implications for the regulation of DNA recognition. *J. Mol. Biol.* **2005**, *348*, 597-607.

(28) Schreiter, E. R.; Wang, S. C.; Zamble, D. B.; Drennan, C. L., NikR-operator complex structure and the mechanism of repressor activation by metal ions. *Proc. Natl. Acad. Sci. U.S.A.* **2006**, *103*, 13676-13681.

(29) Abraham, L. O.; Li, Y. J.; Zamble, D. B., The metal- and DNA-binding activities of *Helicobacter pylori* NikR. *J. Inorg. Biochem.* **2006**, *100*, 1005-1014.

(30) Iwig, J. S.; Rowe, J. L.; Chivers, P. T., Nickel homeostasis in *Escherichia coli* - the rcnR-rcnA efflux pathway and its linkage to NikR function. *Mol. Microbiol.* **2006**, *62*, 252-262.

(31) Iwig, J. S.; Leitch, S.; Herbst, R. W.; Maroney, M. J.; Chivers, P. T., Ni(II) and Co(II) sensing by *Escherichia coli* RcnR. *J. Am. Chem. Soc.* **2008**, *130*, 7592-7606.

(32) Busenlehner, L. S.; Pennella, M. A.; Giedroc, D. P., The SmtB/ArsR family of metalloregulatory transcriptional repressors: structural insights into prokaryotic metal resistance. *FEMS Microbiol. Rev.* **2003**, *27*, 131-143.

(33) Tottey, S.; Harvie, D. R.; Robinson, N. J., Understanding how cells allocate metals using metal sensors and metallochaperones. *Acc. Chem. Res.* **2005**, *38*, 775-783.

(34) Cave, J. S.; Meng, W. M.; Pennella, M. A.; Applehoff, R. J.; Giedroc, D. P.; Robinson, N. J., A nickel-cobalt-sensing ArsR-SmtB family repressor - Contributions of cytosol and effector binding sites to metal selectivity. *J. Biol. Chem.* **2002**, *277*, 38441-38448.

(35) Barondeau, D. P.; Kassmann, C. J.; Bruns, C. K.; Tainer, J. A.; Getzoff, E. D., Nickel Superoxide Dismutase Structure and Mechanism. *Biochemistry* **2004**, *43*, 8038-8047.

(36) Wuerges, J.; Lee, J.-W.; Yim, Y.-I.; Yim, H.-S.; Kang, S.-O.; Carugo, K. D., Crystal structure of nickel-containing superoxide dismutase reveals another type of active site. *Proc. Natl. Acad. Sci. U.S.A.* **2004**, *101*, 8569-8574.

(37) Darnault, C.; Volbeda, A.; Kim, E. J.; Legrand, P.; Vernede, X.; Lindahl, P. A.; Fontecilla-Camps, J. C., Ni-Zn-[Fe_4-S_4] and Ni-Ni-[Fe_4-S_4] clusters in closed and open α subunits of acetyl-CoA synthase/carbon monoxide dehydrogenase. *Nat. Struct. Mol. Biol.* **2003**, *10*, 271-279.

(38) Doukov, T. I.; Iverson, T. M.; Seravalli, J.; Ragsdale, S. W.; Drennan, C. L., A Ni-Fe-Cu center in a bifunctional carbon monoxide dehydrogenase/acetyl-CoA synthase. *Science* **2002**, *298*, 567-572.

(39) Dobbek, H.; Svetlitchnyi, V.; Gremer, L.; Huber, R.; Meyer, O., Crystal structure of a carbon monoxide dehydrogenase reveals a [Ni-4Fe-5S] cluster. *Science* **2001**, *293*, 1281-1285.

(40) Volbeda, A.; Charon, M. H.; Piras, C.; Hatchikian, E. C.; Frey, M.; Fontecilla-Camps, J. C., Crystal-Structure of the Nickel-Iron Hydrogenase from *Desulfovibrio-Gigas*. *Nature* **1995**, *373*, 580-587.

(41) Ermler, U.; Grabarse, W.; Shima, S.; Goubeaud, M.; Thauer, R. K., Crystal structure of methyl coenzyme M reductase: The key enzyme of biological methane formation. *Science* **1997**, *278*, 1457-1462.

(42) Jabri, E.; Carr, M. B.; Hausinger, R. P.; Karplus, P. A., The Crystal-Structure of Urease from *Klebsiella-Aerogenes*. *Science* **1995**, *268*, 998-1004.

(43) He, M. M.; Clugston, S. L.; Honek, J. F.; Matthews, B. W., Determination of the structure of *Escherichia coli* glyoxalase I suggests a structural basis for differential metal activation. *Biochemistry* **2000**, *39*, 8719-8727.

(44) Ryan, K. C.; Johnson, O. E.; Cabelli, D. E.; Brunold, T. C.; Maroney, M. J., Nickel superoxide dismutase: structural and functional roles of Cys2 and Cys6. *J. Biol. Inorg. Chem.* **2010**, *15*, 795-807.

(45) Al-Mjeni, F.; Ju, T.; Pochapsky, T. C.; Maroney, M. J., XAS investigation of the structure and function of Ni in acireductone dioxygenase. *Biochemistry* **2002**, *41*, 6761-6769.

(46) Pochapsky, T. C.; Pochapsky, S. S.; Ju, T. T.; Mo, H. P.; Al-Mjeni, F.; Maroney, M. J., Modeling and experiment yields the structure of acireductone dioxygenase from *Klebsiella pneumoniae*. *Nat. Struct. Biol.* **2002**, *9*, 966-972.

(47) Desguin, B.; Goffin, P.; Viaene, E.; Kleerebezem, M.; Martin-Diaconescu, V.; Maroney, M. J.; Declercq, J. P.; Soumillion, P.; Hols, P., Lactate racemase is a nickel-dependent enzyme activated by a widespread maturation system. *Nat. Commun.* **2014**, *5*.

(48) Zilbermann, I.; Maimon, E.; Cohen, H.; Meyerstein, D., Redox chemistry of nickel complexes in aqueous solutions. *Chem. Rev.* **2005**, *105*, 2609-2625.

(49) Koppenol, W. H.; Stanbury, D. M.; Bounds, P. L., Electrode potentials of partially reduced oxygen species, from dioxygen to water. *Free Radical Biol. Med.* **2010**, *49*, 317-322.

(50) Phillips, S. A.; Thornalley, P. J., The Formation of Methylglyoxal from Triose Phosphates - Investigation Using a Specific Assay for Methylglyoxal. *Eur. J. Biochem.* **1993**, *212*, 101-105.

(51) Boer, J. L.; Mulrooney, S. B.; Hausinger, R. P., Nickel-dependent metalloenzymes. *Arch. Biochem. Biophys.* **2014**, *544*, 142-152.

(52) Maroney, M. J.; Ciurli, S., Nonredox Nickel Enzymes. *Chem. Rev.* **2014**, *114*, 4206-4228.

(53) Silva, M. S.; Gomes, R. A.; Ferreira, A. E. N.; Freire, A. P.; Cordeiro, C., The glyoxalase pathway: the first hundred years ... and beyond. *Biochem. J.* **2013**, *453*, 1-15.

(54) Clugston, S. L.; Yajima, R.; Honek, J. F., Investigation of metal binding and activation of *Escherichia coli* glyoxalase I: kinetic, thermodynamic and mutagenesis studies. *Biochem. J.* **2004**, *377*, 309-316.

(55) Clugston, S. L.; Barnard, J. F. J.; Kinach, R.; Miedema, D.; Ruman, R.; Daub, E.; Honek, J. F., Overproduction and characterization of a dimeric non-zinc glyoxalase I from *Escherichia coli*: Evidence for optimal activation by nickel ions. *Biochemistry* **1998**, *37*, 8754-8763.

(56) Ly, H. D.; Clugston, S. L.; Sampson, P. B.; Honek, J. F., Syntheses and kinetic evaluation of hydroxamate-based peptide inhibitors of glyoxalase I. *Bioorg. Med. Chem. Lett.* **1998**, *8*, 705-710.

(57) Davidson, G.; Clugston, S. L.; Honek, J. F.; Maroney, M. J., An XAS investigation of product and inhibitor complexes of Ni-containing GlxI from *Escherichia coli*: Mechanistic implications. *Biochemistry* **2001**, *40*, 4569-4582.

(58) Dai, Y.; Wensink, P. C.; Abeles, R. H., One protein, two enzymes. *J. Biol. Chem.* **1999**, *274*, 1193-1195.

(59) Sekowska, A.; Denervaud, V.; Ashida, H.; Michoud, K.; Haas, D.; Yokota, A.; Danchin, A., Bacterial variations on the methionine salvage pathway. *BMC Microbiol.* **2004**, *4*.

(60) Ju, T. T.; Goldsmith, R. B.; Chai, S. C.; Maroney, M. J.; Pochapsky, S. S.; Pochapsky, T. C., One protein, two enzymes revisited: A structural entropy switch interconverts the two isoforms of acireductone dioxygenase. *J. Mol. Biol.* **2006**, *363*, 523-534.

(61) Dai, Y.; Pochapsky, T. C.; Abeles, R. H., Mechanistic studies of two dioxygenases in the methionine salvage pathway of *Klebsiella pneumoniae*. *Biochemistry* **2001**, *40*, 6379-6387.

(62) Sparta, M.; Valdez, C. E.; Alexandrova, A. N., Metal-Dependent Activity of Fe and Ni Acireductone Dioxygenases: How Two Electrons Reroute the Catalytic Pathway. *J. Mol. Biol.* **2013**, *425*, 3007-3018.

(63) Allpress, C. J.; Grubel, K.; Szajna-Fuller, E.; Arif, A. M.; Berreau, L. M., Regioselective Aliphatic Carbon-Carbon Bond Cleavage by a Model System of Relevance to Iron-Containing Acireductone Dioxygenase. *J. Am. Chem. Soc.* **2013**, *135*, 659-668.

(64) Szajna, E.; Arif, A. M.; Berreau, L. M., Aliphatic carbon-carbon bond cleavage reactivity of a mononuclear Ni(II) *cis*- β -keto-enolate complex in the presence of base and O_2: A model reaction for acireductone dioxygenase (ARD). *J. Am. Chem. Soc.* **2005**, *127*, 17186-17187.

(65) Callahan, B. P.; Yuan, Y.; Wolfenden, R., The burden borne by urease. *J. Am. Chem. Soc.* **2005**, *127*, 10828-10829.

(66) Desguin, B.; Zhang, T.; Soumillion, P.; Hols, P.; Hu, J.; Hausinger, R. P., A tethered niacin-derived pincer complex with a nickel-carbon bond in lactate racemase. *Science* **2015**, *349*, 66-69.

(67) Belenky, P.; Bogan, K. L.; Brenner, C., NAD(+) metabolism in health and disease. *Trends Biochem. Sci.* **2007**, *32*, 12-19.

(68) Xu, T.; Bauer, G.; Hu, X. L., A Novel Nickel Pincer Complex in the Active Site of Lactate Racemase. *ChemBioChem* **2016**, *17*, 31-32.

(69) Wang, B.; Shaik, S., The Nickel-Pincer Complex in Lactate Racemase Is an Electron Relay and Sink that acts through Proton-Coupled Electron Transfer. *Angew. Chem. Int. Ed.* **2017**.

(70) Svetlitchnyi, V.; Peschel, C.; Acker, G.; Meyer, O., Two membrane-associated NiFeS-carbon monoxide dehydrogenases from the anaerobic carbon-monoxide-utilizing eubacterium *Carboxydothermus hydrogenoformans*. *J. Bacteriol.* **2001**, *183*, 5134-5144.

(71) Ragsdale, S. W., Metals and their scaffolds to promote difficult enzymatic reactions. *Chem. Rev.* **2006**, *106*, 3317-3337.

(72) Ha, S. W.; Korbas, M.; Klepsch, M.; Meyer-Klaucke, W.; Meyer, O.; Svetlitchnyi, V., Interaction of potassium cyanide with the [Ni-4Fe-5S] active site cluster of CO dehydrogenase from *Carboxydothermus hydrogenoformans*. *J. Biol. Chem.* **2007**, *282*, 10639-10646.

(73) Ragsdale, S. W., Nickel-based Enzyme Systems. *J. Biol. Chem.* **2009**, *284*, 18571-18575.

(74) Doukov, T. I.; Blasiak, L. C.; Seravalli, J.; Ragsdale, S. W.; Drennan, C. L., Xenon in and at the end of the tunnel of bifunctional carbon monoxide dehydrogenase/acetyl-CoA synthase. *Biochemistry* **2008**, *47*, 3474-3483.

(75) Raybuck, S. A.; Ramer, S. E.; Abbanat, D. R.; Peters, J. W.; Ormejohnson, W. H.; Ferry, J. G.; Walsh, C. T., Demonstration of Carbon-Carbon Bond-Cleavage of Acetyl Coenzyme-a by Using Isotopic Exchange Catalyzed by the Co Dehydrogenase Complex from Acetate-Grown *Methanosarcina-Thermophila*. *J. Bacteriol.* **1991**, *173*, 929-932.

(76) Darnault, C.; Volbeda, A.; Kim, E. J.; Legrand, P.; Vernède, X.; Lindahl, P. A.; Fontecilla-Camps, J. C., Ni-Zn-[Fe_4-S_4] and Ni-Ni-[Fe_4-S_4] clusters in closed and open α subunits of acetyl-CoA synthase/carbon monoxide dehydrogenase. *Nat. Struct. Mol. Biol.* **2003**, *10*, 271-279.

(77) Barondeau, D. P.; Lindahl, P. A., Methylation of carbon monoxide dehydrogenase from *Clostridium thermoaceticum* and mechanism of acetyl coenzyme A synthesis. *J. Am. Chem. Soc.* **1997**, *119*, 3959-3970.

(78) Harrop, T. C.; Mascharak, P. K., Structural and spectroscopic models of the A-cluster of acetyl coenzyme a synthase/carbon monoxide dehydrogenase: Nature's Monsanto acetic acid catalyst. *Coord. Chem. Rev.* **2005**, *249*, 3007-3024.

(79) Lubitz, W.; Ogata, H.; Rudiger, O.; Reijerse, E., Hydrogenases. *Chem. Rev.* **2014**, *114*, 4081-4148.

(80) Montet, Y.; Amara, P.; Volbeda, A.; Vernede, X.; Hatchikian, E. C.; Field, M. J.; Frey, M.; Fontecilla-Camps, J. C., Gas access to the active site of Ni-Fe hydrogenases probed by X-ray crystallography and molecular dynamics. *Nat. Struct. Biol.* **1997**, *4*, 523-526.

(81) Ash, P. A.; Hidalgo, R.; Vincent, K. A., Proton Transfer in the Catalytic Cycle of [NiFe] Hydrogenases: Insight from Vibrational Spectroscopy. *ACS Catal.* **2017**, *7*, 2471-2485.

(82) Volbeda, A.; Martin, L.; Liebgott, P. P.; De Lacey, A. L.; Fontecilla-Camps, J. C., [NiFe]-hydrogenases revisited: nickel-carboxamido bond formation in a variant with accrued O_2-tolerance and a tentative re-interpretation of Ni-SI states. *Metallomics* **2015**, *7*, 710-718.

(83) Fritsch, J.; Scheerer, P.; Frielingsdorf, S.; Kroschinsky, S.; Friedrich, B.; Lenz, O.; Spahn, C. M. T., The crystal structure of an oxygen-tolerant hydrogenase uncovers a novel iron-sulphur centre. *Nature* **2011**, *479*, 249-252.

(84) Shomura, Y.; Yoon, K. S.; Nishihara, H.; Higuchi, Y., Structural basis for a [4Fe-3S] cluster in the oxygen-tolerant membrane-bound [NiFe]-hydrogenase. *Nature* **2011**, *479*, 253-256.

(85) Volbeda, A.; Amara, P.; Darnault, C.; Mouesca, J. M.; Parkin, A.; Roessler, M. M.; Armstrong, F. A.; Fontecilla-Camps, J. C., X-ray crystallographic and computational studies of the O_2-tolerant [NiFe]-hydrogenase 1 from *Escherichia coli*. *Proc. Natl. Acad. Sci. U.S.A.* **2012**, *109*, 5305-5310.

(86) Evans, R. M.; Parkin, A.; Roessler, M. M.; Murphy, B. J.; Adamson, H.; Lukey, M. J.; Sargent, F.; Volbeda, A.; Fontecilla-Camps, J. C.; Armstrong, F. A., Principles of Sustained Enzymatic Hydrogen Oxidation in the Presence of Oxygen - The Crucial Influence of High Potential Fe-S Clusters in the Electron Relay of [NiFe]-Hydrogenases. *J. Am. Chem. Soc.* **2013**, *135*, 2694-2707.

(87) Volbeda, A.; Amara, P.; Iannello, M.; De Lacey, A. L.; Cavazza, C.; Fontecilla-Camps, J. C., Structural foundations for the O_2 resistance of *Desulfomicrobium baculatum* [NiFeSe]-hydrogenase. *Chem. Commun.* **2013**, *49*, 7061-7063.

(88) Fontecilla-Camps, J. C.; Volbeda, A.; Cavazza, C.; Nicolet, Y., Structure/function relationships of [NiFe]- and [FeFe]-hydrogenases. *Chem. Rev.* **2007**, *107*, 4273-4303.

(89) Lamle, S. E.; Albracht, S. P. J.; Armstrong, F. A., Electrochemical potential-step investigations of the aerobic interconversions of [NiFe]-hydrogenase from *Allochromatium vinosum*: Insights into the puzzling difference between unready and ready oxidized inactive states. *J. Am. Chem. Soc.* **2004**, *126*, 14899-14909.

(90) Fernandez, V. M.; Hatchikian, E. C.; Cammack, R., Properties and Reactivation of 2 Different Deactivated Forms of *Desulfovibrio-Gigas* Hydrogenase. *Biochim. Biophys. Acta* **1985**, *832*, 69-79.

(91) Ragsdale, S. W., Nickel and the carbon cycle. *J. Inorg. Biochem.* **2007**, *101*, 1657-1666.

(92) Horng, Y. C.; Becker, D. F.; Ragsdale, S. W., Mechanistic studies of methane biogenesis by methyl-coenzyme M reductase: Evidence that coenzyme B participates in cleaving the C-S bond of methyl-coenzyme M. *Biochemistry* **2001**, *40*, 12875-12885.

(93) Pelmenschikov, V.; Blomberg, M. R. A.; Siegbahn, P. E. M.; Crabtree, R. H., A mechanism from quantum chemical studies for methane formation in methanogenesis. *J. Am. Chem. Soc.* **2002**, *124*, 4039-4049.

(94) Ghosh, A.; Wondimagegn, T.; Ryeng, H., Deconstructing F_{430}: quantum chemical perspectives of biological methanogenesis. *Curr. Opin. Chem. Biol.* **2001**, *5*, 744-750.

(95) Valentine, J. S.; Wertz, D. L.; Lyons, T. J.; Liou, L.-L.; Goto, J. J.; Gralla, E. B., The dark side of dioxygen biochemistry. *Curr. Opin. Chem. Biol.* **1998**, *2*, 253-262.

(96) Fortunato, G.; Pastinese, A.; Intrieri, M.; Lofrano, M. M.; Gaeta, G.; Censi, M. B.; Boccalatte, A.; Salvatore, F.; Sacchetti, L., Serum Mn-Superoxide Dismutase in Acute Myocardial Infarction. *Clin. Biochem.* **1997**, *30*, 569-571.

(97) Kocatürk, P. A.; Akbostanci, M. C.; Tan, F.; Kavas, G. Ö., Superoxide dismutase activity and zinc and copper concentrations in Parkinson's disease. *Pathophysiology* **2000**, *7*, 63-67.

(98) De Leo, M. E.; Borrello, S.; Passantino, M.; Palazzotti, B.; Mordente, A.; Daniele, A.; Filippini, V.; Galeotti, T.; Masullo, C., Oxidative stress and overexpression of manganese superoxide dismutase in patients with Alzheimer's disease. *Neurosci. Lett.* **1998**, *250*, 173-176.

(99) Sawyer, D. T.; Valentine, J. S., How Super is Superoxide? *Acc. Chem. Res.* **1981**, *14*, 393-400.

(100) Sheng, Y.; Abreu, I. A.; Cabelli, D. E.; Maroney, M. J.; Miller, A.-F.; Teixeira, M.; Valentine, J. S., Superoxide Dismutases and Superoxide Reductases. *Chem. Rev.* **2014**, *114*, 3854-3918.

(101) Auchère, F.; Rusnak, F., What is the ultimate fate of superoxide anion in vivo? *J. Biol. Inorg. Chem.* **2002**, *7*, 664-667.

(102) Fridovich, I., Superoxide Dismutases: An Adaptation to a Paramagnetic Gas. *J. Biol. Chem.* **1989**, *264*, 7761-7764.

(103) Abreu, I. A.; Cabelli, D. E., Superoxide dismutases–a review of the metal-associated mechanistic variations. *Biochim. Biophys. Acta* **2010**, *1804*, 263-274.

(104) Tierney, D. L.; Fee, J. A.; Ludwig, M. L.; Penner-Hahn, J. E., X-ray Absorption Spectroscopy of the Iron Site in *Escherichia coli* Fe(III) Superoxide Dismutase. *Biochemistry* **1995**, *34*, 1661-1668.

(105) Miller, A.-F., Superoxide dismutases: active sites that save, but a protein that kills. *Curr. Opin. Chem. Biol.* **2004**, *8*, 162-168.

(106) Borgstahl, G. E. O.; Parge, H. E.; Hickey, M. J.; Beyer, W. F., Jr.; Hallewell, R. A.; Tainer, J. A., The structure of human mitochondrial manganese superoxide dismutase reveals a novel tetrameric interface of two 4-helix bundles. *Cell* **1992**, *71*, 107-118.

(107) Tainer, J. A.; Getzoff, E. D.; Richardson, J. S.; Richardson, D. C., Structure and Mechanism of Copper, Zinc Superoxide-Dismutase. *Nature* **1983**, *306*, 284-287.

(108) Imlay, J. A.; Fridovich, I., Assay of Metabolic Superoxide Production in *Escherichia-Coli*. *J. Biol. Chem.* **1991**, *266*, 6957-6965.

(109) Hjalmarsson, K.; Marklund, S. L.; Engstrom, A.; Edlund, T., Isolation and Sequence of Complementary-DNA Encoding Human Extracellular Superoxide-Dismutase. *Proc. Natl. Acad. Sci. U.S.A.* **1987**, *84*, 6340-6344.

(110) Alscher, R. G.; Erturk, N.; Heath, L. S., Role of superoxide dismutases (SODs) in controlling oxidative stress in plants. *J. Exp. Bot.* **2002**, *53*, 1331-1341.

(111) Oury, T. D.; Crapo, J. D.; Valnickova, Z.; Enghild, J. J., Human extracellular superoxide dismutase is a tetramer composed of two disulphide-linked dimers: A simplified, high-yield purification of extracellular superoxide dismutase. *Biochem. J.* **1996**, *317*, 51-57.

(112) Rosen, D. R.; Siddique, T.; Patterson, D.; Figlewicz, D. A.; Sapp, P.; Hentati, A.; Donaldson, D.; Goto, J.; Oregan, J. P.; Deng, H. X.; Rahmani, Z.; Krizus, A.; Mckennayasek, D.; Cayabyab, A.; Gaston, S. M.; Berger, R.; Tanzi, R. E.; Halperin, J. J.; Herzfeldt, B.; Vandenbergh, R.; Hung, W. Y.; Bird, T.; Deng, G.; Mulder, D. W.; Smyth, C.; Laing, N. G.; Soriano, E.; Pericakvance, M. A.; Haines, J.; Rouleau, G. A.; Gusella, J. S.; Horvitz, H. R.; Brown, R. H., Mutations in Cu/Zn Superoxide-Dismutase Gene Are Associated with Familial Amyotrophic-Lateral-Sclerosis. *Nature* **1993**, *362*, 59-62.

(113) Valentine, J. S.; Doucette, P. A.; Potter, S. Z., Copper-zinc superoxide dismutase and amyotrophic lateral sclerosis. *Annu. Rev. Biochem* **2005**, *74*, 563-593.

(114) Ellerby, L. M.; Cabelli, D. E.; Graden, J. A.; Valentine, J. S., Copper-zinc superoxide dismutase: Why not pH-dependent? *J. Am. Chem. Soc.* **1996**, *118*, 6556-6561.

(115) Fisher, C. L.; Cabelli, D. E.; Tainer, J. A.; Hallewell, R. A.; Getzoff, E. D., The Role of Arginine-143 in the Electrostatics and Mechanism of Cu,Zn Superoxide-Dismutase - Computational and Experimental Evaluation by Mutational Analysis. *Proteins: Struct. Funct. and Genet.* **1994**, *19*, 24-34.

(116) Meier, B.; Barra, D.; Bossa, F.; Calabrese, L.; Rotilio, G., Synthesis of Either Fe-Superoxide or Mn-Superoxide Dismutase with an Apparently Identical Protein Moiety by an Anaerobic Bacterium Dependent on the Metal Supplied. *J. Biol. Chem.* **1982**, *257*, 3977-3980.

(117) Gregory, E. M.; Dapper, C. H., Isolation of Iron-Containing Superoxide-Dismutase from *Bacteroides-Fragilis* - Reconstitution as a Mn-Containing Enzyme. *Arch. Biochem. Biophys.* **1983**, *220*, 293-300.

(118) Brock, C. J.; Harris, J. I., Superoxide-Dismutase from *Bacillus-Stearothermophilus* - Reversible Removal of Manganese and Its Replacement by Other Metals. *Biochem. Soc. Trans.* **1977**, *5*, 1537-1539.

(119) Ose, D. E.; Fridovich, I., Manganese-Containing Superoxide-Dismutase from *Escherichia-Coli* - Reversible Resolution and Metal Replacements. *Arch. Biochem. Biophys.* **1979**, *194*, 360-364.

(120) Yamakura, F., Study on Reconstitution of Iron Superoxide Dismutase from *Pseudomonas-Ovalis*. *J. Biochem.* **1978**, *83*, 849-857.

(121) Vance, C. K.; Miller, A. F., Simple proposal that can explain the inactivity of metal-substituted superoxide dismutases. *J. Am. Chem. Soc.* **1998**, *120*, 461-467.

(122) Vance, C. K.; Miller, A. F., Novel insights into the basis for *Escherichia coli* superoxide dismutase's metal ion specificity from Mn-substituted FeSOD and its very high E(m). *Biochemistry* **2001**, *40*, 13079-13087.

(123) Miller, A. F.; Padmakumar, K.; Sorkin, D. L.; Karapetian, A.; Vance, C. K., Proton-coupled electron transfer in Fe-superoxide dismutase and Mn-superoxide dismutase. *J. Inorg. Biochem.* **2003**, *93*, 71-83.

(124) Dooley, D. M.; Jones, T. F.; Karas, J. L.; Mcguirl, M. A.; Brown, R. D.; Koenig, S. H., Azide and Fluoride Binding to *Escherichia-Coli* Iron Superoxide-Dismutase as Studied by Solvent Proton Magnetic-Relaxation Dispersion. *J. Am. Chem. Soc.* **1987**, *109*, 721-725.

(125) Lah, M. S.; Dixon, M. M.; Pattridge, K. A.; Stallings, W. C.; Fee, J. A.; Ludwig, M. L., Structure-Function in Escherichia-Coli Iron Superoxide-Dismutase - Comparisons with the Manganese Enzyme from *Thermus-Thermophilus*. *Biochemistry* **1995**, *34*, 1646-1660.

(126) Edwards, R. A.; Baker, H. M.; Whittaker, M. M.; Whittaker, J. W.; Jameson, G. B.; Baker, E. N., Crystal structure of *Escherichia coli* manganese superoxide dismutase at 2.1-angstrom resolution. *J. Biol. Inorg. Chem.* **1998**, *3*, 161-171.

(127) Schmidt, M.; Scherk, C.; Iakovleva, O.; Nolting, H. F.; Meier, B.; Parak, F., The structure of the azide coordinated superoxide dismutase of *Propionibacterium shermanii* investigated by X-ray structure analysis, extended X-ray absorption fine structure, Mossbauer and electron paramagnetic resonance spectroscopy. *Inorg. Chim. Acta* **1998**, *276*, 65-72.

(128) Slykhouse, T. O.; Fee, J. A., Physical and Chemical Studies on Bacterial Superoxide Dismutases - Purification and Some Anion Binding Properties of Iron-Containing Protein of *Escherichia-Coli-B*. *J. Biol. Chem.* **1976**, *251*, 5472-5477.

(129) Miller, A.-F.; Sorkin, D. L.; Padmakumar, K., Anion binding properties of reduced and oxidized iron-containing superoxide dismutase reveal no requirement for tyrosine 34. *Biochemistry* **2005**, *44*, 5969-5981.

(130) Bull, C.; Fee, J. A., Steady-State Kinetic-Studies of Superoxide Dismutases - Properties of the Iron Containing Protein from *Escherichia-Coli*. *J. Am. Chem. Soc.* **1985**, *107*, 3295-3304.

(131) Aruoma, O. I.; Halliwell, B., Superoxide-Dependent and Ascorbate-Dependent Formation of Hydroxyl Radicals from Hydrogen-Peroxide in the Presence of Iron - Are Lactoferrin and Transferrin Promoters of Hydroxyl-Radical Generation. *Biochem. J.* **1987**, *241*, 273-278.

(132) Miller, A. F.; Yikilmaz, E.; Vathyam, S., N^{15} NMR characterization of His residues in and around the active site of FeSOD. *Biochim. Biophys. Acta, Proteins Proteomics* **2010**, *1804*, 275-284.

(133) Jackson, T. A.; Karapetian, A.; Miller, A. F.; Brunold, T. C., Probing the geometric and electronic structures of the low-temperature azide adduct and the product-inhibited form of oxidized manganese superoxide dismutase. *Biochemistry* **2005**, *44*, 1504-1520.

(134) Pick, M.; Rabani, J.; Yost, F.; Fridovich, I., Catalytic Mechanism of Manganese-Containing Superoxide-Dismutase of *Escherichia-Coli* Studied by Pulse-Radiolysis. *J. Am. Chem. Soc.* **1974**, *96*, 7329-7333.

(135) Mcadam, M. E.; Fox, R. A.; Lavelle, F.; Fielden, E. M., Pulse-Radiolysis Study of Manganese-Containing Superoxide-Dismutase from *Bacillus-Stearothermophilus* - Kinetic-Model for Enzyme Action. *Biochem. J.* **1977**, *165*, 71-79.

(136) Mcadam, M. E.; Lavelle, F.; Fox, R. A.; Fielden, E. M., Pulse-Radiolysis Study of Manganese-Containing Superoxide-Dismutase from *Bacillus-Stearothermophilus* - Further-Studies on Properties of Enzyme. *Biochem. J.* **1977**, *165*, 81-87.

(137) Bull, C.; Niederhoffer, E. C.; Yoshida, T.; Fee, J. A., Kinetic-Studies of Superoxide Dismutases - Properties of the Manganese-Containing Protein from *Thermus-Thermophilus*. *J. Am. Chem. Soc.* **1991**, *113*, 4069-4076.

(138) Hsu, J. L.; Hsieh, Y. S.; Tu, C. K.; OConnor, D.; Nick, H. S.; Silverman, D. N., Catalytic properties of human manganese superoxide dismutase. *J. Biol. Chem.* **1996**, *271*, 17687-17691.

(139) Oberley, L. W., Anticancer therapy by overexpression of superoxide dismutase. *Antioxid. Redox Signaling* **2001**, *3*, 461-472.

(140) Policastro, L.; Molinari, B.; Larcher, F.; Blanco, P.; Podhajcer, O. L.; Costa, C. S.; Rojas, P.; Dur n, H., Imbalance of antioxidant enzymes in tumor cells and inhibition of proliferation and malignant features by scavenging hydrogen peroxide. *Mol. Carcinog.* **2004**, *39*, 103-113.

(141) Buettner, G. R.; Ng, C. F.; Wang, M.; Rodgers, V. G. J.; Schafer, F. Q., A new paradigm: Manganese superoxide dismutase influences the production of H_2O_2 in cells and thereby their biological state. *Free Radical Biol. Med.* **2006**, *41*, 1338-1350.

(142) Youn, H. D.; Youn, H.; Lee, J. W.; Yim, Y. I.; Lee, J. K.; Hah, Y. C.; Kang, S. O., Unique isozymes of superoxide dismutase in *Streptomyces griseus*. *Arch. Biochem. Biophys.* **1996**, *334*, 341-348.

(143) Youn, H.-D.; Kim, E.-J.; Roe, J.-H.; Hah, Y. C.; Kang, S.-O., A novel nickel-containing superoxide dismutase from *Streptomyces* spp. *Biochem. J.* **1996**, *318*, 889-896.

(144) Fiedler, A. T.; Bryngelson, P. A.; Maroney, M. J.; Brunold, T. C., Spectroscopic and Computational Studies of Ni Superoxide Dismutase: Electronic Structure Contributions to Enzymatic Function. *J. Am. Chem. Soc.* **2005**, *127*, 5449-5462.

(145) Krüger, H.-J.; Peng, G.; Holm, R. H., Low-Potential Nickel(III,II) Complexes: New Systems Based on Tetradentate Amidate-Thiolate Ligands and the Influence of Ligand Structure on Potentials in Relation to the Nickel Site in [NiFe]-Hydrogenases. *Inorg. Chem.* **1991**, *30*, 734-742.

(146) Herbst, R. W.; Guce, A.; Bryngelson, P. A.; Higgins, K. A.; Ryan, K. C.; Cabelli, D. E.; Garman, S. C.; Maroney, M. J., Role of Conserved Tyrosine Residues in NiSOD Catalysis: A Case of Convergent Evolution. *Biochemistry* **2009**, *48*, 3354-3369.

(147) Szilagyi, R. K.; Bryngelson, P. A.; Maroney, M. J.; Hedman, B.; Hodgson, K. O.; Solomon, E. I., S K-edge X-ray absorption spectroscopic investigation of the Ni-containing superoxide dismutase active site: New structural insight into the mechanism. *J. Am. Chem. Soc.* **2004**, *126*, 3018-3019.

(148) Hatlevik, O.; Blanksma, M. C.; Mathrubootham, V.; Arif, A. M.; Hegg, E. L., Modeling carbon monoxide dehydrogenase/acetyl-CoA synthase (CODH/ACS): a trinuclear nickel complex employing deprotonated amides and bridging thiolates. *J. Biol. Inorg. Chem.* **2004**, *9*, 238-246.

(149) Kaasjager, V. E.; Bouwman, E.; Gorter, S.; Reedijk, J.; Grapperhaus, C. A.; Reibenspies, J. H.; Smee, J. J.; Darensbourg, M. Y.; Derecskei-Kovacs, A.; Thomson, L. M., Unique reactivity of a tetradentate N_2S_2 complex of nickel: Intermediates in the production of sulfur oxygenates. *Inorg. Chem.* **2002**, *41*, 1837-1844.

(150) Grapperhaus, C. A.; Mullins, C. S.; Kozlowski, P. M.; Mashuta, M. S., Synthesis and oxygenation of a nickel(II) and zinc(II) dithiolate: An experimental and theoretical comparison. *Inorg. Chem.* **2004**, *43*, 2859-2866.

(151) Green, K. N.; Brothers, S. M.; Jenkins, R. M.; Carson, C. E.; Grapperhaus, C. A.; Darensbourg, M. Y., An experimental and computational study of sulfur-modified nucleophilicity in a dianionic NiN_2S_2 complex. *Inorg. Chem.* **2007**, *46*, 7536-7544.

(152) Shearer, J.; Zhao, N., $[Me_4N](Ni^{II}(BEAAM))$: A Synthetic Model for Nickel Superoxide Dismutase That Contains Ni in a Mixed Amine/Amide Coordination Environment. *Inorg. Chem.* **2006**, *45*, 9637-9639.

(153) Shearer, J.; Long, L. M., A Nickel Superoxide Dismutase Maquette That Reproduces the Spectroscopic and Functional Properties of the Metalloenzyme. *Inorg. Chem.* **2006**, *45*, 2358-2360.

(154) Mullins, C. S.; Grapperhaus, C. A.; Kozlowski, P. M., Density functional theory investigations of NiN_2S_2 reactivity as a function of nitrogen donor type and N-H···S hydrogen bonding inspired by nickel-containing superoxide dismutase. *J. Biol. Inorg. Chem.* **2006**, *11*, 617-625.

(155) Bellefeuille, J. A.; Grapperhaus, C. A.; Derecskei-Kovacs, A.; Reibenspies, J. H.; Darensbourg, M. Y., Correlation of electrochemistry, nucleophilicity and density functional calculations of the cis-dithiolate (bme*-daco)Ni. *Inorg. Chim. Acta* **2000**, *300*, 73-81.

(156) Broering, E. P.; Truong, P. T.; Gale, E. M.; Harrop, T. C., Synthetic Analogues of Nickel Superoxide Dismutase: A New Role for Nickel in Biology. *Biochemistry* **2013**, *52*, 4-18.

(157) Mathrubootham, V.; Thomas, J.; Staples, R.; McCraken, J.; Shearer, J.; Hegg, E. L., Bisamidate and Mixed Amine/Amidate NiN_2S_2 Complexes as Models for Nickel-Containing Acetyl Coenzyme A Synthase and Superoxide Dismutase: An Experimental and Computational Study. *Inorg. Chem.* **2010**, *49*, 5393-5406.

(158) Miller, A.-F., Redox Tuning over Almost 1 V in a Structurally Conserved Active Site: Lessons from Fe-Containing Superoxide Dismutase. *Acc. Chem. Res.* **2008**, *41*, 501-510.

(159) Tietze, D.; Breitzke, H.; Imhof, D.; Kothe, E.; Weston, J.; Buntkowsky, G., New Insight into the Mode of Action of Nickel Superoxide Dismutase by Investigating Metallopeptide Substrate Models. *Chem. –Eur. J.* **2009**, *15*, 517-523.

(160) Choudhury, S. B.; Lee, J.-W.; Davidson, G.; Yim, Y.-I.; Bose, K.; Sharma, M. L.; Kang, S.-O.; Cabelli, D. E.; Maroney, M. J., Examination of the Nickel Site Structure and Reaction Mechanism in *Streptomyces seoulensis* Superoxide Dismutase. *Biochemistry* **1999**, *38*, 3744-3752.

(161) Getzoff, E. D.; Tainer, J. A.; Weiner, P. K.; Kollman, P. A.; Richardson, J. S.; Richardson, D. C., Electrostatic Recognition between Superoxide and Copper, Zinc Superoxide-Dismutase. *Nature* **1983**, *306*, 287-290.

(162) Getzoff, E. D.; Cabelli, D. E.; Fisher, C. L.; Parge, H. E.; Viezzoli, M. S.; Banci, L.; Hallewell, R. A., Faster Superoxide-Dismutase Mutants Designed by Enhancing Electrostatic Guidance. *Nature* **1992**, *358*, 347-351.

(163) Huang, W. J.; Jia, J.; Cummings, J.; Nelson, M.; Schneider, G.; Lindqvist, Y., Crystal structure of nitrile hydratase reveals a novel iron centre in a novel fold. *Structure* **1997**, *5*, 691-699.

(164) Mayer, S. M.; Lawson, D. M.; Gormal, C. A.; Roe, S. M.; Smith, B. E., New insights into structure-function relationships in nitrogenase: A 1.6 angstrom resolution X-ray

crystallographic study of *Klebsiella pneumoniae* MoFe-protein. *J. Mol. Biol.* **1999**, *292*, 871-891.

(165) Kovacs, J. A., Synthetic analogues of cysteinate-ligated non-heme iron and non-corrinoid cobalt enzymes. *Chem. Rev.* **2004**, *104*, 825-848.

(166) Collins, T. J., Designing Ligands for Oxidizing Complexes. *Acc. Chem. Res.* **1994**, *27*, 279-285.

(167) Noveron, J. C.; Olmstead, M. M.; Mascharak, P. K., Effect of carboxamido N coordination to iron on the redox potential of low-spin non-heme iron centers with N,S coordination: Relevance to the iron site of nitrile hydratase. *Inorg. Chem.* **1998**, *37*, 1138-1139.

(168) Brewer, J. C.; Collins, T. J.; Smith, M. R.; Santarsiero, B. D., Neutral Square-Planar Cobalt(III) Complexes. *J. Am. Chem. Soc.* **1988**, *110*, 423-428.

(169) Lanzilotta, W. N.; Schuller, D. J.; Thorsteinsson, M. V.; Kerby, R. L.; Roberts, G. P.; Poulos, T. L., Structure of the CO sensing transcription activator CooA. *Nat. Struct. Biol.* **2000**, *7*, 876-880.

(170) Chan Chung, K. C.; Cao, L.; Dias, A. V.; Pickering, I. J.; George, G. N.; Zamble, D. B., A High-Affinity Metal-Binding Peptide from *Escherichia coli* HypB. *J. Am. Chem. Soc.* **2008**, *130*, 14056-14056.

(171) Harford, C.; Sarkar, B., Amino terminal Cu(II)- and Ni(II)-binding (ATCUN) motif of proteins and peptides: Metal binding, DNA cleavage, and other properties. *Acc. Chem. Res.* **1997**, *30*, 123-130.

(172) Johnson, O. E.; Ryan, K. C.; Maroney, M. J.; Brunold, T. C., Spectroscopic and computational investigation of three Cys-to-Ser mutants of nickel superoxide dismutase: insight into the roles played by the Cys2 and Cys6 active-site residues. *J. Biol. Inorg. Chem.* **2010**, *15*, 777-793.

(173) Fridovich, I., Oxygen toxicity: A radical explanation. *J. Exp. Biol.* **1998**, *201*, 1203-1209.

(174) Bielski, B. H. J.; Cabelli, D. E., Highlights of Current Research Involving Superoxide and Perhydroxyl Radicals in Aqueous-Solutions. *Int. J. Radiat Biol.* **1991**, *59*, 291-319.

(175) Pelmenschikov, V.; Siegbahn, P. E. M., Nickel Superoxide Dismutase Reaction Mechanism Studied by Hybrid Density Functional Methods. *J. Am. Chem. Soc.* **2006**, *128*, 7466-7475.

(176) Prabhakar, R.; Morokuma, K.; Musaev, D. G., A DFT Study of the Mechanism of Ni Superoxide Dismutase (NiSOD): Role of the Active Site Cysteine-6 Residue in the Oxidative Half-Reaction. *J. Comput. Chem.* **2006**, *27*, 1438-1445.

(177) Campecino, J. O.; Dudycz, L. W.; Tumelty, D.; Berg, V.; Cabelli, D. E.; Maroney, M. J., A Semisynthetic Strategy Leads to Alteration of the Backbone Amidate Ligand in the NiSOD Active Site. *J. Am. Chem. Soc.* **2015**, *137*, 9044-9052.

(178) Bertini, I.; Banci, L.; Piccioli, M.; Luchinat, C., Spectroscopic Studies on Cu_2Zn_2SOD - a Continuous Advancement of Investigation Tools. *Coord. Chem. Rev.* **1990**, *100*, 67-103.

(179) Banci, L.; Bertini, I.; Cabelli, D. E.; Hallewell, R. A.; Luchinat, C.; Viezzoli, M. S., Advances in the Understanding of the Structure-Function Relationship in Cu,Zn Superoxide-Dismutase. *Free Rad. Res. Com.* **1991**, *12-3*, 239-251.

(180) Leveque, V. J. P.; Vance, C. K.; Nick, H. S.; Silverman, D. N., Redox properties of human manganese superoxide dismutase and active-site mutants. *Biochemistry* **2001**, *40*, 10586-10591.

(181) Ryan, K. C.; Guce, A. I.; Johnson, O. E.; Brunold, T. C.; Cabelli, D. E.; Garman, S. C.; Maroney, M. J., Nickel Superoxide Dismutase: Structural and Functional Roles of His1 and Its H-Bonding Network. *Biochemistry* **2015**, *54*, 1016-1027.

(182) Neupane, K. P.; Shearer, J., The Influence of Amine/Amide versus Bisamide Coordination in Nickel Superoxide Dismutase. *Inorg. Chem.* **2006**, *45*, 10552-10566.

(183) Neupane, K. P.; Gearty, K.; Francis, A.; Shearer, J., Probing Variable Axial Ligation in Nickel Superoxide Dismutase Utilizing Metallopeptide-Based Models: Insight into the Superoxide Disproportionation Mechanism. *J. Am. Chem. Soc.* **2007**, *129*, 14605–14618.

(184) Rao, P. V.; Bhaduri, S.; Jiang, J. F.; Holm, R. H., Sulfur bridging interactions of cis-planar Ni^{II}-S_2N_2 coordination units with nickel(II), copper(I,II), zinc(II), and mercury(Il): A library of bridging modes, including $Ni^{II}(\mu_2\text{-}SR)_2M^{I,II}$ rhombs. *Inorg. Chem.* **2004**, *43*, 5833-5849.

(185) Shearer, J.; Dehestani, A.; Abanda, F., Probing Variable Amine/Amide Ligation in $Ni^{II}N_2S_2$ Complexes Using Sulfur K-Edge and Nickel L-Edge X-ray Absorption Spectroscopies: Implications for the Active Site of Nickel Superoxide Dismutase. *Inorg. Chem.* **2008**, *47*, 2649-2660.

(186) Shearer, J., Insight into the Structure and Mechanism of Nickel-Containing Superoxide Dismutase Derived from Peptide-Based Mimics. *Acc. Chem. Res.* **2014**, *47*, 2332-2341 and references therein.

(187) Shearer, J.; Neupane, K. P.; Callan, P. E., Metallopeptide Based Mimics with Substituted Histidines Approximate a Key Hydrogen Bonding Network in the Metalloenzyme Nickel Superoxide Dismutase. *Inorg. Chem.* **2009**, *48*, 10560-10571.

(188) Shearer, J., Use of a Metallopeptide-Based Mimic Provides Evidence for a Proton-Coupled Electron-Transfer Mechanism for Superoxide Reduction by Nickel-Containing Superoxide Dismutase. *Angew. Chem. Int. Ed.* **2013**, *52*, 2569-2572.

(189) Shearer, J.; Peck, K. L.; Schmitt, J. C.; Neupane, K. P., Cysteinate Protonation and Water Hydrogen Bonding at the Active-Site of a Nickel Superoxide Dismutase Metallopeptide-Based Mimic: Implications for the Mechanism of Superoxide Reduction. *J. Am. Chem. Soc.* **2014**, *136*, 16009-16022.

(190) Allan, C. B.; Davidson, G.; Choudhury, S. B.; Gu, Z. J.; Bose, K.; Day, R. O.; Maroney, M. J., Protonation and alkylation of a dinuclear nickel thiolate complex. *Inorg. Chem.* **1998**, *37*, 4166-4167.

(191) Nakane, D.; Funahashi, Y.; Ozawa, T.; Masuda, H., Synthesis of an N_3S_2 Ni(II) Complex Directed to NiSOD Active Site and Its Structural, Electrochemical, and Spectroscopic Properties. *Trans. Mater. Res. Soc. Jpn.* **2009**, *34*, 513-516.

(192) Nakane, D.; Funahashi, Y.; Ozawa, T.; Masuda, H., A Square-planar Ni(II) Complex with an Asymmetric N_2S_2 Donor Set as a Model for the Active Site of Nickel-containing SOD: Structural Conversion Driven by Addition of a Strong Donor Ligand in the High Oxidation State. *Chem. Lett.* **2010**, *39*, 344-346.

(193) Nakane, D.; Kuwasako, S.; Tsuge, M.; Kubo, M.; Funahashi, Y.; Ozawa, T.; Ogura, T.; Masuda, H., A square-planar Ni(II) complex with an N_2S_2 donor set similar to the active centre of nickel-containing superoxide dismutase and its reaction with superoxide. *Chem. Commun.* **2010**, *46*, 2142-2144.

(194) Yao, S.; Bill, E.; Milsmann, C.; Wieghardt, K.; Driess, M., A "Side-on" Superoxonickel Complex [LNi(O_2)] with a Square-Planar Tetracoordinate Nickel(II) Center and Its Conversion into [LNi(μ-OH)$_2$NiL]. *Angew. Chem., Int. Ed.* **2008**, *47*, 7110-7113.

(195) Dey, A.; Green, K. N.; Jenkins, R. M.; Jeffrey, S. P.; Darensbourg, M.; Hodgson, K. O.; Hedman, B.; Solomon, E. I., S K-Edge XAS and DFT Calculations on Square-Planar Ni^{II}-Thiolate Complexes: Effects of Active and Passive H-bonding. *Inorg. Chem.* **2007**, *46*, 9655-9660.

(196) Farmer, P. J.; Reibenspies, J. H.; Lindahl, P. A.; Darensbourg, M. Y., Effects of Sulfur Site Modification on the Redox Potentials of Derivatives of [*N*,*N*'-Bis(2-Mercaptoethyl)-1,5-Diazacyclooctanato]Nickel(II). *J. Am. Chem. Soc.* **1993**, *115*, 4665-4674.

(197) Kopf, M. A.; Varech, D.; Tuchagues, J. P.; Mansuy, D.; Artaud, I., New intermediate-spin chloroiron(III) complex with a mixed nitrogen-sulfur co-ordination. *J. Chem. Soc., Dalton Trans.* **1998**, 991-998.

(198) Gennari, M.; Orio, M.; Pecaut, J.; Neese, F.; Collomb, M. N.; Duboc, C., Reversible Apical Coordination of Imidazole between the Ni(III) and Ni(II) Oxidation States of a Dithiolate Complex: A Process Related to the Ni Superoxide Dismutase. *Inorg. Chem.* **2010**, *49*, 6399-6401.

(199) Gennari, M.; Orio, M.; Pecaut, J.; Bothe, E.; Neese, F.; Collomb, M. N.; Duboc, C., Influence of Mixed Thiolate/Thioether versus Dithiolate Coordination on the

Accessibility of the Uncommon +I and +III Oxidation States for the Nickel Ion: An Experimental and Computational Study. *Inorg. Chem.* **2011**, *50*, 3707-3716.

(200) Gennari, M.; Retegan, M.; DeBeer, S.; Pecaut, J.; Neese, F.; Collomb, M. N.; Duboc, C., Experimental and Computational Investigation of Thiolate Alkylation in Ni-II and Zn-II Complexes: Role of the Metal on the Sulfur Nucleophilicity. *Inorg. Chem.* **2011**, *50*, 10047-10055.

(201) Weber, K.; Kramer, T.; Shafaat, H. S.; Weyhermuller, T.; Bill, E.; van Gastel, M.; Neese, F.; Lubitz, W., A Functional [NiFe]-Hydrogenase Model Compound That Undergoes Biologically Relevant Reversible Thiolate Protonation. *J. Am. Chem. Soc.* **2012**, *134*, 20745-20755.

(202) Cantekin, S.; de Greef, T. F. A.; Palmans, A. R. A., Benzene-1,3,5-tricarboxamide: a versatile ordering moiety for supramolecular chemistry. *Chem. Soc. Rev.* **2012**, *41*, 6125-6137.

(203) Lightfoot, M. P.; Mair, F. S.; Pritchard, R. G.; Warren, J. E., New supramolecular packing motifs: π -stacked rods encased in triply-helical hydrogen bonded amide strands. *Chem. Commun.*, **1999**, 1945-1946.

(204) Arunachalam, M.; Ghosh, P., A Versatile Tripodal Amide Receptor for the Encapsulation of Anions or Hydrated Anions via Formation of Dimeric Capsules. *Inorg. Chem.* **2010**, *49*, 943-951.

(205) Stals, P. J. M.; Haveman, J. F.; Palmans, A. R. A.; Schenning, A. P. H. J., The Self-Assembly Properties of a Benzene-1,3,5-tricarboxamide Derivative. *J. Chem. Educ.* **2009**, *86*, 230-233.

(206) van Hameren, R.; Schön, P.; van Buul, A. M.; Hoogboom, J.; Lazarenko, S. V.; Gerritsen, J. W.; Engelkamp, H.; Christianen, P. C. M.; Heus, H. A.; Maan, J. C.; Rasing, T.; Speller, S.; Rowan, A. E.; Elemans, J. A. A. W.; Nolte, R. J. M., Macroscopic Hierarchical Surface Patterning of Porphyrin Trimers via Self-Assembly and Dewetting. *Science* **2006**, *314*, 1433-1436.

(207) dos Santos, C. M. G.; Boyle, E. M.; De Solis, S.; Kruger, P. E.; Gunnlaugsson, T., Selective and tuneable recognition of anions using C_{3V}-symmetrical tripodal urea-amide receptor platforms. *Chem. Commun.* **2011**, *47*, 12176-12178.

(208) Jaffe, H. H., A Reexamination of the Hammett Equation. *Chem. Rev.* **1953**, *53*, 191-261.

(209) Gale, E. M.; Narendrapurapu, B. S.; Simmonett, A. C.; Schaefer, H. F., III; Harrop, T. C., Exploring the Effects of H-Bonding in Synthetic Analogues of Nickel Superoxide Dismutase (Ni-SOD): Experimental and Theoretical Implications for Protection of the Ni-SCys Bond. *Inorg. Chem.* **2010**, *49*, 7080-7096.

(210) Mullins, C. S.; Grapperhaus, C. A.; Kozlowski, P. M., Density functional theory investigations of NiN_2S_2 reactivity as a function of nitrogen donor type and N–H···S

hydrogen bonding inspired by nickel-containing superoxide dismutase. *J. Biol. Inorg. Chem.* **2006**, *11*, 617-625.

(211) Smith, J. N.; Hoffman, J. T.; Shirin, Z.; Carrano, C. J., H-bonding Interactions and Control of Thiolate Nucleophilicity and Specificity in Model Complexes of Zinc Metalloproteins. *Inorg. Chem.* **2005**, *44*, 2012-2017.

(212) McGuire, D. G.; Khan, M. A.; Ashby, M. T., Discontinuum between a Thiolate and a Thiol Ligand. *Inorg. Chem.* **2002**, *41*, 2202-2208.

(213) Ashby, M. T.; Enemark, J. H.; Lichtenberger, D. L., Destabilizing D(π)-P(π) Orbital Interactions and the Alkylation Reactions of Iron(II) Thiolate Complexes. *Inorg. Chem.* **1988**, *27*, 191-197.

CHAPTER 2

SYNTHESIS AND SPECIATION-DEPENDENT PROPERTIES OF A MULTIMETALLIC MODEL COMPLEX OF NISOD THAT EXHIBITS UNIQUE H-BONDING[1]

Steiner, R. A.;* Dzul, S. P.; Stemmler, T. L.; Harrop, T. C. Synthesis and Speciation-Dependent Properties of a Multimetallic Model Complex of NiSOD That Exhibits Unique Hydrogen- Bonding. *Inorg. Chem.* **2017**, *56*, 2849-2862.

2.1 Abstract

The complex, [{Ni^{II}(nmp)}$_3$$S_3$$BTA^{alk}$)] (**1**) ($nmp^{2-}$ = deprotonated form of *N*-(2-mercaptoethyl)picolinamide; $H_3S_3BTA^{alk}$ = N^1,N^3,N^5-tris(2-mercaptoethyl)benzene-1,3,5-tricarboxamide, where H = dissociable protons), supported by the thiolate-benzenetricarboxamide scaffold (S_3BTA^{alk}) has been synthesized as a trimetallic model of nickel-containing superoxide dismutase (NiSOD). X-ray absorption spectroscopy (XAS) and ^{1}H NMR measurements on **1** indicate that the Ni^{II} centers are square-planar with N_2S_2 coordination, and Ni-N and Ni-S distances of 1.95 Å and 2.16 Å, respectively. Additional evidence from IR indicates the presence of H-bonds in **1** from the ~-200 cm^{-1} shift in ν_{NH} from free ligand. The presence of H-bonds allows for speciation that is temperature, concentration, and solvent dependent. In unbuffered water and low temperature, a dimeric complex (**1**$^{\mathbf{A}}$; λ = 410 nm) that aggregates through intermolecular NH···O=C bonds of BTA units is observed. Dissolution of **1** in pH 7.4 buffer or in unbuffered water at temperatures above 50 °C results in monomeric complex (**1**$^{\mathbf{M}}$; λ = 367 nm) linked through intramolecular NH···S bonds. DFT computations indicate a low energy barrier between **1**$^{\mathbf{A}}$ and **1**$^{\mathbf{M}}$ with nearly identical frontier MOs and Ni-ligand metrics. Notably, **1**$^{\mathbf{A}}$ and **1**$^{\mathbf{M}}$ exhibit remarkable stability in protic solvents such as MeOH and H_2O, in stark contrast to monometallic [Ni^{II}(nmp)(SR)]$^-$ complexes. The reactivity of **1** with excess O_2, H_2O_2, and $O_2^{\bullet-}$ is species dependent. IR and UV-vis reveal that **1**$^{\mathbf{A}}$ in MeOH reacts with excess O_2 to yield an S-bound sulfinate, but does not react with $O_2^{\bullet-}$. In contrast, **1**$^{\mathbf{M}}$ is stable to O_2 in pH 7.4 buffer, but reacts with $O_2^{\bullet-}$ to yield a putative [Ni^{II}(nmp)(O_2)]$^-$ complex from release of the BTA-thiolate based on EPR.

2.2 Introduction

The bioinorganic synthetic model approach has been valuable in evaluating mechanism and understanding the intrinsic properties of the metal active site(s) in question by isolating the metal coordination unit(s) from the protein bulk.[1,2] While insightful in many ways, especially with respect to the proposal/identification of probable reaction intermediates, this approach can be limited due to the variable stability and solubility of the model in question, especially under physiological conditions. Additional restrictions arise from utilizing mononuclear metal complexes with limited accessible oxidation states to carry out multi-electron, often accompanied by multi-proton, substrate transformations. Some of these complications have been overcome by employing multimetallic clusters,[3-8] strategically designed monometallic complexes with stabilizing second-sphere H-bonds,[9] and protein complex hybrids.[10-13] For example, the thiolate-bridged di-Fe complex, $Fe_2[(SCH_2)_2NH](CO)_6$,[14] is a close structural model of the active site of Fe-hydrogenase yet is not functional. Hydrogenase activity is turned-on, however, when the complex is covalently-linked through a cysteine thiolate residue of a generic protein scaffold.[15,16] The di-Fe complex alone is poised to be a functional hydrogenase, but the protein provides additional steric and electronic protection to make this complex an active catalyst. This theme is common in enzymes containing metal clusters or a single metal active site in oligomeric protein architectures.

Ni-containing superoxide dismutase (NiSOD), isolated from *Streptomyces*[17] and found in the genome of cyanobacteria,[18] is one such metalloenzyme that exemplifies this theme. Aerobes possess SODs to catalyze the disproportionation of $O_2^{\bullet-}$ a cytotoxic byproduct of metabolism, into H_2O_2 and O_2 via alternate oxidation/reduction cycles of a first-row metal, i.e., Fe, Cu, Mn, Ni.[19-22] NiSOD is a peculiar member of the SOD family because it employs cysteine-sulfur

(CysS) donors that are susceptible to oxidation ($RS^{\bullet}$/RSSR) or oxygenation (RSO_x anions, x = 1-3).[23-27] NiSOD is a homohexamer comprised of six four-helix bundle subunits that form two interdigitated three-legged piano-stool dimers (Figure 2.S1).[25,26] Each subunit houses a $Ni^{III/II}$ ion coordinated to the first six residues of the N-terminus, which is buried in the space between two four-helix bundles of the opposing trimer. The reduced enzyme contains a square-planar Ni^{II}-N_2S_2 active site from two CysS (Cys2, Cys6), the deprotonated peptide of Cys2, and the N-terminal amine of His1 (Chart 2.1). In the oxidized enzyme, the imidazole-Nδ of His1 coordinates to form a square-pyramidal Ni^{III}-N_3S_2 unit (Chart 2.1). A number of second-sphere H-bonds have been identified as playing key roles in catalysis by controlling access to the active site, communication between subunits, and tuning active site geometry and electronics (Figure 2.S1).[25,28-30] Notably, mutations of residues involved in these interactions result in lowered stability and loss of activity, suggesting H-bond intersubunit interactions are necessary for function.[28-30]

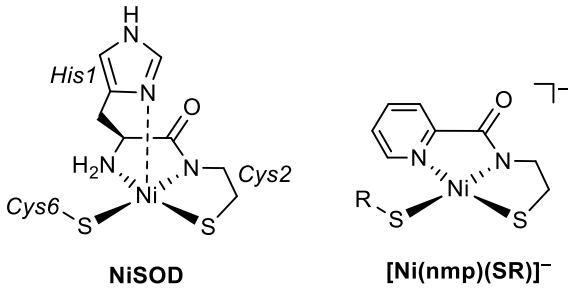

Chart 2.1. *Left*: NiSOD active site. Dotted line indicates the fluxional His1-Nδ coordination; bound in Ni^{III} and unbound in Ni^{II}. *Right*: General structure of the anion of the NiSOD model complex $[Ni^{II}(nmp)(SR)]^-$ (where nmp^{2-} = deprotonated form of *N*-(2-mercaptoethyl)picolinamide; R is variable).

In general, secondary interactions play an important role in protecting M-SCys bonds and peptide-NH H-bonds, i.e., NH···SCys, tune the electronic structure and control the reactivity of these active sites. Indeed, the potential of the electron-transfer protein rubredoxin is modulated by ~0.15 V through H-bonds around the $[Fe(SCys)_4]$ site.[31] Additionally, P450 models demonstrate that the covalent nature of the Fe-SCys bond is reduced by H-bonds to the coordinated CysS with a subsequent increase in redox potential.[32] Perhaps most relevant to SOD is the role of the NH···SCys bond in the $[Fe(NHis)_4(SCys)]$ active site of superoxide reductase (SOR). Indeed, the modulated $S(p\pi) \rightarrow Fe(d_{yz})$, π-to-π* bonding is essential for SOR activity; a proposed inner-sphere mechanism for $O_2^{\bullet-}$ reduction involves coordination to an axial position trans to SCys. The SCys plays the role of pushing electron density to Fe in order to promote electron-transfer and eventual H_2O_2 product dissociation.[33,34] The lengthening of the Fe-SCys

bond and subsequent changes in the pK_a of peroxo-bound intermediates can be attributed, in part, to NH···SCys bonding from a peptide-NH.[35, 36]

Over the past decade, our group[37-41] and others[42-58] have interrogated the structural and electronic properties of NiSOD utilizing the synthetic analogue approach. It thus follows that suitably designed models may answer the question of how this enzyme employs Ni-based redox with notable CysS stability. Since 2009, our group has synthesized Ni^{II}-N_2S_2 complexes utilizing the tridentate nmp^{2-} ligand (nmp^{2-} = deprotonated form of *N*-(2-mercaptoethyl)picolinamide), which structurally and electronically replicates the asymmetric donor environment of NiSOD (Chart 2.1).[37,39,41] This ligand allows manipulation of one specific S in the N_2S_2 coordination sphere. For example, $[Ni^{II}(nmp)(SR)]^-$ complexes that exhibit H-bonds to SR result in stabilization of S-based MOs relative to Ni-based AOs, allowing for enhanced Ni contribution to the HOMO and protection against S-oxidation.[39,58-60] Furthermore, incorporation of H-bonds capable of forming intramolecular bonds with metal thiolates is a synthetic challenge. While some degree of oxidative stability is observed, chemical oxidation, O_2 exposure, or addition of protic solvents, to these complexes ultimately result in *S*,*S*-bridged $[Ni_4(nmp)_4]$, RSSR, RSO_x, or RSH.[39,58-60] An objective of this work is to create an H-bond scaffold to generate secondary structure that emulates NiSOD, to an extent, as a means of protecting the Ni–thiolate bonds. Specifically, we employed the trithiolate ligand based on the 1,3,5-benzenetricarboxamide (BTA) scaffold to engage H-bonds to thiolates of multiple Ni-nmp units (Chart 2.2, complex **1**). Reports on derivatized BTAs reveal the formation of threefold intermolecular H-bonds among the carboxamides to form self-assembled helical aggregates[61-66] that inspired this design (Chart 2.2). Given the capability of the RS-ligands in $[Ni^{II}(nmp)(SR)]^-$ complexes to accept H-bonds, the proposal is that a multimeric complex would overcome the limits of traditional monometallic

analogues and impart additional stability onto individual Ni-nmp units such that a functional NiSOD model could be realized. As a proof of concept, we report herein the synthesis and properties of a multimeric NiSOD model employing a BTA-trithiolate scaffold.

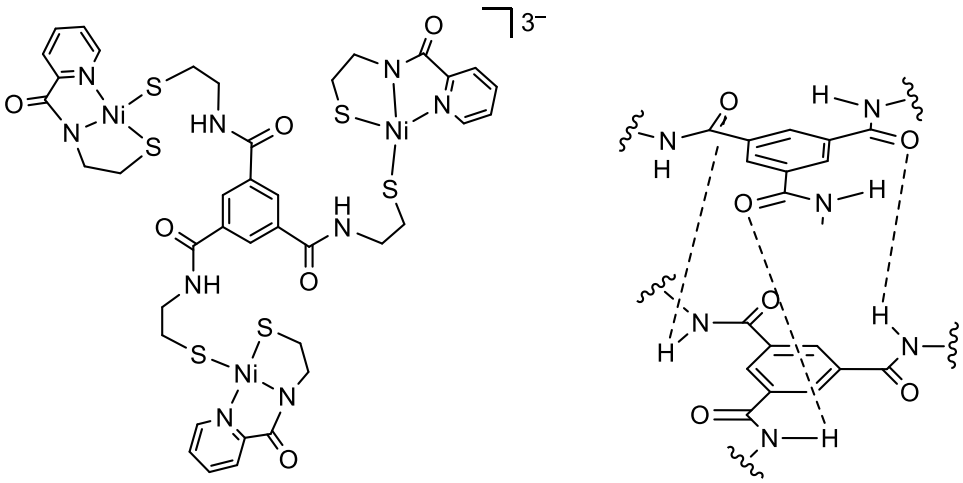

Chart 2.2. *Left*: Structure of the trianion of the NiSOD model $Na_3[\{Ni(nmp)\}_3(S_3BTA^{alk})]$ (**1**). *Right*: One mode of BTA aggregation forming helical stacks.

2.3 Results and Discussion

2.3.1 Synthesis. To model the H-bonding environment surrounding multiple Ni sites in NiSOD, we synthesized the trimetallic compound bearing three Ni-nmp units coordinated to sulfur of the BTA-trithiolate scaffold N^1,N^3,N^5-tris(2-mercaptoethyl)benzene-1,3,5-tricarboxamide) ($H_3S_3BTA^{alk}$, where H = dissociable protons), namely

$Na_3[\{Ni(nmp)\}_3(S_3BTA^{alk})]$ (**1**) (Chart 2.2).[67] The trithiol was synthesized via standard procedures (Scheme 2.S1): S-trityl cysteamine reacted with 1,3,5-benzenetricarbonyltrichloride to afford the S-trityl protected Tr-S_3BTA^{alk} as an air-stable white solid in 86% yield. Subsequent deprotection of the trityl groups with Et_3SiH in TFA/CH_2Cl_2 (1:1) resulted in $H_3S_3BTA^{alk}$ as a white solid in 80% yield. Expanding on previous procedures,[37,39,41] complex **1** was synthesized in 73% yield by reacting deprotonated ligand with the *S*,*S*-bridged complex $[Ni_4(nmp)_4]$ (**2**) (1:0.75) in MeOH at room temperature (RT) (Scheme 2.S1). Uniquely, **1** is stable in protic solvents (MeOH, H_2O, Figure 2.S10) as monitored by ^{1}H NMR and UV-vis spectroscopies (vide infra). The stability of **1** contrasts previously reported $[Ni^{II}(nmp)(SR)]^-$ complexes that revert back to **2** via protonation and release of RSH in protic media.[37,39,41] Indeed, **1** is stable in D_2O over the course of several days, as monitored by ^{1}H NMR (Figure 2.S13). Thus, the BTA scaffold provides protection at the Ni–S-BTA coordination site to inhibit protonation at the Ni–SR bond by likely depressing the thiolate pK_a.

2.3.2 Structural, Spectroscopic, and Theoretical Properties of 1. Complex **1** exhibits sharp signals in its ^{1}H NMR spectrum in a variety of solvents, consistent with square-planar Ni^{II} coordination (Figure 2.1, 2.S10; note: the properties presented here are likely representative of an aggregated species, vide infra). The solid-state FTIR spectrum of **1** (Figure S2.12) confirms the presence of both nmp (1619, 1592 cm^{-1}) and S_3BTA^{alk} ν_{CO} bands (1659 cm^{-1}), representing coordinated and free carboxamide groups, respectively. Other notable bands arise from the N–H stretch of the BTA carboxamide (ν_{NH} = 3246 cm^{-1}) to indicate coordination as the trithiolate and the presence of H-bonding (vide infra). Additional structural confirmation comes from negative-mode high-resolution electrospray ionization mass spectrometry (HR-ESI-MS(–)) where a peak with the appropriate isotope pattern, corresponding to $[M–Na]^-$ at *m*/*z*: 1143.946 (calcd. *m*/*z*:

1143.943) (Figure S2.11), is observed. The UV-vis spectrum of **1** is dominated by intense charge-transfer (CT) transitions between 350-410 nm that are solvent, concentration, and temperature dependent (vide infra), but similar in nature to $[Ni^{II}(nmp)(SR)]^-$ complexes.[47,68,69]

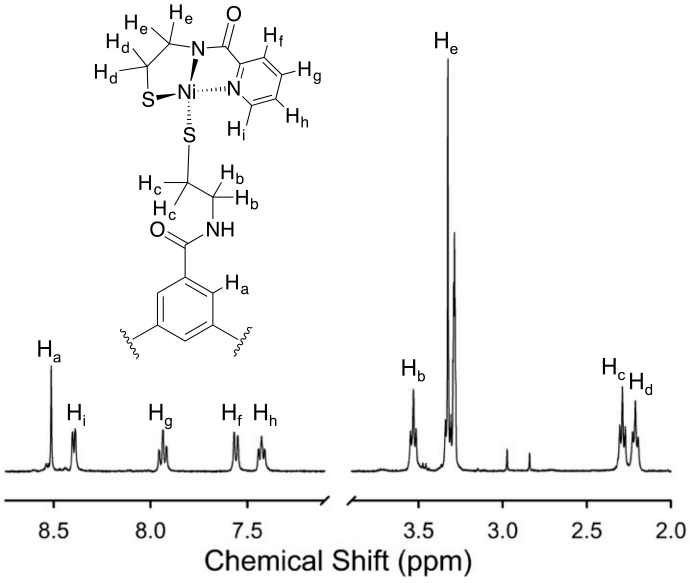

Figure 2.1. Partial ^{1}H NMR spectrum of **1** in CD_3OD at RT. Residual solvent peak is at 3.31 ppm. DMF from workup is also present between 2.8-3.0 ppm. Full ^{1}H NMR spectrum is shown in Figure 2.S10.

Nickel K-edge X-ray absorption spectroscopy (XAS) was used to provide structural details of the metal coordination geometry for **1**. The X-ray absorption near edge spectrum (XANES) for **1** shows a set of weak pre-edge 1s→3d transitions between 8332 and 8334 eV

(Figure 2.2) with a prominent 1s→4p feature at 8338 eV, coupled with the 1s→3d features, consistent with Ni^{II} existing in a distorted square-planar geometry.[70,71] Simulations of the extended X-ray absorption fine structure (EXAFS) for **1** indicate Ni is coordinated to both O/N- and S-scattering ligands at 1.95 Å (with a coordination number (CN) of 0.5) and 2.16 Å (CN of 2.0), respectively. These bond distances are comparable to Ni-ligand distances in other four-coordinate planar $[Ni^{II}(nmp)(SR)]^-$ complexes characterized by XAS and/or X-ray diffraction (XRD) (Table 2.S1).[38] Comparing the XAS simulation parameters for **1** to other $[Ni^{II}(nmp)(SR)]^-$ complexes suggest that **1** is a four-coordinate, distorted square-planar Ni complex with two S and two N/O scattering ligands (Table 2.S14).[37,39,41] The low CN for the O/N-donor from the EXAFS simulations for **1** is likely the result of dampening of the Ni-O/N signal due to the dominant S-scattering present, a condition observed in four-coordinate zinc-binding sites.[72] The XAS for (Et_4N)[Ni(nmp)(S-meb)] (**3**), a monometallic analogue of **1** (S-meb = thiolate of *N*-(2-mercaptoethyl)benzamide), afforded congruent distances to the data from the crystal structure of **3**.[39] Based on our XAS comparisons, the coordination sphere in **1** is nearly identical to that in **3**.

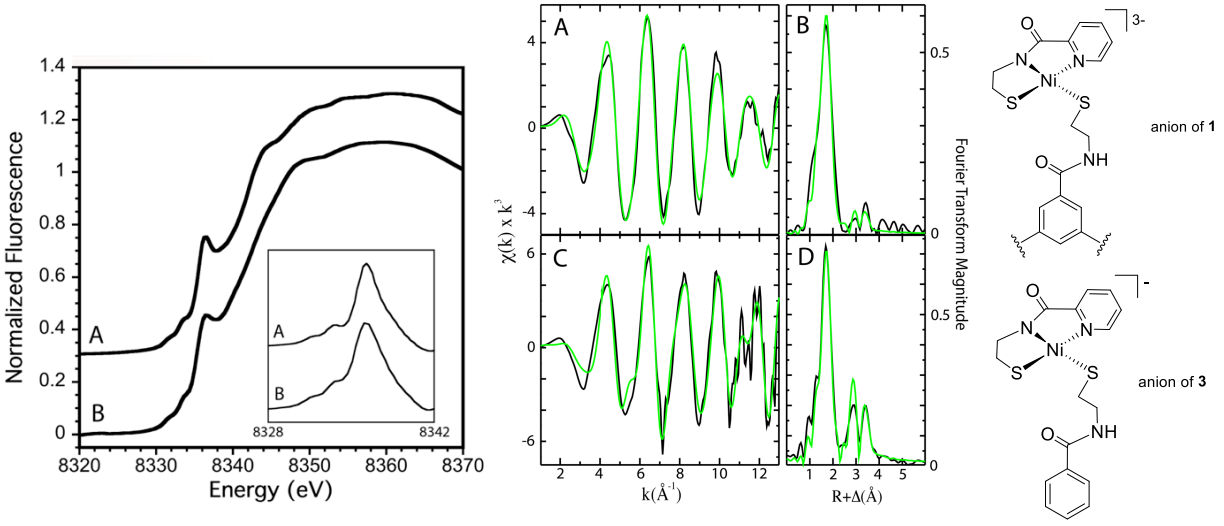

Figure 2.2. *Left*: Ni K-edge XANES for **3** (A) and **1** (B), offset for clarity. *Inset*: expansion of the pre-edge region; in both spectra, background subtracted for normalization and offset for clarity. *Center*: EXAFS (A, C) and Fourier Transform simulations (B, D) comparing raw data (black) to best-fit model (green) for **3** (A, B) and **1** (C, D). *Right*: Structural depiction of the anion portion of **1** (top; wavy lines represent the points of attachment of the two other Ni-nmp units) and $(Et_4N)[Ni(nmp)(S\text{-}meb)]$ (**3**, bottom).

2.3.3 Models of 1 (Aggregation Behavior/Properties). FTIR and ^{1}H NMR spectral changes have been utilized as indicators for the presence/absence of intra- or intermolecular H-bonds in a variety of metal-thiolate complexes.[58,59,73-79] The IR provides evidence for these interactions by monitoring changes in ν_{NH} of the carboxamide engaged in the H-bond when compared to free ligand.[80] Ultimately, the extent of the shift in ν_{NH} reports the strength of the resulting NH···S bond.[73] We have established that thiolate H-bonds exist in specially designed

$[Ni^{II}(nmp)(SR)]^-$ complexes, which has implications in protecting the RS^- ligand from oxidants.[39] When comparing free ligand[81] with **1**, we observe a dramatic change in ν_{NH} ($\Delta\nu_{NH}$) as evidenced by the –222 cm^{-1} shift of **1** (3220 cm^{-1}) from free ligand (3442 cm^{-1}) in CH_2Cl_2 (Figure 2.3). Indeed, this ν_{NH} value is indicative of a columnar stack of BTA units, as observed in a phosphine-derivatized BTA appended to a Rh complex.[82] Evidence for H-bonding is further supported by the observed 2.35 ppm downfield shift of δ_{NH} in the ^1H NMR spectrum of **1** in $CDCl_3$ (Table 2.S2). The singular δ_{NH} indicates uniformity in speciation as a mixture would result in multiple δ_{NH} shifts.[83] If a large self-assembly formed, then broadening and disappearance of signals would occur at 25 °C; shorter supramolecular assemblies generally form in protic solvents.[84] Comparing these results to those reported for **3** and free S-meb, we observe larger $\Delta\delta_{NH}$ (+1.78 ppm for **3**) and $\Delta\nu_{NH}$ (–191 cm^{-1} for **3**).[39] This comparison suggests H-bonding involving the BTA-carboxamide N–H of **1** is strong and the multimetallic nature likely facilitates this interaction.

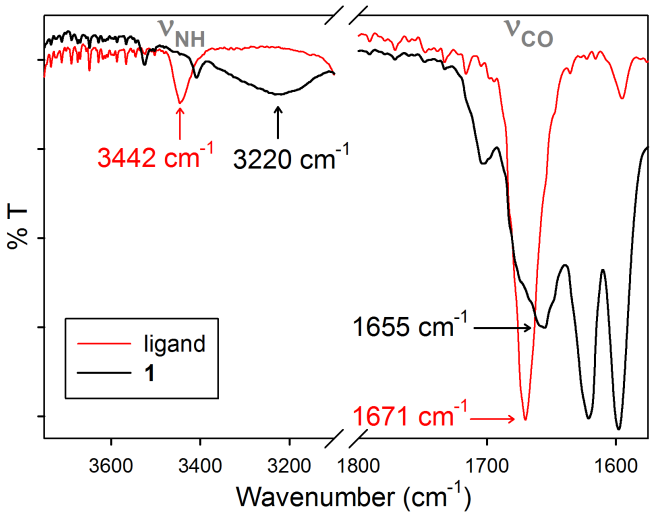

Figure 2.3. FTIR spectra of 25 mM CH_2Cl_2 solutions of **1** (black) and Tr-S_3BTA^{alk} (red) at RT. %T is scaled to match.

The UV-vis of **1** provides additional evidence for aggregation. Spectral monitoring of **1** revealed shifts in λ_{max} based on concentration, temperature, and solvent. For example, the λ_{max} of **1** in H_2O is 410 nm when [**1**] = 130 μM. As [**1**] decreases, a new feature appears at 367 nm that dominates at low concentration ([**1**] ≤ 1.67 μM) (Figure 2.S15). A temperature-dependence is also observed between these two λ_{max} extremes when monitoring aqueous solutions of **1** (100 μM) from 20-80 °C in 10 °C increments and further confirmed with variable temperature ^{1}H NMR measurements (Figure 2.S13). From 20 to 50 °C, **1** exhibits isosbestic behavior, where the 410 nm feature decreases and the 367 nm feature increases (Figure 2.S16). Degradation was observed above 50 °C. Interestingly, from 20-80 °C, a feature at 990 nm appears, possibly due to tetrahedral twisting of the planar complex, as seen in other Ni^{II}-N/S complexes.[85-88] After

returning to 20 °C, the 367 and 990 nm bands disappear and the 410 nm predominates, suggesting a reversible process. Our working model is that **1** exists as a trimetallic monomer ($\mathbf{1}^{\mathbf{M}}$) at low concentration/high temperature (λ = 367 nm) and an aggregate ($\mathbf{1}^{\mathbf{A}}$) at high concentration/low temperature (λ = 410 nm). Complex $\mathbf{1}^{\mathbf{M}}$ likely interacts via a strong intramolecular H-bond between the BTA-carboxamide N–H and the BTA thiolate (Chart 2.3, vide infra). The electron-withdrawing ability of the carboxamide H-bond results in a decrease in electron density at this S-ligand and the resulting blue-shift of λ_{max}.[73,89] In pH 7.4 phosphate-buffered saline (PBS), the dominant species is $\mathbf{1}^{\mathbf{M}}$ (367 nm), however, the dominant species in neutral unbuffered H_2O is $\mathbf{1}^{\mathbf{A}}$.[90] Assembly of $\mathbf{1}^{\mathbf{A}}$ likely occurs from H-bonds among the BTA-carboxamide N–H and C=O, in accordance with the IR and UV-vis data (Figure 2.3, vide supra). Ueyama reports similar UV-vis trends in a series of planar Pt^{II}-N_2S_2 complexes. In these complexes the electronic transition is proposed to originate from a S(p)-Pt(d) π^* HOMO to a bipy(p) π^*-based LUMO, similar frontier MOs for **1** (vide infra) and other $[Ni^{II}(nmp)(SR)]^-$ complexes, where intramolecular NH···S bonding results in a blue-shift of λ_{max}.[73]

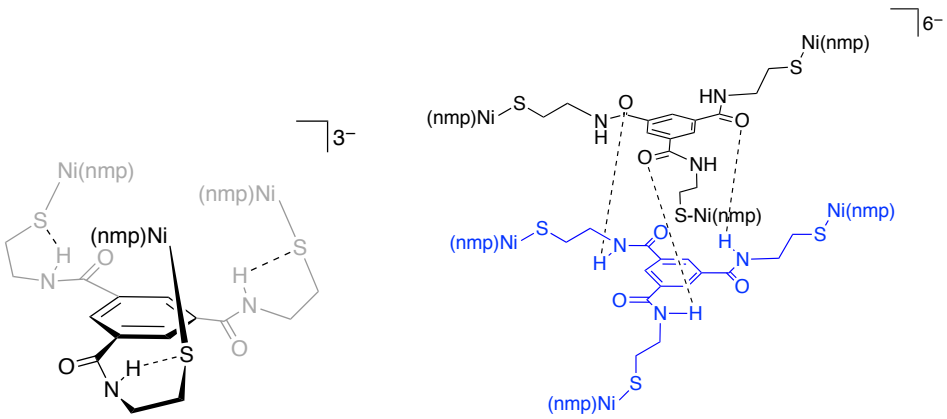

Chart 2.3. Proposed models of $\mathbf{1}^{\mathbf{M}}$ (left) and $\mathbf{1}^{\mathbf{A}}$ (right).

Speciation of $\mathbf{1}^{\mathbf{A}}/\mathbf{1}^{\mathbf{M}}$ has also been investigated by circular dichroism (CD) spectroscopy. For example, 12-35 μM MeOH solutions of $\mathbf{1}^{\mathbf{M}}$ display no CD signal (Figure 2.4), however, a negative Cotton effect at 210 nm appears at [**1**] ≥ 45 μM from a π-π* transition suggesting that $\mathbf{1}^{\mathbf{A}}$ forms a highly-ordered, self-assembled, left-handed superstructure imparted by conformation of the peripheral alkyl side-chains to give directionality to the aggregates. [61,91,92]

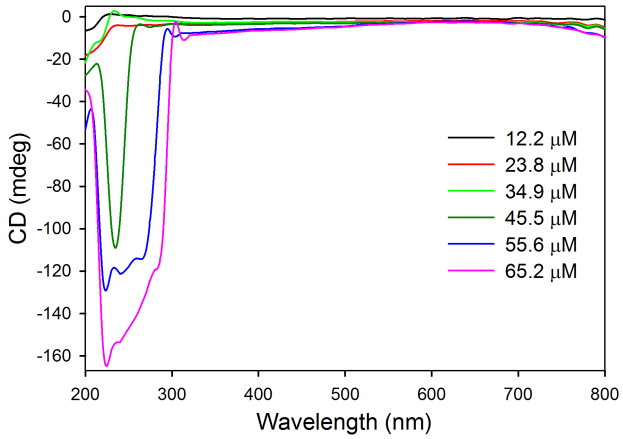

Figure 2.4. Concentration-dependent changes in the CD spectrum of **1** in MeOH at RT.

2.3.4 Electrochemistry. Initial electrochemical measurements of $\mathbf{1^A}$ were performed in DMF (2.5 mM **1**, 0.1 M ^{n}Bu$_4$NPF$_6$ supporting electrolyte, *E* vs. Fc/Fc$^+$) to discern possible Ni and/or thiolate redox events. The cyclic voltammogram (CV) of $\mathbf{1^A}$ displayed an irreversible oxidation (E_{ox}) event at -0.32 V, suggestive of thiolate oxidation to afford disulfide, similar to CVs of [Ni^{II}(nmp)(SR)]$^-$ complexes (Figure 2.S19).[37,39,41,93] Thus, the extensive H-bonding of the BTA scaffold does not provide access to an isolable Ni^{III} complex. Two reduction events at -1.40 and -1.70 V are also observed, the latter of which is revealed only after traversing E_{ox}. The more positive event at -1.40 V correlates to free ligand, while the weaker E_{red} at -1.70 V may indicate disulfide reduction, i.e., only observed after thiolate oxidation to RSSR.

The CV of **1** was performed in water to compare the implications of electronic structure on the speciation of **1** (*E* vs. Ag/AgCl, 0.5 M KNO$_3$ supporting electrolyte). As observed in DMF, the CV of $\mathbf{1^A}$ exhibits irreversible thiolate-based oxidation at 0.32 V, whereas $\mathbf{1^M}$ displays

E_{ox} at 0.40 V (Figure 2.5). In addition to E_{ox}, the CV of **1^{M}** contains a (partially masked) quasi-reversible couple that is also observed in the CV of the free tri-thiolate $[S_3BTA^{alk}]^{3-}$ centered at $E_{1/2}$ = 0.75 V. This feature suggests **1^{M}** may undergo partial ligand dissociation in buffer. Notably, the ~0.08 V cathodic shift in E_{ox} of **1^{M}**, and the lability of **1^{M}** when compared to **1^{A}**, is in-line with reported $[Ni^{II}(nmp)(SR)]^-$ complexes, where E_{ox} is correlated to the basicity of the monodentate thiolate (RS^-). That is, a stronger induced dipole from the H-bond results in a cathodic shift in E_{ox}, as demonstrated with **3** (~+0.20 V in MeCN) from the H-bond free complex $(Et_4N)[Ni(nmp)(S^tBu)]$, and also reported for a number of metalloproteins and small molecules involving H-bonded metal-thiolates.[39,73,94,95] The cathodic shift in E_{ox} and ligand lability of **1^{M}** supports an intramolecular H-bond between the thiolate and carboxamide of S_3BTA^{alk}. One hypothesis is that the intramolecular NH···S bond in **1^{M}** stabilizes the thiolate by effectively lowering the pK_a leading to a more labile RS^- ligand. In biology, H-bonds are known to lower the pK_a of CysS residues to stabilize the thiolate over the thiol.[96] At pH ~7.4, this may have implications on NiSOD and the role of the Ni-bound cysteinate as a proton shuttle for H_2O_2 generation. By tuning the pK_a of the thiolate ligands, a proton shuttle can be realized. DFT studies by Brunold show that the HOMO of $NiSOD_{red}$ is a π-antibonding MO primarily between the Ni(dπ) and S(pπ) orbitals.[97] Upon protonation of Cys6, alleviation of the filled-filled repulsion is more significant than the reduced basicity of the thiol, resulting in a shorter Ni-SCys bond. Given the presence of unligated $[S_3BTA^{alk}]^{3-}$ in the CV of **1^{M}**, the HOMO of **1^{M}** must not be as destabilized as $NiSOD_{red}$, resulting in reduced ligand donor strength of S_3BTA^{alk}. Collectively, these results provide direct experimental evidence to a difference in complex speciation, which is in-line with the proposed **1^{A}/1^{M}** model. Complex **1^{A}** may engage in H-

bonding involving the BTA carboxamide groups and the carbonyl of nmp to preclude a strong intramolecular H-bond with the thiolate of S_3BTA^{alk} to result in the lower E_{ox}.

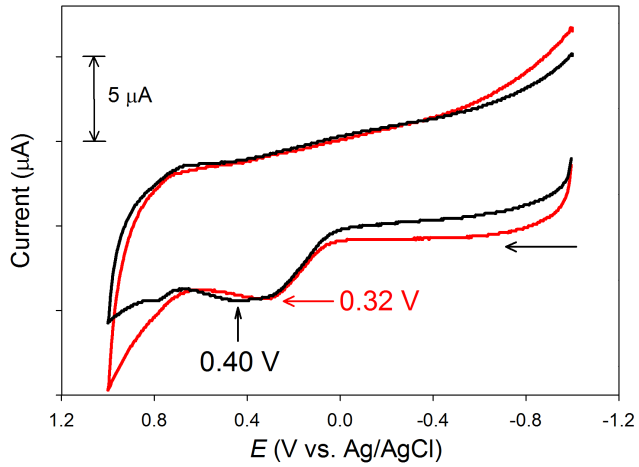

Figure 2.5. Aqueous CVs of $\mathbf{1}^{M}$ (black; 2.5 mM, 0.01 M PBS, pH 7.4) and $\mathbf{1}^{A}$ (red; 2.5 mM, non-buffered H_2O) with E_{ox} values indicated. Conditions: glassy carbon working electrode, 0.5 M KNO_3 supporting electrolyte, scan rate = 100 mV/s, RT. Arrow shows direction of scan.

2.3.5 Reactivity. The property that governs how the CysS ligands are protected from oxidative damage caused by $O_2^{\bullet-}$ and its disproportionation products (O_2, H_2O_2) remain a principle question in NiSOD. The mechanism of NiSOD has yet to be defined and some discussion remains over whether electron transfer occurs by an inner- or outer-sphere mechanism. However, most biochemical evidence suggest the latter.[24-26,98] How the ROS stability of **1** compares to other models and NiSOD will shed insight into the role of H-bonding on the

stability of the Ni-thiolates, and whether NiSOD relies on sterics or electronic tuning, or some combination of both, to prevent S-oxygenation/oxidation. Notably, intramolecular NH···S bonds in Zn^{II}-thiolate complexes reduce the rate of S-methylation by up to two orders of magnitude, experimental evidence of a significant decrease in thiolate nucleophilicity.[59,99,100, 101] Therefore, the ROS reactivity was characterized for both $\mathbf{1^A}$ and $\mathbf{1^M}$: 100 μM **1** in MeOH, where $\mathbf{1^A}$ predominates (λ_{max} = 435 nm) or pH 7.4 PBS, where $\mathbf{1^M}$ (λ_{max} = 367 nm) is present. Reactions were monitored by UV-vis after addition of either KO_2, H_2O_2, or O_2.

For $\mathbf{1^A}$, after a 60 s O_2 purge (O_2 saturation in MeOH = 1.99 ± 0.18 mM,[102] ~20 equiv), isosbestic behavior is observed over 30 min, where λ_{max} shifts to 355 nm (Figure 2.6). The solution maintained a red-orange color and FTIR analysis revealed ν_{SO} bands at 1096 and 1022 cm^{-1}, that correlate to an S-coordinated sulfinate (RSO_2^-) and have been confirmed by $^{18}O_2$ experiments (Figure 2.S22).[103,104] The blue-shift in λ_{max} is likely due to decreased electron density at the thiolate sulfur, analogous to the intramolecular H-bond in $\mathbf{1^M}$. The pseudo first-order rate constant (k_{obs} 1.84 ± 0.2 × 10^{-4} s^{-1}) compares to O_2 reactions with other $[Ni^{II}(nmp)(SR)]^-$ complexes (k_{obs} ~ 10^{-4}–10^{-5} s^{-1})[39] and planar Ni^{II}–thiolate complexes (ex. $[Ni^{II}(NS_2)(CN)]^-$ and $NiNS_3$; k_{obs}: 10^{-4} – 10^{-6} s^{-1} in DMF at 40 °C).[105,106] For the same reaction with $\mathbf{1^M}$ (O_2 saturation in H_2O = 0.34 ± 0.06 mM,[102] ~3.4 equiv), no reaction was observed over 20 min (Figure 2.7). The lack of reactivity of $\mathbf{1^M}$ to O_2 is unique and suggests that H-bonding is protective of S-oxygenation; the intramolecular H-bond reduces the S-nucleophilicity of the BTA-thiolate, which has been effective in H-bonded Zn-thiolates. [59,99,100]

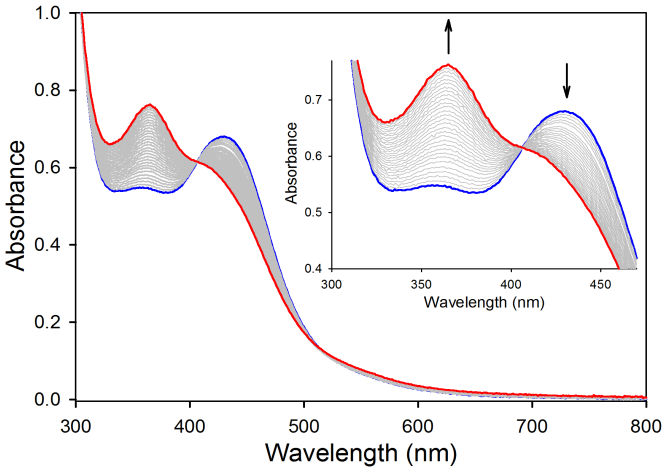

Figure 2.6. UV-vis spectral monitor of a 100 μM MeOH solution of $\mathbf{1}^{\mathbf{A}}$ (blue trace) and immediately after a 60 s O_2(g) purge. Final trace in red. Traces recorded at intervals of 1 scan/min for 30 min at 25 °C. *Inset*: zoom-in of 300-470 nm range. Arrow shows direction of change.

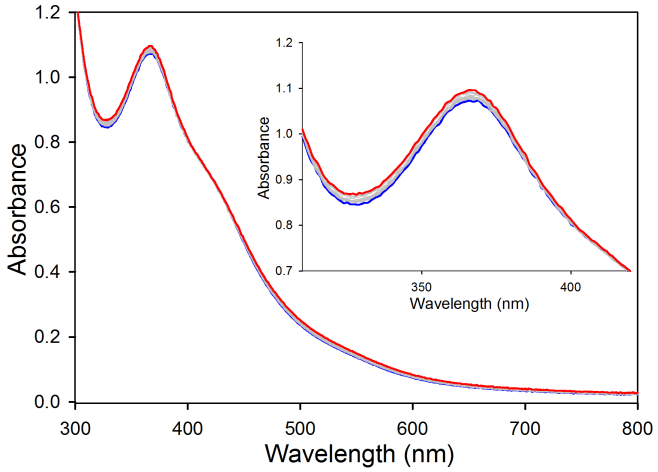

Figure 2.7. UV-vis spectral monitor of a 100 μM buffer solution of $\mathbf{1^M}$ (blue trace) and immediately after a 60 s O_2(g) purge (PBS, pH 7.4). Final trace in red. Traces recorded at intervals of 1 scan/min for 20 min at 25 °C. *Inset*: zoom-in of 300-450 nm range. Traces essentially superimpose onto one another.

Not surprisingly, addition of 100 equiv of H_2O_2·urea to either $\mathbf{1^A}$ or $\mathbf{1^M}$ resulted in rapid bleaching of the red-orange solution, a decrease in the CT band (Figure 2.S23-24), and formation of a red precipitate (*S*,*S*-bridged tetramer **2**). IR characterization of the $\mathbf{1^A}$/H_2O_2 reaction indicated ν_{SO} stretches (1155 and 1044 cm^{-1}) that, along with the loss of absorbance, correlate to free RSO_x species (Figure 2.S25). This degradation in the presence of H_2O_2 is consistent with previously reported models and suggests rapid removal of H_2O_2 in NiSOD.[38,46]

Addition of 100 equiv of KO_2 to $\mathbf{1^A}$ resulted in minimal changes to the characteristic CT band (Figure 2.8). Removal of solvent after 30 min and characterization of the resulting residue revealed no RSO_x. In contrast, addition of 100 equiv of KO_2 to $\mathbf{1^M}$ resulted in isosbestic behavior

in the UV-vis, where the 367 nm band decreases and a band at 410 nm increases (Figure 2.9). Attempts to probe the nature of the $O_2^{\bullet-}$ reaction have been made utilizing nitroblue tetrazolium (NBT),[107] which undergoes reduction of the colorless tetrazolium by $O_2^{\bullet-}$ to form blue formazan (λ_{max} = 530 nm).[108] Unfortunately, NBT has poor solubility in buffer and **1** alone reduced NBT resulting in formazan (34% yield, Figure 2.S26), precluding the quantification of $O_2^{\bullet-}$ sequestering activity in both buffer and MeOH. While others have utilized this assay to probe $O_2^{\bullet-}$ sequestration with NiSOD models,[44,54,56,109] we observe formazan after addition of NBT to **1** under anaerobic conditions in the absence of $O_2^{\bullet-}$. To probe the reactivity of $\mathbf{1^M}$ and $O_2^{\bullet-}$, we can compare the O_2 and H_2O_2 reactivity of $\mathbf{1^M}$. S-oxygenation is unlikely as this transformation would result in a blue-shift of the CT due to reduced S-contribution to the HOMO. Analogously, full S-oxygenation to the sulfonate (RSO_3^-) is unlikely because reformation of **2** would accompany the loss of the BTA-thiolate and result in bleaching. One possibility is ligand substitution, as observed in $[Ni^{II}(nmp)(S\text{-}o\text{-}babt)]^-$ (S-*o*-babt = thiolate of *o*-benzoylaminobenzenethiol), which also contains an intramolecular H-bond.[39] Interestingly, mixing 100 equiv of azide (N_3^-), an electronic mimic of $O_2^{\bullet-}$, to aqueous solutions of either $\mathbf{1^A}$ or $\mathbf{1^M}$ resulted in no UV-vis changes. Based on reactivity studies with H_2O_2 and O_2, it is unlikely that any catalytic disproportionation or redox transformation occurs between $O_2^{\bullet-}$ and $\mathbf{1^M}$ or $\mathbf{1^A}$. One proposal is that $O_2^{\bullet-}$ is substituting for the BTA-thiolate in $\mathbf{1^M}$ to yield $[Ni^{II}(nmp)(O_2)]^-$, which correlates to the reduced donor strength of S-BTA and is a reaction observed with (Et_4N)[Ni(nmp)(S-*o*-babt)] and excess azide (confirmed by ESI-MS).[39]

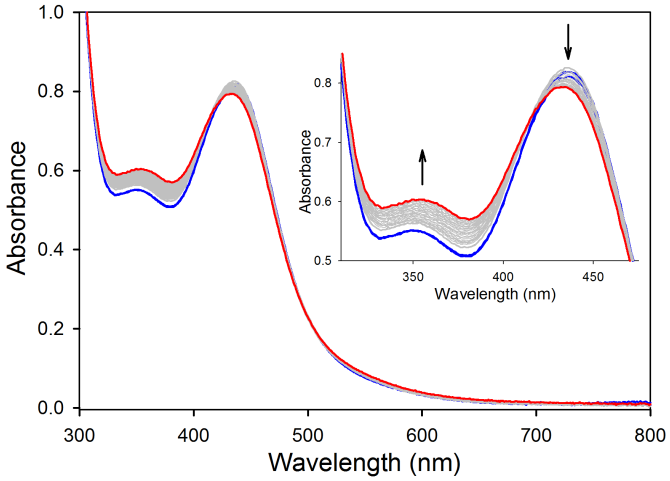

Figure 2.8. UV-vis spectral monitor of a 100 μM MeOH solution of $\mathbf{1}^{\mathbf{A}}$ (blue trace) and immediately after the addition of 100 equiv of KO_2. Final trace in red. Traces recorded at intervals of 1 scan/min for 30 min at 25 °C. *Inset*: zoom-in of 300-470 nm range. Arrow shows direction of change.

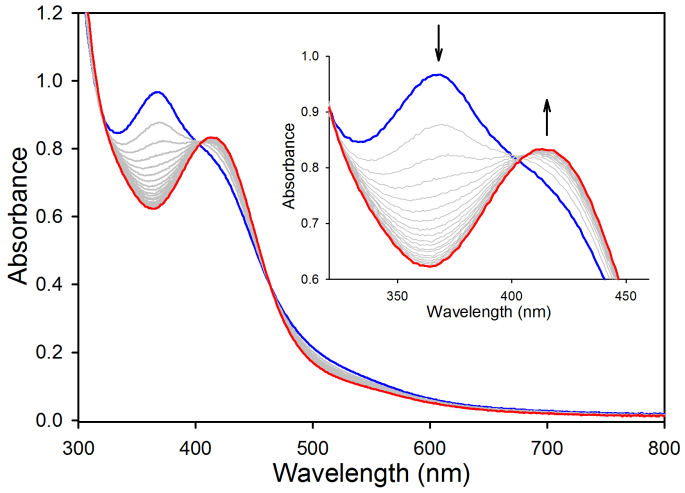

Figure 2.9. UV-vis spectral monitor of a 100 μM buffer solution of $\mathbf{1}^{\mathbf{M}}$ (blue trace) and immediately after the addition of 100 equiv of KO_2 (PBS, pH 7.4). Final trace in red. Traces recorded at intervals of 1 scan/min for 20 min at 25 °C. *Inset*: zoom-in of 300-470 nm range. Arrow shows direction of change.

Electron paramagnetic resonance (EPR) spectroscopy was employed to further probe the nature of the product formed in the $\mathbf{1}^{\mathbf{M}}$/100 equiv KO_2 reaction under identical conditions used for the UV-vis experiment. In addition to the expected free superoxide radical signal (g = 2.100, 2.008), an additional signal appears at $g_{\|}$ = 2.223 (Figure 2.S27). This new g-value is consistent with studies on other M^{II}-superoxos that report spin-density centered on the bound superoxide, with a lower field $g_{\|}$ upon interaction with the metal ion.[43] The EPR spectrum supports an end-on Ni^{II}- $O_2^{\bullet-}$ as suggested by another NiSOD model where $g_{\|}$ = 2.21. [43] In contrast, side-on bonding of superoxide results in rhombic EPR spectra with significant spin-density residing on the

metal.[110,111] The working model is that $[S_3BTA]^{3-}$ interacts with the nmp-Ni^{II}- $O_2^{\bullet-}$ adduct via O···HN H-bonding, which stabilizes the Ni^{II}-$O_2^{\bullet-}$ species and prevents bridging (see Scheme 2.1). However, it is also likely and more entropically favored for solvent to provide this H-bond. By quantifying the deviation of $g_{\parallel}$ from the free spin value, we calculate ΔE = 0.13 eV, the energy splitting of the π_g^* levels of superoxide.[112] Indeed, this interaction is quite weak compared to the interaction of superoxide with alkali and alkali earth metals (ΔE = 0.34-0.65 eV), but compares well to a putative Ni^{II}-$O_2^{\bullet-}$ bond in a NiSOD model complex (ΔE = 0.29 eV).[43,112] Analogous to our model, H-bonding in this complex from an amide-NH is hypothesized to stabilize the Ni^{II}-$O_2^{\bullet-}$ intermediate by nearly 30 kJ/mol based on computations.[43] Collectively, the EPR is consistent with the proposal that superoxide displaces the exogenous thiolate ligand to form the product as depicted in Scheme 2.1, albeit via a rather weak Ni-superoxide interaction (vide supra). Attempts to further confirm the Ni-superoxo product by independent synthesis of $[Ni^{II}(nmp)(O_2)]^-$ have not been successful,[113] supporting the stabilizing nature of this species by H-bonding to the BTA scaffold, which are well-known anion receptors.[63,66]

Scheme 2.1. Ligand substitution of $\mathbf{1^M}$ with superoxide to form a weak Ni(II)-$O_2^{\bullet-}$ adduct assisted by putative H-bonding from a dissociated $[S_3BTA]^{3-}$ or H^+ from solvent (entropically favored).

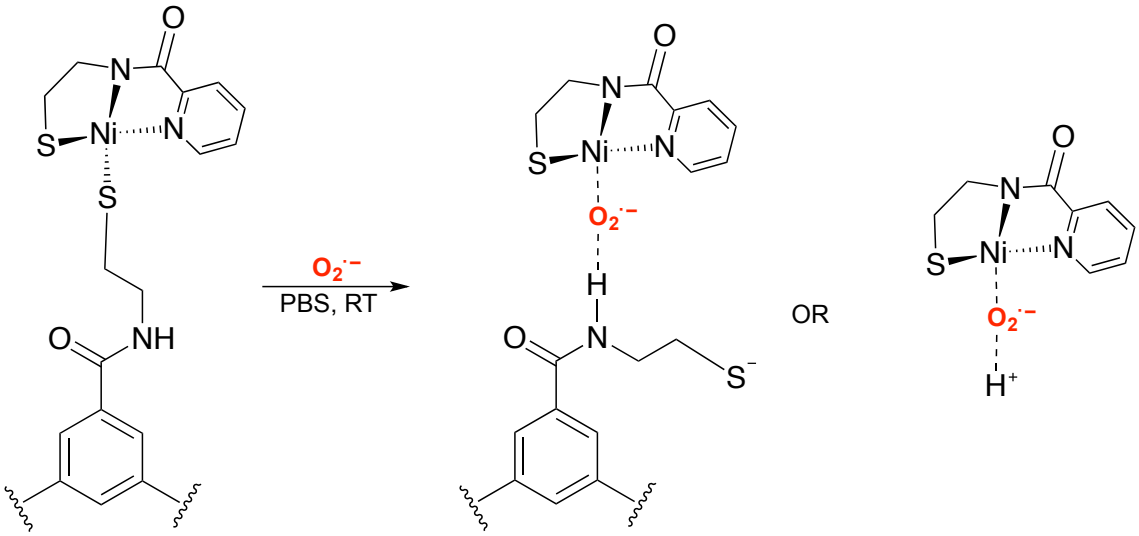

2.3.6 Electronic Structure. To supplement the spectroscopic measurements on **1** and provide details on the structure and frontier MOs, density functional theory (DFT) calculations were employed at the OLYP/def2-TZVPP level of theory. Initial coordinates for $\mathbf{1^A}$ were obtained from the X-ray structure of **3**, in which the Ni-S$(CH_2)_2$NH unit of S_3BTA^{alk} is in a trans configuration with respect to the carboxamide; coordinates for $\mathbf{1^M}$ were obtained from the DFT-optimized structure of **3**, in which the Ni-S$(CH_2)_2$-NH of S_3BTA^{alk} is constrained in a cis conformation from NH···S bonds (Figure 2.10).[39,114] The two structures are within ~0.25 kcal/mol, suggesting that dual speciation is feasible.

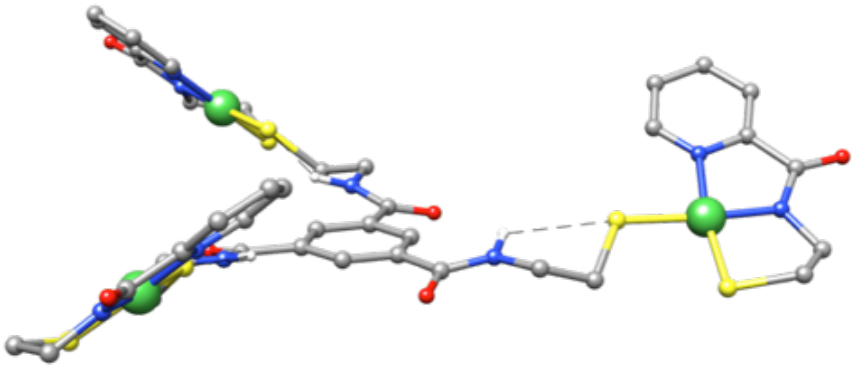

Figure 2.10. Geometry-optimized structure of $\mathbf{1^M}$ (BP86/def2-TZVPP). Ni = green; C = grey; N = blue; S = yellow; O = red. Bond distances: Ni-$N_{carboxamide}$ = 1.891 Å; Ni-N_{py} = 1.933 Å, Ni-S_{nmp} = 2.164 Å; Ni-S_{BTA} = 2.203 Å; Ni···Ni_{avg} ~ 15 Å.

Bond distances in the optimized structures of $\mathbf{1^A}$ and $\mathbf{1^M}$ replicate the asymmetric donor set, with shorter distances for Ni-$N_{carboxamide}$ (avg: $\mathbf{1^A}$ 1.890; $\mathbf{1^M}$ 1.891 Å) than Ni-N_{py} (avg: $\mathbf{1^A}$ 1.930; $\mathbf{1^M}$ 1.933 Å). As expected, a longer Ni-S_3BTA distance (avg: $\mathbf{1^A}$ 2.193; $\mathbf{1^M}$ 2.203 Å) is observed versus Ni-S_{nmp} (avg: $\mathbf{1^A}$ 2.157; $\mathbf{1^M}$ 2.164 Å). Overall, the Ni-N/S bond lengths in $\mathbf{1^M}$ and $\mathbf{1^A}$ are largely the same. The largest difference being Ni-S_3BTA^{alk} in $\mathbf{1^M}$, which is only 0.01 Å longer than $\mathbf{1^A}$. This change contrasts the contraction of this Ni-thiolate bond (~0.03 Å) and Ni-$N_{carboxamide}$ (~0.01 Å) of monometallic **3** with an NH···S bond compared to non-H-bonded $[Ni(nmp)(S^tBu)]^-$.[39] As stated, similar contraction of Ni-SCys was seen in a truncated $NiSOD_{red}$ DFT model, where Ni-SCys decreases 0.03 Å upon protonation.[97] The uncharacteristic lengthening of Ni-S/N bonds upon incorporation of the intramolecular H-bond in $\mathbf{1^M}$, however, correlates with the reduced donor strength of S_3BTA^{alk} as suggested in the CV. Overall, the geometry-optimized structures are in close agreement with the XAS data (vide supra), and

crystallographically-determined structures of $[Ni(nmp)(SR)]^-$ and other NiSOD models that contain an $N_{carboxamide}N_{amine}S_2$ donor set.[43,47,48,52]

The electronic structure of **1**, regardless of speciation, involves large contributions from Ni-AOs and S-based orbitals. Focusing on the HOMO, the nature of which dictates the Ni^{II}-to-Ni^{III} redox conversion, reveals a π-antibonding MO comprised of ~52% Ni-d(π) and ~32% S-p(π) character arising from isoenergetic MOs of all three Ni-nmp units (Figure 2.11 and 2.S29-30). Not surprisingly, this result is comparable to monometallic **3** (58% Ni-d(π) and 26% S-p(π)), suggesting that neither the multimetallic nature nor the $\mathbf{1^A}/\mathbf{1^M}$ speciation drastically change the frontier MOs (Figure 2.S31). Moreover, the negative of the HOMO energies of $\mathbf{1^A}$ and $\mathbf{1^M}$ (-1.5 and -1.7 eV, respectively) correlate with the observed E_{ox} (see Figure 2.5), in accordance with Koopman's theorem.[115] Although a reversible $Ni^{III/II}$ couple is not observed in **1**, installation of H-bonds result in a significant decrease in S-contributions when compared to $[Ni(nmp)(S^tBu)]^-$ (48% Ni-d(π), 39% S-d(π)) that lacks the NH···S bond. Thus, the decreased reactivity at the thiolate of S_3BTA^{alk} in **1** is likely due to a combination of the decreased S-character, observed first in **3**, in addition to the steric factor of the H-bonds. This highlights the use of the protein scaffold in NiSOD as a means of protecting the thiolate donors.

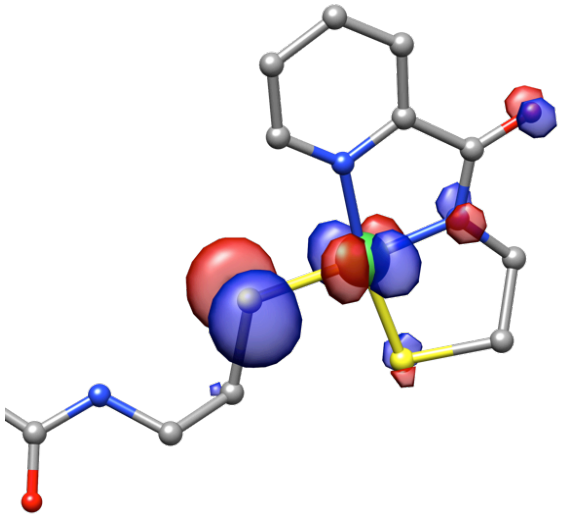

Figure 2.11. DFT-generated isosurface plot of one of the three isoenergetic MOs that contribute to the HOMO of $\mathbf{1}^{\mathbf{M}}$. Atom color scheme is identical to that used in Figure 2.10.

2.4 Conclusions

In summary, the synthesis and properties of the first multimetallic analogue of NiSOD is reported. From the presented results, it is clear that complex **1** exhibits condition-dependent speciation, designated as $\mathbf{1}^{\mathbf{A}}$ and $\mathbf{1}^{\mathbf{M}}$. Both species demonstrate unprecedented stability in protic solvents in contrast to their monometallic counterparts, indicating the multimetallic scaffold prevents protonation of the Ni–S-BTA bond due to H-bonding from the BTA-carboxamide. This protection is in-line with the decreased nucleophilicity observed in Zn-thiolates that incorporate NH···S bonds.[59,99,100] This bonding creates a rigid supramolecular entity (see Charts 2.2, 2.3) based on the large ν_{NH}/δ_{NH} shifts and negative ellipticity in the CD. The proposal is dimer or oligomer aggregation as opposed to polymer formation based on the observation of: (i) no gelation under saturation conditions;[65,116] (ii) no fibril formation under crystallization

conditions;[117] and (iii) a large solubility profile in organic and aqueous solvents. The aggregates form classic BTA helices (Chart 2.3), which may additionally engage in H-bonding with carboxamide-nmp moieties resulting in end-capping of the aggregates.[83] While $\mathbf{1^A}$ is sterically protected from protonation of the Ni–S bond, the thiolate-p(π) orbitals are exposed and susceptible to oxidants, i.e., formation of RSO_x, as they do not engage in H-bonding. In contrast, NH···S intramolecular bonding in $\mathbf{1^M}$ (Chart 2.3) is evidenced by the cathodic-shift in E_{ox} and a blue-shifted λ_{max}. This bonding provides greater thiolate protection against O_2 due to stabilization of S-based orbitals. However, the lack of a supramolecular structure in $\mathbf{1^M}$ makes it vulnerable to ligand exchange. Collectively, these models are in-line with the observed protic solvent stability and discrepancy in ROS reactivity.

The overall hexameric structure and ligand environment of NiSOD evolved to adjust the $Ni^{III/II}$ potential for catalysis, control anion access to the active site, protect against S-oxidation/oxygenation, and provide a proton source for H_2O_2 generation.[118] Model complexes such as **1** emphasize the necessity for both steric protection as in $\mathbf{1^A}$ and electronic protection of $\mathbf{1^M}$ to protect against unwanted thiolate reactivity with ROS. Future generation multimetallic models must consider this aspect in the design, as well as incorporating an additional axial N-ligand to generate five coordinate Ni^{III} (and likely Ni^{II}) coordination spheres as observed in the enzyme. Indeed, BTA units provide synthetically-accessible building blocks for spontaneous organization of ordered superstructures utilized for a variety of applications.[61] BTA scaffolds can be engineered to control reactivity, induce self-assembly, and create secondary structure. For example, an achiral rhodium catalyst comprised of BTA-derived phosphine ligands was incorporated into helical stacks of an enantiopure comonomer to promote enantioselective and catalytic hydrogenation reactions.[82] Additionally, self-folding protein analogues were realized by

integrating multiple BTA moieties into a single chain polymer, which self-assembles into helical aggregates to afford domains that mimic α-helices.[82] We envision further applications of the self-assembling properties of BTAs, specifically multimetallic scaffolds designed to perform catalytic redox chemistry at single metal sites as in NiSOD and to emulate multi-electron redox in metalloclusters.

2.5 Experimental

2.5.1 General Information. All reagents were purchased from commercial suppliers and used as received unless otherwise noted. Acetonitrile (MeCN), methylene chloride (CH_2Cl_2), tetrahydrofuran (THF), and diethyl ether (Et_2O) were purified by passage through activated alumina columns using an MBraun MB-SPS solvent purification system and stored under a dinitrogen (N_2) atmosphere before use. *N*,*N*-dimethylformamide (DMF) was purified with a VAC solvent purifier containing 4 Å molecular sieves and stored under N_2. Methanol (MeOH) was dried over 3 Å molecular sieves and stored under similar conditions. All airfree reactions were performed under an inert atmosphere of N_2 using Schlenk-line techniques or in an N_2-filled MBraun Unilab glovebox. S-trityl cysteamine, S-trityl-nmp, $nmpH_2$, $[Ni_4(nmp)_4]$ (**2**), and $Et_4N[Ni(nmp)(S\text{-}meb)]$ (**3**) were synthesized according to published procedures.[37,39,41] $^{18}O_2$ (97 atom % ^{18}O) was purchased from Sigma-Aldrich and used as received.

2.5.2 Physical Methods. FTIR spectra were collected on a ThermoNicolet 6700 spectrophotometer running the OMNIC software. Solid-state samples were prepared as pressed KBr pellets. Solution samples were prepared in an airtight Graseby-Specac solution cell with CaF_2 windows and 0.1 mm Teflon spacers. Electronic absorption spectra were performed at 25 ºC using a Cary-50 spectrophotometer. UV-vis samples were prepared in gas-tight Teflon-lined screw cap quartz cells with an optical pathlength of 1 cm. Cyclic voltammetry (CV)

measurements were performed with a PAR Model 273A potentiostat using an Ag/Ag^+ (0.01 M $AgNO_3$/0.1 M $^nBu_4NPF_6$ in MeCN) reference electrode, Pt counter electrode, and a Glassy Carbon working milli-electrode (surface area = 2 mm) when measuring in DMF. An Ag/AgCl reference electrode was used when measuring aqueous samples. CV measurements were performed at ambient temperature using ~0.25 mM analyte in the appropriate Ar-purged solvent containing 0.1 M $^nBu_4NPF_6$ as the supporting electrolyte in DMF or 0.5 M KNO_3 in H_2O. The "Maximize stability" mode and a low-pass 5.3 Hz filter were used in the PAR PowerCV software. To ensure accuracy in the measured CVs, these experiments were performed in triplicate while polishing the working electrode between each run, and we report an average E_{ox}. Additionally, potentials were checked and corrected by recording the CV of a ferrocene standard in DMF or a potassium ferricyanide standard in H_2O. Potentials were referenced to ferrocene in DMF and Ag/AgCl in H_2O (checked against a ferro/ferricyanide couple in 50 mM pH 7.0 phosphate buffer)[119] before each run. NMR spectra were recorded in the listed deuterated solvent on a 400 MHz Bruker BZH 400/52 S3 NMR spectrometer or 500 MHz Varian Unity INOVA NMR spectrometer at ambient temperature with chemical shifts referenced to TMS or residual protio signal of the deuterated solvent.[120] Low resolution electrospray ionization mass spectrometry (ESI-MS) data were collected using a Bruker Esquire 3000 plus ion trap mass spectrometer. Matrix Assisted Laser Desorption Ionization (MALDI) data were collected using a Bruker Daltonics autoflex mass spectrometer. High resolution ESI-MS data were collected using an Orbitrap Elite system with precision to the third decimal place. CD spectra were obtained using a Jasco J715 spectropolarimeter. X-band (9.60 GHz) EPR spectra were obtained using a Bruker ESP 300E EPR spectrometer controlled with a Bruker microwave bridge at 10 K. The

EPR was equipped with a continuous-flow liquid He cryostat and a temperature controller (ESR 9) made by Oxford Instruments Inc.

2.5.3 N^1, N^3, N^5-tris(2-(tritylthio)ethyl)benzene-1,3,5-tricarboxamide (Tr-S_3BTA^{alk}). To a homogeneous yellow CH_2Cl_2 (~5 mL) solution containing 1.997 g (6.251 mmol) of S-trityl-cysteamine and 3.5 mL (25 mmol) of Et_3N was added dropwise a 5 mL CH_2Cl_2 solution containing 0.553 g (2.08 mmol) of 1,3,5-benzenetricarbonyl trichloride at RT. The initially colorless solution turned pale yellow and a light precipitate and gas evolution were observed. This solution was allowed to stir at RT for 7 h. After this time, the solution was concentrated to a yellow oil via rotary evaporation. Addition of ~25 mL of MeOH to this oil, accompanied with vigorous stirring for 12 h, resulted in a white insoluble material. The solid was filtered off, dissolved in ~10 mL of THF, and subsequently filtered to remove the insoluble $Et_3N{\cdot}HCl$ byproduct. The THF filtrate was then removed *in vacuo* and the residue triturated with MeOH (3 × 5 mL) to produce a pale yellow solid that was isolated by vacuum filtration and washed with ~10 mL of cold MeOH (2.002 g, 1.796 mmol, 86%). mp: 164.0 °C dec. ^{1}H NMR (500 MHz, $CDCl_3$ with 0.05% v/v TMS, δ from TMS): 8.18 (s, 1H, Ar*H* of BTA), 7.41 (d, 6H, *J* = 7.5 Hz), 7.26 (t, 7H, *J* = 7.6 Hz, integrates high due to overlap with residual protio solvent), 7.19 (t, 3H, *J* = 7.3 Hz), 6.38 (t, 1H, *J* = 5.6 Hz, C(=O)N*H*, verified by exchange with D_2O), 3.28 (q, 2H, *J* = 6.2 Hz, -NCH_2CH$_2$S-), 2.52 (t, 2H, *J* = 6.5 Hz, -NCH$_2$CH_2S-). ^{13}C NMR (125 MHz, $CDCl_3$ with 0.05% v/v TMS, δ from TMS): 165.35 (*C*=O), 144.53, 134.93, 129.51, 128.17, 128.01, 126.84, 67.03 (S*C*Ph$_3$), 39.03 (-N*C*H$_2$CH$_2$S-), 31.72 (-NCH$_2$*C*H$_2$S-). FTIR (KBr), ν_{max} (cm^{-1}): 3409 (br w, ν_{NH}), 3291 (br w, ν_{NH}), 3054 (w), 3029 (w), 2924 (w), 1727 (w), 1652 (s, ν_{CO}), 1594 (m), 1515 (s), 1488 (s), 1443 (s), 1360 (w), 1261 (s br), 1183 (w), 1081 (w), 1033 (w), 1001 (w), 911 (w), 848 (w), 742 (s), 699 (vs), 675 (m), 616 (w), 504 (w). LRMS-MALDI (*m*/*z*): [M+Na]$^+$ calcd for

$C_{72}H_{63}N_3O_3S_3Na$, 1136.4 (100.0), 1137.4 (81.4), 1138.4 (45.4), 1139.4 (18.1); found, 1136.4 (100.0), 1137.5 (73.2), 1138.5 (36.4), 1139.5 (11.2).

2.5.4 N^1, N^3, N^5-tris(2-mercaptoethyl)benzene-1,3,5-tricarboxamide ($H_3S_3BTA^{alk}$). A batch of 0.580 g (0.520 mmol) of Tr-S_3BTA^{alk} was stirred in 10 mL of CH_2Cl_2/TFA (1:1) at RT resulting in a bright orange solution. Then, 499 μL (3.12 mmol) of Et_3SiH was added dropwise, causing immediate bleaching of the color to produce a clear, homogeneous solution. After 90 min stirring at RT, the solution was concentrated to ~50% of its original volume, and the resulting insoluble triphenylmethane (Ph_3CH) byproduct was filtered off and washed with TFA. The filtrate was then concentrated to a beige oil and triturated with Et_2O (3 × 5 mL) to produce a white solid. This solid was stirred in ~15 mL of hexanes for 30 min to remove residual Ph_3CH. Filtering this solution and washing with ~5 mL hexanes yielded 0.162 g (0.418 mmol, 80%) of product as a white solid. mp: 219.0 °C dec. ^{1}H NMR (500 MHz, CD_3OD, δ from solvent residual signal): 8.89 (t, 1H, N*H*, *J* = 5.5 Hz), 8.42 (s, 1H), 3.45 (q, 2H, *J* = 6.6 Hz, -NC*H*$_2$CH$_2$S-), 2.67 (q, 2H, *J* = 7.4 Hz, -NCH$_2$C*H*$_2$S). ^{13}C NMR (125 MHz, $(CD_3)_2SO$, δ from solvent residual signal): 165.48 (*C*=O), 134.85, 128.58, 42.89 (-N*C*H$_2$CH$_2$S-), 23.24 (-NCH$_2$*C*H$_2$S-). FTIR (KBr), ν_{max} (cm^{-1}): 3340 (br m, ν_{NH}), 3062 (w), 2943 (w), 2551 (w, ν_{SH}), 1709 (w), 1644 (s, ν_{CO}), 1527 (s), 1436 (m), 1385 (w), 1360 (w), 1282 (s), 1235 (w), 1187 (m) 1071 (w), 955 (w), 912 (w), 743 (w), 685 (m), 539 (w), 408 (w). LR-ESI-MS (*m*/*z*): [M-H]$^-$ calcd for $C_{15}H_{20}N_3O_3S_3$, 386.1 (100.0), 387.1 (19.7), 388.1 (14.8); found, 385.9 (100.0), 386.9 (23.5), 387.9 (16.7).

2.5.5 $Na_3[S_3BTA^{alk}]$. A batch of sodium metal (0.0209 g, 0.908 mmol) was added to ~5 mL of MeOH, which resulted in immediate and vigorous bubbling to generate NaOMe. Once all the sodium was consumed, the solution was added pipet-wise to a white slurry of 0.1066 g (0.7251 mmol) of $H_3S_3BTA^{alk}$ in ~5 mL MeOH, which resulted in immediate effervescence and a

pale yellow, homogenous solution. The solution was placed under vacuum for 20 min to aid in the removal of H_2(g). The solution was then filtered through a medium porosity glass frit and the solvent was removed *in vacuo* to yield 91.2 mg of a pale yellow solid (0.201 mmol, 73%). The product was used for aqueous electrochemistry comparisons to $\mathbf{1^A}$ and $\mathbf{1^M}$. ^{1}H NMR (500 MHz, CD_3OD, δ from solvent residual signal): 8.45 (s, 1H), 3.52 (t, 2H, *J* = 7.5 Hz, -NC*H*$_2$CH$_2$S-), 2.73 (t, 2H, *J* = 6.0 Hz, -NCH$_2$C*H*$_2$S-). ^{13}C NMR (125 MHz, $(CD_3)_2SO$, δ from solvent residual signal): 167.98 (*C*=O), 136.80, 129.72, 47.02 (-N*C*H$_2$CH$_2$S-), 25.61 (-NCH$_2$*C*H$_2$S-).

2.5.6 Na_3[{Ni(nmp)}$_3$(S^{alk}_3BTA)] (1). To a white slurry containing 0.048 g (0.12 mmol) of $H_3S_3BTA^{alk}$ in ~5 mL MeOH was added sodium metal (0.009 g, 0.4 mmol) at RT resulting in immediate effervescence (H_2), and the mixture became pale yellow and homogeneous. After stirring the mixture for ~20 min, 0.089 g (0.093 mmol) of [$Ni_4(nmp)_4$] (**2**) was added and the solution immediately became dark-red and heterogeneous (likely due to unreacted and insoluble **2**). After ~12 h stirring at RT, the solution appeared more dark-red in color with a minor amount of insoluble material. The solution was then filtered to remove unreacted **2** and the dark-red filtrate was concentrated to dryness and subsequently treated with ~10 mL of Et_2O to form free-flowing solids. The product was collected as a dark-red solid after vacuum filtration on a medium porosity glass frit and was washed with ~10 mL of Et_2O (0.106 g, 0.0906 mmol, 73%). ^{1}H NMR (400 MHz, CD_3OD, δ from solvent residual signal): 8.53 (s, 1H), 8.40 (d, 1H, *J* = 5.3 Hz), 7.93 (t, 1H, *J* = 7.7 Hz), 7.55 (d, 1H, *J* = 7.5 Hz), 7.43 (t, 1H, *J* = 6.0 Hz), 3.53 (t, 2H, *J* = 6.7 Hz), 3.34 (m, 4H integrates high due to overlap with residual protio solvent), 2.29 (t, 2H, *J* = 6.3 Hz), 2.21 (t, 2H, *J* = 6.5 Hz). FTIR (KBr), ν_{max} (cm^{-1}): 3246 (br w, ν_{NH}), 3055 (br), 2916 (w), 2848 (w), 1659 (s, ν_{CO} BTA), 1619 (s, ν_{CO} nmp), 1592 (s, ν_{CO} nmp), 1560 (w), 1531 (m), 1435 (m), 1399 (m), 1290 (w), 1260 (w), 1207 (w), 1179 (w), 1133 (w), 1097 (w), 802 (w), 758 (w),

722 (w), 687 (w), 664 (w), 562 (w), 487 (w), 436 (w). UV-vis (H_2O, 298 K) λ_{max}, nm: 365, 410. Note that accuracy of ε is difficult to determine due to solution speciation of **1**. LR-ESI-MS (*m/z*): $[M–Na]^-$ calcd for $C_{39}H_{42}N_9Na_2Ni_3O_6S_6$, 1145.9 (100.0), 1147.9 (74.5), 1143.9 (64.9), 1146.9 (49.1), 1149.9 (33.5), 1148.9 (33.4), 1144.9 (32.7), 1150.9 (11.6); found, 1145.8 (100.0), 1147.8 (88.4), 1143.8 (63.6), 1146.8 (64.0), 1149.8 (46.0), 1148.7 (60.0), 1144.8 (48.4), 1150.7 (29.6).

2.5.7 $[Na(18C6)]_3$[1]. To a batch of **1** (0.147 g, 0.126 mmol) dissolved in ~5 mL MeOH was added 0.212 g (0.803 mmol) of 18-crown-6 ether (18C6) in ~3 mL of MeOH. The resulting red solution was allowed to stir for 50 min at RT. The solution was then concentrated to a dark red residue and was taken up in ~10 mL of MeCN and stirred for 2 h. After this time, the solution was filtered to remove unreacted **1** and was subsequently concentrated to a dark red residue. This solid was then treated with ~10 mL of Et_2O for ~12 h to form free-flowing solids and dissolve any excess 18C6. The product was collected as a dark red solid via vacuum filtration and washed with ~10 mL of Et_2O (0.142 g, 0.0723 mmol, 58%). HRMS-ESI (*m/z*): $[M–Na–3(18C6)]^-$ calcd for $C_{39}H_{42}N_9Na_2Ni_3O_6S_6$, 1145.944 (100.0), 1147.944 (75.3), 1143.944 (63.8), 1146.944 (51.4), 1149.944 (37.7), 1148.944 (37.1), 1144.944 (32.6), 1150.944 (17.5), 1151.944 (14.2); found: 1145.942 (100.0), 1147.939 (70.2), 1143.947 (66.1), 1146.945 (51.1), 1149.935 (32.1), 1148.940 (34.5), 1144.950 (33.3), 1150.937 (14.6), 1151.933 (12.0).

2.5.8 X-ray Absorption Spectroscopy (XAS). Solid **1** and **3** were prepared anaerobically at a 3:1 stoichiometric dilution with boron nitride, loaded into transmission cells wrapped with Kapton® tape and immediately frozen in liquid nitrogen. XAS data were collected at the Stanford Synchrotron Radiation Light Source (SSRL) on beamline 7-3. Beamline 7-3 utilizes a Si[220] double crystal monochromator with an inline mirror for X-ray focusing and for

harmonic rejection. During data collection, samples were maintained at 12 K using a liquid He continuous flow cryostat. Transmittance XAS spectra were collected using ion chamber detectors filled with nitrogen gas. Spectra were measured in 5 eV increments in the pre-edge region (8265-8325 eV), 0.25 eV increments in the edge region (8325-8405 eV), and 0.05 $Å^{-1}$ increments in the EXAFS region (out to k = 14 $Å^{-1}$), integrating from 1 to 25 s in a k^3-weighted manner for a total scan length of approximately 50 min. X-ray energies were individually calibrated by collecting a Ni-foil absorption spectrum simultaneously with the compound; the first inflection point of the Ni-foil spectrum was assigned to 8333 eV. Data represent the average of 8 scans for **1** and 2 scans for **3**.

XAS spectra were processed using the Macintosh OS X version of the EXAFSPAK program suite[121] integrated with the Feff v8 software[122] for theoretical model generation. Data reduction utilized a Gaussian spline for background removal in the pre-edge region and a three-region cubic spline throughout the EXAFS. Data were converted to k-space using a Ni E_0 value of 8333 eV. The k^3 weighted EXAFS was truncated between 1.0 and 13.0 $Å^{-1}$ for filtering purposes. This k-range corresponds to a spectral resolution of ca. 0.12 Å for all nickel-ligand interactions; therefore only independent scattering environments outside 0.12 Å were considered resolvable in the EXAFS fitting analysis.[123] EXAFS fitting analysis was performed first on filtered data and then verified on the raw unfiltered data. EXAFS data were fit using both single and multiple scattering amplitude and phase functions calculated with the program Feff v8. Single scattering theoretical models were calculated for carbon, nitrogen, oxygen, and sulfur coordination to simulate nickel nearest-neighbor ligand environments. Scale factor (Sc) and E_0 values, used in a static manner during the simulations, were calibrated by fitting crystallographically characterized Ni models; specific values include a Scale Factor of 0.9 and E_0

values of -10.55 eV for O/N/C and -12.22 eV for S. Criteria for judging the best-fit simulation utilized both the lowest mean square deviation between data and fit (F'), corrected for the number of degrees of freedom, and a reasonable Debye-Waller factor.[124,125] Pre-edge analysis was done using EDG_FIT software. A spline function was best-fit between 8328 eV and 8342 eV and a 3-peak model was applied to accommodate the three pre-edge features.

2.5.9 Reactivity Studies with O_2, KO_2, H_2O_2·urea, and NaN_3. All measurements were carried out in gas-tight Teflon-lined screw-cap quartz UV-vis cells of 1 cm pathlength equipped with a rubber septum. Samples were prepared under an anaerobic atmosphere in a glovebox prior to addition of oxidants. For each study, 100 equiv KO_2, NaN_3, or H_2O_2·urea was added or O_2(g) was bubbled (saturation of O_2(g) in MeOH = 1.99 ± 0.18 mM[102]; saturation of O_2(g) in H_2O = 0.34 ± 0.06 mM[102]) into a solution of 100 μM **1** in either MeOH or pH = 7.4 PBS buffer and monitored every 1 min for 20-60 min. The kinetic data were obtained by monitoring the decay of λ_{max} with respect to time at 25 ºC. The average rate constant (k_{obs}) along with standard deviation was calculated from triplicate runs under identical experimental conditions. An absorbance versus time plot was generated in the Cary-50 Scanning Kinetics program and the data was fit according to the equation $y = (A^0 - A)e^{-kt} + A$ where y is the absorbance at λ_{max}, A^0 is the absorbance at time = 0, A is the absorbance at time t, t is time (s), and k (or k_{obs}) is the observed pseudo first-order rate constant. To determine k_{obs}, λ_{max} was monitored at 5 min intervals for 6 h.

2.5.10 O_2 reactions. Dry O_2 gas (via passage through a Drierite column) was bubbled directly into a solution of **1** into a septum-capped cuvette through a stainless steel syringe needle for 60 s. After mixing for 30 min, an FTIR spectrum of the mixture was obtained after evaporation of the reaction solvent to dryness as a KBr pellet.

2.5.11 $^{18}O_2$ reactions. To confirm the uptake of O_2 and formation of a Ni-sulfinate species, $^{18}O_2$ (^{18}O 97%) was bubbled directly into a 100 μM solution of **1** in MeOH into a septum-capped Schlenk flask for 60 s and allowed to mix for 15 h. After mixing, an FTIR spectrum of the mixture was obtained after evaporation of the reaction solvent to dryness as a KBr pellet.

2.5.12 H_2O_2 reactions. Solutions containing 100 equiv of H_2O_2·urea were added to a septum-capped solution of **1** in a UV-vis cuvette via a stainless steel syringe needle. FTIR data were obtained as described above for the O_2(g) experiments.

2.5.13 KO_2 reactions. Solutions containing 100 equiv of KO_2 were added to UV-vis cuvettes containing solutions of **1** via a stainless steel syringe needle. The KO_2 was dissolved in a glovebox and injected into the cuvette within 2 min of dissolution to minimize spontaneous disproportionation; 100 equiv excess ensures KO_2 exceeds H_2O_2 and O_2 concentrations. FTIR data were obtained as described above for the O_2(g) experiments. The reactivity of $\mathbf{1^M}$ and KO_2 was investigated using X-band EPR spectroscopy by incubating a solution of 0.5 mM $\mathbf{1^M}$ with 0.05 M KO_2 in 0.01 M PBS (pH 7.4) for 30 min before freezing in liquid N_2.

2.5.14 Computational Details. Calculations were performed with the ORCA electronic structure package, version 3.0.3., using density functional theory (DFT). The geometries of the models of **1** were optimized with the BP86 functional and the def2-TZVPP basis set was applied for all atoms. The auxiliary basis set was automatically chosen by ORCA. Single-point energy calculations were performed on the optimized structures with the OPTX pure exchange functional of Handy and Cohen used in conjunction with the Lee-Yang-Parr correlation functional (OLYP).[126,127] The def2-TZVPP basis set, and the def2-TZVPP/J auxiliary basis set, were utilized along with COSMO models (water and DMF) with dielectric employed. To

correctly describe the more diffuse regions of the charge density within each molecule, where the negative charge resides, the large def2-TZVPP basis set was used.[128] Contributions from each atom to the highest occupied molecular orbital (HOMO), and orbital compositions were obtained with the Löwdin population analysis.[129] Molecular graphics and analyses were performed with the UCSF Chimera package. Chimera is developed by the Resource for Biocomputing, Visualization, and Informatics at UCSF (supported by NIGMS P41-GM103311). Frequency analysis reveals that no imaginary vibrational frequencies were found. ***Note on Aggregate Model***: While the models $\mathbf{1^A}$ and $\mathbf{1^M}$ have been simplified to ease the calculations, $\mathbf{1^A}$ is truly only one 'layer' of the aggregated stack and there is some inherent energy or thermodynamic driving force upon stacking that is missing in this model. Complex $\mathbf{1^M}$ is also simplified, as the intramolecular H-bonding interactions are oriented upwards; it is feasible that the 'arms' may orient above or below the plane in a variety of combinations and thus is admittedly not all-encompassing.

2.6 Supporting Information

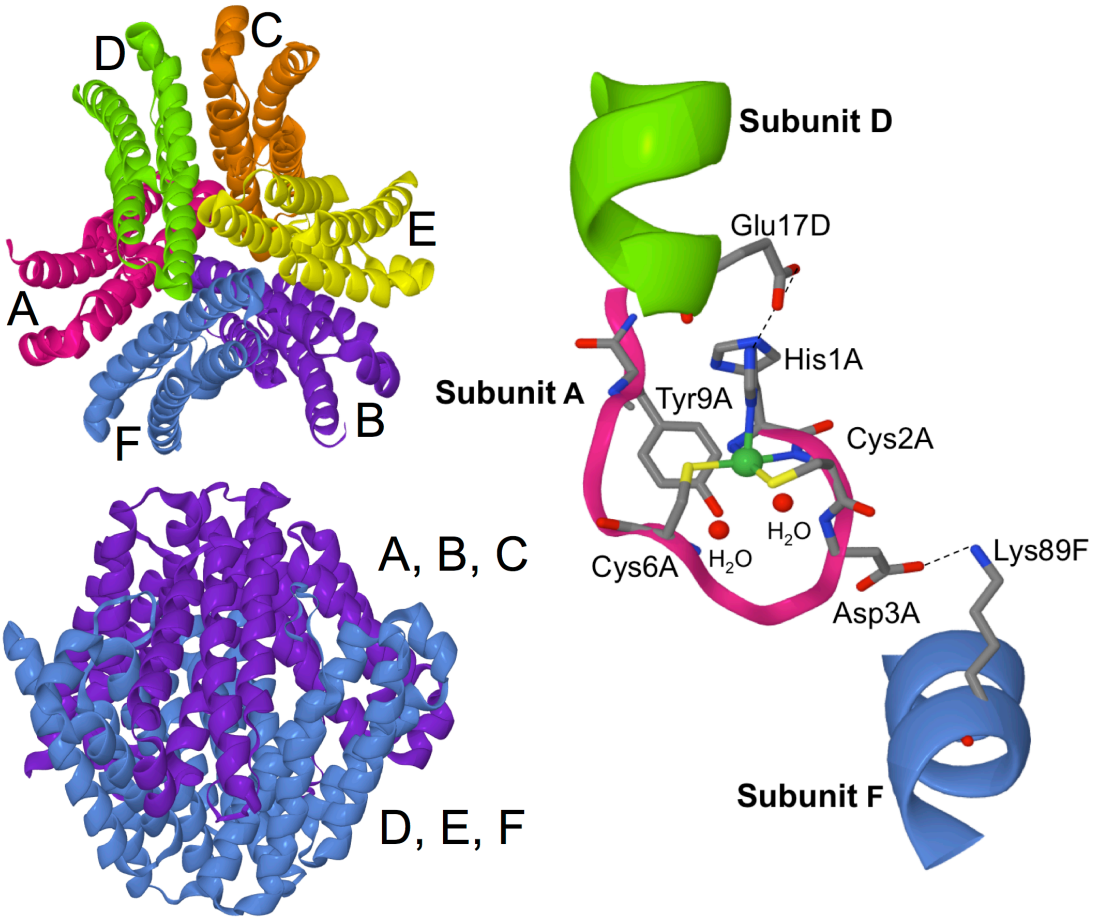

Figure 2.S1. X-ray structure of NiSOD from *S. coelicolo*r (1.20 Å resolution, PDB: 1T6U). *Top left*: Hexameric assembly of four-helix bundles (subunits A-F); *Bottom left*: Dimer of three-legged piano stool trimers; *Right*: Intersubunit interactions; dashed lines represent H-bonds.

Scheme 2.S1. Synthesis of **1.**

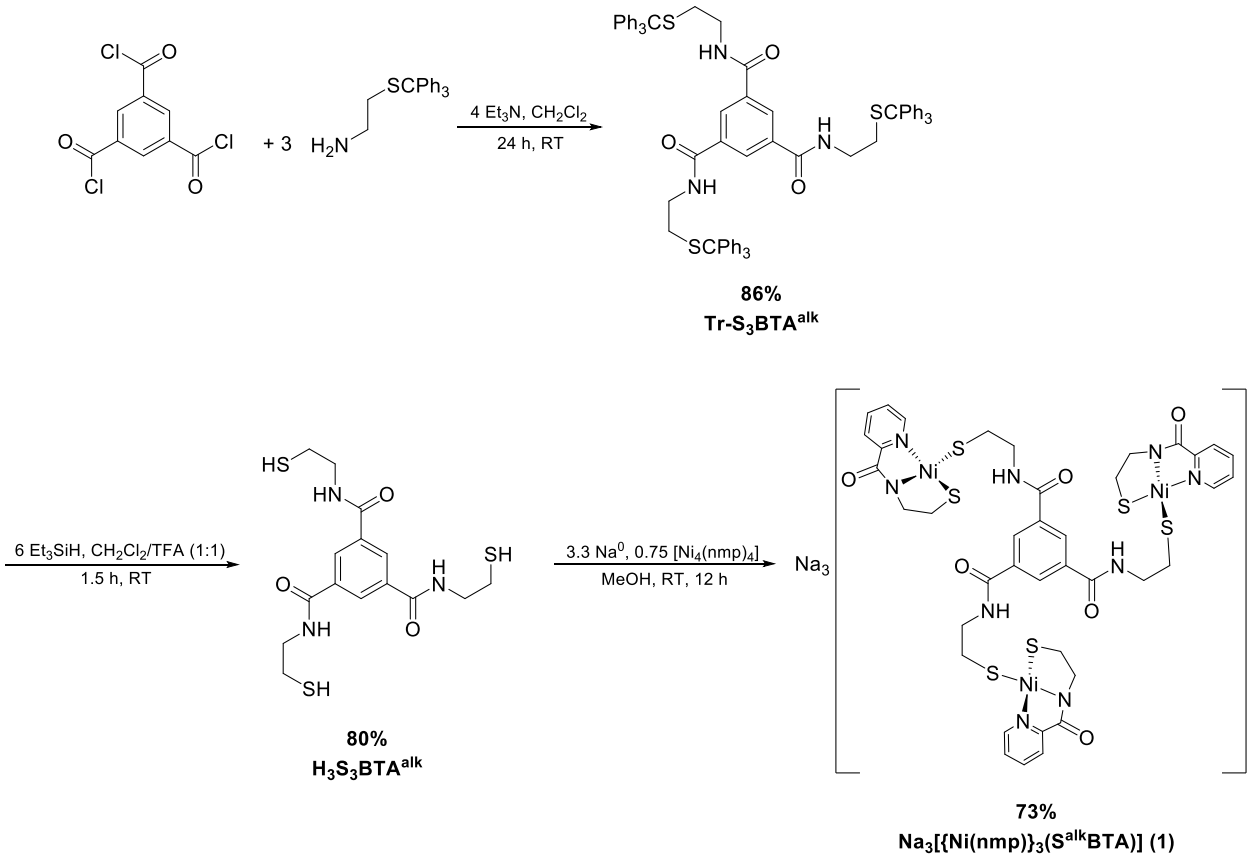

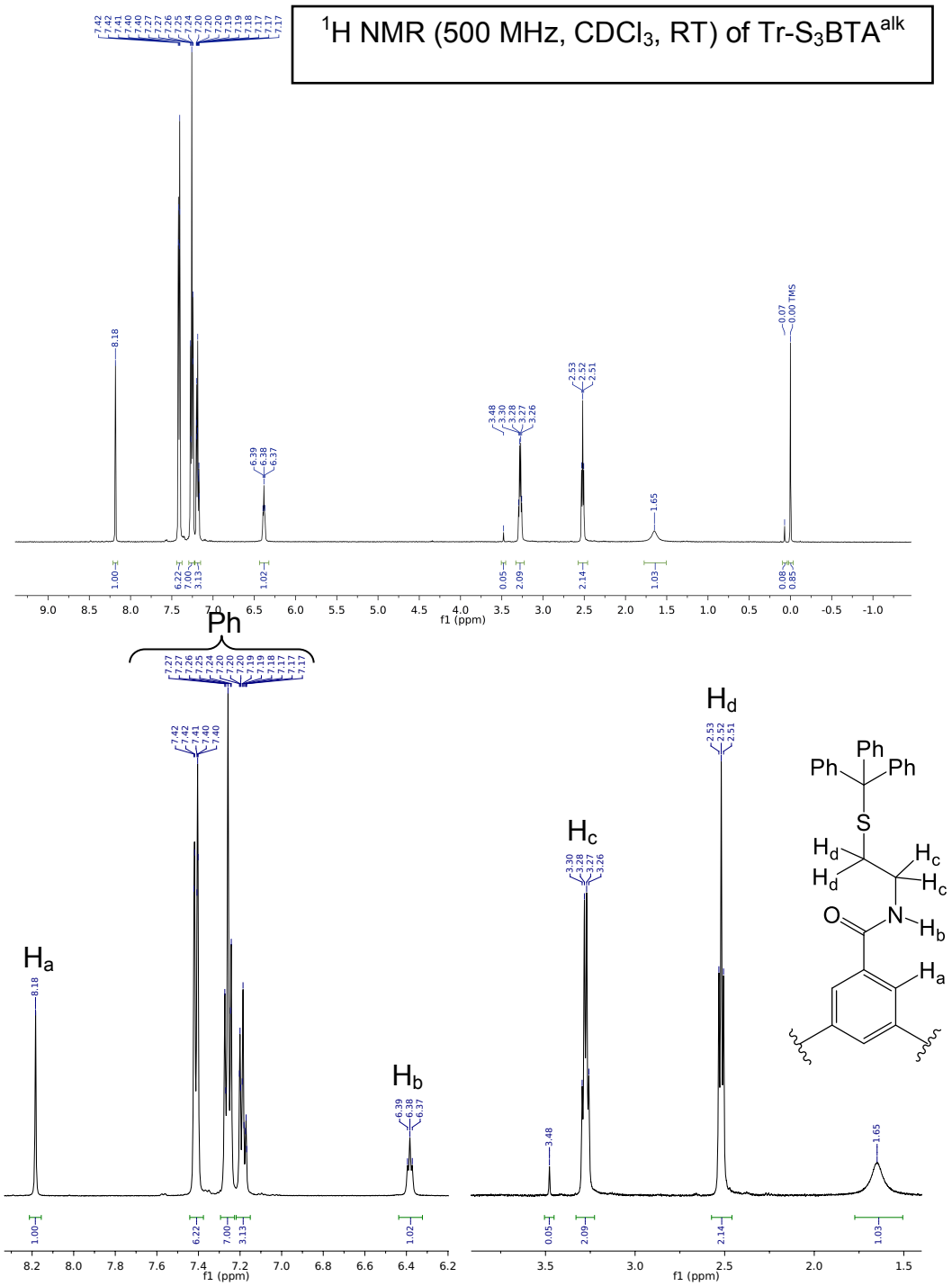

Figure 2.S2. ^{1}H NMR spectrum of Tr-S_3BTA^{alk} in $CDCl_3$ with 0.05% v/v TMS at RT. The peaks at 7.27 and 1.65 ppm are from residual protio solvent and trace H_2O, respectively. Bottom: Zoom-in of top spectrum with peak labels.

^{13}C NMR (125 MHz, $CDCl_3$, RT) of Tr-S_3BTA^{alk}

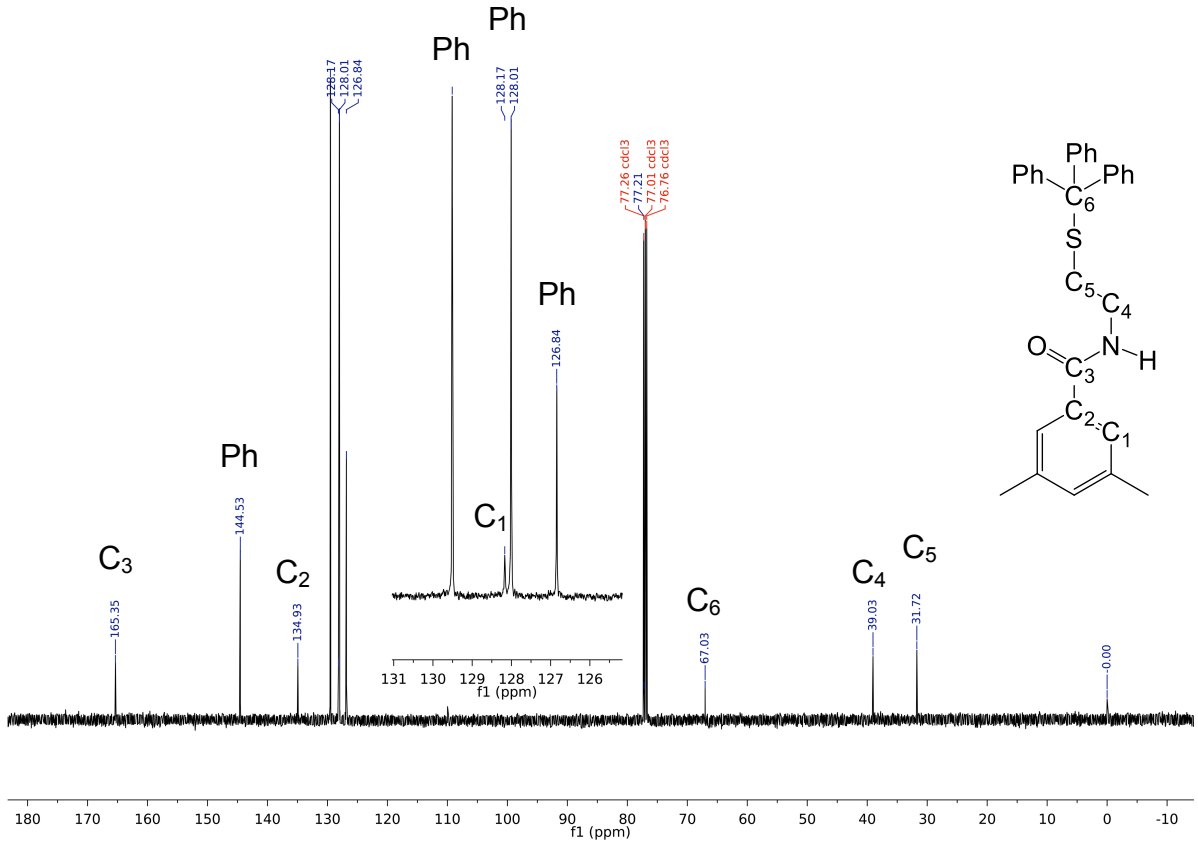

Figure 2.S3. ^{13}C NMR spectrum of Tr-S_3BTA^{alk} in $CDCl_3$ with 0.05% v/v TMS at RT. The solvent peak is identified in red. *Inset*: zoom-in of 125-131 ppm region.

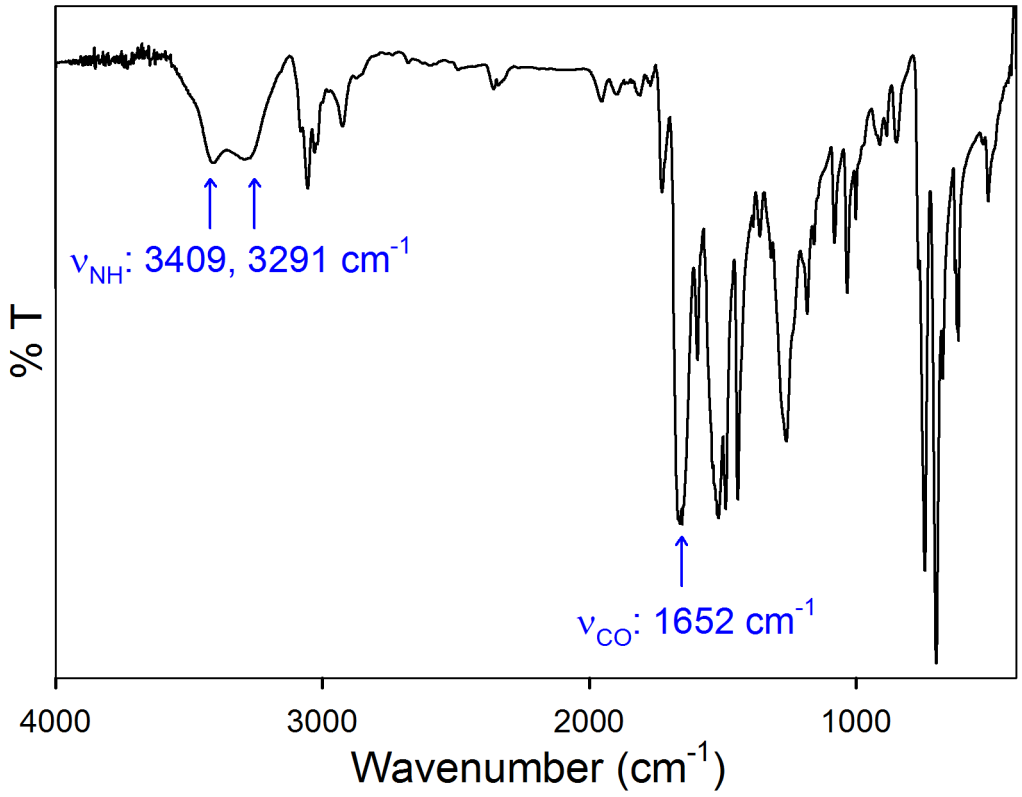

Figure 2.S4. Solid-state FTIR spectrum of Tr-S_3BTA^{alk} in a KBr matrix.

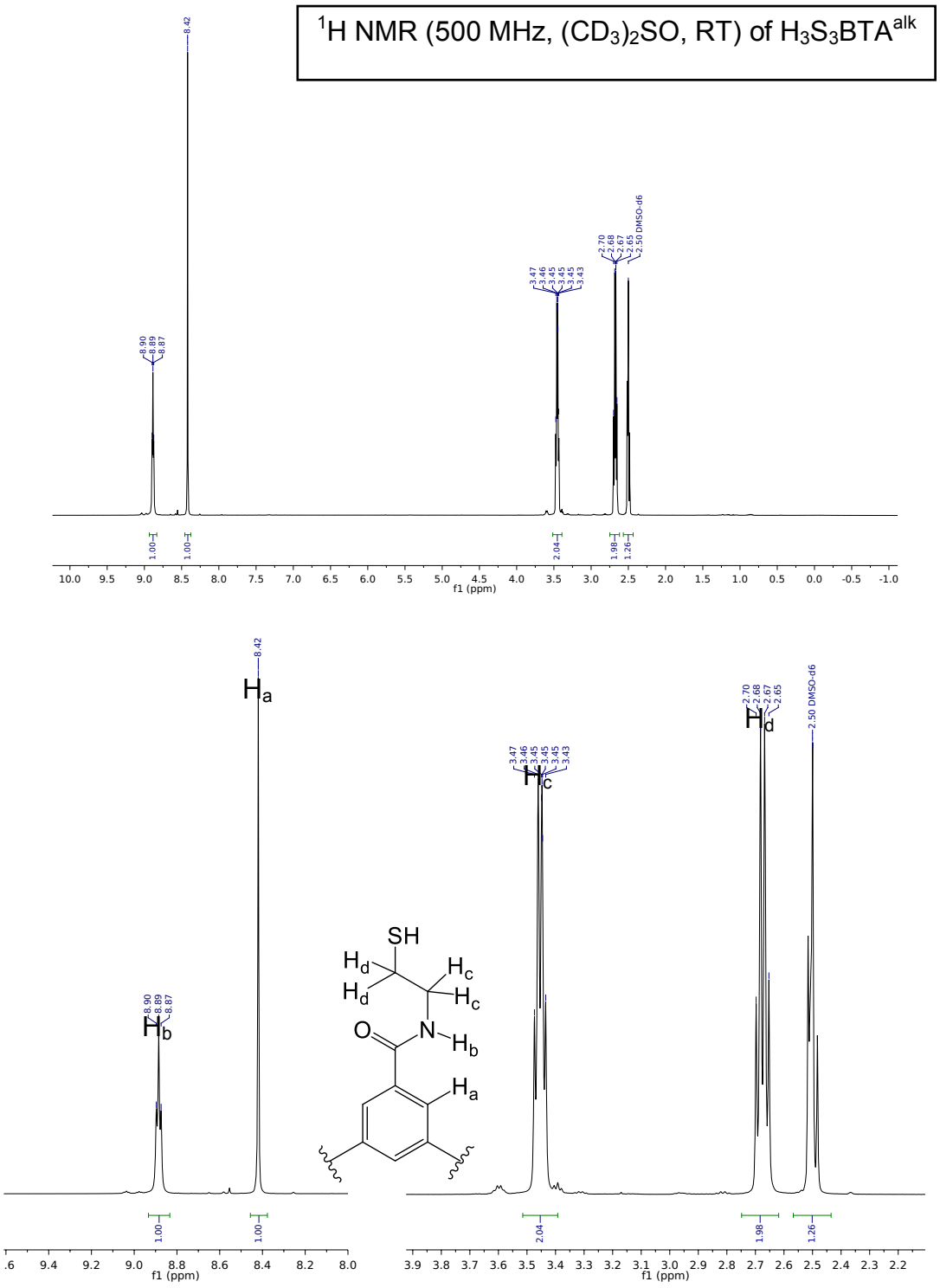

Figure 2.S5. *Top*: ^{1}H NMR spectrum of $H_3S_3BTA^{alk}$ in $(CD_3)_2SO$ at RT. The peak at 2.50 ppm is from residual protio solvent. *Bottom*: Zoom-in of top spectrum with peak labels.

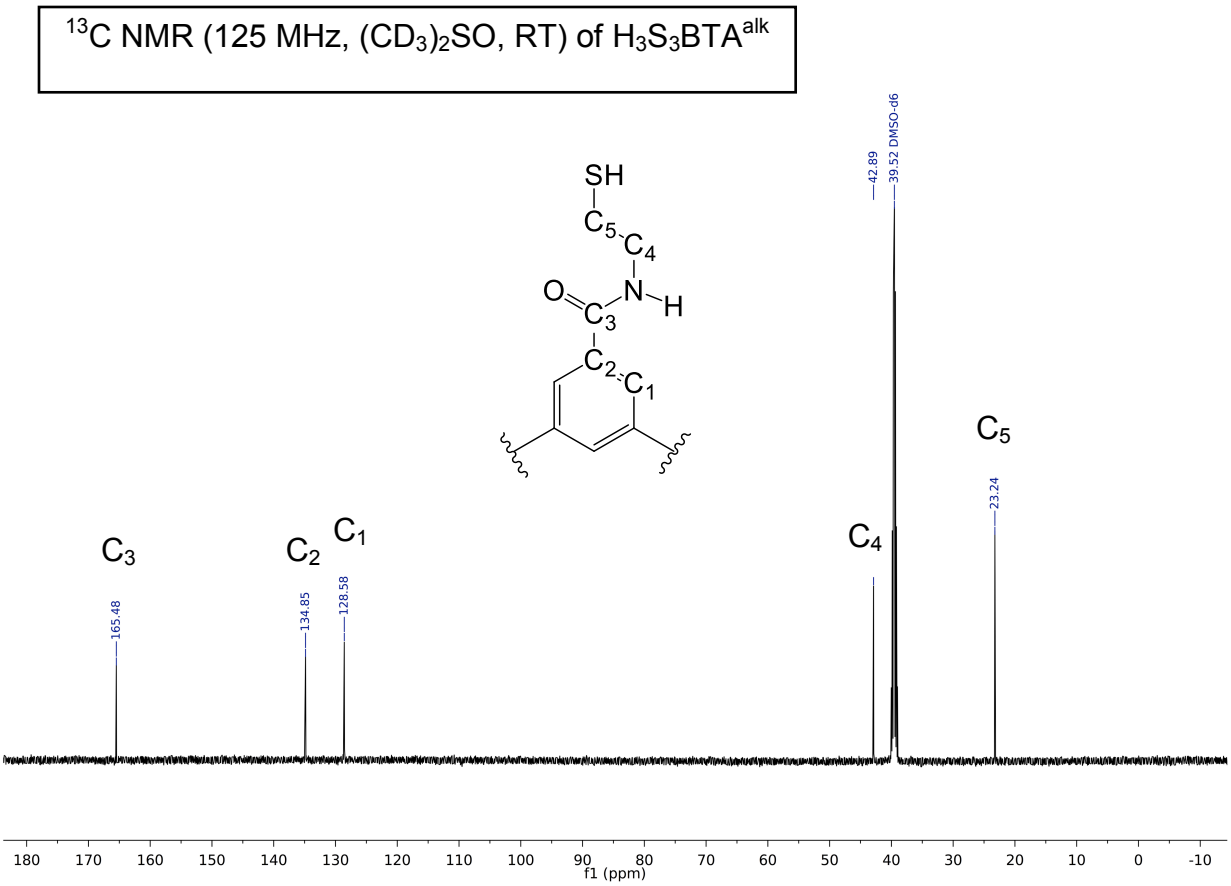

Figure 2.S6. ^{13}C NMR spectrum of $H_3S_3BTA^{alk}$ in $(CD_3)_2SO$ at RT. The peak at 39.52 ppm is from solvent.

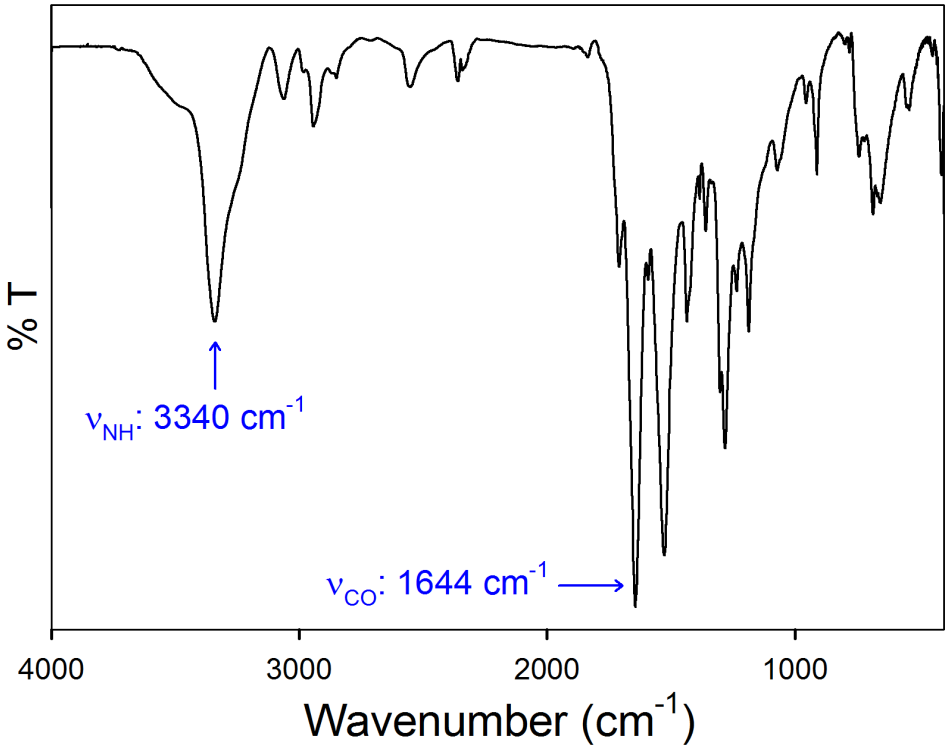

Figure 2.S7. Solid-state FTIR spectrum of $H_3S_3BTA^{alk}$ in a KBr matrix.

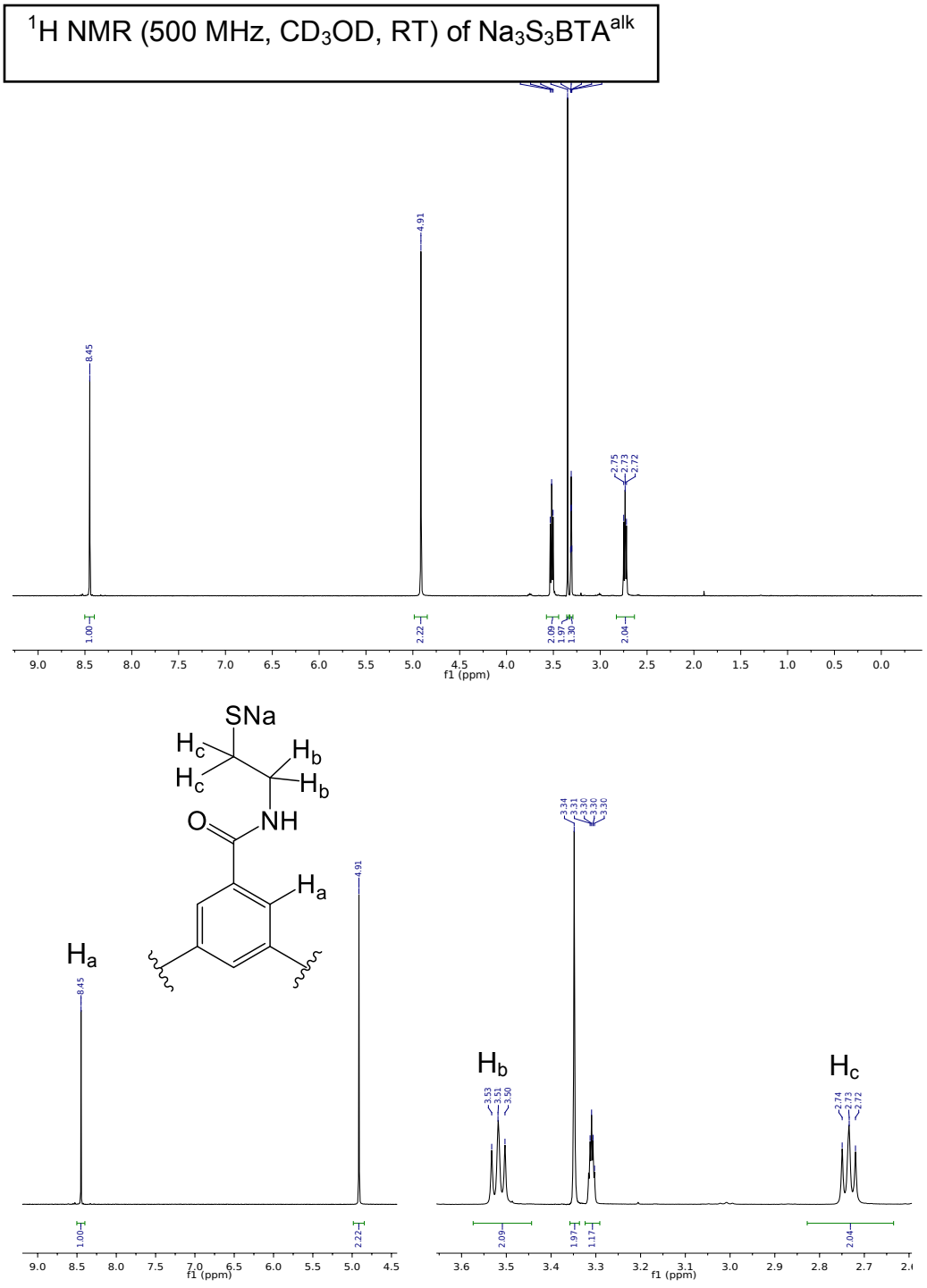

Figure 2.S8. *Top*: ^{1}H NMR spectrum of $Na_3S_3BTA^{alk}$ in CD_3OD at RT. The peaks at 4.91 and 3.30 ppm are from H_2O and residual protio solvent, respectively. The peak at 3.34 ppm is from MeOH. *Bottom*: Zoom-in of top spectrum with peak labels.

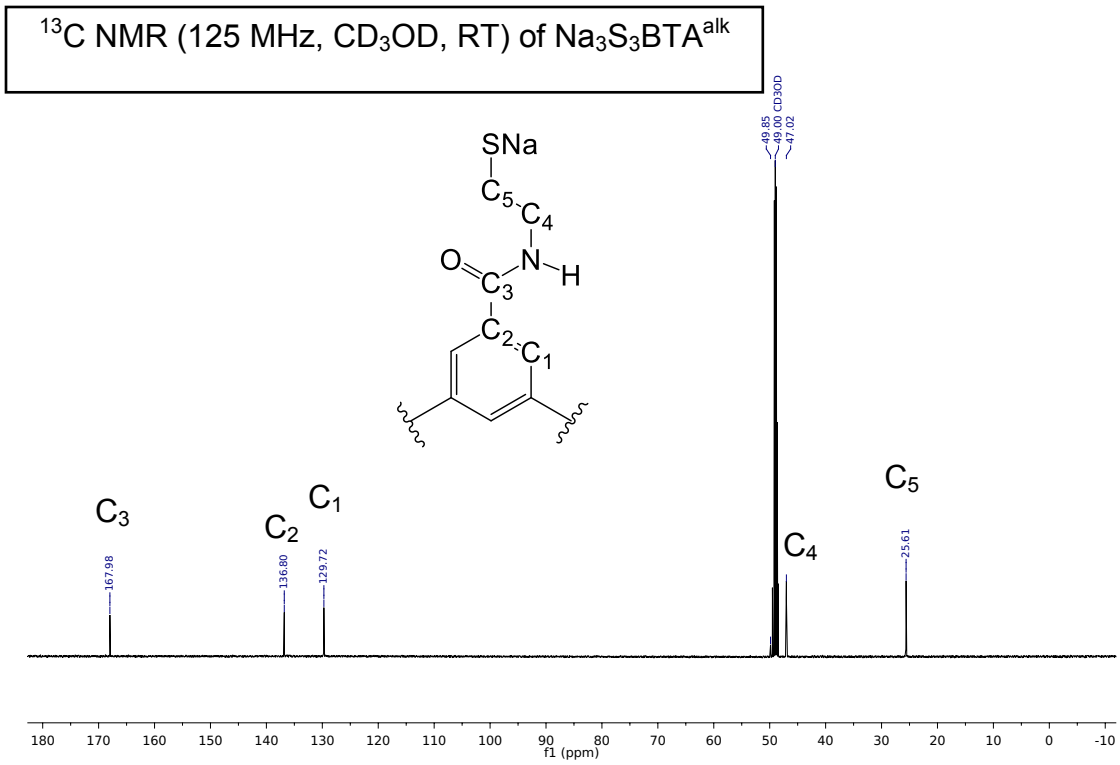

Figure 2.S9. ^{13}C NMR spectrum of $Na_3S_3BTA^{alk}$ in CD_3OD at RT. The peak at 49.00 ppm is from solvent.

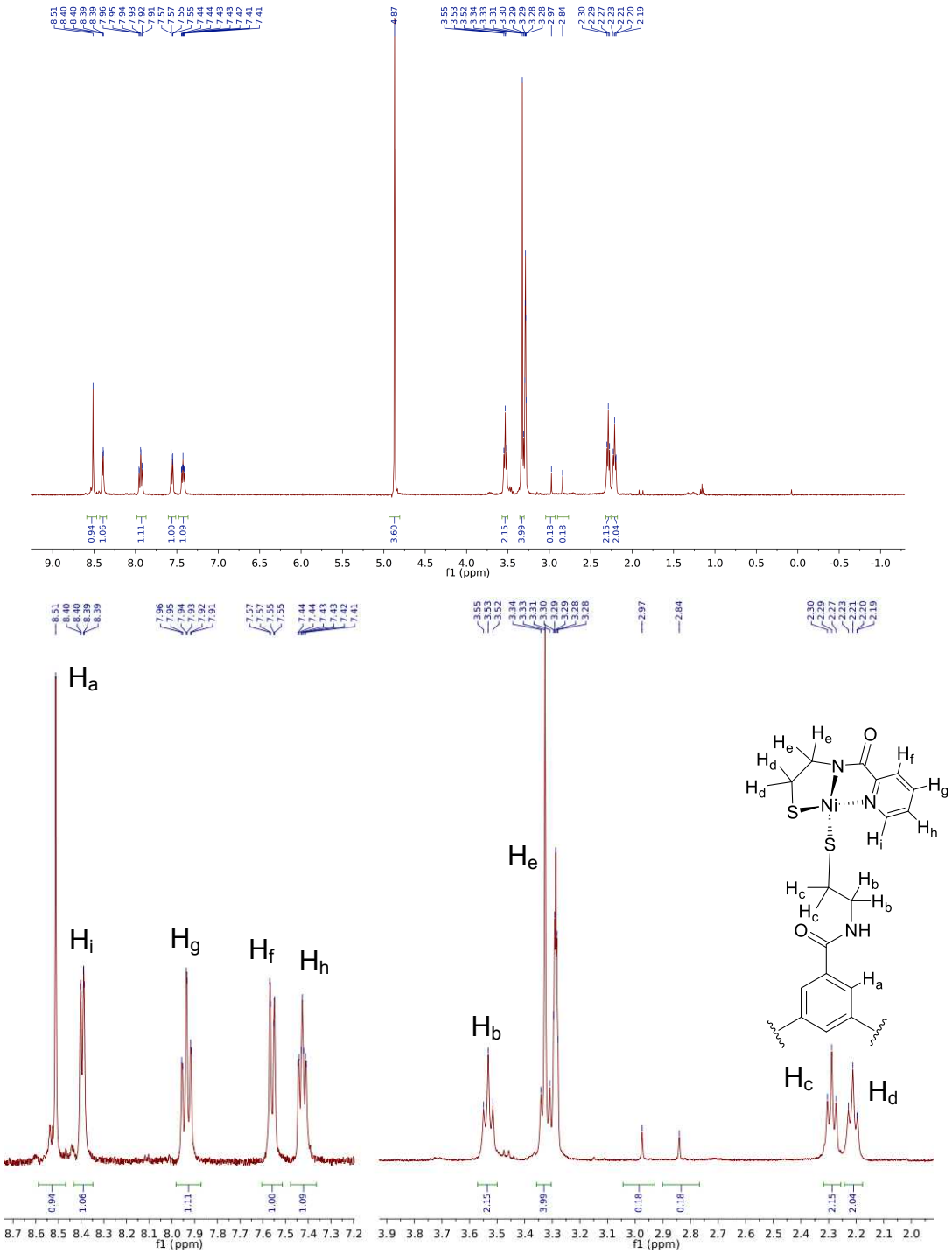

Figure 2.S10. *Top*: ^{1}H NMR spectrum of $Na_3[\{Ni(nmp)\}_3(S_3BTA^{alk})]$ (**1**) in CD_3OD at RT. The peaks at 3.30 and 4.87 ppm are from protio solvent and trace H_2O, respectively. Peaks at 2.97 and 2.84 ppm are DMF from reaction workup; the other DMF peak at 7.97 ppm is masked by H_g.

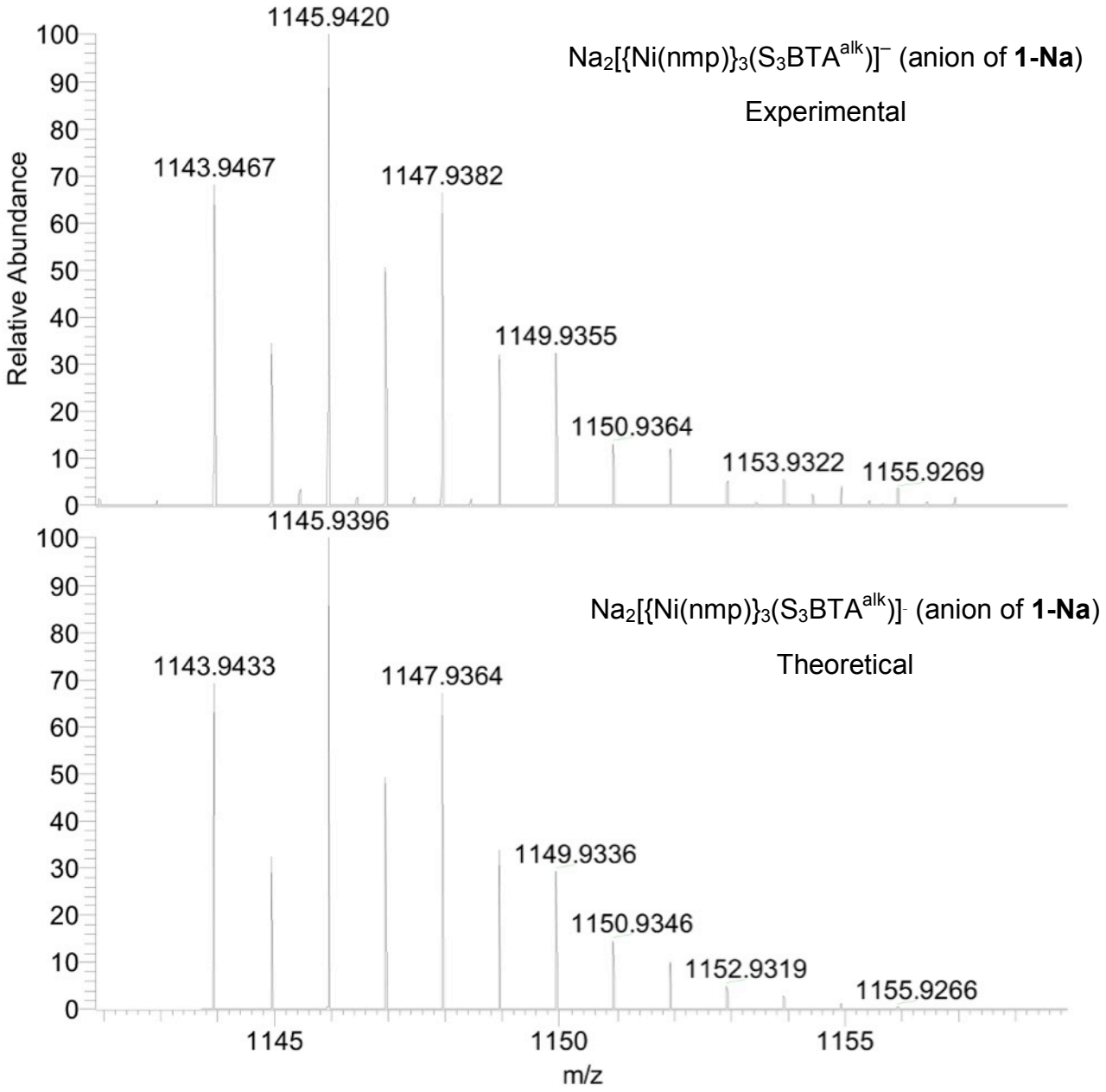

Figure 2.S11. *Top*: High-resolution ESI-MS (negative mode) of the anion form of **1** due to loss of Na^+ counterion, $[M–Na^+–3(18C6)]^–$. *Bottom*: Theoretical isotopic distribution.

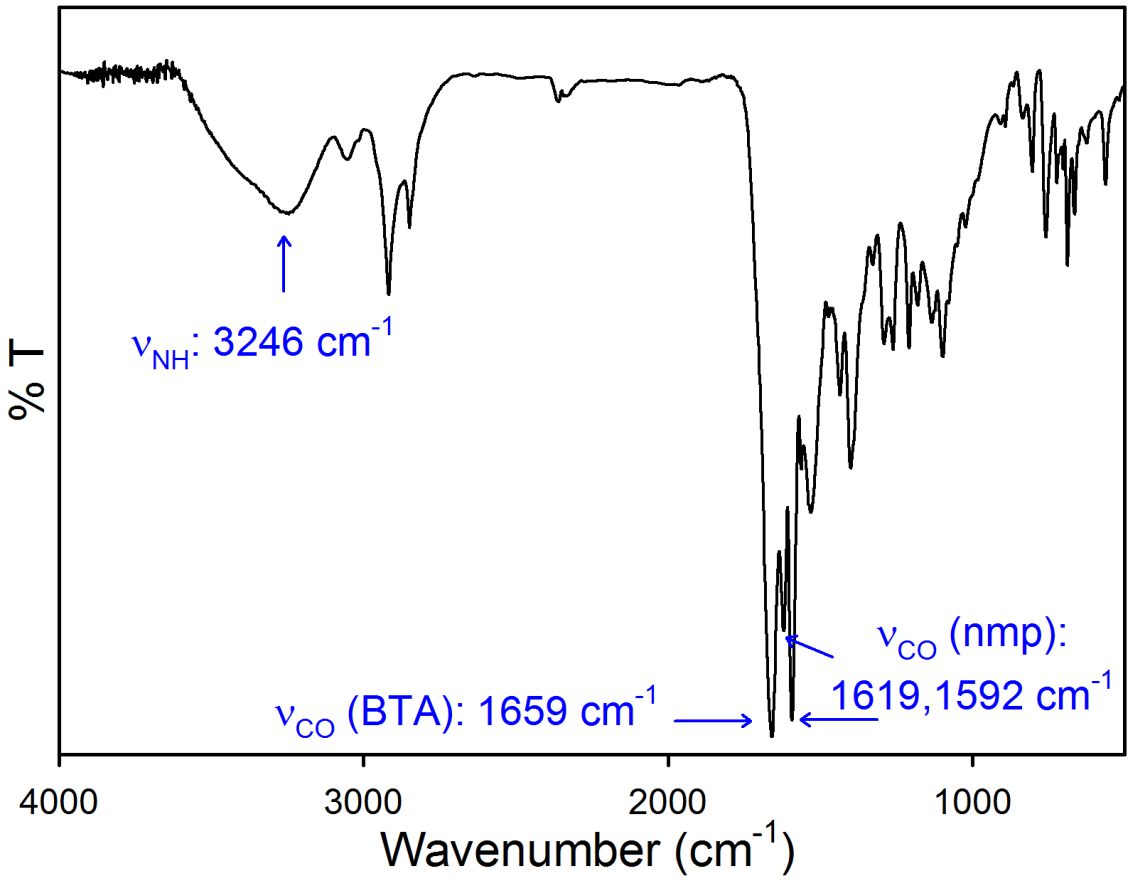

Figure 2.S12. Solid-state FTIR spectrum of **1** in a KBr matrix.

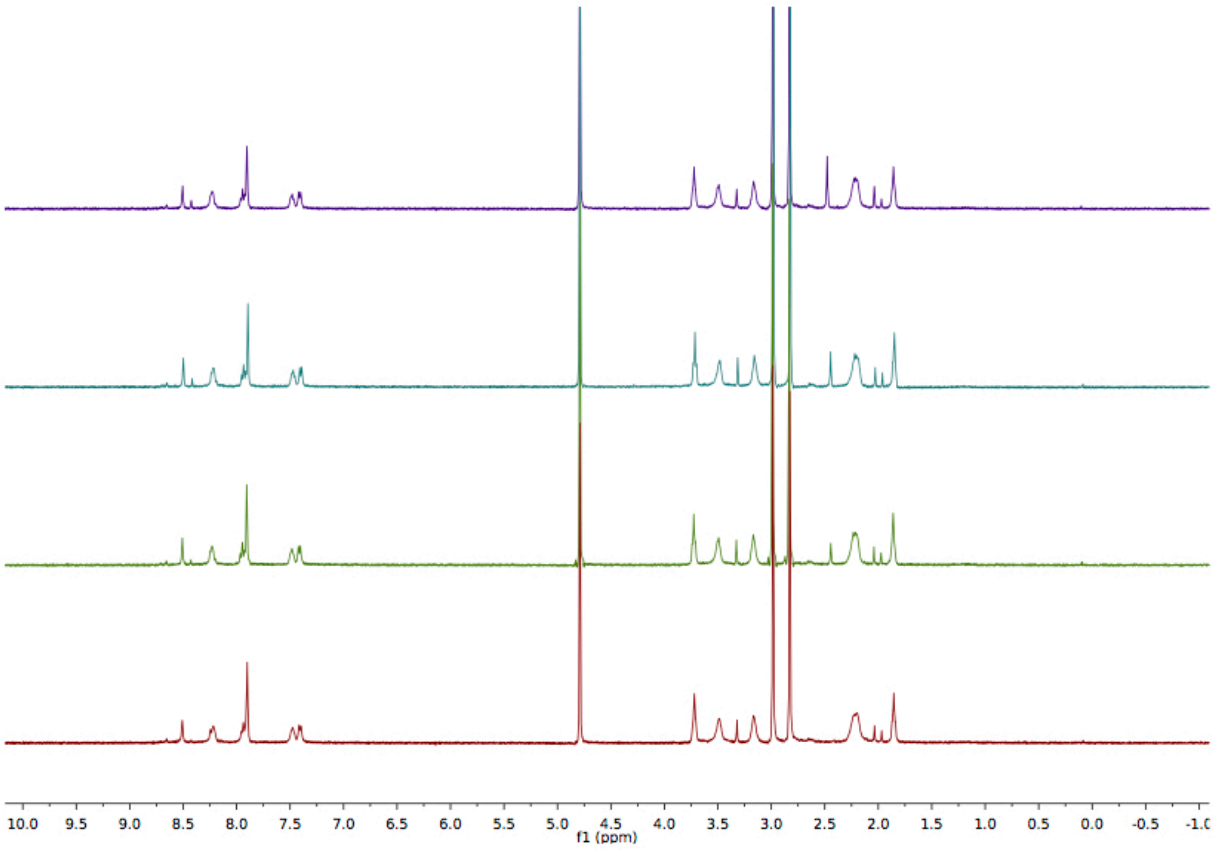

Figure 2.S13. ^{1}H NMR stability study of **1** in D_2O at RT. From bottom to top: 0 h, 24 h, 48 h, 4 d. Major residual solvent peaks are from DMF and H_2O.

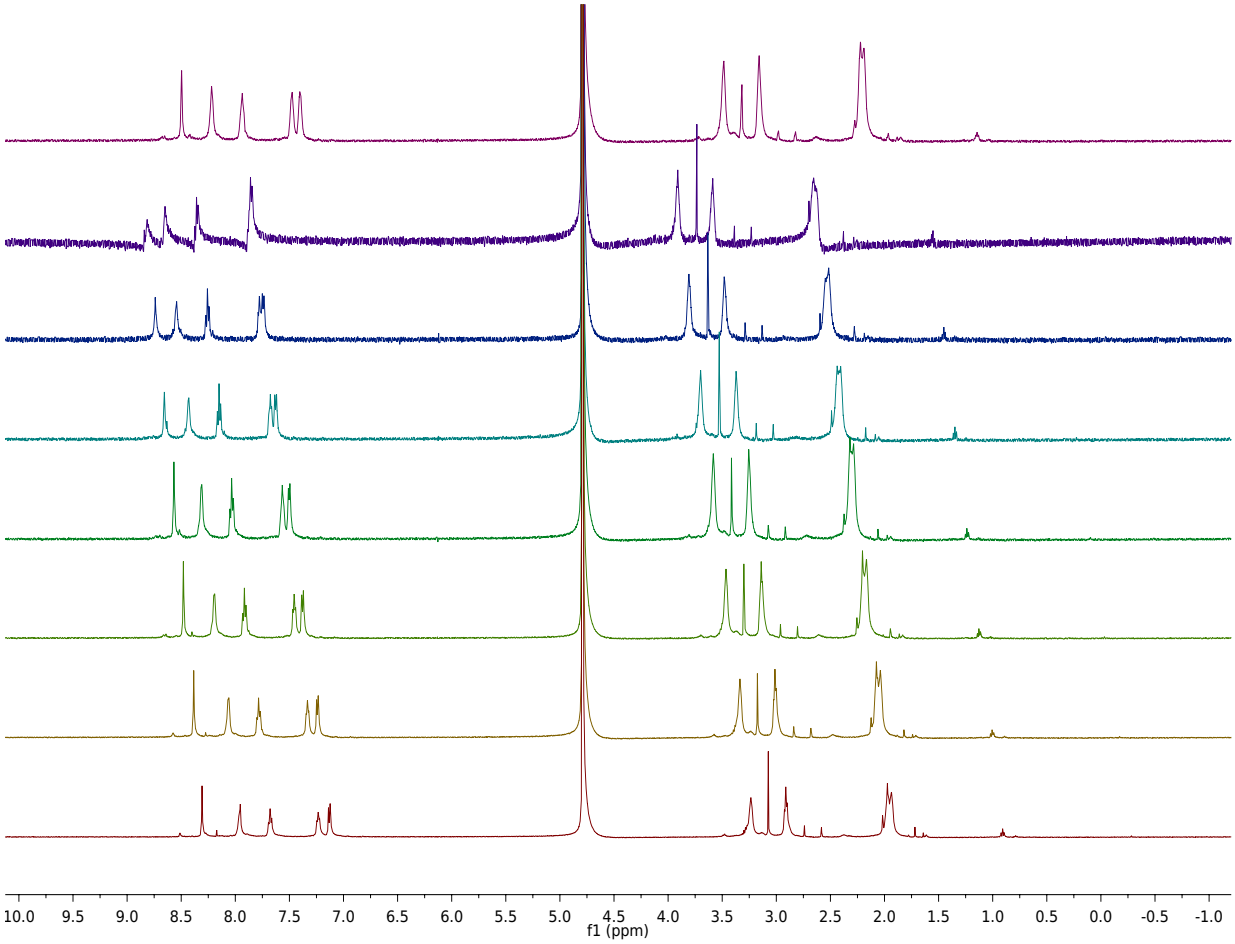

Figure 2.S14. Temperature-dependence study of **1** in D_2O. From bottom to top: 2, 10, 20, 30, 40, 50, 60 ºC and return to 20 ºC after 60 ºC. Peak at 4.79 ppm is from residual solvent.

Table 2.S1. Summary of best fit simulations to Ni EXAFS for **1** and **3** EXAFS[a]

Complex	Nearest Neighbor Ligand Environment[b]				Long Range Ligand Environment[b]				*F'*[g]
	Atom[c]	**R(A)**[d]	**CN**[e]	σ^{2}[f]	**Atom**[c]	**R(A)**[d]	**CN**[e]	σ^{2}[f]	
1	O/N	1.95	0.5	3.86	C	3.323	4.0	1.04	0.85
	S	2.16	2.0	4.65	C	3.835	4.0	0.44	
3	O/N	1.89	1.0	4.37	C	3.341	1.0	2.85	0.20
	S	2.17	2.0	4.07	C	3.829	2.0	3.41	

[a]Data were fit over a *k* range of 1 to 13.0 $Å^{-1}$.

[b]Independent metal-ligand scattering environment.

[c]Scattering atoms: N (nitrogen), S (sulfur) and C (carbon).

[d]Average metal-ligand bond length from two scans.

[e]Average metal-ligand coordination number from two scans.

[f]Average Debye-Waller factor in $Å^2 \times 10^3$ from two scans.

[g]Number of degrees of freedom weighted mean square deviation between data and fit.

Table 2.S2. Changes in the ^{1}H NMR chemical shift (ppm) of δ_{NH} and IR stretching frequencies (cm^{-1}) of ν_{CO} and ν_{NH} of the carboxamide group of Tr-S_3BTA^{alk} (L) upon binding to Ni(nmp) ([a]$CDCl_3$, [b]CH_2Cl_2, [c]CD_3CN, [d]MeCN recorded at RT).

	L	**1**	
δ_{NH}	6.38[a]	8.73[a]	8.65[c]
$\Delta\delta_{NH}$		+2.35	+2.27
$\nu_{NH\ (liquid)}$	3442[b]	3220[b]	3164[d]
$\Delta\nu_{NH\ (liquid)}$		-222	-278
$\nu_{CO\ (liquid)}$	1671[b]	1655[b]	1695[d]
$\Delta\nu_{CO}$		-16	+24
$\nu_{NH\ (KBr)}$	3409, 3291	3246	
$\Delta\nu_{NH\ (KBr)}$		-163, -45	
$\nu_{CO\ (KBr)}$	1652	1659	
$\Delta\nu_{CO\ (KBr)}$		+7	

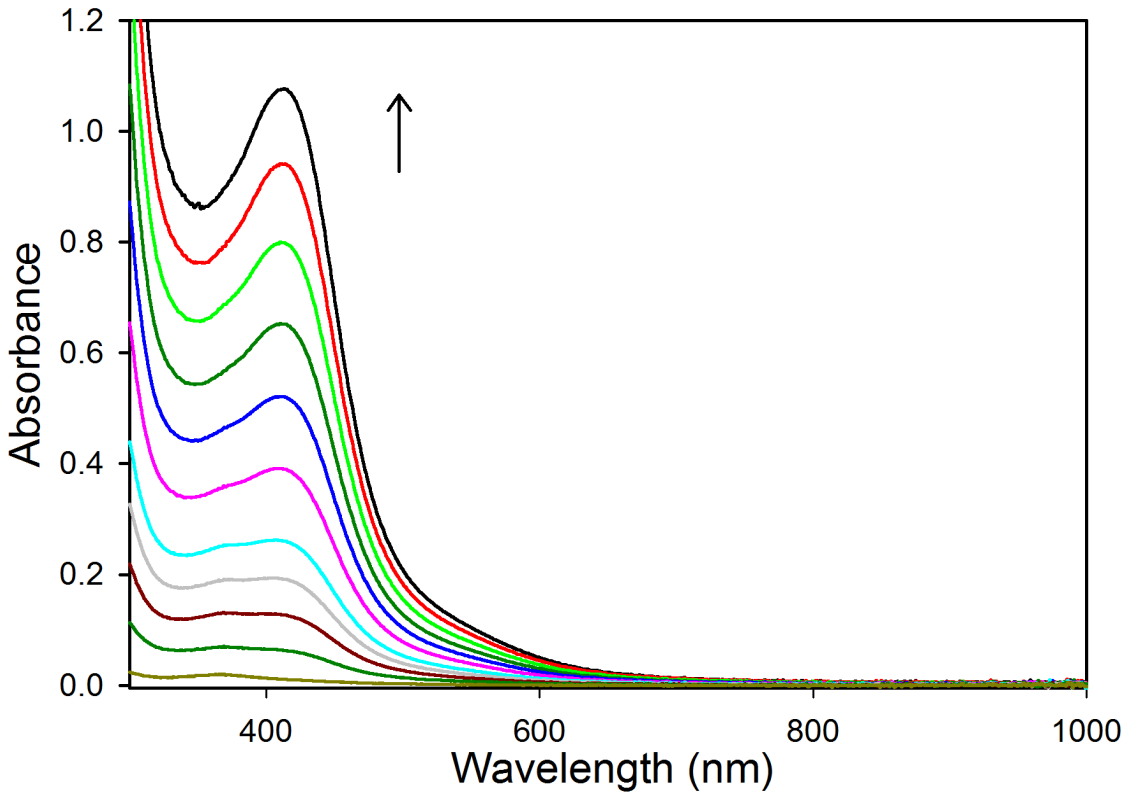

Figure 2.S15. Concentration-dependent UV-vis of **1** in H_2O in 16 μM increments (1.67-130 μM), 25 ºC. Arrow shows direction of change with increasing concentration.

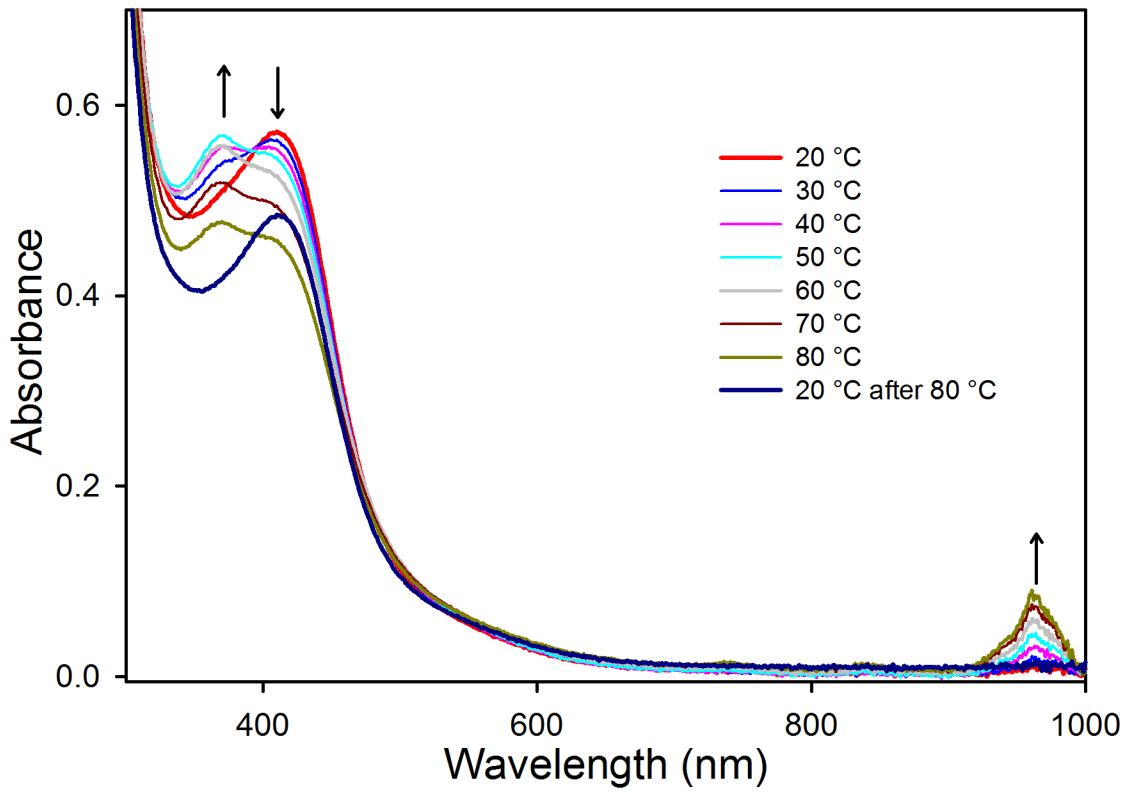

Figure 2.S16. UV-vis spectral changes of a 100 μM H_2O solution of **1** at variable temperatures. Arrows show direction of change with increasing temperature. Dark blue trace represents return to original temperature after temperature ramp.

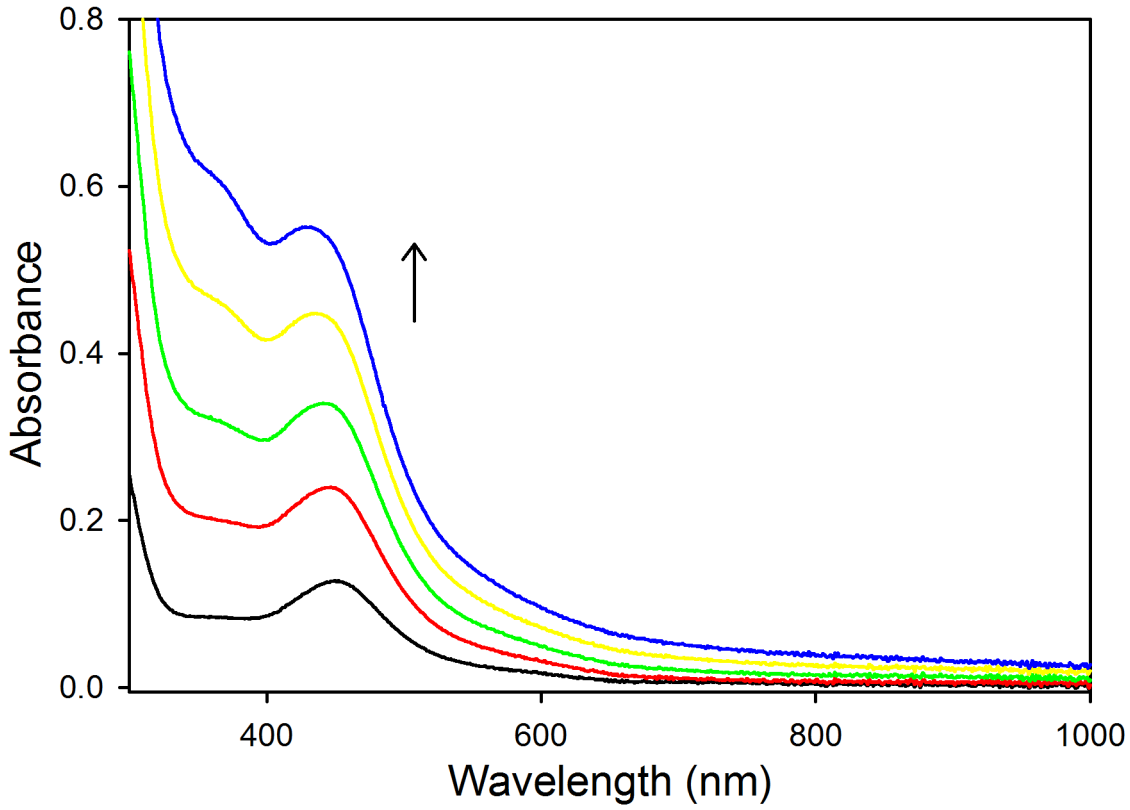

Figure 2.S17. Concentration-dependence in the UV-vis of CH_2Cl_2 solutions of **1** in 16 μM increments (16.6-80.6 μM), 25 ºC. Arrow shows change with respect to increasing concentration.

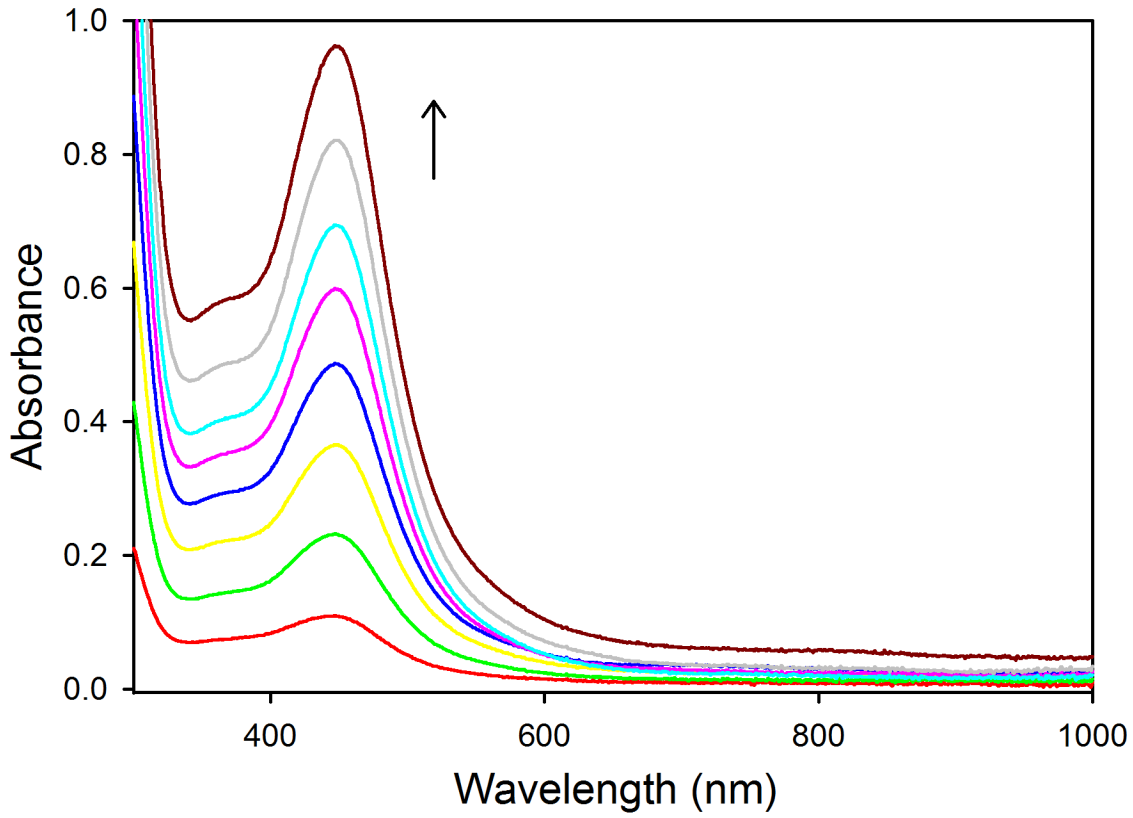

Figure 2.S18. Concentration-dependence in the UV-vis of MeCN solutions of **1** in 16 μM increments (16.6-127 μM), 25 ºC. Arrow shows change with respect to increasing concentration.

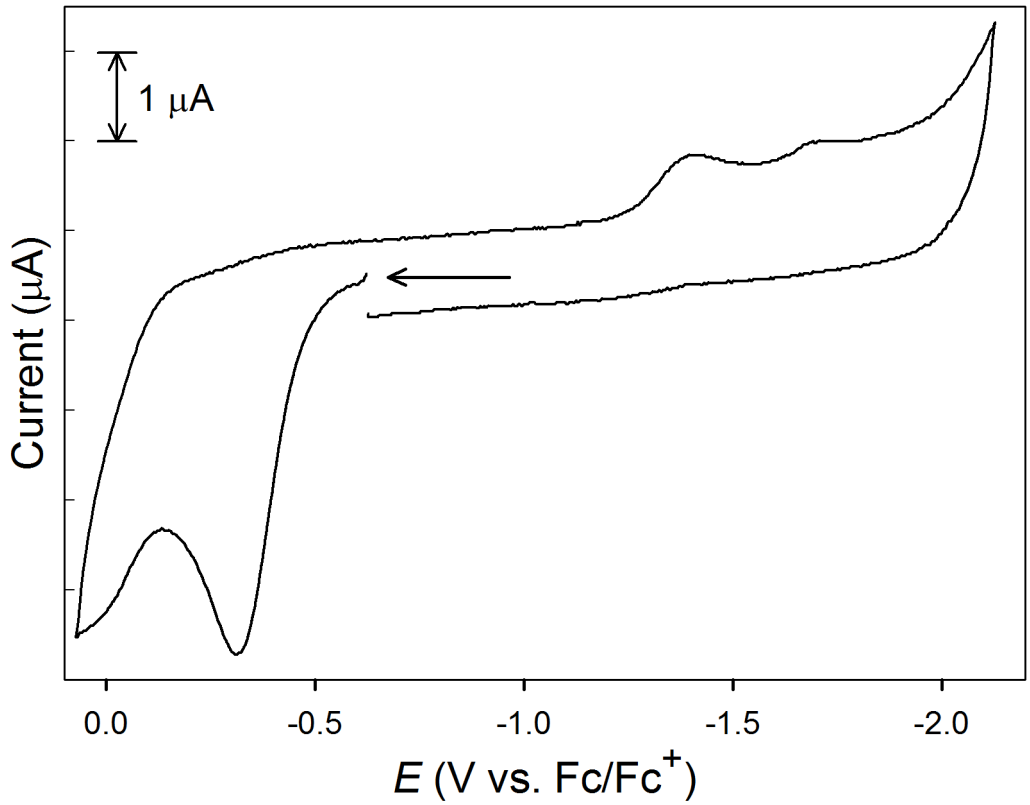

Figure 2.S19. CV of a 2.5 mM DMF solution of **1**$^{\mathbf{A}}$ (0.1 M $^{n}Bu_4NPF_6$ supporting electrolyte, scan rate = 100 mV/s, RT). Arrow shows direction of scan.

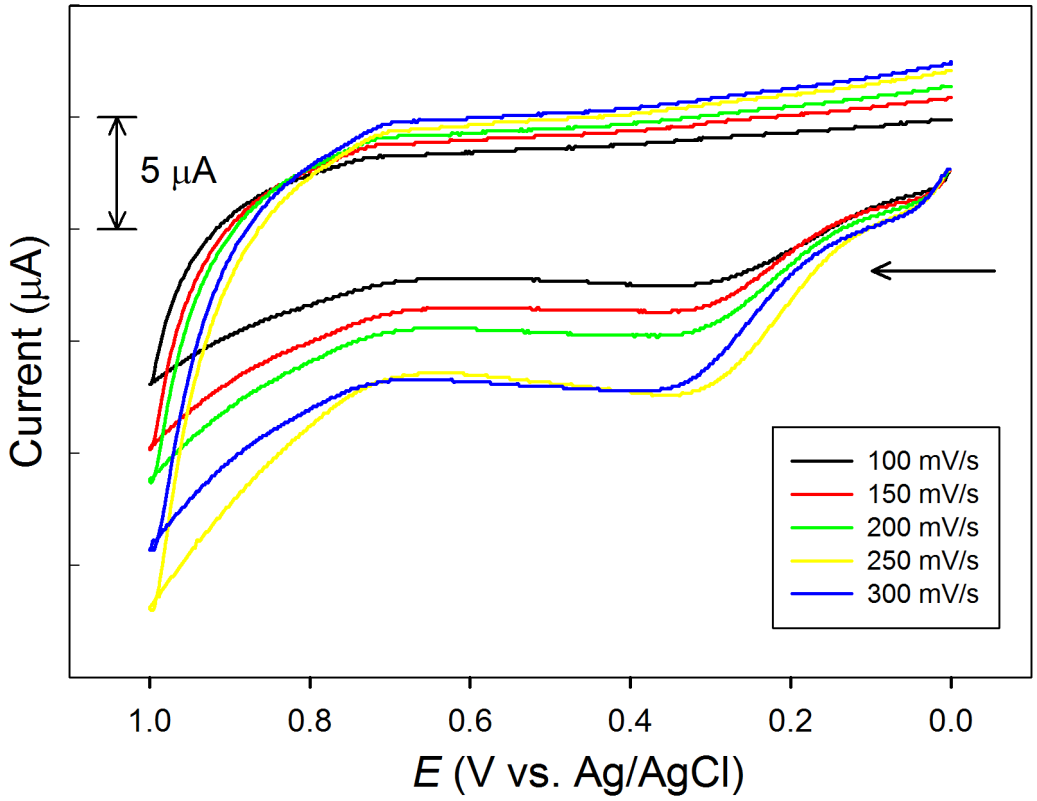

Figure 2.S20. CV of a 2.5 mM H_2O solution of $\mathbf{1}^{\mathbf{A}}$ at different scan rates (0.5 M KNO_3 supporting electrolyte, RT). Arrow shows direction of scan.

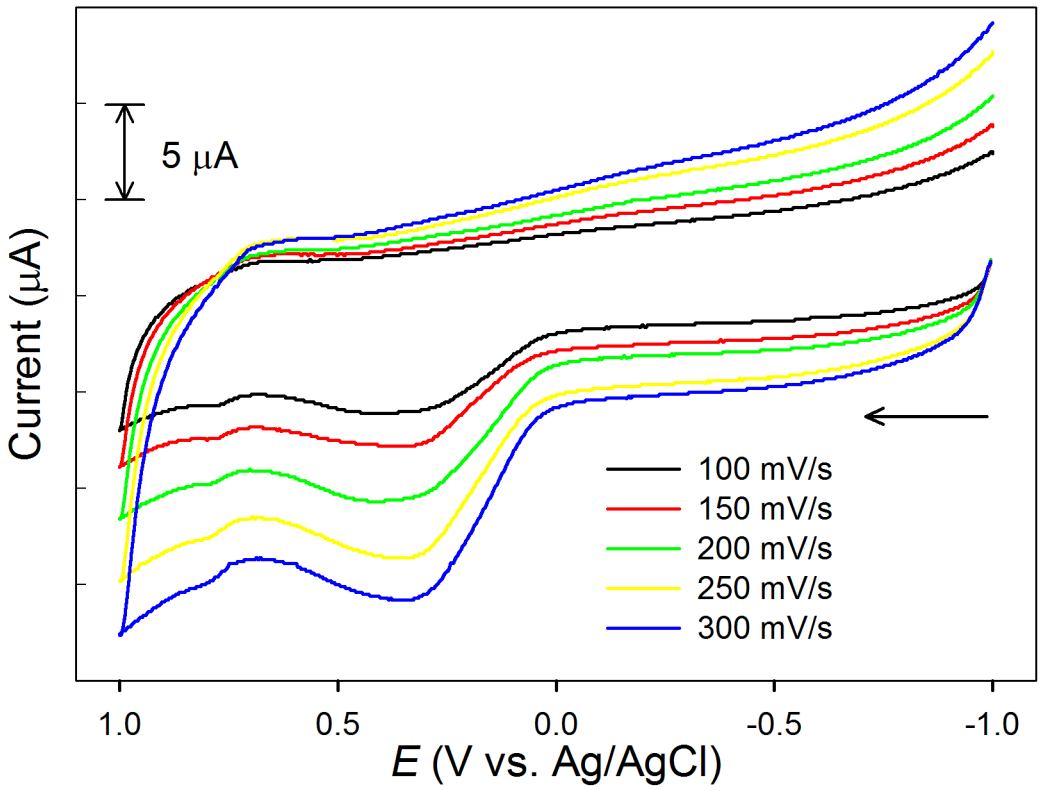

Figure 2.S21. CV of a 2.5 mM PBS solution (pH 7.4) of $\mathbf{1}^{\mathbf{M}}$ at different scan rates (0.5 M KNO_3 supporting electrolyte, RT). Arrow shows direction of scan.

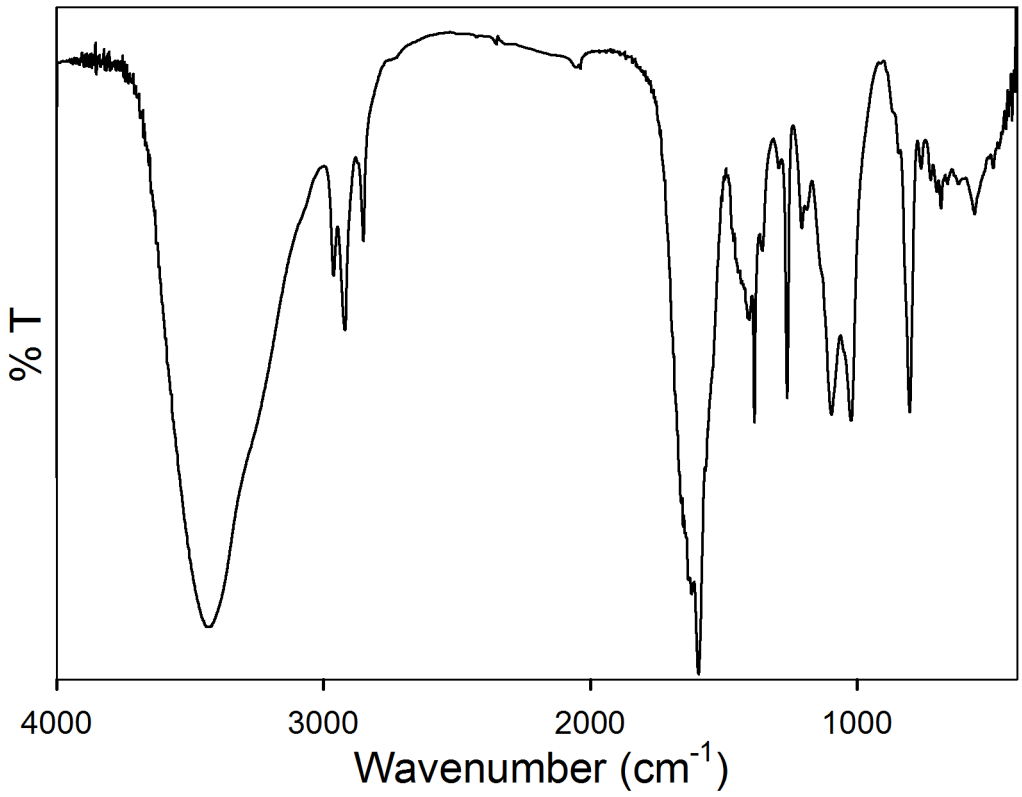

Figure 2.S22. Solid-state FTIR spectrum of $\mathbf{1}^{\mathbf{A}}$ + O_2 in a KBr matrix after removing MeOH reaction solvent.

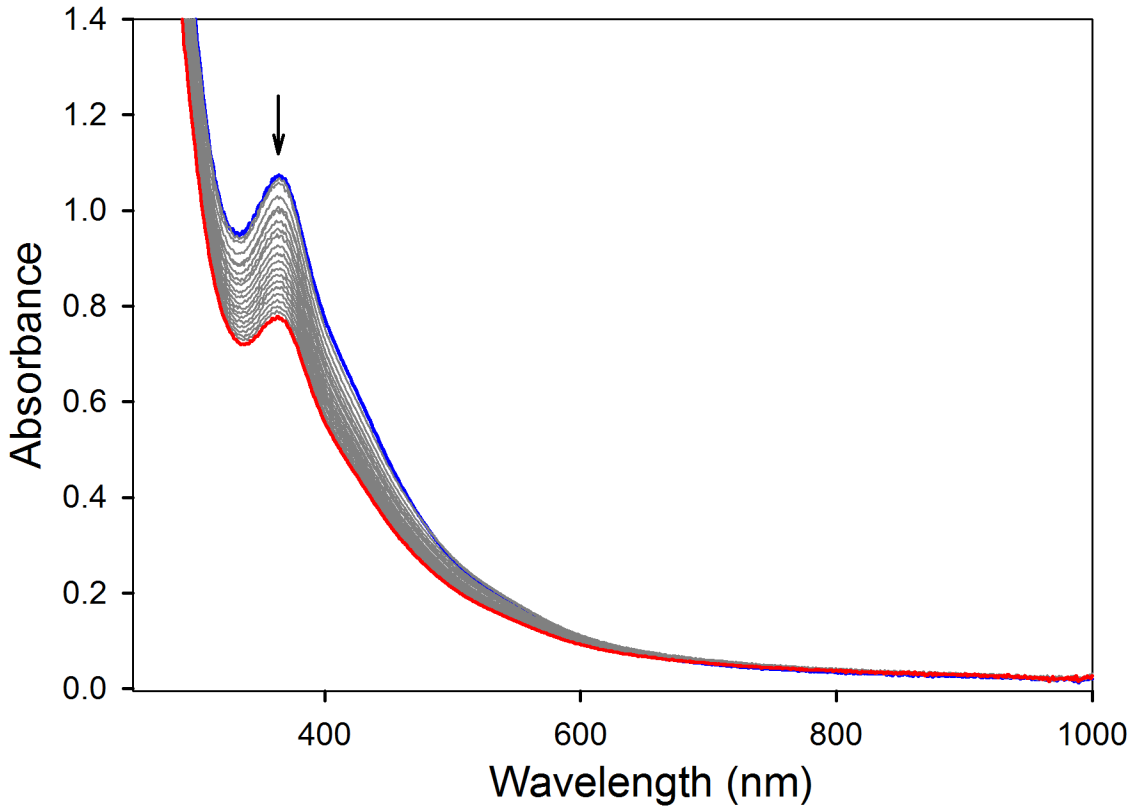

Figure 2.S23. UV-vis spectral monitor of a 100 μM PBS solution (pH 7.4) of $\mathbf{1^M}$ (blue trace) and immediately after addition of 100 equiv of H_2O_2·urea. Final trace in red. Traces recorded at 1 scan/min intervals for 20 min at 25 °C. Arrow shows direction of change. Complete degradation is observed after 2 h.

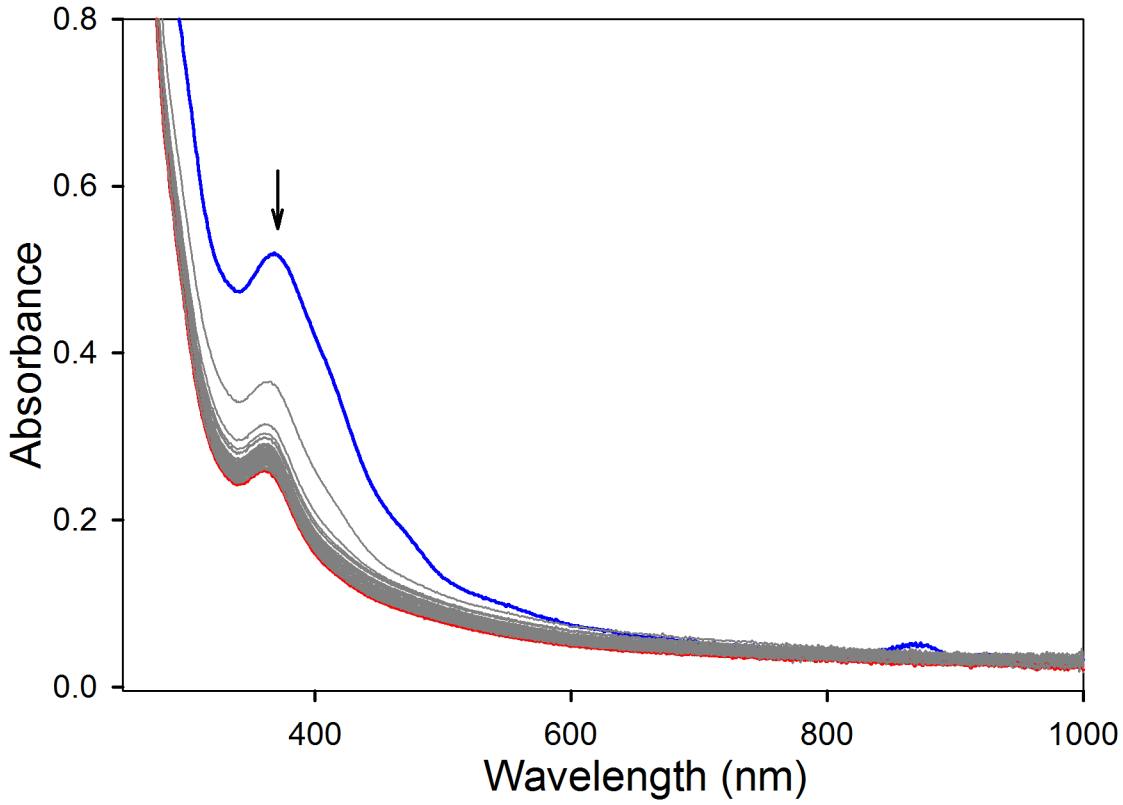

Figure 2.S24. UV-vis spectral monitor of a 100 μM MeOH solution of $\mathbf{1}^{\mathbf{A}}$ (blue trace) and immediately after addition of 100 equiv of H_2O_2·urea. Final trace in red. Traces recorded at 1 scan/min intervals for 60 min at 25 °C. Arrow shows direction of change. Complete degradation is observed after 2 h.

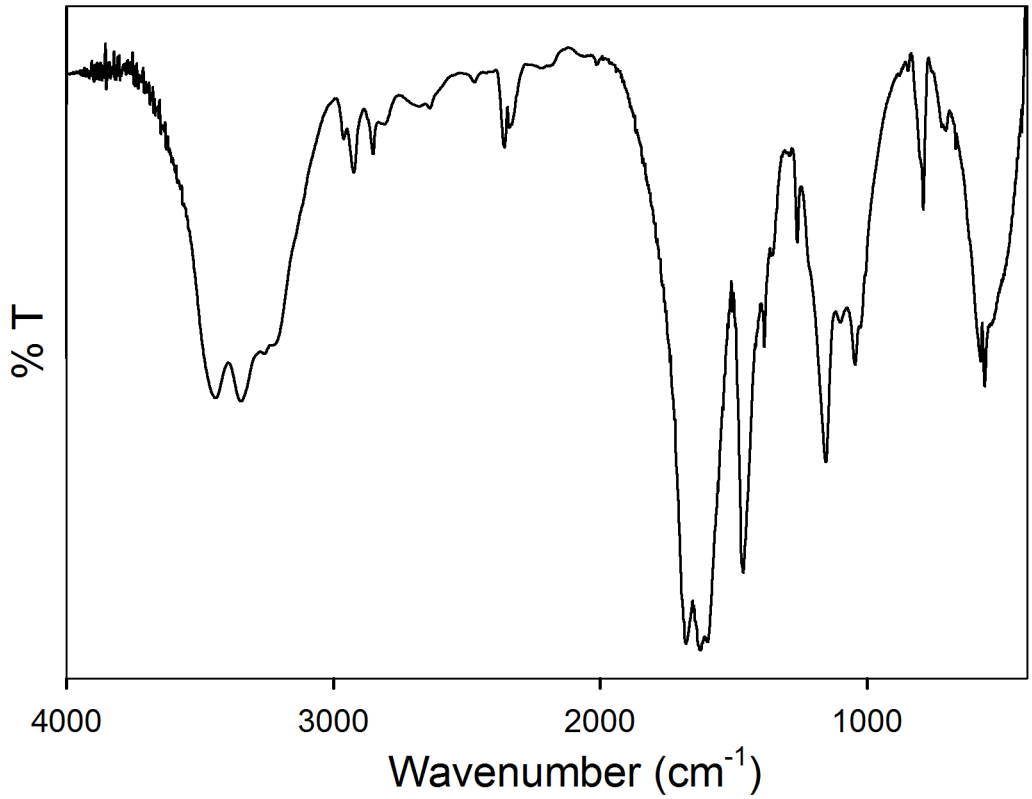

Figure 2.S25. Solid-state FTIR spectrum of the reaction product of **1**^{A} and 100 equiv of H_2O_2·urea in a KBr matrix after removing MeOH reaction solvent.

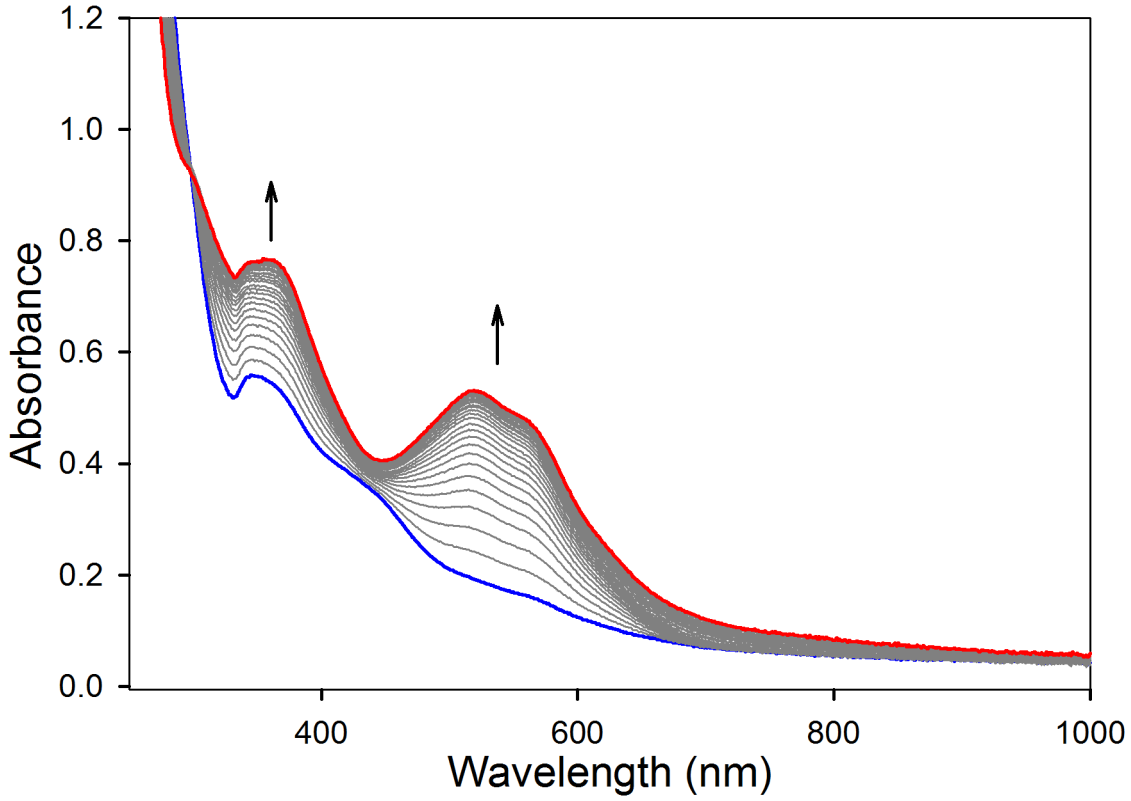

Figure 2.S26. UV-vis spectral monitor of a MeOH solution containing a 1:1 mixture of **1** and NBT (each 61 μM, blue trace). Final trace in red. Traces recorded at 1 scan/min intervals for 30 min at 25 °C. Arrow shows direction of change.

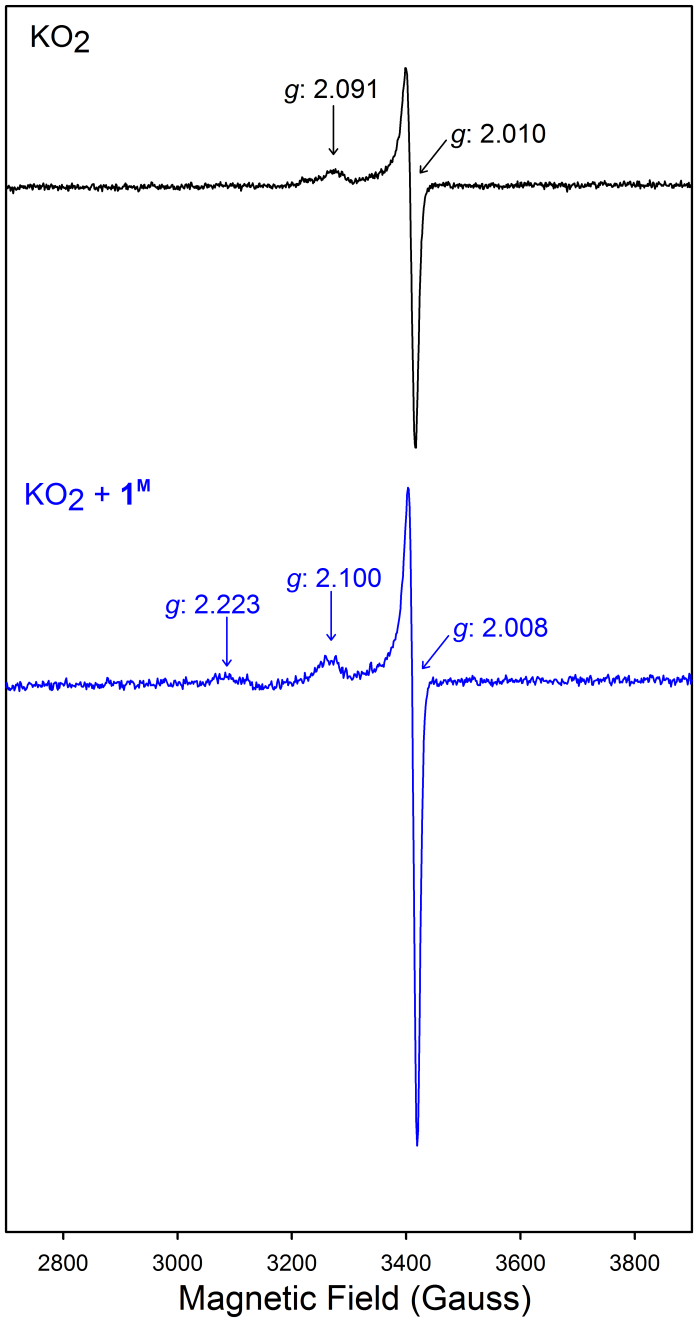

Figure 2.S27. X-band EPR of KO_2 (black) and of the reaction of 0.5 mM $\mathbf{1^M}$ with 0.05 M KO_2 (blue); both spectra recorded in pH 7.4 PBS at 10 K. Spectrometer settings: microwave frequency, 9.585 GHz (black), 9.584 GHz (blue); microwave power, 1.0 mW; modulation frequency, 100 kHz; modulation amplitude, 6.48 G.

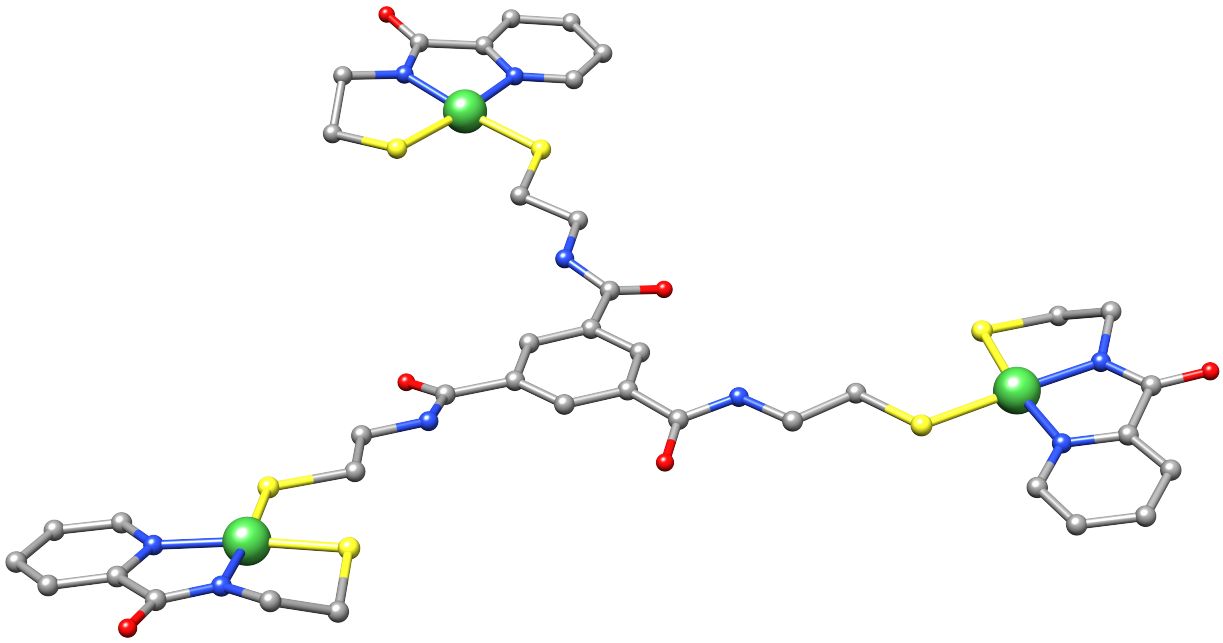

Figure 2.S28. Geometry-optimized structure of $\mathbf{1}^{\mathbf{A}}$ (BP86/def2-TZVPP). Ni = green; C = grey; N = blue; S = yellow; O = red. Bond distances: Ni-$N_{carboxamide}$ = 1.890 Å; Ni-N_{py} = 1.930 Å, Ni-S_{nmp} = 2.157 Å; Ni-S_{BTA} = 2.193 Å; Ni···Ni_{avg} ~ 16 Å.

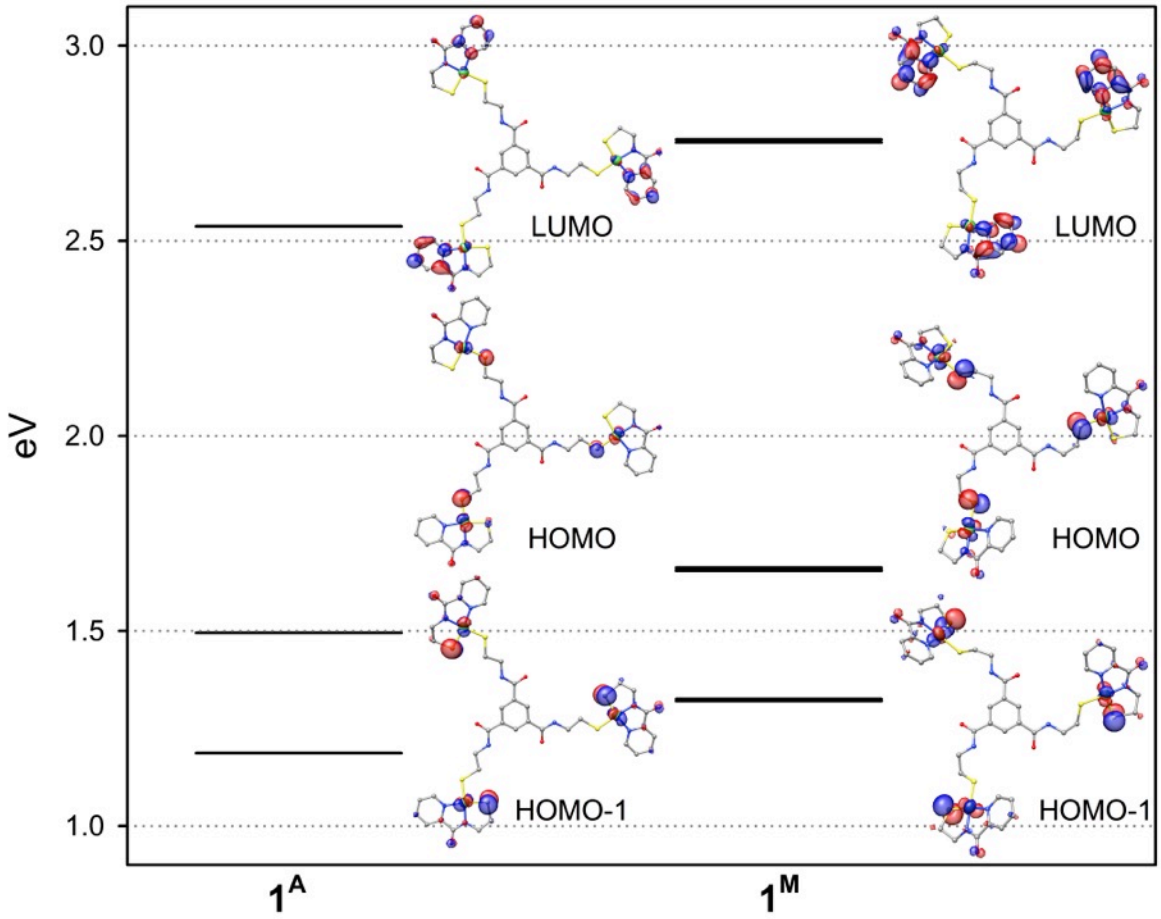

Figure 2.S29. DFT-generated isosurface plots of the frontier MOs of the geometry optimized structure of $\mathbf{1}^{\mathbf{A}}$ and $\mathbf{1}^{\mathbf{M}}$ in the gas phase. In each column, the orbitals descend in the order LUMO, HOMO, HOMO-1.

Table 2.S3. Löwdin orbital compositions derived from the DFT calculations for selected MOs of **1**^{A} in the gas phase. Only s- and p-orbital contributions calculated for N, S. Bonding interactions are represented with a + and antibonding interactions are denoted with a –. The coordinate system used for figuring out the type of AO on Ni, N and S are as follows: z-axis is normal to the square-planar ligand field; x-axis is parallel to S_{nmp}-Ni-N_{py}; y-axis is parallel to S_{BTA}-Ni-N_{am}.

MO label	MO #	E (eV)	%Ni	%N	%S_{total}	%S_{nmp}	%S_{BTA}	Orbital Composition
HOMO-1	280	1.1868	41.5	2.3	35.5	35.1	0.4	Ni(d_{xy})–$S_{nmp}(p_z)$,$N_{am}(p_z)$
HOMO-1	281	1.1871	41.5	2.3	35.6	35.1	0.5	
HOMO-1	282	1.1872	41.6	2.3	35.5	35.1	0.4	
HOMO	283	1.4945	51.8	2.1	33	5.7	27.3	Ni(d_{yz})–$S_{BTA}(p_z)$, $N_{am}(p_z)$, $N_{nmp}(p_z)$
HOMO	284	1.4947	51.7	2.1	32.9	5.6	27.3	
HOMO	285	1.495	51.9	2.2	32.9	5.6	27.3	
LUMO	286	2.5367	9	18.8	2.5	1.8	0.7	Ni(d_{xz})–$N_{py}(p_z)$, $N_{am}(p_z)$
LUMO	287	2.5369	9.1	18.9	2.5	1.8	0.7	
LUMO	288	2.5373	8.8	18.9	2.6	1.8	0.8	

Table 2.S4. Löwdin orbital compositions derived from the DFT calculations for selected MOs of $\mathbf{1^M}$ in the gas phase. Details are the same as in Table 2.S3.

MO label	MO #	E (eV)	%Ni	%N	$\%S_{total}$	$\%S_{nmp}$	$\%S_{BTA}$	Orbital Composition
HOMO-1	280	1.3204	44.4	2	34	33.8	0.2	
HOMO-1	281	1.321	44.6	1.3	34.2	33.9	0.3	$Ni(d_{xy})$–$S_{nmp}(p_z)$,$N_{am}(p_z)$
HOMO-1	282	1.3255	44.8	2.1	34	33.8	0.2	
HOMO	283	1.6545	52.6	2.4	32	4.4	27.6	
HOMO	284	1.6561	52.8	2.3	31.9	4.4	27.5	$Ni(d_{yz})$–$S_{BTA}(p_z)$, $N_{am}(p_z)$, $S_{nmp}(p_z)$
HOMO	285	1.6624	52.8	2.4	32.1	4.5	27.6	
LUMO	286	2.7519	8.7	19.1	2.3	1.6	0.7	
LUMO	287	2.7519	8.8	19.2	2.2	1.5	0.7	$Ni(d_{xz})$–$N_{py}(p_z)$, $N_{am}(p_z)$
LUMO	288	2.7595	8.6	19.2	2.1	1.5	0.6	

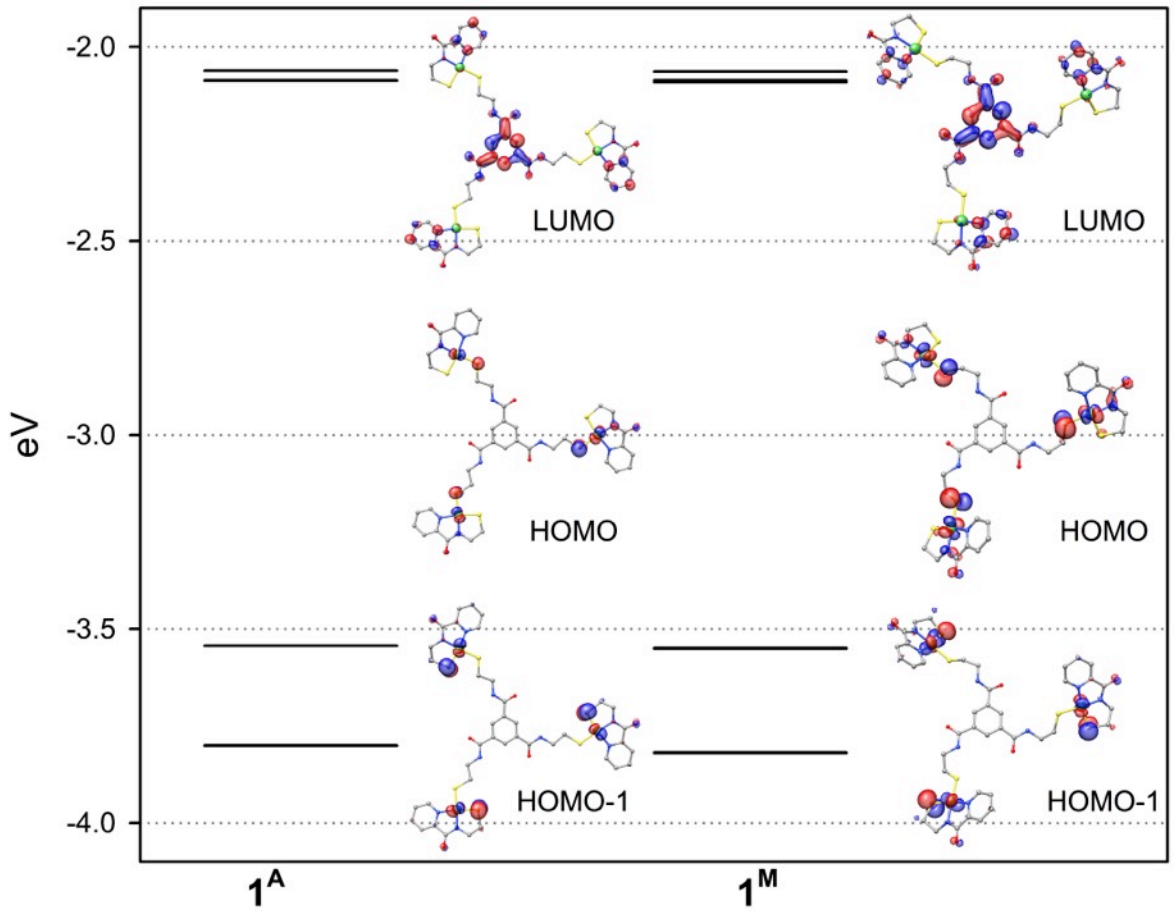

Figure 2.S30. DFT-generated isosurface plots of the frontier MOs of the geometry optimized structure of $\mathbf{1}^{\mathbf{A}}$ and $\mathbf{1}^{\mathbf{M}}$ in water. In each column, the orbitals descend in the order LUMO, HOMO, HOMO-1.

Table 2.S5. Löwdin orbital compositions derived from the DFT calculations for selected MOs of **1**^{A} in water. Details are the same as in Table 2.S3.

MO label	MO #	E (eV)	%Ni	%N	%S_{total}	%S_{nmp}	%S_{BTA}	Orbital Composition
HOMO-1	280	-3.8005	50.8	1.4	30.7	30.5	0.2	Ni(d_{xy})–S_{nmp}(p_z), N_{am}(p_z)
HOMO-1	281	-3.8003	50.8	1.4	30.8	30.6	0.2	
HOMO-1	282	-3.8002	50.8	1.4	30.8	30.6	0.2	
HOMO	283	-3.5437	57.8	3.2	25.9	3.7	22.2	Ni(d_{yz})–N_{am}(p_z), S_{BTA}(p_z)
HOMO	284	-3.5435	57.9	2.9	25.9	3.6	22.3	
HOMO	285	-3.5434	58	2.8	26	3.7	22.3	
LUMO	286	-2.087	0.9	2.2	0.2	0.2	0	C($p\pi$) AO from py and 1,3,5-BTA
LUMO	287	-2.0863	0.9	2.4	0.1	0.1	0	
LUMO	288	-2.0616	7.7	19	1.8	1.2	0.6	

Table 2.S6. Löwdin orbital compositions derived from the DFT calculations for selected MOs of $\mathbf{1^M}$ in water. Details are the same as in Table 2.S3.

MO label	MO #	E (eV)	%Ni	%N	$\%S_{total}$	$\%S_{nmp}$	$\%S_{BTA}$	Orbital Composition
HOMO-1	280	-3.8195	51.7	1.3	30.1	30	0.1	
HOMO-1	281	-3.8189	51.6	1.3	30.1	30.1	0	Ni(d_{xy})–S_{nmp}(p_z), N_{am}(p_z)
HOMO-1	282	-3.8187	51.6	1.3	30.1	30	0.1	
HOMO	283	-3.5505	58.1	3.3	25.6	3.4	22.2	
HOMO	284	-3.5498	58.1	3.1	25.6	3.4	22.2	Ni(d_{yz})–N_{am}(p_z), S_{BTA}(p_z), S_{nmp}(p_z)
HOMO	285	-3.5487	58.1	3.2	25.7	3.5	22.2	
LUMO	286	-2.0909	1.2	0.3	0.2	0.2	0	
LUMO	287	-2.0865	1.3	0.3	0.4	0.3	0.1	C($p\pi$) AO from py and 1,3,5-BTA
LUMO	288	-2.0634	7.8	19.2	1.9	1.2	0.7	

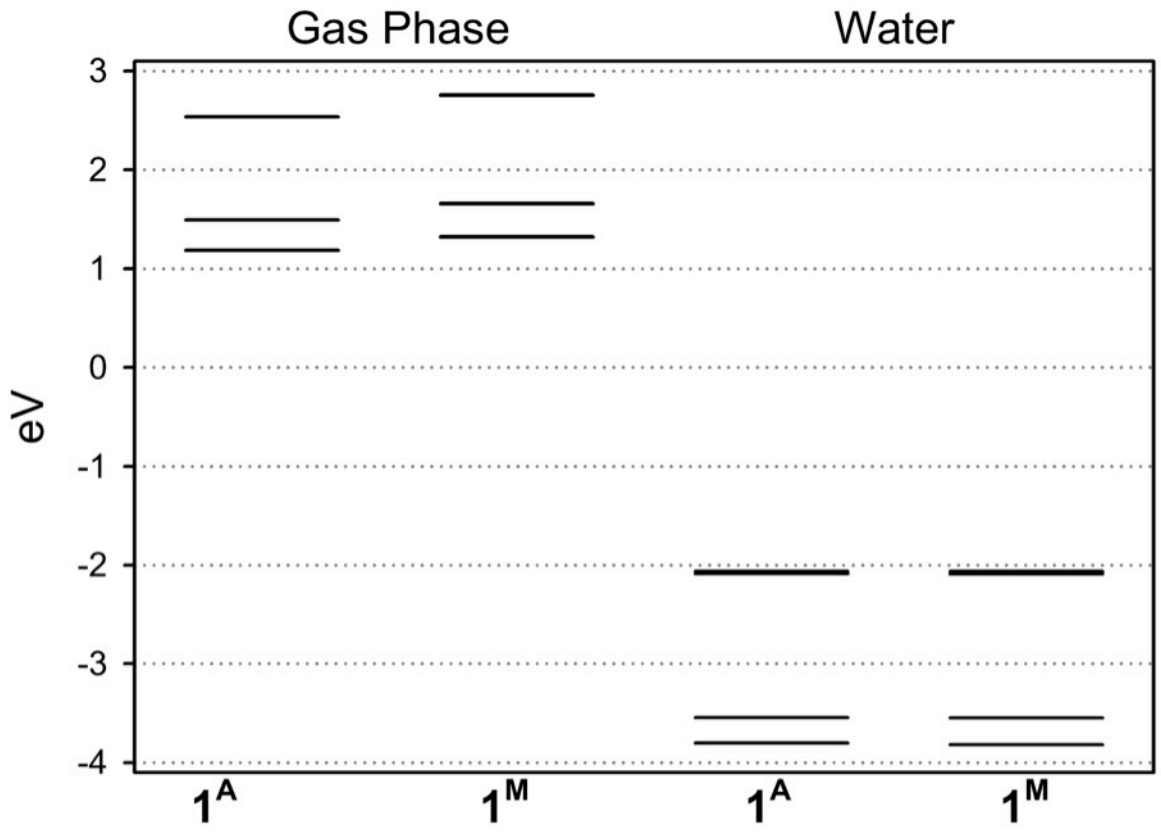

Figure 2.S31. DFT-generated energy plots of the frontier MOs of the geometry optimized structure of $\mathbf{1}^{\mathbf{A}}$ and $\mathbf{1}^{\mathbf{M}}$ in the gas phase and water. In each column, the orbitals descend in the order LUMO, HOMO, HOMO-1.

Table 2.S7. Optimized BP86/def2-TZVPP Cartesian coordinates for $\mathbf{1}^{\mathbf{A}}$.

Ni	-4.255087549	-9.090340618	-2.224383045
Ni	-7.555591472	7.012962474	-2.435868221
Ni	8.049368929	1.816204912	-2.450971931
S	-2.152895488	-8.615639048	-2.131565743
S	-4.920495419	-7.01775658	-2.492881714
S	-8.198269977	4.956642364	-2.328270046
S	-5.423379444	6.548815189	-2.657050723
S	6.581422666	0.199232483	-2.653995848
S	6.589801155	3.402066344	-2.363019485
O	-4.707555732	-13.0566288	-1.699247684
O	-4.561993799	-1.692364696	-3.299490106
O	-10.77260066	9.395466717	-2.004047063
O	-0.983880733	3.561329811	-3.367111916
O	11.7208586	3.415755677	-2.034493347
O	1.775569113	-2.163717735	-3.326667278
N	-3.810292634	-10.90421463	-1.935545792
N	-6.047997673	-9.796453851	-2.341556343
N	-3.116643012	-3.371782115	-2.786599672
N	-9.353772882	7.538902725	-2.188251513
N	-7.267616282	8.916879489	-2.573383185
N	-3.1644928	3.159234301	-2.861346395
N	2.516629936	-0.065654798	-2.855686862
N	9.554279046	0.613269653	-2.573103576
N	9.40378128	3.11329114	-2.217483747
C	-2.443910941	-11.30461842	-1.622083698
C	-1.499493689	-10.33285683	-2.311915042
C	-4.794473168	-11.82126587	-1.916118371
C	-6.103791059	-11.15459637	-2.188292193
C	-7.304005646	-11.86140978	-2.260535863
C	-8.492625223	-11.17500473	-2.502942184
C	-3.556402416	-5.795505425	-2.549068799
C	-7.20475375	-9.135443282	-2.5725817
C	-8.433995211	-9.783017519	-2.660653583
C	-3.408293789	-2.069706649	-3.056579628
C	-4.156963333	-4.4048609	-2.742525211
C	-10.38992321	6.560270463	-1.881254952
C	-10.00825293	5.247411546	-2.546713684
C	-9.655611998	8.849950109	-2.192346435
C	-8.418294586	9.646505851	-2.45194283
C	-8.428339091	11.03820613	-2.543516586
C	-7.234908289	11.72078826	-2.772713542
C	-6.112318146	9.584732563	-2.791706491
C	-6.056265152	10.971722	-2.897809821

C	-5.046810306	4.755644858	-2.680568449
C	-1.889243714	2.755681463	-3.114787337
C	-3.539193421	4.577243662	-2.845843319
C	3.931994216	-0.449774775	-2.831265194
C	4.840213622	0.769310175	-2.686291632
C	-0.261696086	0.882059244	-3.079781268
C	9.555126517	-0.723652048	-2.775697609
C	10.72831866	-1.466953954	-2.871940183
C	-1.61162444	1.267799449	-3.072267258
C	11.96627202	-0.819391624	-2.753297429
C	10.76141735	1.246298096	-2.457975513
C	11.97172679	0.558047689	-2.540295617
C	1.530029606	-0.972728089	-3.095022019
C	0.102602614	-0.468759642	-3.06327595
C	10.69007721	2.719071696	-2.215685151
C	9.074108485	4.503411164	-1.926880342
C	-2.5994065	0.276903864	-3.061037632
C	7.746793015	4.821546298	-2.597049086
C	-0.90632061	-1.44501551	-3.051788852
C	-2.258329924	-1.084893786	-3.043926082
H	-10.5547314	4.396081171	-2.112487315
H	-10.23404291	5.287155421	-3.623216047
H	-0.573448001	-2.483716221	-3.084910984
H	-2.278667317	-12.35187841	-1.930787532
H	-0.488105253	-10.37012836	-1.878716512
H	-2.288150235	-11.25587621	-0.52781707
H	-1.423048011	-10.57289972	-3.383337906
H	-7.250872699	-12.94119466	-2.117605075
H	-2.870927286	-6.044997527	-3.372099683
H	-9.444705533	-11.70497497	-2.567033778
H	-2.981279413	-5.839620739	-1.610660551
H	-7.113615771	-8.053125631	-2.689095512
H	-9.331535843	-9.193440426	-2.849491318
H	-2.175003427	-3.630551594	-2.513420725
H	-4.733872055	-4.360855794	-3.677350702
H	-4.865383361	-4.180011203	-1.92912208
H	-11.37333433	6.936895255	-2.213541152
H	-10.44625674	6.415490659	-0.785846479
H	-9.392363307	11.53414585	-2.425664072
H	-7.216154413	12.8093117	-2.85143821
H	-5.591679018	4.274679016	-3.505943984
H	-5.388772706	4.293631842	-1.740899798
H	-5.218783228	8.962956613	-2.882718898
H	-5.093295862	11.45142901	-3.075044663
H	-3.861592796	2.478331541	-2.580843053

H	-3.19656512	5.039625413	-3.782486682
H	-3.004037541	5.091336682	-2.031284912
H	4.108576495	-1.155796178	-2.003894587
H	2.274785408	0.88268768	-2.590269545
H	0.470618797	1.689250982	-3.134167606
H	4.61142385	1.311819388	-1.755330519
H	8.569940105	-1.18757189	-2.862186481
H	10.66236394	-2.542776302	-3.036553018
H	4.162287524	-0.994161669	-3.758139154
H	12.89962314	-1.380832549	-2.824517836
H	8.976111037	4.637322144	-0.833023636
H	4.695734053	1.46797082	-3.523222626
H	12.88316509	1.14623455	-2.428470552
H	-3.665429282	0.506881306	-3.099987155
H	7.282448549	5.725445678	-2.173604082
H	9.892226649	5.162857058	-2.266256763
H	7.894887415	4.984738259	-3.675405127

Table 2.S8. Optimized BP86/def2-TZVPP Cartesian coordinates for $\mathbf{1^M}$.

Ni	6.510869905	5.013389973	1.475011395
Ni	1.997449866	-9.138079217	1.813968666
Ni	-7.844914873	1.723086204	-0.160125076
S	5.185067129	3.257691472	1.351894174
S	8.22001011	4.066457532	0.545937534
S	0.761165548	-10.12213388	0.336041015
S	1.164047352	-7.122810749	1.498727334
S	-5.669525158	1.472949552	0.085320035
S	-7.721333698	3.372610751	-1.554698864
O	7.548889905	8.770929859	2.484296311
O	3.906352772	-1.843410589	0.296585355
O	-2.165560238	-3.460034883	-0.563400066
O	4.330942164	-11.91917149	3.556273903
O	-0.486017267	2.661219218	-0.583751134
O	-11.73523092	0.962513969	0.548308824
N	5.175438231	6.090025559	2.365320667
N	7.557415394	6.577429065	1.662968356
N	3.874894022	0.408777104	0.645468605
N	2.774530177	-10.81980496	2.194150965
N	-0.36255079	-4.55838943	0.294929354
N	3.18629482	-8.541522916	3.215811264
N	-2.479355004	1.591866569	-0.309685736
N	-8.254925332	0.310641572	1.093346646
N	-9.728513155	1.854626086	-0.266282245
C	3.049466121	6.640780367	3.34940203
C	3.511816905	7.914693569	3.70432518
C	3.902963817	5.764773519	2.684019577
C	4.820306148	8.259380461	3.369864349
C	5.625297932	7.334963692	2.705358937
C	7.023509642	7.647311691	2.27974775
C	8.89319143	6.673414585	1.087596546
C	9.502064476	5.279994388	1.082899083
C	5.307963893	0.50792348	0.910778361
C	5.90754835	1.833598489	0.448863953
C	3.271090076	-0.782610516	0.378147994
C	1.02749853	-11.85824276	0.901565692
C	2.455814183	-12.00185842	1.403130502
C	-1.005714041	-3.43445294	-0.127963723
C	-0.048615173	-7.022048485	0.125908432
C	-1.021996404	-5.861901655	0.315463669
C	3.695679699	-10.90507445	3.171053313
C	3.910951481	-9.555720907	3.776410936
C	4.813754118	-9.336545905	4.816158269

C	3.369753447	-7.290252866	3.692491447
C	4.991963512	-8.045242082	5.309612149
C	4.253256252	-7.005383511	4.730180055
C	1.000261082	0.382999801	0.011007766
C	1.769754122	-0.773108056	0.181757083
C	1.134960864	-2.025754431	0.146218357
C	-0.246880348	-2.127160545	-0.048659729
C	-1.000097608	-0.953578008	-0.217398424
C	-0.388740812	0.304534719	-0.18309606
C	-1.118966378	1.61647754	-0.375247986
C	-3.277687386	2.810150885	-0.423405879
C	-4.666365278	2.556362095	-1.003326303
C	-7.403876587	-0.495252365	1.766254614
C	-7.84176305	-1.466296365	2.662830666
C	-9.21565218	-1.629925602	2.882732263
C	-10.09869624	-0.807850921	2.184766196
C	-9.595668272	0.147642092	1.302651588
C	-10.48161717	1.037279117	0.491944015
C	-10.37642862	2.762833522	-1.204304812
C	-9.462955984	3.96247998	-1.400991407
H	2.032624799	6.319966305	3.575053016
H	2.859938137	8.620052757	4.222581645
H	3.579643386	4.767315516	2.379262281
H	5.262002287	9.23112647	3.59258679
H	8.821072257	7.045929077	0.048057141
H	9.496423981	7.402230428	1.657306032
H	9.847615145	5.013372717	2.09361625
H	10.36113368	5.213447722	0.3967684
H	5.497715549	0.380890924	1.990930856
H	6.990695101	1.812263884	0.639814754
H	3.324863407	1.249207505	0.802801821
H	5.781427079	-0.33671265	0.390561644
H	5.758290449	1.962241033	-0.633567634
H	0.820851657	-12.53933182	0.06096484
H	0.316420852	-12.08504474	1.710871927
H	2.606939652	-12.91213777	2.009898723
H	3.143927214	-12.06359931	0.538693289
H	0.479610471	-6.923236453	-0.834178492
H	-1.771725614	-5.847194591	-0.488359977
H	0.545467308	-4.500771537	0.748849848
H	-0.623312637	-7.959564367	0.098728961
H	-1.56283911	-5.992999639	1.268978657
H	5.353657977	-10.20499774	5.194687556
H	2.782762159	-6.508516812	3.206002597
H	5.69368226	-7.845754045	6.121318094

H	4.3588531	-5.974439177	5.067619589
H	1.438257289	1.382178777	-0.010362572
H	1.778637016	-2.901211767	0.245448326
H	-2.067146442	-1.081572841	-0.406061283
H	-3.378414588	3.285912512	0.567776607
H	-2.709046377	3.500417068	-1.062687371
H	-5.183530788	3.521584229	-1.107288151
H	-4.58495677	2.108853686	-2.005156886
H	-6.343130112	-0.341768337	1.557438174
H	-7.105096792	-2.087362019	3.172197284
H	-9.582865466	-2.387230974	3.577497051
H	-11.18302111	-0.87122057	2.280736595
H	-10.52201369	2.249499605	-2.173765021
H	-11.37571678	3.043053975	-0.826802966
H	-9.725318565	4.529503692	-2.308099595
H	-9.536914415	4.641434986	-0.537509595
H	-2.973987281	0.748867021	-0.029325764

2.7 References

(1) Ibers, J. A.; Holm, R. H., Modeling Coordination Sites in Metallobiomolecules. *Science* **1980**, *209*, 223-235.

(2) Lee, S. C.; Holm, R. H., Speculative synthetic chemistry and the nitrogenase problem. *Proc. Natl. Acad. Sci. U.S.A.* **2003**, *100*, 3595-3600.

(3) Fitzpatrick, J.; Kim, E., Synthetic Modeling Chemistry of Iron-Sulfur Clusters in Nitric Oxide Signaling. *Acc. Chem. Res.* **2015**, *48*, 2453-2461.

(4) Buchwalter, P.; Rosé, J.; Braunstein, P., Multimetallic Catalysis Based on Heterometallic Complexes and Clusters. *Chem. Rev.* **2015**, *115*, 28-126.

(5) Kanady, J. S.; Tran, R.; Stull, J. A.; Lu, L.; Stich, T. A.; Day, M. W.; Yano, J.; Britt, R. D.; Agapie, T., Role of Oxido Incorporation and Ligand Lability in Expanding Redox Accessibility of Structurally Related Mn_4 Clusters. *Chem. Sci.* **2013**, *4*, 3986-3996.

(6) Kanady, J. S.; Tsui, E. Y.; Day, M. W.; Agapie, T., A Synthetic Model of the Mn_3Ca Subsite of the Oxygen-Evolving Complex in Photosystem II. *Science* **2011**, *333*, 733-736.

(7) McWilliams, S. F.; Holland, P. L., Dinitrogen Binding and Cleavage by Multinuclear Iron Complexes. *Acc. Chem. Res.* **2015**, *48*, 2059-2065.

(8) Yano, J.; Yachandra, V., Mn_4Ca Cluster in Photosynthesis: Where and How Water is Oxidized to Dioxygen. *Chem. Rev.* **2014**, *114*, 4175-4205.

(9) Cook, S. A.; Borovik, A. S., Molecular Designs for Controlling the Local Environments around Metal Ions. *Acc. Chem. Res.* **2015**, *48*, 2407-2414.

(10) Artero, V.; Berggren, G.; Atta, M.; Caserta, G.; Roy, S.; Pecqueur, L.; Fontecave, M., From Enzyme Maturation to Synthetic Chemistry: The Case of Hydrogenases. *Acc. Chem. Res.* **2015**, *48*, 2380-2387.

(11) Manesis, A. C.; Shafaat, H. S., Electrochemical, Spectroscopic, and Density Functional Theory Characterization of Redox Activity in Nickel-Substituted Azurin: A Model for Acetyl-CoA Synthase. *Inorg. Chem.* **2015**, *54*, 7959-7967.

(12) Slater, J. W.; Shafaat, H. S., Nickel-Substituted Rubredoxin as a Minimal Enzyme Model for Hydrogenase. *J. Phys. Chem. Lett.* **2015**, *6*, 3731-3736.

(13) McLaughlin, M. P.; Retegan, M.; Bill, E.; Payne, T. M.; Shafaat, H. S.; Peña, S.; Sudhamsu, J.; Ensign, A. A.; Crane, B. R.; Neese, F.; Holland, P. L., Azurin as a Protein Scaffold for a Low-coordinate Nonheme Iron Site with a Small-molecule Binding Pocket. *J. Am. Chem. Soc.* **2012**, *134*, 19746-19757.

(14) Li, H.; Rauchfuss, T. B., Iron Carbonyl Sulfides, Formaldehyde, and Amines Condense To Give the Proposed Azadithiolate Cofactor of the Fe-Only Hydrogenases. *J. Am. Chem. Soc.* **2002**, *124*, 726-727.

(15) Esselborn, J.; Lambertz, C.; Adamska-Venkatesh, A.; Simmons, T.; Berggren, G.; Noth, J.; Siebel, J.; Hemschemeier, A.; Artero, V.; Reijerse, E.; Fontecave, M.; Lubitz, W.; Happe, T., Spontaneous activation of [FeFe]-hydrogenases by an inorganic [2Fe] active site mimic. *Nat. Chem. Biol.* **2013**, *9*, 607-609.

(16) Berggren, G.; Adamska, A.; Lambertz, C.; Simmons, T. R.; Esselborn, J.; Atta, M.; Gambarelli, S.; Mouesca, J.-M.; Reijerse, E.; Lubitz, W.; Happe, T.; Artero, V.; Fontecave, M., Biomimetic assembly and activation of [FeFe]-hydrogenases. *Nature* **2013**, *499*, 66-69.

(17) Youn, H.-D.; Youn, H.; Lee, J.-W.; Yim, Y.-I.; Lee, J. K.; Hah, Y. C.; Kang, S.-O., Unique Isozymes of Superoxide Dismutase in *Streptomyces griseus*. *Arch. Biochem. Biophys.* **1996**, *334*, 341-348.

(18) Palenik, B.; Brahamsha, B.; Larimer, F. W.; Land, M.; Hauser, L.; Chain, P.; Lamerdin, J.; Regala, W.; Allen, E. E.; McCarren, J.; Paulsen, I.; Dufresne, A.; Partensky, F.; Webb, E. A.; Waterbury, J., The genome of a motile marine *Synechococcus*. *Nature* **2003**, *424*, 1037-1042.

(19) Valentine, J. S.; Wertz, D. L.; Lyons, T. J.; Liou, L.-L.; Goto, J. J.; Gralla, E. B., The dark side of dioxygen biochemistry. *Curr. Opin. Chem. Biol.* **1998**, *2*, 253-262.

(20) Auchère, F.; Rusnak, F., What is the ultimate fate of superoxide anion in vivo? *J. Biol. Inorg. Chem.* **2002**, *7*, 664-667.

(21) Fridovich, I., Superoxide Dismutases: An Adaptation to a Paramagnetic Gas. *J. Biol. Chem.* **1989**, *264*, 7761-7764.

(22) Abreu, I. A.; Cabelli, D. E., Superoxide dismutases–a review of the metal-associated mechanistic variations. *Biochim. Biophys. Acta* **2010**, *1804*, 263-274.

(23) Uudsemaa, M.; Tamm, T., Density-Functional Theory Calculations of Aqueous Redox Potentials of Fourth-Period Transition Metals. *J. Phys. Chem. A* **2003**, *107*, 9997-10003.

(24) Youn, H.-D.; Kim, E.-J.; Roe, J.-H.; Hah, Y. C.; Kang, S.-O., A novel nickel-containing superoxide dismutase from *Streptomyces* spp. *Biochem. J.* **1996**, *318*, 889-896.

(25) Barondeau, D. P.; Kassmann, C. J.; Bruns, C. K.; Tainer, J. A.; Getzoff, E. D., Nickel Superoxide Dismutase Structure and Mechanism. *Biochemistry* **2004**, *43*, 8038-8047.

(26) Wuerges, J.; Lee, J.-W.; Yim, Y.-I.; Yim, H.-S.; Kang, S.-O.; Carugo, K. D., Crystal structure of nickel-containing superoxide dismutase reveals another type of active site. *Proc. Natl. Acad. Sci. U.S.A.* **2004**, *101*, 8569-8574.

(27) Koppenol, W. H.; Stanbury, D. M.; Bounds, P. L., Electrode potentials of partially reduced oxygen species, from dioxygen to water. *Free Radical Biol. Med.* **2010**, *49*, 317-322.

(28) Ryan, K. C.; Guce, A. I.; Johnson, O. E.; Brunold, T. C.; Cabelli, D. E.; Garman, S. C.; Maroney, M. J., Nickel Superoxide Dismutase: Structural and Functional Roles of His1 and Its H-Bonding Network. *Biochemistry* **2015**, *54*, 1016-1027.

(29) Ryan, K. C.; Johnson, O. E.; Cabelli, D. E.; Brunold, T. C.; Maroney, M. J., Nickel superoxide dismutase: structural and functional roles of Cys2 and Cys6. *J. Biol. Inorg. Chem.* **2010**, *15*, 795-807.

(30) Herbst, R. W.; Guce, A.; Bryngelson, P. A.; Higgins, K. A.; Ryan, K. C.; Cabelli, D. E.; Garman, S. C.; Maroney, M. J., Role of Conserved Tyrosine Residues in NiSOD Catalysis: A Case of Convergent Evolution. *Biochemistry* **2009**, *48*, 3354-3369.

(31) Lin, I.-J.; Gebel, E. B.; Machonkin, T. E.; Westler, W. M.; Markley, J. L., Changes in hydrogen-bond strengths explain reduction potentials in 10 rubredoxin variants. *Proc. Natl. Acad. Sci. U.S.A.* **2005**, *102*, 14581-14586.

(32) Dey, A.; Okamura, T.-a.; Ueyama, N.; Hedman, B.; Hodgson, K. O.; Solomon, E. I., Sulfur K-edge XAS and DFT calculations on P450 model complexes: Effects of hydrogen bonding on electronic structure and redox potentials. *J. Am. Chem. Soc.* **2005**, *127*, 12046-12053.

(33) Clay, M. D.; Jenney, F. E., Jr.; Hagedoorn, P. L.; George, G. N.; Adams, M. W. W.; Johnson, M. K., Spectroscopic Studies of *Pyrococcus furiosus* Superoxide Reductase: Implications for Active-Site Structures and the Catalytic Mechanism. *J. Am. Chem. Soc.* **2002**, *124*, 788-805.

(34) Kovacs, J. A.; Brines, L. M., Understanding How the Thiolate Sulfur Contributes to the Function of the Non-Heme Iron Enzyme Superoxide Reductase. *Acc. Chem. Res.* **2007**, *40*, 501-509.

(35) Tremey, E.; Bonnot, F.; Moreau, Y.; Berthomieu, C.; Desbois, A.; Favaudon, V.; Blondin, G.; Houée-Levin, C.; Nivière, V., Hydrogen bonding to the cysteine ligand of superoxide reductase: acid-base control of the reaction intermediates. *J. Biol. Inorg. Chem.* **2013**, *18*, 815-830.

(36) Clay, M. D.; Emerson, J. P.; Coulter, E. D.; Kurtz, D. M., Jr.; Johnson, M. K., Spectroscopic characterization of the [Fe(His)$_4$(Cys)] site in 2Fe-superoxide reductase from *Desulfovibrio vulgaris*. *J. Biol. Inorg. Chem.* **2003**, *8*, 671-682.

(37) Gale, E. M.; Patra, A. K.; Harrop, T. C., Versatile Methodology Toward NiN_2S_2 Complexes as Nickel Superoxide Dismutase Models: Structure and Proton Affinity. *Inorg. Chem.* **2009**, *48*, 5620-5622.

(38) Gale, E. M.; Simmonett, A. C.; Telser, J.; Schaefer, H. F., III; Harrop, T. C., Toward Functional Ni-SOD Biomimetics: Achieving a Structural/Electronic Correlation with Redox Dynamics. *Inorg. Chem.* **2011**, *50*, 9216-9218.

(39) Gale, E. M.; Narendrapurapu, B. S.; Simmonett, A. C.; Schaefer, H. F., III; Harrop, T. C., Exploring the Effects of H-Bonding in Synthetic Analogues of Nickel Superoxide Dismutase (Ni-SOD): Experimental and Theoretical Implications for Protection of the Ni-SCys Bond. *Inorg. Chem.* **2010**, *49*, 7080-7096.

(40) Gale, E. M.; Cowart, D. M.; Scott, R. A.; Harrop, T. C., Dipeptide-Based Models of Nickel Superoxide Dismutase: Solvent Effects Highlight a Critical Role to Ni–S Bonding and Active Site Stabilization. *Inorg. Chem.* **2011**, *50*, 10460-10471.

(41) Broering, E. P.; Dillon, S.; Gale, E. M.; Steiner, R. A.; Telser, J.; Brunold, T. C.; Harrop, T. C., Accessing Ni(III)-Thiolate Versus Ni(II)-Thiyl Bonding in a Family of Ni-N_2S_2 Synthetic Models of NiSOD. *Inorg. Chem.* **2015**, *54*, 3815-3828.

(42) Neupane, K. P.; Gearty, K.; Francis, A.; Shearer, J., Probing Variable Axial Ligation in Nickel Superoxide Dismutase Utilizing Metallopeptide-Based Models: Insight into the Superoxide Disproportionation Mechanism. *J. Am. Chem. Soc.* **2007**, *129*, 14605–14618.

(43) Nakane, D.; Wasada-Tsutsui, Y.; Funahashi, Y.; Hatanaka, T.; Ozawa, T.; Masuda, H., A Novel Square-Planar Ni(II) Complex with an Amino-Carboxamido-Dithiolato-Type Ligand as an Active-Site Model of NiSOD. *Inorg. Chem.* **2014**, *53*, 6512-6523.

(44) Jenkins, R. M.; Singleton, M. L.; Almaraz, E.; Reibenspies, J. H.; Darensbourg, M. Y., Imidazole-Containing (N_3S)-Ni^{II} Complexes Relating to Nickel Containing Biomolecules. *Inorg. Chem.* **2009**, *48*, 7280-7293.

(45) Mullins, C. S.; Grapperhaus, C. A.; Frye, B. C.; Wood, L. H.; Hay, A. J.; Buchanan, R. M.; Mashuta, M. S., Synthesis and Sulfur Oxygenation of a (N_3S)Ni Complex Related to Nickel-Containing Superoxide Dismutase. *Inorg. Chem.* **2009**, *48*, 9974-9976.

(46) Herdt, D. R.; Grapperhaus, C. A., Kinetic study of nickel-thiolate oxygenation by hydrogen peroxide. Implications for nickel-containing superoxide dismutase. *Dalton Trans.* **2012**, *41*, 364-366.

(47) Shearer, J.; Zhao, N., $[Me_4N](Ni^{II}(BEAAM))$: A Synthetic Model for Nickel Superoxide Dismutase That Contains Ni in a Mixed Amine/Amide Coordination Environment. *Inorg. Chem.* **2006**, *45*, 9637-9639.

(48) Mathrubootham, V.; Thomas, J.; Staples, R.; McCraken, J.; Shearer, J.; Hegg, E. L., Bisamidate and Mixed Amine/Amidate NiN_2S_2 Complexes as Models for Nickel-Containing Acetyl Coenzyme A Synthase and Superoxide Dismutase: An Experimental and Computational Study. *Inorg. Chem.* **2010**, *49*, 5393-5406.

(49) Ma, H.; Chattopadhyay, S.; Petersen, J. L.; Jensen, M. P., Harnessing Scorpionate Ligand Equilibria for Modeling Reduced Nickel Superoxide Dismutase Intermediates. *Inorg. Chem.* **2008**, *47*, 7966-7968.

(50) Ma, H.; Wang, G.; Yee, G. T.; Petersen, J. L.; Jensen, M. P., Scorpionate-supported models of nickel-dependent superoxide dismutase. *Inorg. Chim. Acta* **2009**, *362*, 4563-4569.

(51) Lee, W.-Z.; Chiang, C.-W.; Lin, T.-H.; Kuo, T.-S., A Discrete Five-Coordinate Ni^{III} Complex Resembling the Active Site of the Oxidized Form of Nickel Superoxide Dismutase. *Chem. –Eur. J.* **2012**, *18*, 50-53.

(52) Nakane, D.; Funahashi, Y.; Ozawa, T.; Masuda, H., A Square-planar Ni(II) Complex with an Asymmetric N_2S_2 Donor Set as a Model for the Active Site of Nickel-containing SOD: Structural Conversion Driven by Addition of a Strong Donor Ligand in the High Oxidation State. *Chem. Lett.* **2010**, *39*, 344-346.

(53) Shearer, J., Insight into the Structure and Mechanism of Nickel-Containing Superoxide Dismutase Derived from Peptide-Based Mimics. *Acc. Chem. Res.* **2014**, *47*, 2332-2341 and references therein.

(54) Glass, A. M.; Krause, M. E.; Laurence, J. S.; Jackson, T. A., Controlling the Chiral Inversion Reaction of the Metallopeptide Ni-Asparagine-Cysteine-Cysteine with Dioxygen. *Inorg. Chem.* **2012**, *51*, 10055-10063.

(55) Krause, M. E.; Glass, A. M.; Jackson, T. A.; Laurence, J. S., Novel Tripeptide Model of Nickel Superoxide Dismutase. *Inorg. Chem.* **2010**, *49*, 362-364.

(56) Krause, M. E.; Glass, A. M.; Jackson, T. A.; Laurence, J. S., MAPping the Chiral Inversion and Structural Transformation of a Metal-Tripeptide Complex Having Ni-Superoxide Dismutase Activity. *Inorg. Chem.* **2011**, *50*, 2479-2487.

(57) Krause, M. E.; Glass, A. M.; Jackson, T. A.; Laurence, J. S., Embedding the Ni-SOD Mimetic Ni-NCC within a Polypeptide Sequence Alters the Specificity of the Reaction Pathway. *Inorg. Chem.* **2013**, *52*, 77-83.

(58) Mullins, C. S.; Grapperhaus, C. A.; Kozlowski, P. M., Density functional theory investigations of NiN_2S_2 reactivity as a function of nitrogen donor type and N-H···S hydrogen bonding inspired by nickel-containing superoxide dismutase. *J. Biol. Inorg. Chem.* **2006**, *11*, 617-625.

(59) Smith, J. N.; Hoffman, J. T.; Shirin, Z.; Carrano, C. J., H-bonding Interactions and Control of Thiolate Nucleophilicity and Specificity in Model Complexes of Zinc Metalloproteins. *Inorg. Chem.* **2005**, *44*, 2012-2017.

(60) McGuire, D. G.; Khan, M. A.; Ashby, M. T., Discontinuum between a Thiolate and a Thiol Ligand. *Inorg. Chem.* **2002**, *41*, 2202-2208.

(61) Cantekin, S.; de Greef, T. F. A.; Palmans, A. R. A., Benzene-1,3,5-tricarboxamide: a versatile ordering moiety for supramolecular chemistry. *Chem. Soc. Rev.* **2012**, *41*, 6125-6137.

(62) Lightfoot, M. P.; Mair, F. S.; Pritchard, R. G.; Warren, J. E., New supramolecular packing motifs: π -stacked rods encased in triply-helical hydrogen bonded amide strands. *Chem. Commun.*, **1999**, 1945-1946.

(63) Arunachalam, M.; Ghosh, P., A Versatile Tripodal Amide Receptor for the Encapsulation of Anions or Hydrated Anions via Formation of Dimeric Capsules. *Inorg. Chem.* **2010**, *49*, 943-951.

(64) Stals, P. J. M.; Haveman, J. F.; Palmans, A. R. A.; Schenning, A. P. H. J., The Self-Assembly Properties of a Benzene-1,3,5-tricarboxamide Derivative. *J. Chem. Educ.* **2009**, *86*, 230-233.

(65) van Hameren, R.; Schön, P.; van Buul, A. M.; Hoogboom, J.; Lazarenko, S. V.; Gerritsen, J. W.; Engelkamp, H.; Christianen, P. C. M.; Heus, H. A.; Maan, J. C.; Rasing, T.; Speller, S.; Rowan, A. E.; Elemans, J. A. A. W.; Nolte, R. J. M., Macroscopic Hierarchical Surface Patterning of Porphyrin Trimers via Self-Assembly and Dewetting. *Science* **2006**, *314*, 1433-1436.

(66) dos Santos, C. M. G.; Boyle, E. M.; De Solis, S.; Kruger, P. E.; Gunnlaugsson, T., Selective and tuneable recognition of anions using C_{3V}-symmetrical tripodal urea-amide receptor platforms. *Chem. Commun.* **2011**, *47*, 12176-12178.

(67) In some cases, **1** was treated with 18-crown-6 ether (18C6) to encapsulate the Na^+ counterion, $(18C6)_3 \cdot \mathbf{1}$, which affords additional solubility in solvents such as MeCN and CH_2Cl_2.

(68) Krüger, H.-J.; Peng, G.; Holm, R. H., Low-Potential Nickel(III,II) Complexes: New Systems Based on Tetradentate Amidate-Thiolate Ligands and the Influence of Ligand Structure on Potentials in Relation to the Nickel Site in [NiFe]-Hydrogenases. *Inorg. Chem.* **1991**, *30*, 734-742.

(69) Harrop, T. C.; Mascharak, P. K., Structural and spectroscopic models of the A-cluster of acetyl coenzyme a synthase/carbon monoxide dehydrogenase: Nature's Monsanto acetic acid catalyst. *Coord. Chem. Rev.* **2005**, *249*, 3007-3024.

(70) Colpas, G. J.; Maroney, M. J.; Bagyinka, C.; Kumar, M.; Willis, W. S.; Suib, S. L.; Baidya, N.; Mascharak, P. K., X-Ray Spectroscopic Studies of Nickel-Complexes, with Application to the Structure of Nickel Sites in Hydrogenases. *Inorg. Chem.* **1991**, *30*, 920-928.

(71) Higgins, K. A.; Chivers, P. T.; Maroney, M. J., Role of the N-terminus in Determining Metal-Specific Responses in the *E. coli* Ni- and Co-Responsive Metalloregulator, RcnR. *J. Am. Chem. Soc.* **2012**, *134*, 7081-7093.

(72) Clark-Baldwin, K.; Tierney, D. L.; Govindaswamy, N.; Gruff, E. S.; Kim, C.; Berg, J.; Koch, S. A.; Penner-Hahn, J. E., The Limitations of X-ray Absorption Spectroscopy for Determining the Structure of Zinc Sites in Proteins. When Is a Tetrathiolate Not a Tetrathiolate? *J. Am. Chem. Soc.* **1998**, *120*, 8401-8409.

(73) Kato, M.; Okamura, T.-a.; Yamamoto, H.; Ueyama, N., Effects of the Intramolecular NH···S Hydrogen Bond in Mononuclear Platinum(II) and Palladium(II) Complexes with 2,2'-Bipyridine and Benzenethiol Derivatives. *Inorg. Chem.* **2005**, *44*, 1966-1972.

(74) Ueyama, N.; Yamada, Y.; Okamura, T.-a.; Kimura, S.; Nakamura, A., Structure and Properties of $[Fe_4S_4\{2,6\text{-bis(acylamino)benzenethiolato-}S\}_4]^{2-}$ and $[Fe_2S_2\{2,6\text{-bis(acylamino)benzenethiolato-}S\}_4]^{2-}$: Protection of the Fe–S Bond by Double NH···S Hydrogen Bonds. *Inorg. Chem.* **1996**, *35*, 6473-6484.

(75) Huang, J.; Ostrander, R. L.; Rheingold, A. L.; Leung, Y.; Walters, M. A., Hydrogen-Bonding and Polar Group Effects on Redox Potentials in $Mo[HB(Me_2pz)_3](NO)(SR)_2$. *J. Am. Chem. Soc.* **1994**, *116*, 6769-6776.

(76) Huang, J.; Ostrander, R. L.; Rheingold, A. L.; Walters, M. A., Synthesis and Electrochemistry of $Mo[BH(Me_2pz)_3](NO)[S(CH_2)_2CONH(CH_2)_2S]$ as a Probe of the Effects of N–H···S Hydrogen Bonding on Redox Potentials. *Inorg. Chem.* **1995**, *34*, 1090-1093.

(77) Walters, M. A.; Dewan, J. C.; Min, C.; Pinto, S., Models of Amide–Cysteine Hydrogen Bonding in Rubredoxin: Hydrogen Bonding between Amide and Benzenethiolate in $[(CH_3)_3NCH_2CONH_2]_2[Co(SC_6H_5)_4]\cdot\frac{1}{2}CH_3CN$ and $[(CH_3)_3NCH_2CONH_2][SC_6H_5]$. *Inorg. Chem.* **1991**, *30*, 2656-2662.

(78) Walters, M. A.; Roche, C. L.; Rheingold, A. L.; Kassel, S. W., N–H···S Hydrogen Bonds in a Ferredoxin Model. *Inorg. Chem.* **2005**, *44*, 3777-3779.

(79) Dey, A.; Green, K. N.; Jenkins, R. M.; Jeffrey, S. P.; Darensbourg, M.; Hodgson, K. O.; Hedman, B.; Solomon, E. I., S K-Edge XAS and DFT Calculations on Square-Planar Ni^{II}-Thiolate Complexes: Effects of Active and Passive H-bonding. *Inorg. Chem.* **2007**, *46*, 9655-9660.

(80) Steiner, T., The Hydrogen Bond in the Solid State. *Angew. Chem., Int. Ed.* **2002**, *41*, 48-76.

(81) Liquid IR measurements were made on $Tr\text{-}S_3BTA^{alk}$ due to lack of solubility of $H_3S_3BTA^{alk}$ in organic solvents.

(82) Desmarchelier, A.; Caumes, X.; Raynal, M.; Vidal-Ferran, A.; van Leeuwen, P. W. N. M.; Bouteiller, L., Correlation between the Selectivity and the Structure of an Asymmetric Catalyst Built on a Chirally Amplified Supramolecular Helical Scaffold. *J. Am. Chem. Soc.* **2016**, *138*, 4908-4916.

(83) Zhang, W.; Horoszewski, D.; Decatur, J.; Nuckolls, C., A Folded, Secondary Structure in Step-Growth Oligomers from Covalently Linked, Crowded Aromatics. *J. Am. Chem. Soc.* **2003**, *125*, 4870-4873.

(84) Berrocal, J. A.; Di Meo, F.; García-Iglesias, M.; Gosens, R. P. J.; Meijer, E. W.; Linares, M.; Palmans, A. R. A., Consequences of conformational flexibility in hydrogen-bond-driven self-assembly processes. *Chem. Commun.* **2016**, *52*, 10870-10873.

(85) Chattopadhyay, S.; Deb, T.; Ma, H.; Petersen, J. L.; Young, V. G., Jr.; Jensen, M. P., Arylthiolate Coordination and Reactivity at Pseudotetrahedral Nickel(II) Centers: Modulation by Noncovalent Interactions. *Inorg. Chem.* **2008**, *47*, 3384-3392.

(86) Frydendahl, H.; Toftlund, H.; Becher, J.; Dutton, J. C.; Murray, K. S.; Taylor, L. F.; Anderson, O. P.; Tiekink, E. R. T., Changes in Geometries and Spin States of Thiolato-Schiff Base NiN_2S_2 Complexes Containing *N*,*N*'-Biphenyl Backbones. *Inorg. Chem.* **1995**, *34*, 4467-4476.

(87) Goswami, N.; Eichhorn, D. M., A New Method for Incorporating Thiolate Donors into a Metal Coordination Sphere. Synthesis and Crystal Structures of the First Nickel Complexes of an N_3S Ligand. *Inorg. Chem.* **1999**, *38*, 4329-4333.

(88) Martin, E. M.; Bereman, R. D.; Dorfman, J., An investigation into the electronic and structural properties of nickel complexes of tetradentate N_2S_2 ligands. *Inorg. Chim. Acta* **1990**, *176*, 247-254.

(89) The concentration-independent ratios of $\mathbf{1^M/1^A}$ in MeCN are in agreement with IR data (red-shift of ν_{CO} of **1** from free ligand suggests a disruption in the H-bonding of the carbonyl moiety by MeCN, a H-bond acceptor).

(90) Breaking up $\mathbf{1^A}$ with salts such as NaCl, $MgSO_4$, $^n Bu_4NPF_6$ has been unsuccessful. Addition of polyhydric alcohols (50% v/v ethylene glycol, 10% v/v glycerol) or urea, reagents with multiple H-bonding sites, partially disrupts $\mathbf{1^A}$ based on UV-vis and confirms the speciation model, but does not completely push the equilibrium towards $\mathbf{1^M}$.

(91) Palmans, A. R. A.; Vekemans, J. A. J. M.; Havinga, E. E.; Meijer, E. W., Sergeants-and-Soldiers Principle in Chiral Columnar Stacks of Disc-Shaped Molecules with C_3 Symmetry. *Angew. Chem., Int. Ed.* **1997**, *36*, 2648-2651.

(92) Brunsveld, L.; Schenning, A. P. H. J.; Broeren, M. A. C.; Janssen, H. M.; Vekemans, J. A. J. M.; Meijer, E. W., Chiral Amplification in Columns of Self-Assembled *N*,*N*',*N*''-Tris((*S*)-3,7-dimethyloctyl)benzene-1,3,5-tricarboxamide in Dilute Solution. *Chem. Lett.* **2000**, 292-293.

(93) Stenson, P. A.; Board, A.; Marin-Becerra, A.; Blake, A. J.; Davies, E. S.; Wilson, C.; McMaster, J.; Schröder, M., Molecular and Electronic Structures of One-Electron Oxidized Ni^{II}–(Dithiosalicylidenediamine) Complexes: Ni^{III}–Thiolate versus Ni^{II}-Thiyl Radical States. *Chem. –Eur. J.* **2008**, *14*, 2564-2576.

(94) Carter, C. W., Jr., New Stereochemical Analogies between Iron-Sulfur Electron-Transport Proteins. *J. Biol. Chem.* **1977**, *252*, 7802-7811.

(95) Adman, E.; Watenpaugh, K. D.; Jensen, L. H., NH··· S Hydrogen-Bonds in *Peptococcus aerogenes* ferredoxin, *Clostridium pasteurianum* rubredoxin, and *Chromatium* high potential iron protein. *Proc. Natl. Acad. Sci. U.S.A.* **1975**, *72*, 4854-4858.

(96) Roos, G.; Foloppe, N.; Messens, J., Understanding the pK_a of Redox Cysteines: The Key Role of Hydrogen Bonding. *Antioxid. Redox Signaling* **2013**, *18*, 94-127.

(97) Fiedler, A. T.; Bryngelson, P. A.; Maroney, M. J.; Brunold, T. C., Spectroscopic and Computational Studies of Ni Superoxide Dismutase: Electronic Structure Contributions to Enzymatic Function. *J. Am. Chem. Soc.* **2005**, *127*, 5449-5462.

(98) Choudhury, S. B.; Lee, J.-W.; Davidson, G.; Yim, Y.-I.; Bose, K.; Sharma, M. L.; Kang, S.-O.; Cabelli, D. E.; Maroney, M. J., Examination of the Nickel Site Structure and Reaction Mechanism in *Streptomyces seoulensis* Superoxide Dismutase. *Biochemistry* **1999**, *38*, 3744-3752.

(99) Smith, J. N.; Shirin, Z.; Carrano, C. J., Control of Thiolate Nucleophilicity and Specificity in Zinc Metalloproteins by Hydrogen Bonding: Lessons from Model Compound Studies. *J. Am. Chem. Soc.* **2003**, *125*, 868-869.

(100) Chiou, S.-J.; Riordan, C. G.; Rheingold, A. L., Synthetic modeling of zinc thiolates: Quantitative assessment of hydrogen bonding in modulating sulfur alkylation rates. *Proc. Natl. Acad. Sci. U.S.A.* **2003**, *100*, 3695-3700.

(101) Fox, D. C.; Fiedler, A. T.; Halfen, H. L.; Brunold, T. C.; Halfen, J. A., Electronic Structure Control of the Nucleophilicity of Transition Metal–Thiolate Complexes: An Experimental and Theoretical Study. *J. Am. Chem. Soc.* **2004**, *126*, 7627-7638.

(102) Quaranta, M.; Murkovic, M.; Klimant, I., A new method to measure oxygen solubility in organic solvents through optical oxygen sensing. *Analyst* **2013**, *138*, 6243-6245.

(103) Buonomo, R. M.; Font, I.; Maguire, M. J.; Reibenspies, J. H.; Tuntulani, T.; Darensbourg, M. Y., Study of Sulfinate and Sulfenate Complexes Derived from the Oxygenation of Thiolate Sulfur in [1,5-Bis(2-mercapto-2-methylpropyl)-1,5-diazacyclooctanato(2–)]nickel(II). *J. Am. Chem. Soc.* **1995**, *117*, 963-973.

(104) Farmer, P. J.; Solouki, T.; Mills, D. K.; Soma, T.; Russell, D. H.; Reibenspies, J. H.; Darensbourg, M. Y., Isotopic Labeling Investigation of the Oxygenation of Nickel-Bound Thiolates by Molecular-Oxygen. *J. Am. Chem. Soc.* **1992**, *114*, 4601-4605.

(105) Mirza, S. A.; Pressler, M. A.; Kumar, M.; Day, R. O.; Maroney, M. J., Oxidation of Nickel Thiolate Ligands by Dioxygen. *Inorg. Chem.* **1993**, *32*, 977-987.

(106) Maroney, M. J.; Choudhury, S. B.; Bryngelson, P. A.; Mirza, S. A.; Sherrod, M. J., Theoretical Study of the Oxidation of Nickel Thiolate Complexes by O_2. *Inorg. Chem.* **1996**, *35*, 1073-1076.

(107) Tabbì, G.; Driessen, W. L.; Reedijk, J.; Bonomo, R. P.; Veldman, N.; Spek, A. L., High Superoxide Dismutase Activity of a Novel, Intramolecularly Imidazolato-Bridged Asymmetric Dicopper(II) Species. Design, Synthesis, Structure, and Magnetism of Copper(II) Complexes with a Mixed Pyrazole–Imidazole Donor Set. *Inorg. Chem.* **1997**, *36*, 1168-1175.

(108) Beauchamp, C.; Fridovich, I., Superoxide Dismutase: Improved Assays and an Assay Applicable to Acrylamide Gels. *Anal. Biochem.* **1971**, *44*, 276-287.

(109) Ueda, J.-i.; Ozawa, T.; Miyazaki, M.; Fujiwara, Y., SOD-like activity of complexes of nickel(II) ion with some biologically important peptides and their novel reactions with hydrogen peroxide. *Inorg. Chim. Acta* **1993**, *214*, 29-32.

(110) Fujita, K.; Schenker, R.; Gu, W.; Brunold, T. C.; Cramer, S. P.; Riordan, C. G., A Monomeric Nickel–Dioxygen Adduct Derived from a Nickel(I) Complex, and O_2. *Inorg. Chem.* **2004**, *43*, 3324-3326.

(111) Yao, S.; Bill, E.; Milsmann, C.; Wieghardt, K.; Driess, M., A "Side-on" Superoxonickel Complex [LNi(O_2)] with a Square-Planar Tetracoordinate Nickel(II) Center and Its Conversion into [LNi(μ-OH)$_2$NiL]. *Angew. Chem., Int. Ed.* **2008**, *47*, 7110-7113.

(112) Fukuzumi, S.; Ohkubo, K., Quantitative Evaluation of Lewis Acidity of Metal Ions Derived from the *g* Values of ESR Spectra of Superoxide: Metal Ion Complexes in Relation to the Promoting Effects in Electron Transfer Reactions. *Chem. Eur. J.* **2000**, *6*, 4532-4535.

(113) The synthesis of $[Ni^{II}(nmp)(O_2^{\bullet-})]^-$ as its $[K(18C6)]^+$ salt was attempted; however, the characterization pointed to mixed products including weak signals in the ^{1}H NMR spectrum and no definitive peaks in the ESI-MS. The product(s) was EPR-silent likely due to bridging interactions. A single peak in the FTIR was observed at 1106 cm^{-1} (KBr pellet) that we tentatively assign as ν_{OO}. This value would be consistent with a terminally bound superoxide (Vaska, L., Dioxygen-Metal Complexes – Toward a Unified View. *Acc. Chem. Res.* **1976**, *9*, 175-183). Unfortunately, the lack of commercial suppliers of ^{18}O-labeled KO_2, and a preparation (Rosenthal, I., The synthesis of ^{18}O-enriched KO_2. *J. Labelled Comp. Radiopharm.* **1976**, *12*, 317-318) that has resulted in explosions (Shearer, J.; Scarrow, R. C.; Kovacs, J. A., Synthetic Models for the Cysteinate-Ligated Non-Heme Iron Enzyme Superoxide Reductase: Observation and Structural Characterization by XAS of an Fe^{III}–OOH Intermediate. *J. Am. Chem. Soc.* **2002**, *124*, 11709-11717), have prevented us from synthesizing the isotopologue. Furthermore, the UV-vis spectrum of the product in the presence of $[S_3BTA^{alk}]^{3-}$ resembled what was observed in the reaction of $\mathbf{1^M}$ with 100 equiv KO_2. Indeed, the isolation/characterization of such a metal-superoxo

species, especially containing thiolate ligands, is novel and will require more dedicated efforts that are beyond the scope of the present work.

(114) While the models $\mathbf{1^A}$ and $\mathbf{1^M}$ have been simplified to ease the calculations, $\mathbf{1^A}$ is truly only one 'layer' of the aggregated stack and there is some inherent energy or thermodynamic driving force upon stacking that is missing in this model. Complex $\mathbf{1^M}$ is also simplified, as the intramolecular H-bonding interactions are oriented upwards; it is feasible that the 'arms' may orient above or below the plane in a variety of combinations and is thus admittedly not all-encompasing.

(115) Perdew, J. P.; Levy, M., Comment on "Significance of the highest occupied Kohn-Sham eigenvalue". *Phys. Rev. B* **1997**, *56*, 16021-16028.

(116) van Hameren, R.; van Buul, A. M.; Castriciano, M. A.; Villari, V.; Micali, N.; Schön, P.; Speller, S.; Scolaro, L. M.; Rowan, A. E.; Elemans, J. A. A. W.; Nolte, R. J. M., Supramolecular Porphyrin Polymers in Solution and at the Solid–Liquid Interface. *Nano Lett.* **2008**, *8*, 253-259.

(117) Friggeri, A.; van der Pol, C.; van Bommel, K. J. C.; Heeres, A.; Stuart, M. C. A.; Feringa, B. L.; van Esch, J., Cyclohexane-Based Low Molecular Weight Hydrogelators: A Chirality Investigation. *Chem. –Eur. J.* **2005**, *11*, 5353-5361.

(118) Sheng, Y.; Abreu, I. A.; Cabelli, D. E.; Maroney, M. J.; Miller, A.-F.; Teixeira, M.; Valentine, J. S., Superoxide Dismutases and Superoxide Reductases. *Chem. Rev.* **2014**, *114*, 3854-3918.

(119) O'Reilly, J. E., Oxidation-reduction potential of ferro-ferricyanide system in buffer solutions. *Biochim. Biophys. Acta* **1973**, *292*, 509-515.

(120) Fulmer, G. R.; Miller, A. J. M.; Sherden, N. H.; Gottlieb, H. E.; Nudelman, A.; Stoltz, B. M.; Bercaw, J. E.; Goldberg, K. I., NMR Chemical Shifts of Trace Impurities: Common Laboratory Solvents, Organics, and Gases in Deuterated Solvents Relevant to the Organometallic Chemist. *Organometallics* **2010**, *29*, 2176-2179.

(121) George, G. N.; George, S. J.; Pickering, I. J. *EXAFSPAK, Stanford Synchotron Radiation Lightsource, Menlo Park, CA.* http://www-ssrl.slac.stanford.edu/~george/exafspak/exafs.htm. *2001.*, EXAFSPAK, Stanford Synchotron Radiation Lightsource, Menlo Park, CA. http://www-ssrl.slac.stanford.edu/~george/exafspak/exafs.htm. 2001.

(122) Rehr, J. J.; Ankudinov, A. L., Progress and challenges in the theory and interpretation of X-ray spectra. *J. Synchrotron Radiat.* **2001**, *8*, 61-65.

(123) Riggs-Gelasco, P. J.; Stemmler, T. L.; Penner-Hahn, J. E., XAFS of dinuclear metal sites in proteins and model compounds. *Coord. Chem. Rev.* **1995**, *144*, 245-286.

(124) Bencze, K. Z.; Kondapalli, K. C.; Stemmler, T. L., *X-Ray Absorption Spectroscopy In Applications of Physical Methods in Inorganic and Bioinorganic Chemistry: Handbook, Encyclopedia of Inorganic Chemistry*. 2nd ed.; John Wiley & Sons, LTD: Chichester, UK, 2007.

(125) Cotelesage, J. J. H.; Pushie, M. J.; Grochulski, P.; Pickering, I. J.; George, G. N., Metalloprotein active site structure determination: Synergy between X-ray absorption spectroscopy and X-ray crystallography. *J. Inorg. Biochem.* **2012**, *115*, 127-137.

(126) Cohen, A. J.; Handy, N. C., Dynamic correlation. *Mol. Phys.* **2001**, *99*, 607-615.

(127) Lee, C.; Yang, W.; Parr, R. G., Development of the Colle-Salvetti correlation-energy formula into a functional of the electron density. *Phys. Rev. B* **1988**, *37*, 785-789.

(128) Weigend, F.; Ahlrichs, R., Balanced basis sets of split valence, triple zeta valence and quadruple zeta valence quality for H to Rn: Design and assessment of accuracy. *Phys. Chem. Chem. Phys.* **2005**, *7*, 3297-3305.

(129) Neese, F., *ORCA - an ab initio, Density Functional and Semiempirical Program Package, version 3.0.3*. University of Bonn: Bonn, Germany.

CHAPTER 3

SYNTHESIS OF A NISOD MODEL WITH A FLEXIBLE AXIAL N-LIGAND[1]

[1] Steiner, R. A. and T. C. Harrop. To be submitted to *Inorganic Chemistry*.

3.1 Abstract

Structural features of the reduced form of NiSOD has been modeled with an asymmetric $N_2S^{Me}S$ thioether ligand (*N*-(2-mercaptoethyl)-2-((2-methylthio)ethyl)amino)acetamide) ($N_2S^{Me}SH_2$, where H represents dissociable protons). This ligand has been designed as a model of potential involvement of Cys6 in NiSOD for H^+ storage between SOD half reactions. Reaction of the $N_2S^{Me}S$ with Ni(II) results in an equilibrium mixture between a monometallic complex (**1**) and dimeric complex (**[1]$_2$**) with a labile thioether ligand based on spectroscopic and structural studies. In addition to a thioether analogue of NiSOD, we have designed and synthesized a ligand poised for coordination to Ni via five donor ligands (N_3S_2); isolation of a square-pyramidal NiN_3S_2 species has remained elusive for structurally-accurate, low-MW models of NiSOD. To address this paucity of five-coordinate (5C) NiN_3S_2 species in the literature, a five-coordinate planar ligand, *N*-(2-mercaptoethyl)-2-((2-mercaptoethyl)(2-(pyridin-2-yl)ethyl)amino)acetamide and its corresponding Ni(II) complex (**2**) have been synthesized. Methylation of **2** and electrochemical characterization results in the expected cathodic shift (–0.739 V to –0.278 V) after S-modification.

3.2 Introduction

Superoxide dismutases (SODs) are metalloenzymes that disproportionate superoxide ($O_2^{\bullet-}$) into hydrogen peroxide (H_2O_2) and molecular oxygen (O_2) via alternate oxidation and reduction of their metal cofactors.[1-3] The most recently discovered SOD, namely NiSOD, has been isolated from *Streptomyces* soil bacteria and contains Ni(III/II) housed in an unusual N/S ligand set.[2,3] This coordination sphere has prompted several investigations into the properties imparted by these donor atoms to favor Ni-based redox and Cys-S oxidative-stability.[4,5] One potential defense against unwanted S-oxygenation/oxidation is through protonation of the

coordinated Cys-S to result in a Ni-coordinated thiol.[6,7] Studies show that modification of one S results in inactivation of the remaining S. Additionally, modification of the anionic *trans*-amide-S is not expected to change Ni coordination due to simultaneous relief of the filled-filled dπ-pπ antibonding interaction between the metal and S-orbitals upon protonation or alkylation.[7-9] A thiol ligand is likely to decrease the S-character of the redox-active molecular orbital (RAMO), promoting Ni-based redox activity.[4]

The Ni-coordinated Cys-thiolates are likely sites of protonation and may serve as the source of H^+ for H_2O_2. X-ray absorption spectroscopy (XAS) analysis by Solomon, Maroney, and coworkers of H_2O_2-reduced NiSOD reveal a broad, structureless S K-edge feature characteristic of a protonated thiolate.[6] One mechanism proposes Ni(III) is initially thiolate-bound, but upon H_2O_2 reduction, Ni(III) is reduced to Ni(II) and a thiolate is protonated via proton-coupled electron transfer (PCET).[6] Indeed, Brunold and coworkers have shown via DFT calculations that Ni-SCys bonds in NiSOD are derived from covalent σ-bonding and S-protonation eliminates the Ni-d(π)/S-p(π) filled-filled repulsions in the π* HOMO without disrupting the σ-interactions.[7] One proposal is that Cys6 is a likely site of protonation due to the more reactive nature of *trans*-amide thiolates vs *trans*-amine thiolates.[8,10-16] In addition, Shearer and coworkers determined computationally that Ni^{II}(SOD-Cys(6)H^+) is minimally thermodynamically more stable than Ni^{II}(SOD-Cys(2)H^+ (ΔG = -4.5 kcal/mol).[17]

Few examples of Ni coordinated thiols exist in the literature and none are reported as models of NiSOD. Synthetically, methylated derivatives can be utilized as an alternative to protonation. Thioether ligands have the benefit of being more robust than the dissociable proton of a thiol and can be structurally characterized via X-ray diffraction (XRD) and NMR spectroscopy. Darensboug and coworkers have extensively studied the effect of methylation on

diamine/dithiolate Ni(II)N_2S_2 complexes and have isolated mono- and dialkylated complexes.[11,13 8,18,19] These spectroscopic benchmarks have shed insight into the nucleophilicity of metal-bound thiolates, but these complexes have not been explored as NiSOD mimics and do not electronically mimic the N-donors found in the NiSOD active site. Indeed, the only example of synthetically controlled thioether placement includes dithioether complexes reported by Masuda and coworkers.[20,21] Maroney and coworkers first reported mono-protonation and mono-alkylation of a dinuclear nickel thiolate complex in 1998. They report this reversible mono-protonation at the terminal thiol based on UV-vis, XRD, where the Ni–S distance is lengthened by ~0.02 Å, and XAS, where there is an increase in the Ni K-edge from 8339.0 to 8339.8 eV upon protonation.[22] The ^{1}H NMR spectrum of {Ni[MeN($CH_2CH_2S)_2$]} indicates a break in symmetry of the dinuclear complex and the ^{2}H NMR (CD_3NO_2) indicates an SH proton at 1.93 ppm.[22] Reactions with benzyl chloride (BnCl) and subsequent analysis by XRD reveals alkylation in the proposed protonation site, where the Ni–S distance of the thioether S-donor is 0.02 Å longer than the Ni–S distance from the terminal thiolate S-donor.[22] Duboc and coworkers have methylated a Ni-2,2′-(2,2′-bipyridine-6,6′-diyl)bis(1,1-diphenylethanethiolate) complex and have obtained an XRD crystal structure on the monomethylated complex that reveals a lengthening of the Ni–$S_{thioether}$ bond by 0.03 Å. These complexes confirm that the relief of the dπ–pπ antibonding interaction between Ni and S upon methylation or protonation counteracts the weak σ-donor character of the thioether ligand, resulting in negligible change in the Ni–S bond distance, as observed in calculations by Brunold, resulting in Ni complexes that maintain the Ni-N_2S_2 coordination sphere upon S-modification.[7,23]

To date (2018) protonation (H^+) and methylation (Me^+) has not been carried out on structurally accurate models of NiSOD. The objective of this work is to investigate the reactions

of H^+/Me^+ sources to observe effects on structure, spectroscopy, electrochemistry, and SOD activity. As proof of concept, we have explored the addition H^+/Me^+ to a 4C NiN_2S_2 complex that contains electronically accurate N/S donors. However, we and others hypothesize that a N_{axial} ligand, like the Ni-NHis (2.3-2.6 Å) found in the enzyme, is required to obtain a Ni(III) species. Therefore, we also explored adding H^+/Me^+ to a 5C NiN_3S_2 complex. Indeed, site-directed mutagenesis and DFT studies indicate that the axial Ni-NHis bond in $NiSOD_{ox}$ is required for maintaining the rate ($k \approx 10^9$ M^{-1} s^{-1}) and depressing the electrochemical potential of the Ni ion (0.090 V vs. Ag/AgCl, pH 7.4, PBS) for catalysis.[24-27] Additionally, only small model mimics of NiSOD that contain an N_{axial} ligand are able to achieve either a Ni(III) oxidation state or SOD activity.[28,34,35]

Since 2011, we have designed, synthesized and characterized five-coordinate (5C) Ni complexes that contain relevant N/S donors (Chart 3.1). One such complex is **K[Ni(N_3S_2)]** (where $[N_3S_2]^{3-}$ = deprotonated form of N-(2-mercaptoethyl)-2-((2-mercaptoethyl)(pyridin-2-ylmethyl)amino)acetamide).[29] Chemical oxidation of **K[Ni(N_3S_2)]**, however, results in a disulfide-linked complex, where the uncoordinated py-N moves into the equatorial plane, displacing the thiolate-S positioned *trans* to the carboxamido-N.[29] Additionally, low-temperature EPR monitoring of the chemical oxidation of **K[Ni(N_3S_2)]** revealed that Ni(III) is traversed on the way to this disulfide species.[29] To prevent this disulfide formation, our group designed and synthesized a new 5C N_3S_2 ligand with additional steric bulk on the thiolate α-carbon (α-C) situated *trans* to the carboxamide-N.[30] Namely, **Na[Ni($N_3S_2^{Me2}$)]** (where $[N_3S_2^{Me2}]^{3-}$ = deprotonated form of 2-((2-mercapto-2-methylpropyl)(pyridin-2- ylmethyl)amino)-N-(2-mercaptoethyl)acetamide).[30] Chemical oxidation of **Na[Ni($N_3S_2^{Me2}$)]**, however, results in a new chemical oxidation product, where py-N also moves into the equatorial plane, but an additional

two electron oxidation takes place at the substituted thiolate and py-CH_2 carbon to generate a thiazolidine heterocycle.[30] In this work, we present the synthesis and characterization of a new NiN_3S_2 complex **Na[Ni($N_3S_2^{py2}$)] (2)** ($N_3S_2^{py2}H_3$ = *N*-(2-mercaptoethyl)-2-((2-mercaptoethyl)(2-(pyridin-2-yl)ethyl)amino)acetamide and H represents dissociable protons) that contains an additional CH_2 group in the py-N ligand. The proposal is that this ligand will provide additional flexibility of the axial N-donor to promote coordinate to the Ni in an axial position, rather than equatorial replacement of the thiolate-S ligand, while also preventing reactivity at the py-CH_2 carbon.

Chart 3.1. Structural representation of NiSOD models with 5C ligands synthesized by Harrop and coworkers.

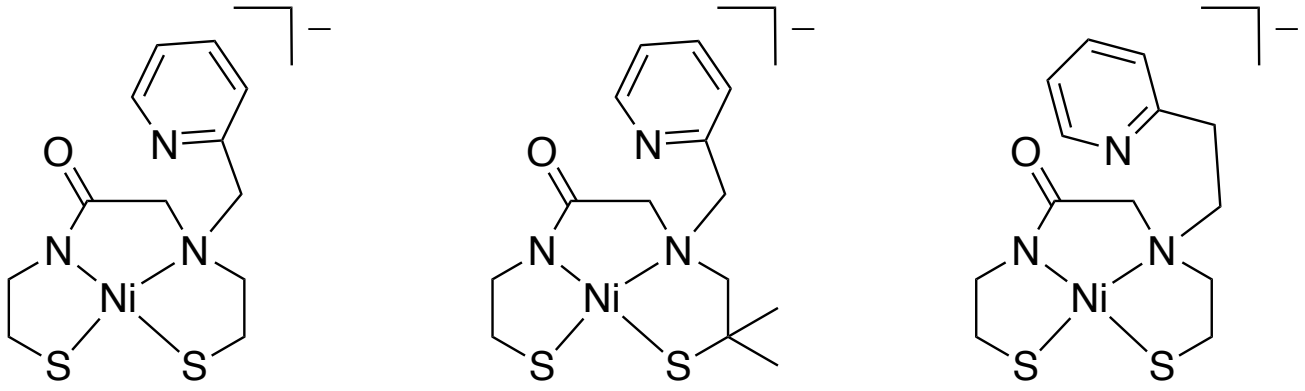

3.3 Results and Discussion

3.3.1 Synthesis of ligands

We will first develop a $N_2S^{Me}S$ monothioether ligand designed for four-coordinate (4C) Ni ligation, which will offer synthetic control over modification at the *trans*-amide-S site. The trityl protected $N_2S^{Me}STr$ ligand, 2-((2-(pyridin-2-yl)ethyl)(2-(tritylthio)ethyl)amino)-*N*-(2-(tritylthio)ethyl)acetamide, containing mixed thioether/thiol moieties was synthesized by reacting 2-bromo-*N*-(2-tritylthio)ethyl)acetamide with 2-(methylthio)ethaneamine with 2 equiv of Et_3N in THF in 58% yield (Scheme 3.1).

Scheme 3.1. Synthesis of $N_2S^{Me}STr$. Tr = trityl or triphenylmethyl (CPh_3) group.

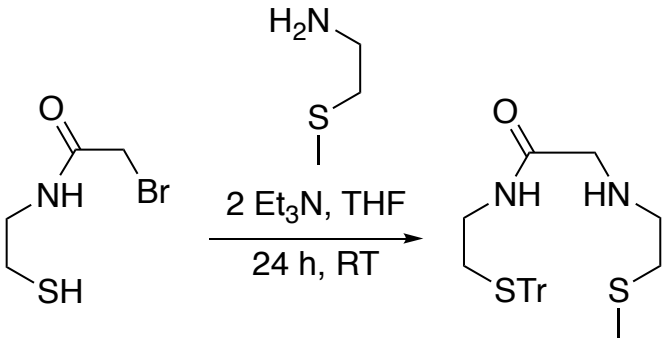

The prominent thioether singlet is present at 2.06 ppm in $CDCl_3$ (Figure 3.S2) and the IR spectrum revealed carboxamide C=O (ν_{CO} = 1657 cm^{-1}) and N–H (ν_{NH} = 3308 cm^{-1}) stretches (Figure 3.S1). Deprotection of the Tr groups using Et_3SiH in TFA afforded *N*-(2-mercaptoethyl)-2-((2-(methylthio)ethyl)amino)acetamide ($N_2S^{Me}SH_2$) as a yellow oil in 78% yield, where the thioether singlet is shifted to 2.12 ppm and a thiol-SH triplet appears at 1.40 ppm in $CDCl_3$ (Figure 3.S7). The IR spectrum of $N_2S^{Me}SH_2$ reveals carboxamide C=O (ν_{CO} = 1647 cm^{-1}), N–H (ν_{NH} = 3303 cm^{-1}), and thiol S–H (ν_{SH} = 2538) stretches (Figure 3.S6).

Scheme 3.2. Synthesis of $N_3S^{py2}H_3 \cdot 2HCl$. Tr = trityl or triphenylmethyl (CPh_3) group.

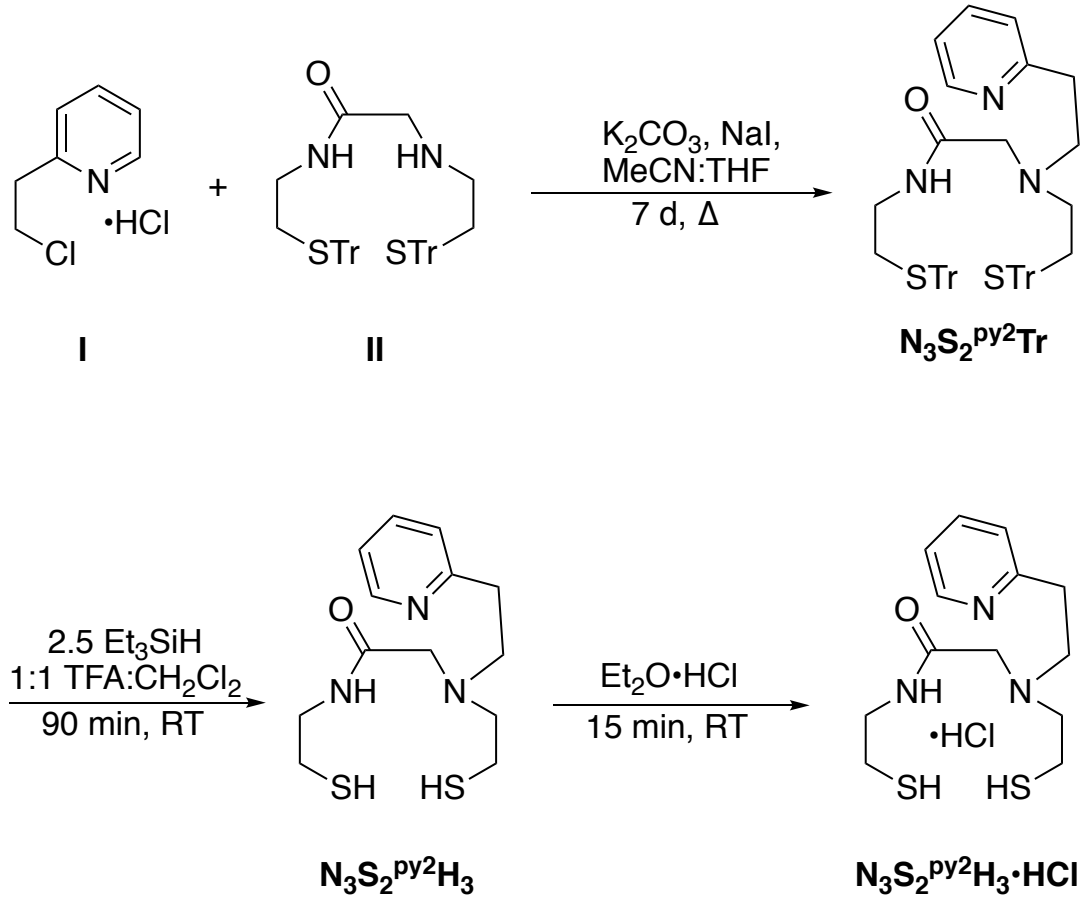

The synthesis begins with in situ generation of 2-(2-chloroethyl)-pyridine (**I**) by treating 2-(2-hydroxyethyl)-pyridine with $SOCl_2$ (Scheme 3.2). The pale brown solid **I** was reacted with *N*-[2-((2-((triphenylmethyl)thio)ethyl)amino)acetyl]-*S*-(triphenylmethyl)-2-aminoethanethiol (**II**), prepared as reported by O'Neil and coworkers.[31] Mixing stoichiometric amounts of **I** and **II** in a refluxing solution of 1:1 THF:MeCN with 1 equiv NaI and 2.5 equiv K_2CO_3 results in $N_3S_2^{py2}Tr$ in 62% yield after an EtOAc/hexane (gradient) column on Si. Deprotection of the Tr groups using Et_3SiH in TFA afforded $N_3S_2^{py2}H_3$ as a yellow oil, isolated as the TFA salt. To remove TFA and make a more tractable solid, $N_3S^{py2}H_3$ was then acidified with $Et_2O \cdot HCl$ to yield $N_3S_2^{py2}H_3 \cdot 2HCl$ in 62% yield as a glassy foam. Some notable spectroscopic features of

$N_3S2^{py2}H_3$ include the different ^1H NMR chemical shifts of the thiol protons at 1.68 and 1.60 ppm (D_2O-exchangeable), which are indicative of the asymmetric carboxamide/amine nature of the ligand (Figure 3.S28). Additionally, the IR spectrum of $N_3S_2^{py2}H_3 \cdot 2HCl$ indicate the presence of the carboxamide C=O (ν_{CO} = 1682 cm^{-1}), N–H (ν_{NH} = 3211 cm^{-1}) and S–H stretch (2538 cm^{-1}) (Figure 3.S27).

3.3.2. Synthesis of Ni(II) complexes

Metalation reactions have been carried out with $N_2S^{Me}SH_2$ with varying deprotonating agents (Na^0, NaH, acac), Ni(II) salts ($[Ni(H_2O)_6](BF_4)_2$, $[Ni(H_2O)_6](SO_4)$, $[Ni(H_2O)_6](ClO_4)_2$, $[Ni(acac)_2]\cdot 6H_2O$ in various solvents (MeOH, MeCN, THF) with different solvent-based workups (Scheme 3.3).

Scheme 3.3 Reaction of $N_2S^HS^{Me}$ with Ni(II) under various conditions to yield an equilibrium mixture of a monometallic and dimeric complex.

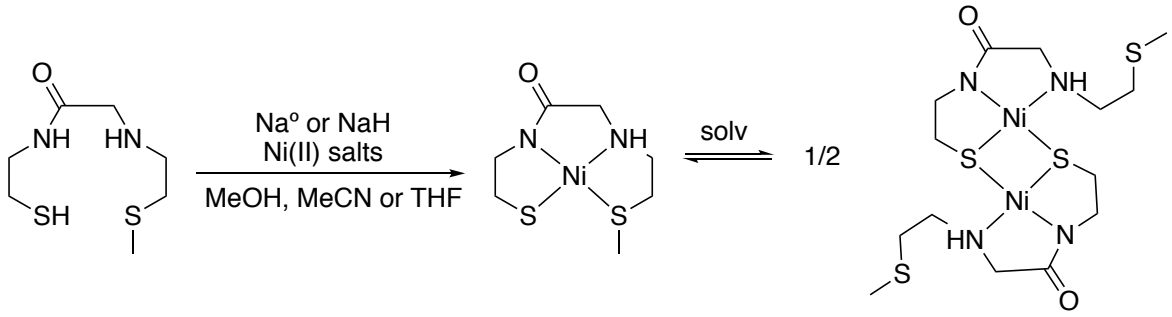

A batch of $N_2S^{Me}SH_2$ was metalated by adding 2.2 equiv NaH, followed by one equiv $[Ni(H_2O)_6](ClO_4)_2$ in MeCN to yield a red solution. The solution was filtered to isolate MeCN insoluble material and remove $NaClO_4$ in the filtrate. The MeCN soluble portion was crystallized

via diffusion of THF into MeCN to reveal a dimeric complex with thioether ligands unbound (Figure 3.1). Crystals of the dimeric species precipitated out of solution while excess $NaClO_4$ remained in the filtrate solution. The Ni–N/S bond distances compare well with the Ni–N/S bond distances of $NiSOD_{red}$ ($Ni–N_{carboxamide}$: 1.853 Å, $Ni–N_{peptide}$ (NiSOD): 1.91-1.94 Å; $Ni–N_{amine}$: 1.941 Å, $Ni–N_{amine}$ (NiSOD) 1.87-2.07 Å; $Ni–S_{trans\text{-}carboxamide}$ (bridged) 2.196 Å, $Ni\text{-}S_{trans\text{-}peptide}$ (NiSOD) 2.19 Å; $Ni–S_{trans\text{-}amine}$ (bridged) 2.169 Å, $Ni–S_{trans\text{-}amine}$ (NiSOD) 2.16-2.24 Å).[2,3] The dimeric species has a boat shape Ni–S core, with an average Ni–S–Ni angle of 80.60º and an average S–Ni–S angle of 84.10º and a Ni---Ni distance of 2.823 Å. The Ni-Ni distance and Ni-S,S-Ni core compares well to a the bond distances and angles of a complex isolated by Boyle and coworkers, where the Ni-Ni bond distance is 2.6733(5) Å. The Ni-Ni bond distance is nearly 0.2 Å shorter and exhibits diamagnetism in the ^1H NMR, providing precedent that the Ni-Ni interaction in $\mathbf{[1]_2}$ would not be close enough to evoke paramagnetism and would remain an S = 0 species.[32] The unbound thioether S2 interacts with a neighboring Ni2 via a distance of 3.564 Å (non-bonding interaction as Van der Waals radii Ni = 1.63 Å, S = 1.80 Å), which is not mirrored with N1 (the closest neighboring thioether ligand is S4, 5.907 Å away). This dimeric species likely arises as a result of the poor basicity of the thioether-S. The lability of the thioether-S results in a broadened species, likely due to exchange at the fourth coordination site, where solvent is able to coordinate and the thioether-S is unbound (vide supra).

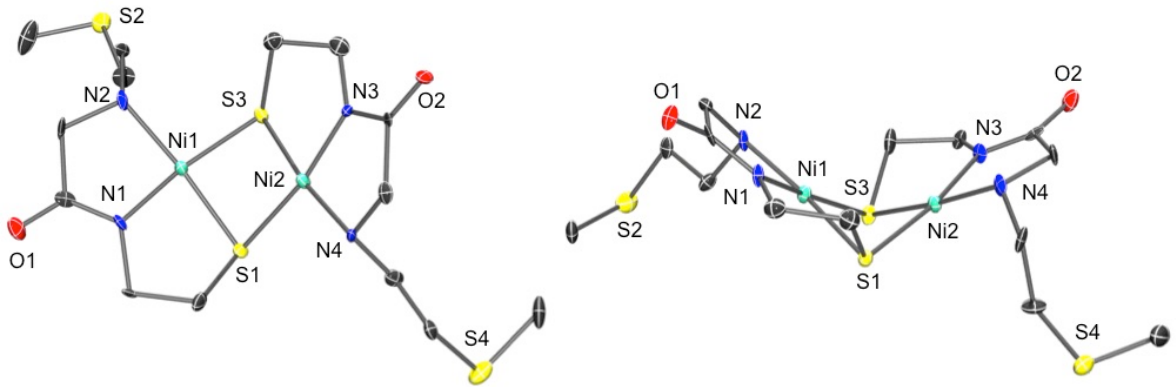

Figure 3.1. ORTEP of $[Ni_2(N_2S_2Me)_2]$ (**1**) at 50% thermal probability. **(*Left*)** View of *S*,*S*-bridged species and uncoordinated thioether ligand. **(*Right*)** ~90° rotation (in plane defined by paper) of the depiction on the left showing the unique configuration of the Ni-S core.

This equilibrium was probed by ^{1}H NMR spectroscopy, as ^{1}H NMR spectra have been obtained as showing an S = 0 species (**[NiL]^D**, where D = diamagnetic) or spectra containing signal broadening due to ligand exchange broadening (**[NiL]^E**, where E = exchange). **[NiL]^D** resulted from reaction of L with (i) Na^0 in MeOH with $[Ni(H_2O)_6](BF_4)_2$, the same reaction conditions have also yielded **[NiL]^E** spectra, usually after equilibrium time in MeCN, vide supra); (ii) NaH in THF with $[Ni(H_2O)_6](BF_4)_2$ (Figure 3.S20)

Our hypothesis is that an initial monometallic complex **[Ni($N_2S^{Me}S$)] (1)** forms with the expected N_2S_2 square-planar coordination sphere, denoted **[NiL]^D**. Due to the weak donor strength of the thioether-S ligand, however, the thioether-S is replaced by a solvent molecule or counterion, resulting in broadening in the ^{1}H NMR spectrum due to exchange; this complex is denoted **[NiL]^E**. Under crystalization conditions, however, the thermodynamic equilibrium results in a dimeric species with a Ni-S,S-Ni core (**[1]$_2$**), where the thioether-S is also unbound (Scheme 3.4). Due to the bridging nature of each Ni(N_2S) moiety in **[1]$_2$**, we suggest that this reorganization occurs via a dissociative mechanism, where the thioether-S becomes unbound and

the Ni(N_2S) moiety is available to loosely coordinate solvent, or bridge to another Ni(N_2S) moiety.

Scheme 3.4. Proposed formation of **[1]$_2$** via solvent interactions and unligated thioether.

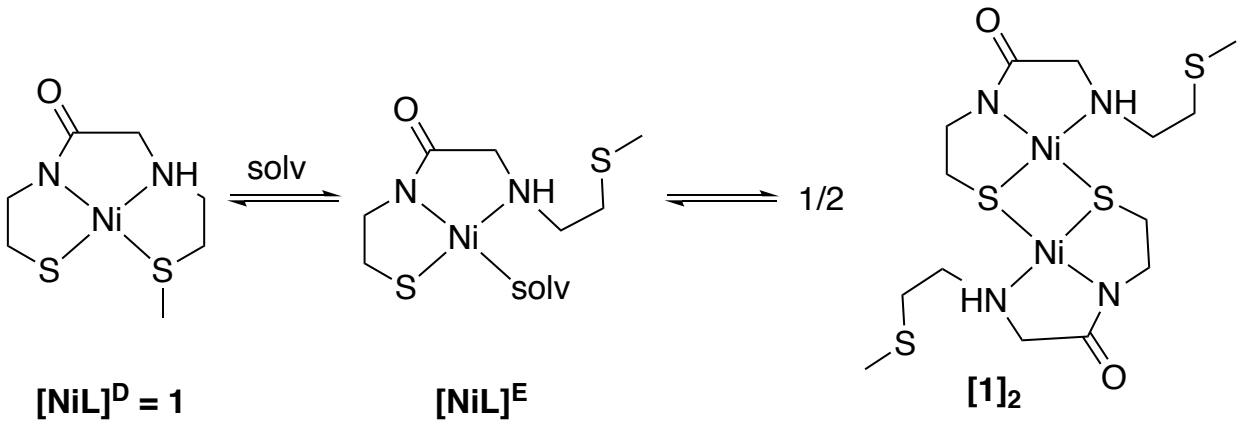

This migration of the thioether-S in a Ni-N/S complex has also been observed by Masuda and coworkers, where X-ray crystallographic shows the binding of the fifth axial pyridine-N donor in the equatorial plane, while the thioether-S is considered unbound with a weak axial interaction with Ni (Chart 3.2, left).[20] Additionally, this group proposed through EPR evidence, that addition of imidazole to their 4C NiN_2S_2 dithioether complex results in imidazole coordination and movement of the thioether ligand from the equatorial plane (Chart 3.2, right). [20] They observe hyperfine coupling in the $g_{\|}$ when their NiN_2S_2 complex is oxidized with ceric ammonium nitrate (CAN) in the presence of 7.5 equiv imidazole, in addition to triplet hyperfine coupling in the g⊥ (g⊥ = 2.20 |A⊥|= 1.7 mT; g‖ = 2.02, |A‖|= 2.3 mT).[20] In the presence of ^{15}N-labeled imidazole, both g‖ and g⊥ changed from triplet hyperfine to doublet hyperfine splitting when oxidized (g⊥ = 2.20 |A⊥|= 2.5 mT; g‖ = 2.02, |A‖|= 3.5 mT).[20] They suggest the amine is coordinated so as to give N-based hyperfine splitting through coordination of the imidazole.[20]

Chart 3.1. Schemes of Ni-N/S complexes containing *trans*-carboxamide thioether ligands that have migrated from coordinating in the equatorial plane in favor of N-ligation.

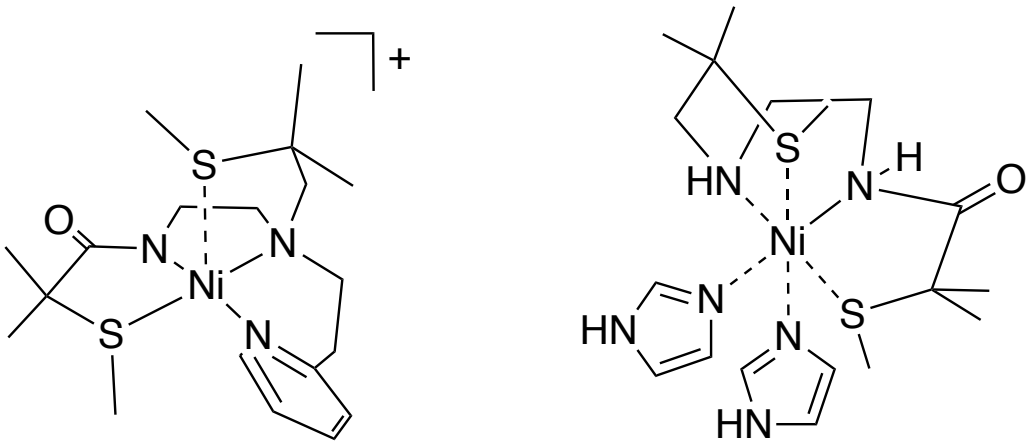

To test our equilibrium hypothesis, a reaction was carried out with NaH in THF, a non-coordinating solvent, with $Ni(ClO_4)_2$ which was dried over 3 Å molecular sieves from their hexa-aquated state. This reaction was filtered and the THF insoluble fractions were isolated, which contains some THF insoluble material in addition to $NaClO_4$. As a qualitative experiment, the UV-vis spectrum was obtained after initially dissolving the material in coordinating MeCN to reveal UV-vis transitions at λ_{max} = 334, 415, 545, corresponding to **[NiL]^{p}**, (Figure 3.2) but after stirring in MeCN overnight, the UV-vis transitions shifted to 430-450 nm, corresponding to **[NiL]^{p}** (Figure 3.2). This study suggests that dissolution in a donor solvent MeCN pushes the equilibrium of **[NiL]^{p}** (λ_{max} = 334, 415, 545) to **[NiL]^{p}** (λ_{max} 430-450 nm), where **[NiL]^{p}** is correlated to the crystallized dimeric species. (Figure 3.2)

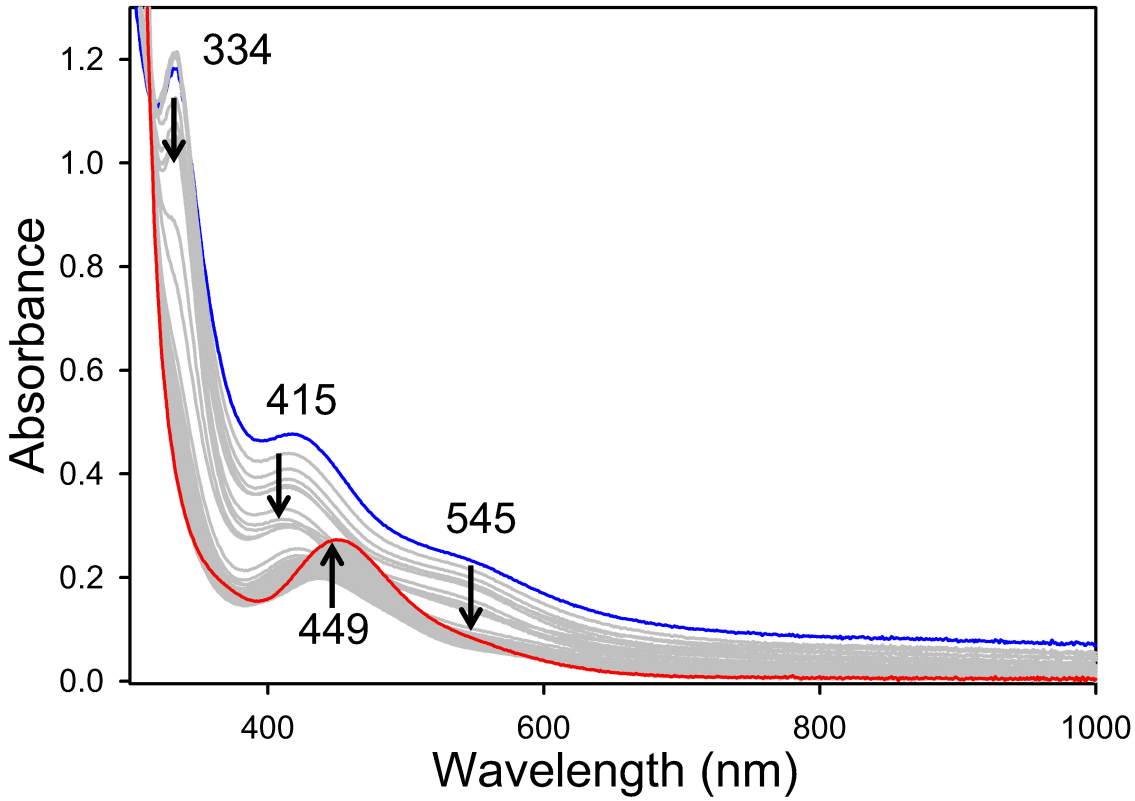

Figure 3.2 UV-vis spectral monitor of a MeCN solution of **[NiL]^{D}** (blue trace). Final trace in red correlates to **[NiL]^{P}**. Traces recorded at intervals of 1 scan/10 min for 12 h at 25 °C. Arrow shows direction of change.

Although both monometallic and dimetallic species are neutral, ESI-MS has revealed that the dimeric species, $[2M+Na]^+$ (calcd: 551.0; found: 551.0) and $[2M+H]^+$ (calcd: 529.0; found: 528.9) in positive mode (Figures 3.S11-3.S12) and the monometallic complex $[M+Na]^+$ (calcd: 287.0; found 287.1) in positive mode and $[M–H]^-$ (calcd: 263.0; found 263.0) in negative mode (Figures 3.S13-3.S14). The equilibration shift from **[NiL]^{D}** (λ_{max} = 334, 415, 545) to **[NiL]^{P}** (λ_{max} 430-450 nm), where **[NiL]^{P}** revealed a *m/z* = 551.0 correlating to $[2M+Na]^+$, providing further evidence that the dimeric species is the product of reaction with donor solvents such as MeCN.

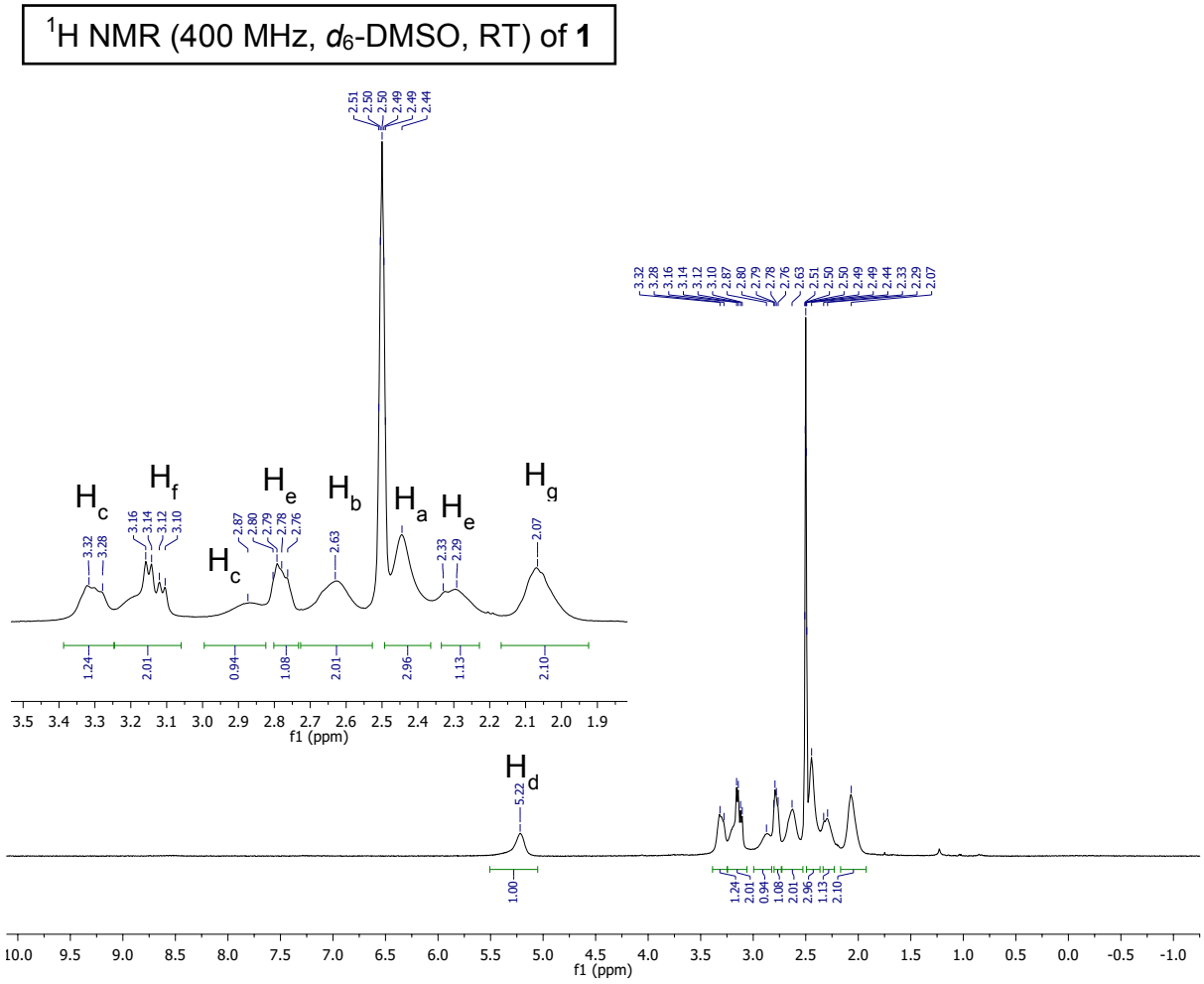

Figure 3.3. ^{1}H NMR spectrum of **1** in d_6-DMSO at RT. The peak at 2.50 ppm is from residual protio solvent. *Inset*: Zoom-in of full spectrum with peak labels.

In order to isolate the 4C diamagnetic Ni complex, a batch $N_2S^{Me}SH_2$ was deprotonated by two equiv Na^o and metalated with 1 equiv $NiSO_4$. Addition of $NiSO_4$ resulted in an immediate color change to dark red upon addition and the complex was purified by extracting with MeOH, cold isopropanol, and washing with MeCN to obtain red solid **[Ni($N_2S^{Me}S$)] (1)** in 66% yield. FTIR analysis reveals a ν_{NH} stretch at 3129 cm^{-1} and a ν_{CO} stretch at 1559 cm^{-1} with a ν_{CO} shift of ~99 cm^{-1} from 1647 cm^{-1} to lower frequency from $N_2S^{Me}SH_2$ (Figure 3.S15). Characterization of **1** by UV-vis spectroscopy in DMF revealed a λ_{max} = 467 nm indicative of ligand-field (LF)

transitions for a Ni(II)-N_2S_2 square-planar complex (Figure 3.S16). The ^{1}H NMR indicates a diamagnetic complex in d_6-DMSO (Figure 3.3), due to the lower donor strength of DMSO, with the appropriate aliphatic signals and diastereotopic splitting of the aliphatic protons closest to the amine proton upon Ni coordination, as confirmed by COSY (Figure 3.S18) and HSQC NMR (Figure 3.S19), Specifically, in the COSY spectrum, the cross-peak located at 3.2 ppm correlates to diastereotopically split protons off of the amine moiety (Figure 3.S18).

Synthesis of **Na[Ni($N_3S_2^{py2}$)] (2)** was carried out in 94% yield by deprotonating $N_3S^{py2}H_3$·2HCl with 6 equiv Na^o in MeOH and adding 1 equiv $NiCl_2$ to yield a dark red solution. The solution was dried to a dark red residue, taken up in MeCN/MeOH (10:1) and filtered to remove NaCl (Scheme 3.5). Analysis by FTIR indicated a ν_{NH} stretch at 3390 cm^{-1} and a ν_{CO} stretch at 1590 cm^{-1}, a ν_{CO} shift of ~ 92 cm^{-1} to lower frequency from $N_3S^{py2}H_3$·2HCl (1682 cm^{-1}) (Figure 3.S35).

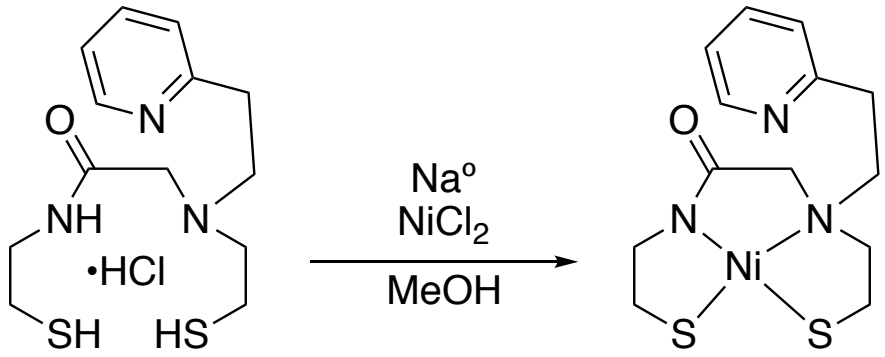

Scheme 3.5 Synthesis of **2**.

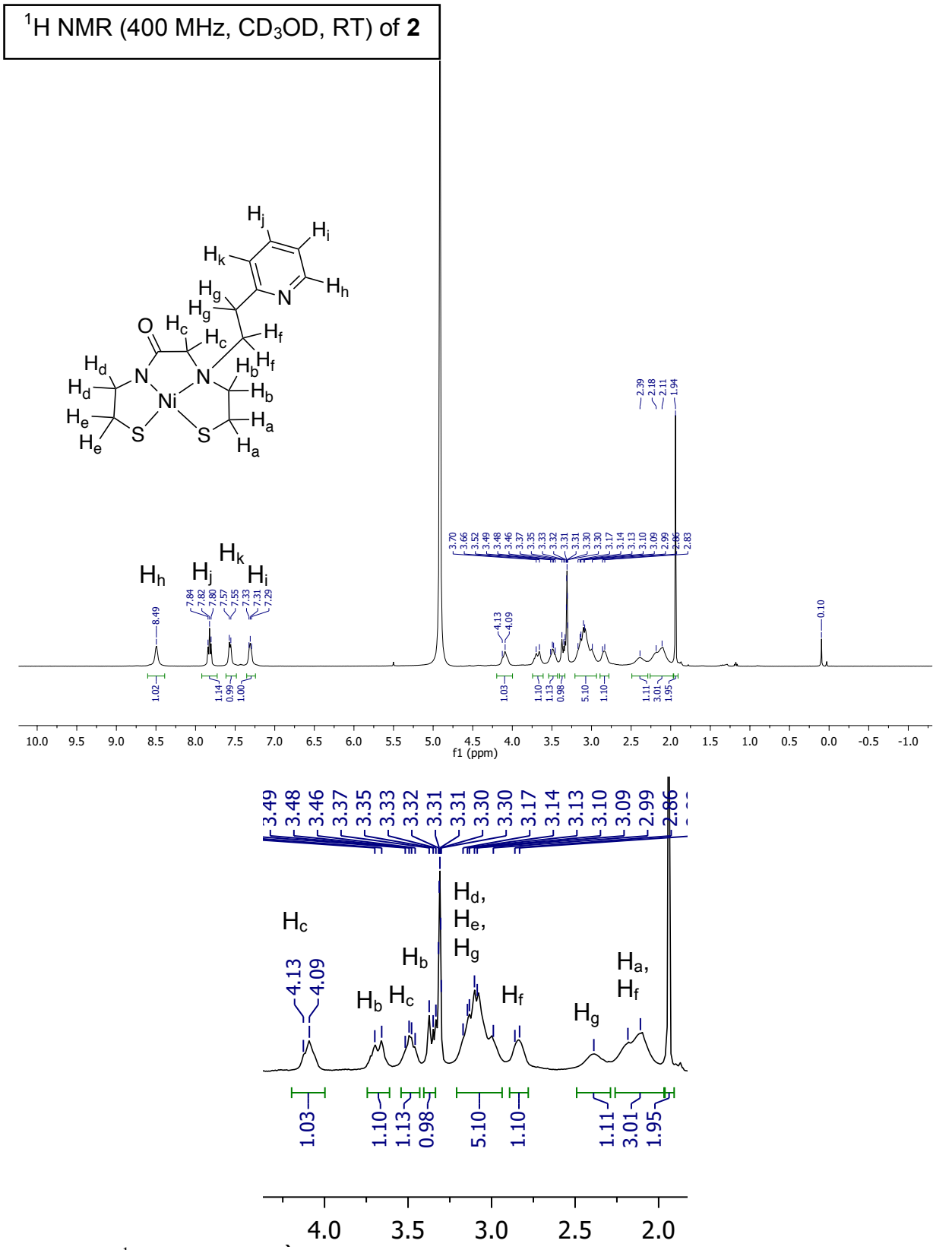

Figure 3.4. ^{1}H NMR spectrum of **2** in CD_3OD at RT. The peaks at 4.87 and 3.31 ppm are from residual protio solvent. The peak 1.94 is due to residual MeCN. Bottom, zoom in of aliphatic region.

Characterization of **2** by UV-vis spectroscopy in MeOH revealed a λ_{max} = 455 nm and a shoulder at 567 nm, indicative of a Ni(II)-N_2S_2 square-planar complex (Figure S.41). Pyridine coordination to Ni can be ruled out, as Ni–NPy coordination often results in a large CT transition and the UV-vis shows ligand-field (LF) transitions.[33] The ^{1}H NMR spectrum of **2** in CD_3OD indicated a diamagnetic species consistent with square planar Ni-N/S (S = 0) complexes, where diastereotopic splitting occurs for the aliphatic protons upon Ni-coordination (Figure 3.4). Additional characterization of **2** via COSY (Figure 3.S37) and HSQC NMR spectroscopy (Figure 3.S38) indicates the presence of two sets of diastereotopically split protons (pairs 7.77 and 6.81 ppm and 6.22 and 5.46 ppm). Taken together, this data is consistent with previously synthesized 5C complexes by our group indicating an Ni(II) square-planar system.[29,30]

3.3.3 Electrochemistry

The cyclic voltammograms (CVs) of $\mathbf{1_2}$ were measured in MeOH (0.1 M ^{n}Bu$_4$NPF$_6$ electrolyte) and potentials are reported versus ferrocene/ferrocenium (Fc/Fc$^+$). Scanning in the negative direction, followed by scanning to positive potentials revealed an E_{red} = –1.380 V and and E_{ox} = 0.356 V corresponding to thiolate E_{ox} /disulfide E_{red} conversion (Figure 3.5).

The cyclic voltammograms (CVs) of **2** were measured in DMF (0.1 M ^{n}Bu$_4$NPF$_6$ electrolyte) and in THF (0.1 M ^{n}Bu$_4$NPF$_6$ electrolyte and 10 equiv 1,4,7,10-tetraoxacyclododecane (12C4) to encapsulate the Na$^+$ cation and aid in solubility) and potentials are reported versus ferrocene/ferrocenium (Fc/Fc$^+$). When scanning in the positive direction (Figure 3.6, black solid trace), the full CV of **2** exhibits three oxidation features at –0.491 V, +0.057 mV, and +0.605 mV, with no corresponding reduction waves that would indicate reversibility of these oxidation events. When scanning first in the negative direction (Figure 3.6,

blue dashed trace), an irreversible reduction feature (E_{red}) at –2.06 V is revealed. After scanning in the positive direction and then switching to negative potentials, however, an additional E_{red} appears at –1.51 V, which correlates to the Ni(III)-thiolate/Ni(II)-thiyl E_{ox} event followed by a chemical reaction to form disulfide, where E_{red} is attributed to disulfide reduction.

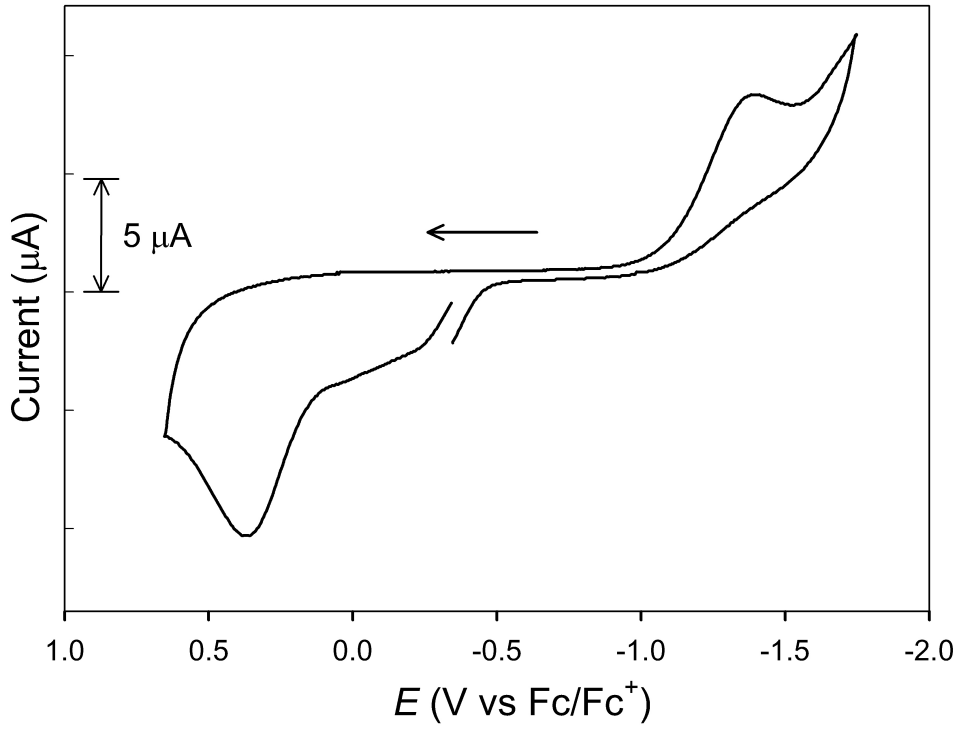

Figure 3.5. CV of 5 mM **1** in MeOH, RT. 0.1 M $^{n}Bu_4NPF_6$ electrolyte, glassy carbon working electrode, Pt counter electrode, 100 mV/s scan rate.

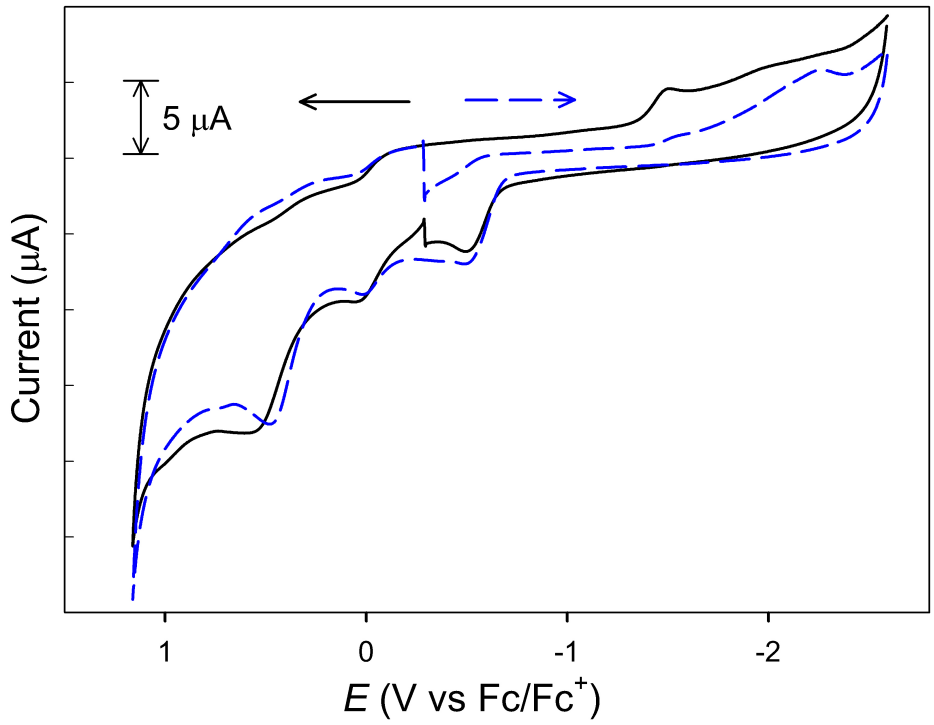

Figure 3.6. CV of 1 mM of **2**, 0.1 M $^{n}Bu_4NPF_6$ in DMF. The black solid trace indicates scanning first in the positive direction. The blue dashed trace indicates scanning first in the negative direction.

CVs were also performed in weakly coordinating THF in order to potentially promote axial pyridine binding. Similar thiolate E_{ox} (–0.312 V)/disulfide E_{red} (–2.47 V) conversion was present with scan rate dependency, which revealed a decrease in current response for E_{red} at higher scan speeds (Figure 3.7, top). This is indicative of an ECE process, where Ni(III)-thiolate/Ni(II)-thiyl oxidation occurs, followed by chemical formation of disulfide (Figure 3.7, bottom). When the scan rate increases, redox is faster than the chemical reaction, leaving less disulfide to be reduced.

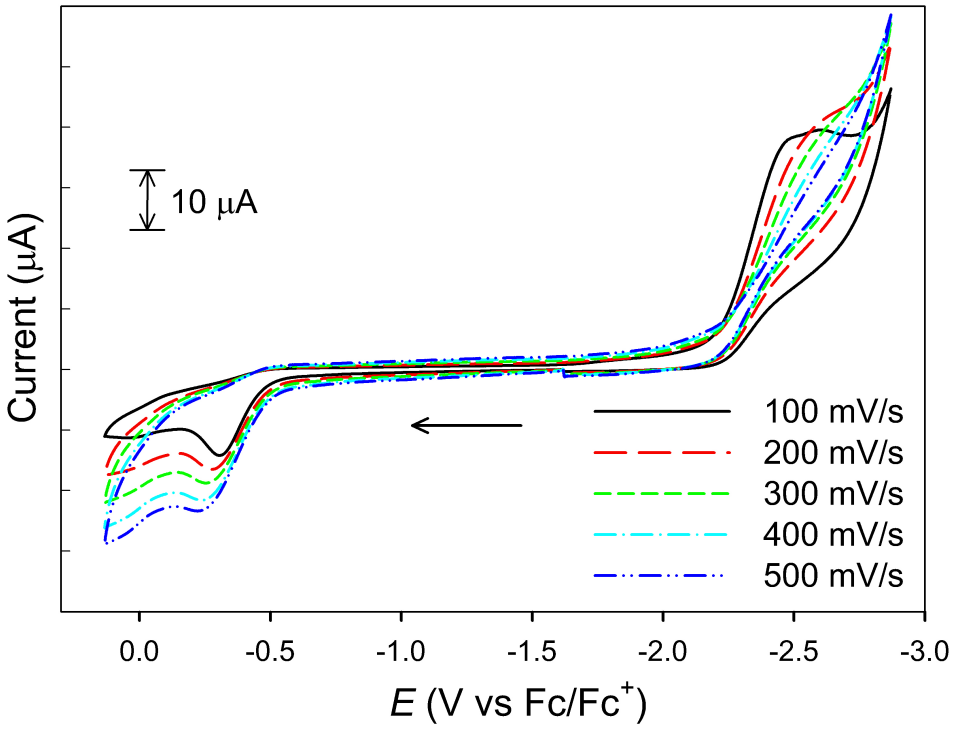

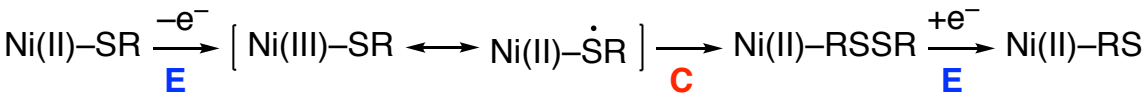

Figure 3.7. (Top) CV of a 5 mM THF solution of **2** (50 mM 12C4, 0.1 M $^{n}Bu_4NPF_6$ supporting electrolyte, varying scan rate, RT). Arrow shows direction of scan. (Bottom) Scheme of proposed ECE process.

3.3.4 Reactivity studies

Attempts to probe the nature of the $O_2^{\bullet-}$ reaction have been made utilizing nitroblue tetrazolium (NBT),[34] which undergoes reduction of the colorless tetrazolium by $O_2^{\bullet-}$ to form blue formazan (λ_{max} = 530 nm).[35] The reaction of **2** with NBT, however, alone resulted in forming formazan (32%), preventing the quantification of $O_2^{\bullet-}$ sequestering activity. Additionally, the electronic effects of methylation with complex **2** was characterized by CV. An aliquot of 5 equiv

MeI was added to the THF solution of **2** causing a color change from red-orange to pale green. As a result, the E_{ox} corresponding to thiolate oxidation was shifted to a more positive potential by ~0.5 V (from –0.739 V to –0.278 V) (Figure 3.8).

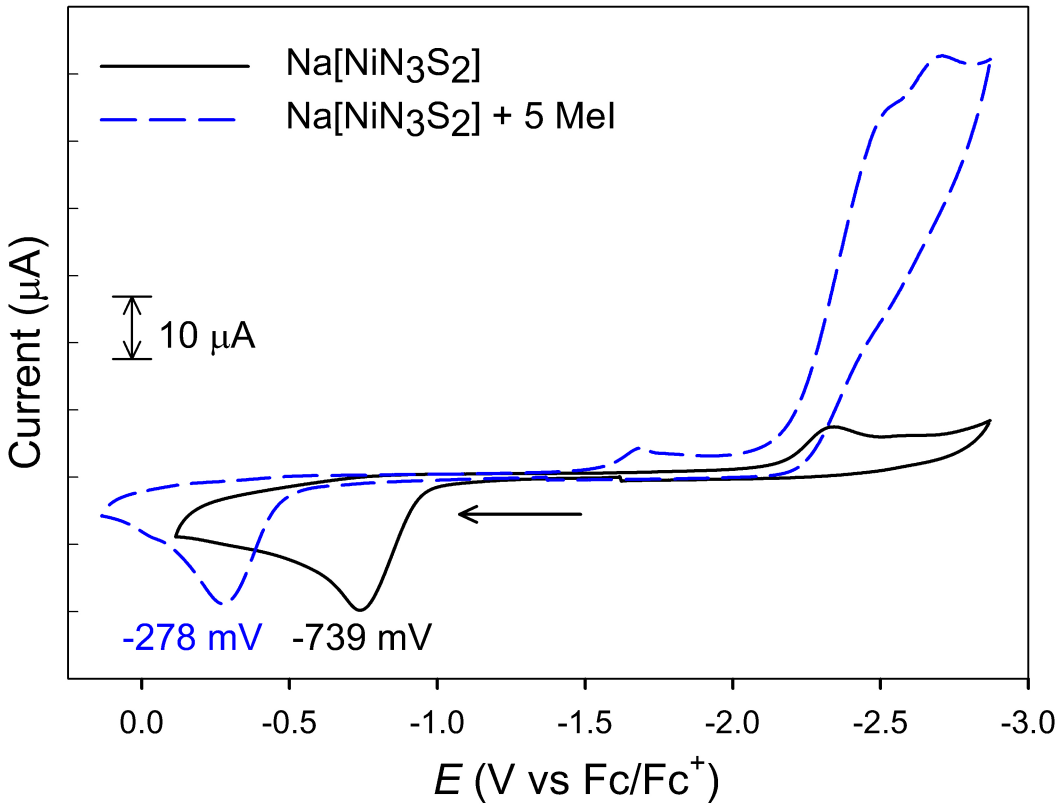

Figure 3.8. CV of 5 mM **2**, 50 mM 12C4, 0.1 M $^{n}Bu_4NPF_6$ in THF, RT, scan rate = 100 mV/s. The solid black trace is the scan of **2** alone. The dashed blue trace is **2** and 5 mM MeI.

This oxidative shift is expected based on the increase in net charge from –1 to 0. The disulfide reduction was also shifted to a more positive potential (from –2.32 V to –1.69 V), in addition to the appearance of a large, new E_{red} feature at –2.68 V, likely corresponding to Ni(II)/Ni(I) reduction. A cathodic shift of both the thiolate E_{ox} and the Ni(II)/Ni(I) couple is consistent with other methylated derivatives.[10,20,23] This methylation was characterized via UV-

vis with in situ reactivity studies with **2** and a methylating agent, either methyl iodide (MeI) or methyl triflate (MeOTf). Methylation reactions with MeOTf were realized with 2 mM **2**, where no change was observed for 1-2 equiv of MeOTf at –30 ºC. No reaction was observed at –30 ºC until 5 equiv of MeOTf was added, which resulted in immediate bleaching of color and disappearance of any spectral features by UV-vis (Table 3.1).

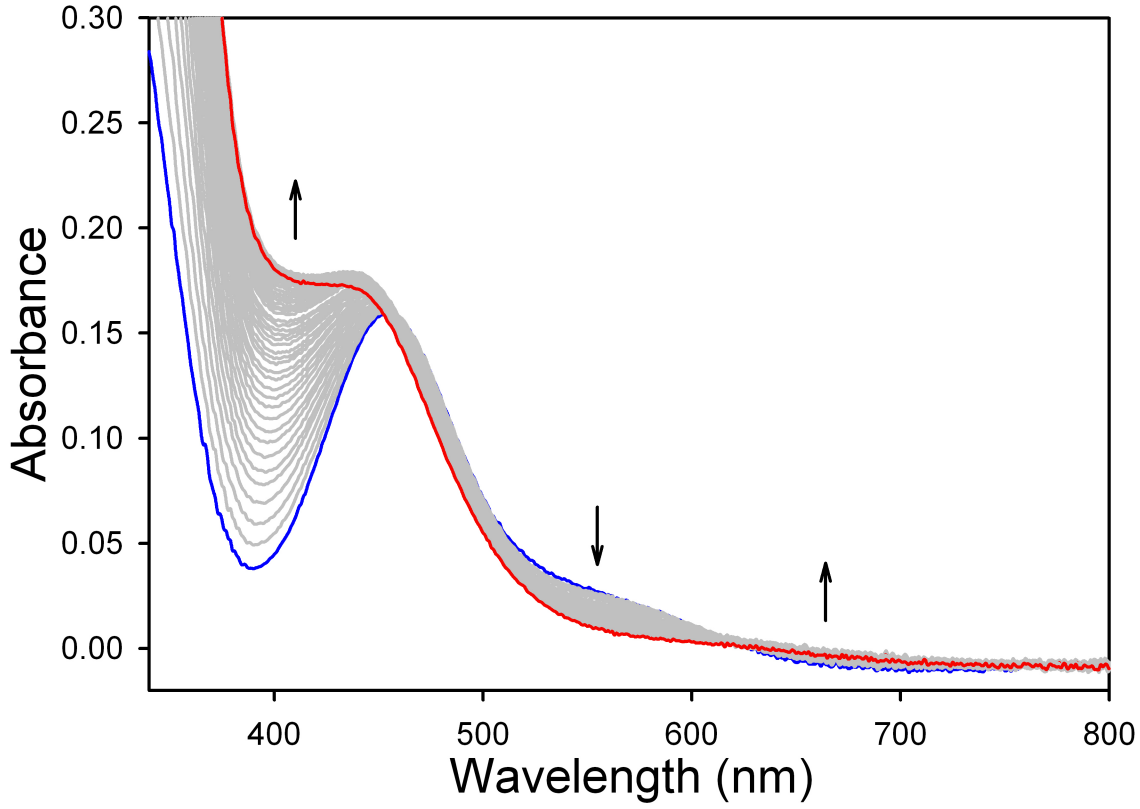

Figure 3.9 UV-vis spectral monitor of a 2 mM MeOH solution of **2** after addition of 5 equiv MeI (blue trace). Traces recorded at intervals of 1 scan/min for 1 h at 25 °C. Final trace is indicated by the red line. Arrow shows direction of change.

Reactions with 2 mM **2** were also carried out with MeI; a change in the UV-vis profile (Figure 3.9) was not observed until 5 equiv of MeI was added at 25 ºC (no change was observed for 1-2 equiv of MeI at –73 ºC or at RT (Table 3.1)). Characterization of this solution by LR-ESI-MS resulted in a positively charged mass correlating to dimethylation. These nucleophilic reactions with **2** are contrary to results observed by Darensbourg and coworkers, where methylation is facile upon addition of one CH_3^+ to a Ni-bound thiolate, but the second methylation is much more difficult and requires excess methylating agent. In comparison, for our mixed carboxamide/amine systems, reaction of 1-2 equiv of methylating agent results in no spectral change by UV-vis, but 5+ equiv results in dimethylation. This suggests that the mixed carboxamide/amine ligand plays a role in changing the nucleophilicity of the thiolate sulfurs by reducing the nucleophilicity of the first methylation, but increases the nucleophilicity of the second sulfur, in comparison to diamine NiN_2S_2 complexes.

Table 3.1 Summary of methylation reactions with **2**.

Reaction	**Temperature**	**Result (UV-vis)**
$Na[NiN_3S_2]$ + MeI	–73 ºC	N/C
$Na[NiN_3S_2]$ + 2MeI	–73 ºC	N/C
$Na[NiN_3S_2]$ + 2MeI	RT	N/C
$Na[NiN_3S_2]$ + 5MeI	25 ºC	↑433 nm ↓ 565 nm
$Na[NiN_3S_2]$ + MeOTf	–30 ºC	N/C
$Na[NiN_3S_2]$ + 2MeOTf	–30 ºC	N/C
$Na[NiN_3S_2]$ + 5MeOTf	–30 ºC	Bleaching

3.4 Conclusions

The asymmetric N_2S_2-CH_3 thioether ligand (*N*-(2-mercaptoethyl)-2-((2-methylthio)ethyl)amino)acetamide) and five-donor ligand *N*-(2-mercaptoethyl)-2-((2-mercaptoethyl)(2-(pyridin-2-yl)ethyl)amino)acetamide have been synthesized and metalated to Ni(II) resulting in isolation and characterization of **1** and **2**. Binding of the thioether ligand to Ni(II) results in equilibrium between a monometallic and dimeric complex (**[1]$_2$**)with a labile thioether ligand, which resulted in modification of the original synthesis in order to isolate the diamagnetic monometallic complex **1**. Reactivity studies of **2** show the expected shift in oxidation potential corresponding to S-based methylation. Further exploration of these complexes will involve detailed reactions, isolation and kinetic studies with protonation and methylation sources.

3.5 Experimental

General Information. All reagents were purchased from commercial suppliers and used as received unless otherwise noted. Acetonitrile (MeCN), methylene chloride (CH_2Cl_2), tetrahydrofuran (THF), pentane and diethyl ether (Et_2O) were purified by passage through activated alumina columns using an MBraun MB-SPS solvent purification system and stored under a dinitrogen (N_2) atmosphere before use. Methanol (MeOH) was dried over 3 Å molecular sieves and stored under similar conditions. All airfree reactions were performed under an inert atmosphere of N_2 using Schlenk-line techniques or in an N_2-filled MBraun Unilab glovebox. S-trityl cysteamine, 2-bromo-*N*-(2-(tritylthio)ethyl)acetamide, and Na[Ni(N_2S_2)] were synthesized according to published procedures.[33,36]

Physical Methods. FTIR spectra were collected on a ThermoNicolet 6700 spectrophotometer running the OMNIC software. Solid-state samples were prepared as pressed

KBr pellets. Electronic absorption spectra were performed at 298 K using a Cary-50 spectrophotometer. UV-vis samples were prepared in gas-tight Teflon-lined screw cap quartz cells with an optical pathlength of 1 cm. NMR spectra were recorded in the listed deuterated solvent on a 400 MHz Bruker BZH 400/52 S3 NMR Spectrometer or 500 MHz Varian Unity INOVA NMR spectrometer at ambient temperature with chemical shifts referenced to TMS or residual protio signal of the deuterated solvent.[37] Low resolution electrospray ionization mass spectrometry (ESI-MS) data were collected using a Perkin Elmer Sciex API I Plus quadrupole mass spectrometer.

2-((2-(methylthio)ethyl)amino)-*N*-(2-(tritylthio)ethyl)acetamide ($N_2S^{Me}STr$). A batch of 1.0381 g (2.3572 mmol) of 2-bromo-*N*-(2-(tritylthio)ethyl)acetamide was dissolved in ~10 mL THF under N_2(g) to form a light brown solution. To this solution was added a THF solution (~5 mL) containing 0.654 mL of Et_3N (4.69 mmol) and 0.219 mL (2.36 mmol) of 2-(methylthio)ethaneamine. White precipitate formed upon addition. The reaction flask was evacuated and refilled with N_2(g) and the solution stirred for 24 h. The solution was then filtered and the filtrate concentrated to a brown oil. Et_2O (~30 mL) was added to the oil and the biphasic solution stirred overnight. The Et_2O was decanted from the brown oil and any remaining Et_2O was removed by vacuum. The oil was taken up in CH_2Cl_2 (~30 mL) and subsequently washed with $NaHCO_3$(aq) and brine. The CH_2Cl_2 layer was dried with $MgSO_4$, filtered, and concentrated to yield a pale yellow oil (0.6197 g, 1.375 mmol, 58%). ^{1}H NMR (400 MHz, $CDCl_3$ with 0.05% v/v TMS, δ from TMS): 7.41 (m, 8H), 7.29 (t, 9H, integrates high due to overlap with residual protio solvent, J = 7.2 Hz), 7.22 (t, 3H, J =7.2 Hz), 3.22 (s, 2H), 3.13 (q, 2H, J = 6.4 Hz), 2.77 (t, 2H, J = 6.0 Hz), 2.60 (t, 2H, J = 6.4 Hz), 2.40 (t, 2H, J = 6.4 Hz), 2.06 (s, 3H), 1.68 (s, 1H, N*H*). ^{13}C NMR (100 MHz, $CDCl_3$ with 0.05% v/v TMS, δ from residual solvent): 171.51 (*C*=O),

144.79, 129.68, 128.08, 126.90, 66.84 (S*C*Ph_3), 52.16, 47.98, 37.82, 34.76, 32.22, 15.47. FTIR (KBr), ν_{max} (cm^{-1}): 3308 (br w ν_{NH}), 3054 (w), 3029 (w), 2914 (w), 2831 (w), 1954 (w), 1905 (w), 1813 (w), 1770 (w), 1657 (s ν_{CO}), 1594 (m), 1518 (m), 1487 (m), 1442 (m), 1358 (w), 1318 (w), 1284 (w), 1242 (w), 1182 (w), 1128 (w), 1082 (w), 1032 (m), 1000 (w), 909 (m), 849 (w), 741 (s), 696 (s), 675 (s), 616 (s), 573 (m), 505 (m). LR-ESI-MS (*m/z*): $[2M+H]^+$ calcd for $C_{52}H_{61}N_4O_2S_4$, 901.4 (100.0), 902.4 (60.9), 903.4 (35.4), 904.4 (12.2), 905.4 (4.0); found, 901.4 (100.0), 902.3 (61.6), 903.3 (36.2), 904.3 (13.3), 905.2 (4.0).

***N*-(2-mercaptoethyl)-2-((2-methylthio)ethyl)amino)acetamide ($N_2S^{Me}SH_2$).** A batch of 0.6197 g (1.375 mmol) of 2-((2-(methylthio)ethyl)amino)-*N*-(2-(tritylthio)ethyl)acetamide was dissolved in ~10 mL CH_2Cl_2 and ~10 mL TFA to form a bright yellow solution. To this solution was added 0.320 mL (2.00 mmol) of Et_3SiH and the color of the solution changed to an almost colorless pale yellow. After 90 min of stirring, the solution was concentrated and the residue was washed with pentanes (~20 mL) to remove $HCPh_3$. The oil was then dissolved in ~10 mL of CH_2Cl_2 and ~3 g of $NaHCO_3$ was added to neutralize any remaining TFA. After 2 h stirring, the solution was filtered and concentrated to afford a yellow oil (0.2245 g, 1.078 mmol, 78%). ^{1}H NMR (400 MHz, $CDCl_3$ with 0.05% v/v TMS, δ from TMS): 7.76 (s, 1H, N*H*), 3.48 (q, 2H, *J* = 6.8 Hz), 3.31 (s, 2H), 2.83 (t, 1H, *J* = 5.6 Hz), 2.68 (m, 4H), 2.12 (s, 3H), 1.83 (s, 1H, N*H*), 1.40 (t, 1H, *J* = 8.4 Hz, S*H*). ^{13}C NMR (100 MHz, $CDCl_3$ with 0.05% v/v TMS, δ from residual solvent): 171.81 (*C*=O), 52.14, 48.02, 41.99, 34.78, 24.84, 15.51. FTIR (KBr), ν_{max} (cm^{-1}): 3303 (br m, ν_{NH}), 3076 (w), 2915 (m), 2832 (m), 2538 (w, ν_{SH}), 1768 (w), 1647 (s, ν_{CO}), 1522 (s), 1425 (m), 1358 (w), 1334 (w), 1286 (w), 1243 (m), 1197 (m), 1130 (m), 1036 (w), 922 (w), 959 (w), 926 (w), 753 (m), 698 (m), 654 (m), 576 (m). LR-ESI-MS (*m/z*): $[M+H]^+$ calcd for

$C_7H_{17}N_2OS_2$, 209.1 (100.0), 210.1 (9.2), 211.1 (9.0); found, 209.1 (100.0), 210.1 (9.2), 211.1 (9.1).

[Ni($N_2S^{Me}S$)] (1). A batch of 0.0300 g of $N_2S^{Me}SH_2$ (0.144 mmol) was dissolved in ~2 mL of MeOH to form a homogeneous pale yellow solution. To this was added a batch of 0.0062 g Na^o (0.27 mmol), which resulted in immediate effervescence and was placed under vacuum for 20 min and allowed to stir. To this solution was added 0.0636 g $NiSO_4$ (0.242 mmol), which was dried over 3 Å sieves in ~9 mL MeOH for 12 h to remove H_2O. Addition of $NiSO_4$ resulted in an immediate color change to dark red upon addition and was allowed to stir for 12 h. The MeOH solution was filtered through a medium porosity glass frit and celite and washed with ~1 mL of MeOH. The filtrate was concentrated *in vacuo*, dissolved in ~10 mL isopropanol, placed in freezer (–22 ºC) for 12 h and then filtered through a medium porosity glass frit and celite and washed with ~1 mL cold isopropanol. The filtrate was concentrated *in vacuo* and washed with ~2 mL of MeCN and filtered to isolate 0.0252 g of red solid (0.0951 mmol, 66%). FTIR (KBr), ν_{max} (cm^{-1}): 3128 (ν_{NH}, br m), 2962 (m), 2916 (m), 2846 (m), 1589 (ν_{CO}, vs), 1408 (m), 1322 (w), 1261 (m), 1204 (w), 1094 (m), 1022 (m), 904 (w), 800 (m), 684 (w). LR-ESI-MS (*m/z*): $[M–H]^–$ calcd for $NiC_7H_{13}N_2OS_2$, 263.0 (100.0), 264.0 (9.2), 265.0 (47.5), 266.0 (4.6), 267.0 (8.7); found, 262.9 (100.0), 263.9 (12.7), 264.9 (51.1), 265.9 (7.8), 266.9 (12.3). ^{1}H NMR (400 MHz, d_6-DMSO, δ from residual protio solvent): 5.22 (br s, 1H, N*H*), 3.22-3.28 (br s, 1H), 3.16-3.10 (m, 2H), 2.87 (br s, 1H), 2.78 (br s, 1H), 2.63 (br s, 2H), 2.44 (br s, 3H), 2.33-2.29 (br s, 1H), 2.07 (br s, 2H). $[2M+Na]^+$ calcd for $Ni_2C_{14}H_{28}N_4O2S_4Na$, 551.0 (100.0), 552.0 (19.8), 553.0 (96.1), 554.0 (21.2), 555.0 (40.5), 556.0 (7.2), 557.0 (9.4), 559 (1.0); found, 550.9 (100.0), 551.9 (19.9), 552.9 (98.0), 553.9 (22.6), 554.9 (41.2), 555.9 (10.2), 556.9 (12.2), 559.0 (4.0). UV-vis (MeOH, 25 ºC) λ_{max}, nm (ε, M^{-1} cm^{-1}): 467 (143).

2-((2-(pyridin-2-yl)ethyl)(2-(tritylthio)ethyl)amino)-*N*-(2-(tritylthio)ethyl)acetamide ($N_3S_2^{py^2}Tr$) An aliquot of 0.161 mL (1.43 mmol) of 2-(2-hydroxylethyl)-pyridine was dissolved in ~ $CH_2Cl_2/SOCl_2$ (1:1, ~6 mL) and was allowed to stir for 12 h. The solution was concentrated and the pale brown solid was triturated with CH_2Cl_2 (3 × ~5 mL). This solid was then dissolved in MeCN/THF (1:1, ~10 mL) to yield a pale yellow, homogenous solution and a batch of 0.195 g (1.30 mmol) of NaI was added and allowed to stir for ~15 min, followed by a batch of 0.451 g (3.26 mmol) of K_2CO_3. To this slurry was added 0.884 g (1.30 mmol) of *N*-(2-(tritylthio)ethyl)-2-((2(tritylthio)ethyl)amino)acetamide in MeCN/THF (1:1, ~10 mL) and the solution refluxed for 9 d with a $CaSO_4$ drying tube, after which the slurry became brown. The slurry was then filtered and the brown filtrate was concentrated, dissolved in CH_2Cl_2 (~100 mL), and subsequently washed with D.I. H_2O, sat. $NaHCO_3$(aq), and brine. The solution was dried over $MgSO_4$, filtered, and concentrated to a brown oil. Flash chromatography on silica gel (EtOAc/hexanes) with a stepwise gradient of 40% → 67% → 100% EtOAc, followed by concentration yielded a yellow-brown glassy foam 0.630 g (0.803 mmol, 62%). Mp: 45-47 ºC. ^{1}H NMR (500 MHz, $CDCl_3$ with 0.05% v/v TMS, δ from TMS): 8.41 (m, 1H), 7.44 (m, 2H, overlap of C(=O)N*H* and pyridine C*H*), 7.40 (d, 6H, *J* = 8.0), 7.34 (d, 6H, *J* = 8.0), 7.21 (m, 13H, integrates high due to overlap with residual protio solvent), 7.18 (m, 6H), 7.02 (m, 2H), 2.99 (q, 2H, *J* = 6.5), 2.90 (s, 2H), 2.77 (dt, 4H, *J* = 6.0), 2.40 (t, 2H, *J* = 6.5), 2.30 (t, 2H, *J* = 7.0), 2.20 (t, 2H, *J* = 7.0). ^{13}C NMR (125 MHz, $CDCl_3$ with 0.05% v/v TMS, δ from residual solvent): 171.17 (*C*=O), 159.81, 149.39, 144.88, 144.86, 136.43, 129.69, 129.68, 128.04, 128.03, 126.82, 126.81, 123.58, 121.41, 66.85 (S*C*Ph_3), 66.78 (S*C*Ph_3), 58.39, 54.41, 53.95, 38.13, 36.01, 32.02, 29.86. FTIR (KBr), ν_{max} (cm^{-1}): 3344 (br m, ν_{NH}), 3360 (br m, ν_{NH}), 3054 (m), 2919 (m), 2848 (m), 2822 (m), 1954 (w), 1896 (w), 1811 (w), 1773 (w), 1734 (m), 1674 (s, ν_{CO}),

1592 (s), 1513 (s), 1488 (s), 1442 (s), 1358 (w), 1293 (w), 1240 (m), 1182 (m), 1082 (m), 1033 (m), 885 (w), 848 (w), 743 (s), 699 (s), 616 (m), 506 (m), 416 (m). LRMS-ESI (*m*/*z*): $[M+H]^+$ calcd for $C_{51}H_{50}ON_3S_2$ 784.3 (100.0), 785.3 (55.9), 786.3 (26.0), 787.3 (8.5), 788.3 (2.2); found, 784.3 (100.0), 785.3 (55.9), 786.3 (25.1), 787.3 (9.4), 788.3 (2.6).

***N*-(2-mercaptoethyl)-2-((2-mercaptoethyl)(2-(pyridin-2-yl)ethyl)amino)acetamide ($N_3S_2^{py^2}H_3$·2HCl)** A batch of $N_3S^{py^2}Tr$ (0.6684 g, 0.8525 mmol) was dissolved in TFA/CH_2Cl_2 (1:1, ~16 mL) to yield a bright red-orange solution. To this was added 0.545 mL of Et_3SiH (3.41 mmol), which caused a lightening of the solution to a yellow color, which was allowed to stir for 2 h. The solution was concentrated, then subsequently washed with pentane (5 × 10 mL). The residue was taken up in MeCN/CH_2Cl_2 (1:1, ~5 mL) and $NaHCO_3$ (~10% w/v) was added as a solid and stirred for 12 h. The solution was filtered, concentrated, dissolved in CH_2Cl_2 (~10 mL) and the slurry was filtered through celite and a medium porosity glass frit and washed with CH_2Cl_2 (~5 mL) and concentrated. ^{1}H NMR (500 MHz, CD_3CN, δ from residual protio solvent): 8.51 (d, 1H, *J* = 5.5), 7.71 (s, 1H, C(=O)N*H*), 7.68 (t, 1H, *J* = 7.7), 7.22 (m, 2H), 3.29 (q, 2H, *J* = 6.5), 3.10 (s, 2H), 2.91 (m, 4H), 2.67 (t, 2H, *J* = 6.8), 2.54 (dq, 4H, *J* = 14.9, 6.9), 1.68 (S*H*, t, 1H, *J* = 8.4), 1.60 (S*H*, t, 1H, *J* = 8.0). LRMS-ESI (*m*/*z*): $[M+H]^+$ calcd for $C_{13}H_{22}ON_3S_2$ 300.1 (100.0), 301.1 (16.8), 302.1 (9.0), 303.1 (1.3); found, 300.0 (100.0), 301.0 (16.6), 302.0 (9.6), 303.0 (4.9). To remove TFA, the solution was dissolved in MeCN (~1 mL) and acidified with 1.25 mL 1M Et_2O·HCl, which caused immediate precipitation of a white solid. After 15 min, the solid was washed with Et_2O (~10 mL) and dried to a glassy foam to yield 184.5 mg (0.495 mmol, 58%). Mp: 112-113 ºC ^{1}H NMR (500 MHz, CD_3OD, δ from residual protio solvent): 8.84 (d, 1H, *J* = 5.2), 8.61 (t, 1H, *J* = 8.0), 8.14 (d, 1H, *J* = 8.1), 8.02 (t, 1H, *J* = 6.6), 4.26 (s, 2H), 3.81 (m, 2H), 3.66 (m, 2H), 3.59 (m, 2H), 3.46 (t, 2H, *J* = 6.7), 2.96 (m, 2H), 2.67 (t, 2H, *J* =

6.7). ^{13}C NMR (125 MHz, CD_3OD with δ from residual solvent): 165.84 (*C*=O), 152.78, 148.20, 143.31, 129.17, 127.21, 59.00, 55.81, 52.10, 44.03, 29.27, 24.44, 19.23. FTIR (KBr pellet), ν_{max} (cm^{-1}): 3211 (br m, ν_{NH}), 3052 (m), 2975 (m), 2941 (m), 2869 (w), 2811 (w), 2426 (m, br), 2057 (m, ν_{NH}), 1993 (m, ν_{SH}), 1682 (s, ν_{CO}), 1634 (s), 1618 (s), 1559 (s), 1545 (s), 1469 (m), 1443 (m), 1420 (m), 1397 (m), 1358 (m), 1284 (m), 1246 (m), 1199 (m), 1170 (m), 1046 (m), 1002 (m), 932 (m), 771 (s), 661 (w), 627 (w), 583 (w), 498 (w).

Na[Ni($N_3S_2^{py2}$)] (2) A batch of 1.786 g $N_3S_2^{py2}H_3 \cdot 2HCl$ (0.4798 mmol) was dissolved in ~7 mL MeOH and Na° (0.0854 g, 2.85 mmol) was added as a solid to cause immediate effervescence and was allowed to stir for 10 min after which a peachy heterogenous solution formed. A yellow solution of dissolved 0.0652 g (0.503 mmol) $NiCl_2$ in ~5 mL MeOH was added, resulting in an immediate color change to red and was allowed to stir for 12 h. The solution was concentrated to a red residue, and then stirred in ~5 mL MeCN and ~0.5 mL MeOH for 1 h, and was then filtered to yield 0.1700 g of a red solid (94%). ^{1}H NMR (400 MHz, CD_3OD, δ from residual protio solvent): 8.54 (d, 1H, *J* = 4.9), 7.69 (t, 1H, *J* = 7.6), 7.33 (d, 1H, *J* = 7.8), 7.20 (t, 1H, *J* = 7.2), 3.90 (m, 1H), 3.44 (m, 4H, integrates high due to overlap with residual Et_2O), 2.95 (m, 6H), 2.64 (m, 1H), 2.22 (m, 2H, integrates high due to overlap with H_2O), 2.04 (m, 1H, integrates high due to overlap with residual protio solvent). FTIR (KBr pellet), ν_{max} (cm^{-1}): 3390 (br m, ν_{NH}), 2919 (m), 2848 (m), 1590 (s, ν_{CO}), 1435 (m), 1416 (m), 1385 (w), 1325 (w), 1263 (w), 1206 (w), 1181 (w), 1141 (w), 1095 (w), 1033 (w), 802 (w), 768 (w), 607 (w), 463 (w). LRMS-ESI (*m/z*): $[M]^-$ calcd for $C_{13}H_{18}ON_3S_2Ni$ 354.0 (100.0), 355.0 (17.0), 356.0 (49.1), 357.0 (9.8), 358.0 (10.1); found, 353.8 (100.0), 354.8 (17.5), 355.8 (49.3), 356.8 (10.9), 357.8 (10.8). HRMS-ESI (*m/z*): $[M]^-$ calcd for $C_{13}H_{18}ON_3S_2Ni$ 354.025 (100.0), 355.028 (14.1), 356.020 (47.2), 357.024 (5.4), 358.017 (7.7) 360.018 (1.4); found, 354.025

(100.0), 355.028 (13.2), 356.020 (49.7), 357.024 (5.3), 358.017 (7.8), 360.018 (1.3). UV-vis (MeOH, 25 ºC) λ_{max}, nm (ε, M^{-1} cm^{-1}): 453 (221), 550 (sh).

Na[Ni(N_2S_2)] + 50 MeI: A batch of 0.0531 g of N_2S_2 (0.195 mmol) was dissolved in ~ 3 mL of MeOH to form a red solution and an aliquot of 0.606 mL of MeI (9.75 mmol) was added, which caused an immediate color change to pale green. The solution was filtered and the filtrate was concentrated *in vacuo* to form a green-brown solid (0.0409, 0.147 mmol) The reaction was characterized by FTIR, CV, UV-vis, and ESI-MS.

X-ray Crystallographic Data Collection and Structure Solution and Refinement. Brown, blade-shaped crystals of **$[1]_2$** were grown by THF diffusion into a CH_3CN solution at –22 ºC under anaerobic atmosphere. The crystals were obtained from the following synthesis:

$[1]_2$. A batch of 0.1154 g of $N_2S^{Me}SH_2$ (0.5539 mmol) was dissolved in 1 mL of MeCN to form a homogeneous pale yellow solution. To this was added a slurry of 0.0292 g NaH (1.22 mmol), which resulted in immediate effervescence and was placed under vacuum for 30 min and allowed to stir. This ligand solution was added to a solution of 0.2026 g $Ni(ClO_4)_2$ (0.5540 mmol), which was dried over 3 Å sieves in ~3 mL MeCN for 12 h to remove H_2O. Addition of ligand resulted in an immediate color change to dark red and was allowed to stir for 1 h. The MeCN solution was filtered through a medium porosity glass frit and washed with ~1 mL of MeCN. The filtrate was concentrated *in vacuo* to isolate 0.0227 g red solid (0.0857 mmol, 15%). Suitable crystals were mounted on a glass fiber. The X-ray intensity data were measured at 100 K on a Bruker SMART APEX II X-ray diffractometer system with graphite-monochromatic Mo Kα radiation (λ = 0.71073 Å) using ω-scan technique controlled by the SMART software package.[38] The data were corrected for Lorentz and polarization effects[39] and integrated with the manufacturer's SAINT software. Absorption corrections were applied with the program

SADABS.[40] Subsequent structure refinement was performed using the SHELXTL 6.1 solution package operating on a Pentium computer. The structure was solved by direct methods using the SHELXTL 6.1 software package.[41,42] All non-hydrogen atoms were refined anisotropically.[43] Non-hydrogen atoms were located from successive difference Fourier map calculations. The crystal structure contains an Alert B as a result of a very small number of equivalent reflections (4491, typically >20,000 for our group), which may lead to artificially high values of different reflections with average R equivalents. Selected data and metric parameters for complex **[1]$_2$** are summarized in Tables S.1-3 Perspective views of the complexes were obtained using ORTEP.[44]

Computations. All computations were performed using the ORCA 3.0.1 program developed by Dr. Frank Neese.[45] The crystallographically determined coordinates from $[NiN_3S_2]^-$ from Gale et al. provided the initial structures for the computational models of **2** and **2·Me**.[46] Both models were then subjected to unconstrained geometry optimizations within the framework of density functional theory (DFT) using Becke's three-parameter hybrid functional and the Lee-Yang-Parr correlation functional (B3LYP).[47,48] Ahlrichs' valence triple-ζ basis set, TZV(P) basis set,[49,50] was chosen for the Ni, N, and S atoms, respectively, while Ahlrichs' polarized split valence and auxiliary basis sets,[49] SV(P) and SV/C, were selected for all of the remaining atoms. Single-point DFT calculations on the geometry-optimized models were performed using the OLYP functional and same basis sets as those used in the geometry optimizations. The Pymol program[51] was utilized to generate isosurface plots of MOs and spin densities with isodensity values of 0.05 a.u. and 0.005 a.u., respectively.

3.6 References

(1) Sheng, Y.; Abreu, I. A.; Cabelli, D. E.; Maroney, M. J.; Miller, A.-F.; Teixeira, M.; Valentine, J. S., Superoxide Dismutases and Superoxide Reductases. *Chem. Rev.* **2014**, *114*, 3854-3918.

(2) Barondeau, D. P.; Kassmann, C. J.; Bruns, C. K.; Tainer, J. A.; Getzoff, E. D., Nickel Superoxide Dismutase Structure and Mechanism. *Biochemistry* **2004**, *43*, 8038-8047.

(3) Wuerges, J.; Lee, J.-W.; Yim, Y.-I.; Yim, H.-S.; Kang, S.-O.; Carugo, K. D., Crystal structure of nickel-containing superoxide dismutase reveals another type of active site. *Proc. Natl. Acad. Sci. U.S.A.* **2004**, *101*, 8569-8574.

(4) Fiedler, A. T.; Brunold, T. C., Spectroscopic and computational studies of Ni(III) complexes with mixed S/N ligation: Implications for the active site of nickel superoxide dismutase. *Inorg. Chem.* **2007**, *46*, 8511-8523.

(5) Broering, E. P.; Truong, P. T.; Gale, E. M.; Harrop, T. C., Synthetic Analogues of Nickel Superoxide Dismutase: A New Role for Nickel in Biology. *Biochemistry* **2013**, *52*, 4-18.

(6) Szilagyi, R. K.; Bryngelson, P. A.; Maroney, M. J.; Hedman, B.; Hodgson, K. O.; Solomon, E. I., S K-edge X-ray absorption spectroscopic investigation of the Ni-containing superoxide dismutase active site: New structural insight into the mechanism. *J. Am. Chem. Soc.* **2004**, *126*, 3018-3019.

(7) Fiedler, A. T.; Bryngelson, P. A.; Maroney, M. J.; Brunold, T. C., Spectroscopic and Computational Studies of Ni Superoxide Dismutase: Electronic Structure Contributions to Enzymatic Function. *J. Am. Chem. Soc.* **2005**, *127*, 5449-5462.

(8) Bellefeuille, J. A.; Grapperhaus, C. A.; Derecskei-Kovacs, A.; Reibenspies, J. H.; Darensbourg, M. Y., Correlation of electrochemistry, nucleophilicity and density functional calculations of the cis-dithiolate (bme*-daco)Ni. *Inorg. Chim. Acta* **2000**, *300*, 73-81.

(9) Ashby, M. T.; Enemark, J. H.; Lichtenberger, D. L., Destabilizing d(π)-p(π) Orbital Interactions and the Alkylation Reactions of Iron(II) Thiolate Complexes. *Inorg. Chem.* **1988**, *27*, 191-197.

(10) Hatlevik, O.; Blanksma, M. C.; Mathrubootham, V.; Arif, A. M.; Hegg, E. L., Modeling carbon monoxide dehydrogenase/acetyl-CoA synthase (CODH/ACS): a trinuclear nickel complex employing deprotonated amides and bridging thiolates. *J. Biol. Inorg. Chem.* **2004**, *9*, 238-246.

(11) Kaasjager, V. E.; Bouwman, E.; Gorter, S.; Reedijk, J.; Grapperhaus, C. A.; Reibenspies, J. H.; Smee, J. J.; Darensbourg, M. Y.; Derecskei-Kovacs, A.; Thomson, L. M., Unique

reactivity of a tetradentate N_2S_2 complex of nickel: Intermediates in the production of sulfur oxygenates. *Inorg. Chem.* **2002**, *41*, 1837-1844.

(12) Grapperhaus, C. A.; Mullins, C. S.; Kozlowski, P. M.; Mashuta, M. S., Synthesis and oxygenation of a nickel(II) and zinc(II) dithiolate: An experimental and theoretical comparison. *Inorg. Chem.* **2004**, *43*, 2859-2866.

(13) Green, K. N.; Brothers, S. M.; Jenkins, R. M.; Carson, C. E.; Grapperhaus, C. A.; Darensbourg, M. Y., An experimental and computational study of sulfur-modified nucleophilicity in a dianionic NiN_2S_2 complex. *Inorg. Chem.* **2007**, *46*, 7536-7544.

(14) Shearer, J.; Zhao, N., $[Me_4N](Ni^{II}(BEAAM))$: A Synthetic Model for Nickel Superoxide Dismutase That Contains Ni in a Mixed Amine/Amide Coordination Environment. *Inorg. Chem.* **2006**, *45*, 9637-9639.

(15) Shearer, J.; Long, L. M., A Nickel Superoxide Dismutase Maquette That Reproduces the Spectroscopic and Functional Properties of the Metalloenzyme. *Inorg. Chem.* **2006**, *45*, 2358-2360.

(16) Mullins, C. S.; Grapperhaus, C. A.; Kozlowski, P. M., Density functional theory investigations of NiN_2S_2 reactivity as a function of nitrogen donor type and N-H···S hydrogen bonding inspired by nickel-containing superoxide dismutase. *J. Biol. Inorg. Chem.* **2006**, *11*, 617-625.

(17) Shearer, J.; Peck, K. L.; Schmitt, J. C.; Neupane, K. P., Cysteinate Protonation and Water Hydrogen Bonding at the Active-Site of a Nickel Superoxide Dismutase Metallopeptide-Based Mimic: Implications for the Mechanism of Superoxide Reduction. *J. Am. Chem. Soc.* **2014**, *136*, 16009-16022.

(18) Dey, A.; Green, K. N.; Jenkins, R. M.; Jeffrey, S. P.; Darensbourg, M.; Hodgson, K. O.; Hedman, B.; Solomon, E. I., S K-Edge XAS and DFT Calculations on Square-Planar Ni^{II}-Thiolate Complexes: Effects of Active and Passive H-bonding. *Inorg. Chem.* **2007**, *46*, 9655-9660.

(19) Farmer, P. J.; Reibenspies, J. H.; Lindahl, P. A.; Darensbourg, M. Y., Effects of Sulfur Site Modification on the Redox Potentials of Derivatives of [*N*,*N*'-Bis(2-Mercaptoethyl)-1,5-Diazacyclooctanato]Nickel(II). *J. Am. Chem. Soc.* **1993**, *115*, 4665-4674.

(20) Nakane, D.; Funahashi, Y.; Ozawa, T.; Masuda, H., A Square-planar Ni(II) Complex with an Asymmetric N_2S_2 Donor Set as a Model for the Active Site of Nickel-containing SOD: Structural Conversion Driven by Addition of a Strong Donor Ligand in the High Oxidation State. *Chem. Lett.* **2010**, *39*, 344-346.

(21) Nakane, D.; Kuwasako, S.; Tsuge, M.; Kubo, M.; Funahashi, Y.; Ozawa, T.; Ogura, T.; Masuda, H., A square-planar Ni(II) complex with an N_2S_2 donor set similar to the active centre of nickel-containing superoxide dismutase and its reaction with superoxide. *Chem. Commun.* **2010**, *46*, 2142-2144.

(22) Allan, C. B.; Davidson, G.; Choudhury, S. B.; Gu, Z. J.; Bose, K.; Day, R. O.; Maroney, M. J., Protonation and alkylation of a dinuclear nickel thiolate complex. *Inorg. Chem.* **1998**, *37*, 4166-4167.

(23) Gennari, M.; Orio, M.; Pecaut, J.; Bothe, E.; Neese, F.; Collomb, M. N.; Duboc, C., Influence of Mixed Thiolate/Thioether versus Dithiolate Coordination on the Accessibility of the Uncommon +I and +III Oxidation States for the Nickel Ion: An Experimental and Computational Study. *Inorg. Chem.* **2011**, *50*, 3707-3716.

(24) Herbst, R. W.; Guce, A.; Bryngelson, P. A.; Higgins, K. A.; Ryan, K. C.; Cabelli, D. E.; Garman, S. C.; Maroney, M. J., Role of Conserved Tyrosine Residues in NiSOD Catalysis: A Case of Convergent Evolution. *Biochemistry* **2009**, *48*, 3354-3369.

(25) Ryan, K. C.; Guce, A. I.; Johnson, O. E.; Brunold, T. C.; Cabelli, D. E.; Garman, S. C.; Maroney, M. J., Nickel Superoxide Dismutase: Structural and Functional Roles of His1 and Its H-Bonding Network. *Biochemistry* **2015**, *54*, 1016-1027.

(26) Fiedler, A. T.; Bryngelson, P. A.; Maroney, M. J.; Brunold, T. C., Spectroscopic and Computational Studies of Ni Superoxide Dismutase: Electronic Structure Contributions to Enzymatic Function. *J. Am. Chem. Soc.* **2005**, *127*, 5449-5462.

(27) Bryngelson, P. A.; Arobo, S. E.; Pinkham, J. L.; Cabelli, D. E.; Maroney, M. J., Expression, Reconstitution, and Mutation of Recombinant *Streptomyces coelicolor* NiSOD. *J. Am. Chem. Soc.* **2004**, *126*, 460-461.

(28) Lee, W.-Z.; Chiang, C.-W.; Lin, T.-H.; Kuo, T.-S., A Discrete Five-Coordinate Ni^{III} Complex Resembling the Active Site of the Oxidized Form of Nickel Superoxide Dismutase. *Chem.-Eur. J.* **2012**, *18*, 50-53.

(29) Gale, E. M.; Simmonett, A. C.; Telser, J.; Schaefer, H. F., III; Harrop, T. C., Toward Functional Ni-SOD Biomimetics: Achieving a Structural/Electronic Correlation with Redox Dynamics. *Inorg. Chem.* **2011**, *50*, 9216-9218.

(30) Truong, P. T.; Gale, E. M.; Dzul, S. P.; Stemmler, T. L.; Harrop, T. C., Steric Enforcement about One Thiolate Donor Leads to New Oxidation Chemistry in a NiSOD Model Complex. *Inorg. Chem.* **2017**, *56*, 7761-7780.

(31) O'Neil, J. P.; Wilson, S. R.; Katzenellenbogen, J. A., Preparation and Structural Characterization of Monoamine-Monoamide Bis(Thiol) Oxo Complexes of Technetium(V) and Rhenium(V). *Inorg. Chem.* **1994**, *33*, 319-323.

(32) Cornman, C. R.; Jantzi, K. L.; Wirgau, J. I.; Stauffer, T. C.; Kampf, J. W.; Boyle, P. D., Coordination Chemistry of a Tripodal S_2ON Ligand: Syntheses, Structures, and Reactivity of the Molybdenum(VI) and Nickel(II) Complexes of Bis(2-mercaptoethyl)-2-amino-4-methylphenol (H_3btap) and Comparison to VVO(btap) *Inorg. Chem.* **1998**, *37*, 5851-5855.

(33) Gale, E. M.; Patra, A. K.; Harrop, T. C., Versatile Methodology Toward NiN_2S_2 Complexes as Nickel Superoxide Dismutase Models: Structure and Proton Affinity. *Inorg. Chem.* **2009**, *48*, 5620-5622.

(34) Tabbì, G.; Driessen, W. L.; Reedijk, J.; Bonomo, R. P.; Veldman, N.; Spek, A. L., High Superoxide Dismutase Activity of a Novel, Intramolecularly Imidazolato-Bridged Asymmetric Dicopper(II) Species. Design, Synthesis, Structure, and Magnetism of Copper(II) Complexes with a Mixed Pyrazole–Imidazole Donor Set. *Inorg. Chem.* **1997**, *36*, 1168-1175.

(35) Beauchamp, C.; Fridovich, I., Superoxide Dismutase: Improved Assays and an Assay Applicable to Acrylamide Gels. *Anal. Biochem.* **1971**, *44*, 276-287.

(36) Mathrubootham, V.; Thomas, J.; Staples, R.; McCraken, J.; Shearer, J.; Hegg, E. L., Bisamidate and Mixed Amine/Amidate NiN_2S_2 Complexes as Models for Nickel-Containing Acetyl Coenzyme A Synthase and Superoxide Dismutase: An Experimental and Computational Study. *Inorg. Chem.* **2010**, *49*, 5393-5406.

(37) Fulmer, G. R.; Miller, A. J. M.; Sherden, N. H.; Gottlieb, H. E.; Nudelman, A.; Stoltz, B. M.; Bercaw, J. E.; Goldberg, K. I., NMR Chemical Shifts of Trace Impurities: Common Laboratory Solvents, Organics, and Gases in Deuterated Solvents Relevant to the Organometallic Chemist. *Organometallics* **2010**, *29*, 2176-2179.

(38) *SMART v5.626: Software for the CCD Detector System*. Bruker AXS: Madison, WI, 2000.

(39) Walker, N.; Stuart, D., *Acta Crystallogr.* **1983**, *A39*, 158-166.

(40) Sheldrick, G. M., *SADABS, Area Detector Absorption Correction*. University of Göttingen: Göttingen, Germany, 2001.

(41) Sheldrick, G. M., *SHELX-97, Program for Refinement of Crystal Structures*. University of Göttingen: Göttingen, Germany, 1997.

(42) Sheldrick, G. M., *Acta Crystallogr.* **2008**, *A64*, 112-122.

(43) Sheldrick, G. M., *SHELXTL 6.1, Crystallographic Computing System*. Siemens Analytical X-Ray Instruments: Madison, WI, 2000.

(44) Burnett, M. N.; Johnson, C. K., *ORTEP-III, Report ORNL-6895*. Oak Ridge National Laboratory: Oak Ridge, TN, 1996.

(45) Neese, F., The ORCA program system. *Wiley Interdiscip. Rev. Comput. Mol. Sci.* **2012**, *2*, 73-78.

(46) Gale, E. M.; Cowart, D. M.; Scott, R. A.; Harrop, T. C., Dipeptide-Based Models of Nickel Superoxide Dismutase: Solvent Effects Highlight a Critical Role to Ni–S Bonding and Active Site Stabilization. *Inorg. Chem.* **2011**, *50*, 10460-10471.

(47) Becke, A. D., Density-Function Thermochemistry .3. The Role of Exact Exchange. *J. Chem. Phys.* **1993**, *98*, 5648-5652.

(48) Lee, C.; Yang, W.; Parr, R. G., Development of the Colle-Salvetti correlation-energy formula into a functional of the electron-density. *Phys. Rev. B: Condens. Matter Mater. Phys.* **1998**, *37*, 785-789.

(49) Schäfer, A.; Horn, H.; Ahlrichs, R., Fully Optimized Contracted Gaussian Basis Sets for Atoms Lithiium to Krypton. *J. Chem. Phys.* **1992**, *97*, 2571-2577.

(50) Ahlrichs, R.; Coworkers., Unpublished.

(51) The PyMOL Molecular Graphics System, Version 1.5.0.4. Schrödinger, LLC.

3.7 Supporting Information

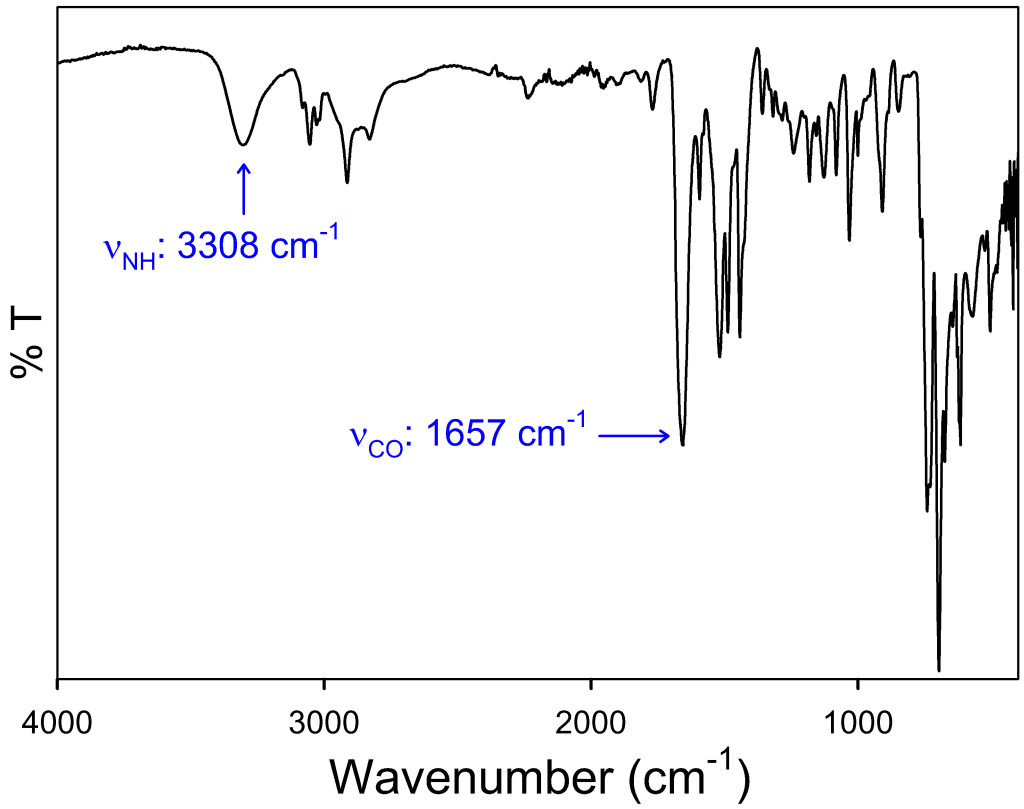

Figure 3.S1. Solid-state FTIR spectrum of $N_2S^{Me}STr$ in a KBr matrix.

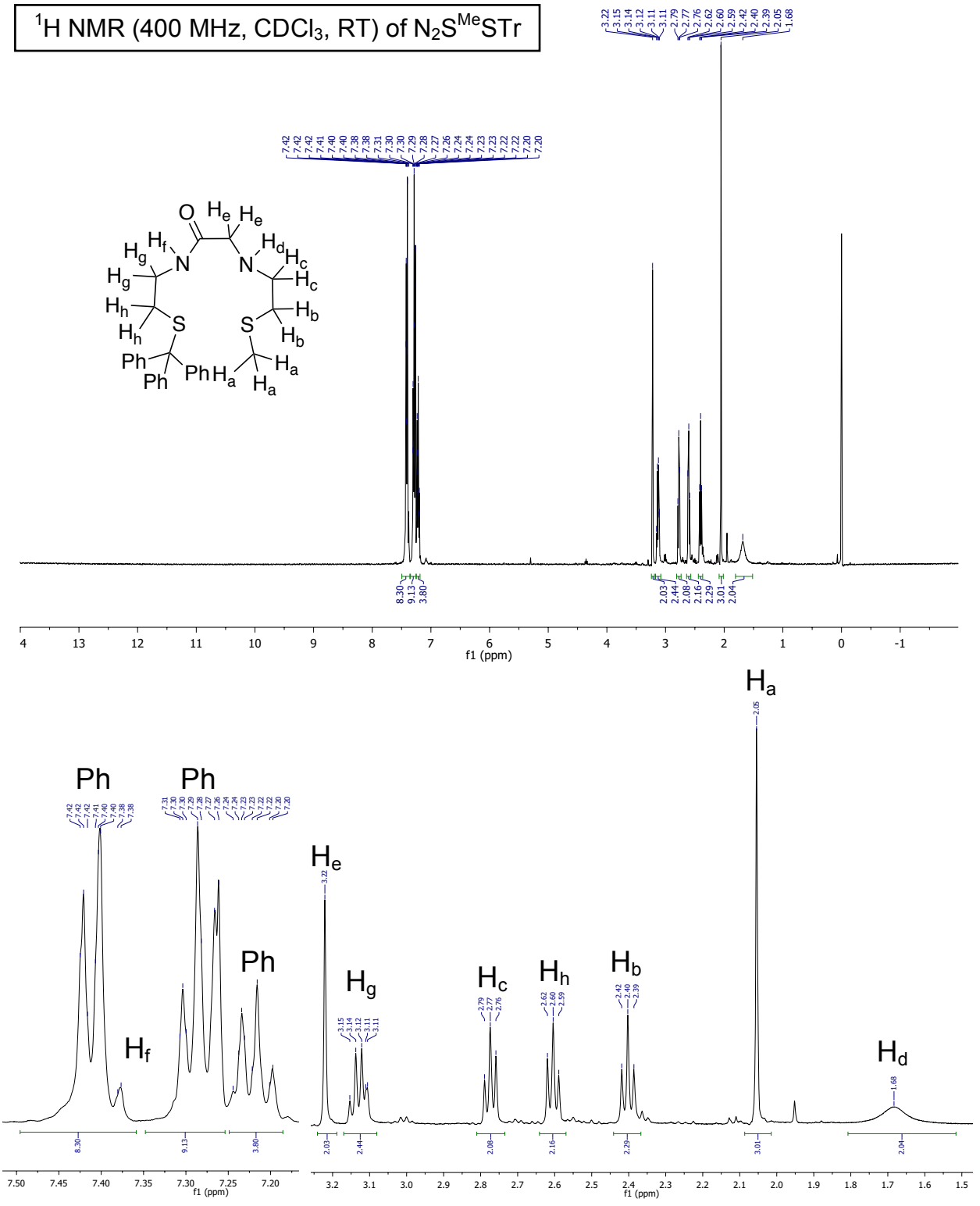

Figure 3.S2. *Top*: ^{1}H NMR spectrum of $N_2S^{Me}STr$ in $CDCl_3$ at RT. The peak at 7.27 ppm is from residual protio solvent. *Bottom*: Zoom-in of top spectrum with peak labels.

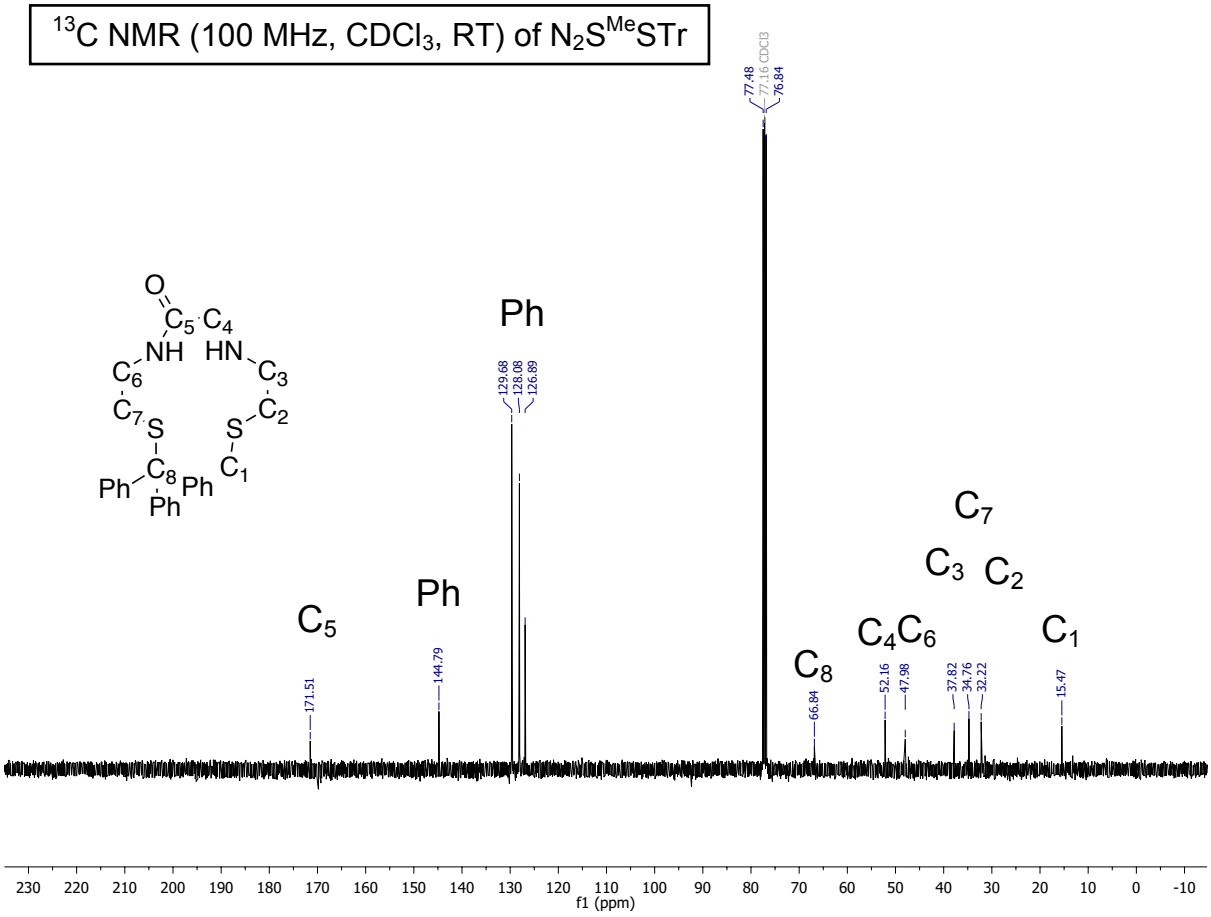

Figure 3.S3. ^{13}C NMR spectrum of $N_2S^{Me}STr$ in $CDCl_3$ at RT. The peak at 77.16 is from solvent.

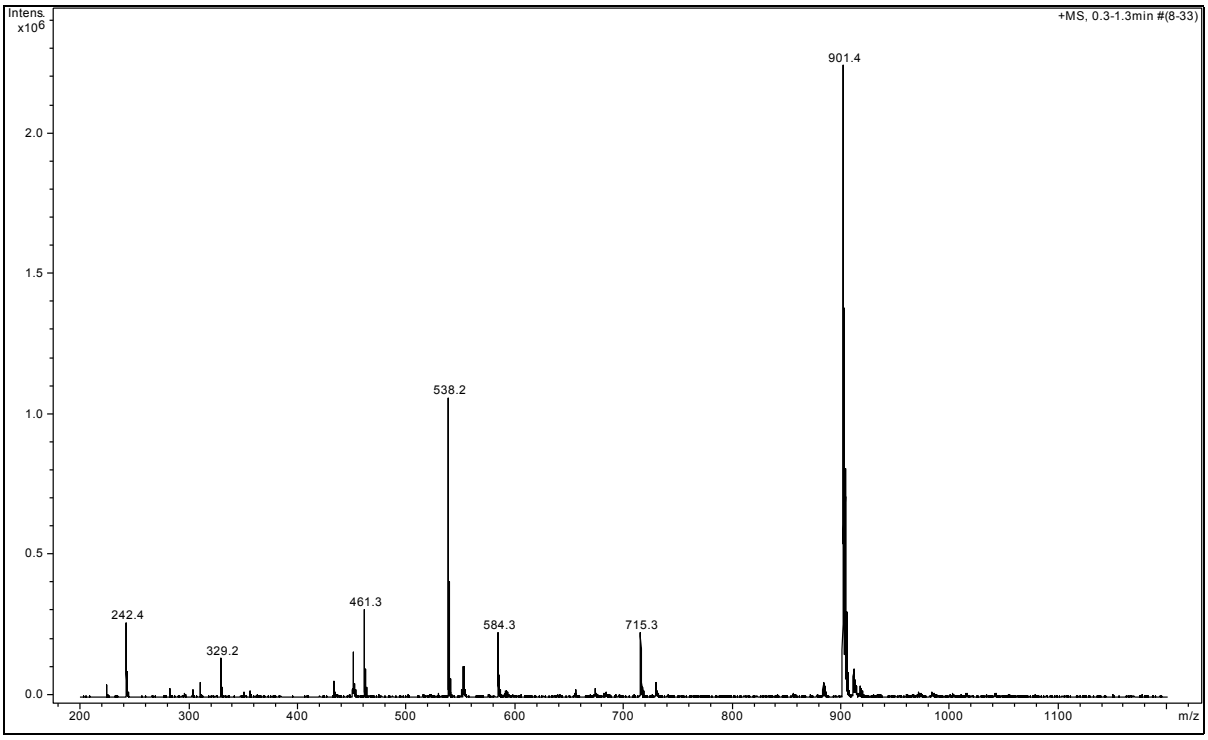

Figure 3.S4. LR-ESI-MS of $N_2S^{Me}STr$ in CH_2Cl_2 RT

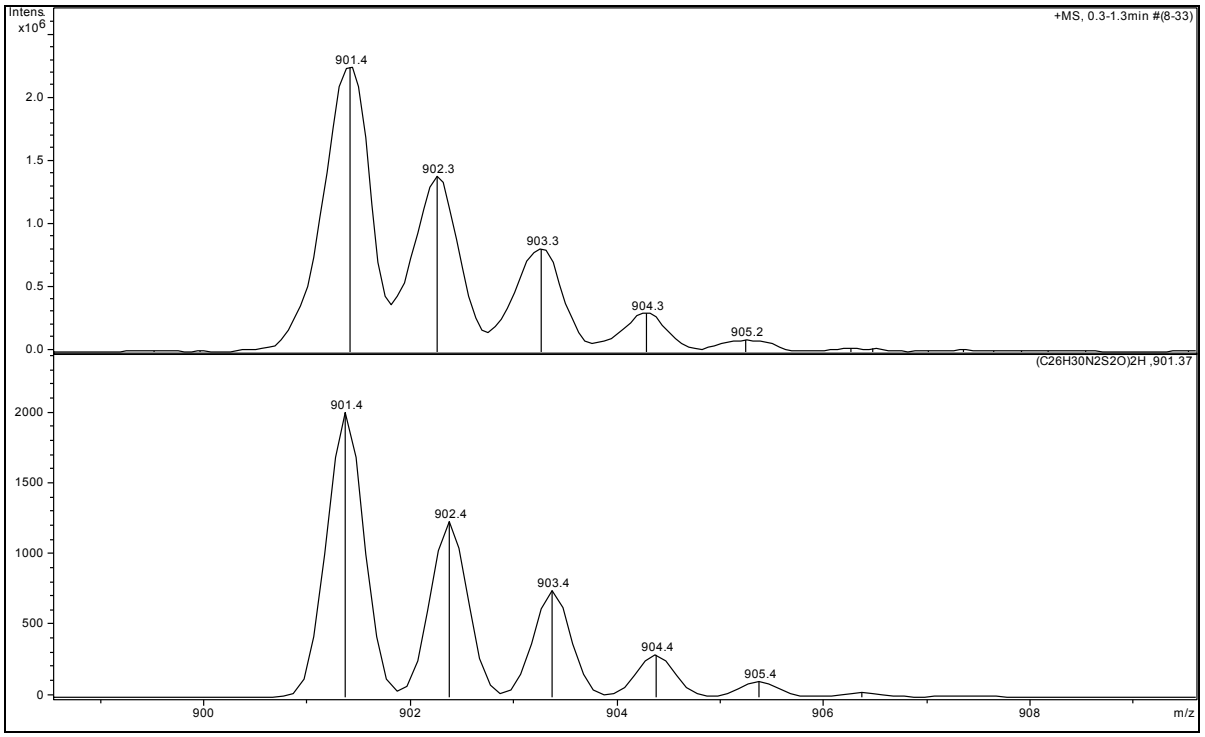

Figure 3.S5. LR-ESI-MS of $N_2S^{Me}STr$ in CH_2Cl_2 RT. *Top*: Low-resolution ESI-MS (positive mode) of the dimeric cation of $N_2S^{Me}STr$, $[2M+H]^+$. *Bottom*: Theoretical isotopic distribution.

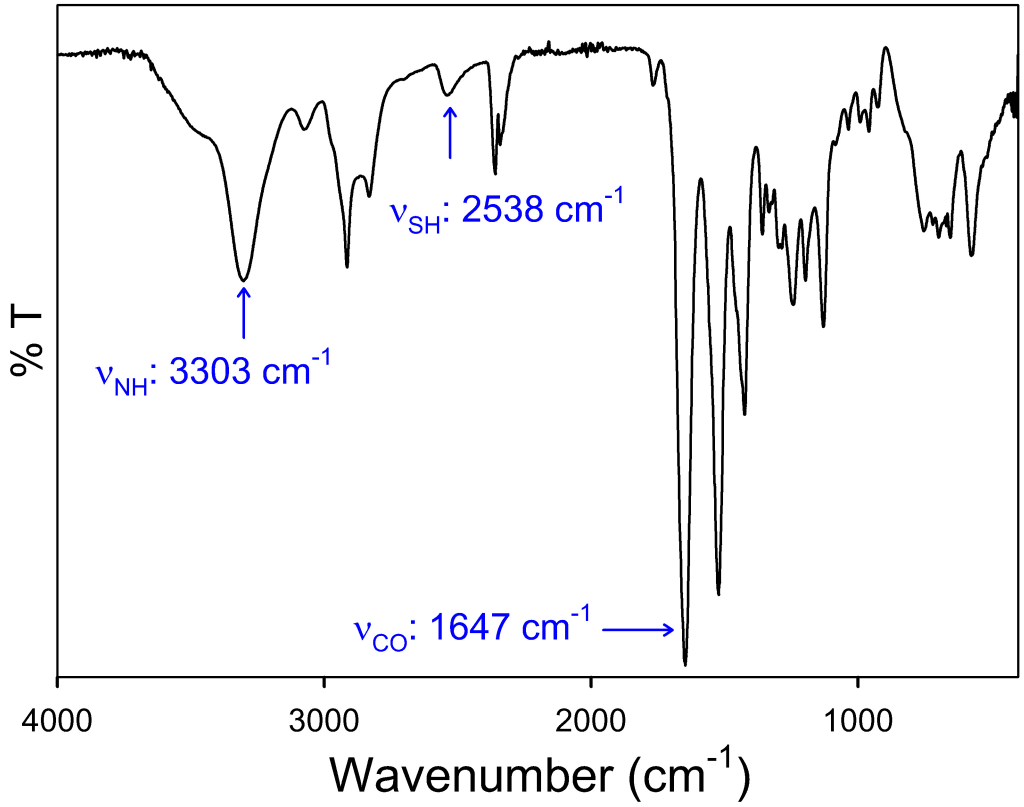

Figure 3.S6. Solid-state FTIR spectrum of $N_2S^{Me}SH_2$ in a KBr matrix.

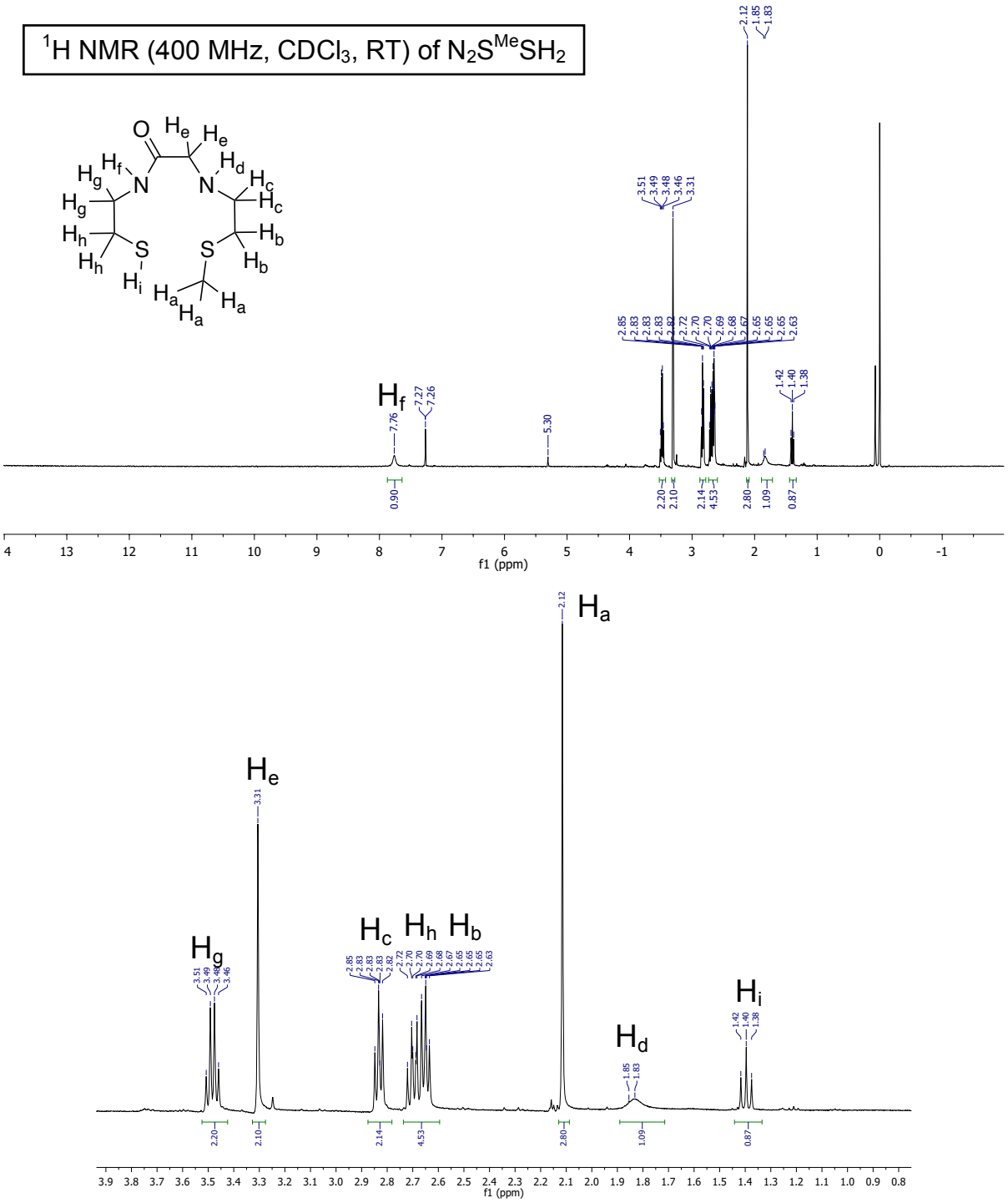

Figure 3.S7. *Top*: ^{1}H NMR spectrum of $N_2S^{Me}SH_2$ in $CDCl_3$ at RT. The peak at 7.27 ppm is from residual protio solvent. *Bottom*: Zoom-in of top spectrum with peak labels.

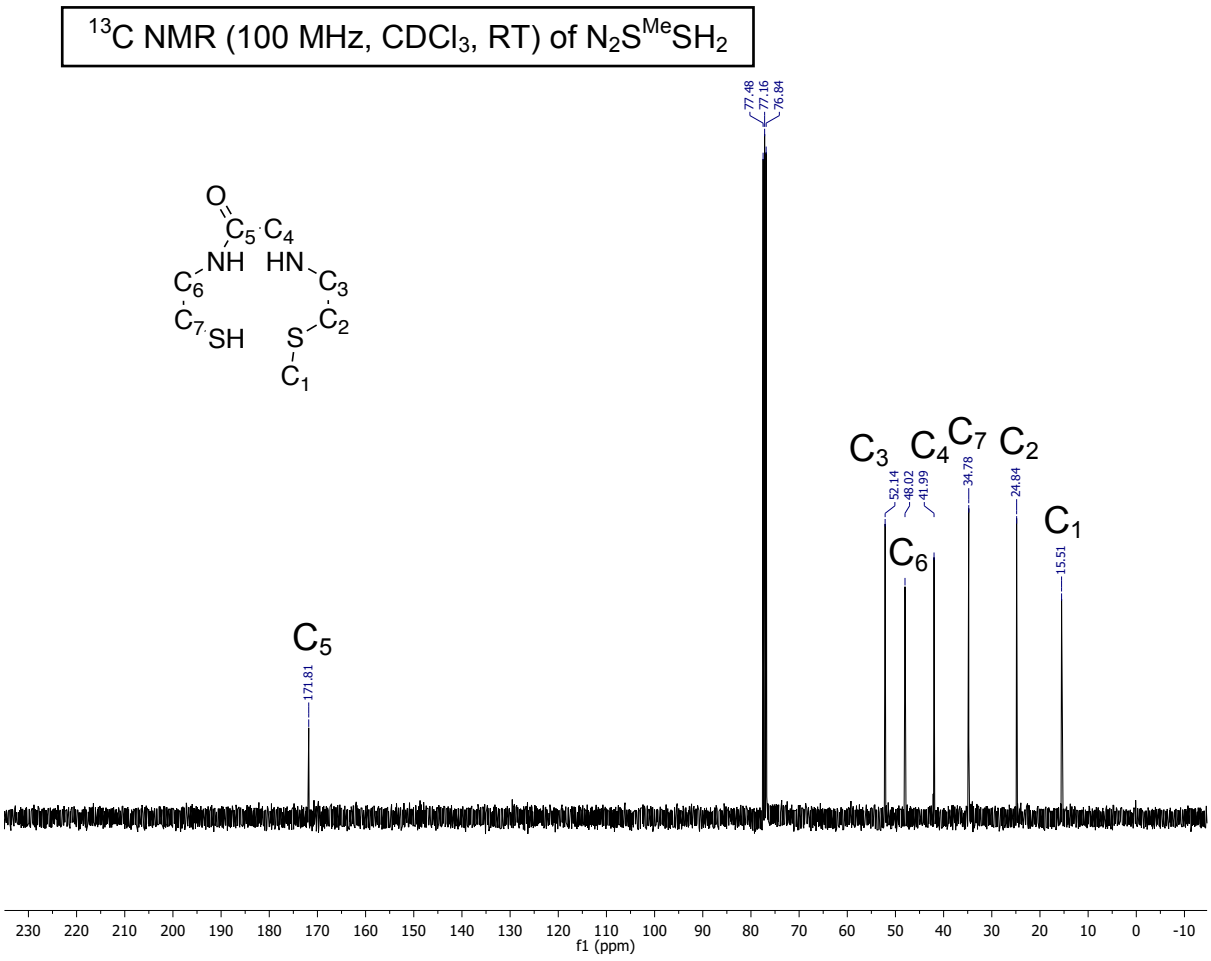

Figure 3.S8. ^{13}C NMR spectrum of $N_2S^{Me}SH_2$ in $CDCl_3$ at RT. The peak at 77.16 is from solvent.

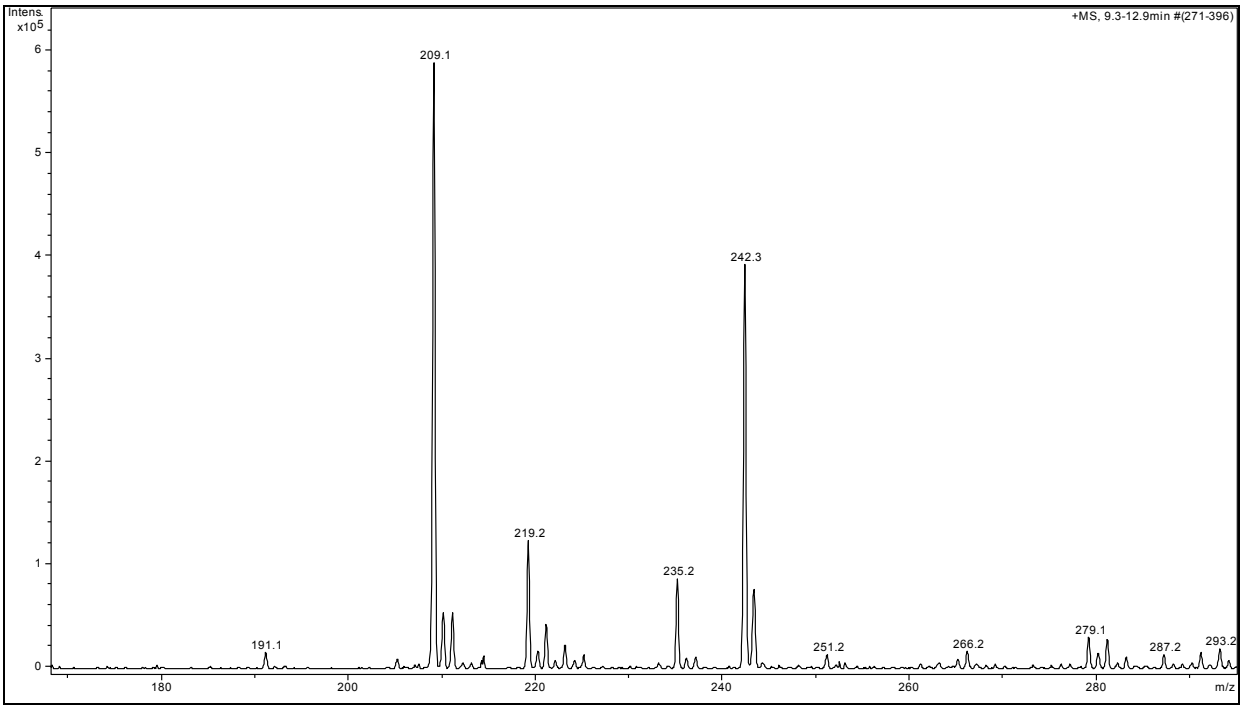

Figure 3.S9. LR-ESI-MS of $N_2S^{Me}SH_2$ in CH_2Cl_2 RT.

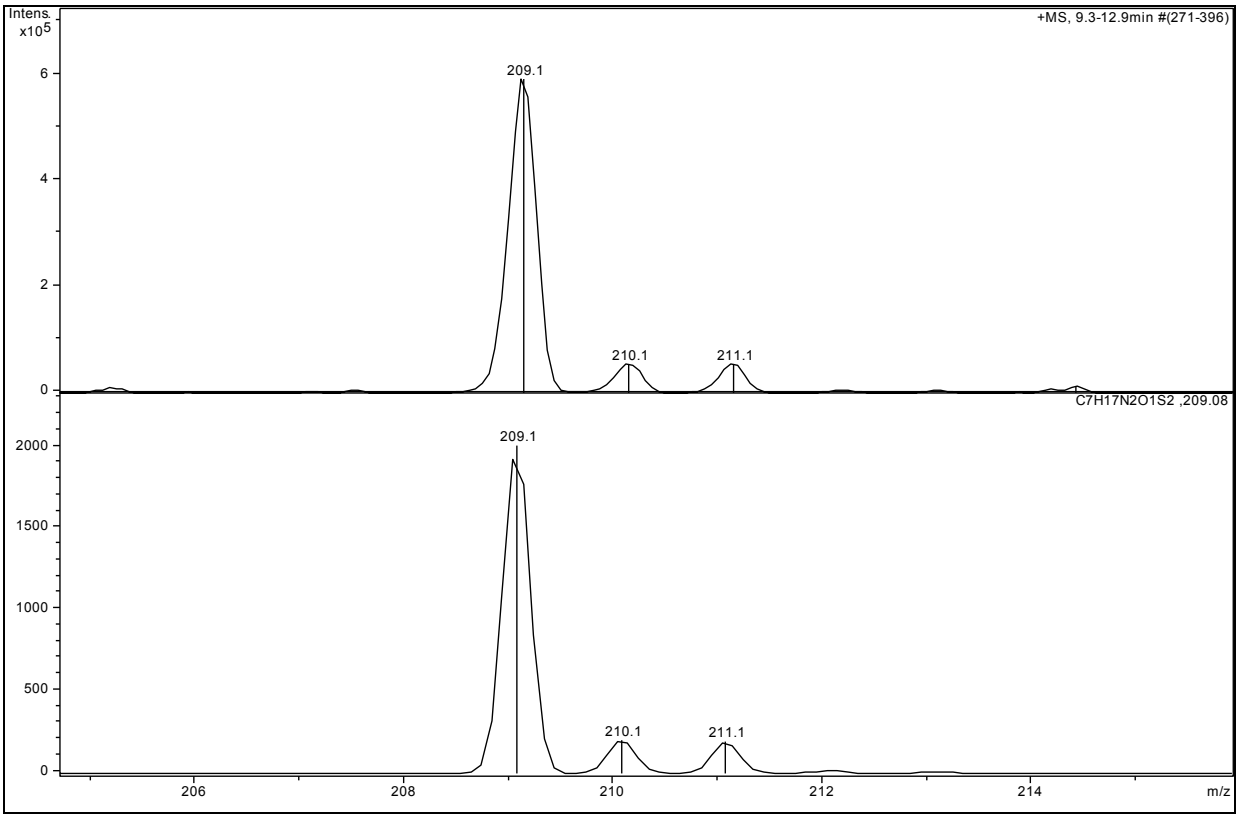

Figure 3.S10. LR-ESI-MS of $N_2S^{Me}SH_2$ in CH_2Cl_2 RT. *Top*: Low-resolution ESI-MS (positive mode) of the cation of $N_2S^{Me}SH_2$, $[M+H]^+$. *Bottom*: Theoretical isotopic distribution.

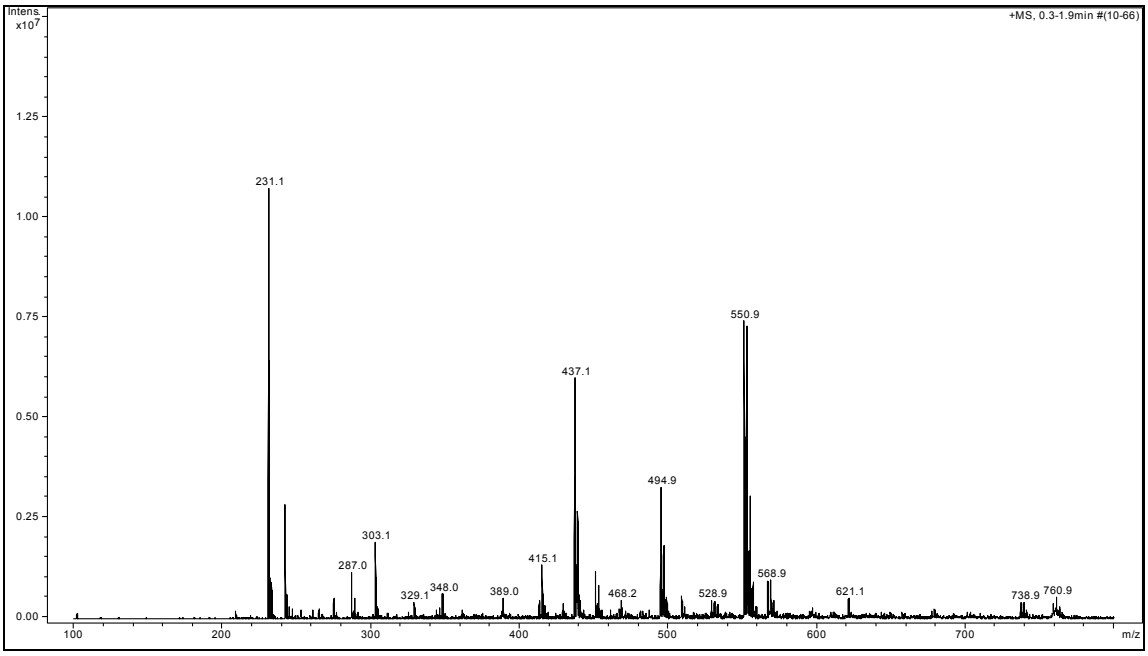

Figure 3.S11. LR-ESI-MS of **1** in MeOH RT.

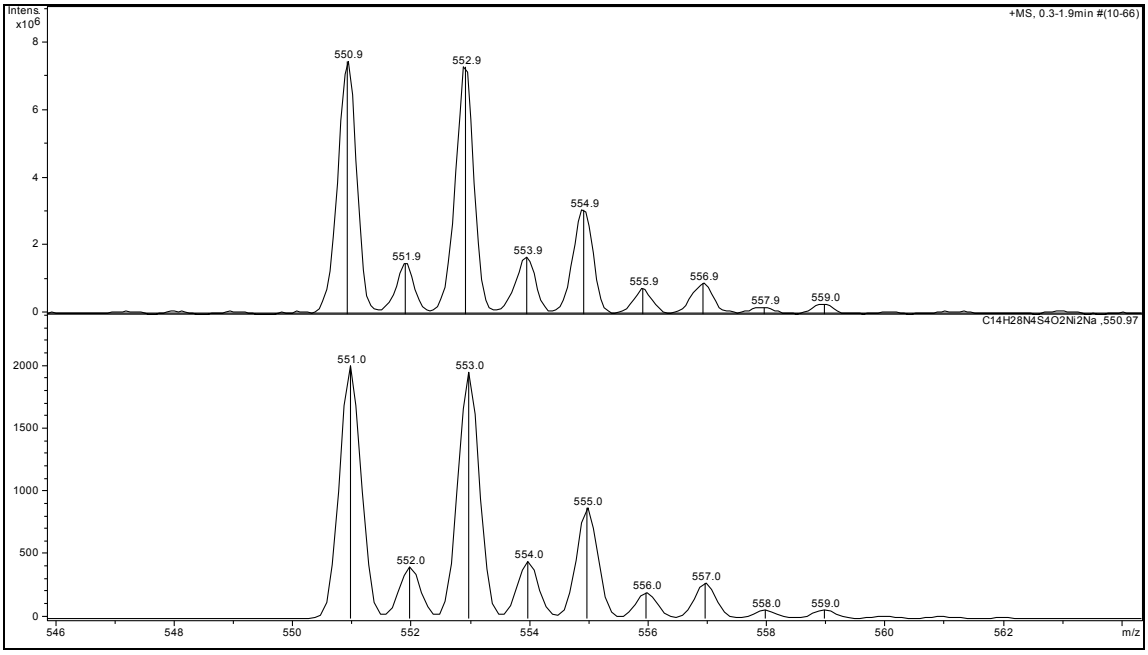

Figure 3.S12. LR-ESI-MS of **1** in MeOH RT. *Top*: Low-resolution ESI-MS (positive mode) of the dimeric cation of **1**, $[2M+Na]^+$. *Bottom*: Theoretical isotopic distribution.

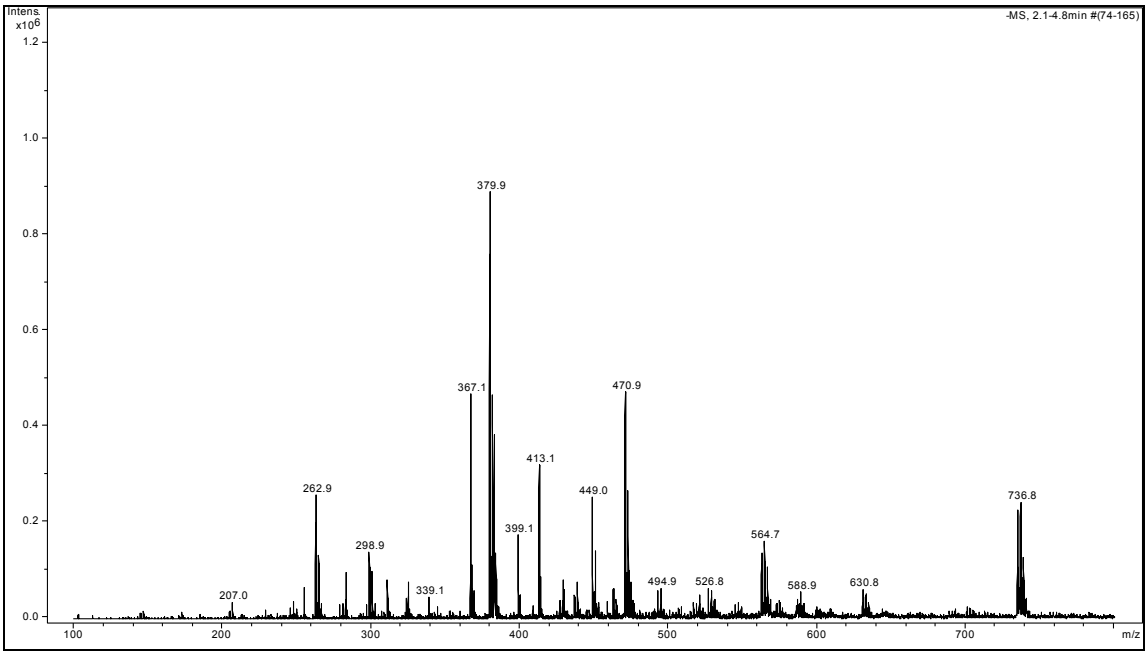

Figure 3.S13. LR-ESI-MS of **1** in MeOH RT.

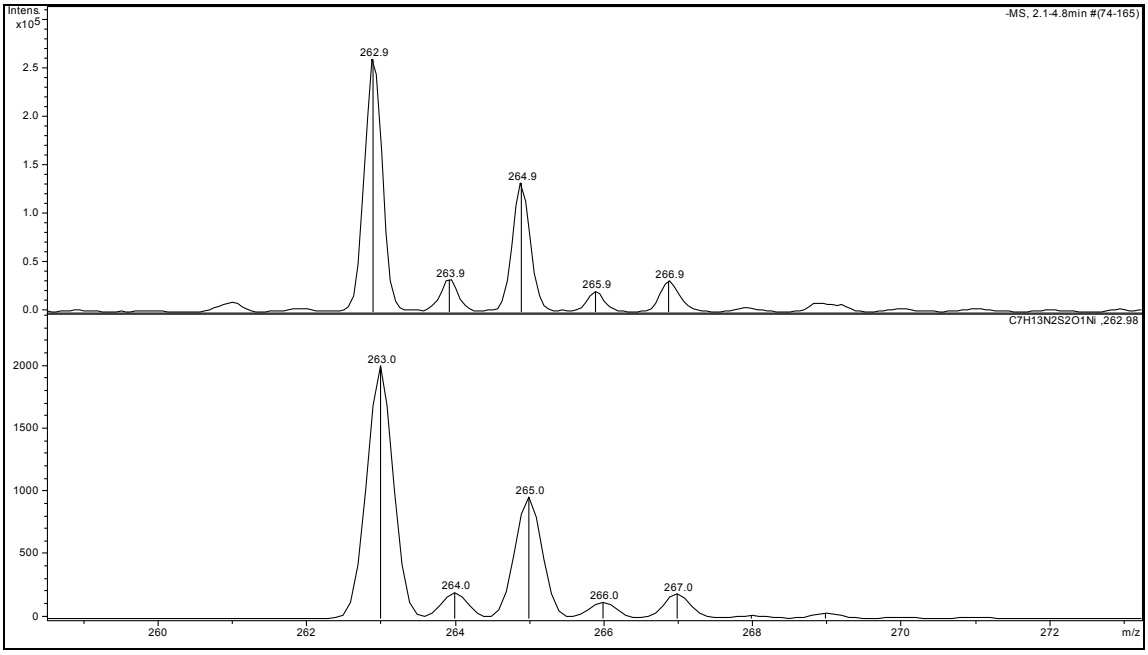

Figure 3.S14. LR-ESI-MS of **1** in MeOH RT. *Top*: Low-resolution ESI-MS (negative mode) of the anion of **1**, $[M–H]^-$. *Bottom*: Theoretical isotopic distribution.

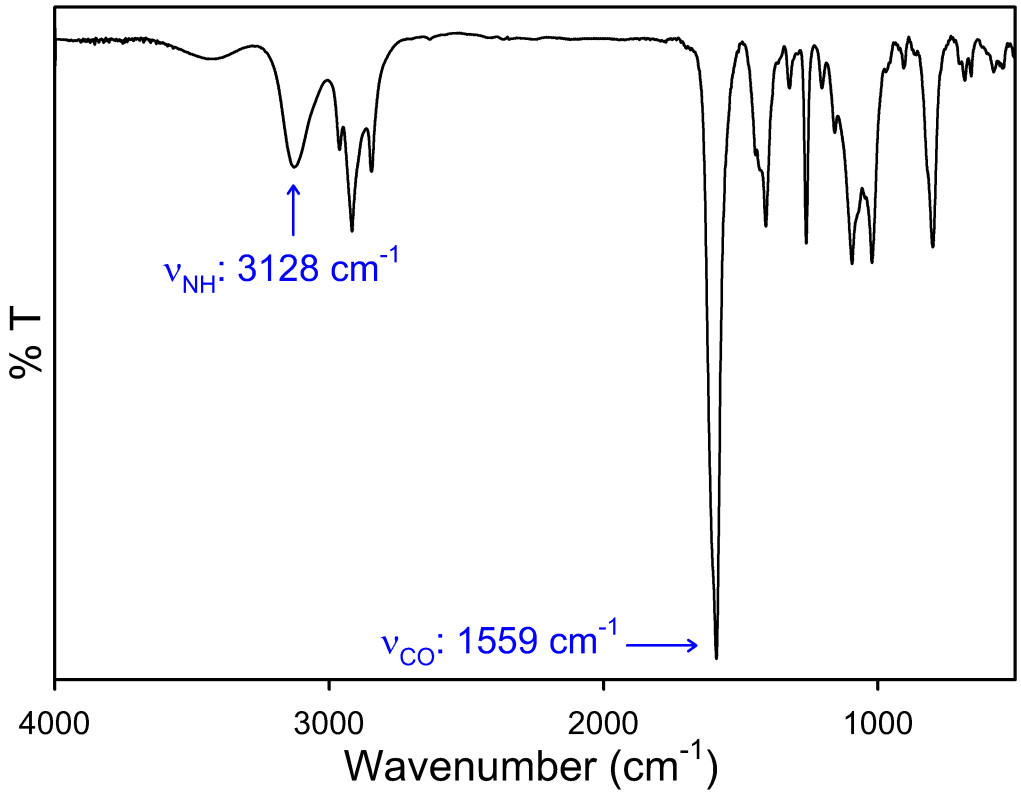

Figure 3.S15. Solid-state FTIR spectrum of **1** in a KBr matrix.

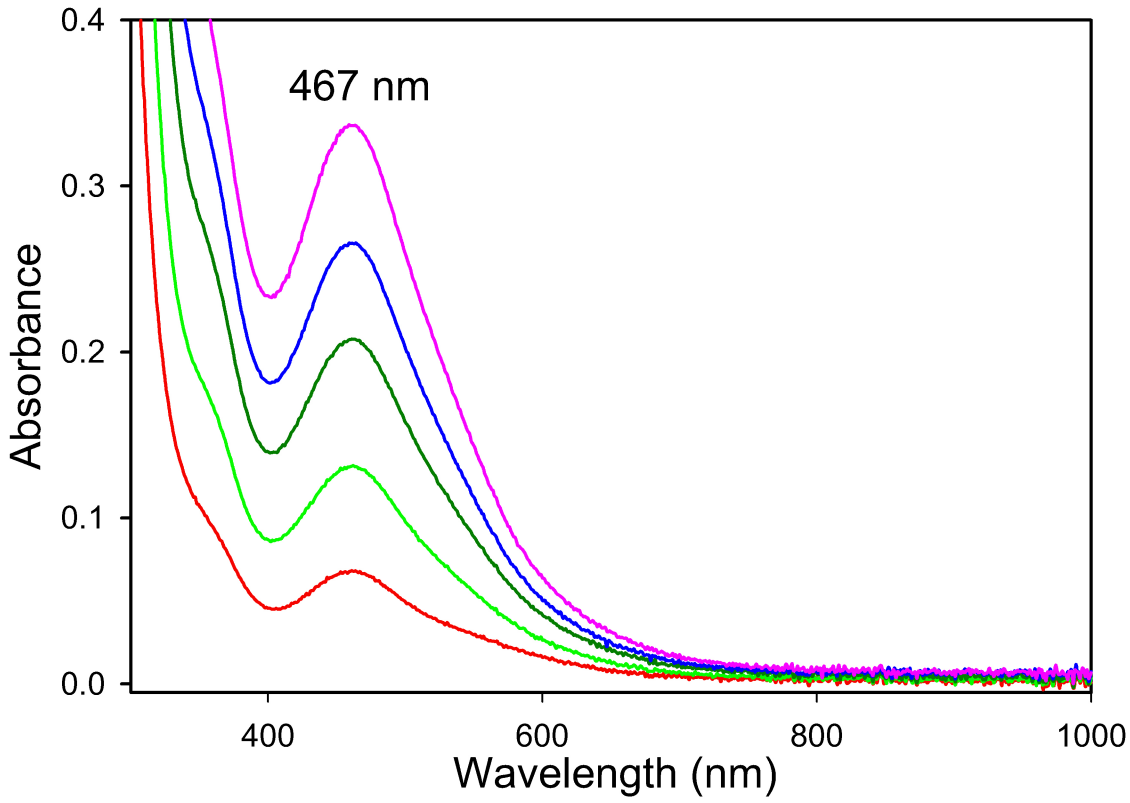

Figure 3.S16. Concentration-dependent UV-vis spectrum of **1** in DMF, 25 ºC. Concentrations of 0.50, 0.98, 1.5, 2.4 and 2.8 mM.

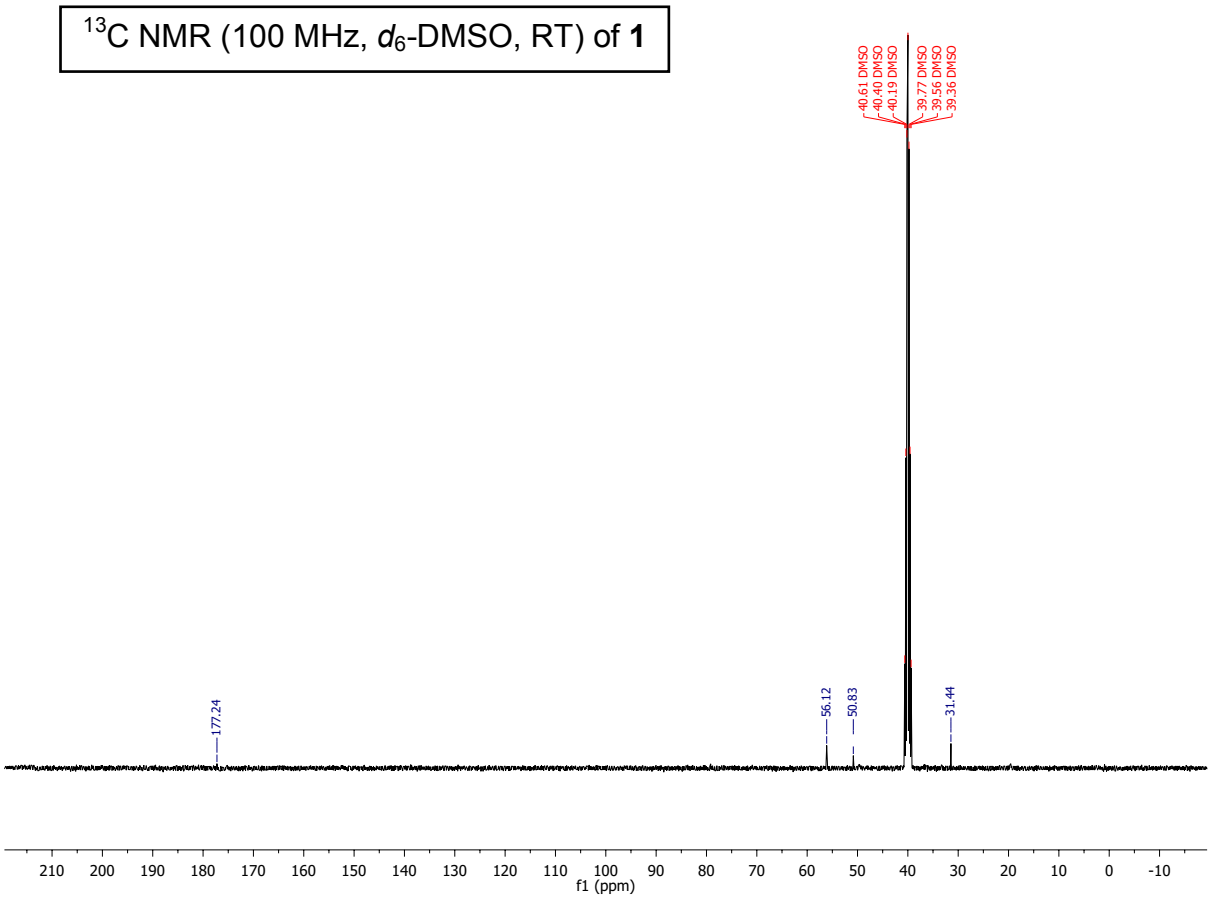

Figure 3.S17. ^{13}C NMR spectrum of **1** in d_6-DMSO at RT. The peak at 39.51 ppm is from residual solvent.

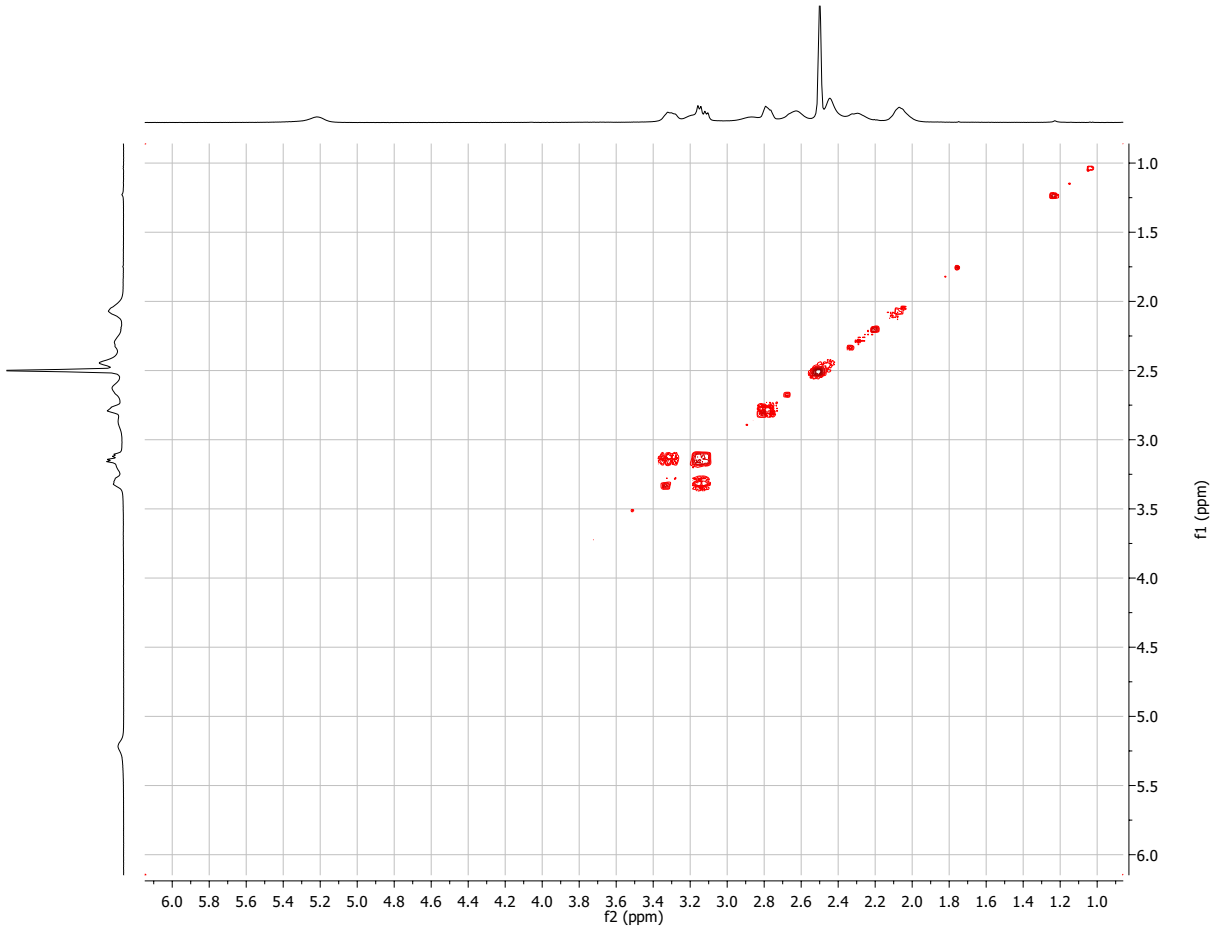

Figure 3.S18. COSY NMR spectrum of **1** in d_6-DMSO at RT.

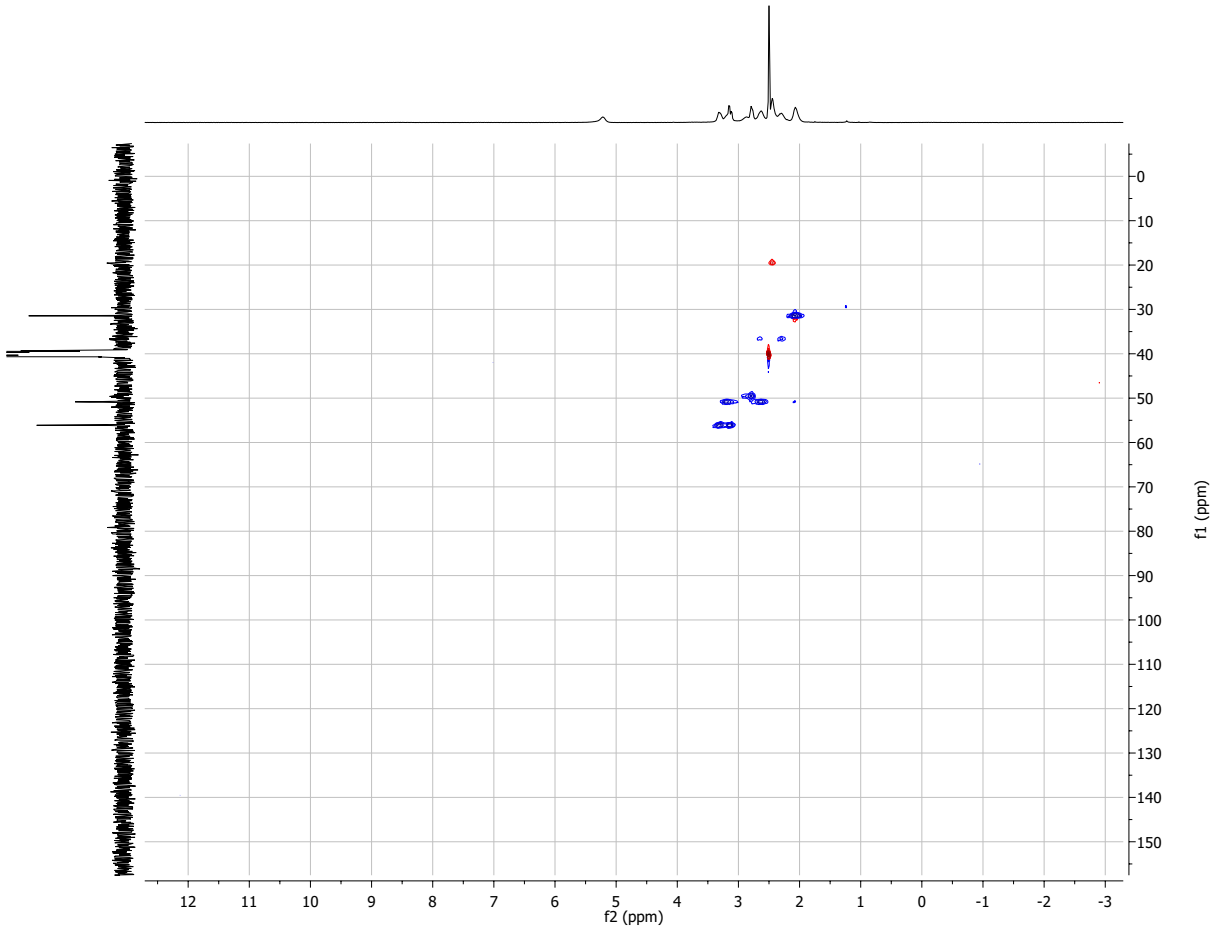

Figure 3.S19. HSQC NMR spectrum of **1** in d_6-DMSO at RT.

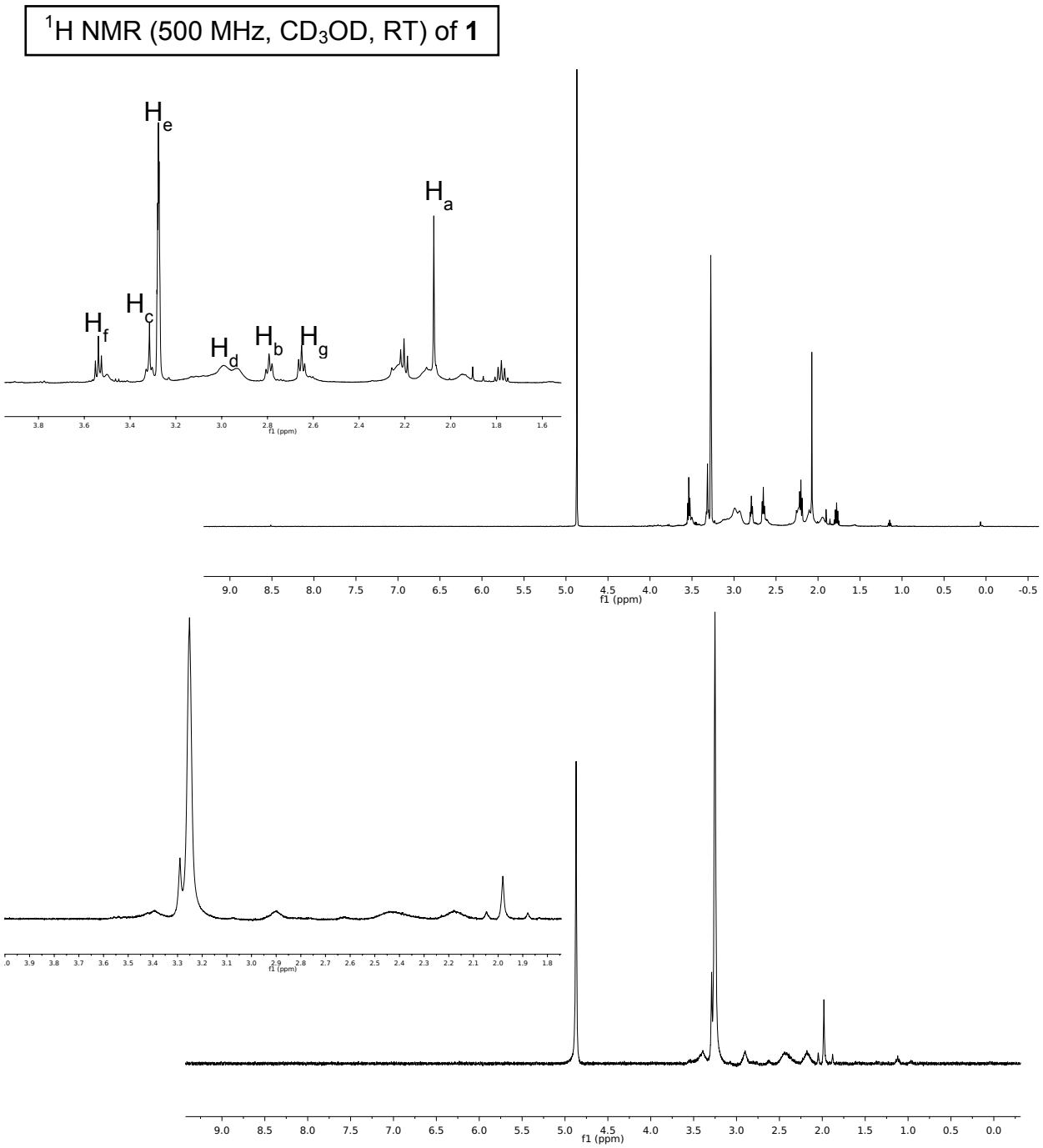

Figure 3.S20. ^{1}H NMR (CD_3OD, RT) from reaction of $Na_3[N_2S^{Me}S]$ with Ni(II) salts. (Top) 500 MHz spectrum of reaction with $[Ni(H_2O)_6](BF_4)_2$ exhibiting sharp signals characteristic of planar Ni(II). (Bottom) 400 MHz spectrum with $[Ni(H_2O)_6](ClO_4)_2$ with signal broadening. 3.31 ppm = residual MeOH; 4.87 ppm = H_2O.

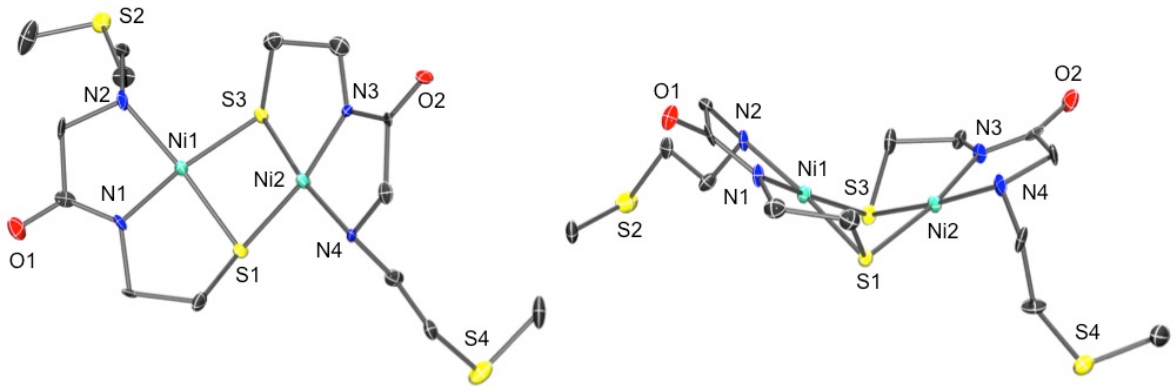

Figure 3.S21. ORTEP of $[Ni_2(N_2S^{Me}S)_2]$ (**[1]$_2$**) at 50% thermal probability. **(*Left*)** View of *S*,*S*-bridged species and uncoordinated thioether ligand. **(*Right*)** ~90° rotation (in plane defined by paper) of the depiction on the left showing the unique configuration of the Ni-S core.

Table 3.S1. Comparison of Ni-N/S bond distances (Å) with those reported from crystal structures of Ni-SOD[a] from *Streptomyces coelicolor* reported by Barondeau et al.[1] and of **[1]$_2$** (Harrop91).

	Ni-SOD [ref]		**Harrop91**
Ni-N1	1.91(3)	Ni(1)-N(1), Ni(2)-N(3)	1.850(12), 1.856(12)
Ni-N2	1.87(6)	Ni(1)-N(2), Ni(2)-N(4)	1.929(12), 1.952(11)
Ni-S1	2.16(2)	Ni(1)-S(1), Ni(2)-S(3)	2.168(4), 2.171(4)
Ni-S2	2.19(2)	Ni(1)-S(3), Ni(2)-S(1)	2.190(4), 2.201(5)

[a]N1, N2, S1, and S2 correspond to N_{amide} from Cys2, N_{His1}, S_{Cys2}, and S_{Cys6}, respectively.

Table 3.S2. Summary of Crystal Data and Intensity Collection and Structure Refinement Parameters for **[1]$_2$** (Harrop91)

Parameters	**Harrop91**
Formula	$C_{14}H_{28}N_4Ni_2O_2S_4$
Formula weight	530.06
Crystal system	Monoclinic
Space group	C2/c
Crystal color, habit	brown, blade
a, Å	20.390(12)
b, Å	10.057(6)
c, Å	21.892(13)
α, deg	90
β, deg	109.319(8)
γ, deg	90
V, Å^3	4236(4)
Z	8
$\rho_{calcd,}$ g/cm^3	1.662
T, K	100
abs coeff, μ (Mo Kα), mm^{-1}	2.189
θ limits, deg	1.97-26.44
total no. of data	4491
no. of unique data	4491
no. of parameters	236
GOF of F^2	1.084
R_1,[a] %	0.1036
wR_2,[b] %	0.2222
max, min peaks, e/Å^3	1.516, -0.943

[a]$R_1 = \Sigma| |F_O| - |F_c| | / \Sigma |F_O|$; [b]$wR_2 = \{\Sigma[w(F_o^2 - F_c^2)^2]/\Sigma[w(F_o^2)^2]\}^{1/2}$

Table 3.S3. Selected Bond Distances (Å) and Bond Angles (deg) for $\mathbf{[1]_2}$ (Harrop91).

	Harrop91
Ni(1)-N(1)	1.850(12)
Ni(1)-N(2)	1.929(12)
Ni(1)-S(1)	2.168(4)
Ni(1)-S(3)	2.190(4)
Ni(1)-Ni(2)	2.823(3)
Ni(2)-N(3)	1.856(12)
Ni(2)-N(4)	1.952(11)
Ni(2)-S(3)	2.171(4)
Ni(2)-S(1)	2.201(5)
N(1)-Ni(1)-N(2)	85.6(6)
N(1)-Ni(1)-S(1)	88.5(4)
N(2)-Ni(1)-S(1)	173.8(4)
N(1)-Ni(1)-S(3)	170.8(4)
N(2)-Ni(1)-S(3)	101.5(4)
S(1)-Ni(1)-S(3)	84.28(15)
N(3)-Ni(2)-N(4)	85.1(5)
N(3)-Ni(2)-S(3)	88.3(4)
N(4)-Ni(2)-S(3)	172.8(4)
N(3)-Ni(2)-S(1)	170.5(4)
N(4)-Ni(2)-S(1)	102.9(4)
S(3)-Ni(2)-S(1)	83.92(15)

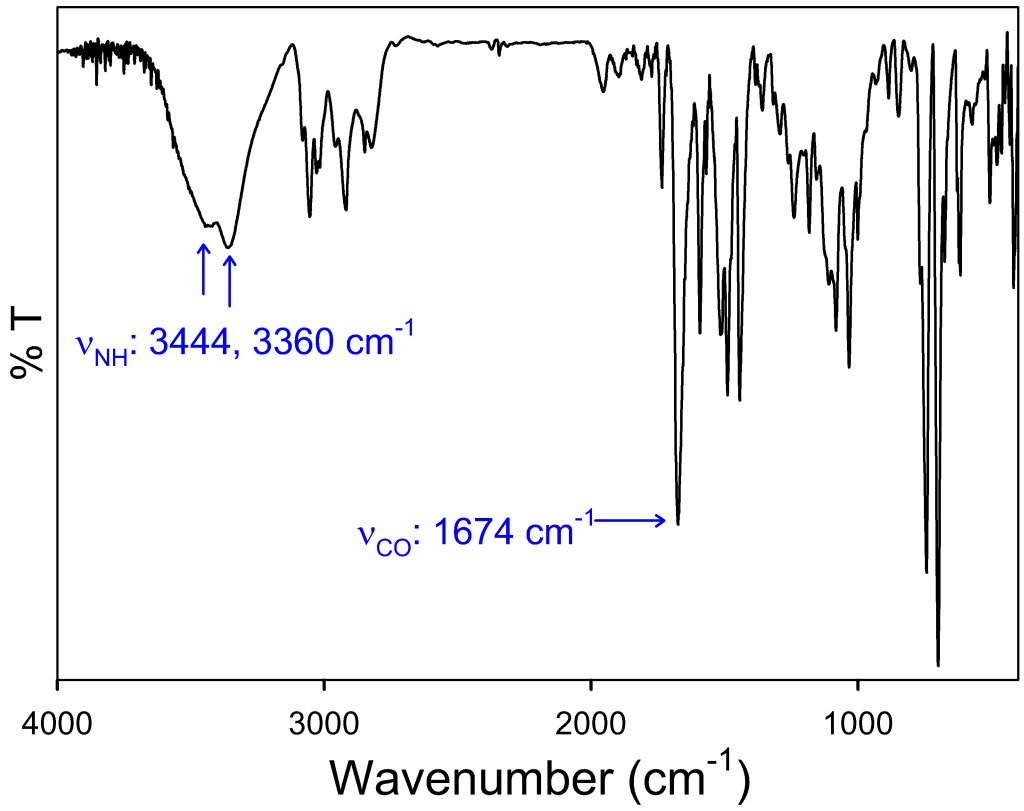

Figure 3.S22. Solid-state FTIR spectrum of $N_3S_2^{py2}Tr$ in a KBr matrix.

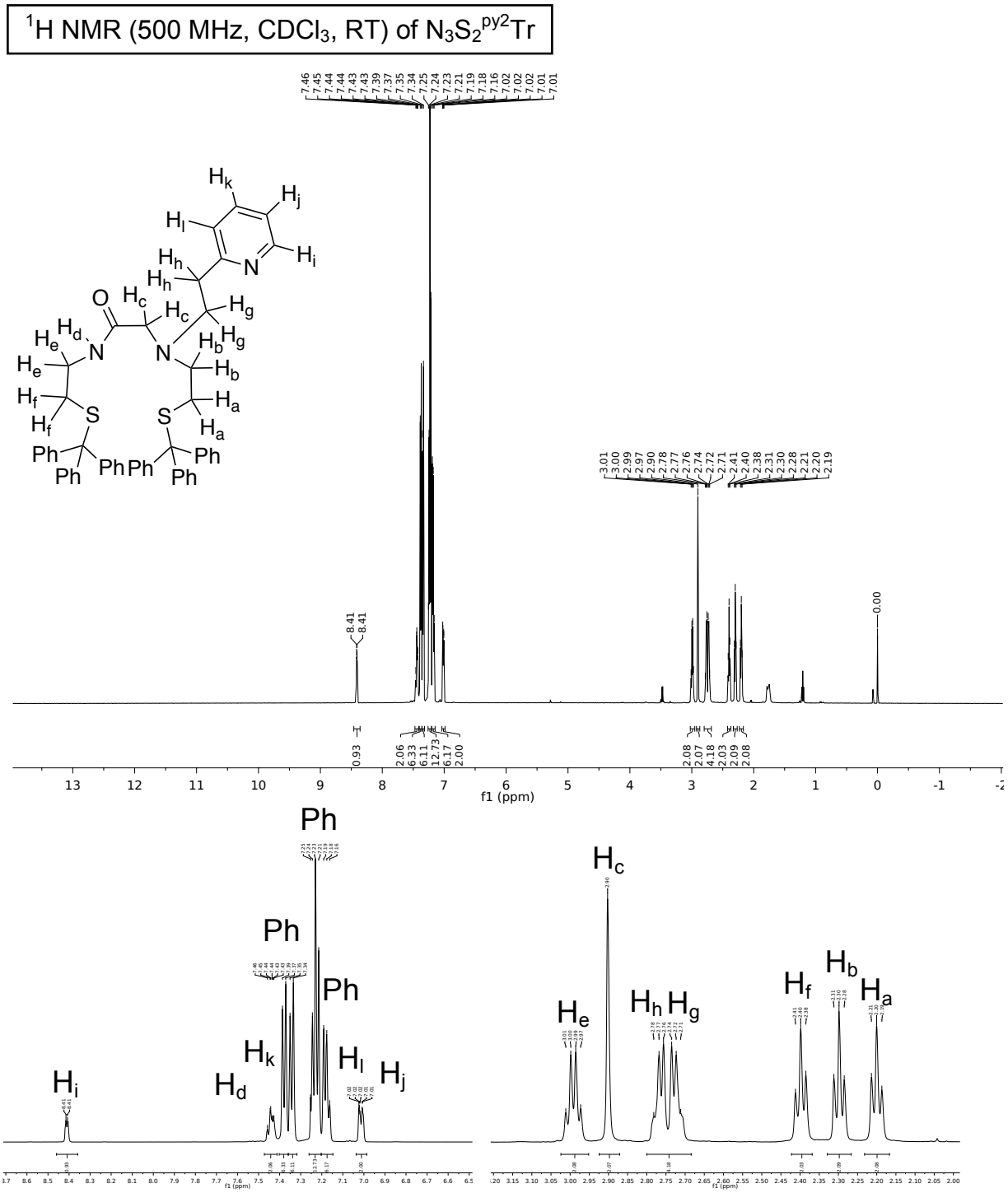

Figure 3.S23. *Top*: ^{1}H NMR spectrum of $N_3S_2^{py2}Tr$ in $CDCl_3$ at RT. The peaks at 7.27 and 1.75 ppm are from residual protio solvent and H_2O, respectively. The peaks at 3.47 and 1.21 ppm are from Et_2O. *Bottom*: Zoom-in of top spectrum with peak labels.

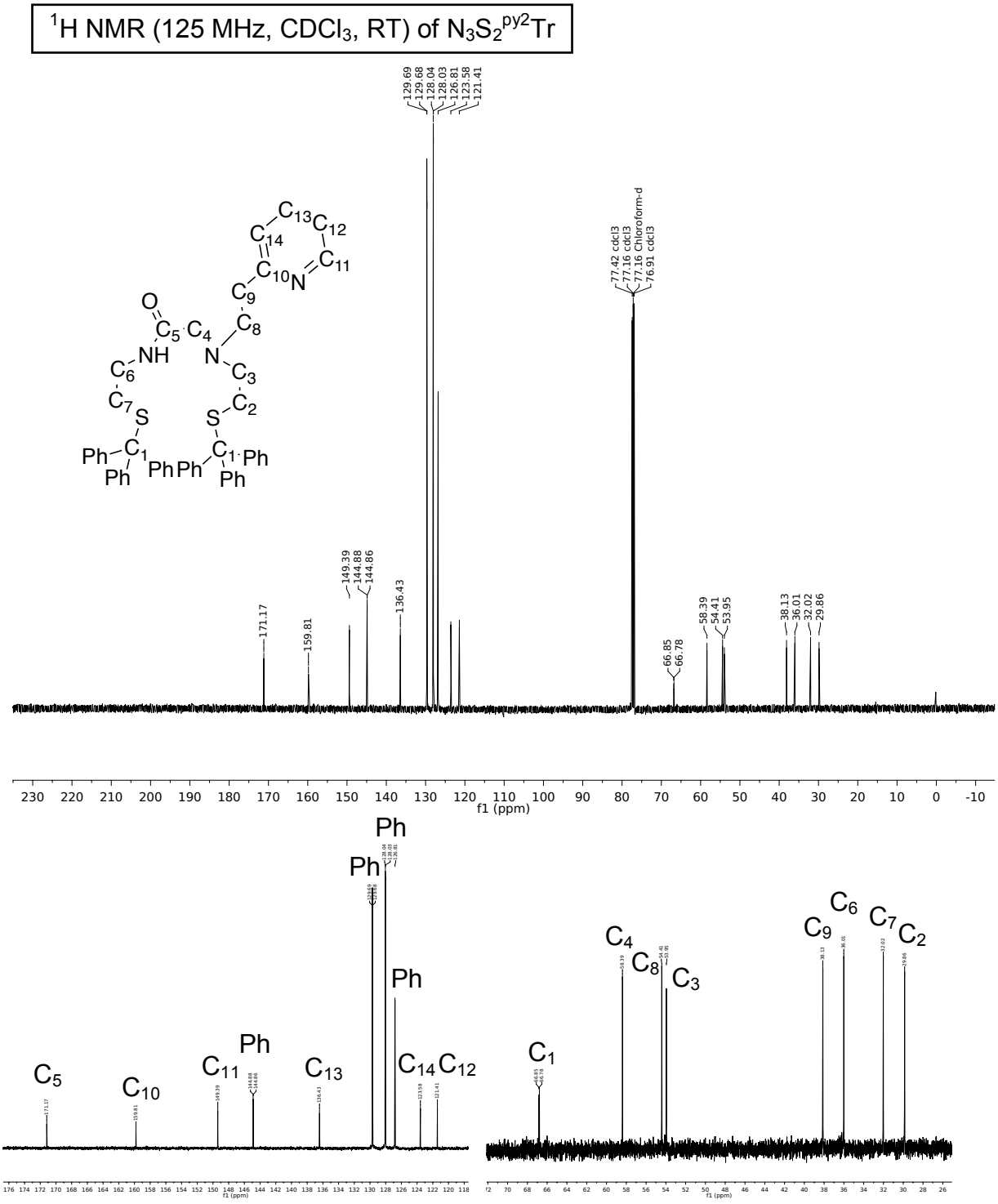

Figure 3.S24. *Top*: ^{13}C NMR spectrum of $N_3S_2^{py2}Tr$ in $CDCl_3$ at RT. The peak at 77.16 is from solvent. *Bottom*: Zoom-in of top spectrum with peak labels.

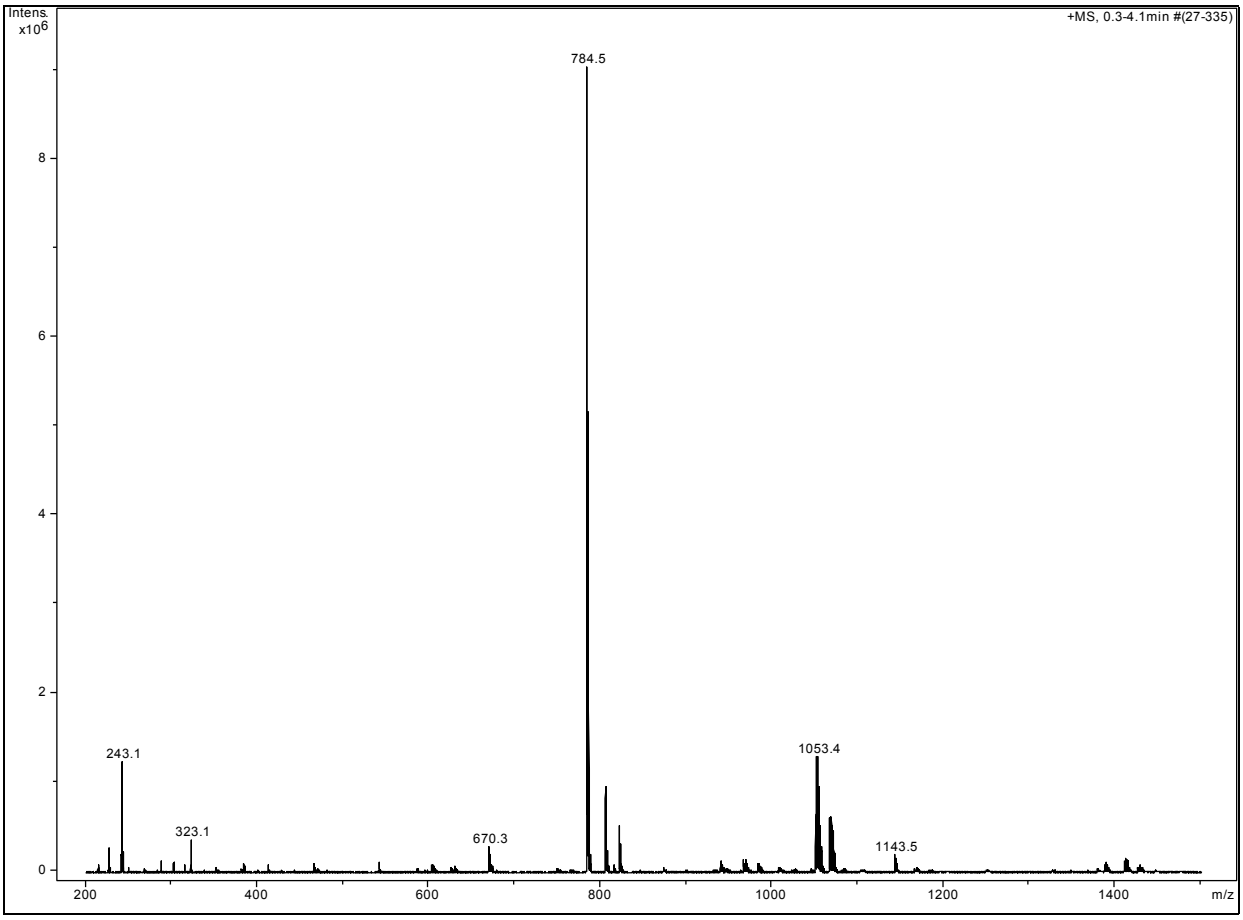

Figure 3.S25. LR-ESI-MS of $N_3S_2^{py2}Tr$ in CH_3OH RT.

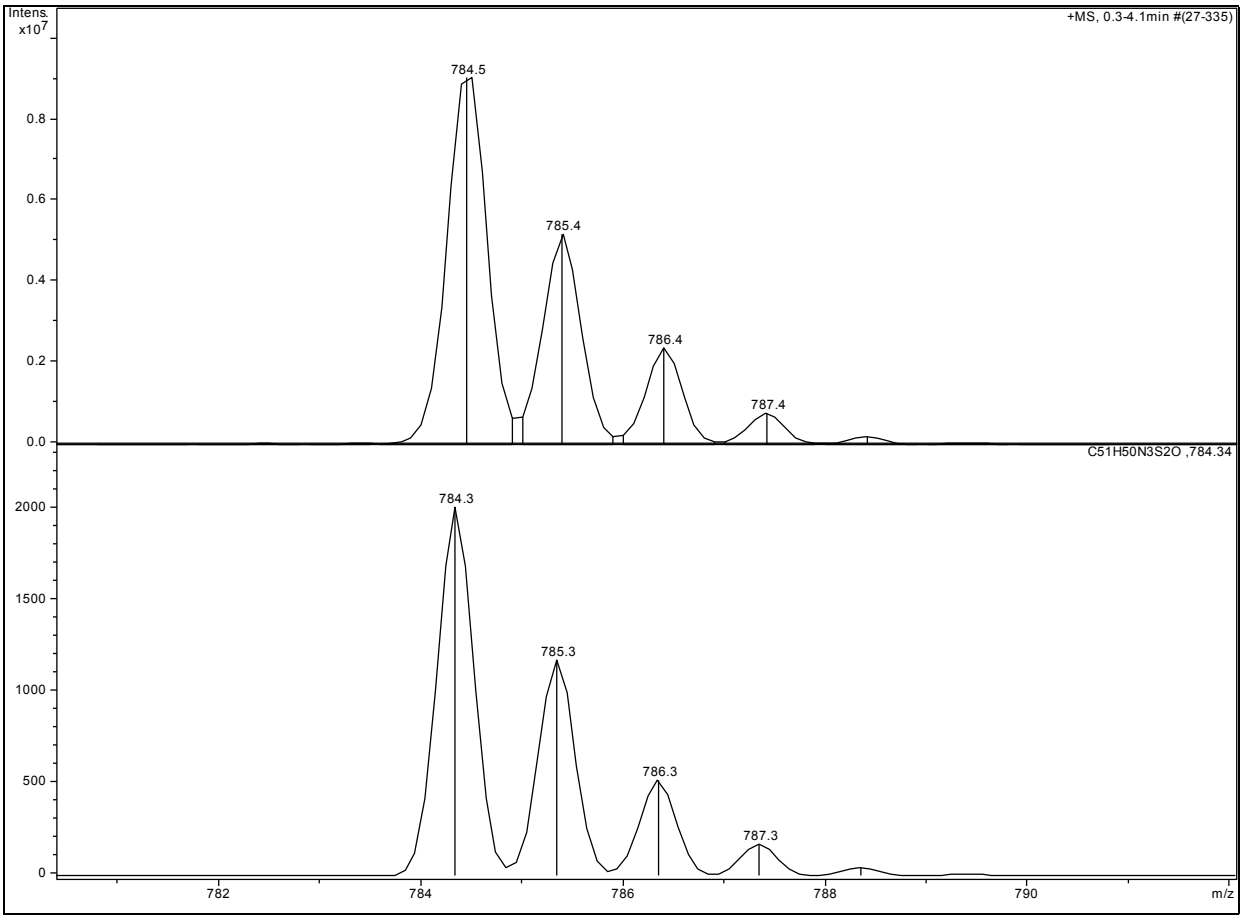

Figure 3.S26. LR-ESI-MS of $N_3S_2^{py2}Tr$ in CH_3OH RT. *Top*: Low-resolution ESI-MS (positive mode) of the cation of $N_3S_2^{py2}Tr$, $[M+H]^+$. *Bottom*: Theoretical isotopic distribution.

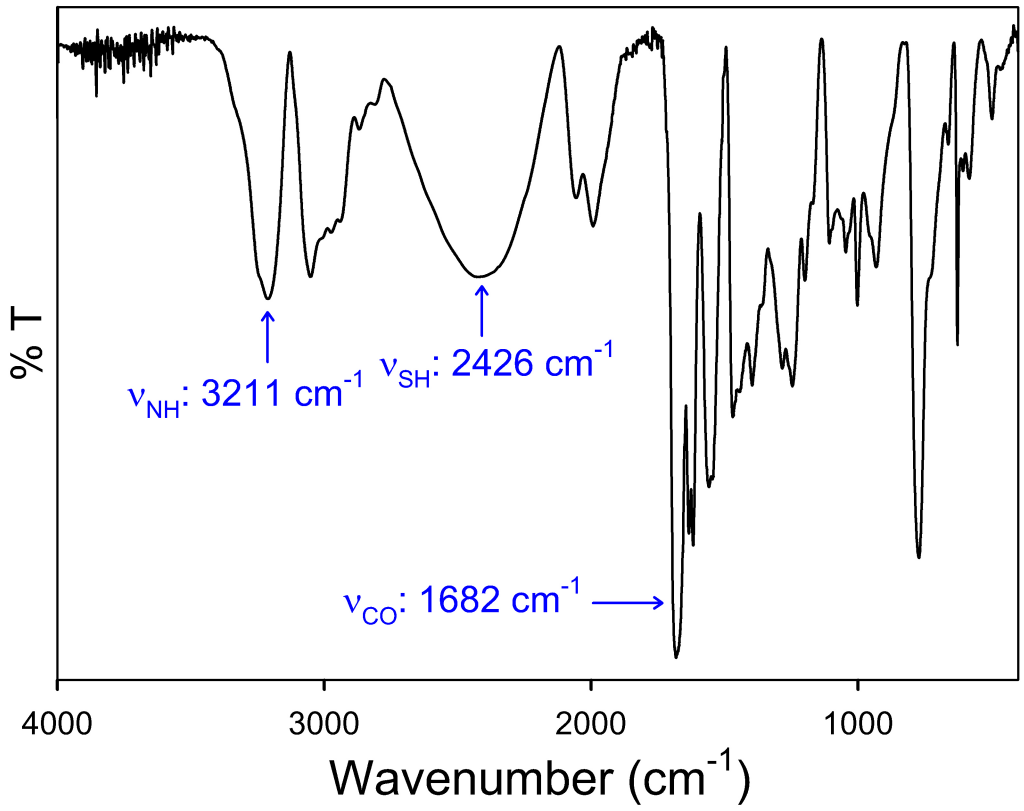

Figure 3.S27. Solid-state FTIR spectrum of $N_3S_2^{py2}H_3 \cdot 2HCl$ in a KBr matrix.

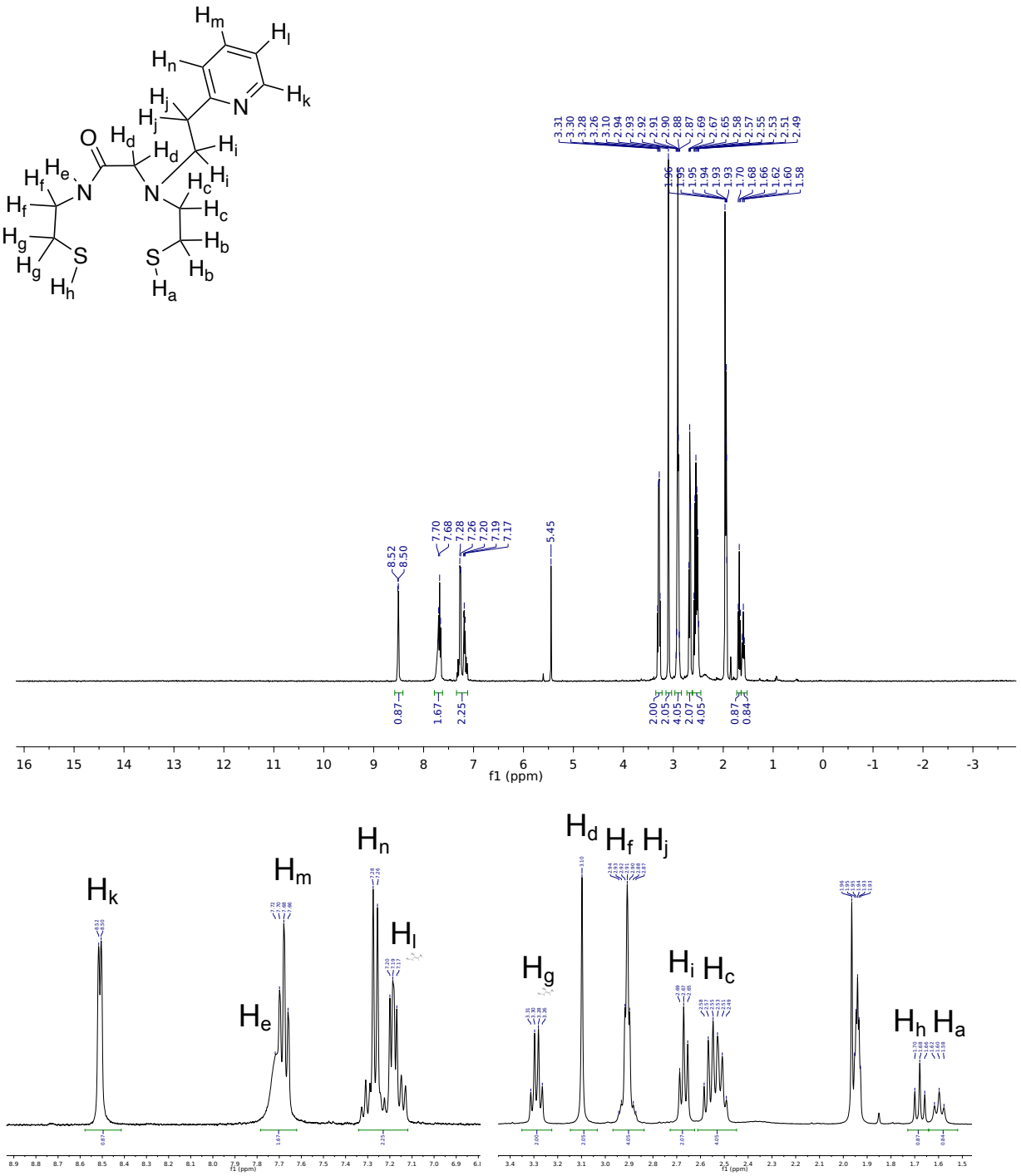

Figure 3.S28. *Top*: ^{1}H NMR spectrum of $N_3S_2{}^{py2}H_3$ in CD_3CN at RT. The peaks at 1.94 and 1.96 ppm are from residual protio solvent. The peak at 5.45 ppm is from CH_2Cl_2. *Bottom*: Zoom-in of top spectrum with peak labels.

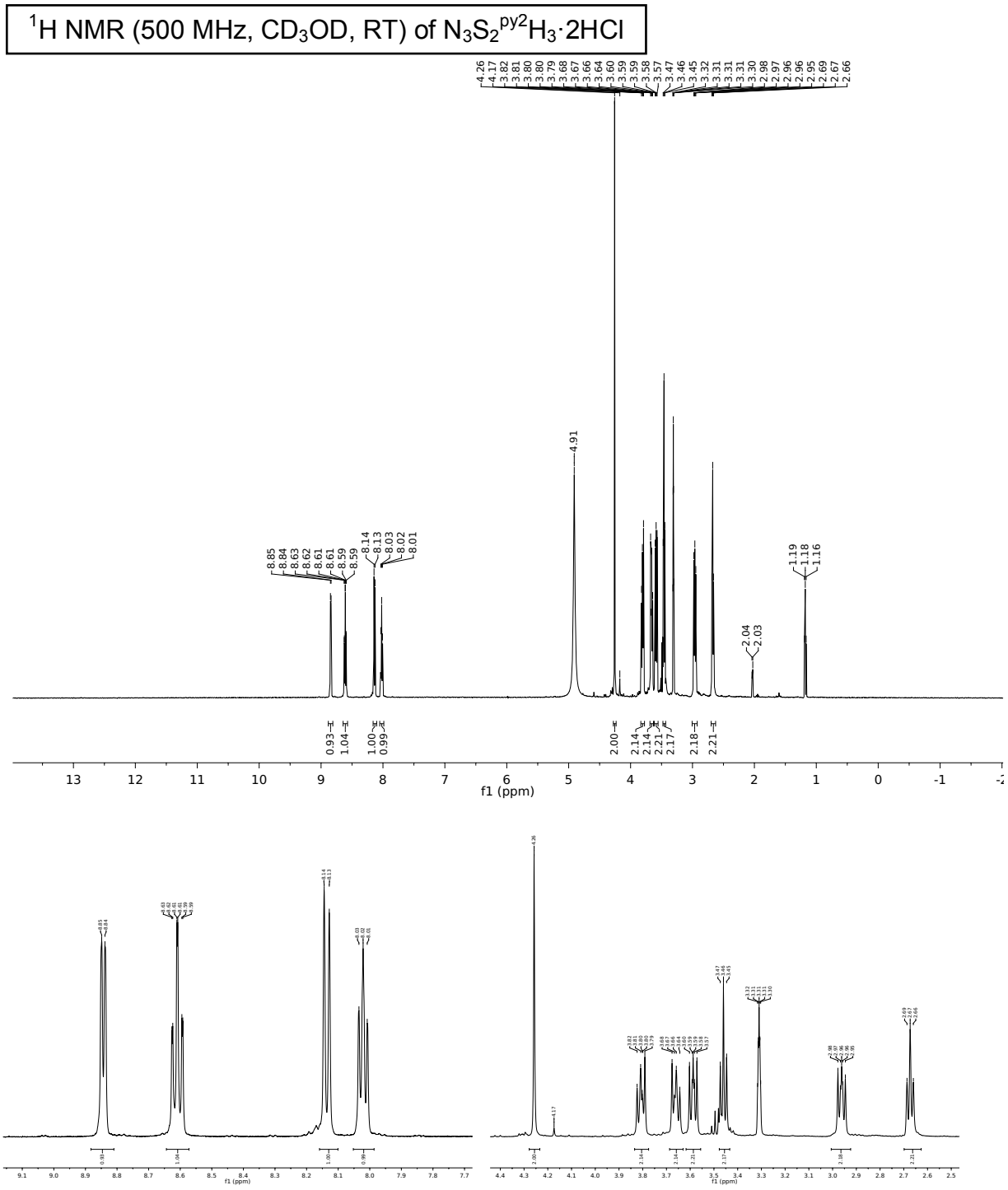

Figure 3.S29. *Top*: ^{1}H NMR spectrum of $N_3S_2{}^{py2}H_3 \cdot 2HCl$ in CD_3OD at RT. The peaks at 3.31 and 4.91 ppm are from residual protio solvent and H_2O. The peaks at 1.18 ppm and 2.03 are from Et_2O and CH_3CN, respectively. *Bottom*: Zoom-in of top spectrum with peak labels.

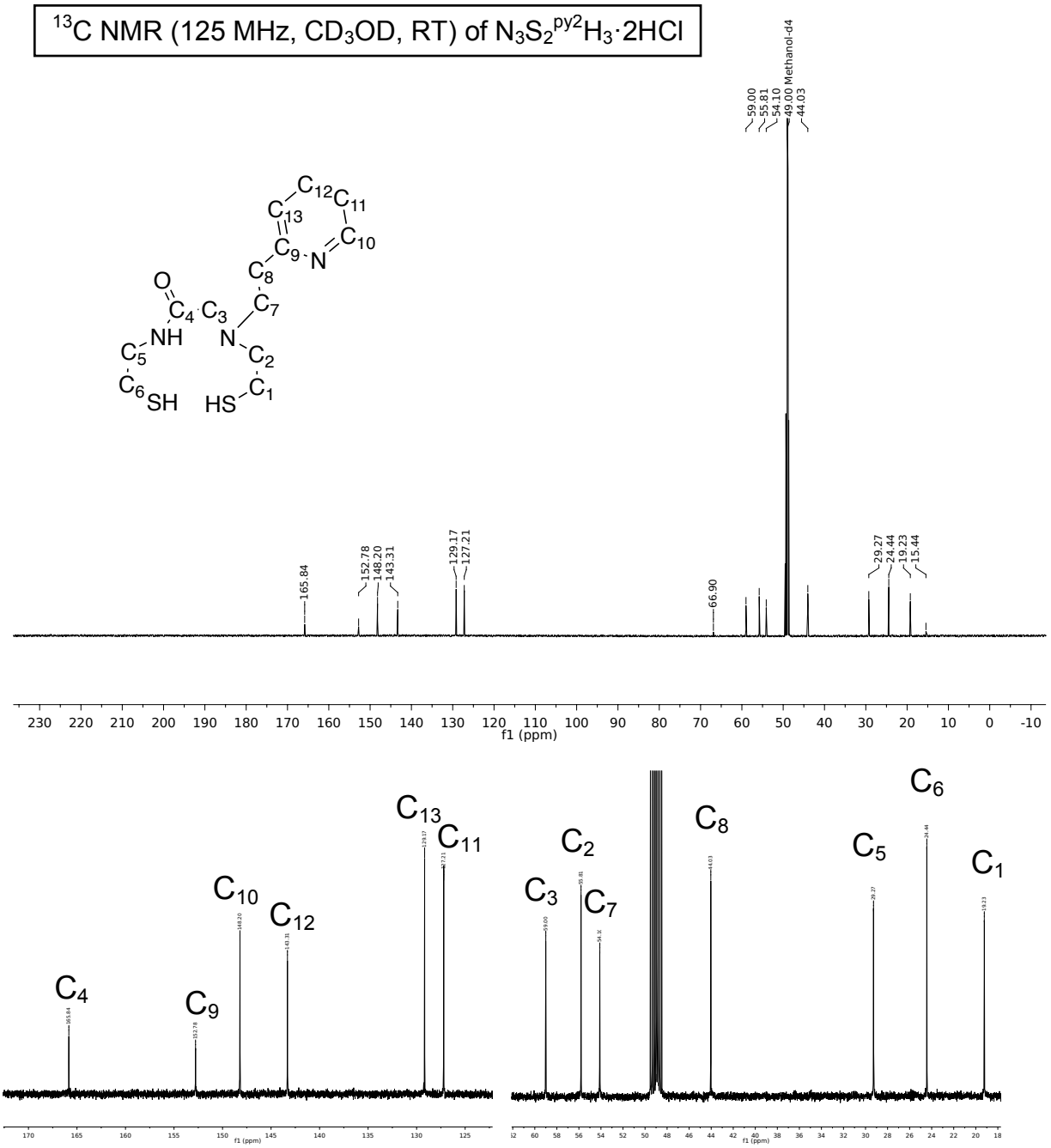

Figure 3.S30. *Top*: ^{13}C NMR spectrum of $N_3S_2^{py2}H_3 \cdot 2HCl$ in CD_3OD at RT. The peak at 77.16 ppm is from solvent. *Bottom*: Zoom-in of top spectrum with peak labels.

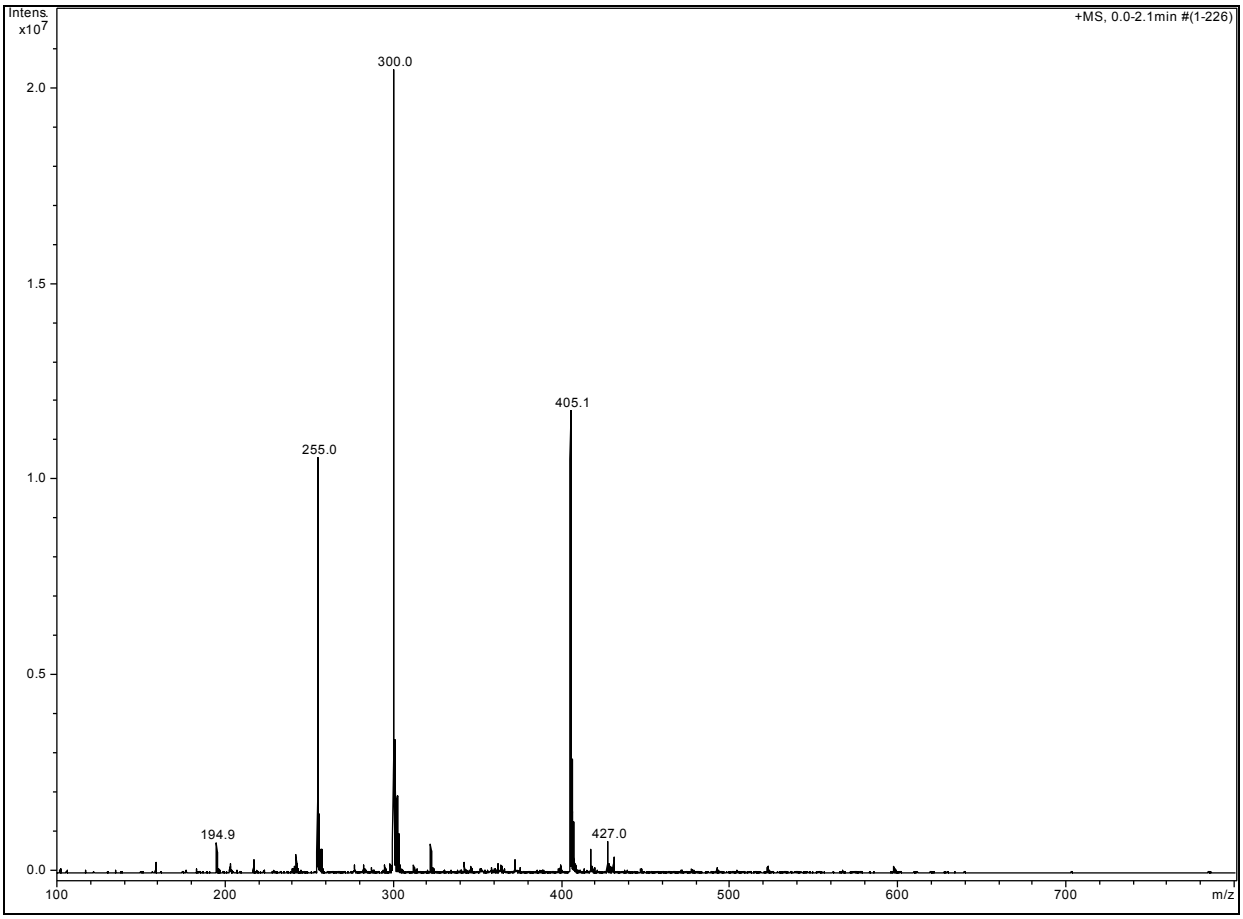

Figure 3.S31. LR-ESI-MS of $N_3S_2^{py2}H_3$ in CH_3OH RT.

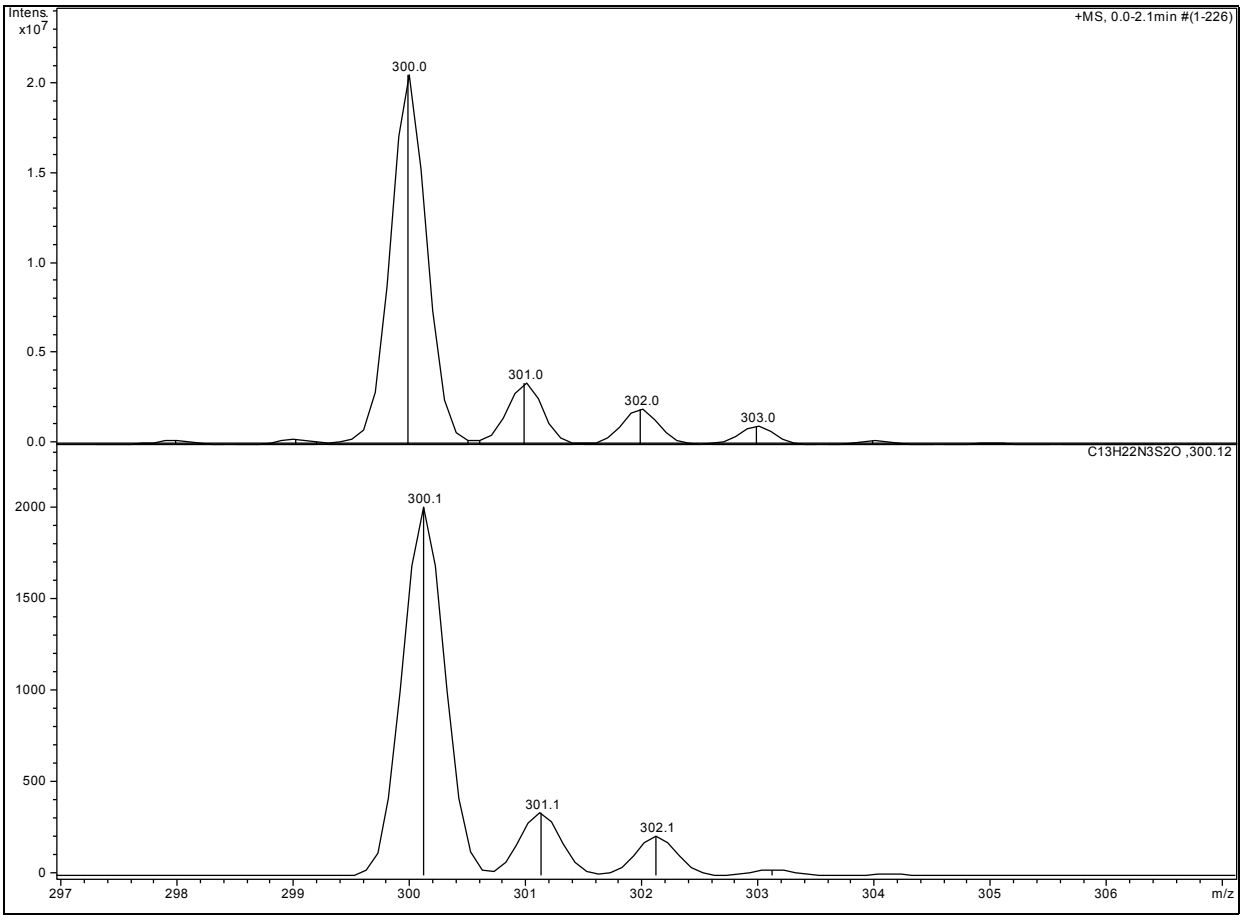

Figure 3.S32. LR-ESI-MS of $N_3S_2^{py2}H_3$ in CH_3OH RT. *Top*: Low-resolution ESI-MS (positive mode) of the cation of $N_3S_2^{py2}H_3$, $[M+H]^+$. *Bottom*: Theoretical isotopic distribution.

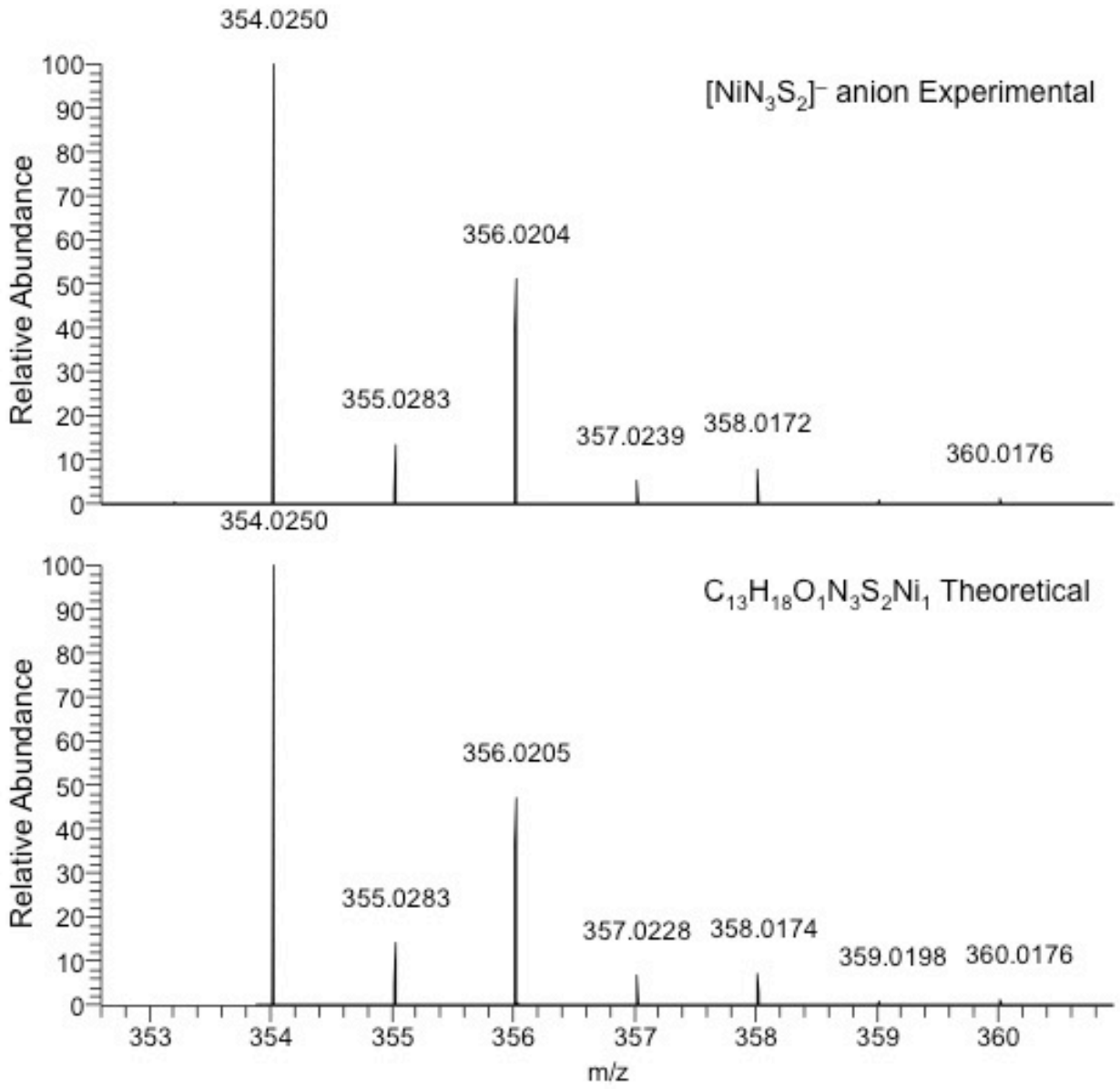

Figure 3.S33. *Top*: High-resolution ESI-MS (negative mode) of the anion of **2**, $[M–Na]^-$.

Bottom: Theoretical isotopic distribution.

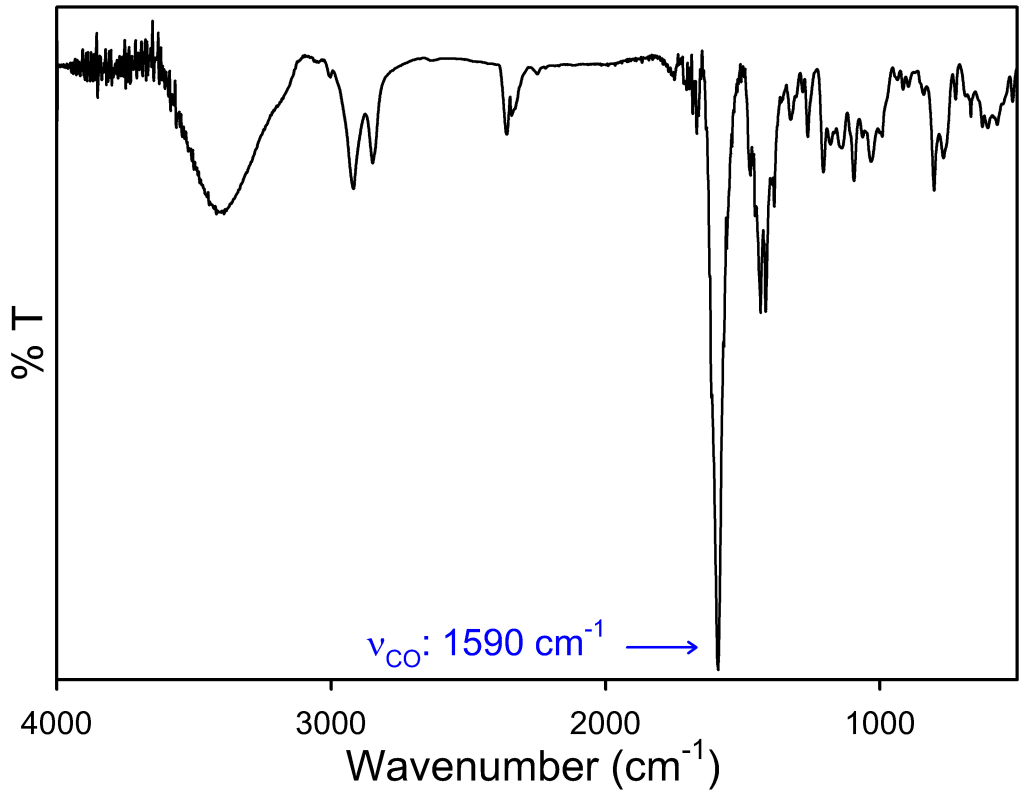

Figure 3.S34. Solid-state FTIR spectrum of **2** in a KBr matrix.

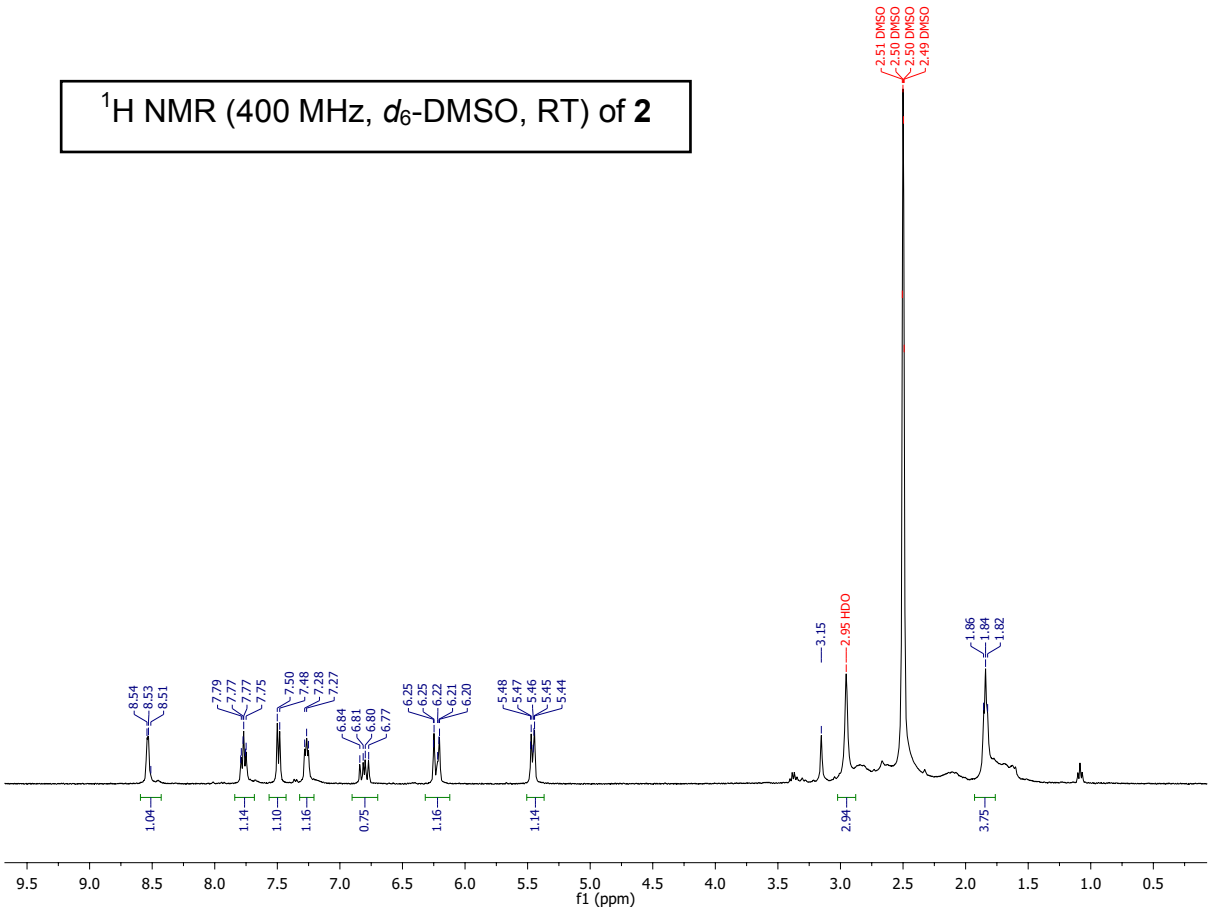

Figure 3.S35. ^{1}H NMR spectrum of **2** in d_6-DMSO at RT. The peak at 2.50 ppm is from residual protio solvent.

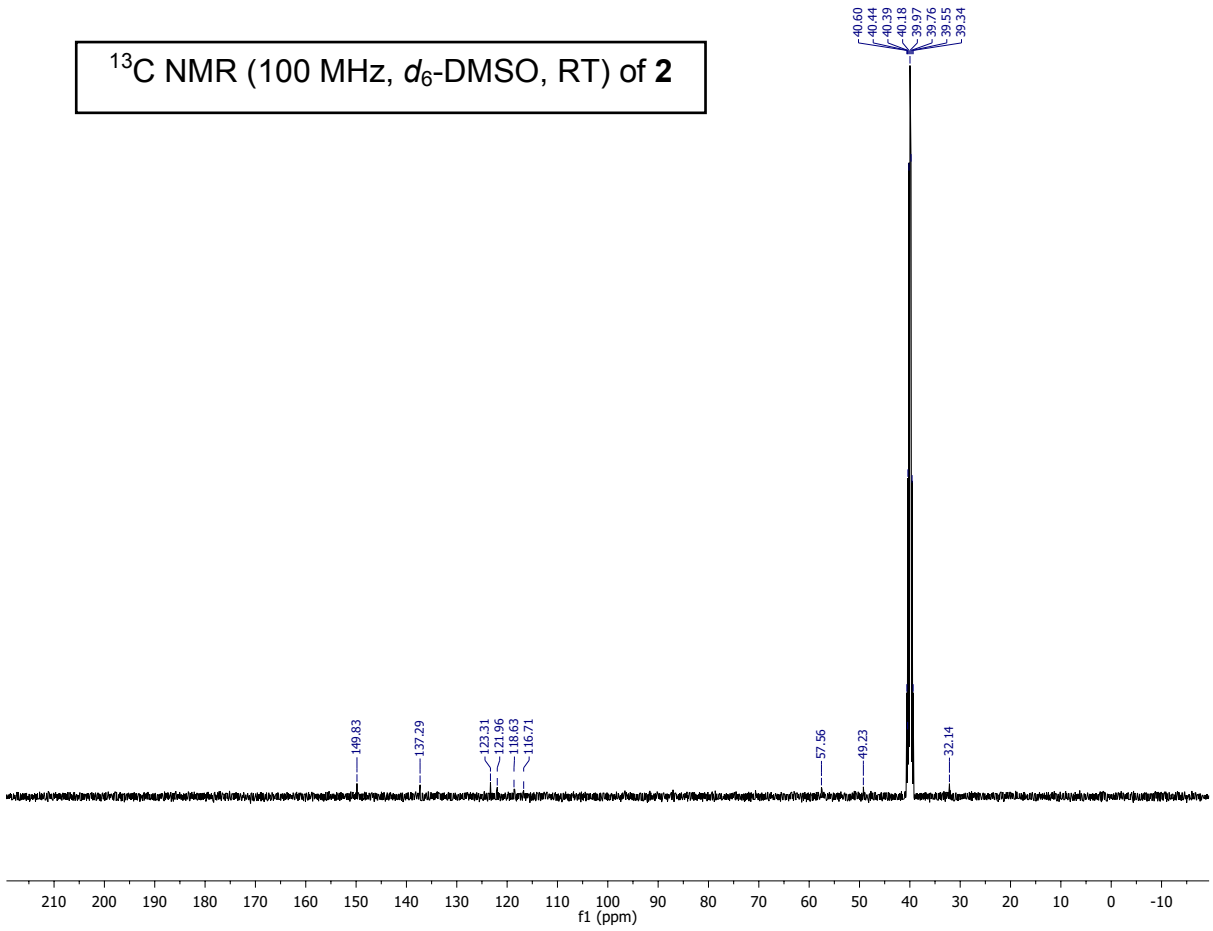

Figure 3.S36. *Top*: ^{13}C NMR spectrum of **2** in d_6-DMSO at RT. The peak at 39.51 ppm is from solvent.

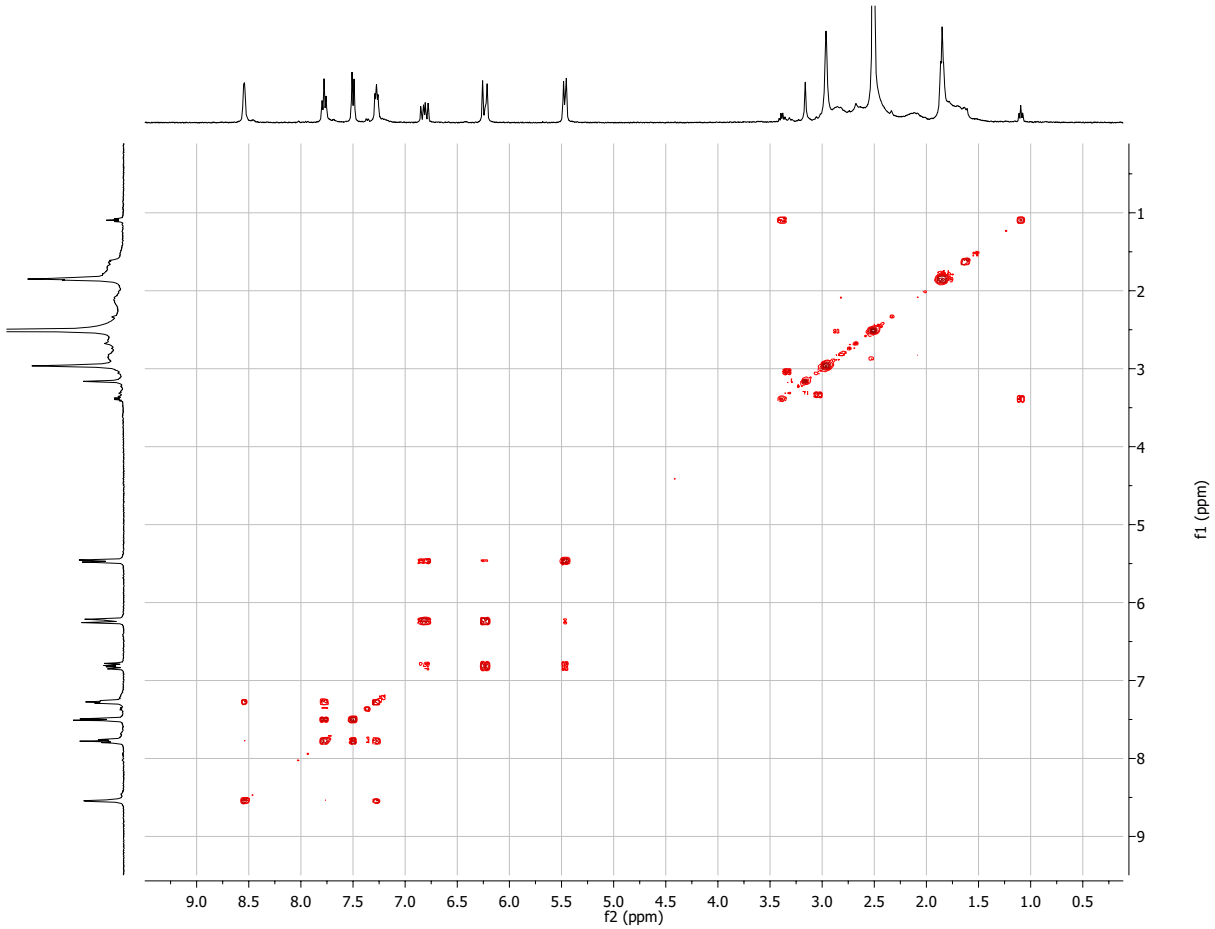

Figure 3.S37. COSY NMR spectrum of **2** in d_6-DMSO at RT.

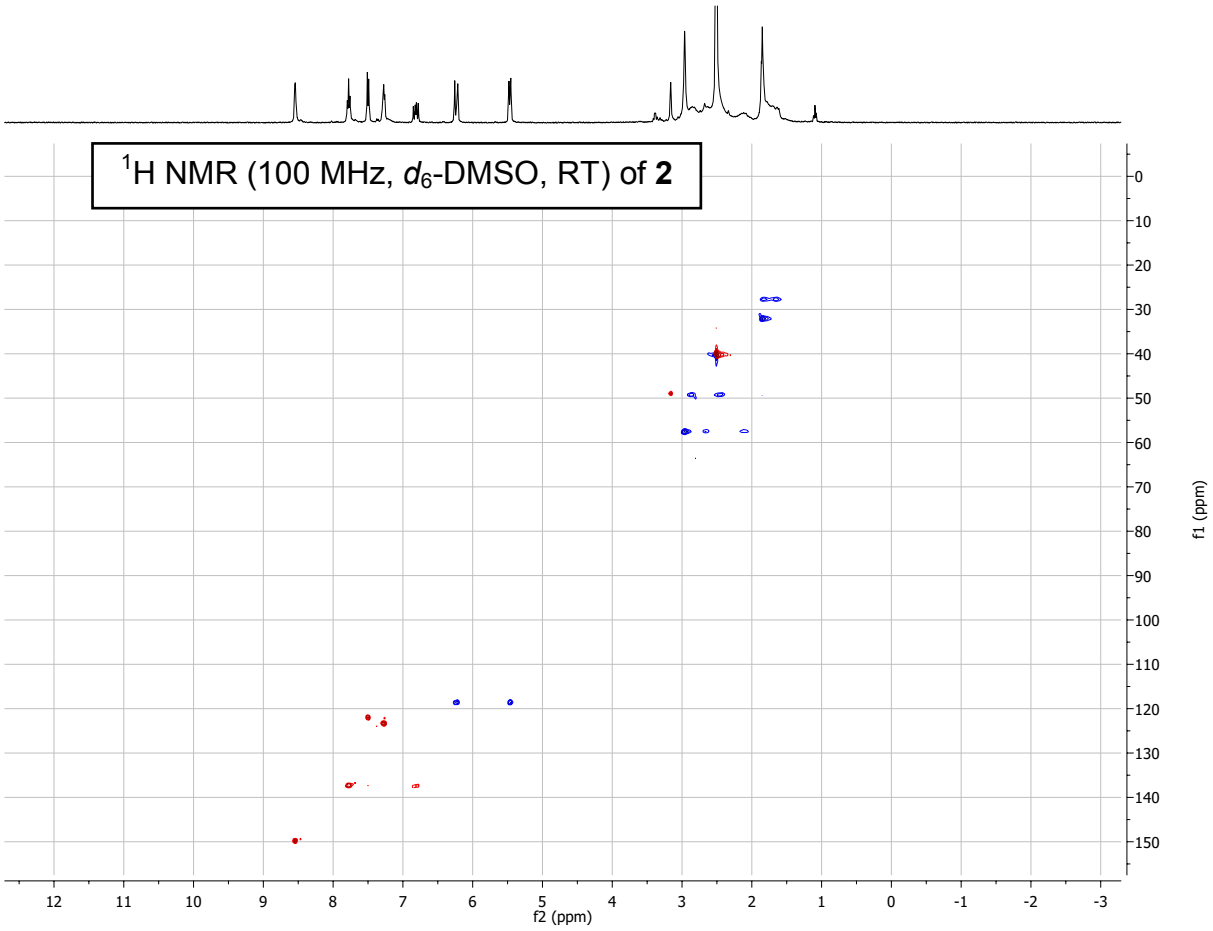

Figure 3.S38. HSQC NMR spectrum of **2** in d_6-DMSO at RT.

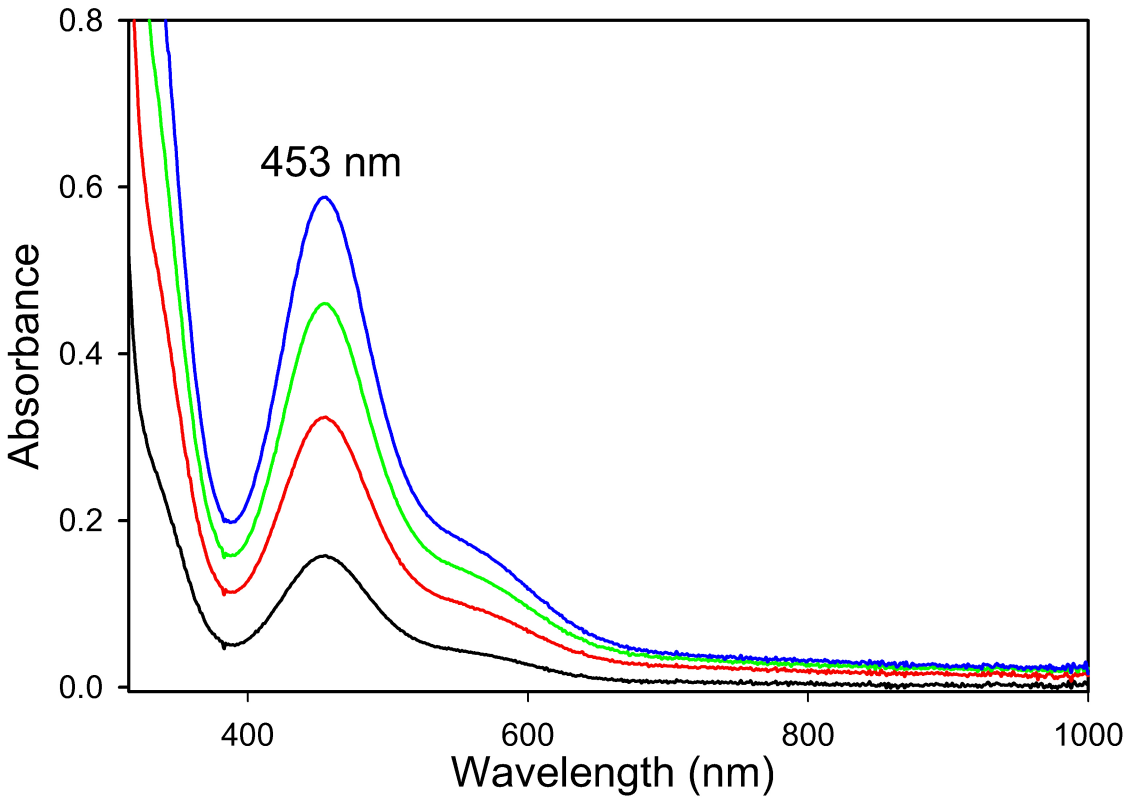

Figure 3.S39. Concentration-dependent UV-vis spectrum of **2** in MeOH, 25 ºC. Concentrations of 0.9, 1.6, 2.2, and 2.7 mM.

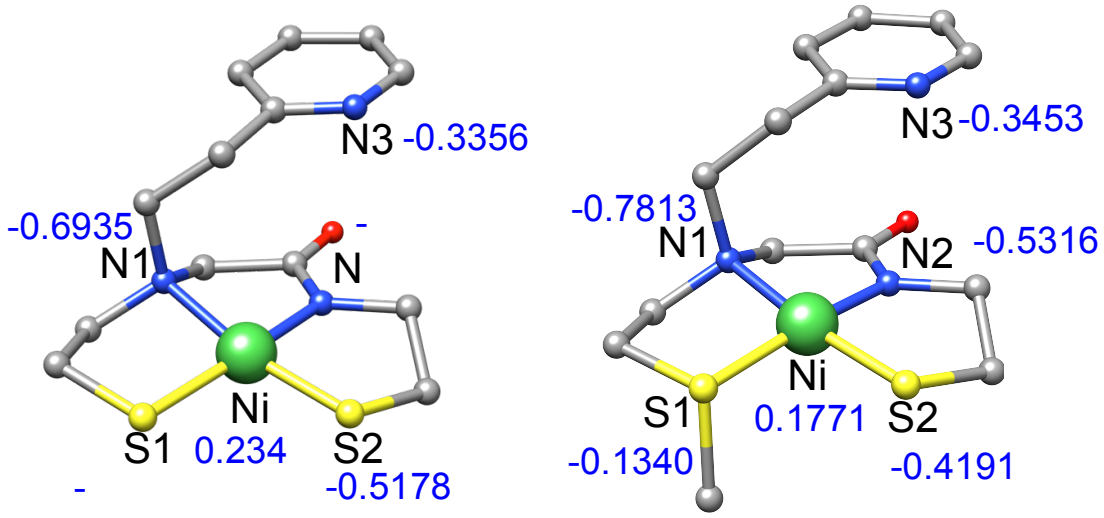

Figure 3.S40. Geometry-optimized structures of $NiN_3S_2^{py2}$ (*left*) and $NiN_3S_2^{py2}Me$ (*right*) with Mulliken atomic charges on Ni, S, and N atoms in blue. Green = Ni; yellow = S; blue = N; red = O; cyan = F; gray = C.

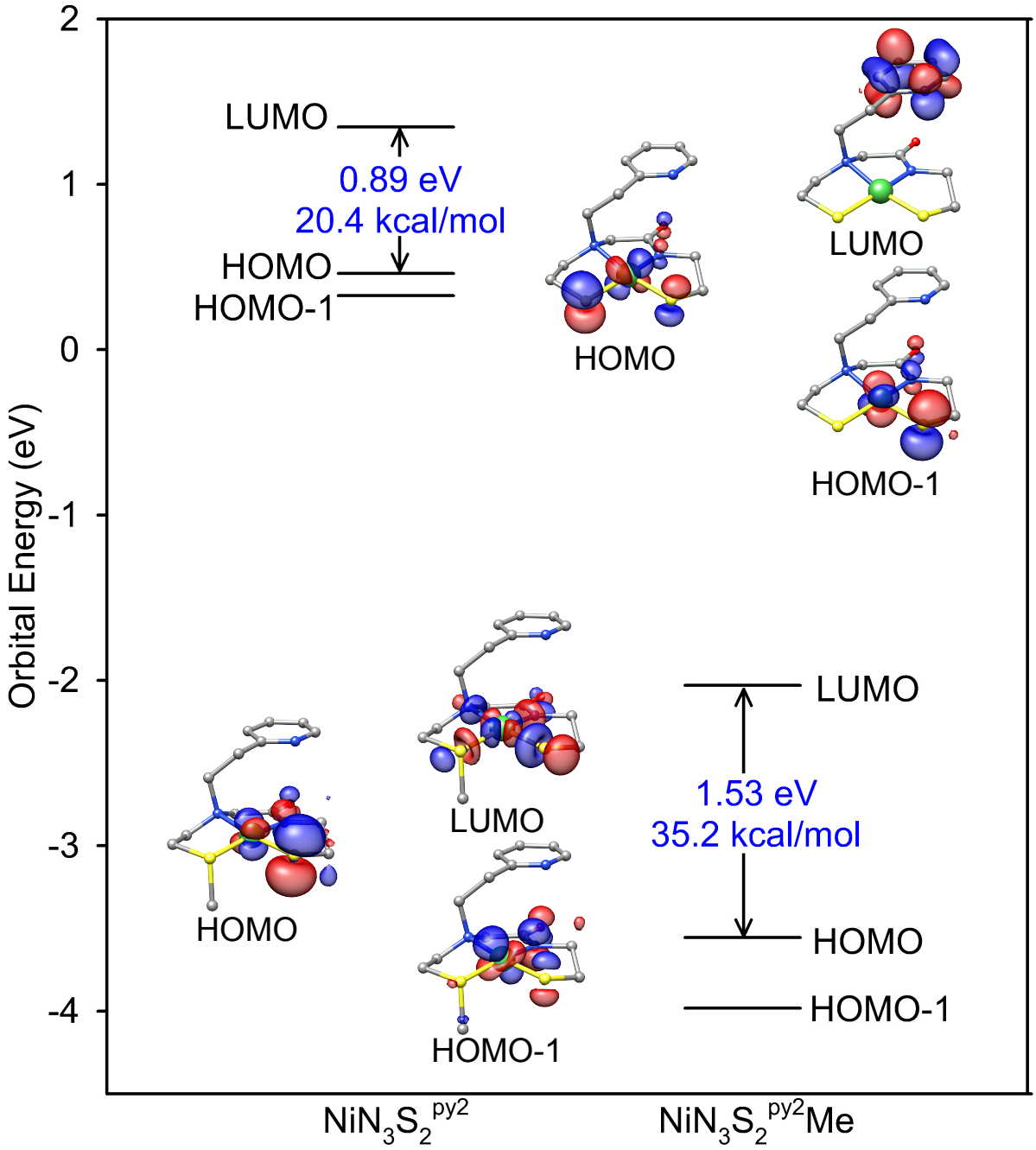

Figure 3.S41. Orbital energy diagram of **2** (left) and $NiN_3S_2^{py2}Me$ (right) with HOMO–LUMO gap in blue. In each column, the MOs descend in order LUMO, HOMO, HOMO–1.

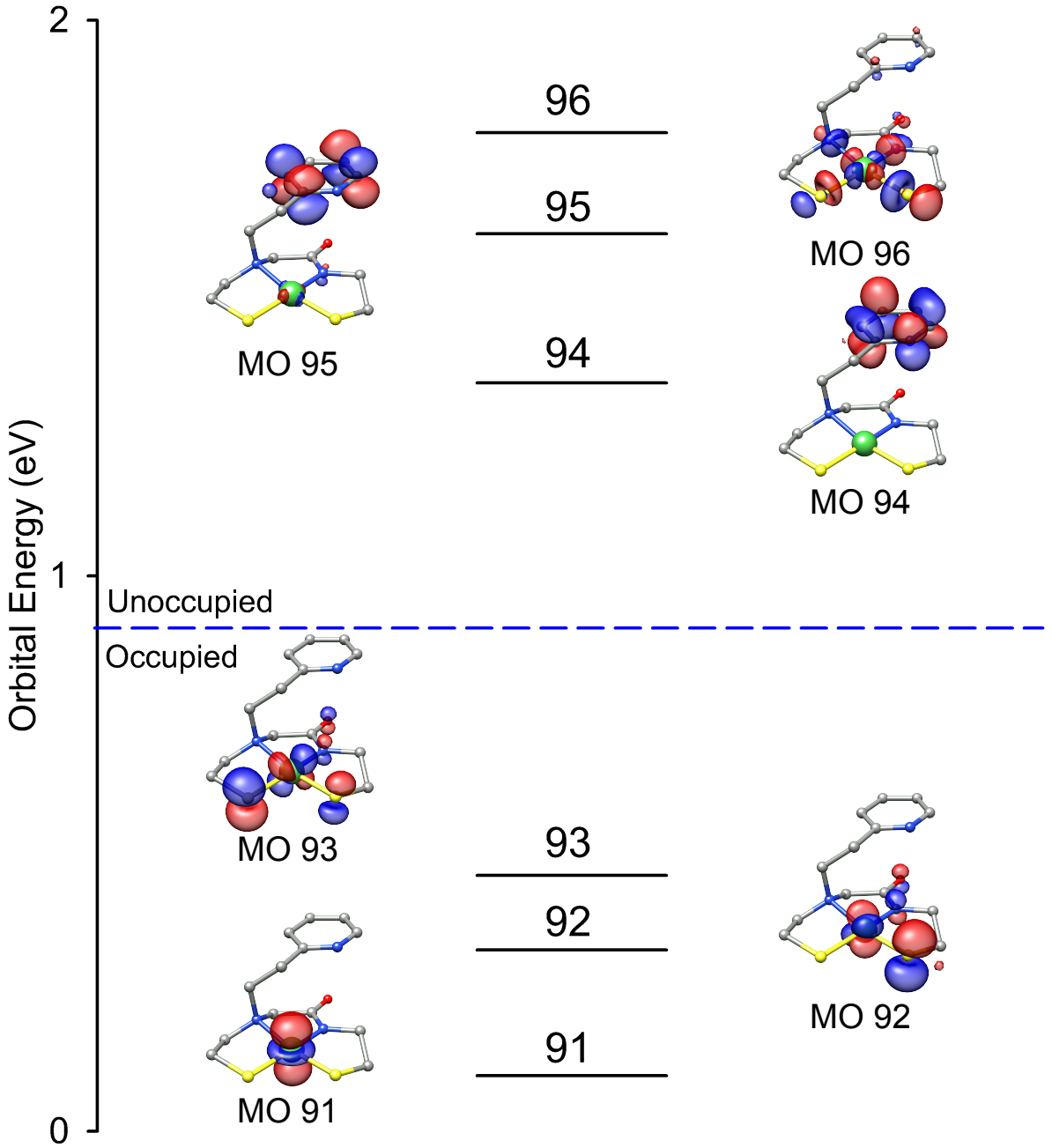

Figure 3.S42. DFT-generated isosurface plots (OLYP/def2-TZVPP) of the frontier MOs of **2**. The MOs descend in order of LUMO+2, LUMO+1, LUMO, HOMO, HOMO–1, HOMO–2.

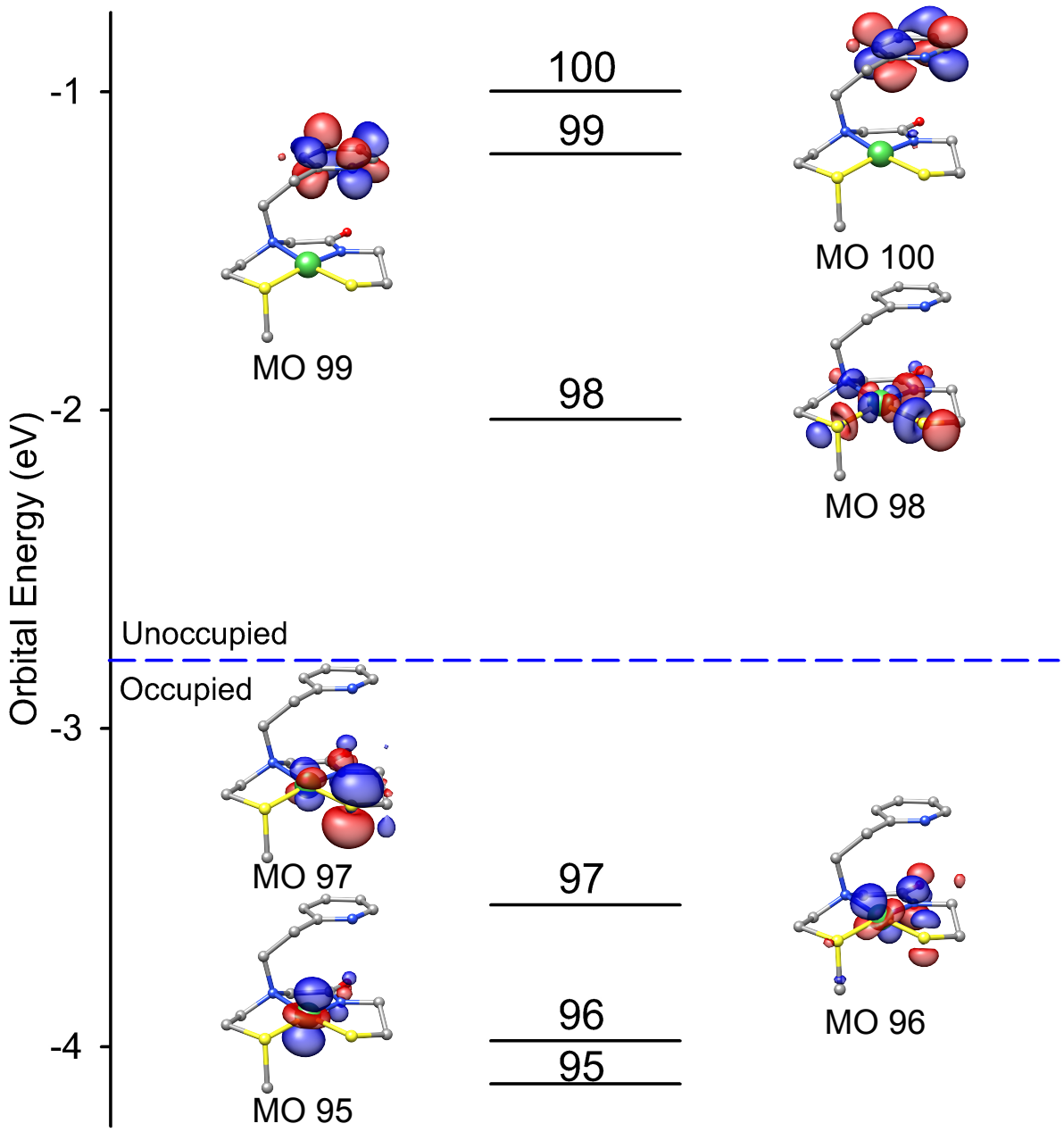

Figure 3.S43. DFT-generated isosurface plots (OLYP/def2-TZVPP) of the frontier MOs of $NiN_3S_2^{py2}Me$. The MOs descend in order of LUMO+2, LUMO+1, LUMO, HOMO, HOMO–1, HOMO–2.

Table 3.S4. Löwdin population analysis derived from the DFT calculations for selected MOs of $NiN_3S_2^{py2}$ from OLYP/def2-TZVPP with NO COSMO. Only s and p contributions were tabulated for N and S atoms. Bonding interactions are represented with a + and antibonding interactions are denoted with a –. N1 = amino-N; N2 = carboxamido-N; N3 = pyridine-N; S1 = $S_{trans\text{-carboxamide}}$; S2 = $S_{trans\text{-amine}}$.

	MO#	Energy (eV)	%Ni	%S1	%S2	%N1	%N2	Type of Interaction
LUMO+2	96	1.7974	48.1	9.0	14.8	5.4	6.2	
LUMO+1	95	1.6156	3.5	0.5	1.0	0.1	1.1	
LUMO	94	1.3471	0.3	0.0	0.0	0.0	0.0	
HOMO	93	0.4603	59.0	21.3	9.1	0.0	2.2	
HOMO–1	92	0.3261	60.5	0.8	25.7	0.2	3.8	
HOMO–2	91	0.1002	91.1	1.2	3.5	0.3	1.0	

Table 3.S5. Löwdin population analysis derived from the DFT calculations for selected MOs of $NiN_3S_2^{py2}$Me from OLYP/def2-TZVPP with NO COSMO. Only s and p contributions were tabulated for N and S atoms. Bonding interactions are represented with a + and antibonding interactions are denoted with a –. N1 = amino-N; N2 = carboxamido-N; N3 = pyridine-N; S1 = $S_{trans\text{-carboxamide}}$; S2 = $S_{trans\text{-amine}}$.

	MO#	Energy (eV)	%Ni	%S1	%S2	%N1	%N2	Type of Interaction
LUMO+2	100	-0.9977	0.3	0.0	0.0	0.1	4	
LUMO+1	99	-1.1956	0.2	0.0	0.0	0.1	13.5	
LUMO	98	-2.0287	48.6	6.4	17.5	5.4	6.6	
HOMO	97	-3.5544	39.9	0.0	41.1	0.1	8.6	
HOMO–1	96	-3.9820	57.7	1.7	8.6	0.1	0.0	
HOMO–2	95	-4.1174	87.2	0.5	1.7	0.5	1.0	

Table 3.S6. Optimized OLYP/def2-TZVPP Cartesian coordinates for $NiN_3S_2^{py2}$.

Ni	2.6984450000	4.2346580000	-0.1987310000
S	3.5625390000	4.3264240000	-2.2168540000
S	4.4021300000	5.0192710000	0.8839820000
N	1.0049180000	3.3061130000	-0.9532580000
N	1.6931670000	4.2679460000	1.4062640000
N	1.3879010000	1.2843050000	2.7692520000
O	-0.4468510000	4.0301030000	2.3199310000
C	2.1400130000	3.6279390000	-3.1559370000
H	2.0252490000	4.1854880000	-4.1130780000
H	2.3206350000	2.5629770000	-3.4361410000
C	0.8430630000	3.7687320000	-2.3627130000
H	0.5765620000	4.8440450000	-2.3043080000
H	-0.0073380000	3.2151460000	-2.8469790000
C	-0.1065030000	3.7608260000	-0.0717860000
H	-0.9566300000	3.0409510000	-0.0750690000
H	-0.4774150000	4.7266600000	-0.4772350000
C	0.3705600000	4.0178490000	1.3767630000
C	2.3554390000	4.5489710000	2.6761160000
H	2.7769450000	3.5977820000	3.0835710000
H	1.6119720000	4.9393220000	3.4101980000
C	3.4850590000	5.5383090000	2.4004500000
H	4.2032780000	5.5845040000	3.2508960000
H	3.0660030000	6.5584690000	2.2438000000
C	1.1899630000	1.8270710000	-0.9305380000
C	0.8131230000	1.1141240000	1.5599610000
C	-0.5610720000	0.8202740000	1.4335170000
H	-1.0048300000	0.6475240000	0.4398580000
C	-1.3639730000	0.7754620000	2.5800550000
H	-2.4461350000	0.5761040000	2.4957590000
C	-0.7718660000	1.0099550000	3.8276080000
H	-1.3647550000	1.0191780000	4.7569570000
C	0.6115080000	1.2483300000	3.8576700000
H	1.1275650000	1.4257110000	4.8206560000
C	1.7408970000	1.2250520000	0.3688000000
H	0.2245040000	1.3438890000	-1.2321400000
H	2.6311600000	1.8181500000	0.6758950000
H	2.1073620000	0.2011130000	0.1123980000
H	1.9310130000	1.5998900000	-1.7194870000

Table 3.S7. Optimized OLYP/def2-TZVPP Cartesian coordinates for $NiN_3S_2^{py2}Me$.

Ni	2.9166130000	3.8549900000	-0.1967730000
S	3.9014500000	3.8183860000	-2.1102560000
S	4.6753110000	4.5412820000	0.8387510000
N	1.2265340000	3.1246670000	-0.9746930000
N	1.9331130000	4.1342080000	1.3399500000
N	1.2340900000	1.3628650000	2.7746440000
O	-0.2293870000	4.2042360000	2.1905400000
C	2.4688890000	3.2963470000	-3.1411030000
H	2.4995850000	3.8363040000	-4.1103630000
H	2.6242130000	2.2198530000	-3.3581470000
C	1.1602290000	3.5670710000	-2.4000570000
H	0.9644400000	4.6582820000	-2.3864030000
H	0.3031820000	3.0733870000	-2.9219150000
C	0.1218080000	3.7225520000	-0.1602240000
H	-0.7716790000	3.0633080000	-0.1419940000
H	-0.1680790000	4.6849450000	-0.6314560000
C	0.5868330000	4.0287090000	1.2769070000
C	2.5999580000	4.4155950000	2.6111740000
H	2.9080930000	3.4503030000	3.0767720000
H	1.8856080000	4.9222540000	3.2980250000
C	3.8232970000	5.2670100000	2.3039010000
H	4.5448300000	5.2807870000	3.1492230000
H	3.5291660000	6.3134370000	2.0711990000
C	1.2192940000	1.6244680000	-0.9150420000
C	0.6787590000	1.0795590000	1.5806540000
C	-0.7056190000	0.8601270000	1.4354110000
H	-1.1336670000	0.5865080000	0.4565320000
C	-1.5399750000	1.0010830000	2.5530660000
H	-2.6288510000	0.8536730000	2.4597920000
C	-0.9644890000	1.3441250000	3.7832410000
H	-1.5796090000	1.4922150000	4.6849860000
C	0.4297170000	1.4982420000	3.8366360000
H	0.9299010000	1.7527010000	4.7890310000
C	1.6433390000	0.9876360000	0.4138990000
H	0.2063780000	1.2747540000	-1.2310830000
H	2.6136740000	1.4223870000	0.7370940000
H	1.8311230000	-0.0895600000	0.1895900000
H	1.9367350000	1.2736770000	-1.6817720000
C	4.0040590000	5.5839660000	-2.5609670000
H	4.3657980000	5.6845330000	-3.6070320000
H	4.7330590000	6.0190830000	-1.8475190000
H	3.0262100000	6.0880640000	-2.4220890000

CHAPTER 4

CONCLUSIONS

This driving force behind this work is determining how nickel superoxide dismutase (NiSOD) promotes both Ni-based redox activity and S-oxidative-stability. A number of proposed mechanisms to prevent S-oxygenation/oxidation chemistry that have been presented include, (i) hydrogen bonding (H-bonding) networks in the hexameric enzyme, (ii) Ni-coordinated Cys-thiol, and (iii) secondary sphere residues to control the access/release of substrate/product from the active site. We have successfully developed, synthesized, and characterized Ni complexes with mixed N/S ligands as low molecular weight synthetic analogues of NiSOD. The design of these complexes focused on mimicking the active site of NiSOD both structurally and via electronically accurate ligands involving carboxamide-N, amine-N, and thiolate-S ligands. These complexes have shed light onto the role of hydrogen bonding (H-bonding) networks in creating sterically protected against unwanted reactivity with ROS. Additonally, H-bonds modulate the S-electron density in the frontier molecular orbitals (FMO). Reactivity of our low molecular weight complexes has also demonstrated reactivity with proton (H^+) or methyl (CH_3^+) donors with NiN_2S_2 complexes containing mixed carboxamide/amine ligands. Our results indicate that S-nucleophilicity of this mixed N-donor set is quite different from the S-nucleophilicity of well-established diamine NiN_2S_2 complexes.

We first designed NiSOD analogues that accurately reproduce the reduced states of NiSOD's active site and emulated the multimetallic nature of the enzyme to determine the role of

H-bonding networks in the oxidative-stability and catalytic activity of Ni-coordinated thiolates. These complexes are of the general formula $[\{Ni(N_{2/3}S)\}_3(S_3R)]^{3-}$, where S_3R represents a trithiolate ligand tethering three $Ni(N_{2/3}S)$ moieties together via an exogenous sulfur (S_{exo}). We synthesized trimetallic complexes by utilizing an established $Ni(N_2S)$ moiety (nmp). We hypothesized that these trimetallic systems will interact via unique inter/intra-molecular H-bonding networks, resulting in properties distinct from their monometallic counterparts. The hexameric structure and ligand environment of NiSOD likely evolved to adjust the redox potential for catalysis, control anion access to the active site, protect against S-oxidation/oxygenation, and provide a H^+ source for H_2O_2 generation.[66] Based on our findings, we propose that NiSOD employs both steric and electronic protection to prevent thiolate reactivity with ROS.

Both $\mathbf{1^M}$ and $\mathbf{1^A}$ have unprecedented stability in protic solvents, indicating the multimetallic scaffold prevents protonation of the Ni–S bond in $\mathbf{1^M}$/$\mathbf{1^A}$. $\mathbf{1^A}$ has strong H-bonds comprised of BTA carboxamides that have rigid supramolecularity based on the large ν_{NH} and δ_{NH} shifts and negative ellipticity, however, an anodic E_{ox} eliminates thiolate-based H-bonds. We propose dimer or oligomer aggregation, where $\mathbf{1^A}$ is sterically protected from protonation of the Ni–S bond and reactivity with $O_2^{\cdot-}$ (ligand exchange), but allow RSO_x to form upon addition of O_2(g), as the thiolates are uninvolved in H-bonding. In contrast, $\mathbf{1^M}$ has an intramolecular H-bond involving the thiolates as evidenced by the cathodic E_{ox} and a blue-shifted λ_{max}, which provides O_2-protection due to stabilization of S-based MOs, but no supramolecular structure to protect from ligand exchange with $O_2^{\cdot-}$. These models are in-line with the observed protic stability in both $\mathbf{1^M}$ and $\mathbf{1^A}$, but the discrepancy in ROS ($O_2^{\cdot-}$, O_2) reactivity. This work

highlights the use of both steric and electronic control to protect the thiolate-S of NiSOD, which promoting diffusion controlled catalytic activity.

We have also designed, synthesized and characterized analogues of NiSOD that model thiol coordination to assess the mechanistic and electronic implications of Cys-protonation as a protective mechanism against S-oxidation. We successfully synthesized a ligand containing mixed carboxamide/amine N-donors and mixed thiolate/thioether S-donors, but coordination to Ni highlighted the weak σ-donor strength of the thioether ligand. We propose that upon coordination to Ni, the complex is in equilibrium between a monometallic complex with NiN_2S_2-CH_3 square planar coordination, and a dimetallic *S*,*S*-bridged species where the thioether ligand is unbound. We also modified $NiN_{2/3}S_2$ complexes with the goal to modify the S-thiolates with H^+ or CH_3^+ agents, while maintaining the S–Ni bond. Modification of the S-thiolate weakens the σ-donor, but also reduced the Ni(dπ)-S(pπ) repulsive interactions, resulting in little change in bond distance between Ni and S. We anticipated the reactivity of the trans-carboxamide thiolate-S would be more reactive than the trans-amine thiolate-S, and that initial modification of a thiolate-S would be facile, while modification of the remaining thiolate-S would be unfavored. Uniquely, we spectrophotometrically observed that modification of the $NiN_{2/3}S_2$ complexes was unfavored and did not occur with less than 2 equiv of H^+ or CH_3^+ source or below 25 ºC. Additionally, ESI-MS data revealed evidence for dimethylation in all of the methylation reactions with $NiN_{2/3}S_2$. This qualitative information on reactivity highlights the unique properties of the mixed carboxamide/amine N-donors in $NiN_{2/3}S_2$ complexes. In contrast, the dimamine $NiN_{2/3}S_2$ indicated immediate reactivity with CH_3^+ sources, while dimethylation is quite difficult and requires excess of CH_3^+ (~50 equiv). Indeed, a mixed carboxamide/amine N-

donor may be required for transient protonation of the Cys ligands in NiSOD to maintain catalysis and generation of H_2O_2.

In summary, this research has aimed to probe the role of secondary-sphere interactions in the activity and stability of NiSOD by creating small-molecule analogues of NiSOD. The goal of this group is to gain insight into the structure-function of redox-active Ni in biology, all of which contain Ni-S bonds. In addition to NiSOD, redox-active Ni can catalyze important transformations for application in alternative energy; NiFe-hydrogenase catalyzes the reversible oxidation of hydrogen and methyl-CoM reductase catalyzes the generation of methane. CO dehydrogenase catalyzes the oxidation of CO to CO_2, an important transformation for environmental remediation. By understanding Ni-based catalytic activity in biology, we can utilize these catalytic transformations for therapeutic, alternative energy, and environmental uses.

APPENDIX A

LIGAND SYNTHESIS AND PROGRESS TOWARDS SYNTHETIC MODELS OF NISOD CONTAINING MULTIMETALLIC AND SECONDARY SPHERE MOITIES

A.1 Introduction

A.1.1 Trithiolate ligands

Due to the alternating redox states and the close contacts between neighboring subunits, the Ni homohexameric structure of NiSOD suggests some degree of intersubunit communication to promote efficient turnover. An electronically accurate NiSOD multimetallic model may provide insight into the potential cooperativity between metal centers. To probe these Ni-Ni interactions in NiSOD, we have synthesized small-molecule, multimetallic models of NiSOD (See Chapter 2). To form these multimetallic models, trithiolate ligands are connected with monomeric Ni(N_2S) complexes previously synthesized by our lab to generate new Ni(N_2S)S′ NiSOD models (S′ originates from the trithiolate platform) with three Ni sites (Figure A.1).[1-5]

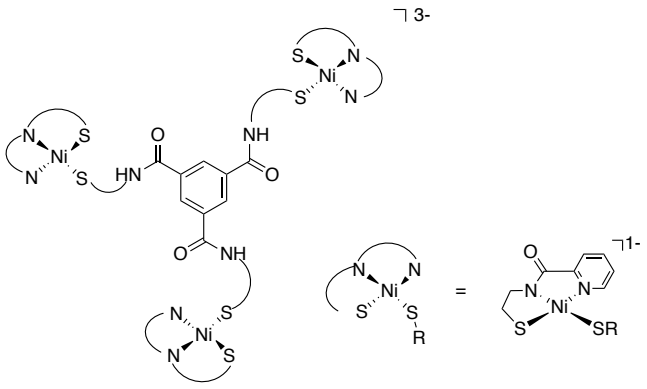

Figure A.1 General platform of Ni(N_2S)S′ NiSOD models.

These systems reveal new insights into the role that metal-metal interactions play in $O_2^{\bullet-}$ disproportionation in NiSOD. The trimeric platform that has been designed utilizes a 1,3,5-benzenetricarboxamide (BTA) base with three thiolate arms branching off of the carboxamide-N untis to form a small molecule tri-peptide/tri-thiolate.

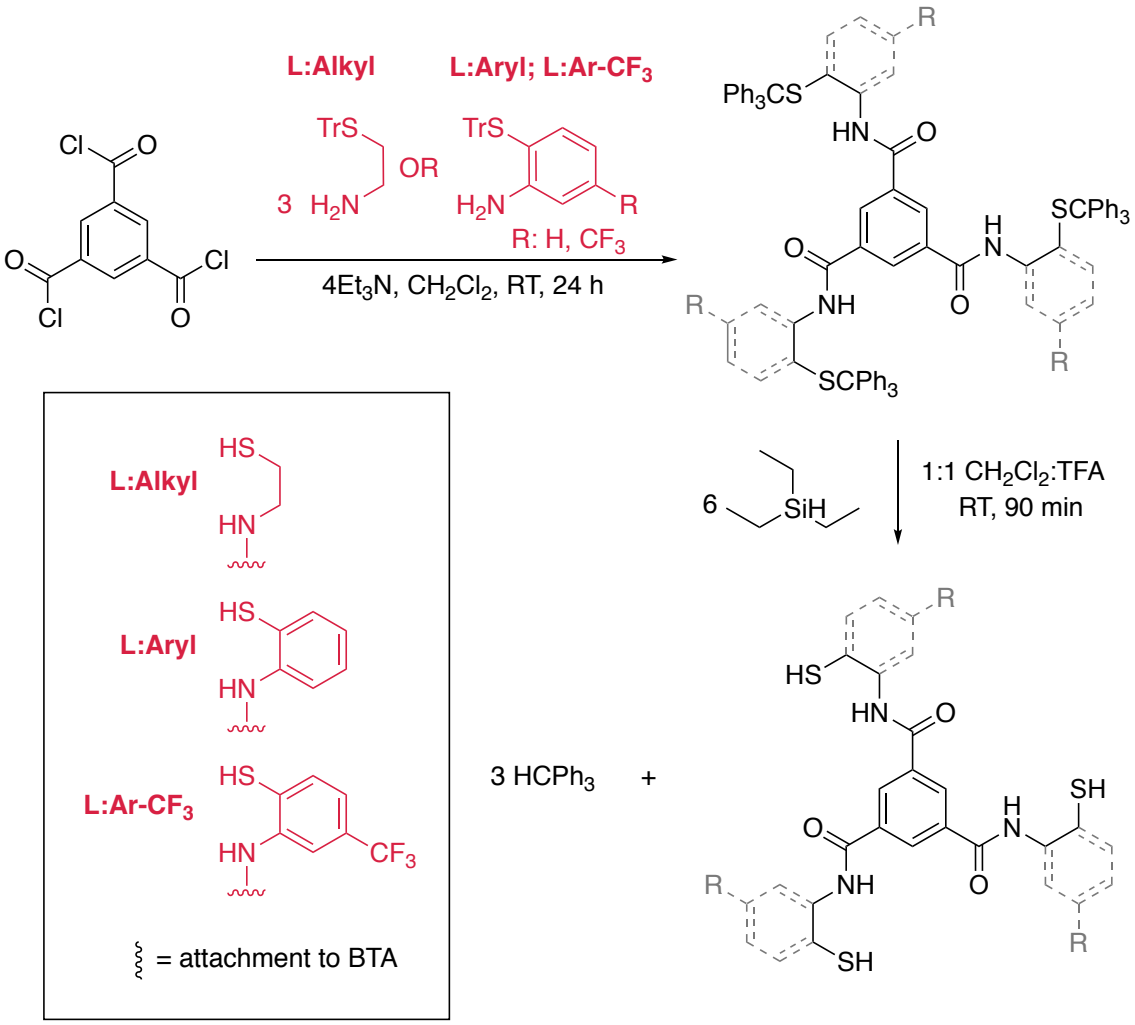

Scheme A.1. Synthesis of trithiolate ligands, where synthesis of L:alkyl is presented in Chapter 2.

Complexes of this type have exhibited strong hydrogen-bonding interactions via the carboxamide-backbone, which is characteristic of BTA compounds.[6-16] Previously reported BTA compounds have encapsulated anions within a dimeric species composed of two BTA units joined via hydrogen-bonding interactions.[17] The behavior of these BTA systems suggests the trimetallic complex may dimerize to form to form a hexameric species, similar to the enzyme. The work here presents the development of the tri-trithiolate ligands, building upon the trithiolate ligand discussed in Chapter 2 (Scheme A.2). Additionally, attempts at synthesizing a dimetallic complex of the same Ni(N_2S)S′ family are discussed.

A.1.2. Schiff-base condensation reactions with S-trityl Cys-Gly

To probe the role of secondary sphere residues on oxidative stability of Ni-thiolates, we have attempted syntheses to create of a family of compounds of the general formula [Ni(N_2^{imine}S)(SR)], where imine functionalization will allow for constrained axial modifications above and below the basal plane. The N_2S trichelate was synthesized via coupling of Cys and Gly and the secondary amine of Gly is available for modification via Schiff-base condensation with a carbonyl to form an imine. Once coordinated to Ni, we suggest the double bond will position new imine substituents axially and create a scaffold to control substrate access/product release to/from the Ni center in a variety of ways: By adding bulky benzene substituents, we can prevent access of $O_2^{\bullet-}$ to the metal center and effectively "turn-off" the possibility of inner-sphere eT and probe the catalytic mechanism of NiSOD. Phenol or methoxyphenol ligands will create a structural mimic of the proposed Tyr9 binding pocket. Additionally, phenol ligands can act as a potential H^+ source for H_2O_2 generation reminiscent of the pendant amines used in the hydrogenase catalyst designed by Dubois and coworkers, while both phenol and

methooxyphenol ligands may act as a Lewis Base (LB) to the axial N-donor and mimic the H-bonding interactions of His1, Glu17, and Arg47 in the enzyme.[18,19] H_2O_2 reporter groups, such as aryl boronates that react with $O_2^{\bullet-}$ to form phenols and can be detected by FTIR and ^{1}H or $^{10/11}B$ NMR spectroscopies, will be positioned to detect H_2O_2 formation as theses moieties can react selectively with H_2O_2 at low concentration.[20-23] Covalently attachment of an aryl boronate would ensure detection of low H_2O_2 formation and functionally mimic the Tyr9 binding pocket by disproportionating H_2O_2. If the proposed complex proves to be catalytically active, an exogenous fluorescent boronate complex could be introduced as an assay.[20-23] This work presents the attempted Schiff base condensation reactions in order to build this family of imine functionalized NiSOD model complexes.

A.2 Results and Discussion

A.2.1 Trithiolate Ligand Synthesis and Properties

Two tri-thiolate ligands were synthesized via reactions with 1,3,5-benzene tricarbonyl trichloride and different S-trityl protected aminothiols in the presence of excess base (Et_3N) to form ligands with a benzene 1,3,5-tricarboxamide (BTA) base and three thiolate arms that branch off of the carboxamide-N units. The aminothiols used were 2-aminobenzenethiol and 2-amino-4-(trifluoromethyl)benzenethiol to form the ligands denoted L:Ar-H and L:Ar-CF_3, respectively (Scheme A.1). These aminothiols were chosen to probe the electronic effects of the exogenous S ligand when ligated to the Ni metal center in the $[Ni(nmp)(SR)]^-$ system. By tuning the electron density of the exogenous S atom, the redox behavior of the Ni metal can be altered to favor Ni-based oxidation over S-based oxidation. Aromatic aminothiols provide conjugated π-systems that can donate or remove electron density with respect to the S atom. The 2-

aminobenzenethiol backbone of L:Ar-H weakly donates electron density to S while the 2-amino-4-(trifluoromethyl)benzenethiol backbone of L:Ar-CF_3 removes electron density from S, as the strong electron withdrawing trifluoromethyl group is para to the S on the benzene ring (Hammet $\sigma_p = 0.54 \pm 0.1$).

A.2.2 Schiff Base Condensation Reactions to form Imine Functionalization Off Cys-Gly

The goal of imine functionalization was to add ketones or aldehydes containing a thioether moiety to S-trityl Cys-Gly (Scheme A.2) to undergo a Schiff-Base condensation and afford the imine product, which would limit thermal motion of the thioether ligand and promote binding to the Ni center. Two different thioether starting materials were used: 3-(methylthio)propionaldehyde and 1-methylthio-2-propanone (Scheme A.3). Tables A.1-2 summarizes and Figures A.2-3 these experiments.

Scheme A.2 Synthesis of S-trityl Cys Gly

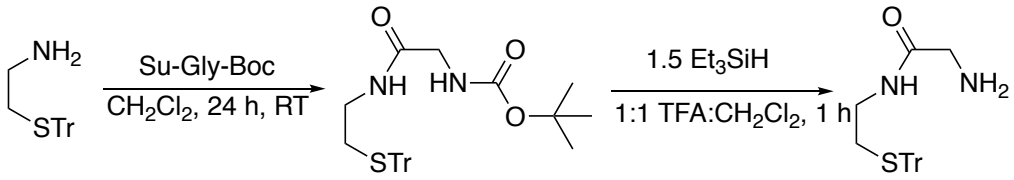

Scheme A.3. Schiff Base condensation reactions.

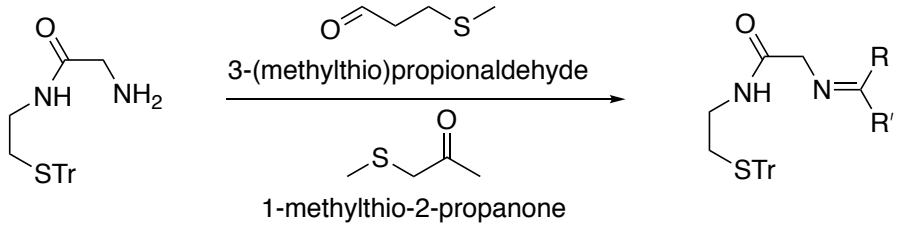

Table A.1. Summary of reaction of S-trityl Cys-Gly with 1-methylthio-2-propanone.

Reaction	Solvent	Temp, time	Result
RAS 2-226	MeOH	RT 12 h	^{1}H NMR ($CDCl_3$) of crude reactions and D_2O exchange indicate formation of Schiff-base intermediate containing a hydroxyl group. This is indicated by quartet at 3.41 with large splitting (J = 20 MHz) that is indicative of a chiral carbon, along with disappearance of two singlets upon D_2O exchange – likely the hydroxyl and 2º amine.
RAS 2-228	MeOH, 3 Å sieves	RT 12 h	
RAS 2-229	EtOH	RT 12 h	
RAS 2-236	MeCN 3 Å sieves	RT 12 h	

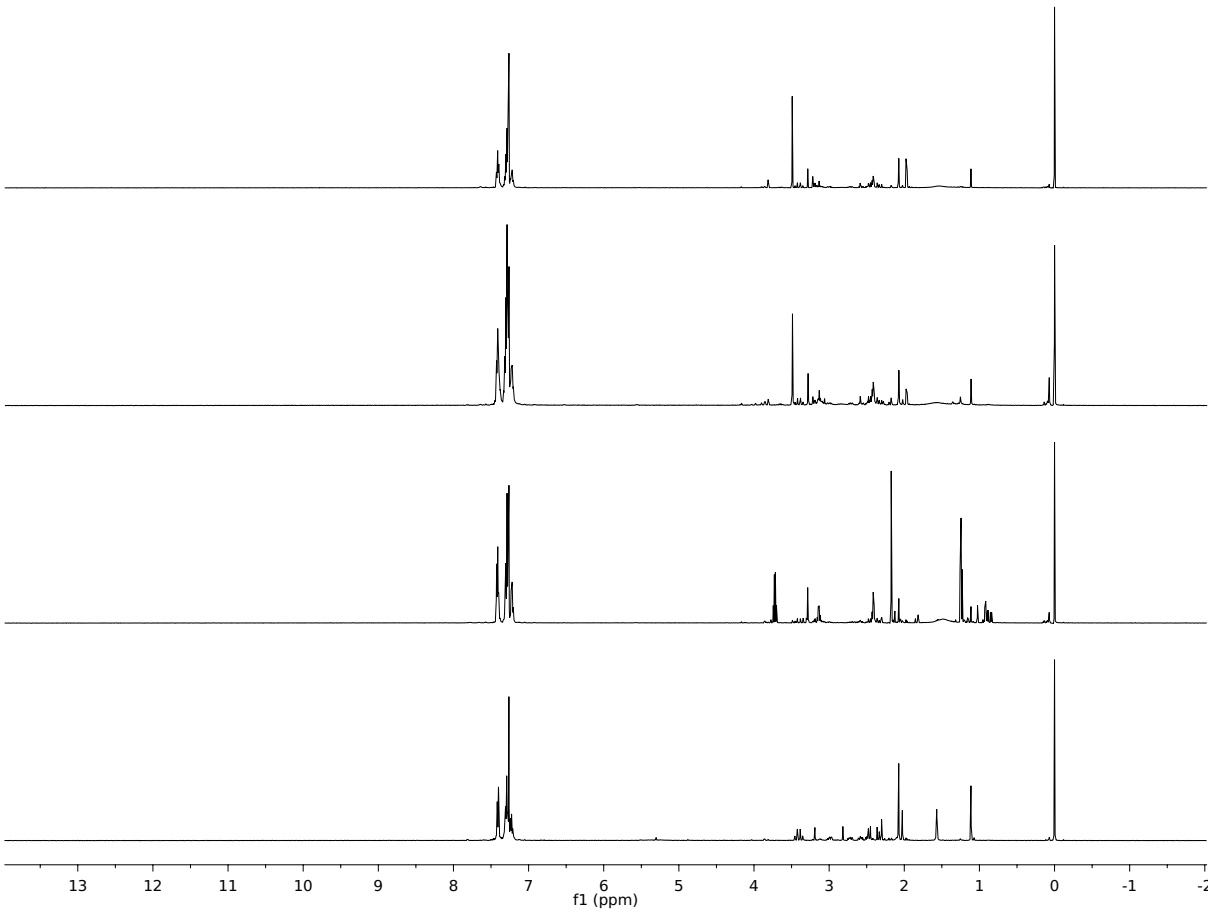

Figure A.2. Summary of 500 mHz ^{1}H NMR spectra of reaction of S-trityl Cys-Gly with 1-methylthio-2-propanone. From top to bottom: 2-226, 2-228, 2-229, 2-236 in CDCl3 at RT.

Table A.2 Summary of reaction of S-trityl Cys-Gly with 3-(methylthio)propionaldehyde.

Reaction	Solvent	Temp, time	Result
RAS 2-223	MeOH	RT 12 h	^{1}H NMR ($CDCl_3$) indicates product mixture – reactant peaks, Schiff Base intermediate peaks, and/or product peaks.
RAS 2-227	MeOH	RT 12 h in GB	
RAS 2-238	MeCN 3 Å sieves	RT 12 h in GB	

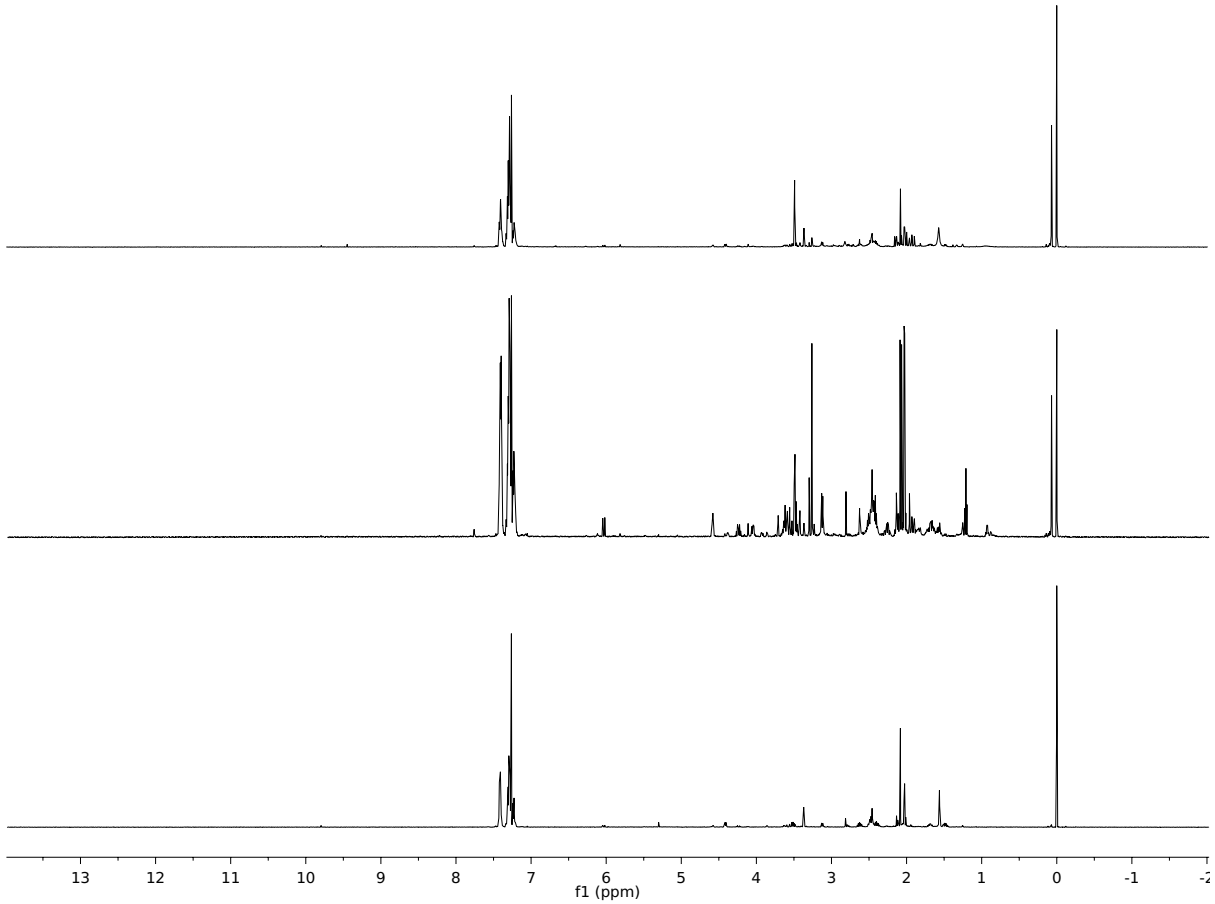

Figure A.3 Summary of 500 mHz ^{1}H NMR spectra of reaction of S-trityl Cys-Gly with 3-(methylthio)propionaldehyde. From top to bottom: 2-223, 2-227, 2-238.

Reactions with Cys-Gly and 1-methylthio-2-propanone provide strong evidence of a Schiff-base intermediate containing a hydroxyl OH. This functional group is indicated by a quartet at 3.41 ppm with large splitting (J = 20 MHz) that is indicative of a chiral carbon, along with disappearance of two singlets upon D_2O exchange, likely the hydroxyl and 2º amine. Reactions with Cys-Gly and 3-(methylthio)propionaldehyde afford a large mixture of peaks in the ^{1}H NMR, including starting material reagents. For both reactions, it appears formation of the imine is inhibited under the reaction conditions utilized, potentially due to the steric bulk of the trityl thiolate impeding access to the primary amine.

A.2.4 Complex Synthesis and Properties

To synthesize complex **Na_2[(Ni(nmp))$_2$(DT)]** (Scheme A.4), a commercially available dithiolate ligand, 2,4,6-trimethyl-1,3-phenylene)dimethanethiol, abbreviated (DT) was deprotonated with NaH and reacted with [Ni_4(nmp)$_4$] to form the complex **[Na_2(Ni(nmp))$_2$(DT)]**.

Scheme A.4. Synthesis of **[Na_2(Ni(nmp))$_2$(DT)]**

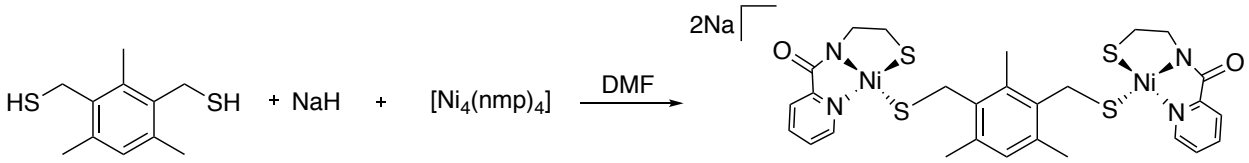

DT **Na_2[(Ni(nmp))$_2$(DT)]**

This complex has been characterized by ^{1}H NMR, UV-vis (MeCN), and KBr FTIR (Figures A.9-11). The λ_{max} of 457 nm was characteristic of other NiN_2S_2 systems. The complex is not purified enough to assign every ^{1}H NMR (*d*-DMSO) peak with confidence, but the four aromatic peaks corresponding to the pyridyl group of nmp were present (8.22, 7.88, 7.42, 7.31 ppm), the aromatic proton on the dithiol benzene was apparent (6.52 ppm), as were the peaks in the aliphatic region indicative of the mercaptoethyl moiety of the nmp ligand (3.17, 2.12 ppm) (Figure A.9).

A.3 Conclusions

In summary, S-trityl protected trithiolate ligands S-trityl L:Ar-CF_3 and S-trityl L:Ar-H have been successfully synthesized, and future directions include metallation to form the desired NiSOD analogues to shed insight into the electronic effects of thiolate on a multimetallic system. Imine functionalization of S-trityl Cys-Gly has not yet been realized. Perhaps Schiff base condensation is not favored when S-trityl Cys-Gly contains the trityl moiety. Future directions include Schiff base functionalization off of the $[Ni(CysGly)SR]^-$ complex (Figure A.3). Additionally, formation of the dimetallic **$Na_2[(Ni(nmp))_2(DT)]$** in acceptable purity has yet to be isolated. The isolated material likely contains a mixture of monometallic and dimetallic material and may be purified by increasing reaction time and/or temperature to favor formation of the dimetallic material, or separation of the material through column chromatography.

A.4 Experimental

General Information. See Chapter 3.

Physical Methods. See Chapter 3.

Synthesis of S-trityl L:Ar-CF_3. A batch of 0.199 g (0.749 mmol) of 1,3,5-benzene tricarbonyl trichloride was dissolved in ~5 mL of CH_2Cl_2 to form a clear solution. A batch of 1.015 g (2.323 mmol) of S-trityl-2-amino-(4-triflouromethyl) benzenethiol (SC_6H_3-*o*-NH_2-*p*-CF_3) was dissolved in ~5 mL of CH_2Cl_2 containing 418 μL (2.999 mmol) of Et_3N to form a homogeneous, yellow solution. Upon addition of the amine solution to the acid chloride, the reaction turned heterogenous, pale yellow with some gas evolution. The solution was capped and allowed to stir for 12 h at RT. White solid had formed and the solution was placed in the freezer to aid in precipitation. The solid was gravity filtered and washed with cold Et_2O. The solid was dissolved in THF and filtered to remove the byproduct $Et_3N{\cdot}HCl$. The solution was concentrated in vacuo and the solid was washed with CH_2Cl_2 to remove any remaining $Et_3N{\cdot}HCl$. A batch of 0.319 g (0.208 mmol, 29%) of the pale yellow solid was collected. ^{1}H NMR (500 MHz, $CDCl_3$, δ from TMS): 9.35 (s, 3H), 9.04 (s, 3H), 8.32 (s, 3H), 7.53 (d, 3H), 7.34 (d, 18H), 7.18 (m, 30H). FTIR (KBr pellet), ν_{max} (cm^{-1}): 3339 (br s, N-H), 3057, 1689 (s, C=O), 1575 (s), 1525 (s), 1490 (m), 1429 (s), 1330 (s), 1289 (m), 1267 (m), 1213 (s), 1173 (s), 1130 (s), 1084 (s), 1035 (w), 923 (m), 901 (m), 824 (m), 761 (m), 732 (m), 700 (m), 660 (m), 630 (w), 616 (w), 594 (w).

Synthesis of S-trityl L:Ar-H. Material synthesized by Prof. Todd Harrop via a similar procedure outlined for S-trityl L:Ar-CF_3 and was purified by removing $Et_3N{\cdot}HCl$ by dissolving in THF, filtering, and concentrating the filtrate. ^{1}H NMR (500 MHz, $CDCl_3$, δ from TMS): 9.11 (s, 3H), 8.61 (d, 3H), 8.21 (s, 3H), 7.48 (t, 3H), 7.42 (d, 3H), 7.29 (m, 18H), 7.11 (m, 27H), 6.96 (t, 3H). ^{13}C NMR (125 MHz, $CDCl_3$, δ): 161.95 (*C*=O), 143.13, 142.32, 137.71, 135.39, 131.50,

129.81, 128.27, 127.83, 127.22, 123.76, 121.30, 119.48, 72.26 (*C*Ph_3) FTIR (KBr pellet), ν_{max} (cm^{-1}): 3341 (m, N-H), 3057 (w), 2978 (w), 2603 (br w), 2496 (w), 1679 (s), 1577 (s), 1514 (s), 1440 (s), 1421 (s), 1306 (s), 1223 (m), 1185 (w), 1035 (m), 1000 (w), 851 (w), 700 (s), 667 (w), 625 (w), 587 (w), 520 (w), 494 (w), 464 (w), 432 (w).

Schiff base condensation attempts with S-trityl Cys-Gly. General reaction procedure with S-trityl Cys-Gly and 1-methylthio-2-propanone or 3-(methylthio)propionaldehyde. S-trityl Cys-Gly was dissolved (EtOH, MeOH, or MeCN) and 1 equiv of ketone or aldehyde was added and allowed to stir for 12 h at RT.

Synthesis of $Na_2[(Ni(nmp))_2(DT)]$. A batch of 51.2 mg (0.241 mmol) of (2,4,6-trimethyl-1,3-phenylene)dimethanethiol was dissolved in of DMF (~3 mL). To this solution was added a slurry of 12.1 mg (0.506 mmol) of NaH in DMF. The solution was put under vacuum for 20 min to aid in removing H_2(g). After 20 min, the cloudy, heterogeneous solution was now colorless and clear. [$Ni_4(nmp)_4$] was then added as a solid and the heterogeneous dark red solution was allowed to stir for 12 h. The solution was filtered through celite and the DMF filtrate was removed via short-path vacuum distillation. The residue was dissolved in ~10 mL MeCN and was allowed to stir for 12 h. The solution was filtered to collect the MeCN insoluble portion, and the MeCN filtrate was removed to collect the MeCN soluble residue. While 51.4 mg of MeCN soluble solid was collected (0.0679 mmol, 28%). UV-vis (qual., MeCN) λ_{max} 460 nm. ^{1}H NMR did not produce discrete product peaks. FTIR (KBr pellet), ν_{max} (cm^{-1}): 3367 (br s), 2917 (m), 2849 (m), 1664 (s), 1617 (s), 1592 (m), 1560 (m), 1533 (m), 1465 (w), 1435 (w), 1397 (m), 1379 (w), 1260 (w), 1207 (w), 1096 (w), 803 (w), 753 (w), 677 (w), 621 (w). 563 (w).

A.5 Supporting Information

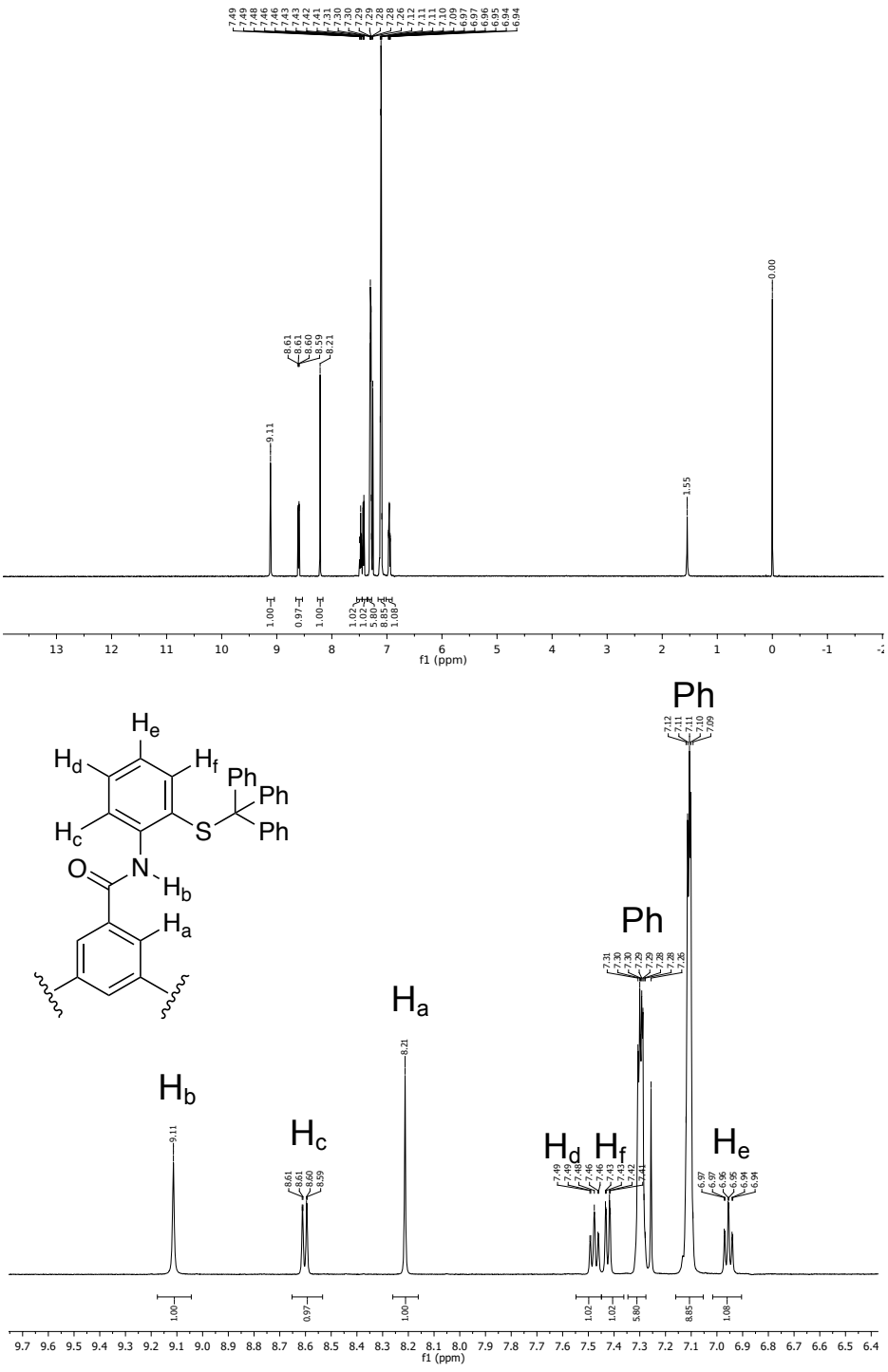

Figure A.4. 500 MHz ^{1}H NMR spectrum of S-trityl L:Ar-H in $CDCl_3$ at RT. (Top) Full Spectrum. (Bottom) Zoom in of aromatic region. Ph = phenyl.

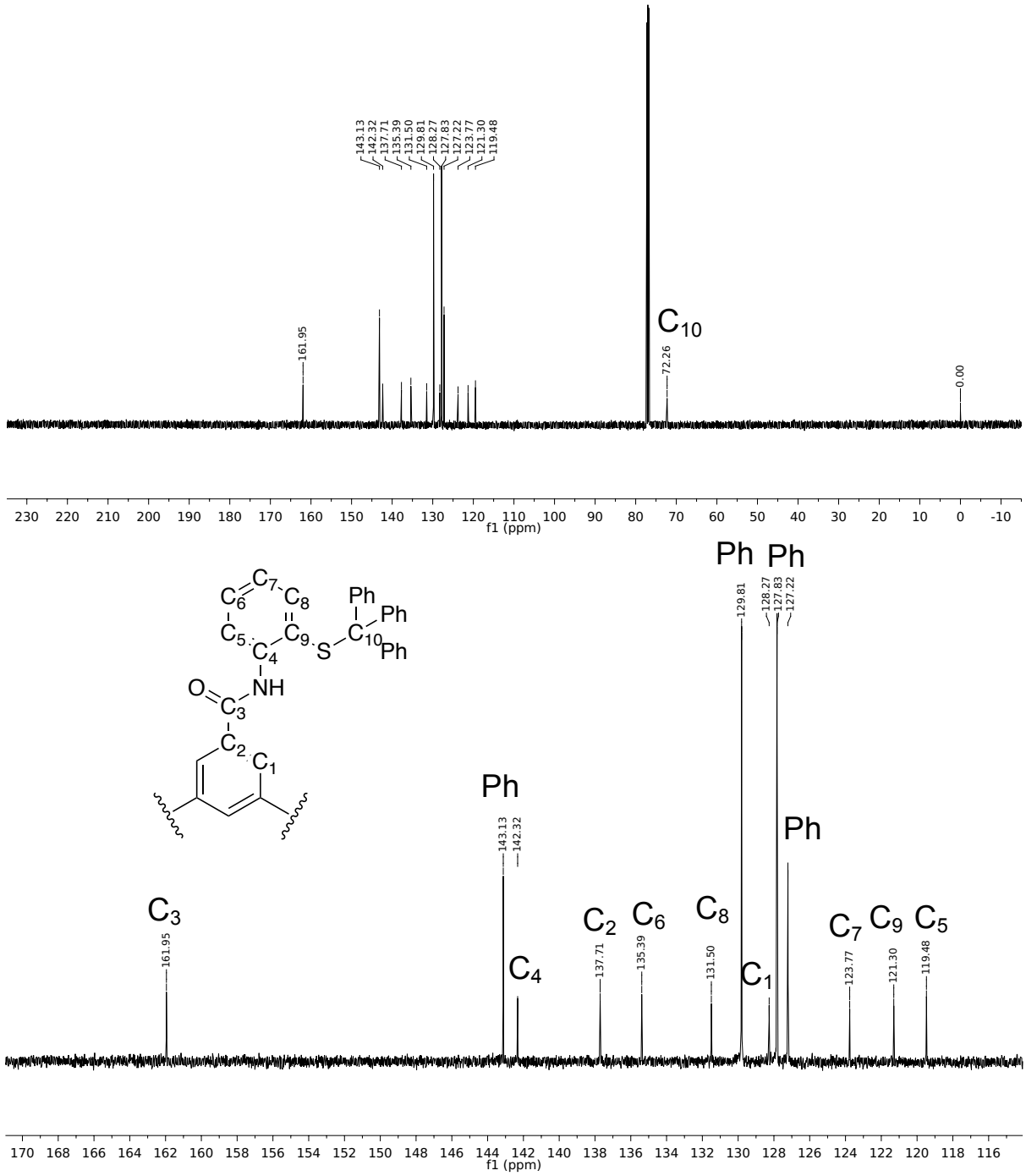

Figure A.5. 125 MHz ^{13}C NMR spectrum of S-trityl L:Ar-H in $CDCl_3$ at RT. (Top) Full Spectrum. (Bottom) Zoom in of aromatic region. Ph = phenyl.

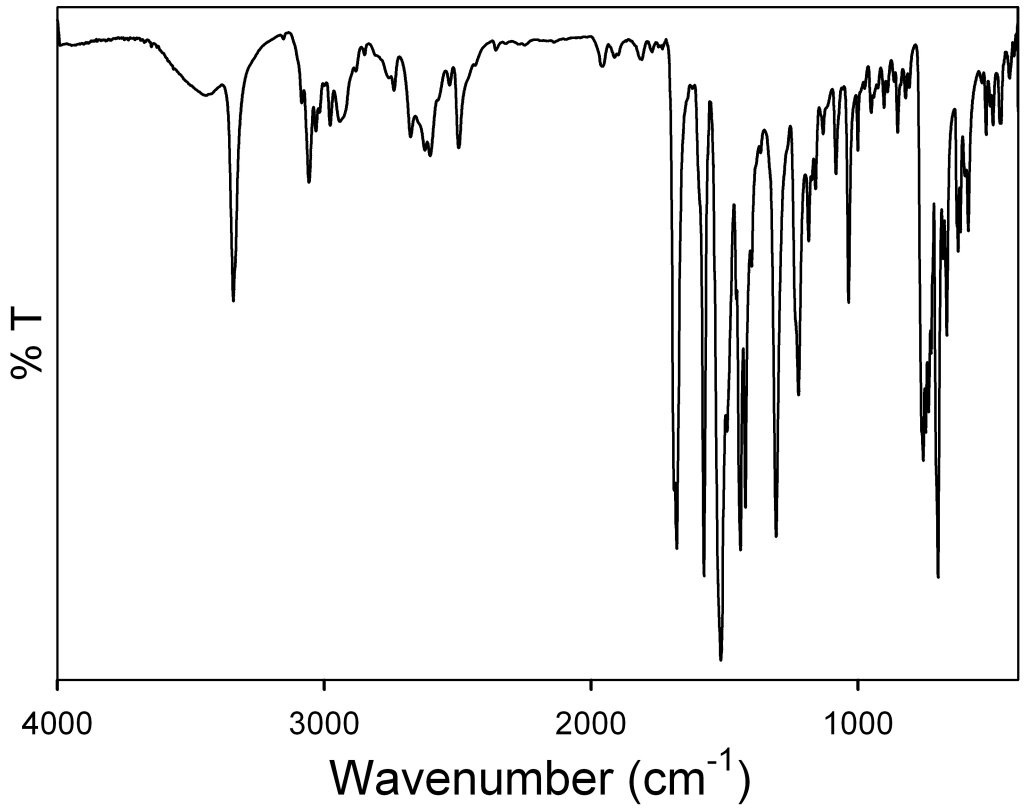

Figure A.6. Solid-state FTIR spectrum of S-trityl L:Ar-H in a KBr matrix.

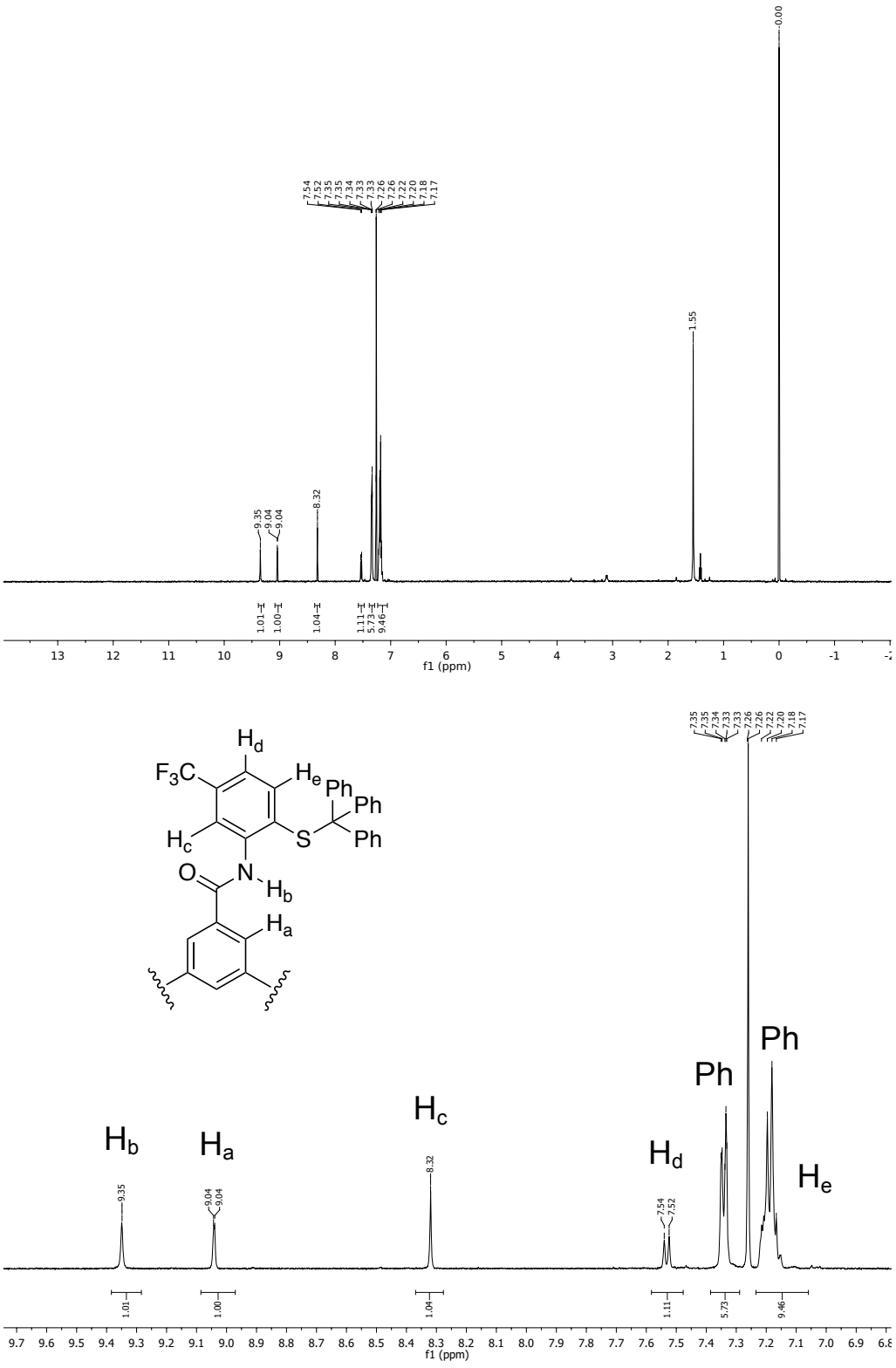

Figure A.7. 500 MHz ^{1}H NMR spectrum of S-trityl L:Ar-CF_3 in $CDCl_3$ at RT. (Top) Full Spectrum. (Bottom) Zoom in of aromatic region. Ph = phenyl.

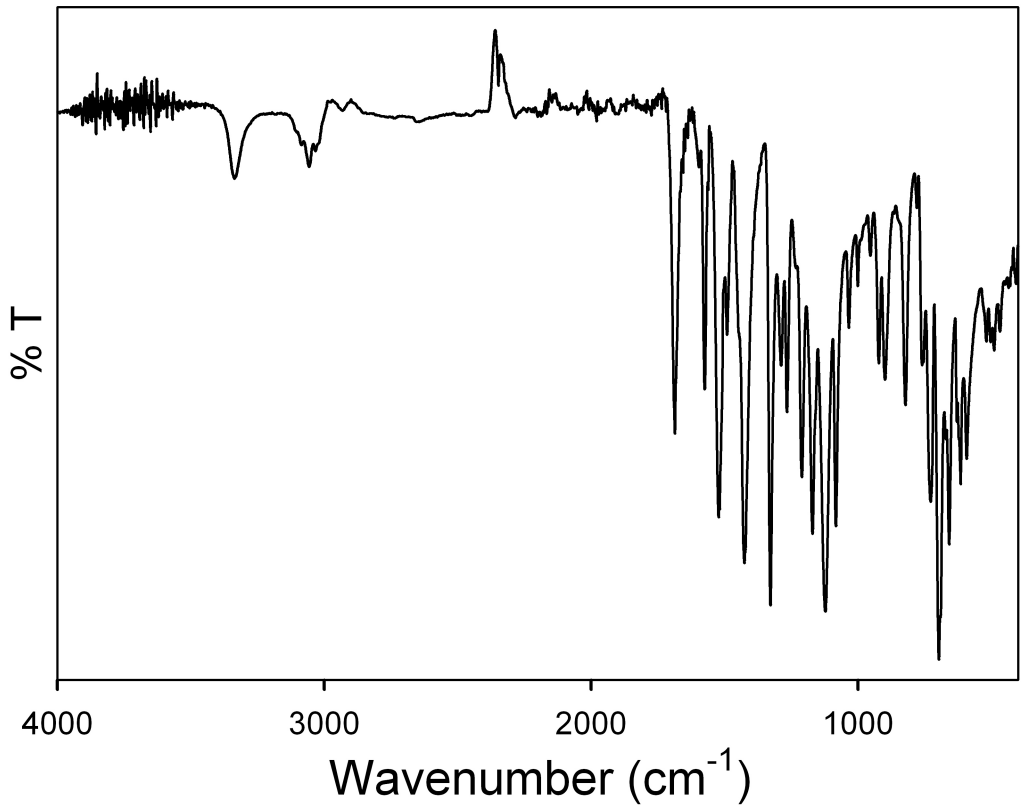

Figure A.8. Solid-state FTIR spectrum of S-trityl L:Ar-CF_3 in a KBr matrix.

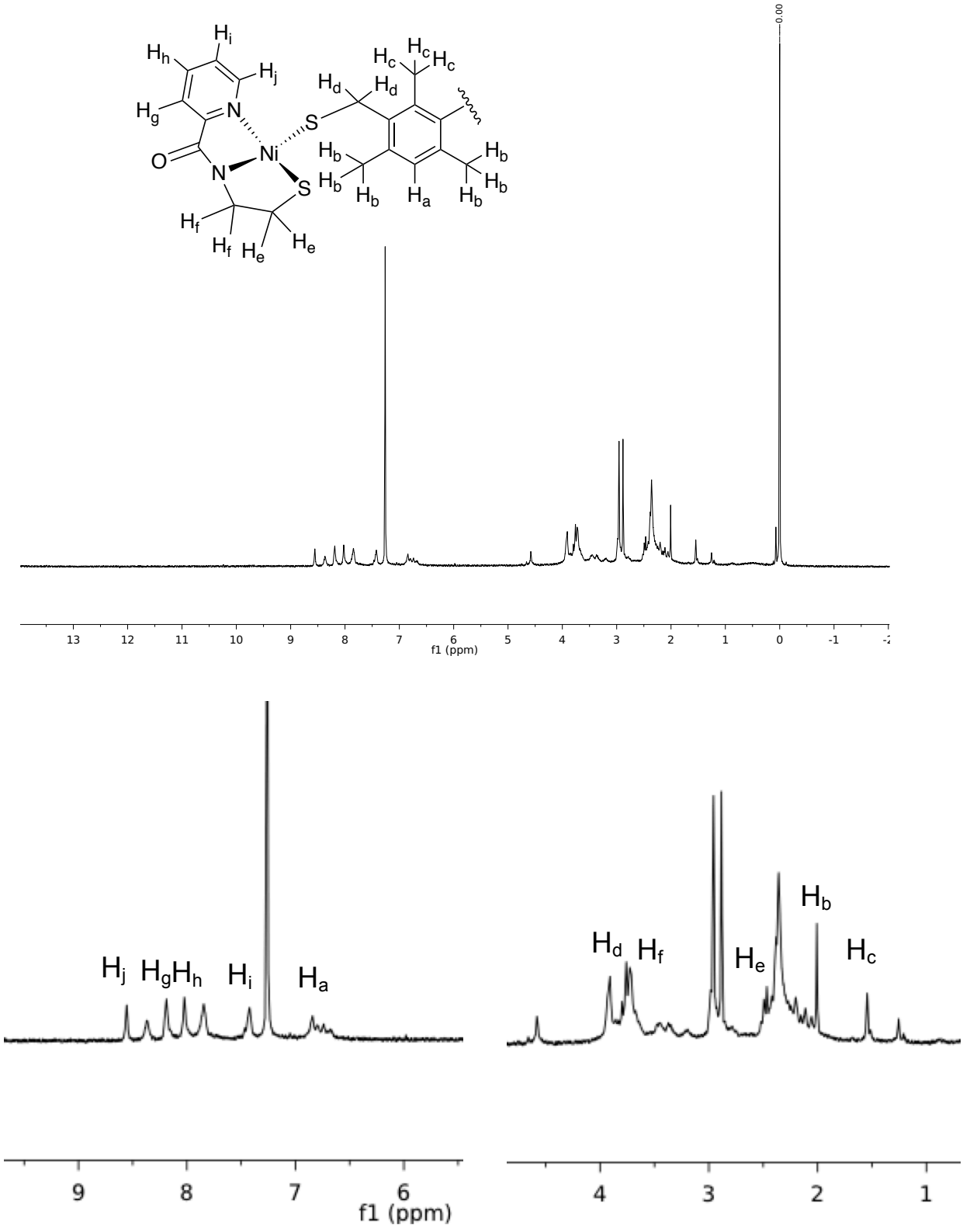

Figure A.9. 500 MHz ^{1}H NMR spectrum of **Na_2[(Ni(nmp))$_2$(DT)]** in $CDCl_3$ at RT.

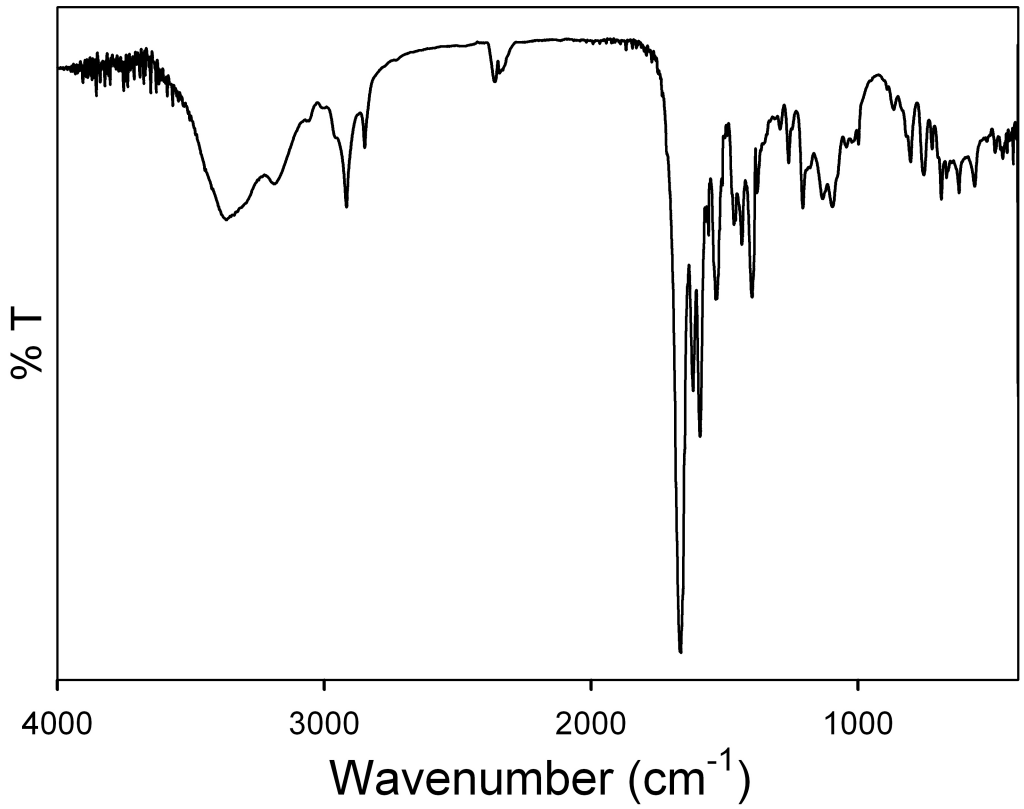

Figure A.10 Solid-state FTIR spectrum of **$Na_2[(Ni(nmp))_2(DT)]$** in a KBr matrix.

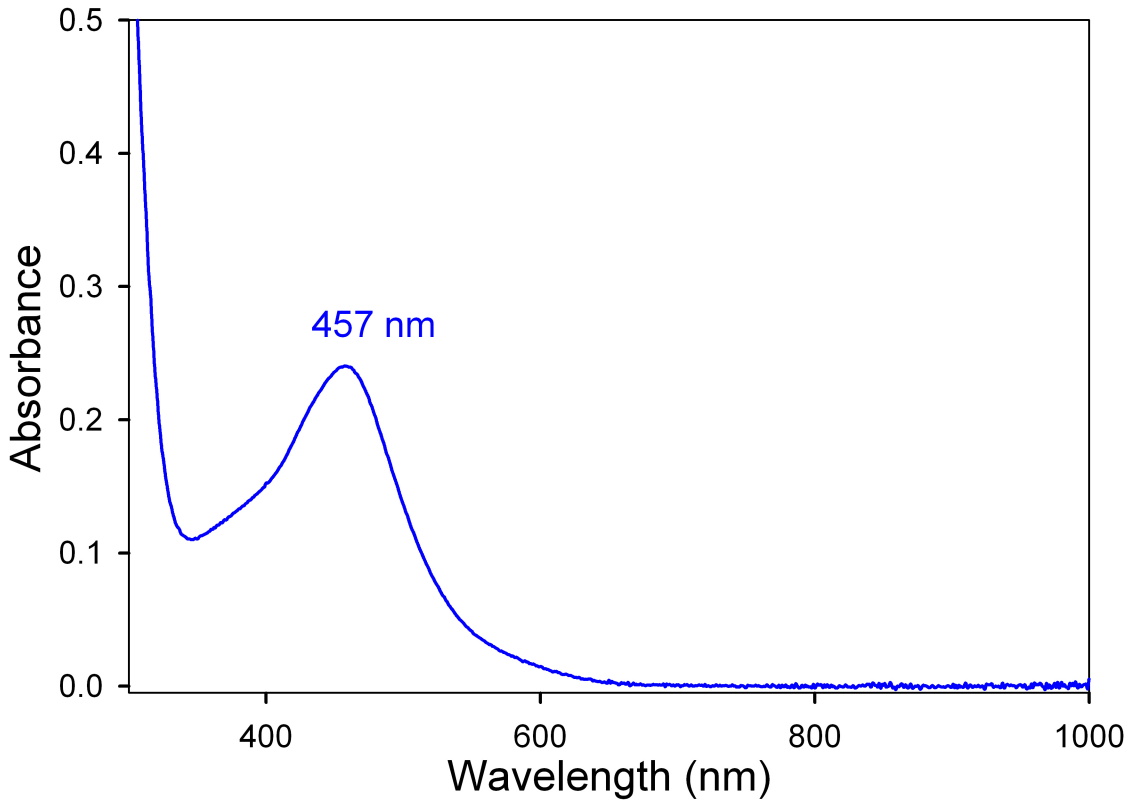

Figure A.11 Qualitative UV-vis spectrum of **Na_2[(Ni(nmp))$_2$(DT)]** in MeCN.

A.6 References

(1) Gale, E. M.; Narendrapurapu, B. S.; Simmonett, A. C.; Schaefer, H. F., III; Harrop, T. C., Exploring the Effects of H-Bonding in Synthetic Analogues of Nickel Superoxide Dismutase (Ni-SOD): Experimental and Theoretical Implications for Protection of the Ni-SCys Bond. *Inorg. Chem.* **2010**, *49*, 7080-7096.

(2) De Leo, M. E.; Borrello, S.; Passantino, M.; Palazzotti, B.; Mordente, A.; Daniele, A.; Filippini, V.; Galeotti, T.; Masullo, C., Oxidative stress and overexpression of manganese superoxide dismutase in patients with Alzheimer's disease. *Neurosci. Lett.* **1998**, *250*, 173-176.

(3) Broering, E. P.; Truong, P. T.; Gale, E. M.; Harrop, T. C., Synthetic Analogues of Nickel Superoxide Dismutase: A New Role for Nickel in Biology. *Biochemistry* **2013**, *52*, 4-18.

(4) Gale, E. M.; Simmonett, A. C.; Telser, J.; Schaefer, H. F., III; Harrop, T. C., Toward Functional Ni-SOD Biomimetics: Achieving a Structural/Electronic Correlation with Redox Dynamics. *Inorg. Chem.* **2011**, *50*, 9216-9218.

(5) Gale, E. M.; Patra, A. K.; Harrop, T. C., Versatile Methodology Toward NiN_2S_2 Complexes as Nickel Superoxide Dismutase Models: Structure and Proton Affinity. *Inorg. Chem.* **2009**, *48*, 5620-5622.

(6) Cantekin, S.; de Greef, T. F. A.; Palmans, A. R. A., Benzene-1,3,5-tricarboxamide: a versatile ordering moiety for supramolecular chemistry. *Chem. Soc. Rev.* **2012**, *41*, 6125-6137.

(7) Lightfoot, M. P.; Mair, F. S.; Pritchard, R. G.; Warren, J. E., New supramolecular packing motifs: π-stacked rods encased in triply-helical hydrogen bonded amide strands. *Chem. Commun.*, **1999**, 1945-1946.

(8) Timme, A.; Kress, R.; Albuquerque, R. Q.; Schmidt, H. W., Phase Behavior and Mesophase Structures of 1,3,5-Benzene- and 1,3,5-Cyclohexanetricarboxamides: Towards an Understanding of the Losing Order at the Transition into the Isotropic Phase. *Chem. Eur. J.* **2012**, *18*, 8329-8339.

(9) Jimenez, C. A.; Belmar, J. B.; Ortiz, L.; Hidalgo, P.; Fabelo, O.; Pasan, J.; Ruiz-Perez, C., Influence of the Aliphatic Wrapping in the Crystal Structure of Benzene Tricarboxamide Supramolecular Polymers. *Crystal Growth & Design* **2009**, *9*, 4987-4989.

(10) Palmans, A. R. A.; Vekemans, J. A. J. M.; Kooijman, H.; Spek, A. L.; Meijer, E. W., Hydrogen-bonded porous solid derived from trimesic amide. *Chem. Commun.* **1997**, 2247-2248.

(11) Stals, P. J. M.; Haveman, J. F.; Palmans, A. R. A.; Schenning, A. P. H. J., The Self-Assembly Properties of a Benzene-1,3,5-tricarboxamide Derivative. *J. Chem. Educ.* **2009**, *86*, 230-233.

(12) Howe, R. C. T.; Smalley, A. P.; Guttenplan, A. P. M.; Doggett, M. W. R.; Eddleston, M. D.; Tan, J. C.; Lloyd, G. O., A family of simple benzene 1,3,5-tricarboxamide (BTA) aromatic carboxylic acid hydrogels. *Chem. Commun.* **2013**, *49*, 4268-4270.

(13) Friggeri, A.; van der Pol, C.; van Bommel, K. J. C.; Heeres, A.; Stuart, M. C. A.; Feringa, B. L.; van Esch, J., Cyclohexane-Based Low Molecular Weight Hydrogelators: A Chirality Investigation. *Chem. –Eur. J.* **2005**, *11*, 5353-5361.

(14) Moure, A.; Luis, S. V.; Alfonso, I., Efficient Synthesis of Pseudopeptidic Molecular Cages. *Chem. Eur. J.* **2012**, *18*, 5496-5500.

(15) Moon, D.; Kang, S.; Park, J.; Lee, K.; John, R. P.; Won, H.; Seong, G. H.; Kim, Y. S.; Kim, G. H.; Rhee, H.; Lah, M. S., Face-driven corner-linked octahedral nanocages: M6L8 cages formed by C-3-symmetric triangular facial ligands linked via C-4-symmetric square tetratopic Pd-II ions at truncated octahedron corners. *J. Am. Chem. Soc.* **2006**, *128*, 3530-3531.

(16) Park, J.; Hong, S.; Moon, D.; Park, M.; Lee, K.; Kang, S.; Zou, Y.; John, R. P.; Kim, G. H.; Lah, M. S., Porous metal-organic frameworks based on metal-organic polyhedra with nanosized cavities as supramolecular building blocks: Two-fold interpenetrating primitive cubic networks of [CU6L8](12+) nanocages. *Inorg. Chem.* **2007**, *46*, 10208-10213.

(17) dos Santos, C. M. G.; Boyle, E. M.; De Solis, S.; Kruger, P. E.; Gunnlaugsson, T., Selective and tuneable recognition of anions using C-3v-symmetrical tripodal urea-amide receptor platforms. *Chem. Commun.* **2011**, *47*, 12176-12178.

(18) Helm, M. L.; Stewart, M. P.; Bullock, R. M.; DuBois, M. R.; DuBois, D. L., A Synthetic Nickel Electrocatalyst with a Turnover Frequency Above 100,000 s(-1) for H-2 Production. *Science* **2011**, *333*, 863-866.

(19) Ryan, K. C.; Guce, A. I.; Johnson, O. E.; Brunold, T. C.; Cabelli, D. E.; Garman, S. C.; Maroney, M. J., Nickel Superoxide Dismutase: Structural and Functional Roles of His1 and Its H-Bonding Network. *Biochemistry* **2015**, *54*, 1016-1027.

(20) Lippert, A. R.; De Bittner, G. C. V.; Chang, C. J., Boronate Oxidation as a Bioorthogonal Reaction Approach for Studying the Chemistry of Hydrogen Peroxide in Living Systems. *Acc. Chem. Res.* **2011**, *44*, 793-804.

(21) Dickinson, B. C.; Huynh, C.; Chang, C. J., A Palette of Fluorescent Probes with Varying Emission Colors for Imaging Hydrogen Peroxide Signaling in Living Cells. *J. Am. Chem. Soc.* **2010**, *132*, 5906-5915.

(22) Dodani, S. C.; He, Q.; Chang, C. J., A Turn-On Fluorescent Sensor for Detecting Nickel in Living Cells. *J. Am. Chem. Soc.* **2009**, *131*, 18020–18021.

(23) Miller, E. W.; Albers, A. E.; Pralle, A.; Isacoff, E. Y.; Chang, C. J., Boronate-based fluorescent probes for imaging cellular hydrogen peroxide. *J. Am. Chem. Soc.* **2005**, *127*, 16652-16659.

APPENDIX B

MODELING THIOLATO-NI COORDINATION IN BIOLOGY VIA NI-N3S2 AND NI-S4 SPECIES

B.1 Introduction

B.1.1. Modeling Thiolato-Ni Coordination in Biology via Ni-N_3S_2 and Ni-S_4 Species

Sulfur ligation from cysteine sulfur (SCys) and iron-sulfur (Fe-S) clusters is ubiquitous with redox-active Ni in nature and includes the enzymes: Ni superoxide dismutase (NiSOD), NiFe hydrogenase (NiFe-H_2ase), CO dehydrogenase (CODH), acetyl-CoA synthase (ACS), and methyl-CoM reductatase (MCR), all of which are involved in the consumption and production of gases involved in the global carbon, nitrogen and oxygen cycles. This group of catalytic active sites are capable of performing redox chemistry over a potential range of ~1.5 V and are able to cycle through three redox states (+1, +2, +3). Their coordination geometries range from mononuclear Ni centers, such as NiSOD – that disproportionate superoxide ($O_2^{\cdot -}$) into hydrogen peroxide (H_2O_2) and oxygen (O_2) – to complex metal clusters such as NiFe-H_2ase – that catalyze the reversible two electron reduction of protons to hydrogen (H_2). This work focuses on constructing small molecule metal-sulfur complexes to probe the structure/function relationships that promote catalytic activity and oxidative stability in these systems. Specifically, we present the syntheses and characterization of small molecule analogues of redox-active Ni enzymes: (i) a planar five coordinate N_3S_2 complex modeling the oxidized state of NiSOD by incorporating a

planar pyridine donor to access a high valent Ni oxidation state, of which there is a paucity of isolated Ni(III)-thiolate species in the literature; and (ii) a tetrathiolate Ni complex with carboxamide moieties poised to engage in intramolecular hydrogen-bonds (H-bonds) between the carboxamide N-H and Ni-coordinated thiolate, which models the tetrathiolate moiety found in NiFe-H_2ase. Indeed, these small molecule analogues provide an opportunity to understand the redox requirements for Ni-S units in biology. Here, we present the synthesis of the ligand N^2,N^6-bis(2-mercaptoethyl)pyridine-2,6-dicarboxamide to be utilized to form a tetrathiolato Ni species and a mononuclear planar 5 coordinate species.

B.2 Results and Discussion

B.2.1 Synthesis of N^2,N^6-bis(2-mercaptoethyl)pyridine-2,6-dicarboxamide

The S-trityl protected N^2,N^6-bis(2(tritylthio)ethyl)pyridine-2,6-dicarboxamide ligand was synthesized via reaction of pyridine dicarbonyl dichloride with two equiv of S-trityl cysteamine in the presence of excess Et_3N and was obtained via 71% yield. The ligand was deprotected after dissolving in 1:1 TFA:CH_2Cl_2 and adding Et_3SiH with 54% yield (Scheme B.1). Spectroscopic properties were comparible to those reported by Jurczak, J. et al.[1]

Scheme B.1 Deprotection of N^2,N^6-bis(2(tritylthio)ethyl)pyridine-2,6-dicarboxamide.

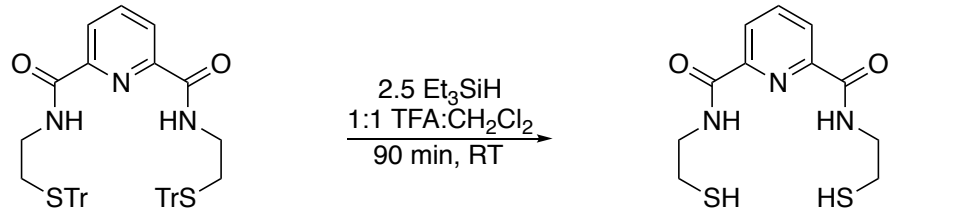

N^2,N^6-bis(2(tritylthio)ethyl) pyridine-2,6-dicarboxamide

N^2,N^6-bis(2-mercaptoethyl) pyridine-2,6-dicarboxamide

B.2.2 Synthesis of Metal Complexes

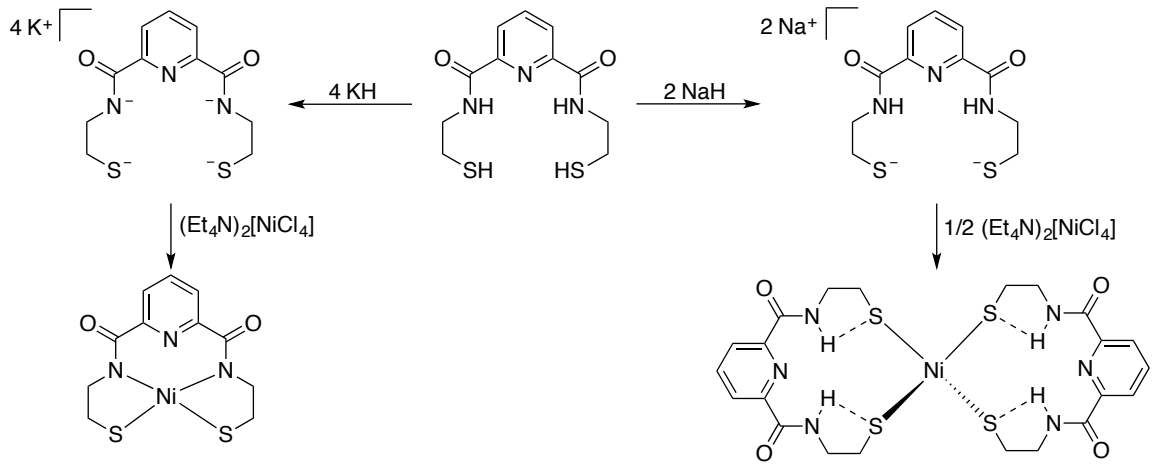

Scheme B.2. Synthesis of 1:1 and 2:1 ligand-metal complexes.

Synthesis of the tetrathiolate Ni^{II} species (Scheme B.2) was attempted by deprotonating 2 equiv of N^2,N^6-bis(2-mercaptoethyl)pyridine-2,6-dicarboxamide with 4 equiv of NaH, so as to deprotonate the 4 thiol protons and not the carboxamide protons. A batch of 0.1076 g (0.3770 mmol) of bis(2-mercaptoethyl)pyridine-2,6-dicarboxamide was dissolved in ~5 mL MeCN to form a pale yellow homogenous solution and 0.0180 g (0.754 mmol) of NaH was added as a slurry in ~5 mL MeCN and was placed under vacuum for ~20 min to aid in removing H_2(g) and the solution became a beige slurry. A batch of 0.0866 g (0.189 mmol) of $(Et_2N)_2NiCl_4$ was added as a bright blue solid and the solution immediately turned a heterogenous brown and then red-brown precipitate and was allowed to stir for ~2 h. The solution was filtered through a medium porosity glass frit and the MeCN soluble portion was characterized by a qualitative UV-vis (MeCN) which revealed two λ_{max} = 333.7 and 422.2 nm, while the MeCN insoluble portion was characterized by FTIR (KBr) with ν_{NH} = 3368 (br m); $\nu_{C=O}$ = 1655 (s). The MeCN soluble portion was filtered through a nylon frit and Et_2O diffusion into MeCN (unsuccessful) crystallizations. The MeCN insoluble portion was insoluble in CH_2Cl_2, THF, and partially

soluble in MeOH and DMF, therefore, the solid was dissolved in ~10 mL MeOH and allowed to stir for ~48 h before filtering through a medium porosity glass frit. An FTIR (KBr) spectrum was taken of the MeOH insoluble solid (15.7 mg), but no $\nu_{C=O}$ was observed. The MeOH soluble portion was dried *in vacuo* and ~10 mL THF was added and let stir overnight until free-floating solids were formed. The solution was filtered through a medium porosity glass frit and washed with ~5 mL Et_2O and dried to yield a ruby red solid (82.3 mg) that was characterized by UV-vis(MeOH) with a λ_{max} = 392 nm, FTIR (KBr) with ν_{NH} = 3306 (br m); $\nu_{C=O}$ = 1666, 1584 (s), ^{1}H NMR(CD_3OD) with many peaks indicating a break in symmetry of the symmetrical ligand (Figure B.1) and ESI-MS(MeOH) with revealed Ni coordinated in a 1:1 ratio with the ligand experimental: $[NiL\text{-}2(Et_2N^+)+H^+]^-$ = 339.9; theoretical: $[C_{11}H_{12}O_2N_3S_2Ni]^-$ = 340.0 (Figure B.2). These results suggest that tetrathiolate coordination of Ni^{II} was unsuccessful by this preparation.

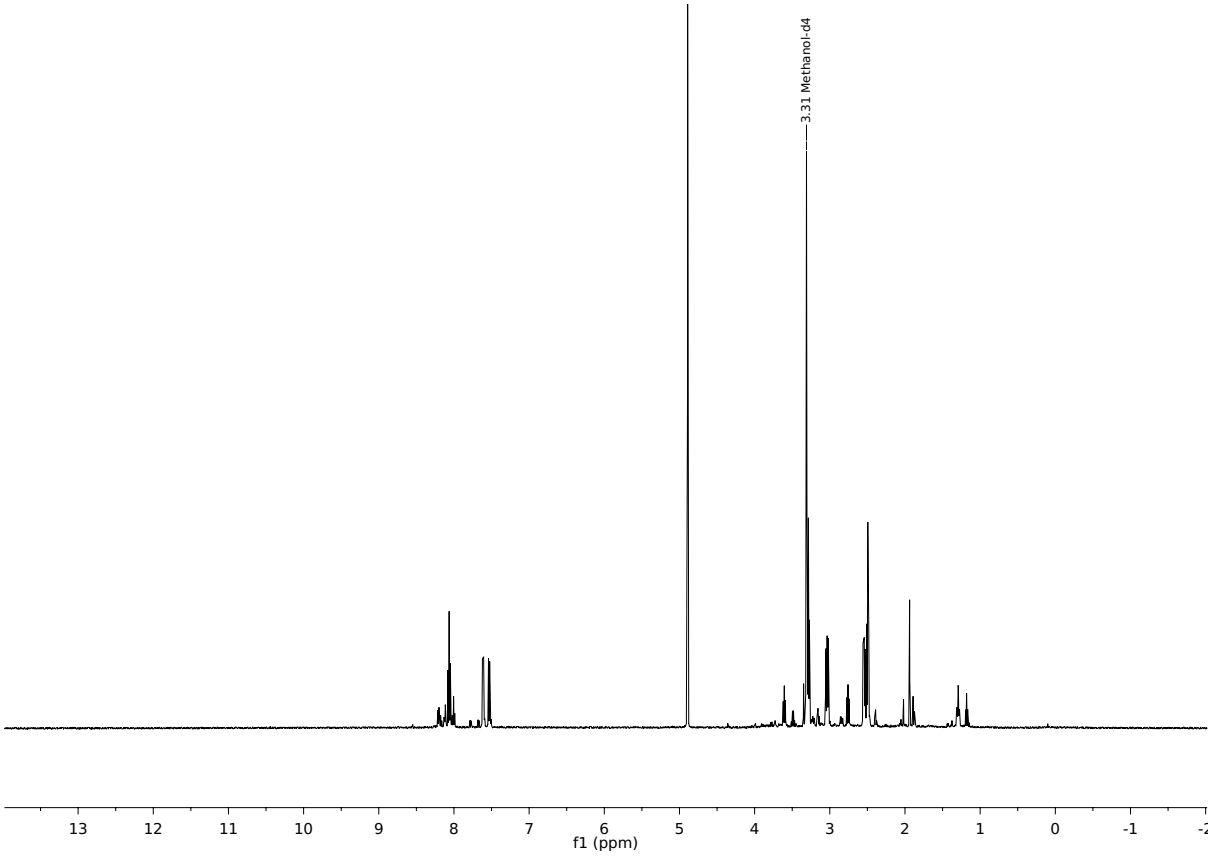

Figure B.1 500 MHz ^{1}H NMR in CD_3OD at RT of synthesis of the tetrathiolate Ni^{II} species.

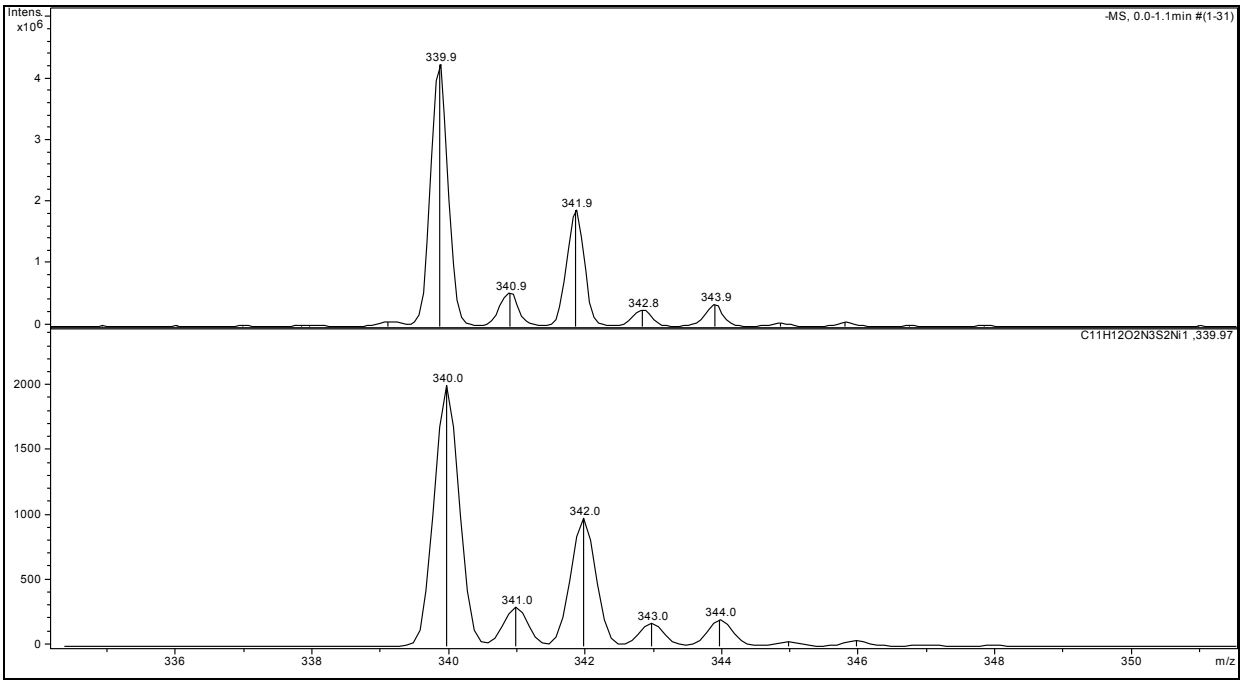

Figure B.2 ESI-MS of synthesis of the tetrathiolate Ni^{II} species.

Synthesis of the N_3S_2 Ni^{II} species (Scheme B.2) was attempted by deprotonating 1 equiv of *N*^{2},*N*^{6}-bis(2-mercaptoethyl)pyridine-2,6-dicarboxamide with 4 equiv of KH, so as to deprotonate the 2 thiol protons and the 2 carboxamide protons. A batch of 0.1155 g (0.4047 mmol) *N*^{2},*N*^{6}-bis(2-mercaptoethyl)pyridine-2,6-dicarboxamide was dissolved in ~5 mL MeCN to form a homogenous, pale yellow solution and 0.0650 g (1.62 mmol) KH was added as a slurry with ~2 mL MeCN. The solution was placed under vacuum for 20 min to aid in removing H_2(g) and became heterogeneous yellow. A batch of $(Et_2N)_2NiCl_4$ was added as a bright blue solid and the solution turned a heterogenous dark maroon-red and was allowed to stir for ~2 h. A qualitative UV-vis(MeCN) revealed λ_{max} = 390 nm. The solution was filtered through a medium porosity frit and the MeCN soluble portion was set up for (unsuccessful) Et_2O diffusion into MeCN crystallizations. The MeCN insoluble portion was dried as a brown-beige solid (0.1270 g)

and characterized by FTIR (KBr) to reveal ν_{NH} = 3336 (br m); $\nu_{C=O}$ = 1667 (s), 1621 (s), 1599 (s). Reconstitution of the MeCN soluble cystallization resulted in a sticky residue that 'gummed-up' even after precipitation and stirring in THF or Et_2O. Another synthesis was attempted where ligand was added to a solution of metal to ensure that Ni^{II} was always in excess. A batch of 0.0880 g (0.308 mmol) N^2,N^6-bis(2-mercaptoethyl)pyridine-2,6-dicarboxamide was deprotonated in ~8 mL MeCN with 0.0552 g (1.38 mmol) KH and stirred under vacuum for ~20 min. A batch of 0.1430 g (0.310 mmol) $(Et_2N)_2NiCl_4$ was dissolved in ~4 mL MeCN and the deprotonated ligand was added pipet-wise and allowed to stir for 40 min. The solution was filtered through a medium porosity glass frit and isolated 0.1020 g MeCN insoluble solid and a MeCN soluble dark oil (0.2366 g) after removing MeCN *in vacuo*. A qualitative UV-vis(MeCN) of the MeCN soluble revealed l_{max} = 399 nm and ESI-MS (MeCN) characterization revealed Ni coordinated in a 1:1 ratio with the ligand experimental: $[NiL\text{-}2(Et_2N^+)+H^+]^-$ = 339.9; theoretical: $[C_{11}H_{12}O_2N_3S_2Ni]^-$ = 340.0 (Figure B.3). Qualitative oxidation experiments were carried out with Fc+ and ceric ammonium nitrate (CAN) that resulted in rapid bleaching of the λ_{max} = 399 nm feature. A CV experiment was also carried out with 0.005 M NiN_3S_2 in 0.10 M Bu_4NPF_6 in MeCN, which resulted in irreversible oxidation ~130 mV when scanned from –750 mV toward positive potential. Perhaps a larger solvent window is necessary to see the $Ni^{III/II}$ couple.

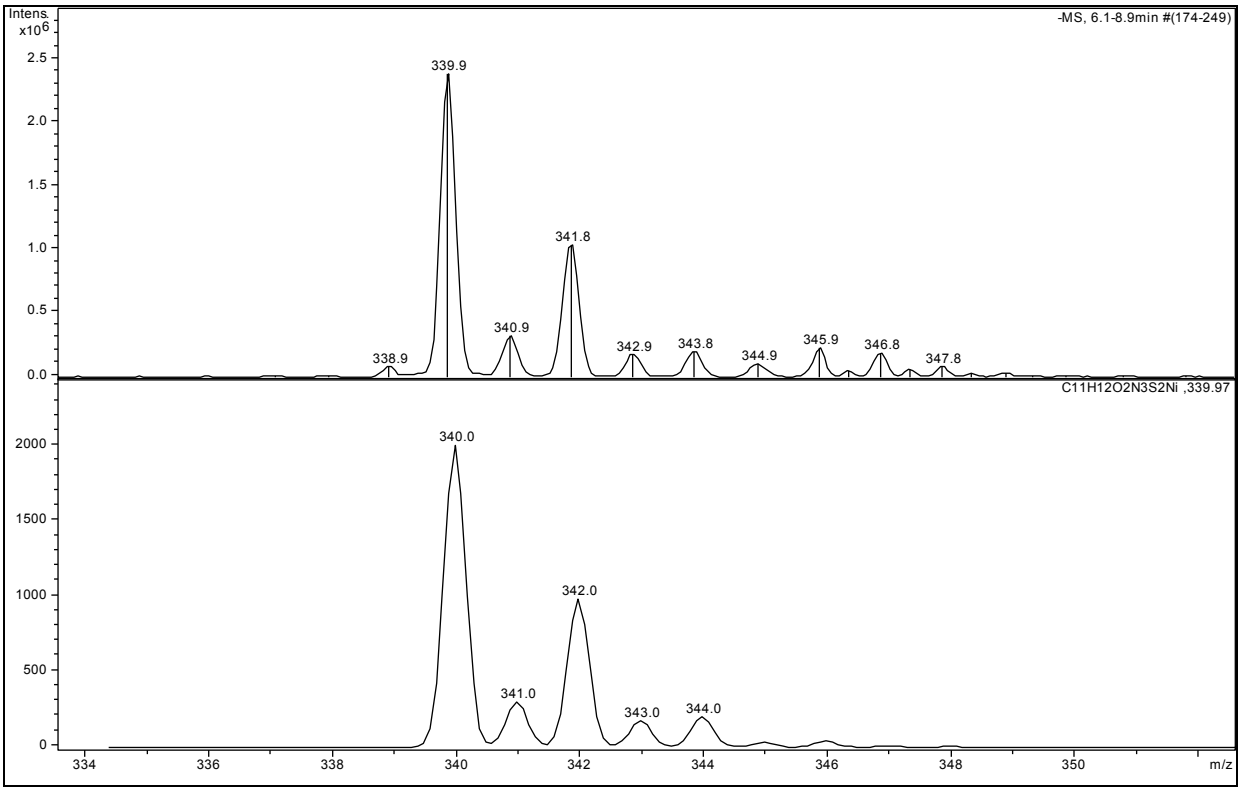

Figure B.3 LR-ESI-MS of synthesis of the N_3S_2 Ni^{II} species

B.3 Conclusions

In summary, the *N*^{2},*N*^{6}-bis(2-mercaptoethyl)pyridine-2,6-dicarboxamide ligand has been successfully synthesized and matches spectroscopic properties reported by Jurczak, J. et al.[1] Preliminary metalation attempts have been made that manipulate stoichiometry in order to promote coordination of either a tetrathiolato species or a mononuclear planar five coordinate species, respectively. Characterization of these reactions has indicated that the monometallic complex is favored over a tetrathiolato species, based on ESI-MS. Tuning the deprotonation conditions in order to promote thiol deprotonation, but not carboxamide deprotonation will ensure thiolate coordination over carboxamide-N binding to Ni.

B.4 Experimental

General Information. See Chapter 3. Synthesis of N^2,N^6-bis(2(tritylthio)ethyl)pyridine-2,6-dicarboxamide and N^2,N^6-bis(2-mercaptoethyl)pyridine-2,6-dicarboxamide were modified from reported preparation by Jurczak, J. et al.[1] ^{1}H NMR spectroscopy matched reported chemical shifts.

Physical Methods. See Chapter 3.

Synthesis of N^2,N^6-bis(2(tritylthio)ethyl)pyridine-2,6-dicarboxamide. A batch of pyridine-2,6-dicarboxylic acid was dissolved in ~10 mL $SOCl_2$ and refluxed for 5 h until the solution was a homogeneous pale yellow color and the acid chloride was formed. $SOCl_2$ was removed *in vacuo* and triturated with CH_2Cl_2 (3 × 5 mL) to yield a white solid, which was dissolved in CH_2Cl_2 (~10 mL) to form a yellow solution. To this solution was then added a 10 mL solution of CH_2Cl_2 containing 3.6495 g (11.423 mmol) of S-trityl cysteamine and 7.947 mL (52.12 mmol) of Et_3N, which was allowed to stir for 12 h under N_2(g). The solution was taken up in ~100 mL CH_2Cl_2 and washed with D.I. H_2O, sat $NaHCO_3$ (aq), dried over $MgSO_4$, filtered and concentrated to yield a pale yellow solid. To remove $Et_3N{\cdot}HCl$, the solid was dissolved in ~10 mL THF and allowed to stir for 2 h and filtered. The filtrate was concentrated to yield a 3.1183 g (4.0510 mmol) pale yellow solid (71%).

Synthesis of N^2,N^6-bis(2-mercaptoethyl)pyridine-2,6-dicarboxamide. A batch of N^2,N^6-bis(2(tritylthio)ethyl)py ridine-2,6-dicarboxamide (3.1183 g, 4.0510 mmol) was dissolved in ~40 mL of 1:1 TFA:CH_2Cl_2 to form a bright yellow solution. Et_3SiH (1.940 mL, 12.149 mmol) was added to the solution causing a color change from bright red to pale yellow and was allowed to stir for 90 min. The solution was concentrated and washed with ~50 mL pentanes in ~5 mL aliquots to remove $HCPh_3$. The oil was dissolved in ~10 mL CH_2Cl_2 and 10 % w/v

$NaHCO_3$ was added and allowed to stir for 20 min, and then filtered through a medium porosity frit and celite to yield 0.6283 g (2.201 mmol) of a yellow oil (54%).

B.5 References

(1) Ulatowski, F.; Sadowska-Kuziola, A.; Jurczak, J., "Choose-a-Size" Approach in Dynamic Combinatorial Chemistry: A Single Substrate Dynamic Combinatorial Library of Oligomacrocycles That Adapts to the Size and Shape of Carboxylates. *J. Org. Chem.* **2014**, *79*, 9762-9770.